EARTHQUAKE BEHAVIOR OF GEOSYNTHETIC-REINFORCED RETAINING STRUCTURES

by
Öznur Selek
B.S., Civil Engineering, Boğaziçi University, 1999
M.S., Civil Engineering, Boğaziçi University, 2002

Submitted to the Institute for Graduate Studies in
Science and Engineering in partial fulfillment of
the requirements for the degree of
Doctor of Philosophy

Graduate Program in Civil Engineering
Boğaziçi University
2011

ACKNOWLEDGEMENTS

I am grateful to my thesis advisor, Prof. Erol Güler for his guidance and support throughout this study. I would like to thank Oktay Çırağ from KOERI shaking table laboratory and Tahir Erdem Öztürk from Boğaziçi University for their help in testing. I owe thanks to my family for their continuous support and motivation.

The shaking table laboratory testing in this study was carried out with the support of Boğaziçi University Scientific Research Project BAP03A404 and TÜBİTAK Scientific Research Project MAG-103I005.

ABSTRACT

EARTHQUAKE BEHAVIOR OF GEOSYNTHETIC-REINFORCED RETAINING STRUCTURES

Geosynthetic-reinforced soil walls have so far shown a very good performance during earthquakes. Nevertheless, additional tests like reduced-scale shaking table testing can be useful in understanding the effects of various parameters.

Eight different reduced-scale models were tested using the shaking table facility at the Kandilli Observatory and Earthquake Research Institute (KOERI) of Boğaziçi University in the scope of this study. A woven geotextile was used as reinforcement and concrete blocks were used as wall facing. Four tests were conducted using 1:2 scale models of two meters height, one test involved a 1:4 scale model with 1 meter height, and the remaining three models were 1:4 scale two meters high walls. The models were instrumented with eight optical laser distance sensors to measure face displacement, ten accelerometers to measure accelerations on face and top of wall, and eight special transducers to measure the strain in geotextiles. The effects of peak ground acceleration, reinforcement length and spacing, model scale, and treatment of top two rows of facing blocks on amplification of acceleration, maximum displacements during shaking, permanent displacements and geotextile stresses were investigated.

Maximum accelerations observed during shaking on the wall face increased from bottom to top and increased linearly with increasing table acceleration. Geotextile length and spacing did not affect the amplification factors for acceleration and affected maximum face displacements during shaking only slightly as long as the geotextile length was meeting the minimum requirements of FHWA design procedure for seismic loading. No noteworthy permanent displacements were observed. Measured geotextile stresses were higher than the design values calculated and the difference was more pronounced in walls with short reinforcements. It is concluded that for the tested type of geosynthetic-

reinforced soil wall with purely frictional reinforcement-block connection, determining the length and spacing of reinforcement using the pseudo-static design approach suggested by FHWA provides satisfactory performance during seismic loading, but geotextile stresses higher than those calculated in design may be encountered.

ÖZET

GEOSENTETİK DONATILI İSTİNAT DUVARLARININ DEPREM YÜKLERİ ALTINDAKİ DAVRANIŞI

Geosentetik donatılı istinat duvarları, deprem yükleri altında son derece iyi davranış göstermektedir. Ancak sarsma masası deneyleri gibi çalışmalar farklı parametrelerin etkilerini değerlendirmek açısından faydalıdır.

Bu çalışma kapsamında, Boğaziçi Üniversitesi Kandilli Rasathanesi ve Deprem Araştırma Enstitüsü'ndeki sarsma masasında sekiz adet küçük ölçekli model üzerinde deney yapılmıştır. Donatı olarak dokunmuş bir geotekstil ve duvar ön yüzünde beton bloklar kullanılmıştır. Deneylerin dördü, 1:2 ölçekli iki metre yüksekliğinde model üzerinde, biri 1:4 ölçekli bir metre yüksekliğinde model üzerinde, geriye kalan üçü ise 1:4 ölçekli iki metre yüksekliğinde model üzerinde yapılmıştır. Modellerde ön yüz deplasmanları sekiz adet optik lazer mesafe ölçüm sensörü ile, ön yüz ve üst yüzey ivmeleri on adet ivmeölçer ile, geotekstildeki gerilmeler ise sekiz adet özel ölçüm cihazıyla ölçülmüştür. Deprem ivmesi, donatı boyu ve aralığı, model ölçeği ve üst iki sıra beton bloğun sabitlenme durumunun ivme büyütmesi, sarsıntı sırasındaki maksimum deplasman, kalıcı deplasmanlar ve geotekstil gerilmeleri üzerindeki etkisi araştırılmıştır.

Ön yüzde sarsıntı sırasında gözlenen maksimum ivmeler duvar boyunca aşağıdan yukarı doğru artmıştır ve masa ivmesinin artışıyla doğrusal olarak artmıştır. FHWA tasarım prosedürünün minimum gereklerini yerine getiren geotekstil uzunluğu ve aralığı ivme büyütme faktörlerini etkilememiş, sarsıntı sırasındaki maksimum ön yüz deplasmanlarını ise çok az etkilemiştir. Kaydadeğer kalıcı deplasman saptanmamıştır. Ölçülen geotekstil gerilmeleri tasarım prosedürleriyle hesaplanana göre yüksek olmuş ve fark daha kısa donatı kullanıldığı durumlarda artmıştır. Çalışmada test edilen, tamamen sürtünme ile çalışan donatı-blok bağlantısı olan geosentetik donatılı istinat duvarı için, FHWA'nın önerdiği eşdeğer deprem yükleriyle tasarım yaklaşımı ile belirlenen donatı boy

ve aralığının, deprem yükleri altındaki performans açısından yeterli olacağı, ancak tasarımda hesaplanandan daha yüksek geotekstil gerilmeleriyle karşılaşılabileceği sonucuna varılmıştır.

TABLE OF CONTENTS

LIST OF FIGURES

LIST OF TABLES

LIST OF SYMBOLS / ABBREVIATIONS

A	Maximum ground acceleration coefficient
A_m	Maximum horizontal acceleration coefficient in the reinforced soil wall
C	Reinforcement effective unit parameter
C_c	Coefficient of curvature
C_u	Coefficient of uniformity
e	Eccentricity
E	Modulus of Elasticity
F^*	Pullout resistance factor
F_T	Total force applied by the retained fill on the back of the reinforced zone
FS_{PO}	Factor of safety against pullout
$\mathrm{FS}_{\mathrm{sliding}}$	Factor of safety against sliding
H	Wall height
h	Height from base at the back of reinforced zone
K_a	Active coefficient of earth pressure
K_{AE}	Total seismic earth pressure coefficient
K_{ar}	Earth pressure coefficient calculated for reinforced zone
k_c	Critical acceleration
k_h	Horizontal seismic coefficient
k_v	Vertical seismic coefficient
L	Reinforcement length
L_a	Length of reinforcement in front of the critical surface
L_e	Length of embedment in the resisting zone
M	Mass
n	Porosity
$\mathrm{P_A}$	Active static earth pressure resultant force
P_{AE}	Total dynamic active earth force
P_d	Driving force
P_I	Inertia force acting on the active zone
P_{IR}	Inertia force
P_R	Resisting force

R_c	Coverage ratio
q_{ult}	Ultimate bearing capacity
s_v	Reinforcement spacing
t	Time
T_a	Allowable tensile force per unit width of reinforcement.
T_{max}	Maximum tension force per unit width of wall
u	Displacement
$\dot{u}$	Velocity
$\ddot{u}$	Acceleration
V_1	Weight of reinforced soil mass
V_2	Weight of sloped zone over reinforced soil mass
x	Length
W_a	Weight of active zone
W_R	Weight of reinforced zone
Z	Depth
α	Scale correction factor
α_{AE}	Inclination of failure surface from horizontal under seismic loading
β	Angle of backfill slope
γ	Unit weight
γ_f	Unit weight of retained fill
δ	Angle of wall friction
ε	Strain
ε_{ult}	Ultimate strain
θ	Face inclination from horizontal
λ	Scaling factor for length
λ_ε	Scaling factor for strain
λ_ρ	Scaling factor for density
μ	Coefficient of friction
ρ	Soil-reinforcement friction angle
ρ_s	Density of soil
σ	Stress
σ_1	Axial stress

σ_3	Confining pressure
τ	Shear stress
σ_H	Horizontal stress
σ_v	Vertical stress
ξ	Seismic inertia angle
φ	Angle of internal friction
φ_f	Angle of internal friction of backfill soil
φ_r	Angle of internal friction of reinforced soil
ΔK_{dyn}	Incremental dynamic active earth pressure coefficient
ΔP_{dyn}	Incremental dynamic component of P_{AE}
$\Delta\sigma_h$	Increment of horizontal stress due to any horizontal concentrated surcharge

AASHTO	American Association of State Highway and Transportation Officials
FHWA	Federal Highway Administration
GRS wall	Geosynthetic Reinforced Soil retaining wall
KOERI	Kandilli Observatory and Earthquake Research Institute
NCMA	National Concrete Masonry Association

1. INTRODUCTION

1.1. General

Geosynthetic-reinforced soil walls (GRS walls) have been in use widely for approximately thirty years, so ample data regarding their performance during earthquakes have started to accumulate. The cost-effectiveness of these walls together with the affirmative records regarding seismic performance has resulted in an increasing rate of preference of these walls over conventional retaining structures. The increase is probably most evident in Japan, where the good seismic performance of GRS walls observed during the 1995 Hyogoken-Nanbu (Kobe) earthquake resulted in a sharp increase in the construction rate of these structures (Tamura, 2006).

The approach that is commonly used in the design of GRS walls to evaluate the seismic stability is a limit equilibrium approach. A destabilizing pseudo-static force is added to represent the effect of the earthquake and the wall is designed to satisfy the required factor of safety under the considered forces. This approach is not helpful in estimating the amount of displacement before failure occurs. Considering the nature of GRS walls, unacceptably large displacements may be observed before failure, so a performance-based design approach in which specified target performance values are met is necessary (Koseki *et al.*, 2006).

One tool available for estimating the earthquake-induced displacements in GRS walls is Newmark's sliding block analysis. As long as the earthquake loads are large enough to form a failure plane in the unreinforced backfill, this method may provide satisfactory results, but before the critical acceleration is exceeded and the failure planes are formed, shear deformations of the foundation and the reinforced backfill will be the prevailing critical component of the seismic response (Koseki *et al.*, 2006).

Testing using shaking tables is the most straightforward method to predict the seismic behavior of GRS walls. Mostly, reduced-scale modeling is preferred so that testing is feasible and information regarding higher walls can be achieved with the limited capacity of shaking table facilities, even though it is hard to define and fulfill scaling laws for GRS walls. These tests provide qualitative insights, and the results can be used to develop and validate numerical codes that will be used to predict the seismic response of the prototype (Koseki *et al.*, 2006).

In this study, a series of reduced-scale shaking table tests were conducted using the shaking table facility at the Kandilli Observatory and Earthquake Research Institute (KOERI) of Bogazici University. Numerous types of GRS walls are used throughout the world and the prevailing type of GRS walls differs in every country due to local requirements and conditions. This study is one of the first studies to test the seismic performance of the GRS wall used in Turkey, in which the facing is constructed using concrete blocks having no shear connections but relying on the interface friction with the geosynthetic.

In order to evaluate seismic performance, eight different setups were tested under El Centro earthquake loading applied at different amplitude scales. Enünlü (2007) evaluated the results for the test runs with full-scale earthquake loadings of the first two test configurations and compared the results with seismic analysis in Plaxis. This study considers all of the scaled earthquake loadings for all eight tests and evaluates the effects of change in peak ground acceleration, reinforcement length, reinforcement spacing, model scale, treatment of top two rows, and applied earthquake frequency on the accelerations on the wall face, maximum displacements of the wall face during shaking, permanent displacements, and stresses in reinforcement and compares the stresses in geotextile reinforcements with those recommended for design.

Information on the pseudo-static design procedures for GRS walls and studies using numerical techniques, and gravity shaking table tests are given in chapter two. Chapter three presents the test setup, starting with the similitude rules used and the shaking table facility employed. Then the materials used for the construction of GRS wall and the instruments utilized are introduced. Final wall arrangement is shown, features of individual test configurations are listed, and the applied earthquake record is given at the end of this chapter.

Chapter four presents and discusses the results, starting with the introduction of data acquisition and analysis procedures. Time records of face and top accelerations, face displacements, and geotextile stresses are given for test runs for the maximum table acceleration in each test. Then the effects of increasing maximum table acceleration, reinforcement length, reinforcement spacing, model scale, treatment of top two rows, and applied earthquake frequency on the accelerations on the wall face, maximum displacements of the wall face during shaking, permanent displacements, and stresses in reinforcement are discussed with the help of comparisons among relevant tests. Afterwards, measured stresses in geotextile reinforcements are compared with those recommended for design by Federal Highway Administration (FHWA) and the National Concrete Masonry Association (NCMA) and illustrations of possible failure planes are given. Observations on a test run with wall failure conclude the chapter.

Conclusions drawn from the study are given in the last chapter. Shaking table acceleration and displacement records and sample spreadsheet calculations used for calculation of design geotextile stresses are given in the appendices.

2. LITERATURE REVIEW

2.1. Geosynthetics

Geosynthetics may be defined as man-made (“synthetic”) materials used in geotechnical works (“geo”). They may be made of plastics, rubber, fiberglass or other materials. Geosynthetics may be grouped into four, according to their structure and technical properties.

Geotextiles form the first group. These are permeable fabrics made of various types of synthetic fibers. Geotextiles may be further grouped according to the manufacturing method as woven, non-woven, and knit geotextiles. Geotextiles are porous to water flow both across their plane and within their plane. They are mainly used for reinforcement, separation, filtration, and drainage in geotechnical applications.

Geogrids, which form the second group of geosynthetics, are geosynthetics formed into an open netlike configuration by stretching uniaxially or biaxially under controlled conditions. They are mainly produced from polypropylene or high-density polyethylene. The stretching process increases the strength and reduces creep sensitivity. Therefore geogrids are mainly used for reinforcement purposes.

The third and fourth groups consist of geomembranes and geocomposites, respectively. Geomembranes are impermeable membranes used as barriers or liners in geotechnical applications. Geocomposites are composites made from two or more geosynthetic materials from the first three groups. They are used for meeting various specific requirements.

2.2. Historical Development of Geosynthetic-Reinforced Soil Walls

The concept of reinforcing soils with other materials has been in existence since ancient history, and various techniques of reinforcement of poor soils by using metal strips or fabrics are in development since 1920s. The patented Reinforced Earth system, which consists of a cover on front face, reinforcing metal strips and granular backfill, is in use since the 1960s. Geosynthetic reinforced soil retaining walls with facings consisting of concrete blocks appeared in the 1980s and continue to increase in popularity ever since.

There are plenty of reasons justifying this rise in popularity: Geosynthetic reinforced soil retaining walls with modular concrete facing are easy to construct, they are suitable for realizing special layouts in a very short time, they are cost-effective and their performance under both static and seismic loads have been observed to be more than satisfactory. They can be used extensively, from small landscape projects to highway walls, bridge abutments, erosion control, and parking area supports. The high compressive strength and low absorption of concrete facing units make these walls durable. Compared to cantilever type retaining walls, only very small earth pressures are activated on the back of facing. The flexible nature prevents the formation of cracks and large deformations can be accommodated, particularly unequal settlement of the supporting ground.

The cross-section of a typical geosynthetic-reinforced soil wall with concrete block facing is shown in Figure 2.1. The elements of a GRS wall can be described as follows: Foundation soil is the soil that supports the leveling pad and the reinforced soil zone of a GRS wall system. The leveling pad consists of crushed stone or unreinforced concrete; it distributes the weight of facing units over a wider area and provides a working surface during construction. Segmental facing units are concrete masonry units that are used to provide stability, durability, and visual enhancement at the face of the wall. Retained soil may be the undisturbed soil for cut walls and the common compacted backfill for fills. Drainage fill is free-draining granular material placed behind the wall to aid the removal of groundwater and reduce the hydrostatic pressure on the wall. It is sometimes also used to fill the cores of the facing units to increase the weight and shear capacity. The dry stacked method of construction used for these GRS walls permits water to drain through the face of the wall, aiding the removal of groundwater. A geotextile filter may be installed between the drainage fill and the infill to protect the drainage fill from clogging. Reinforced soil is the compacted structural fill used behind facing units which contains the geosynthetic reinforcement layers.

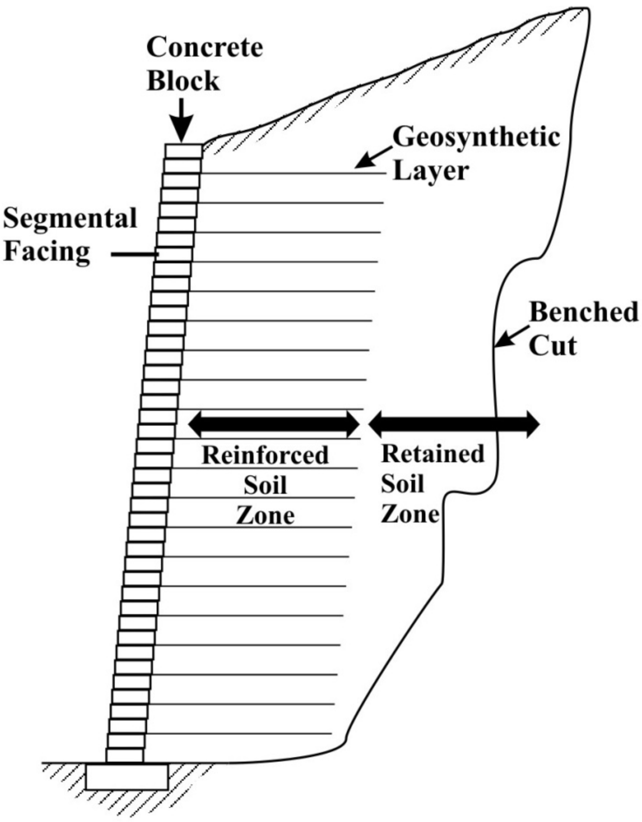

Figure 2.1. Cross-section of typical geosynthetic reinforced segmental retaining wall (Helwany, 2001)

2.3. Design of Geosynthetic-Reinforced Soil Walls Considering Seismic Effects as Pseudo-Static Loading

Numerous methods have been proposed and used in the design of GRS walls using granular soils. In practice, limit equilibrium methods of analysis are used to determine geometry and reinforcement properties to prevent internal and external failure. General agreement has been reached that a complete design approach should consist of working stress analyses, limit equilibrium analyses, and deformation evaluations (Elias *et al.*, 2001).

Design recommendations by FHWA (Elias *et al.*, 2001) consider a Coulomb state of stress for external stability calculations and a Rankine failure surface for internal stability computations. These recommendations are summarized in Sections 2.3.1 and 2.3.2.

2.3.1. Sizing for External Stability (Recommendations by FHWA)

The four potential external failure mechanisms considered in external stability calculations are:

- Sliding on the base
- Overturning
- Bearing capacity failure
- Deep-seated stability problem

These failure mechanisms are illustrated in Figure 2.2. The external stability computation process is summarized in Figure 2.3.

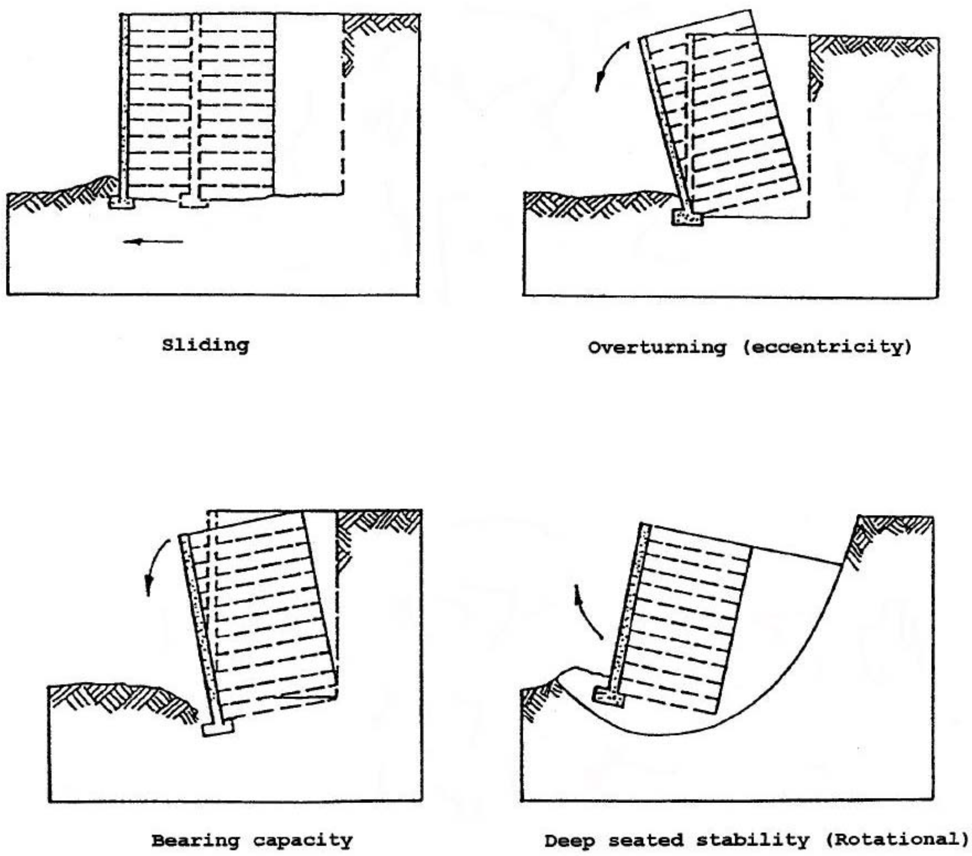

Figure 2.2. Potential external failure mechanisms for a GRS wall (Elias *et al.*, 2001)

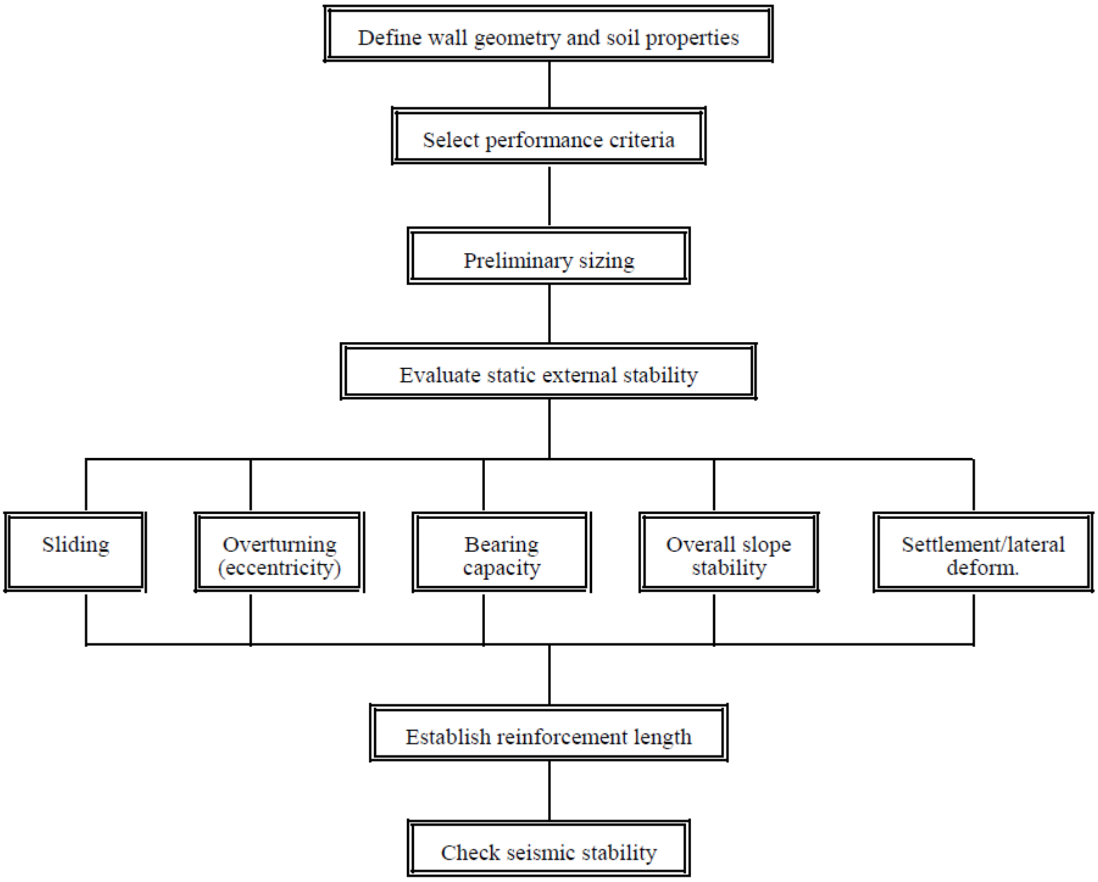

Figure 2.3. Schematic representation of external stability computational sequence (Elias *et al.*, 2001)

FHWA suggests that a length of reinforcement greater than $0.7H$ and 2.5 meters should be chosen in the preliminary sizing stage.

In external stability computations for walls with a vertical face, the GRS wall mass is assumed to act as a rigid body with earth pressures developed on a vertical pressure plane at the back end of the reinforcements, as shown in Figure 2.4. The active coefficient of earth pressure for vertical walls with a horizontal backfill is calculated from:

$$K_a = \tan^2\left(45 - \frac{\varphi_f}{2}\right) \tag{2.1}$$

where: K_a = active coefficient of earth pressure

φ_f = angle of internal friction of backfill soil

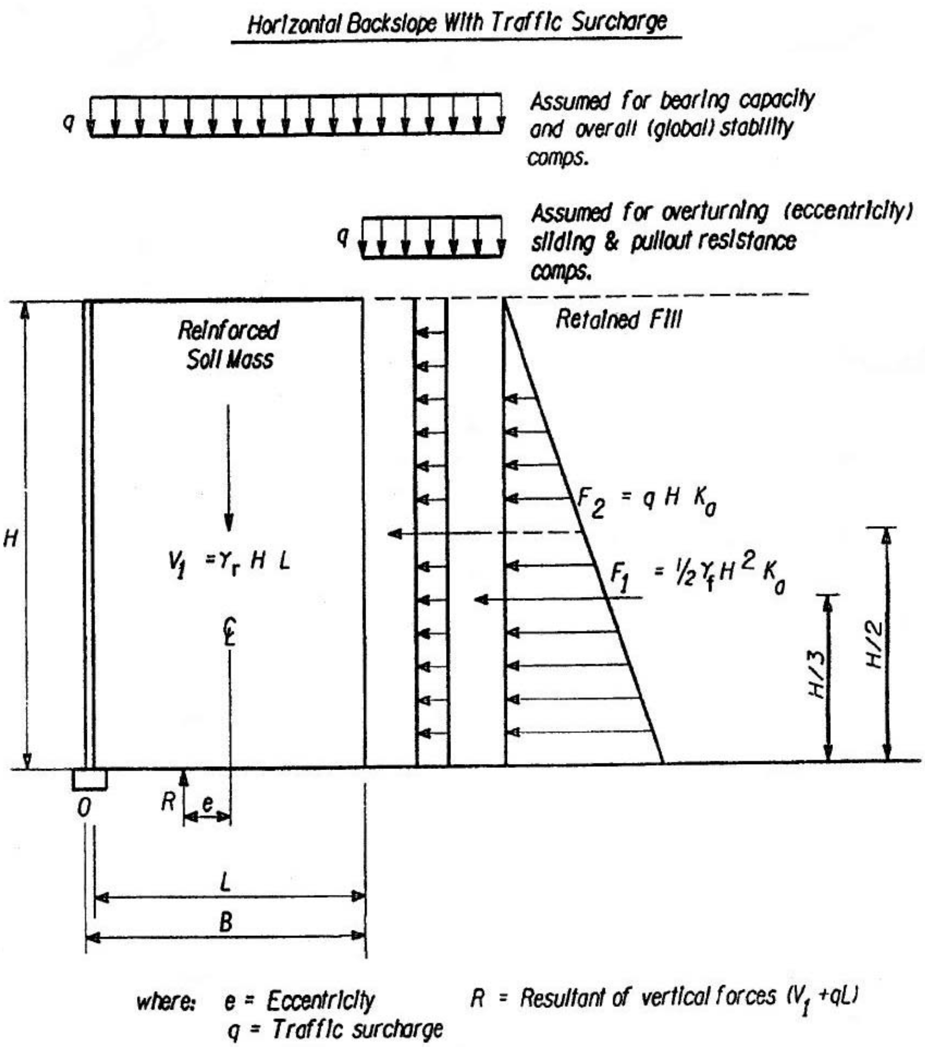

Figure 2.4. External stability analysis for GRS wall with horizontal backfill and traffic surcharge: calculation of earth pressures and eccentricity (Elias *et al.*, 2001)

For vertical walls with a sloping backfill, active coefficient of earth pressure is calculated as:

$$K_a = \cos\beta \left[\frac{\cos\beta - \sqrt{\cos^2\beta - \cos^2\varphi_f}}{\cos\beta + \sqrt{\cos^2\beta - \cos^2\varphi_f}} \right] \tag{2.2}$$

where: β = angle of backfill slope

For an inclined face (batter greater than or equal to eight degrees), the coefficient of earth pressure can be calculated from the general Coulomb case as:

$$K_a = \frac{\sin^2(\theta + \varphi_f)}{\sin^2\theta \sin(\theta - \delta)\left[1 + \sqrt{\frac{\sin(\varphi_f + \delta)\sin(\varphi_f - \beta)}{\sin(\theta - \delta)\sin(\theta + \beta)}}\right]^2} \tag{2.3}$$

where: θ = face inclination from horizontal

δ = angle of wall friction

Figure 2.5 shows computation of vertical stress, σ_v, at the base of the wall. First the total force applied by the retained fill on the back of the reinforced zone is calculated as:

$$F_T = \frac{1}{2} K_a \gamma_f h^2 \tag{2.4}$$

where: F_T = total force applied by the retained fill on the back of the reinforced zone

γ_f = unit weight of retained fill

h = height from base at the back of reinforced zone

Eccentricity is calculated as the next step using Equation 2.5 and the reinforcement length is increased if eccentricity is not less than $L/6$ in soil or $L/4$ in rock to ensure stability against overturning.

$$e = \frac{F_T \cos\beta \frac{h}{3} - F_T \sin\beta \frac{L}{2} - V_2 \frac{L}{6}}{V_1 + V_2 + F_T \sin\beta} \tag{2.5}$$

where: e = eccentricity

L = reinforcement length

V_1 = weight of reinforced soil mass

V_2 = weight of sloped zone over reinforced soil mass

Finally the equivalent uniform vertical stress, σ_v, on the base is calculated from Equation 2.6 and if applicable, the influence of surcharge and concentrated loads are added.

$$\sigma_v = \frac{V_1 + V_2 + F_T \sin\beta}{L - 2e} \tag{2.6}$$

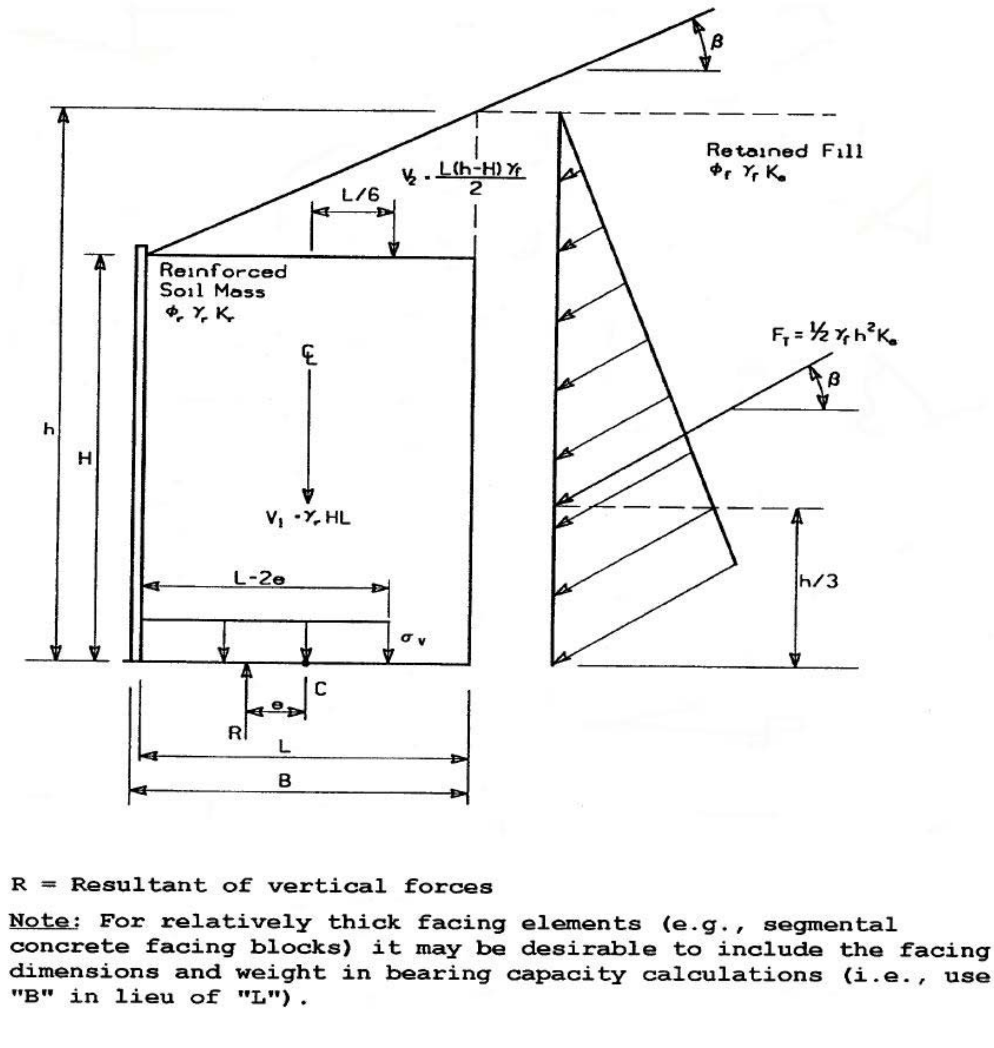

Figure 2.5. Computation of vertical stress, σ_v, at the base of the wall (Elias *et al.*, 2001)

After the calculation of horizontal earth pressures and the vertical stress at the base, sliding stability is checked by:

$$FS_{sliding} = \frac{\sum horizontal\ resisting\ forces}{\sum horizontal\ driving\ forces} = \frac{\sum P_R}{\sum P_d} \geq 1.5 \tag{2.7}$$

$$P_d = F_T \cos\beta \tag{2.8}$$

$$P_R = \left(V_1 + V_2 + F_T \sin\beta\right)\mu \tag{2.9}$$

where: μ = coefficient of friction at the base

The coefficient of friction in Equation 2.9 is determined by taking the tangent of the minimum of these three: internal friction angle of the retained fill, φ_f, internal friction angle of the reinforced soil, φ_r, or the soil-reinforcement friction angle, ρ.

To check stability against bearing capacity failure, the ultimate bearing capacity, q_{ult}, is calculated using classical soil mechanics methods and if the vertical pressure at the base is higher than q_{ult} divided by the chosen factor of safety, it is necessary to increase the reinforcement length.

To check deep-seated stability, the reinforced soil is considered as a rigid body and potential failure surfaces completely outside this rigid body are investigated using slope stability analysis. For complex structures, compound failures involving a failure surface passing both outside and through the reinforced soil should be considered.

After the static external stability of the GRS wall is ensured, effects of seismic loading on the external stability is considered (Figure 2.6). The method that is most commonly used for the seismic analysis and design of GRS walls is the pseudo-static method in which pseudo-static forces related to the ground acceleration are added to the conventional static limit equilibrium analysis. During an earthquake, the retained fill exerts a dynamic thrust, P_{AE}, on the GRS wall in addition to the static force. The reinforced soil mass is also subjected to a horizontal inertia force, P_{IR}, estimated in FHWA recommendations as:

$$P_{IR} = MA_m g \tag{2.10}$$

where: M = Mass of the active portion of the reinforced wall section assumed at a base width of $0.5H$, as shown in Figure 2.6

A_m = maximum horizontal acceleration coefficient in the reinforced soil wall

$$A_m = (1.45 - A)A \tag{2.11}$$

where: A = maximum ground acceleration coefficient

For horizontal backslope condition, the seismic thrust, P_{AE}, is suggested in FHWA recommendations as:

$$P_{AE} = 0.375 A_m \gamma_f H^2 \tag{2.12}$$

FHWA suggests adding the full inertia force P_{IR} and fifty per cent of the seismic thrust P_{AE} to the static forces.

For sloping backfill condition, the seismic thrust, P_{AE}, can be calculated using the Mononobe-Okabe method:

$$P_{AE} = 0.5 \gamma_f (H_2)^2 \Delta K_{AE} \tag{2.13}$$

where: $H_2 = H + \dfrac{0.5H \tan\beta}{1 - 0.5\tan\beta}$

K_{AE}, the total seismic earth pressure coefficient, is calculated based on the general Mononobe-Okabe expression:

$$K_{AE} = \frac{\cos^2(\varphi - \xi - 90 + \theta)}{\cos\xi \cos^2(90 - \theta)\cos(\beta + 90 - \theta + \xi)\left[1 + \sqrt{\dfrac{\sin(\varphi + \beta)\sin(\varphi - \xi - \beta)}{\cos(\beta + 90 - \theta + \xi)\cos(\beta - 90 + \theta)}}\right]^2} \tag{2.14}$$

where: ξ = seismic inertia angle

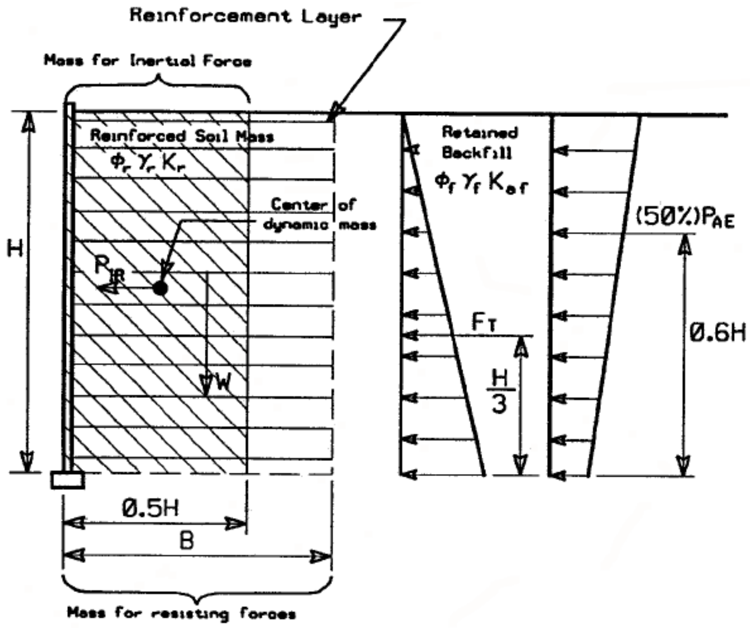

(a)

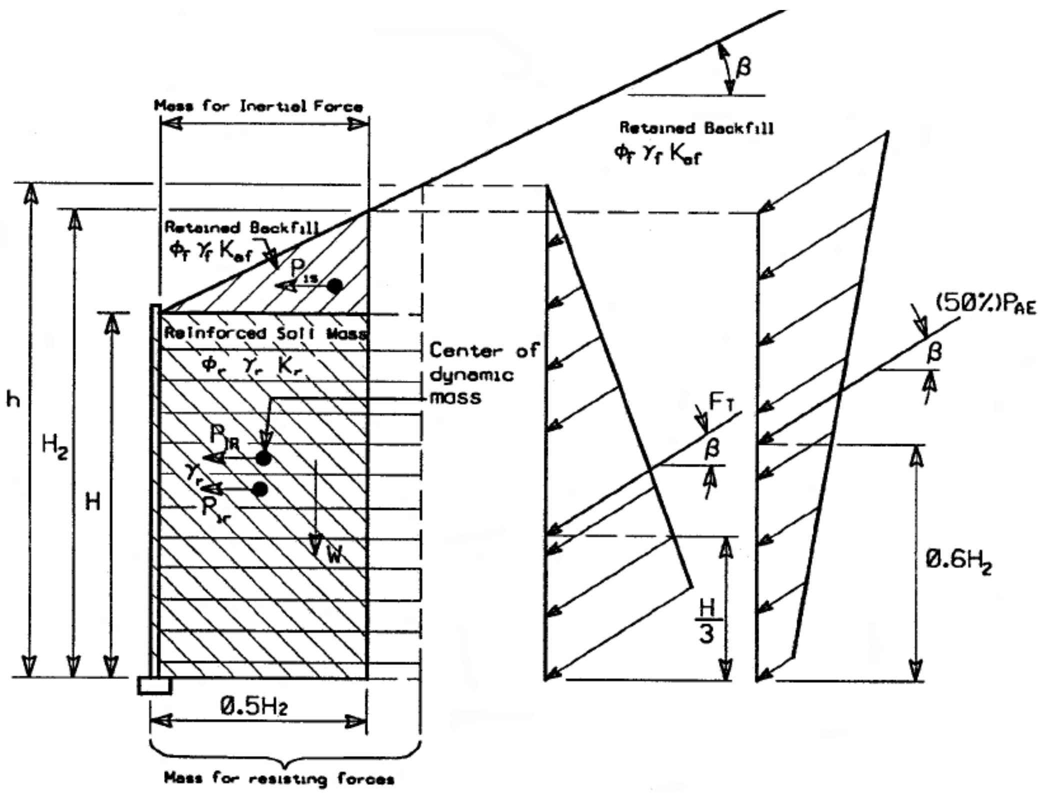

(b)

Figure 2.6. Forces considered in seismic external stability calculations: (a) for level backfill (b) for sloping backfill (Elias *et al.*, 2001)

$$\xi = \tan^{-1}\left(\frac{k_h}{1 \pm k_v}\right) \tag{2.15}$$

where: k_h = horizontal seismic coefficient

k_v = vertical seismic coefficient

The seismic external analysis is completed by evaluating sliding stability, eccentricity and bearing capacity checks as in the static case, this time with the pseudo-static forces added. Computed factors of safety greater than 75 per cent of the static factors of safety and eccentricity falling within $L/3$ is considered as acceptable.

2.3.2. Sizing for Internal Stability (Recommendations by FHWA)

There are two possible mechanisms for internal failure of GRS walls. The first possible mechanism is failure by elongation or breakage of reinforcements when the tensile forces in the reinforcements are larger than that can be carried. The other possible mechanism is failure by pullout, in which the tensile forces in the reinforcement become larger than the pullout resistance. Therefore to prevent internal failure, maximum developed tension forces and the resistance provided are determined in the design process, which is illustrated in Figure 2.7. In design, first the location of the critical surface is determined, a reinforcement spacing compatible with the facing is selected, maximum static and dynamic tensile forces in the reinforcements and at the connection to the facing are computed and the pullout capacity at each reinforcement level is calculated.

The most critical slip surface is assumed to coincide with the maximum tensile forces line. The critical surface suggested in FHWA recommendations is given in Figure 2.8.

Steps for calculation of maximum tensile forces in the reinforcement layers and checking for internal stability against breakage of reinforcement are described below:

- Calculate the horizontal stress, σ_H, and the location of the intersection with the potential failure line at each reinforcement level. The active earth pressure coefficient used in calculating σ_H is determined using a Coulomb earth pressure relationship. For a vertical wall with horizontal backfill, the earth pressure coefficient reduces to Rankine's equation:

$$K_a = \tan^2\left(45 - \frac{\varphi}{2}\right) \tag{2.16}$$

$$\sigma_H = K_{ar}\sigma_v + \Delta\sigma_H \tag{2.17}$$

where: K_{ar} = earth pressure coefficient calculated for reinforced zone
$\Delta\sigma_h$ = increment of horizontal stress due to any horizontal concentrated surcharge
σ_v = total vertical stress including soil self-weight and effects of any surcharge loads present

- Calculate the maximum tension force per unit width of wall, T_{max}, in each reinforcement layer from:

$$T_{\max} = \sigma_H s_v \tag{2.18}$$

where: s_v = reinforcement spacing

- Check internal stability with respect to breakage of the reinforcement by checking that T_{max} is less than or equal to T_a, the allowable tensile force per unit width of reinforcement. The connection of reinforcement with the facing should be designed for T_{max}.

Stability with respect to pullout of the reinforcements requires that the following condition is met:

$$T_{\max} \leq \frac{1}{FS_{PO}} F^* \gamma Z_p L_e C R_c \alpha \tag{2.19}$$

where: FS_{PO} = safety factor against pullout, which should be greater than or equal to 1.5

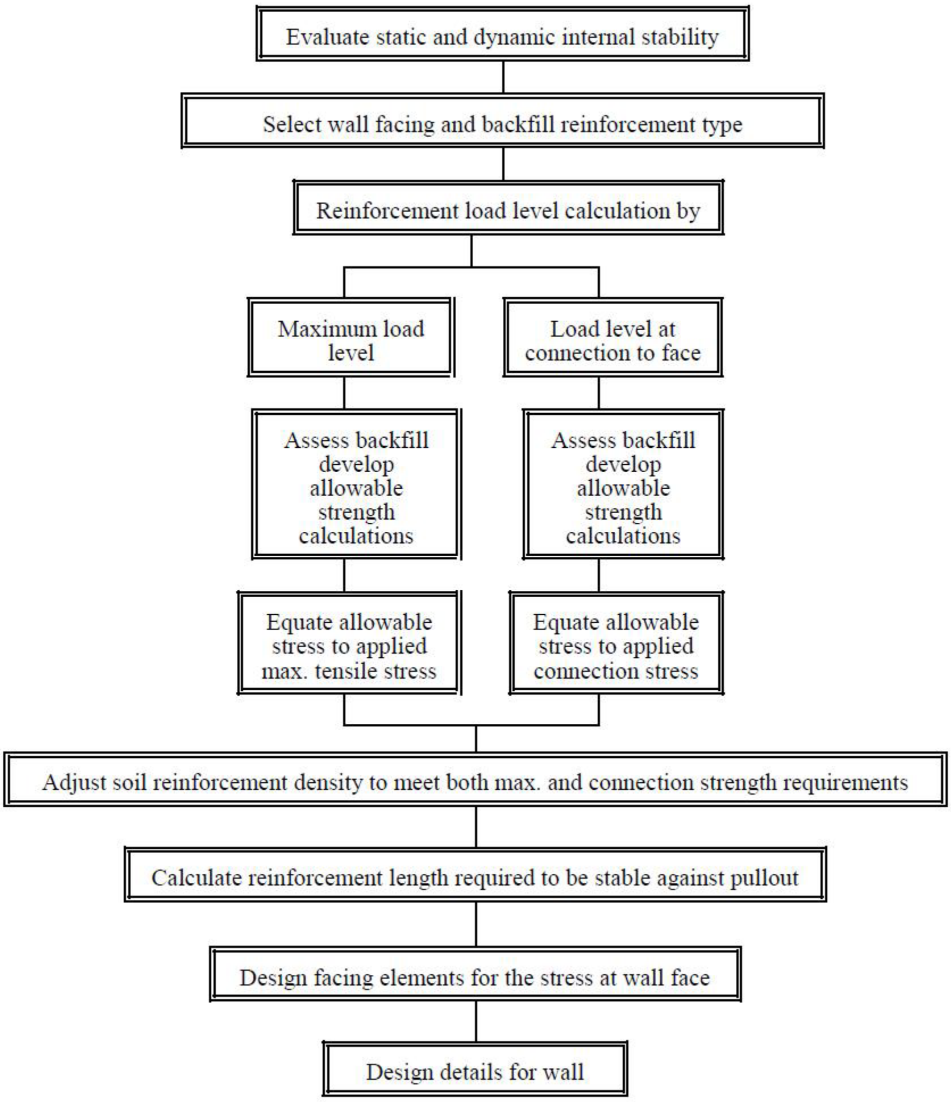

Figure 2.7. Schematic representation of internal stability computation and design sequence (Elias *et al.*, 2001)

C = 2 for strip, grid, and sheet type reinforcement

α = scale correction factor

F^* = pullout resistance factor

R_c = coverage ratio

γZ_p = overburden pressure including distributed dead load surcharges

L_e = length of embedment in the resisting zone

L_e is determined from Equation 2.19 and FHWA recommends it to be kept above one meter.

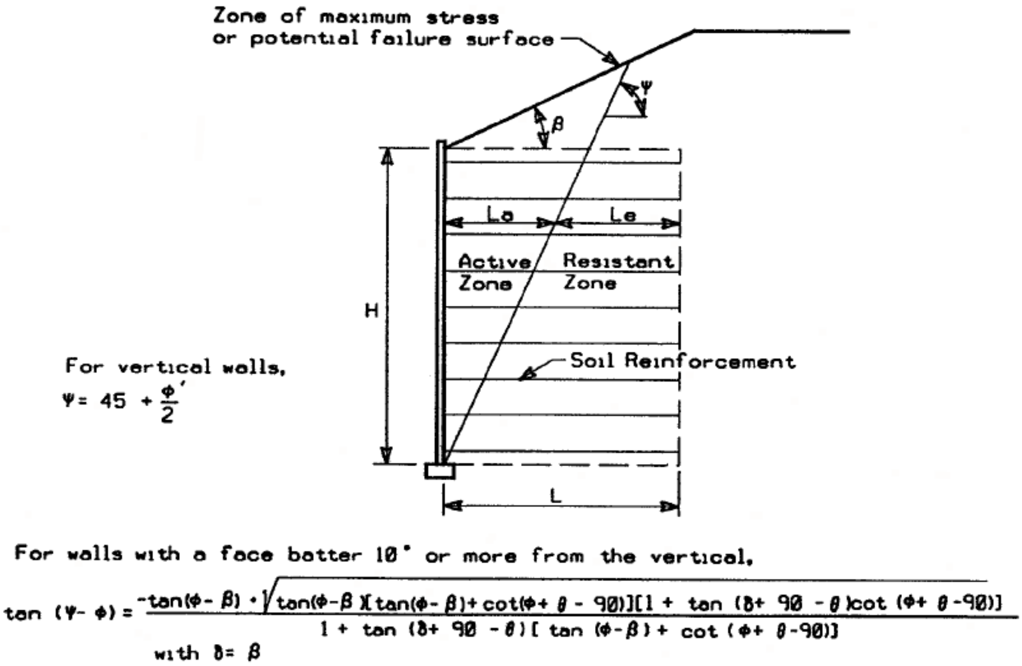

Figure 2.8. Location of potential failure surface for internal stability design of GRS walls (Elias *et al.*, 2001)

The total length of reinforcement, L, required for internal stability is:

$$L = L_a + L_e \tag{2.20}$$

where: L_a = length of reinforcement in front of the critical surface.

For vertical face and horizontal backfill:

$$L_a = (H - Z)\tan(45 - \varphi/2) \tag{2.21}$$

where: Z = depth to the reinforcement level

To check the internal stability under seismic loading, FHWA recommends the addition of dynamic increments calculated at each reinforcement layer to T_{max} calculated by Equation 2.18, as shown in Figure 2.9. The inertia force P_I considered in internal stability calculations and the dynamic increment in tensile force, T_{md}, resulting from the inertia force are calculated by using:

$$P_I = A_M W_A \tag{2.22}$$

where: W_A = weight of active zone

$$T_{md} = P_I \frac{L_{ei}}{\sum_{i=1}^{n} L_{ei}} \tag{2.23}$$

$$T_{total} = T_{\max} + T_{md} \tag{2.24}$$

In the updated recommendations of FHWA (Berg *et al.*, 2009), T_{md} is calculated by distributing the inertial force equally to the reinforcements.

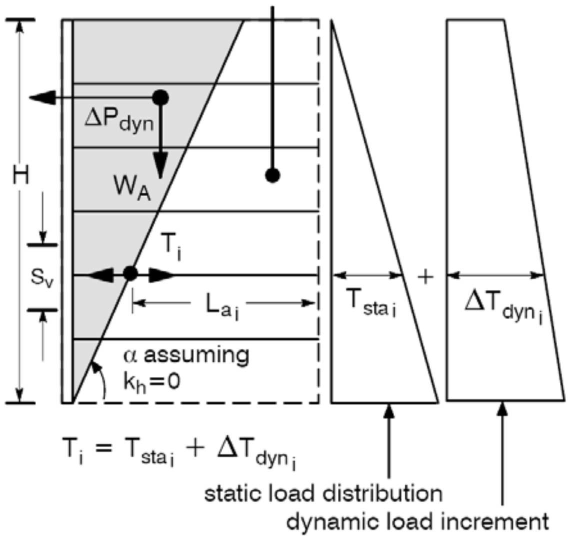

Figure 2.9. Reinforcement tensile load calculation using FHWA method, which utilizes Rankine earth pressure theory (Bathurst and Alfaro, 1996)

2.3.3. Background of Accepted Design Recommendations and Variations in Pseudo-Static Design

Seed and Whitman (1970) decomposed the P_{AE} in Equation 2.13 into static component P_A and incremental dynamic component ΔP_{dyn}:

$$P_{AE} = P_A + \Delta P_{dyn} \tag{2.25}$$

or

$$(1 \pm k_v)K_{AE} = K_A + \Delta K_{dyn} \tag{2.26}$$

where: ΔK_{dyn} = incremental dynamic active earth pressure coefficient

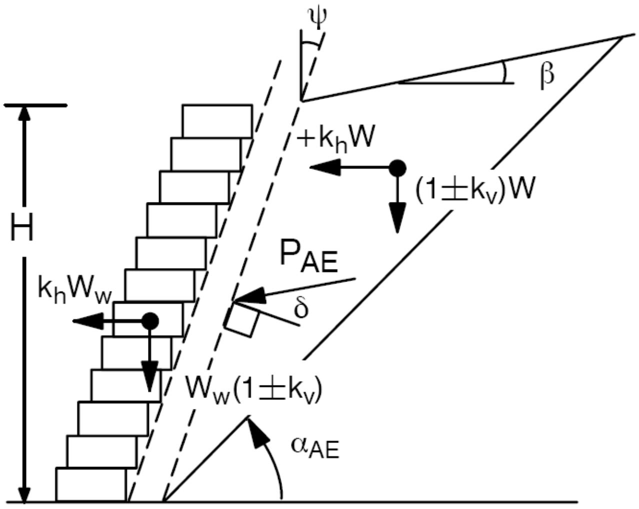

Figure 2.10. Forces and geometry used in pseudo-static seismic analysis (Bathurst and Alfaro, 1996)

Figure 2.10 shows the general geometry used in pseudo-static seismic analysis. Closed-form approximate solutions for α_{AE} developed by Okabe and Zarrabi are given below. These were shown to result in excessive reinforcement lengths, so in practice, the orientation of the internal failure plane for reinforcement design is found using static load conditions (i.e. $k_h = k_v = 0$) (Bathurst *et al.*, 2002).

$$\alpha_{AE} = \phi - \theta + \tan^{-1}\left[\frac{-A_\alpha + D_\alpha}{E_\alpha}\right] \tag{2.27}$$

where: $A_\alpha = \tan(\phi - \theta - \beta)$

$D_\alpha = \sqrt{A_\alpha[A_\alpha + B_\alpha][B_\alpha C_\alpha + 1]}$

$E_\alpha = 1 + [C_\alpha(A_\alpha + B_\alpha)]$

$$B_\alpha = \frac{1}{\tan(\phi - \theta + \psi)}$$

$$C_\alpha = \tan(\delta + \theta - \psi)$$

Bathurst and Cai (1995) proposed the active earth pressure distribution shown in Figure 2.11 for external, internal and facing stability calculations of GRSW with segmental facing upon reviewing the literature for conventional gravity retaining walls. This distribution is accepted by FHWA in external stability calculations. NCMA recommends using ΔP_{dyn} (distributed) added to the inertial force acting on the facing column in order to calculate the tensile forces in reinforcement in internal stability calculations (Bathurst, 1998). Without seismic effects, the distribution becomes the triangular static distribution due to soil weight.

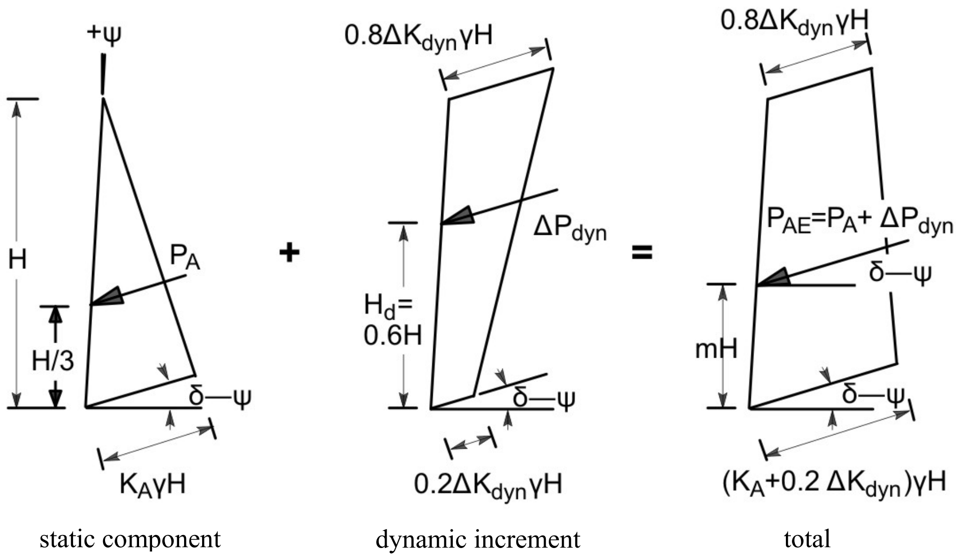

Figure 2.11. Calculation of total earth pressure due to soil self-weight (Bathurst and Cai, 1995)

Selection of seismic coefficients is an issue on which there appears to be no agreement and engineering judgment must be employed for a site and structure specific decision. There are various studies involving a wide range of seismic coefficient values. Equation 2.11 proposed by Segrestin and Bastick (1988) with a note on the specific conditions it is based on is adopted in FHWA guidelines. For the vertical seismic coefficient k_v, Seed and Whitman (1970) and Wolfe *et al.* (1978) suggested that ignoring k_v

is acceptable in pseudo-static analysis. For sites close to the epicenter, vertical accelerations may become significant, so the decision should be made with care.

FHWA guidelines (Elias *et al.*, 2001) restrict the use of pseudo-static methods to sites with A lower than 0.29. For larger accelerations, structural displacements may exceed the acceptable values, so at least a sliding block analysis is required.

External stability calculations are similar to those for conventional gravity retaining walls. Factors of safety against base sliding and overturning for the reinforced soil zone together with the facing column are calculated using the forces and geometry shown in Figure 2.12. There are various suggestions for the value of P_{IR}, the horizontal inertia force, but in all cases it is taken lower than $k_h W_R$ in order not to be too conservative.

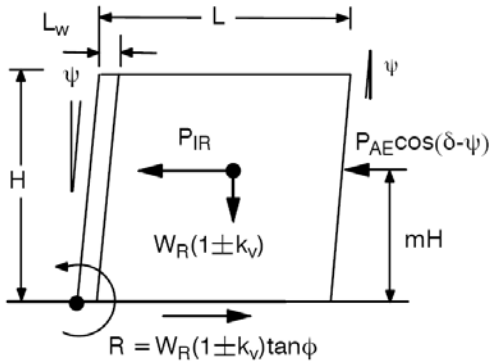

Figure 2.12. Forces and geometry for external stability calculations (Bathurst *et al.*, 2002)

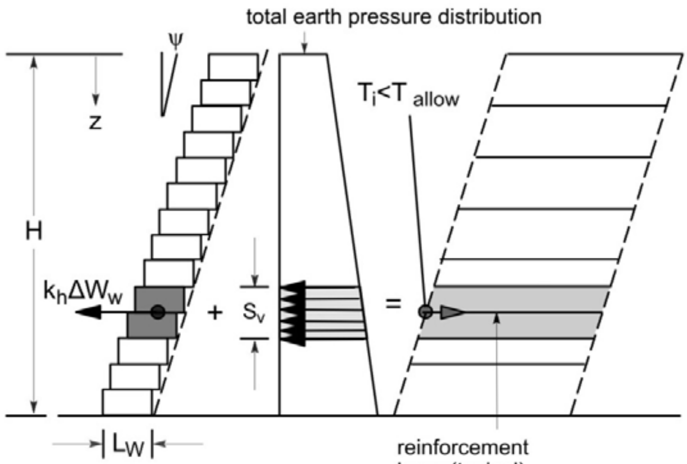

Figure 2.13. Reinforcement tensile load calculation using Bathurst and Cai method (Bathurst and Alfaro, 1996)

For internal stability calculations, each reinforcement layer is required to carry the part of the assumed internal pressure distribution applied to the area S_v in Figure 2.13. Tensile strength, facing connection strength and pullout capacity of the reinforcement layer should be adequate. Various methods used are presented in Figures 2.14 to 2.16.

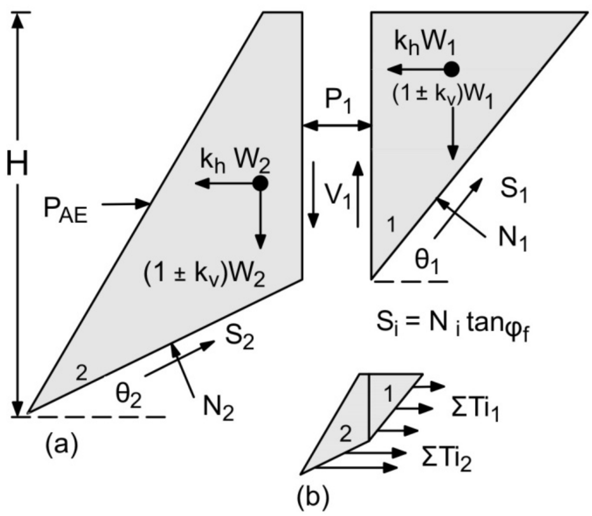

Figure 2.14. Two-part wedge analysis: (a) free-body diagram (b) with reinforcement forces (Bathurst and Alfaro, 1996)

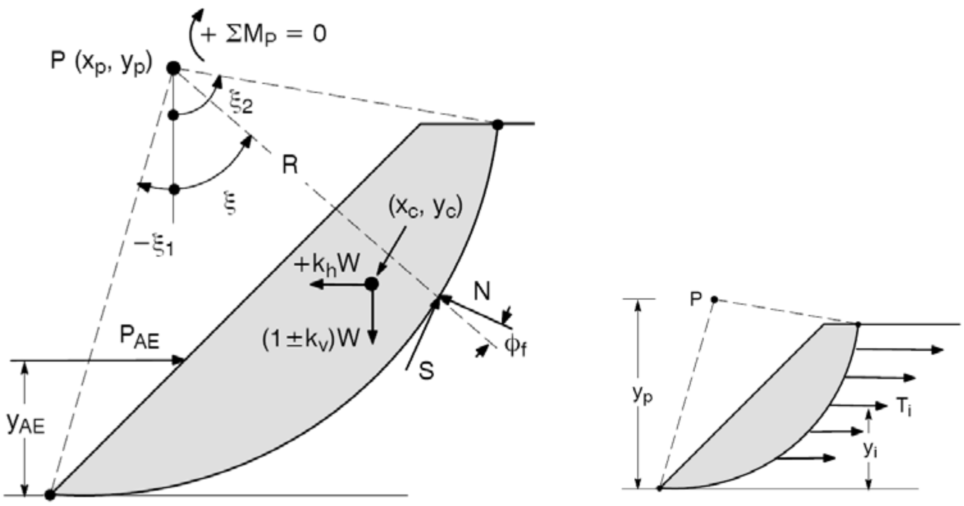

(a) (b)

Figure 2.15. Log-spiral analysis: (a) free-body diagram (b) with reinforcement forces (Bathurst and Alfaro, 1996)

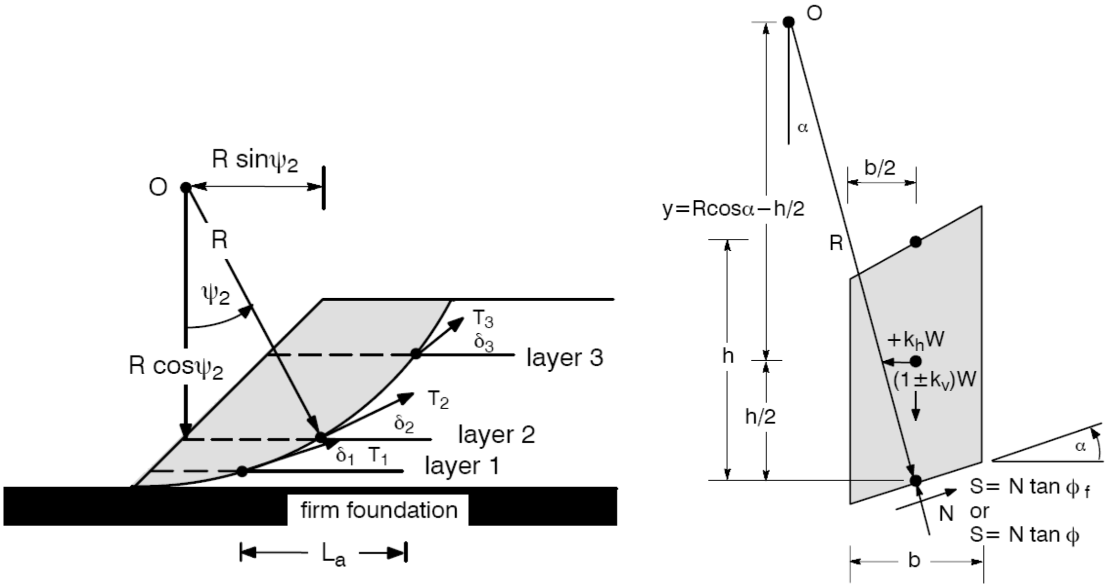

(a) (b)

Figure 2.16. Circular slip analysis: (a) circular slip geometry (b) method of slices (Bathurst and Alfaro, 1996)

2.4. Newmark's Sliding Block Analysis

Pseudo-static approach is inadequate when intolerable movements are expected before the collapse of the structure. Newmark's sliding block analysis may be used to estimate the permanent displacement of a geosynthetic reinforced wall. This method involves double integration of the given input acceleration. It assumes that movement starts when a critical acceleration, $k_c g$, is exceeded, as illustrated in Figure 2.17. In the first integration step, the parts of the acceleration record where the critical acceleration is exceeded are integrated until the velocity becomes zero again. In the second step, integration of the velocity gives the displacement. The values of k_h that give a factor of safety of unity in pseudo-static analysis may be taken as k_c. External sliding and internal sliding of layers need to be considered separately. The major assumption in this method is that the block is allowed to move only in one direction, i.e. when an acceleration greater than $k_c g$ is applied in the backward direction, no movement takes place. Without this assumption, a block free to move in both directions on horizontal uniform ground would be expected to have no permanent displacement. Suggestions from numerous studies involving modifications of this method are available.

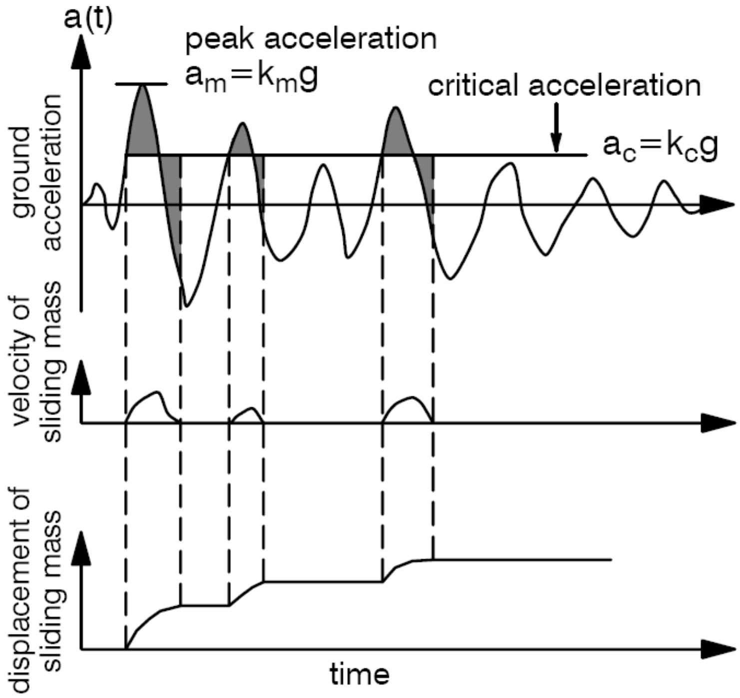

Figure 2.17. Newmark's sliding block calculations (Bathurst and Alfaro, 1996)

2.5. Dynamic Analysis Using Numerical Techniques

The advantages offered by numerical techniques (e.g. the possibility of implementing complex models for the involved materials) make this choice a very promising method for the design and analysis of geosynthetic reinforced soil walls and slopes. Various programs based on finite element method or finite difference method are available or being developed, and many studies involving the comparison of numerical analysis results with the results of physical tests are conducted. Some of the major studies showing the power of numerical techniques are alluded below.

Fujii *et al*. (2006) aimed to simulate results from a series of dynamic centrifuge tests on GRS segmental walls using finite element analyses with the program FLIP. In total, thirteen test cases with different input wave forms and amplitudes were analyzed.

El-Emam *et al.* (2004) reported the results of numerical modeling of 1-m high shaking table tests that investigated full-height panel face GRS walls with different toe boundary conditions using the finite difference-based program FLAC. The numerical models were found to give reasonably accurate predictions of the experimental results (wall facing displacements, reinforcement loads and measured toe loads) despite the complexity of the physical models under investigation.

Bathurst and Hatami (1998) reported the results of a numerical parametric study of an idealized 6-m high GRS wall with a full-height rigid facing and six layers of reinforcement. They showed that the magnitude and distribution of reinforcement loads were sensitive to the stiffness of the reinforcement materials used.

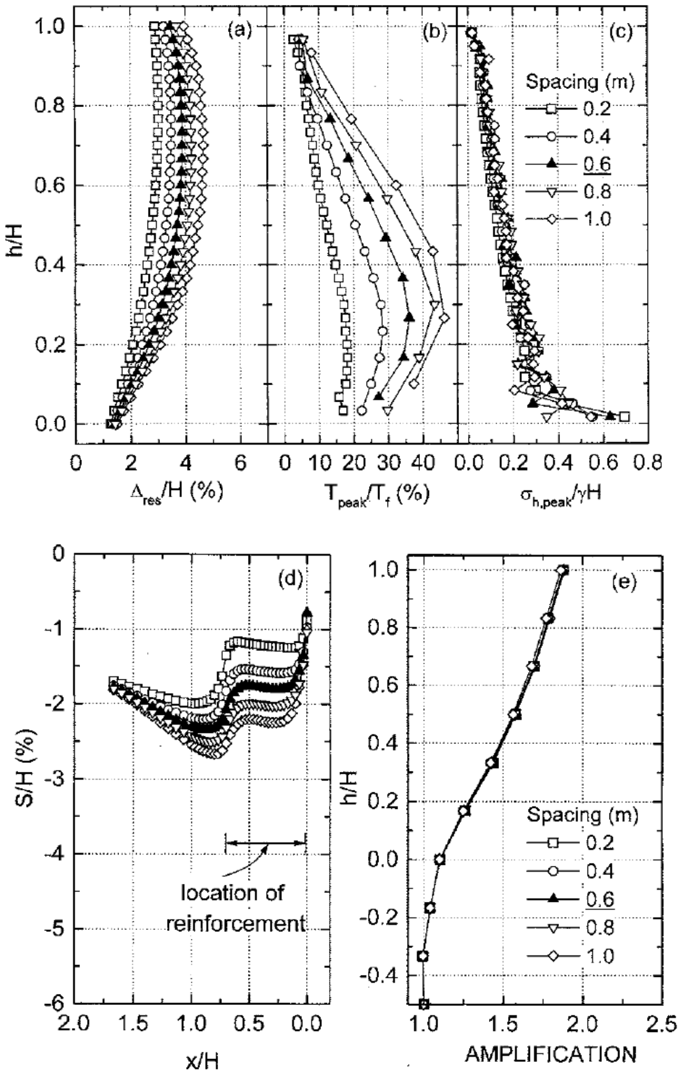

Figure 2.18. Effects of reinforcement spacing on seismic wall performance: (a) facing lateral displacement (b) maximum reinforcement force (c) lateral earth pressure behind facing (d) crest surface settlement (e) acceleration amplification (Ling *et al.*, 2005a)

Ling *et al.* (2005a) conducted a series of two-dimensional plane strain analyses on segmental block-reinforced soil retaining walls using a modified version of Diana-Swandyne-II program, whose procedure was previously validated against full-scale static and dynamic centrifuge tests (Ling *et al*., 2004). The walls considered were six meters high with 0.2 meters high facing blocks. The backfill and foundation soils were expressed using a generalized plasticity model (Ling *et al.*, 2004). The effects of soil properties, earthquake motions, and reinforcement layouts were investigated. In the dynamic analyses, considerable residual displacements were found. Maximum reinforcement force more than doubled compared to that at the end of construction. The reinforcement force mobilized at the bottom was higher and the deformation was larger at the top. Soils that exhibited large plastic deformation gave a smaller soil amplification compared to less deformable soils. Different reinforcement lengths resulted in different lateral displacement and vertical settlement values, but did not affect the acceleration amplification significantly. Maximum reinforcement forces and lateral earth pressure increased as the reinforcement length decreased. Effects of reinforcement spacing were similar to those of reinforcement length, but were more pronounced, as seen in Figure 2.18.

Lee *et al.* (2010) used LS-DYNA, a general purpose nonlinear three dimensional finite element computer code, for the numerical simulation of geosynthetic-reinforced soil walls under seismic shaking. They used the full-scale shaking table tests performed by Ling *et al.* (2005b) for validation. These walls had segmental block facing and the soil fill was reinforced with geogrids. Lateral earth pressures and horizontal displacements calculated were similar to the measured values, but the other parameters investigated did not match closely.

Ling *et al.* (2010) performed a recent finite-element simulation study on four full-scale GRS walls using improved versions of constitutive models for soil and polymeric reinforcement materials. The first three walls were simulations of full-scale GRS wall shaking table tests previously reported (Ling *et al.*, 2005b). The walls were 2.8 m high with geogrid reinforcement and fine sand backfill. Wall deformations, tensile force in geogrids, and time response of horizontal and vertical accelerations obtained from the numerical analysis were compared with the experimental results and were concluded to be in satisfactory agreement. Comparison of maximum calculated and measured accelerations is shown in Figure 2.19.

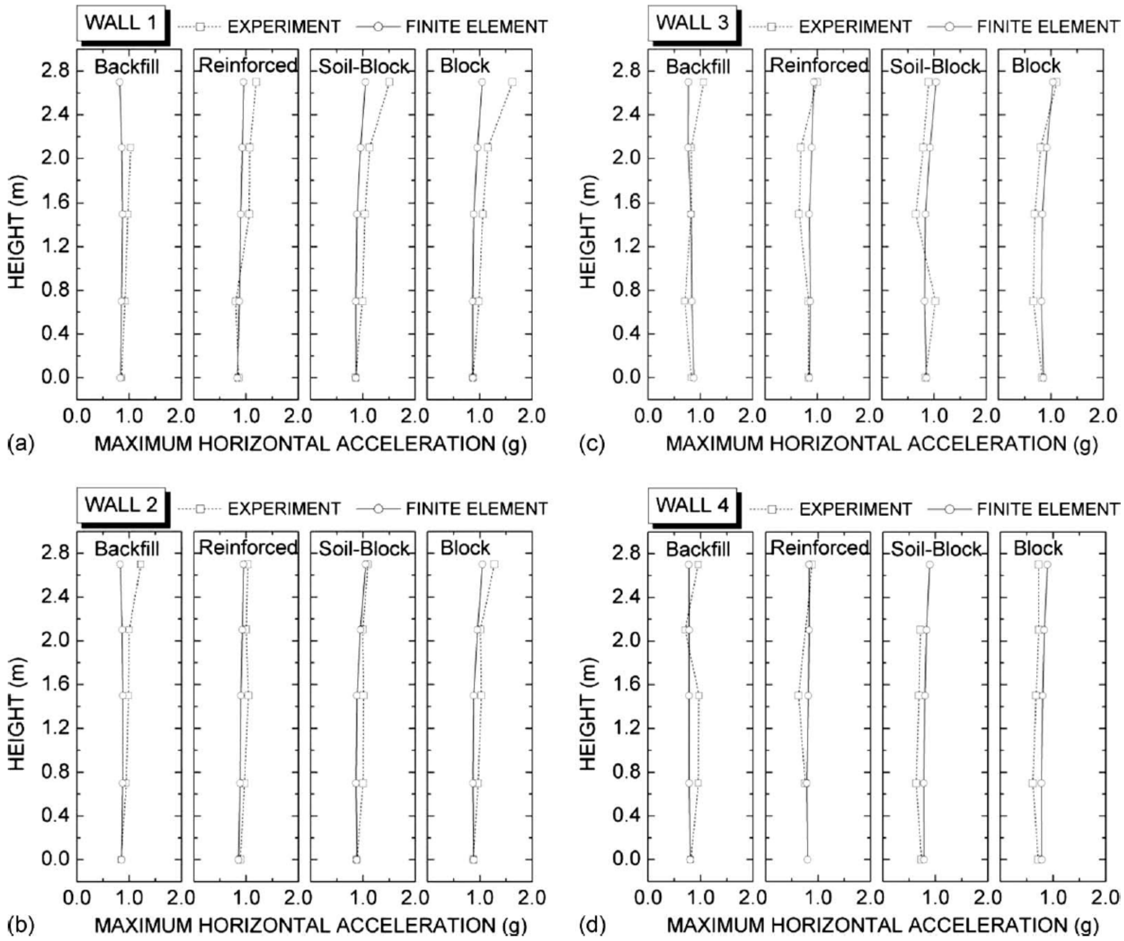

Figure 2.19. Maximum horizontal accelerations: (a) Wall 1 (b) Wall 2 (c) Wall 3 (d) Wall 4 (Ling *et al.*, 2010)

2.6. Gravity Shaking Table Testing of Model GRS Walls

The major difficulty with shaking table tests is to establish scaling rules between the reduced-scale model and the prototype. Various suggestions are offered in the literature for the similitude rules. Rules proposed by Iai (1989) are widely used to scale the geometry of the model and the properties of the components. Details of these rules will be given in Section 3.2.

Main shaking table studies reported in literature are listed and summarized in Table 2.1.

Table 2.1. Shaking table studies on geosynthetic-reinforced soil walls (Based on Bathurst *et al.*, 2002 and updated)

Reference	**Model details**	**Observed behavior and implications to design and analysis**
Koga *et al.*, 1988; Koga and Washida, 1992	1.0-1.8 m high models with vertical and inclined slopes at 1/7 scale. Sandbags with wrapped-face facing. Non-woven geotextile, plastic nets and steel bars with sandy silt backfill.	Deformations decreased with increasing reinforcement stiffness and density, and decreasing face slope angle. Failure volumes were shallower for reinforced structures. Relative reduction in deformation of reinforced structures compared to unreinforced structures increased with steepness of the face. Circular slip method agrees well with experimental results except for steep-faced models.
Murata *et al.*, 1994	2.5 m high 1/2 scale model walls with gabion/rigid concrete panel walls. Geogrid with dry sand backfill. Horizontal shaking using sinusoidal and scaled earthquake record. Base accelerations up to 0.5g at 3.4 Hz.	Increase in reinforcement forces due to shaking was very small. Reinforcement loads increased towards the front of the wall. Acceleration amplification was negligible up to mid-height of wall but increased to about 1.5 at the top. Amplification behavior was similar for reinforced and unreinforced zones. The reinforced zone behaved as a monolithic body. Sinusoidal base input resulted in greater deformations than scaled earthquake record. Rigid facing adds to wall seismic resistance.
Sugimoto *et al.*, 1994; Telekes *et al.*, 1994	1.5 m high model embankment with sand bags and wrapped-face slope surface. Geogrid reinforcement with sand backfill. Model scales 1/6 and 1/9. Sinusoidal and scaled earthquake record. Base acceleration up to 0.5g at 40 Hz.	Reinforced models more stable than unreinforced. Proposed similitude rules for small and large strain deformation modeling. Largest amplification recorded at crest of models. Failure of structures was progressive from top of structure downward. Reinforcement forces increased linearly with acceleration up to start of failure. Failure mechanism difficult to predict using proposed scaling rules. Under seismic loading conditions, there was a tendency for shallow slopes to fail compared to steeper ones. Scale effects due to vertical stress and apparent cohesion of backfill soil influenced the relative performance of steep-faced and shallow-faced models.
Budhu and Halloum, 1994	0.72 m high model wall with wrapped-face facing. Geotextile with dry sand backfill. Base acceleration in increments of 0.05g at 3 Hz.	Sliding progressed with increasing acceleration from the top geotextile/sand interface to the bottom layer. No consistent decreasing trend of critical acceleration was observed with increasing spacing to length ratio. Critical acceleration proportional to the soil/geotextile interface friction value.

Table 2.1. Continued

Reference	Model details	Observed behavior and implications to design and analysis
Sakaguchi *et al.*, 1992; Sakaguchi, 1996	1.5 m high model walls. One wrapped-face and four unreinforced rigid concrete panel walls. Geogrid with dry sand backfill. Sinusoidal loading with base acceleration up to 0.72g at 4 Hz.	Wrapped-face wall behaved as a rigid body and failed at a higher acceleration than unreinforced structures. However, at smaller accelerations (due to stiff facing panels) the displacements of the unreinforced structures were less. A base input acceleration of 0.32g delineated stable wall performance from yielding wall performance for the reinforced structure. Residual strains were greatest closest to the face. Concluded that more rigid light-weight modular block facings may be effective in reducing reinforcement loads.
Koseki *et al.*, 1998; Watanabe *et al.*, 2003; Koseki *et al.*, 2003	0.5-0.53 m high propped-panel models, phosphor-bronze reinforcement strips (with L/H = 0.4) connected together in a· grid form. One uniform length model and one model with extended reinforcement length at the top. 5 Hz sinusoidal base acceleration with stepwise increase in amplitude.	Overturning was observed to be the main failure mode. Simple shear deformation of reinforced zone was observed. The ratio of observed and predicted critical seismic coefficients (corresponding to 5% lateral displacement) was about 1.05 for uniform reinforcement model and 1.15 for the model with extended reinforcement layer length at the top. These ratio values were larger than the values for conventional retaining wall models (values less than one) tested in the same study. Walls on shaking tables were more stable than on equivalent tilting tables. Observed failure plane angle was steeper than the predicted value. Permanent horizontal displacements were lower with the GRS walls than with conventional walls. The presence of extended reinforcement at top further decreased the permanent displacements and the tensile stresses in this extended layer were measured to be larger (Watanabe et al., 2003).
Bathurst *et al.*, 1996; Pelletier, 1996; Bathurst *et al.*, 2002	1020 mm high, 1/6 scale reinforced segmental retaining wall models (Figure 2.20a). Iai similitude rules used. Weak geogrid reinforcement (HDPE bird fencing). 160x100x34 mm facing blocks. Base input frequency 5 Hz, corresponding to 2 Hz in prototype. Input acceleration shown in Figure 2.20b	Four different configurations evaluated the effect of facing batter and interface shear properties of facing. Vertical wall with fixed block-block and block-geosynthetic interfaces had the smallest displacements. Vertical wall with frictional interfaces performed the worst, but increasing the wall batter improved performance. Acceleration amplifications as high as 2.2 recorded (at top). Peak acceleration measured at the middle of the wall height or at the top of the backfill surface shown to give a more accurate estimate to be used in pseudo-static analysis. Geoynthetic tensile loads remained low compared to capacity. Actual failure mechanism difficult to predict, e.g. toppling of top blocks observed whereas pullout of the top reinforcement layer was predicted.

Table 2.1. Continued

Reference	**Model details**	**Observed behavior and implications to design and analysis**
Matsuo *et al.*, 1998	1-1.4m high models with hard facing panel. Reinforcement length, L/H = 0.4 and 0.7. One model with inclined facing. 5 Hz sinusoidal base acceleration with stepwise increase in amplitude. In addition, recorded ground motion was applied.	Walls showed larger margin of safety when subjected to recorded ground motion compared to sinusoidal base acceleration. Did not observe failure of the model walls in spite of predicted factors of safety that were less than 1.
El-Emam and Bathurst, 2004, 2005, 2007	1 m high 1/6 scale models with rigid facing panels (Figure 2.22). A stepped amplitude sinusoidal function at 5 Hz predominant frequency used as base excitation. (Scaling similar to Bathurst *et al.*, 1996)	Horizontally restrained toe attracted 40%-60% of the peak total horizontal earth load, indicating the importance of the rigid facing column in carrying the dynamic loads. Current design methodologies were shown to underestimate the load carried by reinforcement and horizontal toe, meaning non-conservative design. Lateral displacement decreased and the critical acceleration to cause movement increased with increasing length, stiffness and number of reinforcement layers.
Ling *et al.*, 2005b	2.8 m high full-scale GRS segmental retaining wall models tested. Both vertical and horizontal components of the Kobe earthquake accelerogram applied.	At a scaled peak horizontal acceleration of 0.4g, maximum deformations at crest were negligible. Maximum deformation remained below 100 mm at acceleration scaled to 0.86g. Increasing the length of reinforcement at the wall crest and decreasing the reinforcement spacing improved the seismic behavior.
Latha and Krishna, 2008	60 cm high, wrap-faced and rigid-faced model walls in laminar box. Poorly graded, dry sand backfill and geotextile reinforcement. Relative densities between 37 per cent and 87 per cent tested.	Wrap-faced walls had much higher displacements and the effect of relative density was more pronounced compared to rigid-faced walls. Amplification in acceleration was not affected from change in relative density at smaller base excitations. Displacements were more sensitive. Response was affected at higher base excitations. Final relative densities after shaking were higher than 90 per cent in some cases.
Güler and Enünlü, 2009	1:2 scale 1.9 m high models with concrete facing blocks tested with El Centro and sinusoidal harmonic motion excitations. L/H=0.9 and L/H=0.6 models tested.	GRS walls behaved very successfully under the testing conditions; no residual displacements were observed. Accelerations on face were increased at top. Geotextile stresses were higher at the potential failure surface predicted by Rankine theory.

As shown in Table 2.1, Bathurst *et al.* (2002) reported the results from shaking table tests on 1020 mm high, 1/6 scale reinforced segmental retaining wall models, for which the setup and base input acceleration are shown in Figure 2.20. Four different configurations were tested to evaluate the effect of facing batter and interface shear properties of the facing. As seen in Figure 2.21, Wall 4, which had a vertical facing with fixed block-block and block-geosynthetic interfaces, had the smallest displacements. Wall 1, which had a vertical facing with frictional interfaces performed the worst, but increasing the wall batter (Wall 3) or fixing the block-block interface (Wall 2) improved performance.

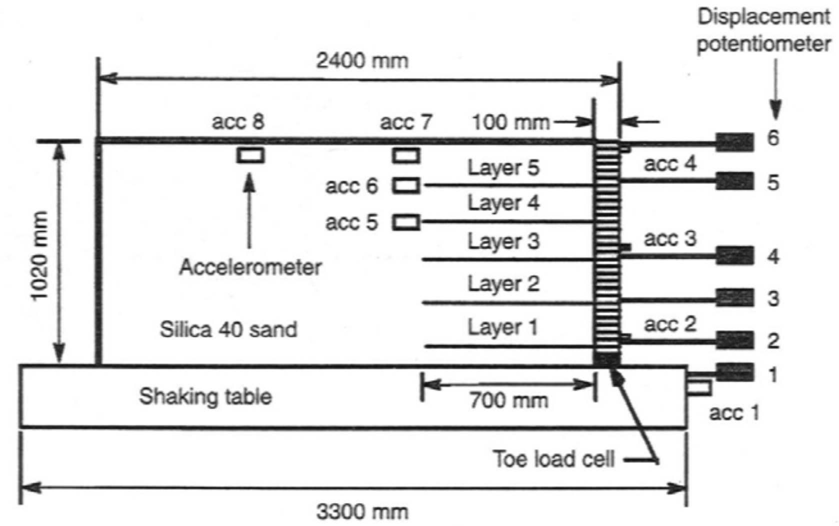

(a)

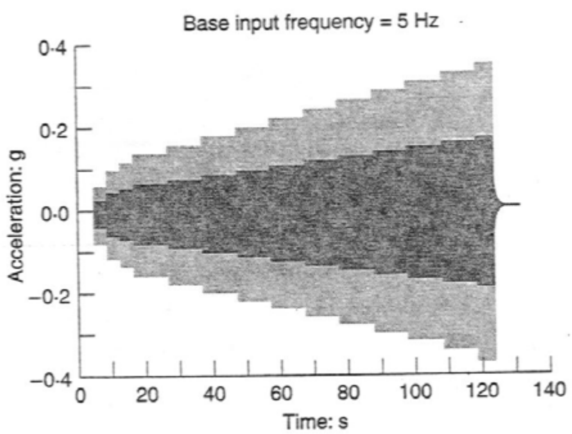

(b)

Figure 2.20. Shaking table test setup for tests by Bathurst *et al.*: (a) typical test arrangement (b) base input acceleration (Bathurst *et al.*, 2002)

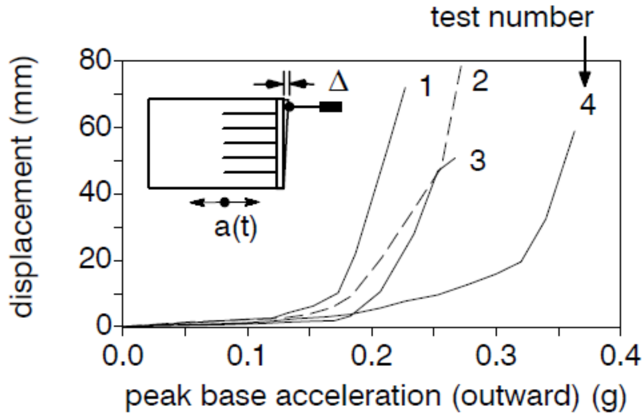

Figure 2.21. Displacement close to top of wall versus peak base acceleration for the different wall configurations tested (Bathurst *et al.,* 2002)

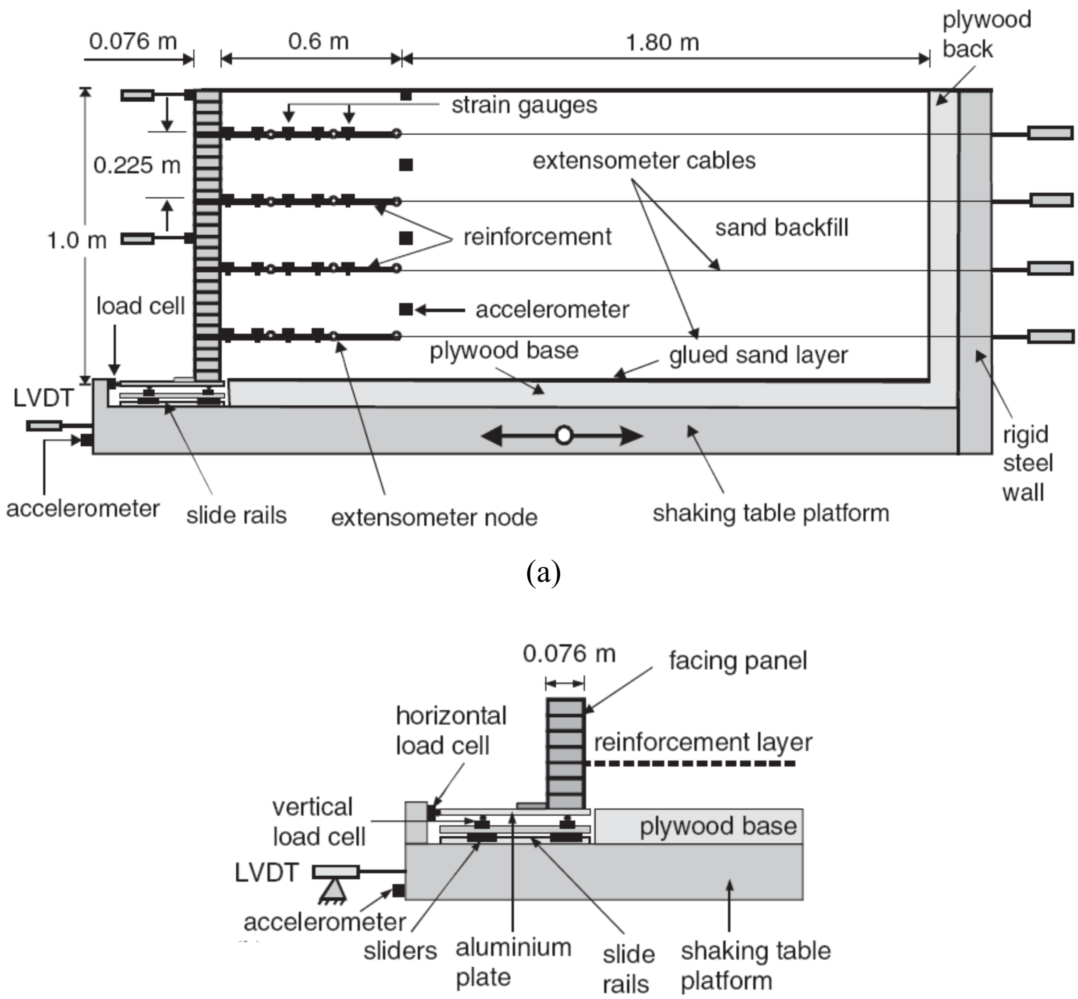

(b)

Figure 2.22. Shaking table test setup for tests by El-Emam and Bathurst: (a) typical test arrangement (b) detail of instrumented toe (El-Emam and Bathurst, 2007)

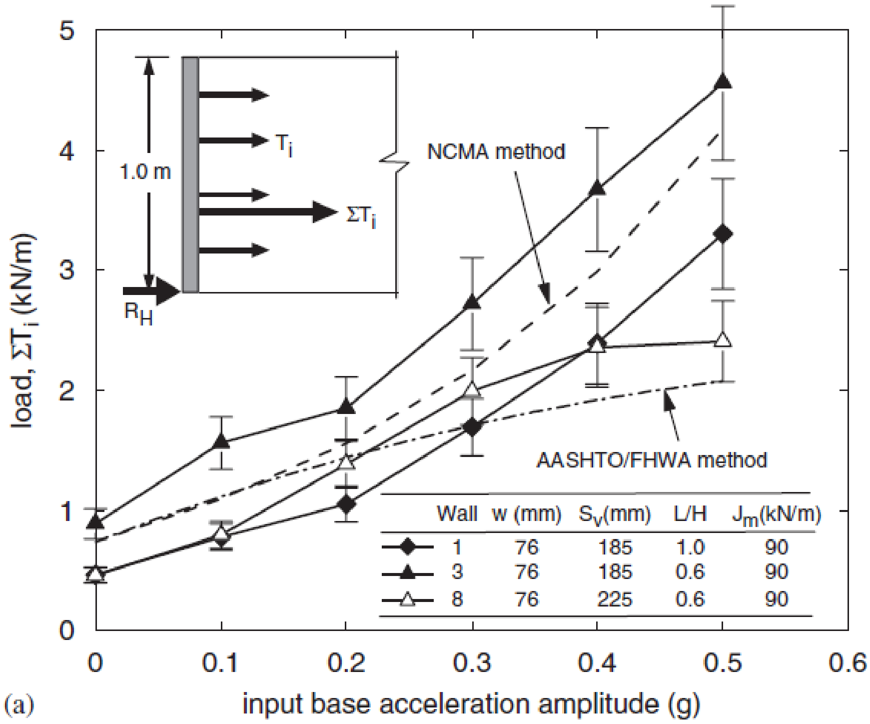

(a)

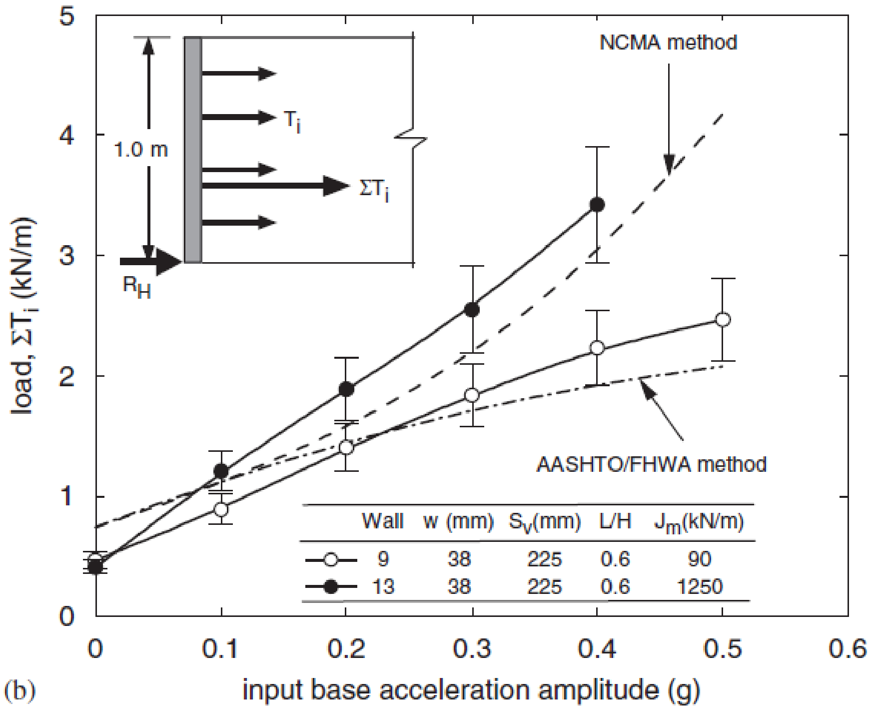

(b)

Figure 2.23. Measured and predicted sum of connection loads for model walls with different reinforcement parameters versus peak input base acceleration amplitude: (a) influence of reinforcement geometry (b) influence of reinforcement stiffness (El-Emam and Bathurst, 2007)

As summarized in Table 2.1, El-Emam and Bathurst (2004, 2005, 2007) conducted shaking table tests on one meter high 1/6 scale models with rigid facing panels. Shaking table test setup they utilized is shown in Figure 2.22. Their studies showed that lateral displacement, acceleration amplification factors, and total reinforcement connection loads decreased and magnitude of critical acceleration increased with increasing reinforcement length and increasing number of reinforcement layers. Increasing the reinforcement length reduced the total seismic-induced earth forces acting at the back of the facing. NCMA and AASHTO/FHWA design methodologies were shown to under-predict the value of total earth forces, as seen in Figure 2.23 comparing the sum of connection loads measured to total seismic-induced earth forces assumed in design.

3. TEST SETUP

3.1. General

In this chapter, the scaling laws used to model the prototype wall and the shaking table, materials and instruments used in testing will be introduced. Then the general test setup will be presented. Finally, the properties of the eight different test setups and description of the earthquake record applied for each of these eight tests will be given.

3.2. Similitude

Iai (Iai, 1989) used the basic equations governing the equilibrium and the mass balance to derive similitude rules for shaking table tests conducted in 1 g gravitational field. His rules are applicable within low and intermediate strain levels, so can be used in tests where the major concern is the deformation rather than the ultimate state of stability. The scaling factors derived by Iai that are applicable in this study are given in Table 3.1 along with the calculated values for 1:2 and 1:4 scale tests performed.

Table 3.1. Scaling factors given by Iai and corresponding values in this study

Variable	**Scaling factor (prototype/ model)**	**Scaling factor value for 1:2 scale tests**	**Scaling factor value for 1:4 scale tests**
x (length)	λ	2	4
ρ_s (density of soil)	λ_ρ	1	1
ε (strain of soil)	λ_ε	1	1
t (time)	$(\lambda\,\lambda_\varepsilon)^{0.5}$	$\sqrt{2}$	2
σ (stress in soil)	$\lambda\,\lambda_\rho$	2	4
u (displacement)	$\lambda\,\lambda_\varepsilon$	2	4
$\dot{u}$ (velocity)	$(\lambda\,\lambda_\varepsilon)^{0.5}$	$\sqrt{2}$	2
$\ddot{u}$ (acceleration)	1	1	1
n (porosity)	1	1	1

3.3. Shaking Table

The uniaxial shaking table ANCO R-148 at the Kandilli Observatory and Earthquake Research Institute (KOERI) of Boğaziçi University was used in this study. This servo-hydraulic actuator driven, 3x3 shaking table was manufactured by Anco Engineers, Inc., and it can be used to test objects up to ten tons weight over a frequency range of 0-50 Hz. The welded steel tabletop has tapped holes for attaching test objects. To be able to produce the required linear horizontal motion, the table has precision ground rails engaging eleven roller linear bearings on the base. The system has two hydraulic pumps to supply a total of 60 GPM at 3000 Psi. There is also a set of accumulators in the hydraulic system to provide for peak flow and return flow capture during high velocity seismic events and to provide sufficient pilot flow for control during main system depressurization.

The actuator has a ±12 cm stroke and has two three-stage 200 GPM Moog servo-valves. The Moog servo-valve and GS actuator are controlled by a GS2000 analog control servo-loop, servo-controller. The digital control system supplies the table displacement signals to the servo-controller and the servo-controller attempts to control the actuator to match this signal. The controller provides for closed-loop control of motion on translation along the horizontal axis.

Earthquake records of acceleration are given as input data to control the motion of shaking table using a sixteen channel Data Physics 550 WIN digital data control and acquisition system, which is also used for data acquisition. A feedback accelerometer mounted on the table sends the acceleration information to the digital control system and this system sends an analog drive signal to the actuator servo-controller. The system has anti-aliasing filters for the sixteen input channels.

Figure 3.1 shows the shaking table dual loop control system. The GS servo controller requires a displacement command whereas the DP digital controller uses an acceleration command. This difference in expectation is adjusted for in the equalization process done in the self test.

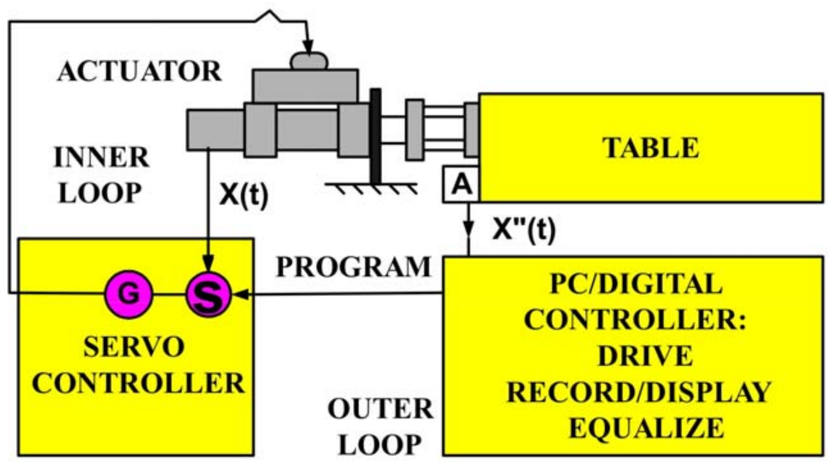

Figure 3.1. Table dual loop control system (ANCO Engineers, 2010)

Figure 3.2 shows the achievable motion and five per cent response spectrum for the shaking table with a test specimen mass of ten tons. The table has a peak nominal table motion (input to test specimens) of 24 cm peak-to-peak displacement, peak velocity of approximately ±1.2 m/s, and peak acceleration (with a ten-ton payload) of approximately ±2.0g (Boğaziçi University Department of Earthquake Engineering, 2009).

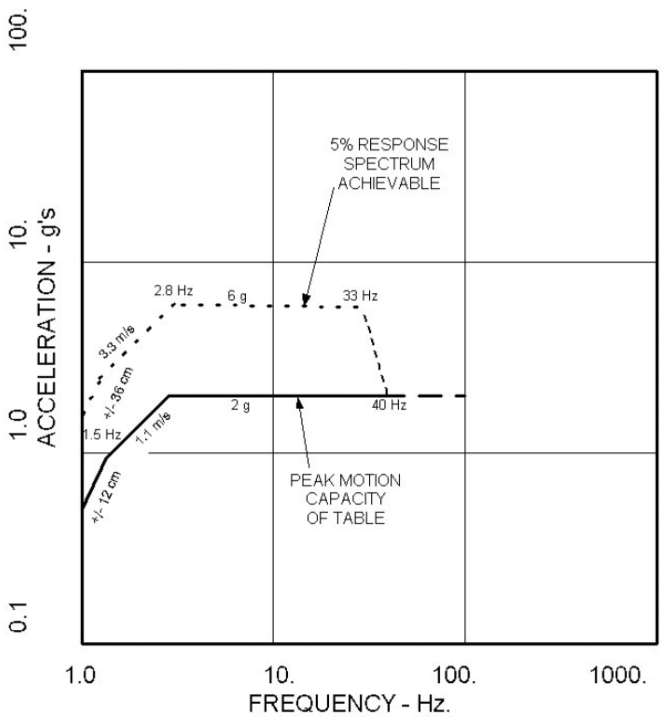

Figure 3.2. Achievable motion and five per cent response spectrum for R-148 table with ten tons test specimen (Boğaziçi University Department of Earthquake Engineering, 2009)

3.4. Materials Constituting the Model GRS Wall

3.4.1. Geotextile

The geosynthetic reinforcement used in testing was a woven polyester geotextile with tensile strength T_{ult} = 40 kN/m and ultimate strain ε_{ult} = 11 per cent. The same geotextile was used in all eight different setups.

3.4.2. Soil Fill

The grain size distribution curve for the soil which was taken from Kilyos and used in this study is shown in Figure 3.3. The coefficient of uniformity, C_u, is found to be 9.13 and the coefficient of curvature, C_c, is 1.17 from the grain size distribution curve. The percentage of fines (passing sieve no. 200) was six per cent, and the fraction passing sieve no. 4 was non-plastic, so the soil is classified as well-graded silty sand (SW-SM) according to the Unified Soil Classification System.

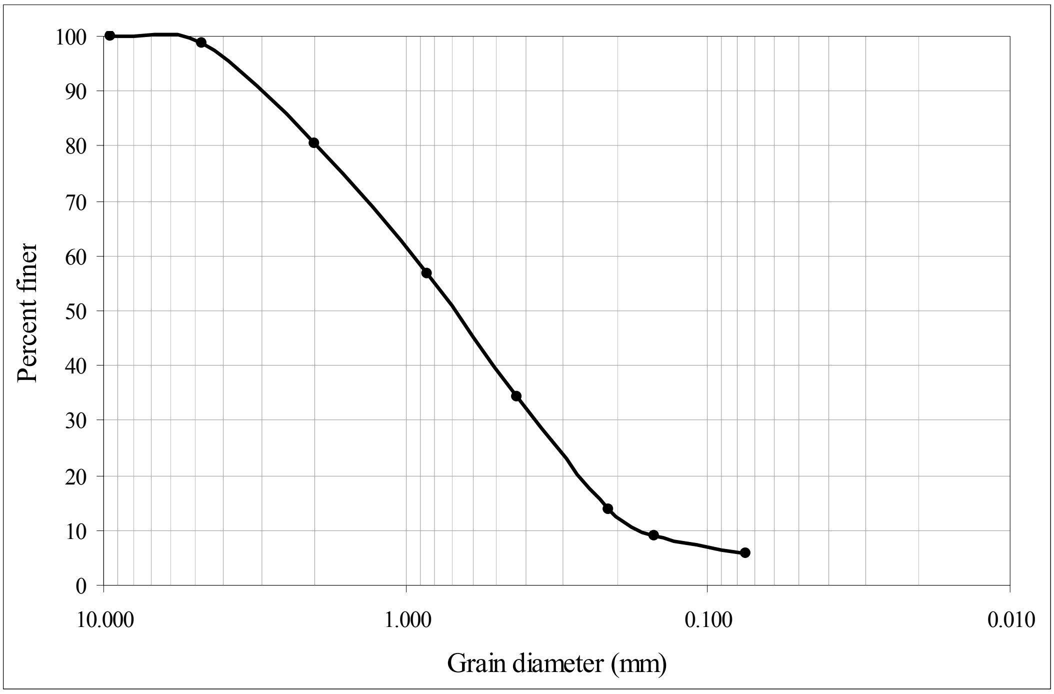

Figure 3.3. Grain size distribution for the soil used in this study

Figure 3.4 and Table 3.2 show the specimen parameters and the CD triaxial test results for the soil used in the study.

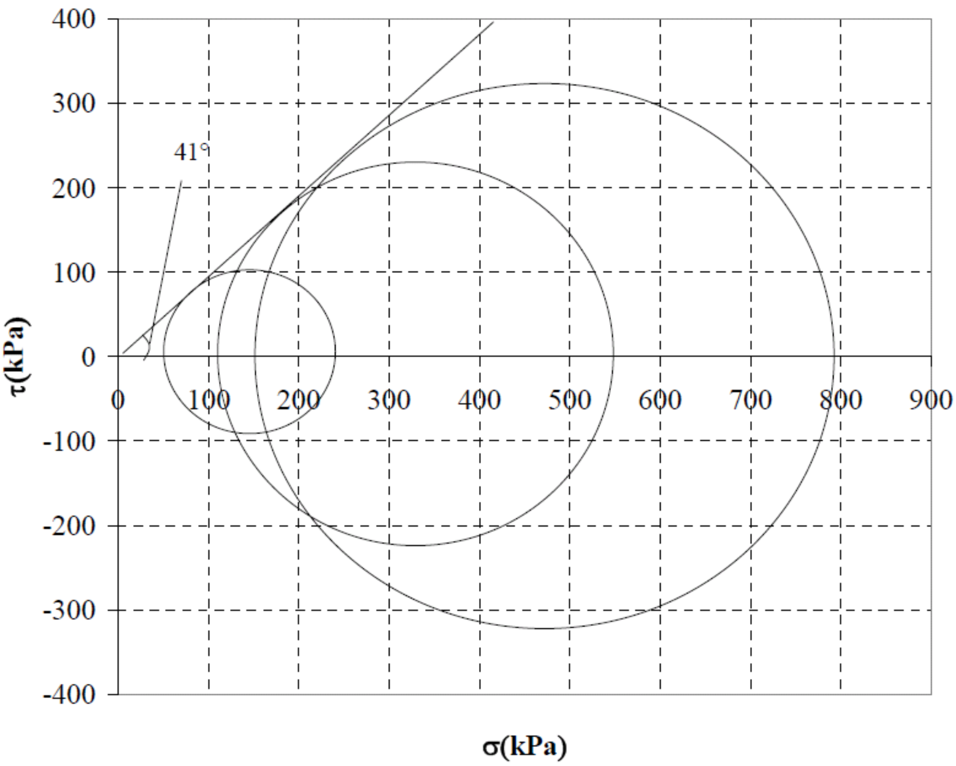

Figure 3.4. Determination of internal friction angle from triaxial test (Enünlü, 2007)

Table 3.2. Specimen parameters and soil properties determined from triaxial test (Enünlü, 2007)

Specimen	γ (kN/m^3)	void ratio	σ_3 (kPa)	σ_1 (kPa)	*E* (kPa)	*E* average (kPa)	φ (°)
S3	17.20	0.51	50	231	17075	29180	41
S6	17.08	0.52	100	545	24722		
S4	17.71	0.47	150	782	45731		

During testing on the shaking table, it was aimed in the compaction process to produce unit weights as close to the triaxial specimens' as possible. The soil was used at its natural water content which was about four per cent. Variations of soil properties among individual tests are presented in Section 3.7.

3.4.3. Facing Blocks

Scaled-down concrete blocks were used to represent the 40x20x20 cm concrete facing blocks with double holes used in the construction of GRS walls. For the 1:2 model walls, the block size was 20x10x10 cm and for the 1:4 scale it was 10x5x5 cm. The 20x20x10 cm block had a single hole that was dimensioned to equate its overall unit weight to the prototype block and the 10x5x5 cm block had no hole due to geometry limitations. The blocks are shown in Figure 3.5.

(a)

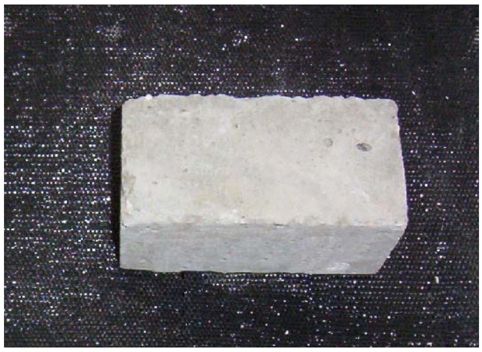

(b)

Figure 3.5. Photographs of facing blocks used: (a) 1:2 scale, 20x20x10 cm concrete blocks (b) 1:4 scale, 10x5x5 cm facing blocks

3.5. Supplementary Materials and Equipment for Constructing the Model Wall

The model wall was constructed in a steel container manufactured for this purpose. The 3x3 meters size and ten tons carrying capacity of the shaking table limited the size of the steel container. The depth of the model wall had to be maximized to represent the prototype as closely as possible. To be able to test a model wall with two meters height, the steel container dimensions were chosen as height = 215 cm, depth = 278 cm, and width = 53 cm. These dimensions resulted in a total weight of about nine tons on the shaking table. The steel container was fastened to the shaking table using eight bolts on each side.

During the construction of the model wall, the back five centimeters was filled with tire-shred rubber to minimize the reflection of earthquake waves from the back of the steel container.

To minimize the friction at the sides of the wall, the inner sides of the steel container were greased and lined with floating rubber sheets with 6 mm thickness for the first two wall setups. For the consequent tests, polyethylene insulation sheets that were much easier to handle were used to serve the same purpose.

A steel bar was welded to the base of the container in the front to prevent the forward movement of the first layer of facing blocks, so the first layer of the fill served as the base soil. After each layer of blocks and soil were placed, the soil was compacted using a Dynapac compactor to achieve the desired amount of compaction (Figure 3.6).

After all the construction and instrumentation was finished, a coated wire mesh was attached to the front frame for safety.

(a)

(b)

Figure 3.6. Photographs showing wall construction: (a) compaction and side linings (b) steel container and the constructed wall on the shaking table

3.6. Measuring Devices and Their Setup

3.6.1. Displacement Transducer to Measure the Shaking Table Displacement

LD600-100 High Accuracy DC Long Stroke Displacement Transducer manufactured by Omega Engineering was used to measure the displacement of shaking table during testing. This transducer has a linear stroke of ±100 mm, sensitivity of 2.00 mV/V/mm, response time 100 Hz, and linearity 0.25 per cent. This transducer was mounted on a heavy concrete block and positioned in front of the shaking table such that the tip of its core touched the shaking table in its central position before testing began (Figure 3.7).

Figure 3.7. Photograph showing the setup of long stroke displacement transducer, optical laser distance sensors, and accelerometers on the wall face

3.6.2. Optical Laser Distance Sensors to Measure Wall Face Displacement

ODSL 8/V4-400-S12 Optical Laser Distance Sensors manufactured by Leuze Electronic were used to measure the displacement of the wall face. These sensors measure distances between 20 and 400 mm with a resolution of 0.1 mm at 200 Hz frequency.

The optical laser distance sensors were fastened on adjustable supports mounted on a post (Figures 3.7, 3.8, 3.14). The positions of the sensors in individual tests are given in Section 3.7. The supports were adjusted so that the sensors were 20 to 30 cm away from the wall face before shaking started. The readings were then corrected by subtracting the intial distance readings to obtain the displacement measurements.

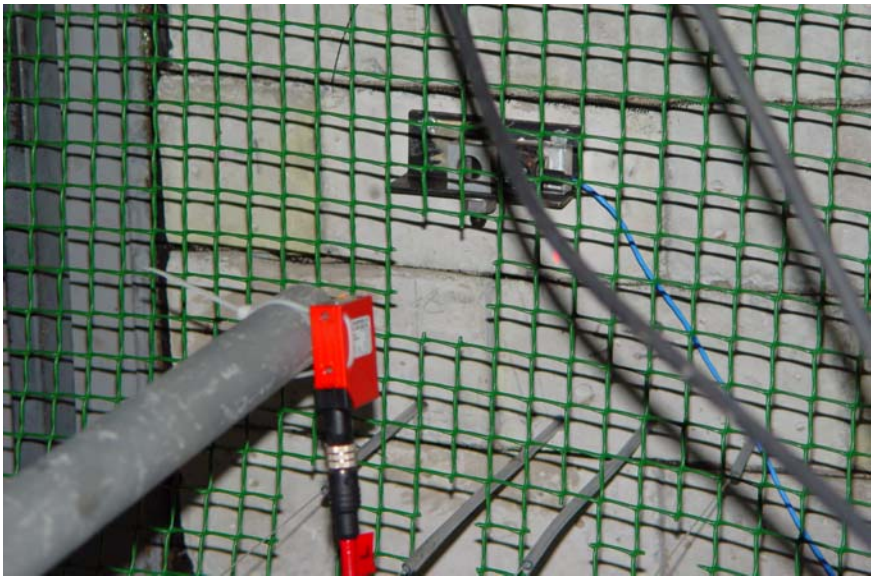

Figure 3.8. Optical laser distance sensor measuring the distance to the wall face through an opening in the wire mesh

3.6.3. Transducers to Measure Geotextile Displacements

Balluff Micropulse AT Transducers (model: BTL6-A110-M200-A1-S115) (Figure 3.9) were used to measure the geotextile displacements. This transducer contains a waveguide enclosed by an aluminum housing. When the magnet manufactured to be used with this transducer is attached to the moving object such that it can move over the top of the transducer’s housing while keeping a distance of four to eight mm, its position is constantly measured and recorded. The nominal stroke for the chosen type of transducer is 200 mm.

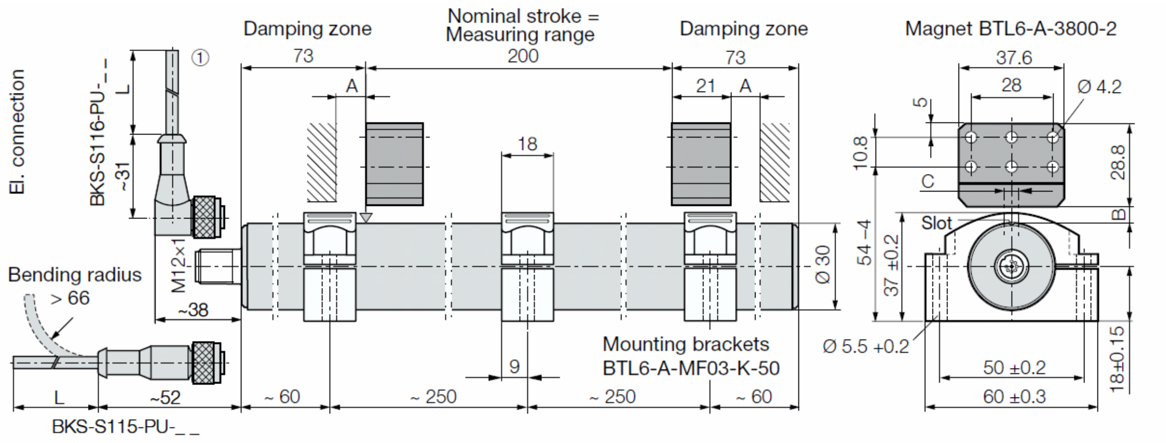

Figure 3.9. Dimensional drawing of BTL6-A110-M200-A1-S115 Micropulse AT Transducer (Balluff Data Sheet)

Eight of these transducers were mounted on a post at two levels to enable the measurement of geotextile displacements at 40 and 160 cm heights (Figure 3.10a). The aim of measuring geotextile displacements was to find the strains in the geotextile during shaking. Therefore for each geotextile reinforcement corresponding to these two heights, three adjacent regions were chosen for taking strain measurements and the magnets transmitting the movement to the transducer were connected to the boundaries of these regions (Figure 3.11). The positions of these boundaries are given in Section 3.7 for each test setup. For transferring the horizontal displacements of one geotextile layer to the magnets, four fishing lines were wrapped around four thin nails attached to the geotextile at the region boundaries. The buried parts of these fishing lines were placed in serum tubes that passed through pre-drilled holes in the facing blocks (seen in Figure 3.8). The ends of fishing lines connected to the geotextile were covered with geotextile patches to avoid damage during construction and testing. Special attention was given to keep these lines straight and horizontal.

The displacement in the horizontal direction was transferred into a vertical displacement using pulleys. The four fishing lines were then attached to the magnets with suspended weights. Each magnet moved on four brass guide rods to ensure that the distance between the magnet and the LVDT was kept between four and eight mm (Figure 3.10b). As a result, the magnets were able to move upward and downward the same distance as the selected points on the geotextiles moved backward and forward.

(a) (b)

Figure 3.10. Setup of the Micropulse AT Transducers measuring the geotextile displacements: (a) the complete post (b) detail of transducer set for one geotextile layer

Figure 3.11. The three regions on geotextile for which strain measurements are sought

After testing, the time histories of average strains in the three regions were calculated by finding the relative displacements between two adjacent boundaries and dividing by the initial distances between the boundaries.

3.6.4. Accelerometers

PCB Piezotronics 3801G3FB3G accelerometers (Figure 3.12) were used to measure the table, wall face and top soil accelerations. One accelerometer was mounted on the shaking table to measure the shaking table acceleration and give the shaking table system the necessary feedback. The accelerometers were connected to the data acquisition system of the shaking table and their readings were recorded at 81 Hz. The accelerometer mounted directly on the shaking table was also connected to the data acquisition system assembled for this study in order to synchronize the data recorded by the two independent systems.

The accelerometers on the face were screwed to metal plates attached rigidly to the concrete blocks (Figure 3.7). The accelerometers on the top were wrapped tightly in plastic bags and buried ten centimeters into the soil. The positions of the available eleven accelerometers in each test are given in Section 3.7.

Figure 3.12. The accelerometer used in the study

3.6. Final Wall Arrangement

A typical drawing and a typical photograph of the test setup constituted from the elements described in the preceding sections are shown in Figures 3.13 and 3.14. Drawings showing the typical locations of the measuring devices are given in Figures 3.15 and 3.16. The exact locations of individual devices will be given in the following section.

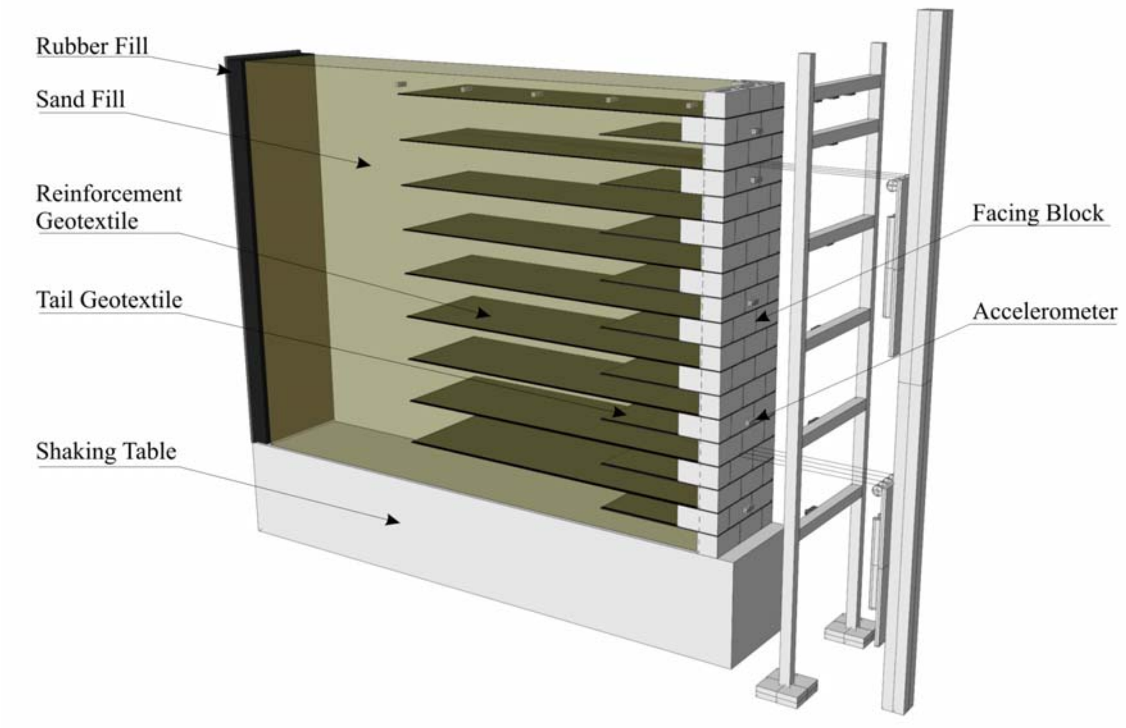

Figure 3.13. Drawing of the typical test setup

Figure 3.14. Typical photograph of test setup

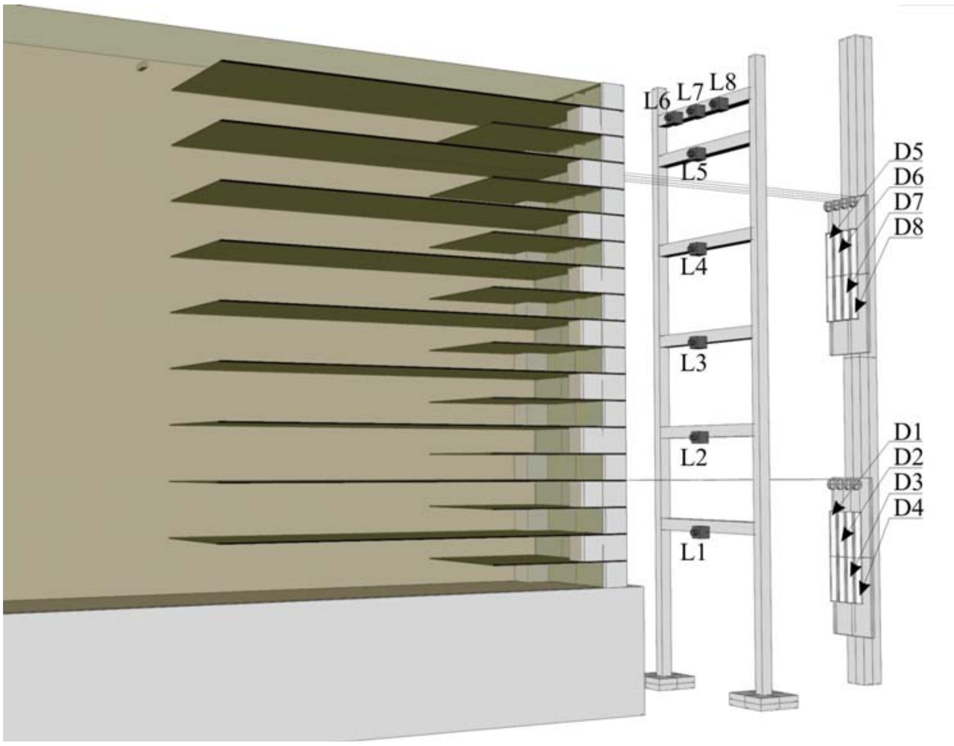

Figure 3.15. Setup of optical laser distance sensors (L1-L8) and geotextile displacement transducers (D1-D8)

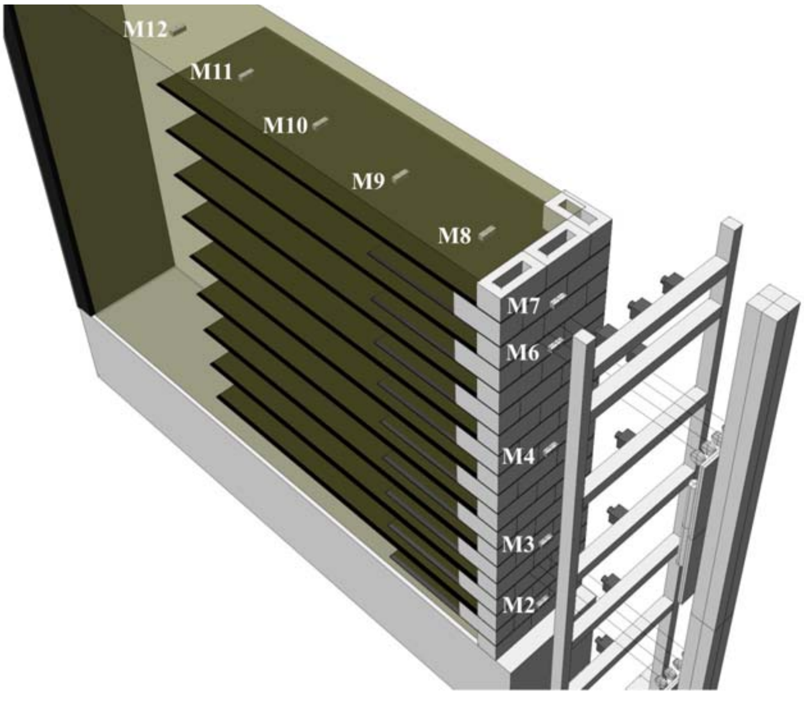

Figure 3.16. Setup of accelerometers on face (M2, M3, M4, M5, M6, M7) and accelerometers on top (M8, M9, M10, M11, M12)

3.7. Individual Test Configurations

Throughout this study, eight different GRS wall configurations were tested. Table 3.3 summarizes the test geometries for the eight configurations. Figures 3.17, 3.18, and 3.19 illustrate the geometries of model and prototype walls. Tables 3.4 and 3.5 give the locations of optical laser distance sensors and accelerometers for each configuration. Table 3.6 gives the locations of boundaries at which geotextile displacement measurements were taken. Properties of the compacted sand fill in each test are given in Table 3.7. The given unit weights were measured during dismounting of the model after the shaking sequence was completed.

Table 3.3. Summary of GRS wall configurations tested

<table>
<tr><th rowspan="2"></th><th colspan="8">Test Number</th></tr>
<tr><th>1</th><th>2</th><th>3</th><th>4</th><th>5</th><th>6</th><th>7</th><th>8</th></tr>
<tr><td>Model scale</td><td colspan="4">1:2</td><td colspan="4">1:4</td></tr>
<tr><td>Total reinforcement geotextile length, L (cm)</td><td>170</td><td>114</td><td colspan="2">85</td><td>42.5</td><td>85</td><td colspan="2">145</td></tr>
<tr><td>Total tail geotextile length, L_t (cm)</td><td colspan="2">50</td><td>N/A</td><td>-</td><td colspan="4">-</td></tr>
<tr><td>Reinforcement geotextile spacing, s_v (cm)</td><td colspan="2">20</td><td>10</td><td>20</td><td colspan="4">10</td></tr>
<tr><td>Wall height (cm)</td><td colspan="4">200</td><td>100</td><td colspan="3">200</td></tr>
<tr><td>Treatment of top two rows</td><td colspan="4">Fixed</td><td colspan="3">Free</td><td>Fixed</td></tr>
</table>

The last row in Table 3.3 gives the condition of top two rows for each test configuration. Treatment of the top two rows of facing blocks affects the performance of GRS walls, so different treatment conditions were used to evaluate the differences in performance. “Free” means only the reinforcing geotextile is placed in between and no other measure is taken to fix the top two layers. In the construction of GRS walls in practice, the top two rows are fixed to each other by filling the holes in the last two rows of blocks with cement mortar and placing steel bars in the mortar. These bars pass through the geosynthetic layer between these blocks. In this study, for the 1:2 scale configurations, the top two rows were “fixed” using the same method. For the 1:4 scale configurations with the top two layers "fixed", nine centimeters long nails were placed in pre-drilled holes to fix the top two block layers, as shown in Figure 3.20.

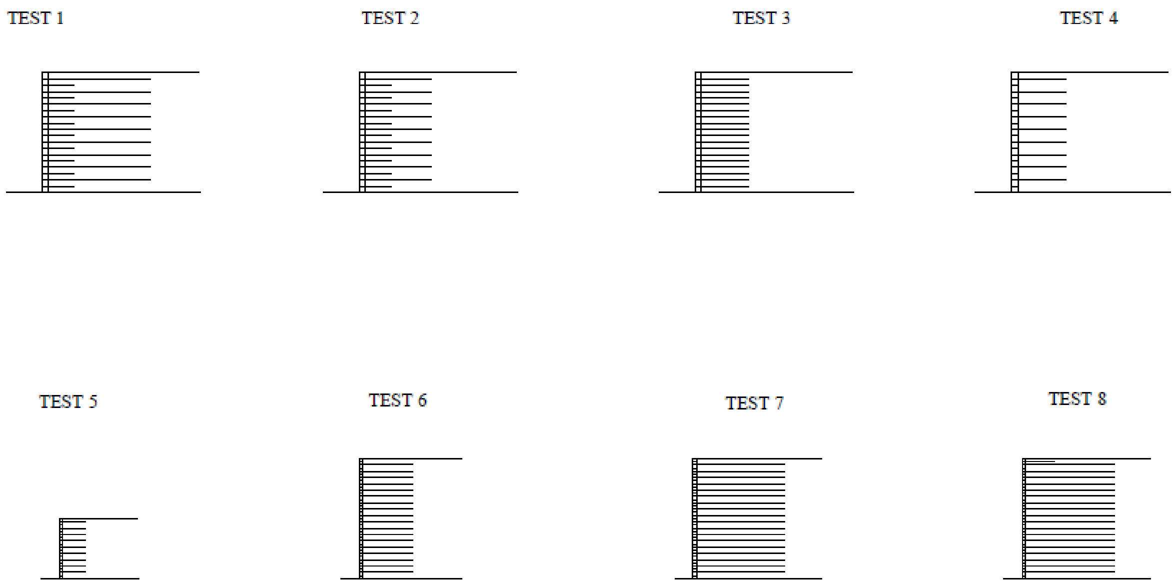

Figure 3.17. Geometries of the model walls tested

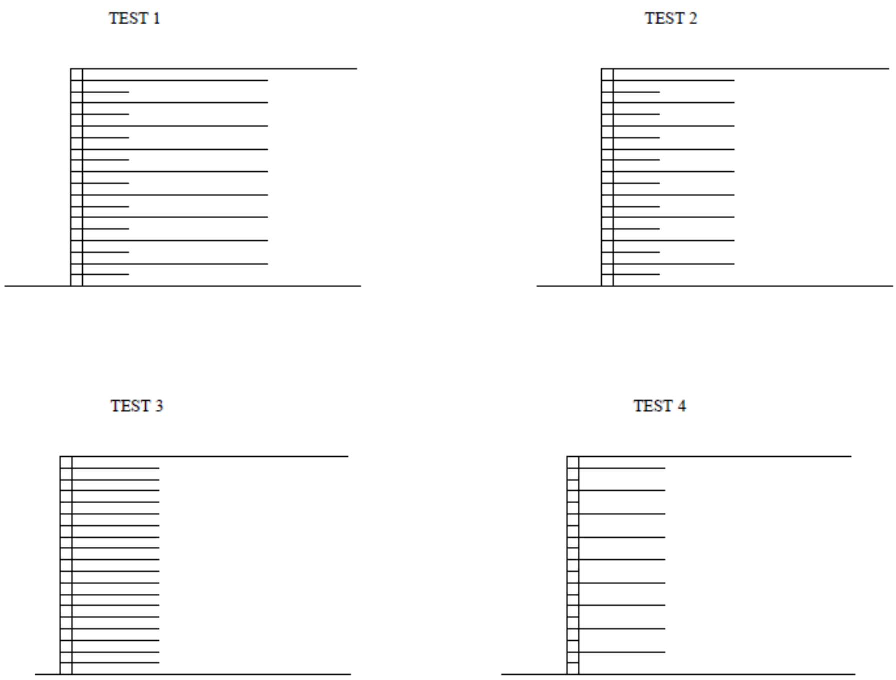

Figure 3.18. Geometries of the prototype walls for 1:2 scale models

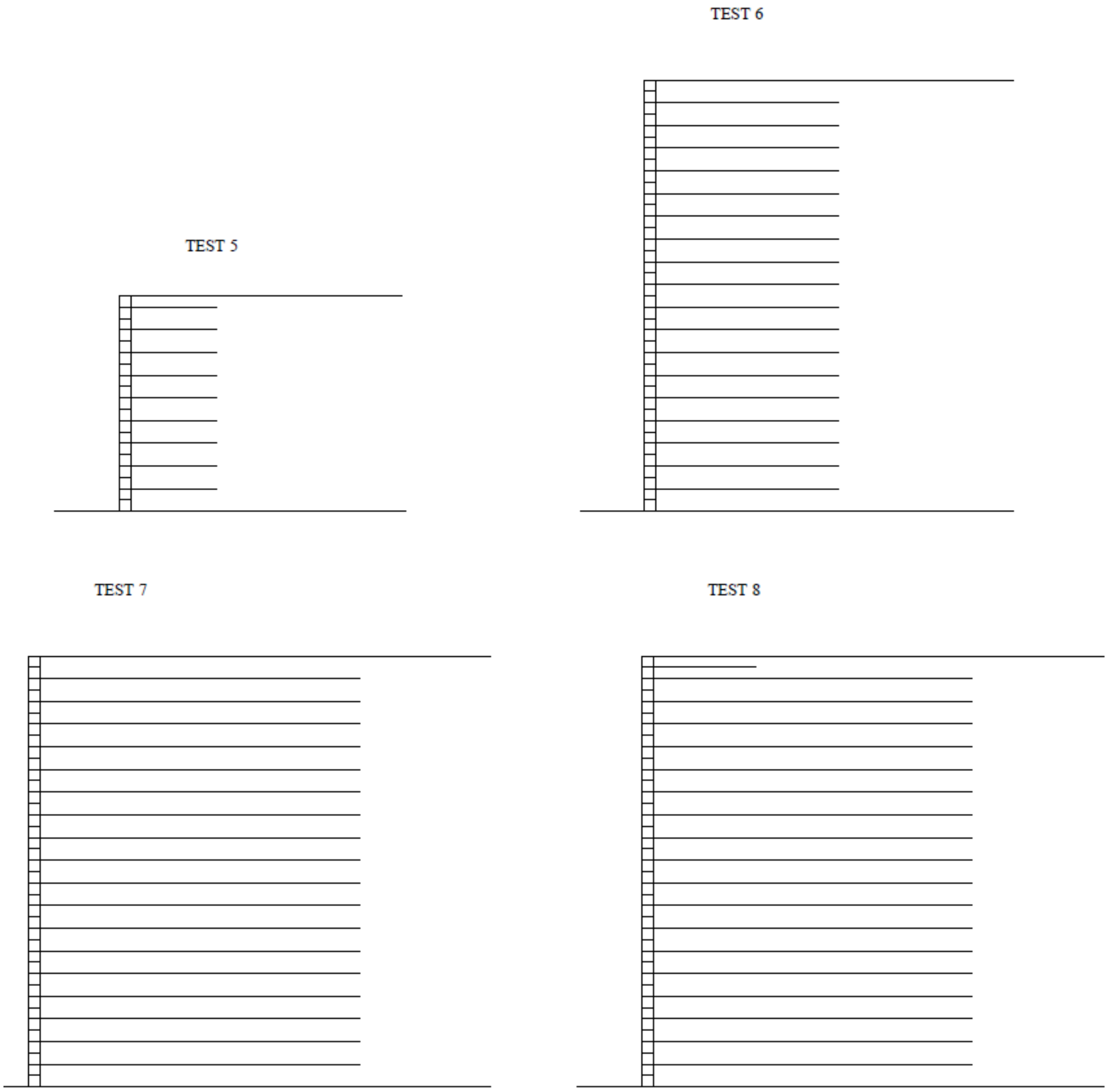

Figure 3.19. Geometries of the prototype walls for 1:4 scale models

Figure 3.20. Fixing the top two block layers in 1:4 scale tests

Table 3.4. Heights of optical laser distance sensors measured from bottom of GRS wall in centimeters

Optical Laser Distance Sensor	**Test Number**							
	1	**2**	**3**	**4**	**5**	**6**	**7**	**8**
L1	19.3				19.3	19.3		
L2	59.3				59.3	59.3		
L3	99.3				99.3	99.3		
L4	139.3				99.3	139.3		
L5	179.3				99.3	179.3		
L6	197.3				-	194.3		
L7	197.3				-	194.3		
L8	197.3				-	194.3		

Table 3.5. Location of accelerometers

	Test Number							
	1	**2**	**3**	**4**	**5**	**6**	**7**	**8**
Accelerometers on face:								
M2	15				18	22		
M3	55				59	59		
M4	108				85	110		
M6	160				-	161		
M7	180				-	182		
Accelerometers at the top:								
M8	30	35						
M9	70	110						
M10	110	185						
M11	150	260						
M12	190	275*						
Note: For accelerometers on face, value gives the height from bottom of GRS wall in cm. For accelerometers at the top, value gives the distance from the wall face in cm. * denotes that the accelerometer is buried in rubber fill.								

Table 3.6. Location of geotextile boundaries for strain measurement

	Test Number							
	1	**2**	**3**	**4**	**5**	**6**	**7**	**8**
Lower Geotextile Layer (h=40 cm):								
Boundary 1 (D1)	70	70	55	55	30	55	110	110
Boundary 2 (D2)	40	40	35	35	20	35	60	60
Boundary 3 (D3)	22.5	22.5	20	20	10	20	35	35
Boundary 4 (D4)	10	10	10	10	5	10	20	20
Upper Geotextile Layer (h=160 cm):								
Boundary 1 (D5)	150	98	55	55	-	55	110	110
Boundary 2 (D6)	90	90	35	35	-	35	60	60
Boundary 3 (D7)	60	60	20	20	-	20	35	35
Boundary 4 (D8)	20	20	10	10	-	10	20	20
Note: Values give the distance from back of facing block in cm. Abbreviation in parentheses indicates the geotextile displacement transducer used to measure the displacement of geotextile at that boundary.								

Table 3.7. Properties of the compacted sand fill

	Test Number							
	1	**2**	**3**	**4**	**5**	**6**	**7**	**8**
Unit weight (kN/m^3)	15.3	16.5	17	16.4	19	18.5	18.5	18.5
Water content (%)	3.7	3.9	5.3	5	4.7	4.6	4.6	4.6
Dry unit weight (kN/m^3)	14.7	15.9	16.1	15.6	18.1	17.7	17.7	17.7
Approximate relative density	0.2	0.4	0.43	0.34	0.76	0.7	0.7	0.7
Internal friction angle	36°	38°	38°	37°	42°	41°	41°	41°

The approximate relative density values given in Table 3.7 were calculated assuming that the minimum dry unit weight is 14 kN/m^3 and the maximum dry unit weight was 20 kN/m^3 for the sand used. The internal friction angle values given in Table 3.7 were determined from the correlation chart given in Figure 3.21, using the borderline between uniform coarse sand and well-graded medium sand.

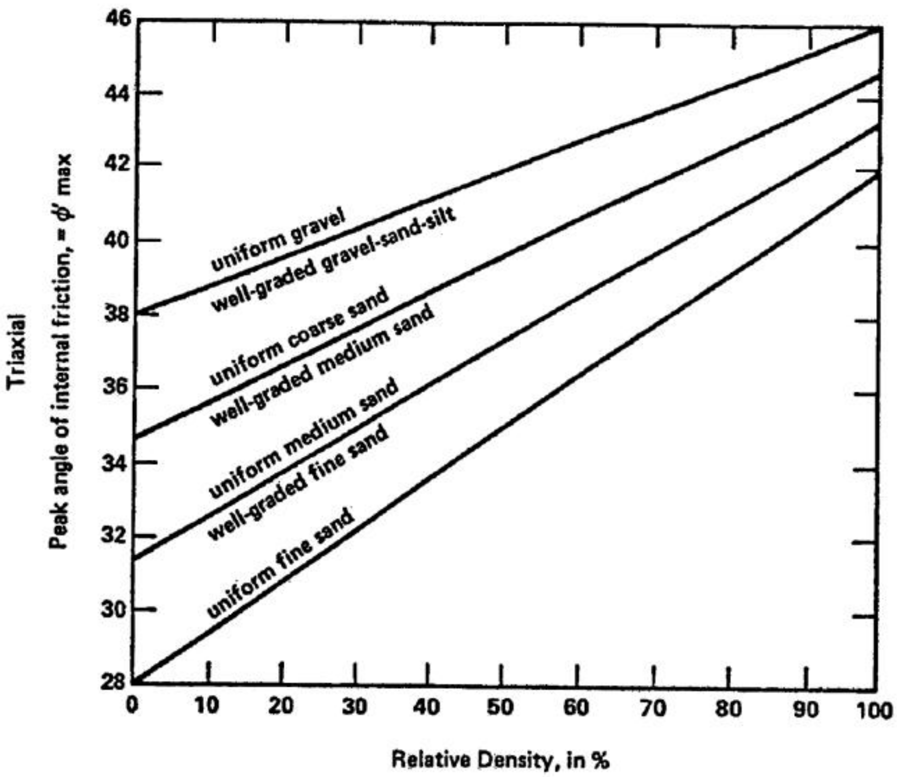

Figure 3.21. Correlation of peak internal friction angle with relative density (Schmertmann, 1978)

3.8. Applied Earthquake Record

The original El Centro Earthquake record shown in Figure 3.22 was scaled by increasing the frequency so that the values on the time axis are divided by square root of two for 1:2 scale tests and by two for 1:4 scale tests, in accordance with the rules given in Section 3.2. In the last test (Test No. 8), which was a 1:4 scale test, the frequency was increased by both square root of two and by two for comparison. The complete list of applied earthquake records is given in Table 3.8. The acceleration records showing the shaking table response to the input record for all runs are presented in Appendix A.

Table 3.8. Testing sequence and list of applied earthquake records: (a) 1:2 scale tests (b) 1:4 scale tests

(a)

Test no.	**1**			**2**			**3**			**4**		
Test date	19.04.2006			02.05.2006			01.02.2007			09.02.2007		
Total geotextile length (cm)	170			114			85			85		
Tail geotextile length (cm)	50			50			85					
Model scale	1/2			1/2			1/2			1/2		
Treatment of top two rows	Fixed			Fixed			Fixed			Fixed		
Frequency (f denotes original El Centro record frequency)	√2 f			√2 f			√2 f			√2 f		
a_{max} (g)	Run	Kandilli*	Study**	Run	Kandilli*	Study**	Run	Kandilli*	Study**	Run	Kandilli*	Study**
	1-1 (10%)	0.04513	0.43582	2-1 (30%)	0.087801	1.44588	3-1 (20%)	0.06753	0.10607	Part 1:		
(Runs are numbered according to testing order)	1-2 (20%)	0.08223	0.12631	2-2 (50%)	0.114969	0.14166	3-2 (30%)	0.08576	0.12898	4-1 (20%)	0.060687	0.0784
	1-3 (30%)	0.0859	0.15233	2-3 (70%)	0.209763	0.22486	3-3 (40%)	0.16097	0.2222	4-2 (30%)	0.08621	0.12294
	1-4 (40%)	0.11074	0.17703	2-4 (80%)	0.210664	0.25128	3-4 (50%)	0.1441	0.24047	4-3 (40%)	0.1147	0.13293
	1-5 (50%)	0.12184	0.14996	2-5 (20%)	0.056944	0.0886	3-5 (60%)	0.14843	0.19783	4-4 (50%)	0.12518	0.18352
	1-6 (60%)	0.184	0.25508	2-6 (100%-1)	0.318752	0.34875	3-6 (70%)	0.19629	0.24562	4-5 (60%)	0.16187	0.1809
	1-7 (70%)	0.20187	0.22487	2-7 (100%-2)	0.249829	0.25934	3-7 (80%)	0.25053	0.2588	4-6 (70%)	0.18876	0.25011
	1-8 (80%)	0.22231	0.29678	2-8 (100%-3)	0.294607	0.31571	3-8 (90%)	0.25303	0.33068	4-7 (80%)	0.25918	0.27677
	1-9 (90%)	0.24461	0.29018	2-9 (30%-2)	0.100118	0.08027	3-9 (100%-1)	0.27172	0.29826	4-8 (90%)	0.26716	0.31317
	1-10 (100%-1)	0.29572	0.36027	2-10 (60%)	0.145496	0.1998	3-10 (100%-2)	0.28038	0.35305	4-9 (100%-1)	0.30339	0.33542
	1-11 (100%-2)	0.27588	0.35341	2-11 (100%-4)	0.271765	0.29108				4-10 (100%-2)	0.2569	0.2875
										Part 2:		
										4-11 (2x20%)	0.11008	0.16668
										4-12 (2x40%)	0.20351	0.24044
										4-13 (2x50%)	0.24021	0.32445
										4-14 (2x60%)	0.33159	0.34073
										4-15 (2x70%)	0.39768	0.50791
										4-16 (2x80%)	0.48884	0.44749
										4-17 (2x90%)	0.57179	0.58686
										4-18 (2x100%-1)	0.6217	0.71764
										4-19 (2x100%-2)	0.6094	0.68514

Table 3.8. Continued

(b)

Configuration no.	5			6			7			8		
Test date	13.02.2007			15.02.2007			20.02.2007			22.02.2007		
Total geotextile length (cm)	42.5			85			145			145		
Tail geotextile length (cm)	-			-			-			-		
Model scale	1/4			1/4			1/4			1/4		
Treatment of top two rows	Free			Free			Free			Fixed		
Frequency (f denotes original El Centro record frequency)	2 f			2 f			2 f			√2 f, 2f		
a_{max} (g)*	Run	Kandilli*	Study**	Run	Kandilli*	Study**	Run	Kandilli*	Study**	Run	Kandilli*	Study**
	5-1 (2x20%)	0.127	0.14432	6-1 (2x20%)	0.093351	0.14945	7-1 (2x20%)	0.09865	0.1219	√2 f		
(Runs are numbered	5-2 (2x30%)	0.15685	0.18618	6-2 (2x30%)	0.133	0.16925	7-2 (2x30%)	0.14081	0.17241	8a-1 (20%)	0.068401	0.08204
according to testing	5-3 (2x40%)	0.20653	0.2535	6-3 (2x40%)	0.22143	0.27121	7-3 (2x40%)	0.26068	0.2765	8a-2 (30%)	0.08367	0.12184
order)	5-4 (2x50%)	0.34828	0.30493	6-4 (2x50%)	0.29025	0.32423	7-4 (2x50%)	0.25156	0.24397	8a-3 (40%)	0.12218	0.1336
	5-5 (2x60%)	0.3027	0.32741	6-5 (2x60%)	0.30506	0.35009	7-5 (2x60%)	0.30512	0.33724	8a-4 (50%)	0.1509	0.1453
	5-6 (2x70%)	0.42121	0.49078	6-6 (2x70%)	0.37434	0.36402	7-6 (2x70%)	0.39719	NaN	8a-5 (60%)	0.21607	0.19975
	5-7 (2x80%)	0.41597	0.3931	6-7 (2x80%)	0.38756	0.38492	7-7 (2x75%)	0.39787	0.4409	8a-6 (70%)	0.22519	0.2133
	5-8 (2x90%)	0.49368	0.55159	6-8 (2x90%)	NaN	~ 2	7-8 (2x80%)	0.52071	0.57261	8a-7 (80%)	0.28444	0.26694
	5-9 (2x100%)	0.58916	0.56955	(Failure)			7-9 (2x85%)	0.44481	0.44557	8a-8 (90%)	0.29265	0.30057
							7-10 (2x90%)	0.46783	0.44757	8a-9 (100%)	0.36535	0.3977
							7-11 (2x95%)	0.51865	0.52879	2 f		
							7-12 (2x100%)	0.5836	0.55372	8b-1 (2x20%)	0.10331	0.16011
										8b-2 (2x30%)	0.13408	0.17937
										8b-3 (2x40%)	0.21407	0.22018
										8b-4 (2x50%)	0.27629	0.31147
										8b-5 (2x60%)	0.32551	0.34732
										8b-6 (2x70%)	0.37246	0.38153
										8b-7 (2x80%)	0.43376	0.45292
										8b-8 (2x90%)	0.50167	0.5165
										8b-9 (2x100%)	0.49392	0.49673

* Value shows the maximum outward acceleration measured by the shaking table facility's own data acquisition system.

** Value shows the maximum outward acceleration measured by the system established for this study.

The expressions in parantheses next to the run number indicate the scale of the input earthquake record to the original El Centro Earthquake record.

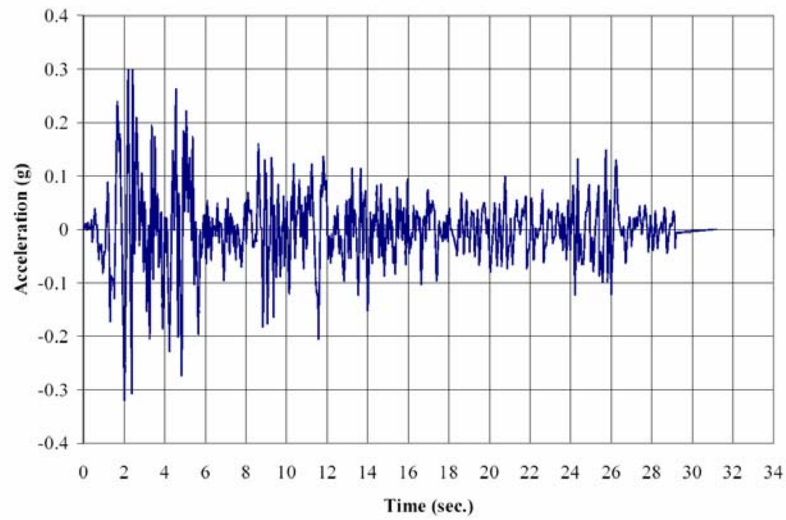

Figure 3.22. Original record of the North-South component of El Centro Earthquake

4. RESULTS

4.1. Data Acquisition and Analysis

Two separate systems of data acquisition were utilized in this study. The data from the accelerometers were recorded by the shaking table facility's own data acquisition system and the data from all the other devices were recorded using the system prepared for this study, which utilized the software VI Logger. The accelerometer on the shaking table (M1) was connected to both of the systems to check and synchronize the data.

Two Matlab codes were written to analyze the data automatically in a standardized way. One code deals with the displacement measurements and the other with the acceleration measurements. Since the data acquisition system utilizing the VI Logger software did not have the ability to start and end data acquisition simultaneously with the shaking table's own data acquisition system and had to be actuated manually, it was necessary to choose the correct duration for the displacement measurements.

The code dealing with displacement measurements, named displacement.m, reads all the recorded raw data and as the first step, matches the table acceleration measurements taken with the two different systems and tries to extract the correct duration. To do this, the first time value (tref1) for which the table acceleration exceeds three times the standard deviation and the time value for the last record are found for the records measured by shaking table's own system. Then the table acceleration data recorded by the manually started system is normalized by subtracting the mean and filtered using an averaging window size of ten (this size is chosen to achieve consistency with the shaking table's system's sampling frequency; it is increased if the visual inspection of the overlapped data shows the matching is not satisfactory). Then the time value (tref2) for which the acceleration exceeds three times the standard deviation is found. This time value is matched with tref1, and the redundant values in the beginning and end of the manually started system's records are truncated. Finally, the two acceleration records are plotted on the same graph and visually inspected. This is necessary since the acceleration records do not match perfectly. If the match is not satisfactory, a higher multiple of standard deviation is chosen to find the acceleration values for which the reference times are matched, or the window size of the filter is increased and visual inspection is repeated.

After the correct duration is obtained, the face displacements are calculated and plotted against time. Then the same process is repeated with face displacements relative to table, displacements of geotextile, geotextile strains and geotextile stresses. The maxima and minima for all these variables, the time values for these maxima and minima, permanent face displacements and permanent geotextile strains are recorded in a separate file in the meanwhile. Finally, a simple animation showing the movement of wall face during shaking is created.

The file acceleration.m starts with reading all the acceleration data and combining them in a single matrix. Accelerations measured by all accelerometers and accelerations relative to shaking table are plotted against time. The maxima and minima for these variables and the time values for these maxima and minima are recorded.

The two codes are executed for each test run, 98 times in total. The most important outcomes are presented in the following sections and in the Appendices.

4.2. Acceleration Records

Accelerations records for all test runs are given in Appendix A. The plots contain the results from both data acquisition systems and show how the systems are matched.

The shaking table acceleration records, the increase in accelerations relative to the shaking table measured by the accelerometers on the wall face, and the increase in accelerations relative to the shaking table measured by the accelerometers buried in the soil at the top are given in Figures 4.1 to 4.27 for the shaking with the highest maximum table acceleration in each of the eight tests. The shaking table acceleration records shown here are the ones measured by the shaking table facility's own system, so all the acceleration records have the same sampling frequency. For the second part of Test 4 and for Tests 5 and 6, only M8 measurements were recorded at the top due to an error in the shaking table facility's system.

It is observed from Figures 4.1 to 4.27 that measured accelerations increase from bottom to top on wall face and back to front on top. Accelerations measured by M7 and M8, uppermost accelerometer on face and front accelerometer on top, respectively, are highest. Peak values obtained from acceleration records are used in Sections 4.5 to 4.10 in evaluating the effects of various parameters on acceleration on wall face and top.

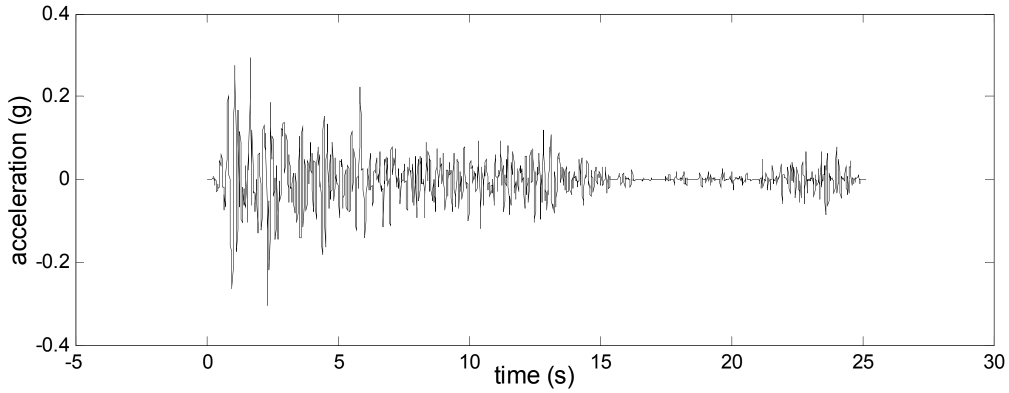

Figure 4.1. Shaking table acceleration record for Test 1-10

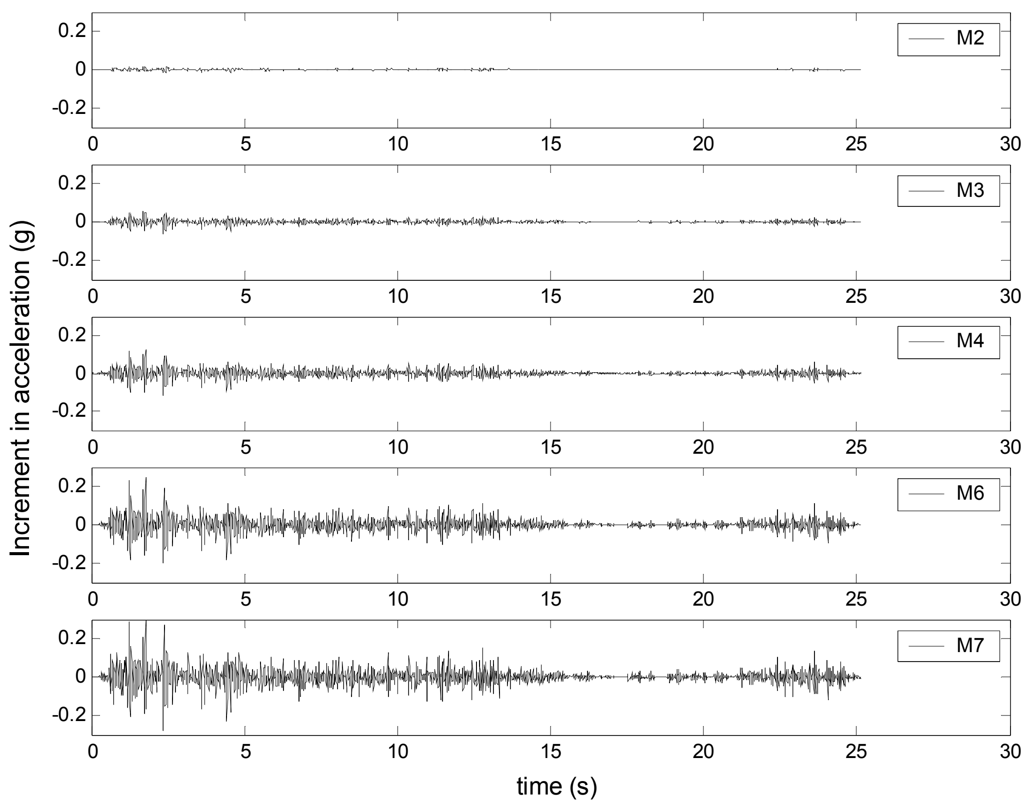

Figure 4.2. Record of increase in acceleration on wall face (bottom to top) for Test 1-10

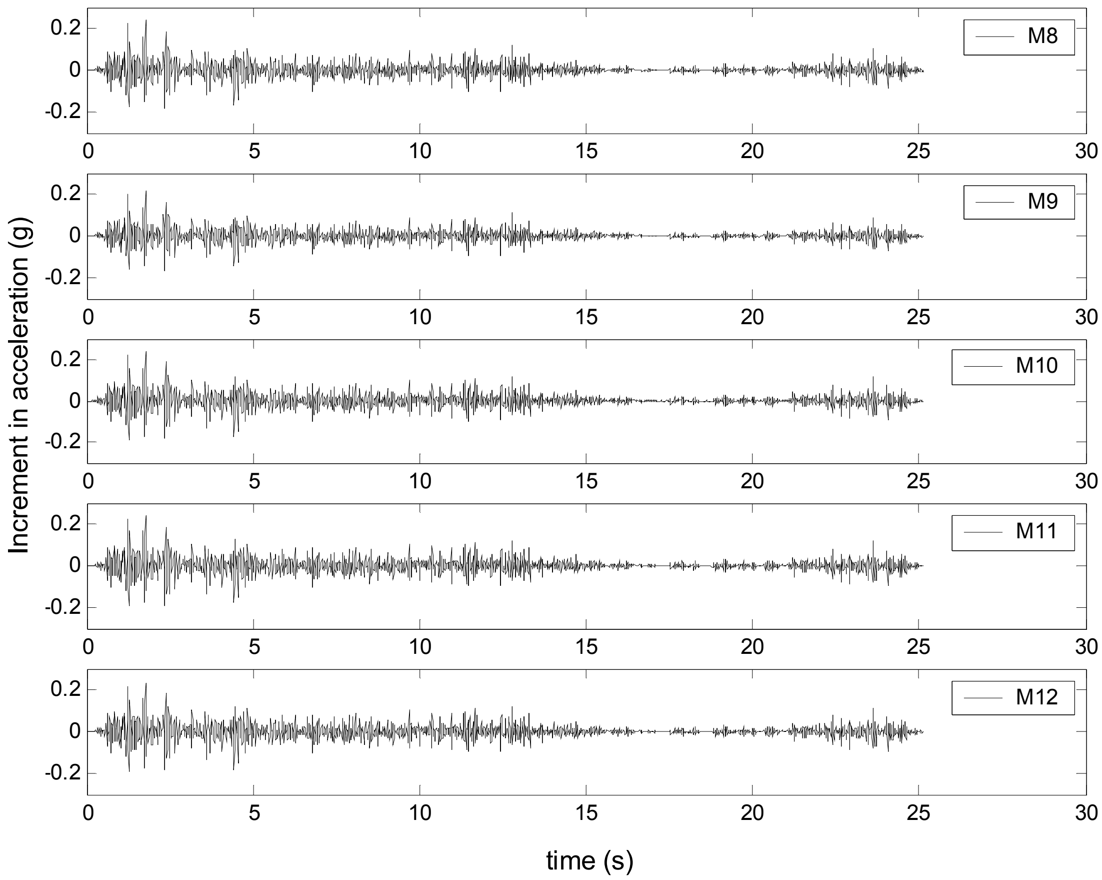

Figure 4.3. Record of increase in acceleration on top (front to back) for Test 1-10

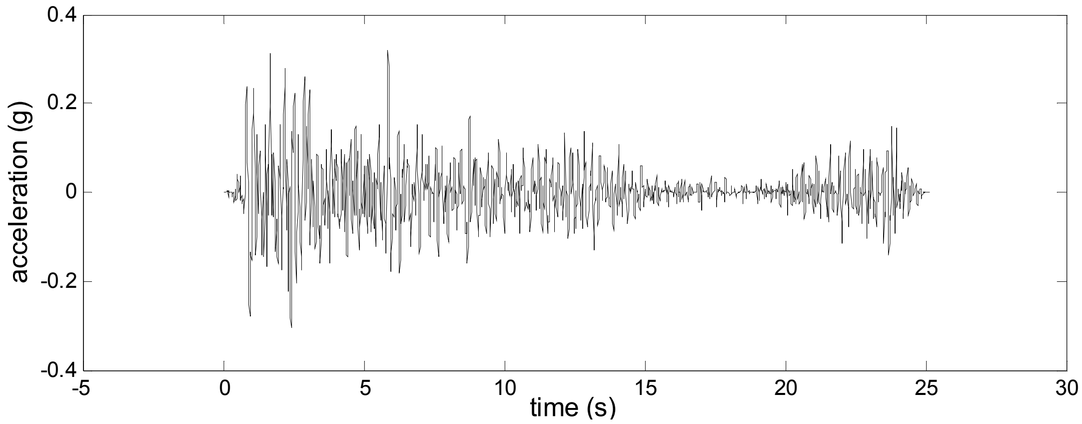

Figure 4.4. Shaking table acceleration record for Test 2-6

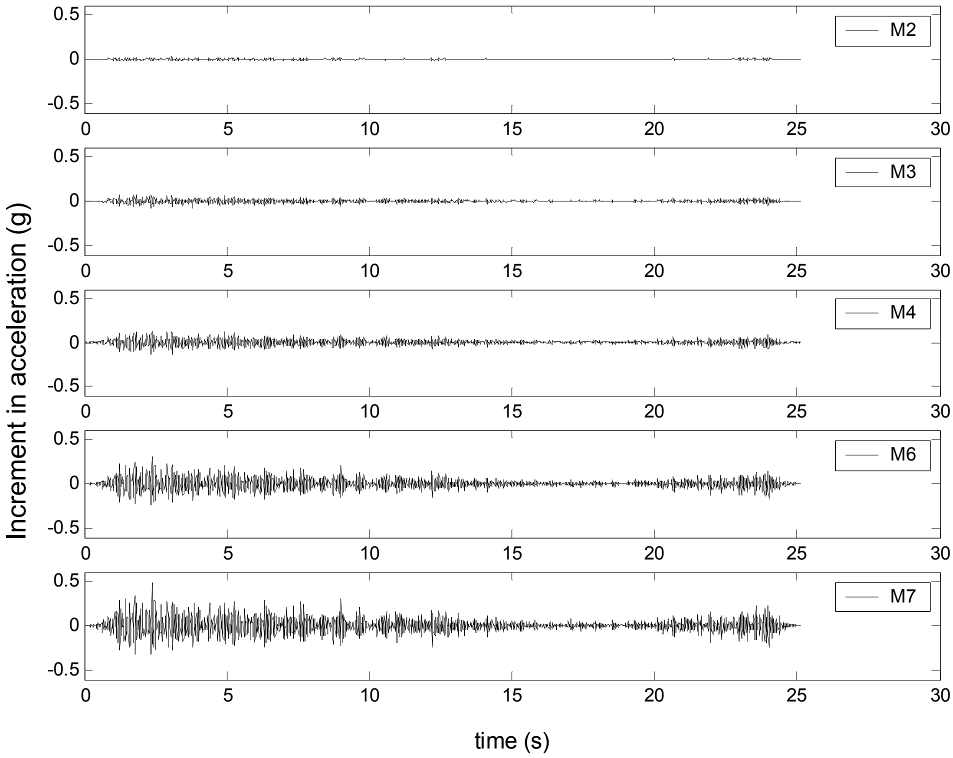

Figure 4.5. Record of increase in acceleration on wall face (bottom to top) for Test 2-6

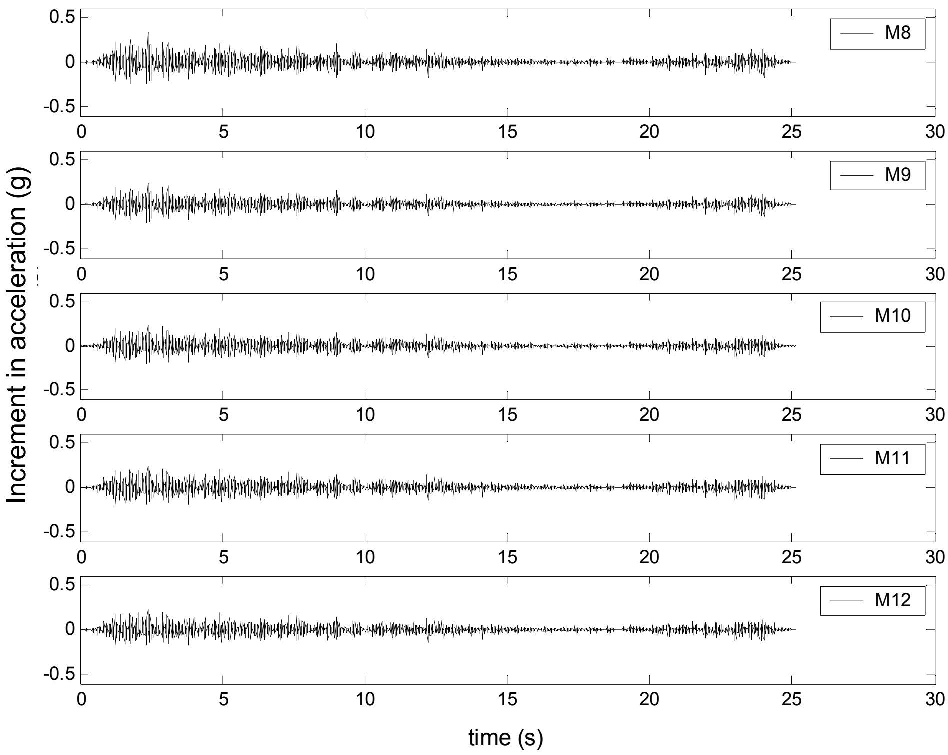

Figure 4.6. Record of increase in acceleration on top (front to back) for Test 2-6

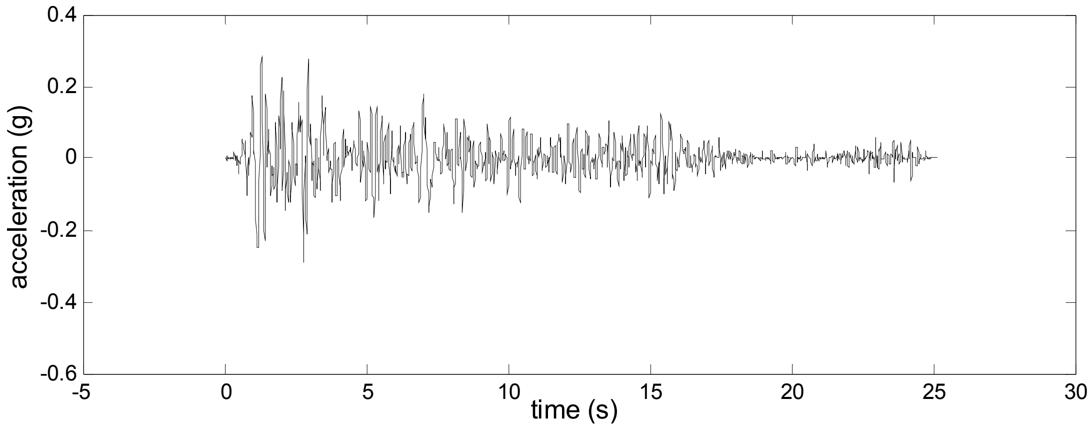

Figure 4.7. Shaking table acceleration record for Test 3-10

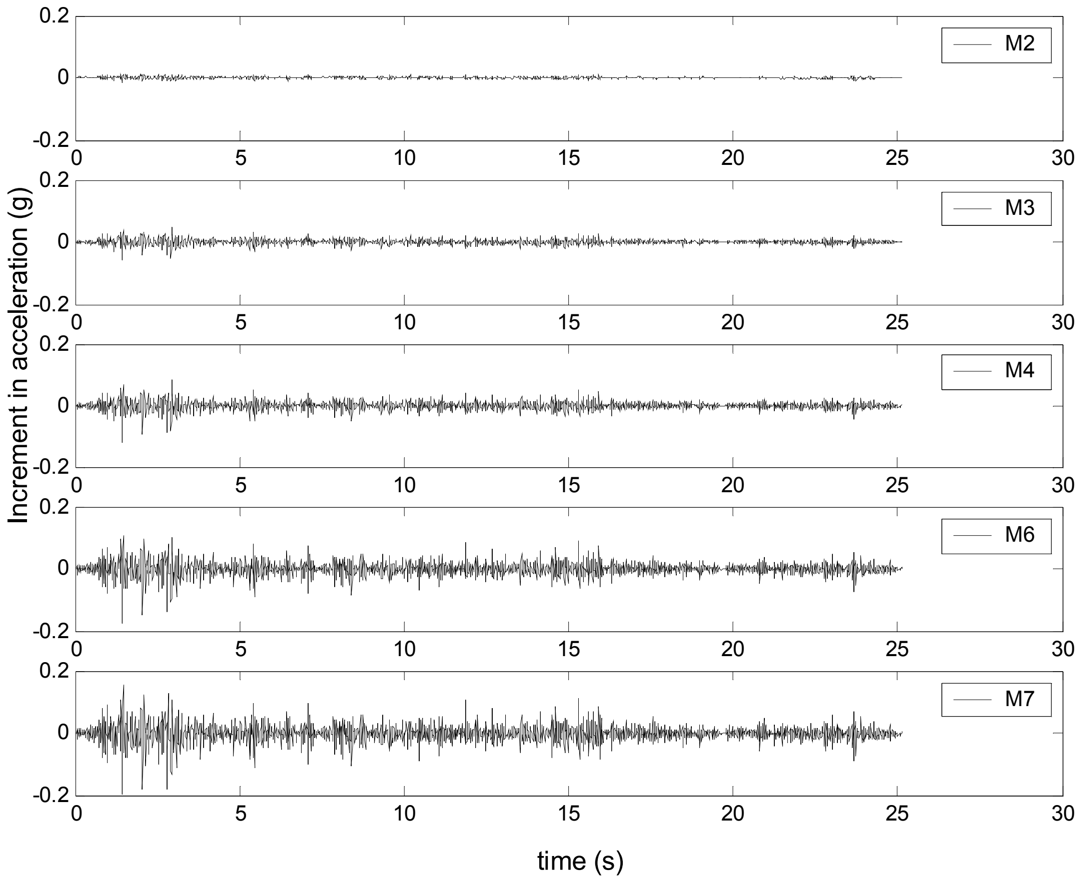

Figure 4.8. Record of increase in acceleration on wall face (bottom to top) for Test 3-10

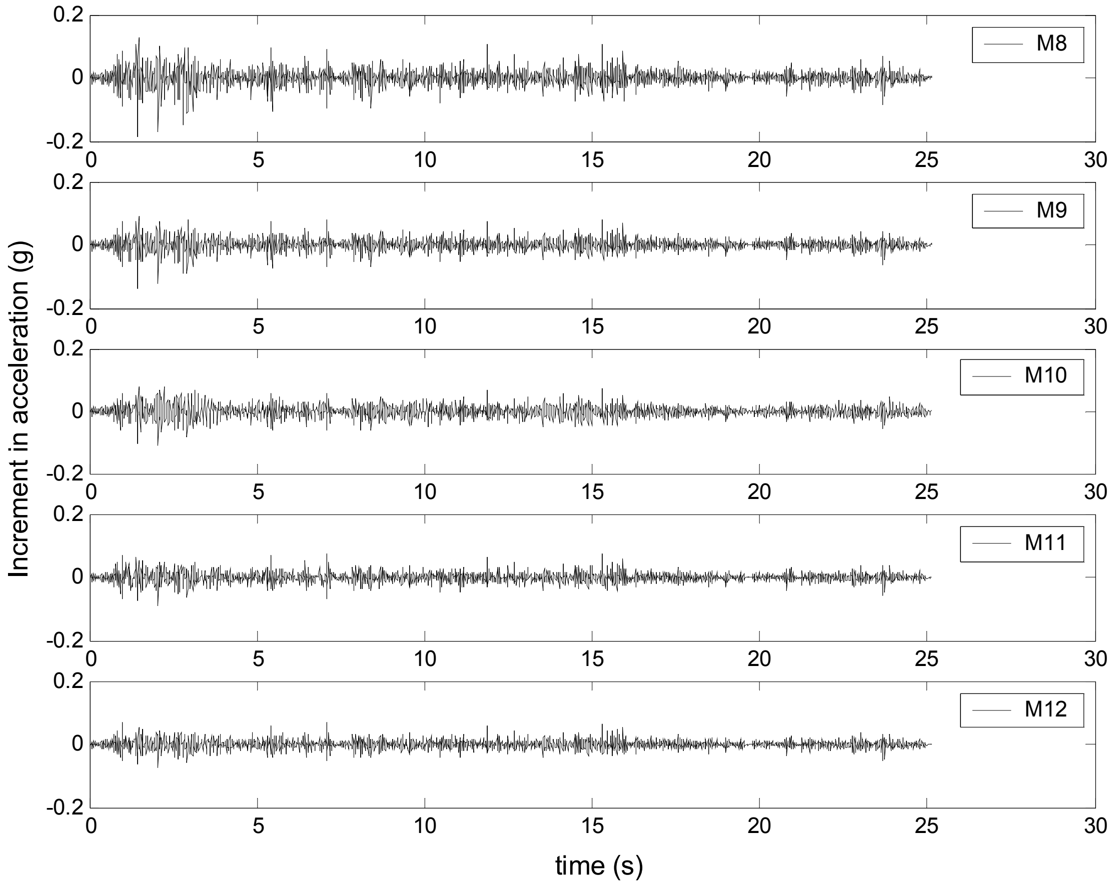

Figure 4.9. Record of increase in acceleration on top (front to back) for Test 3-10

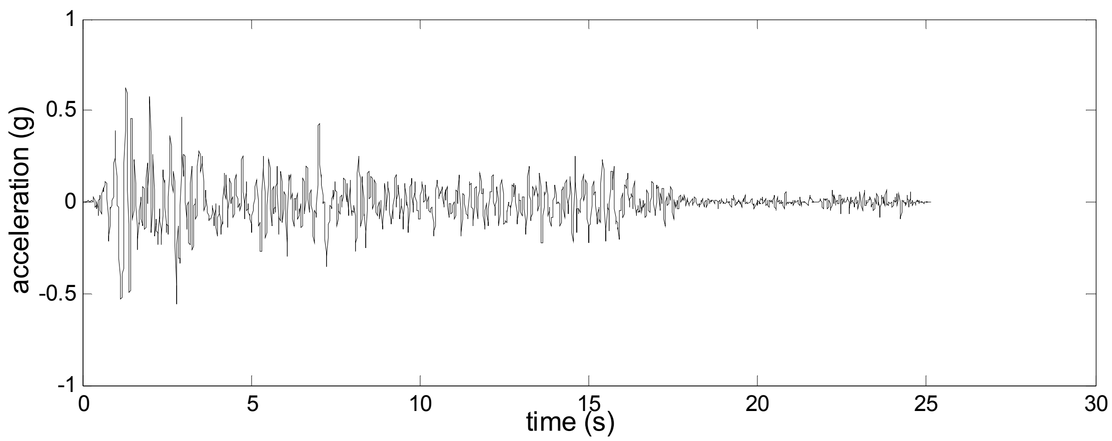

Figure 4.10. Shaking table acceleration record for Test 4-18

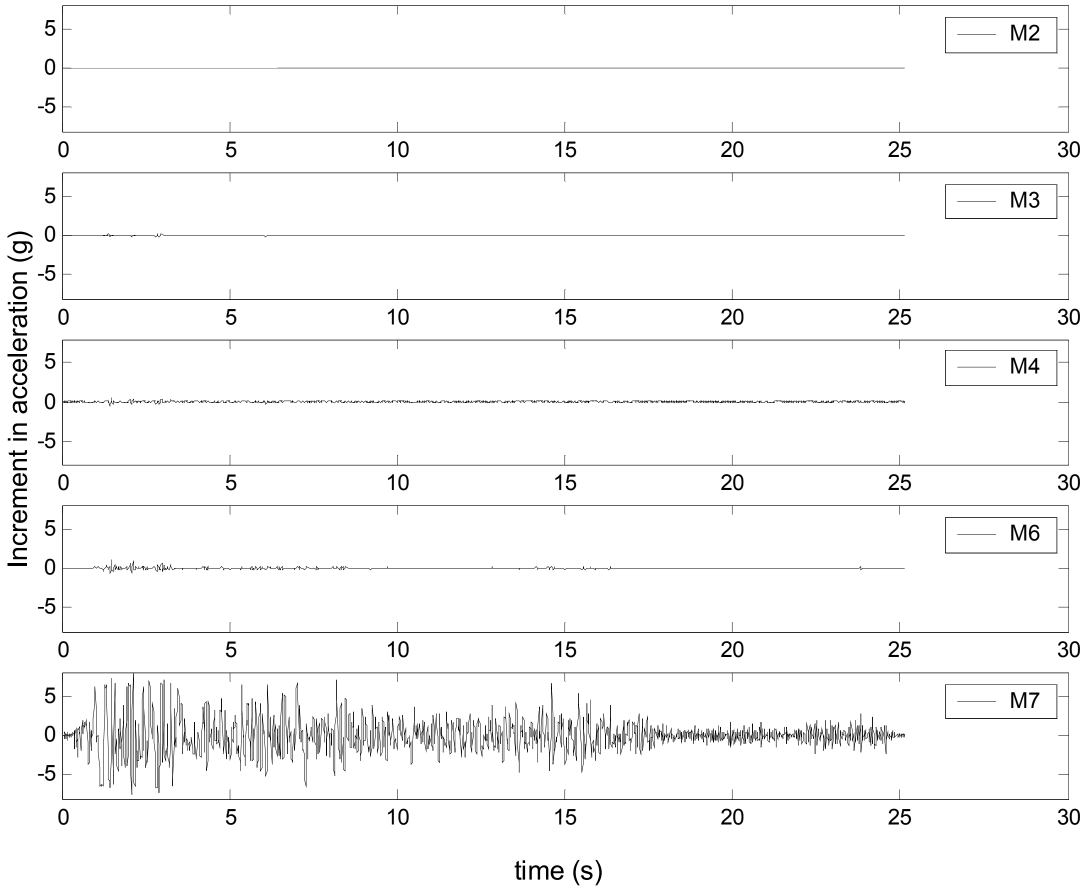

Figure 4.11. Record of increase in acceleration on wall face (bottom to top) for Test 4-18

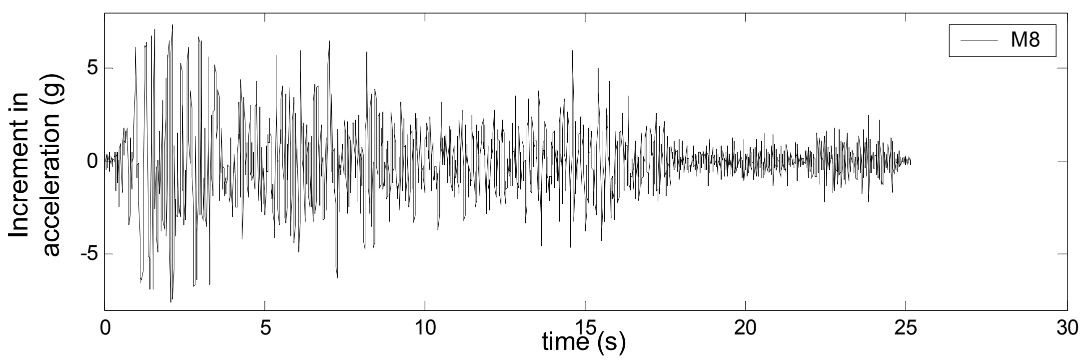

Figure 4.12. Record of increase in acceleration on top for Test 4-18 (only M8 measurement is available)

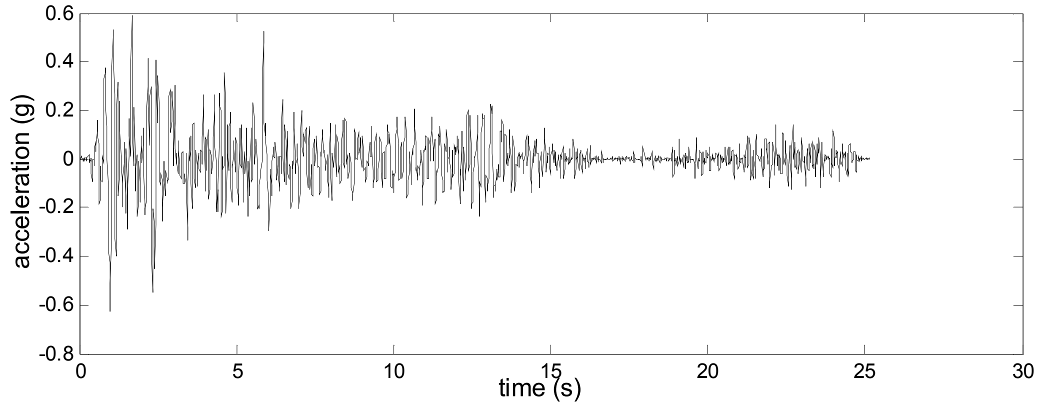

Figure 4.13. Shaking table acceleration record for Test 5-9

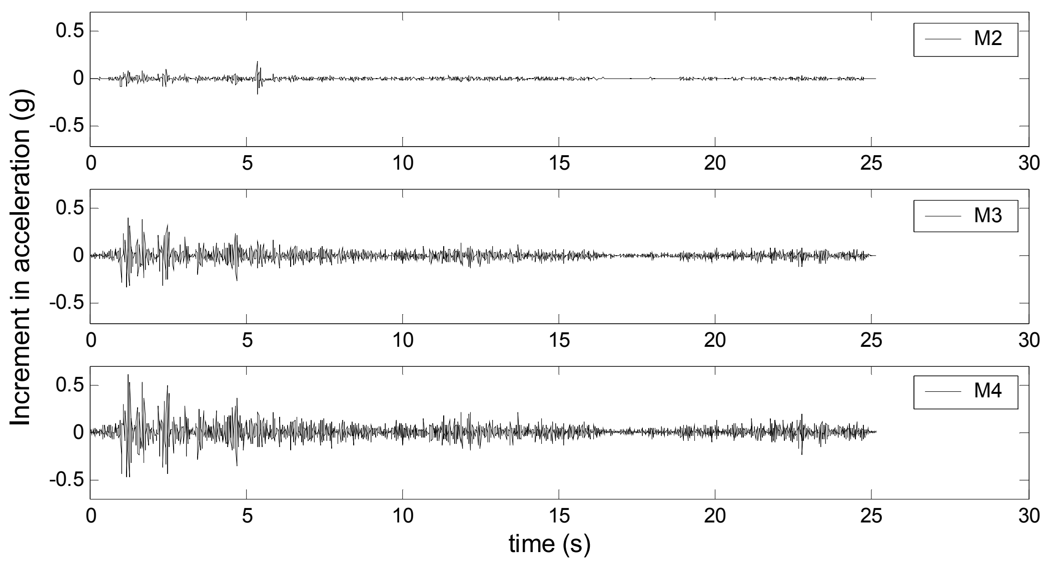

Figure 4.14. Record of increase in acceleration on wall face (bottom to top) for Test 5-9

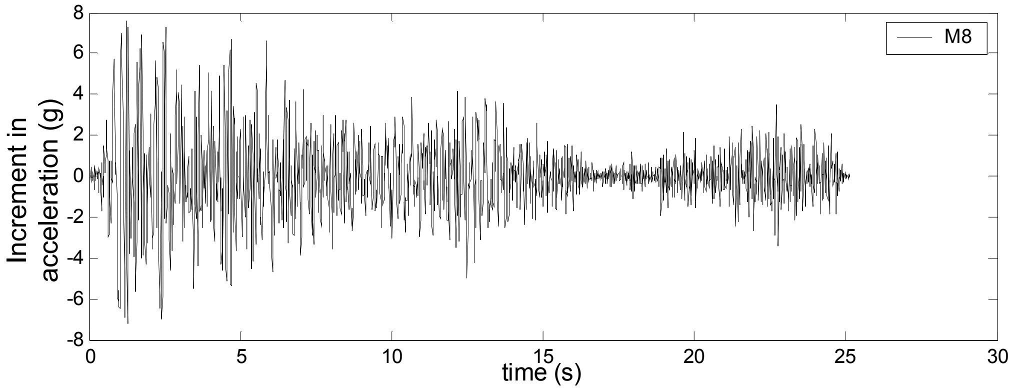

Figure 4.15. Record of increase in acceleration on top for Test 5-9 (only M8 measurement is available)

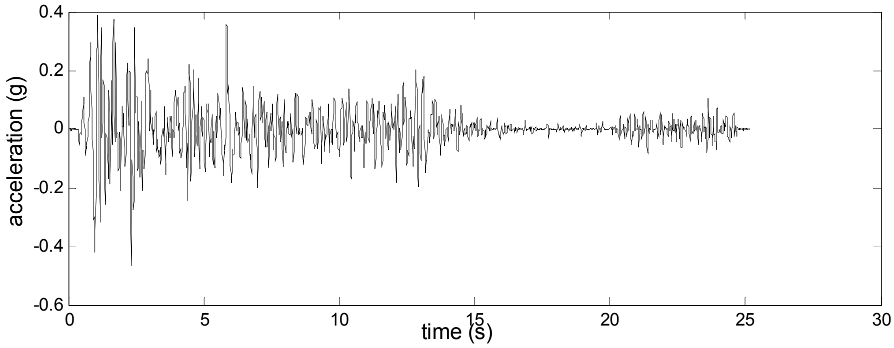

Figure 4.16. Shaking table acceleration record for Test 6-7

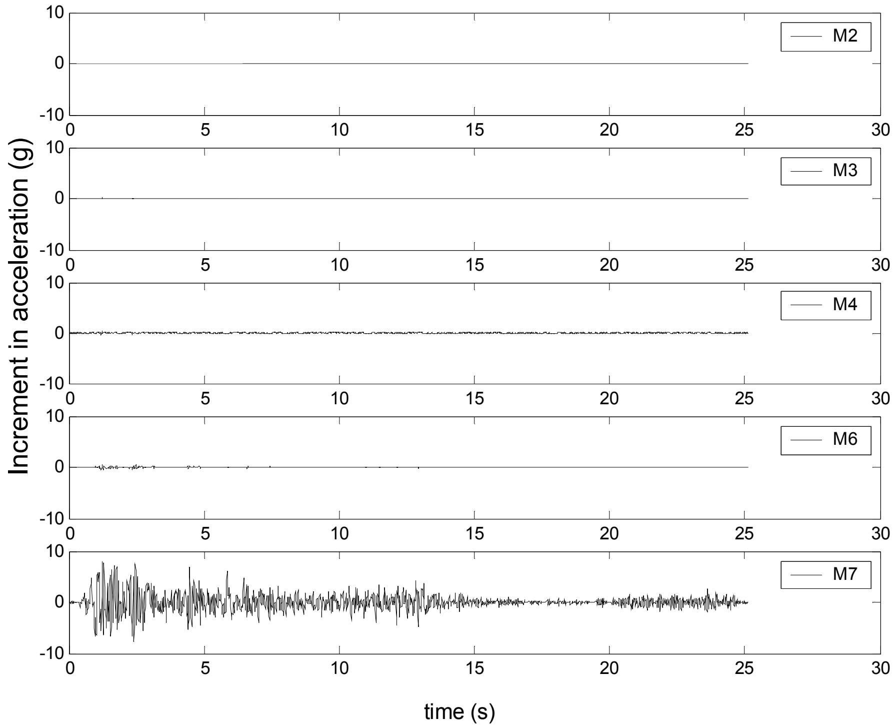

Figure 4.17. Record of increase in acceleration on wall face (bottom to top) for Test 6-7

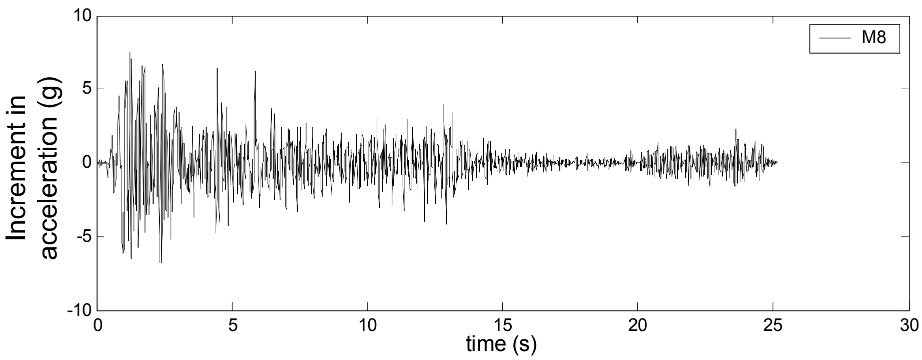

Figure 4.18. Record of increase in acceleration on top for Test 6-7 (only M8 measurement is available)

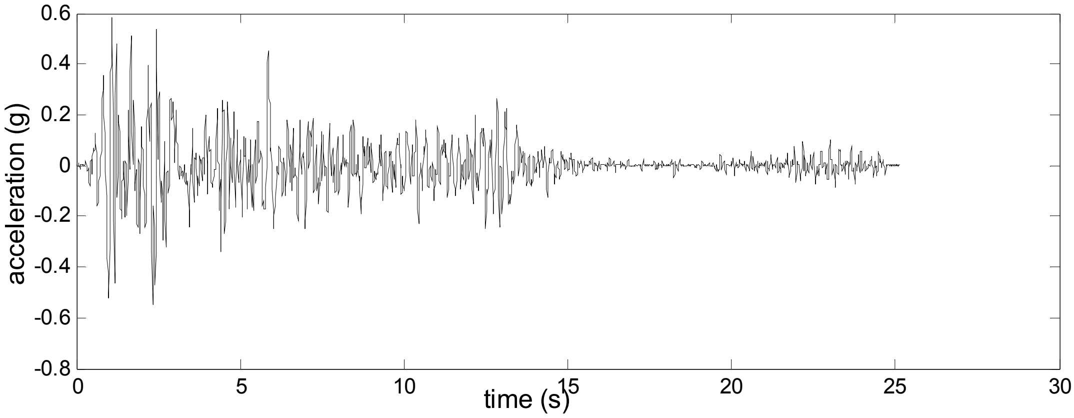

Figure 4.19. Shaking table acceleration record for Test 7-12

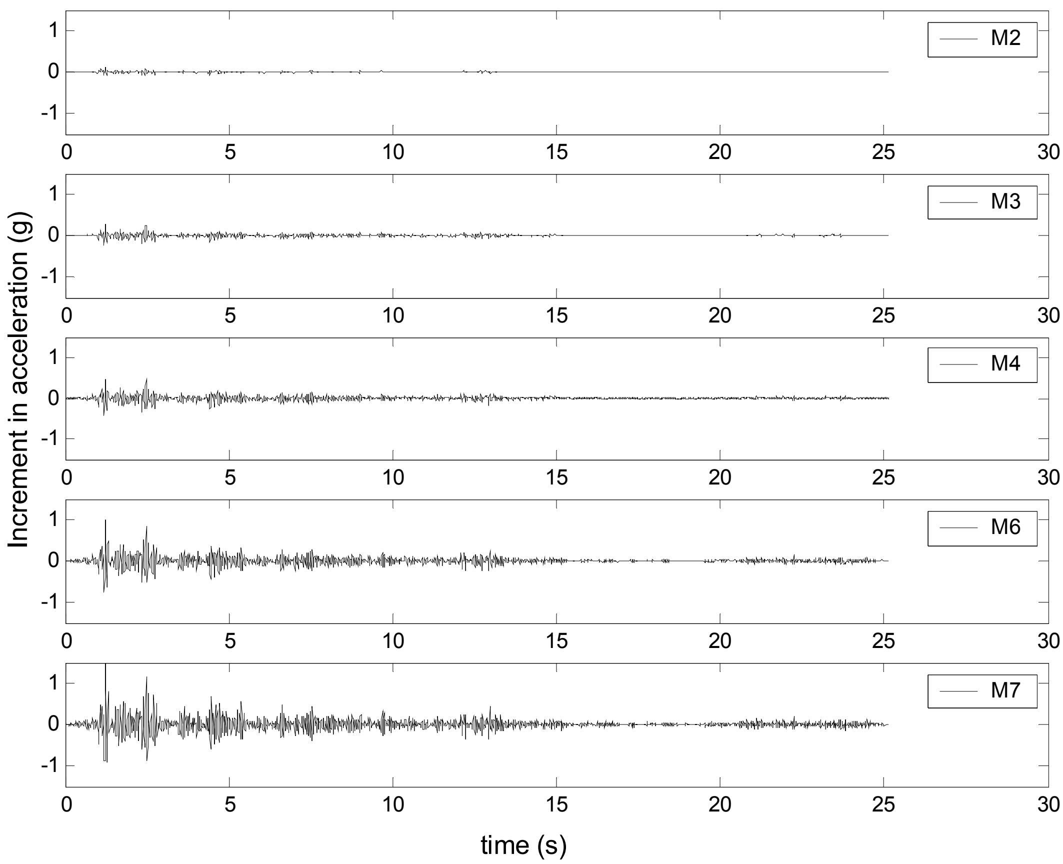

Figure 4.20. Record of increase in acceleration on wall face (bottom to top) for Test 7-12

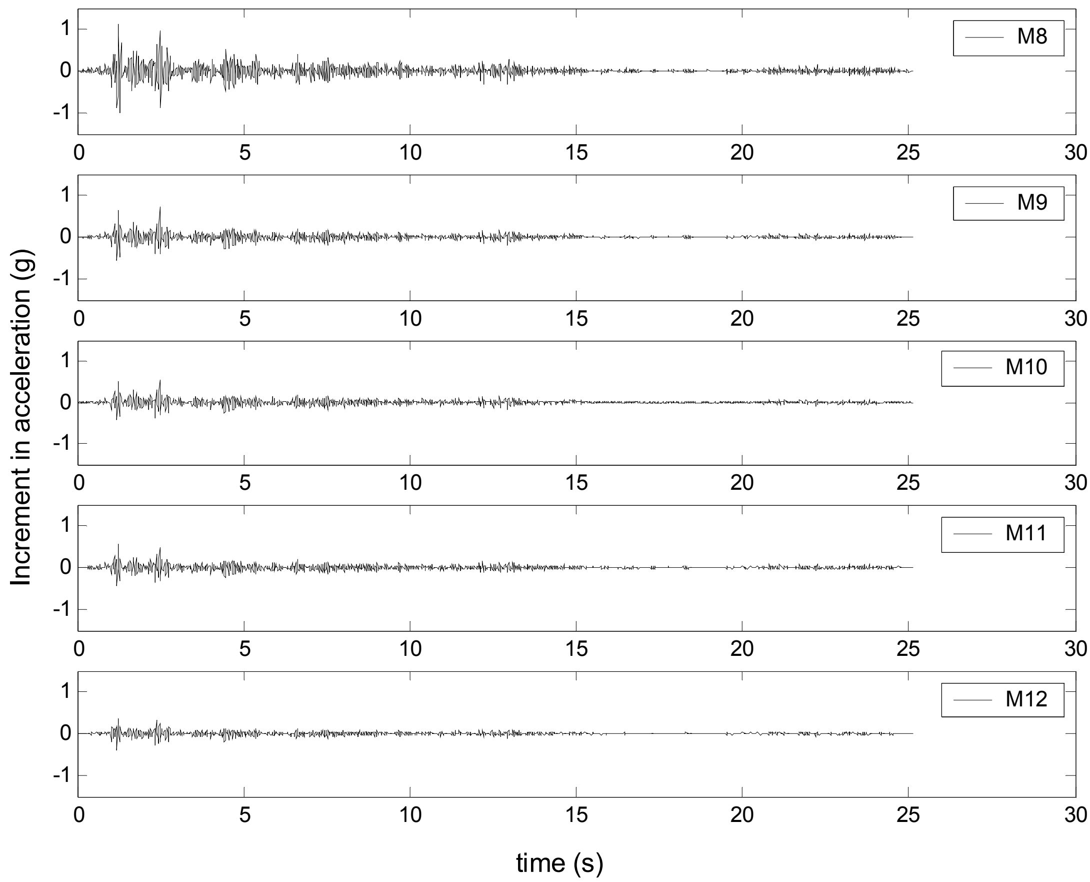

Figure 4.21. Record of increase in acceleration on top (front to back) for Test 7-12

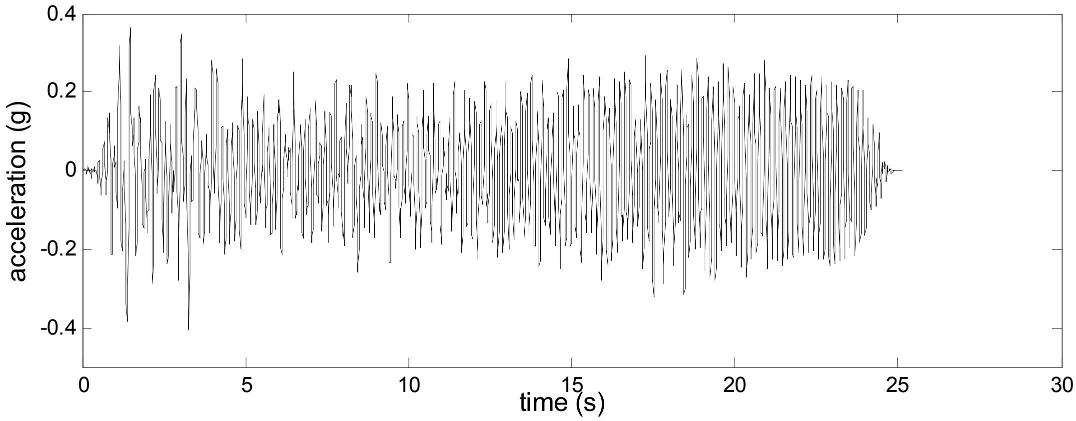

Figure 4.22. Shaking table acceleration record for Test 8a-9

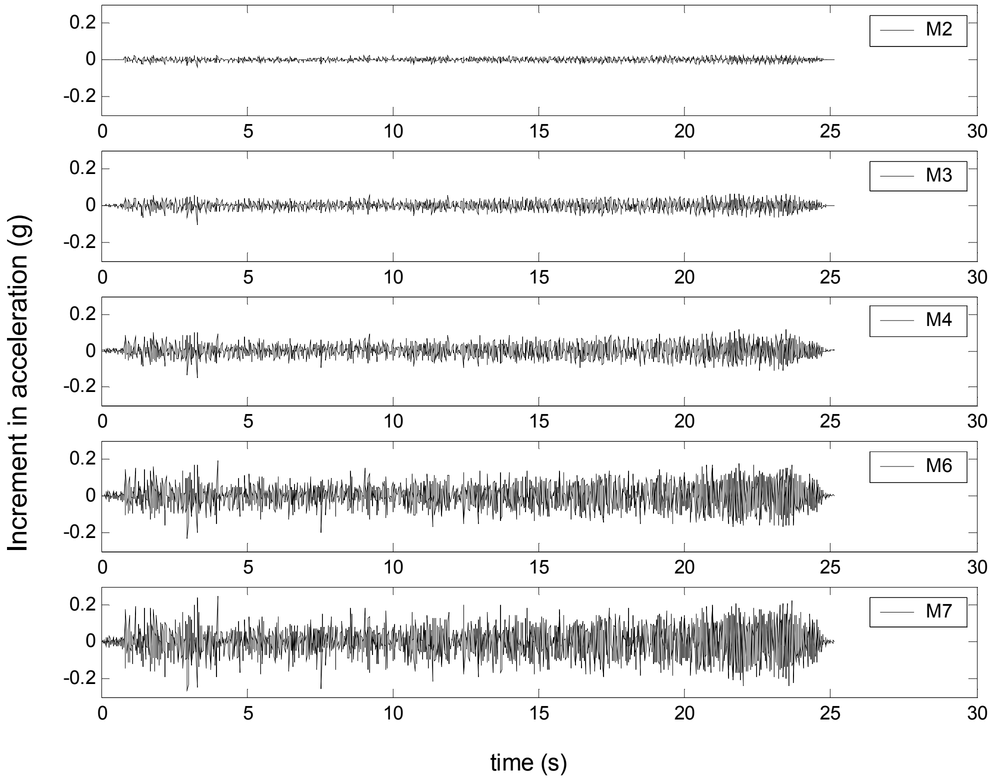

Figure 4.23. Record of increase in acceleration on wall face (bottom to top) for Test 8a-9

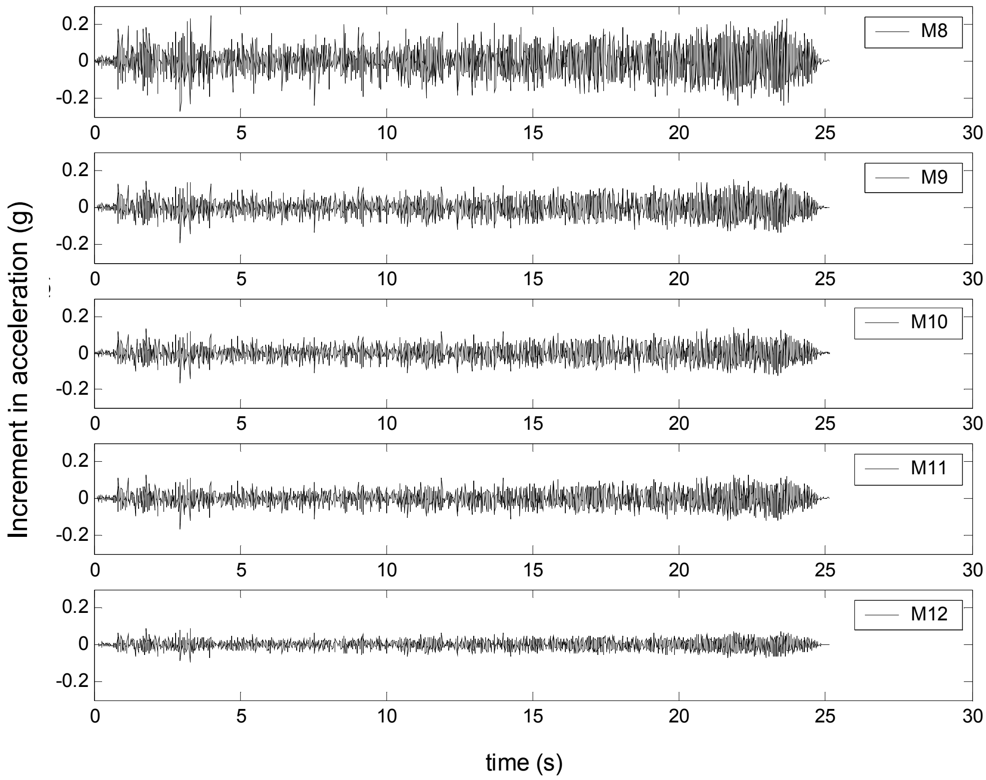

Figure 4.24. Record of increase in acceleration on top (front to back) for Test 8a-9

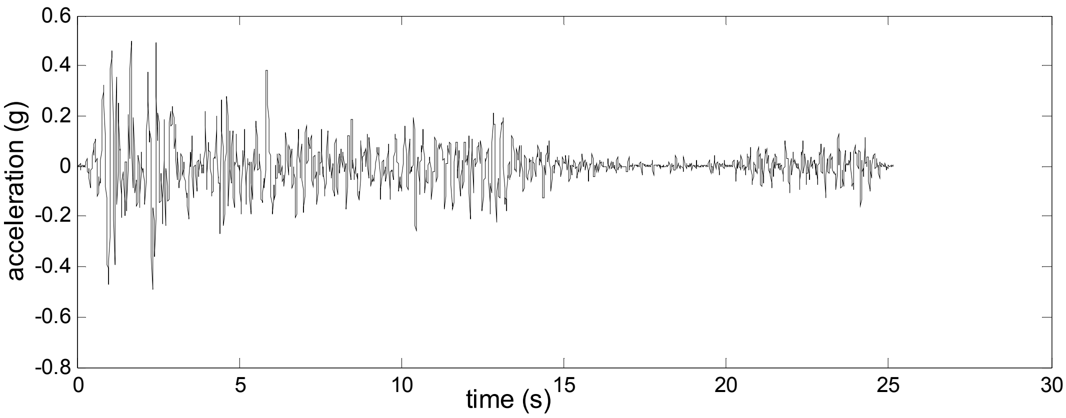

Figure 4.25. Shaking table acceleration record for Test 8b-8

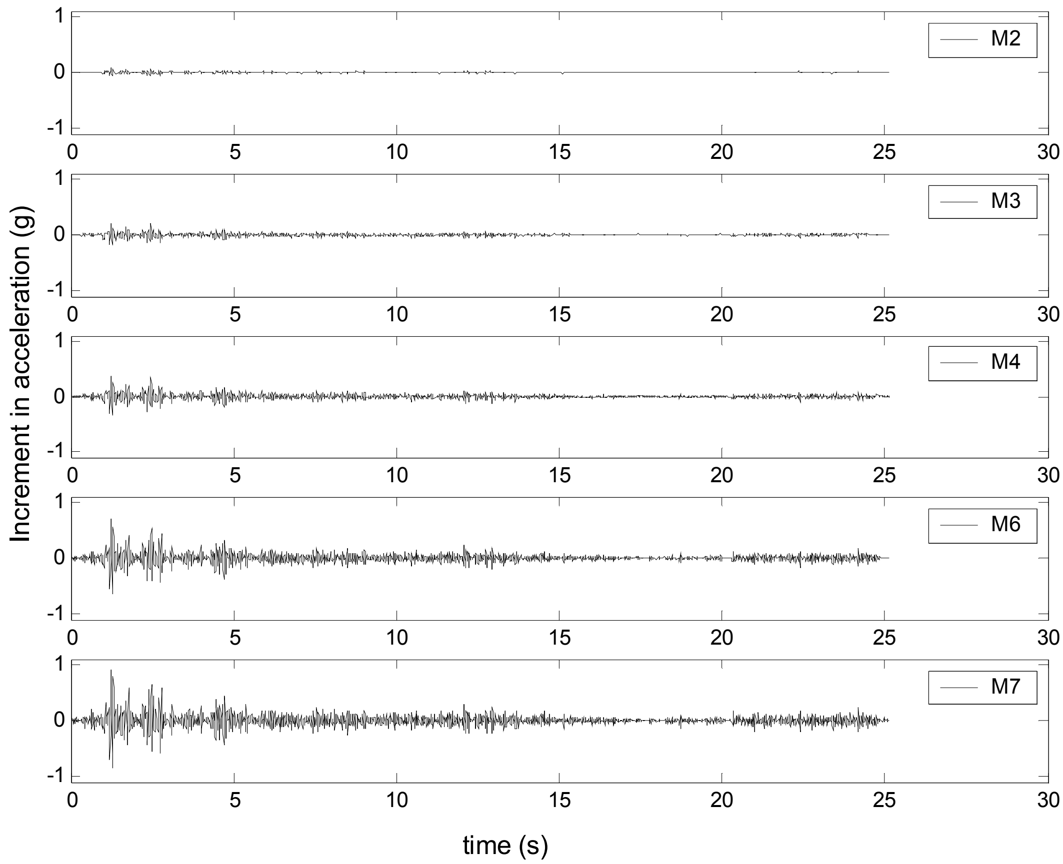

Figure 4.26. Record of increase in acceleration on wall face (bottom to top) for Test 8b-8

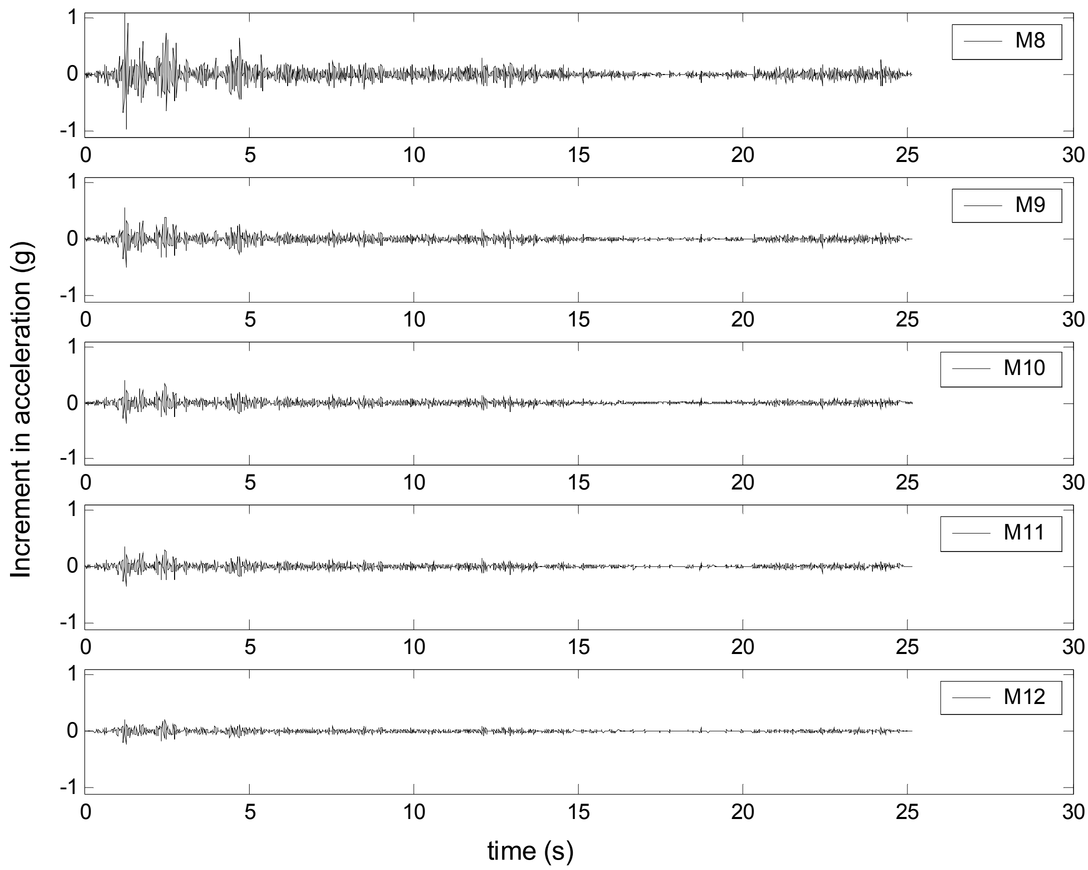

Figure 4.27. Record of increase in acceleration on top (front to back) for Test 8b-8

4.3. Displacement Records

4.3.1. Measured Displacement Records

Measured shaking table displacement records for all test runs are given in Appendix B.

The shaking table displacement records and the wall face displacements relative to the shaking table are presented in the Figures 4.28 to 4.45. Since there were a total of 98 tests, only the shakings with the highest maximum table acceleration in each of the eight tests are presented. The heights of optical laser distance sensors in each test were given in Table 3.4. Sensors L1 to L5 were positioned upward from bottom and sensors L6, L7, and L8 were placed at the same level at the top. Peak values obtained from these figures are used in Sections 4.5 to 4.10 in evaluating the effects of various parameters on maximum face displacements during shaking. For example, effects of increasing table acceleration on maximum face displacements are discussed in Section 4.5.2 with the help of figures in which maximum relative displacements during shaking versus maximum table acceleration are plotted.

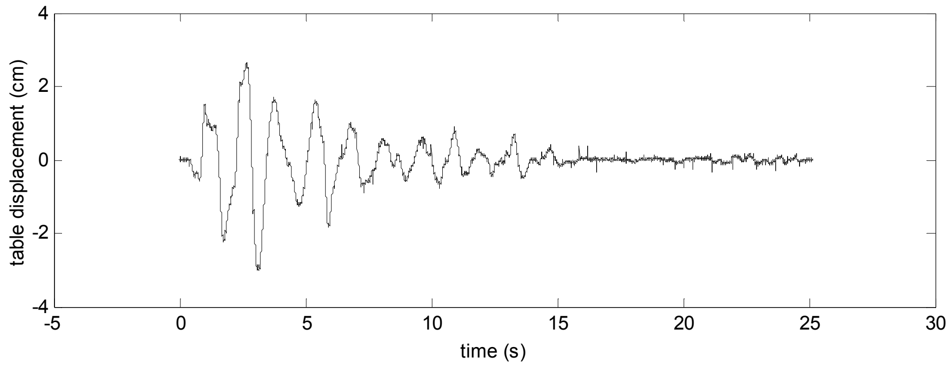

Figure 4.28. Shaking table displacement record for Test 1-10

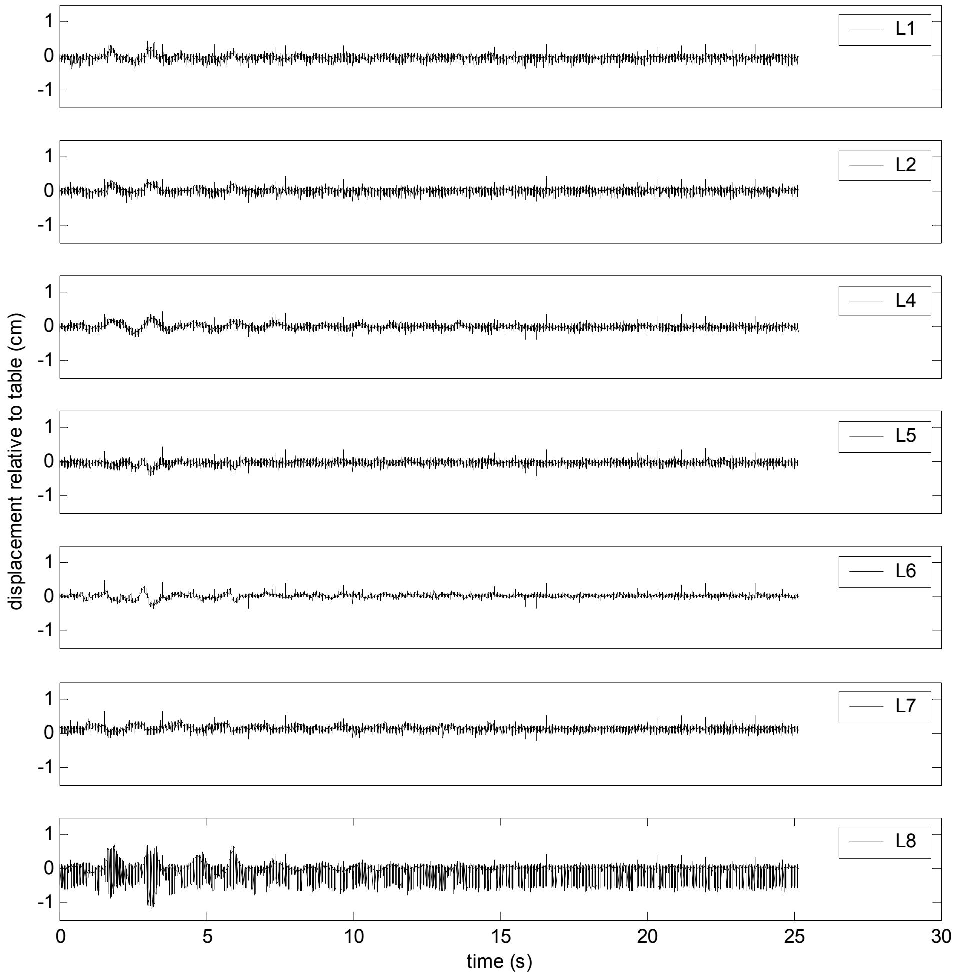

Figure 4.29. Record of relative displacements on wall face (bottom to top) for Test 1-10

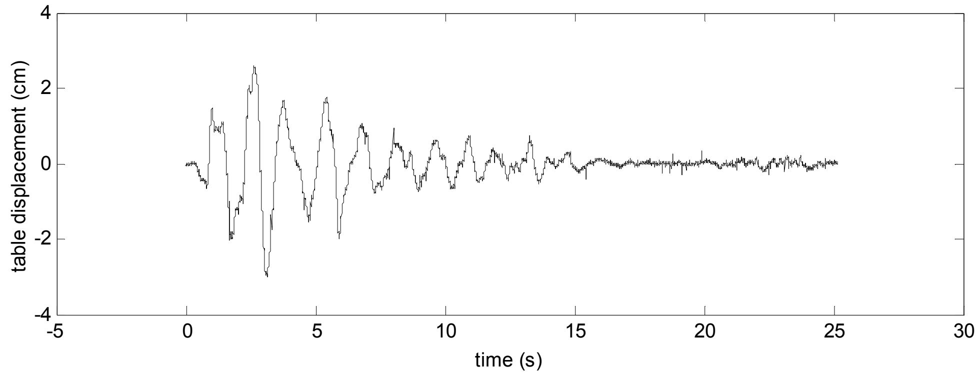

Figure 4.30. Shaking table displacement record for Test 2-6

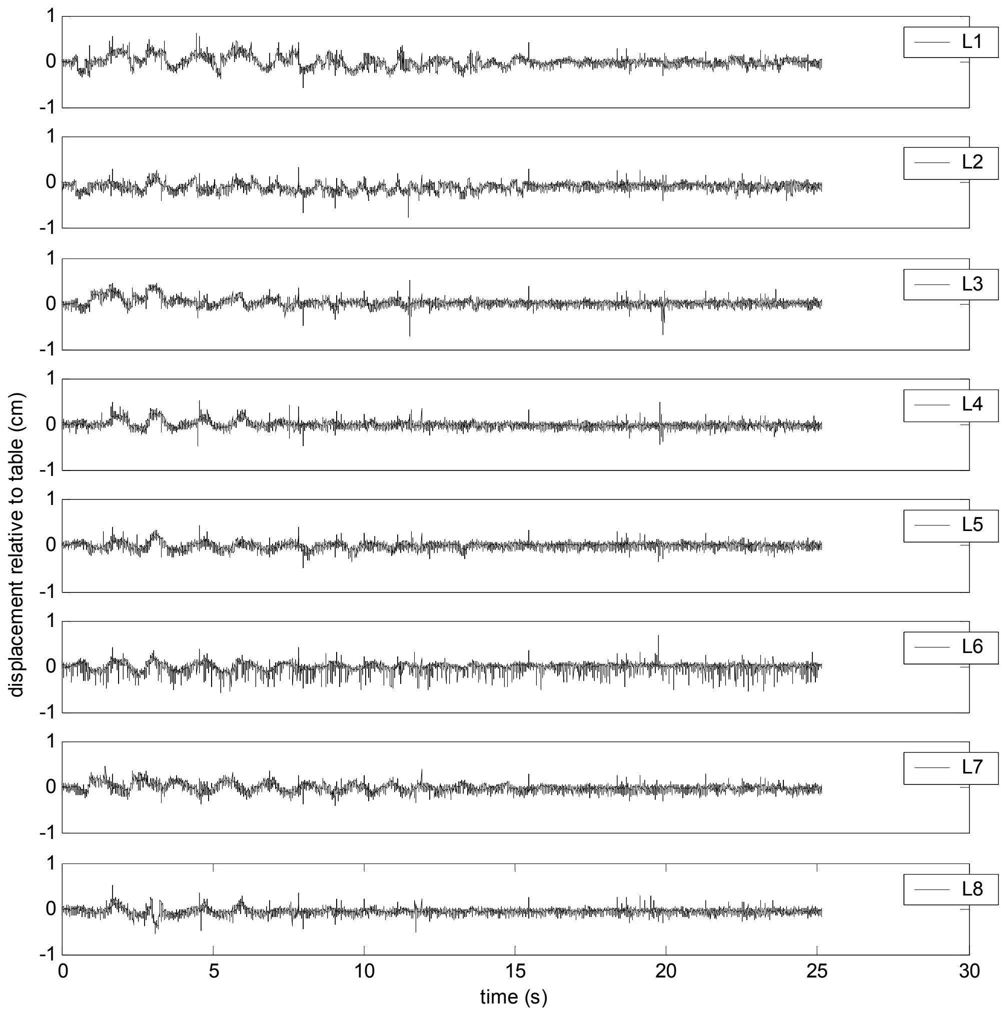

Figure 4.31. Record of relative displacements on wall face (bottom to top) for Test 2-6

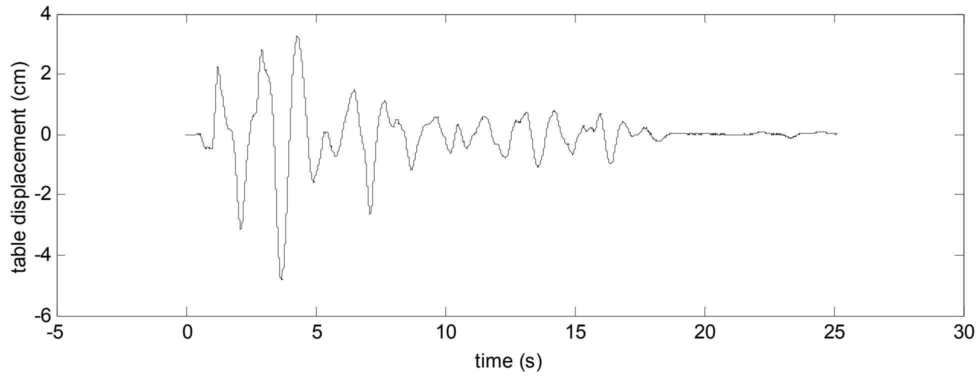

Figure 4.32. Shaking table displacement record for Test 3-10

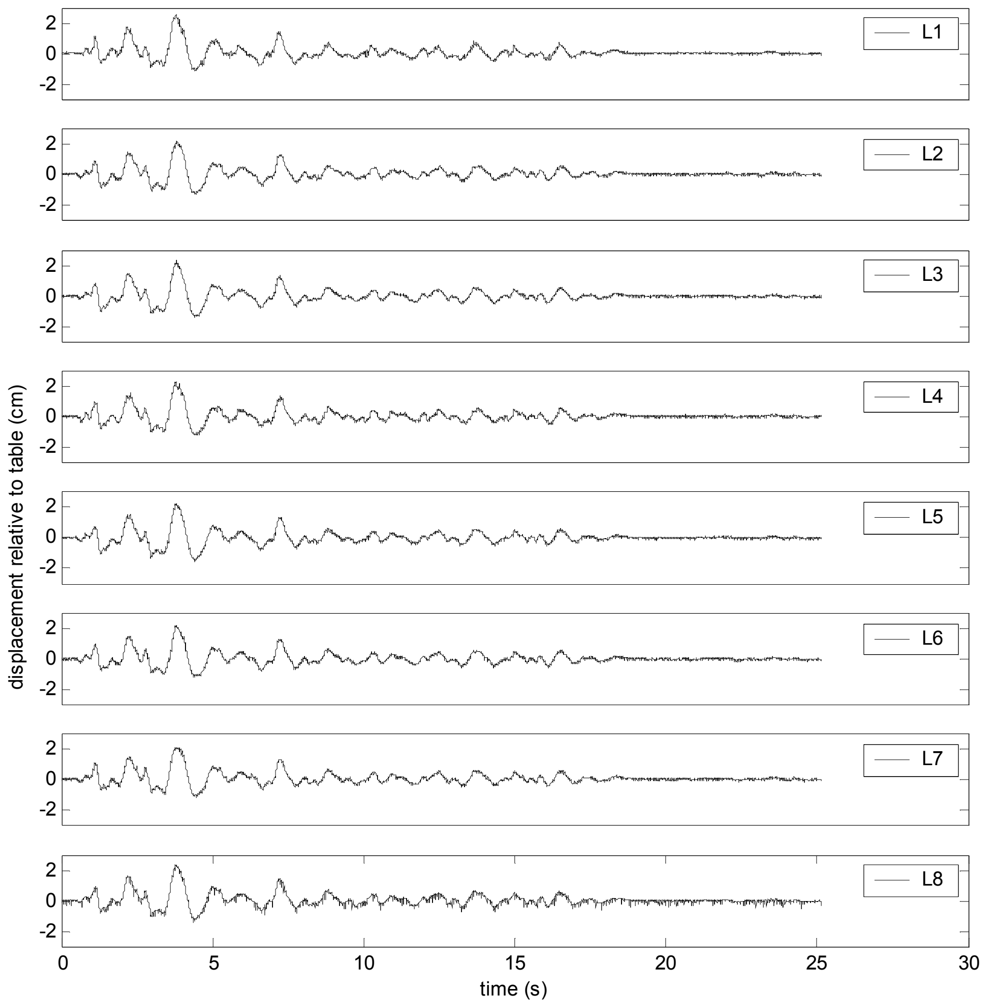

Figure 4.33. Record of relative displacements on wall face (bottom to top) for Test 3-10

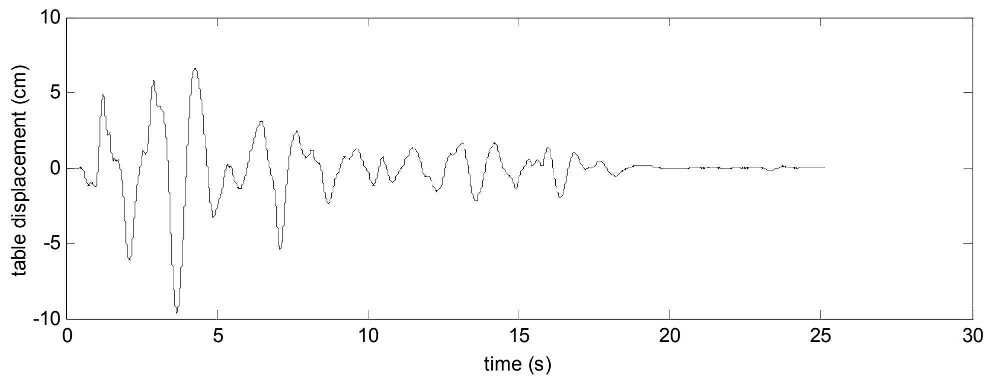

Figure 4.34. Shaking table displacement record for Test 4-18

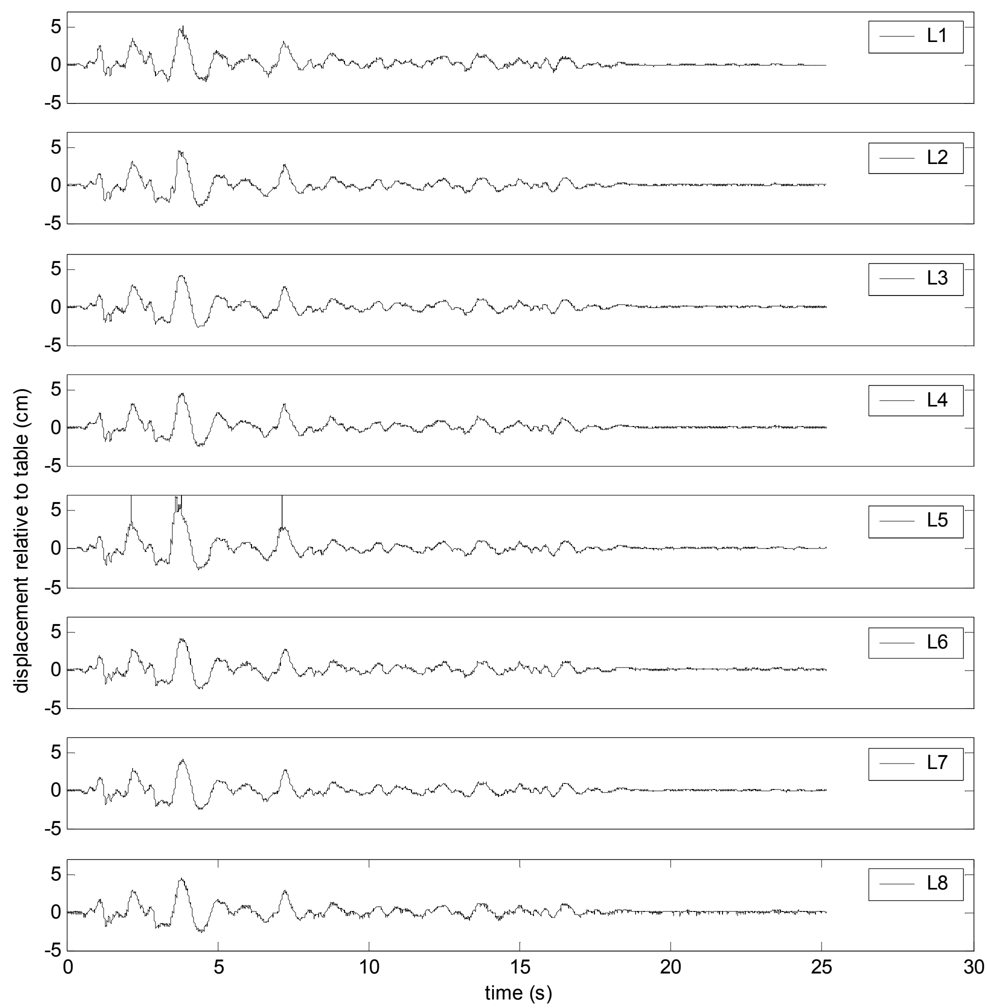

Figure 4.35. Record of relative displacements on wall face (bottom to top) for Test 4-18

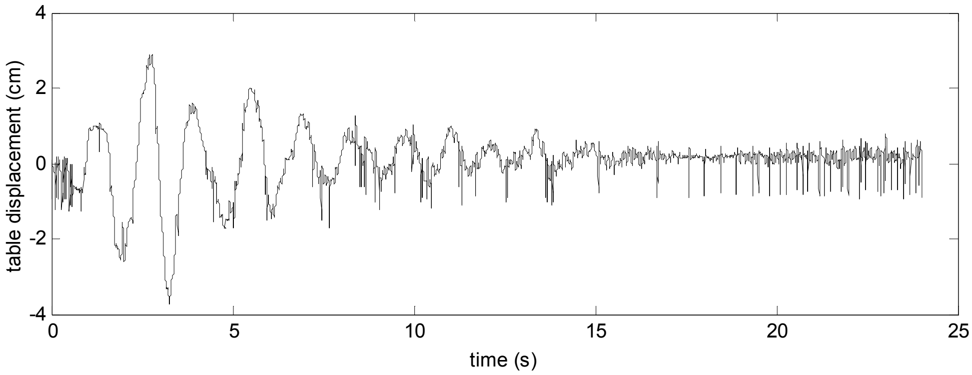

Figure 4.36. Shaking table displacement record for Test 5-9

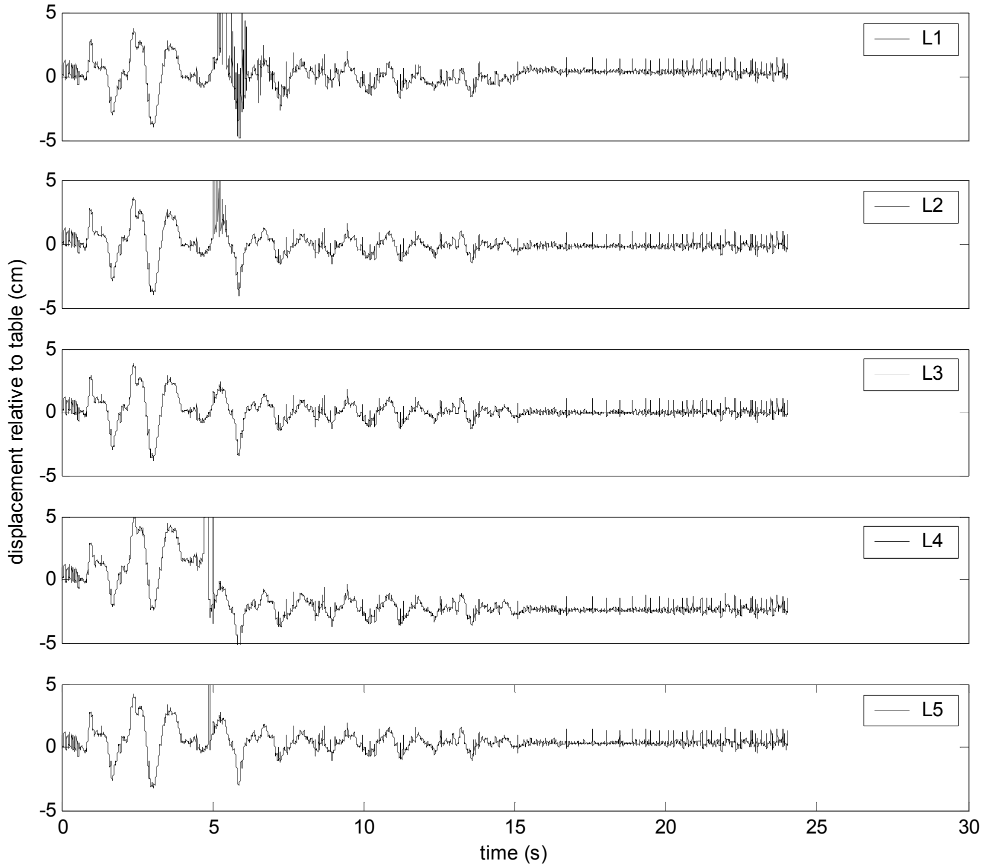

Figure 4.37. Record of relative displacements on wall face (bottom to top) for Test 5-9

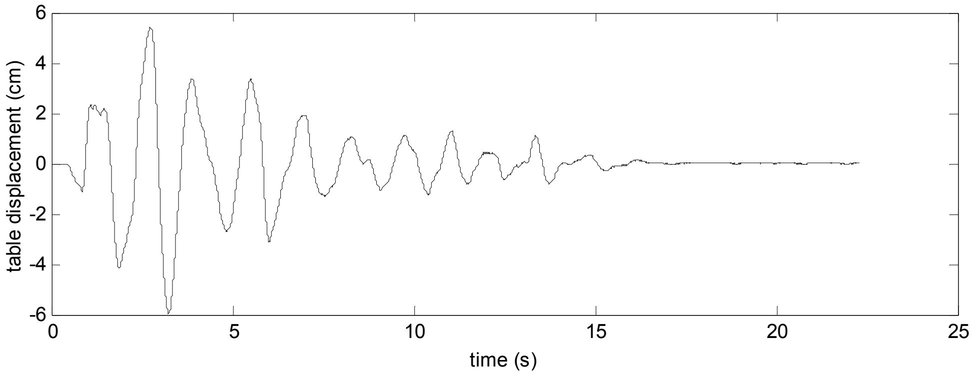

Figure 4.38. Shaking table displacement record for Test 6-7

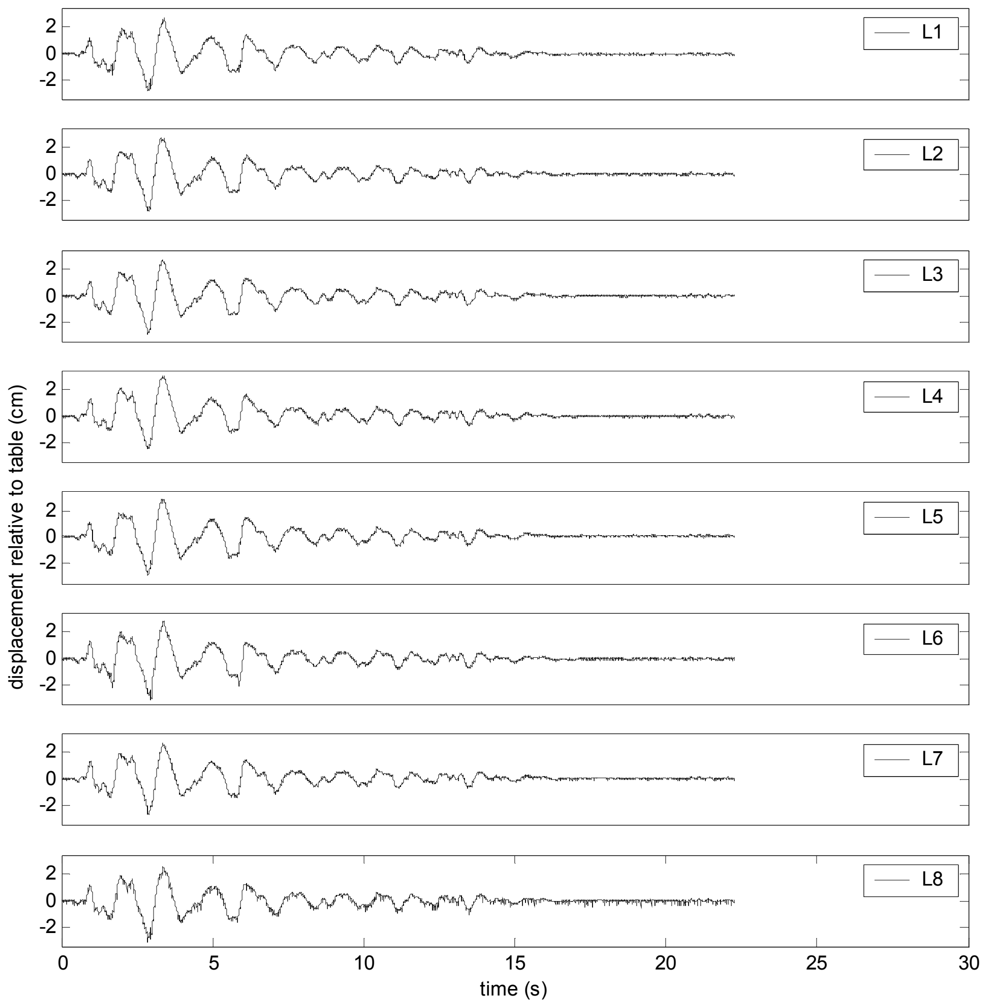

Figure 4.39. Record of relative displacements on wall face (bottom to top) for Test 6-7

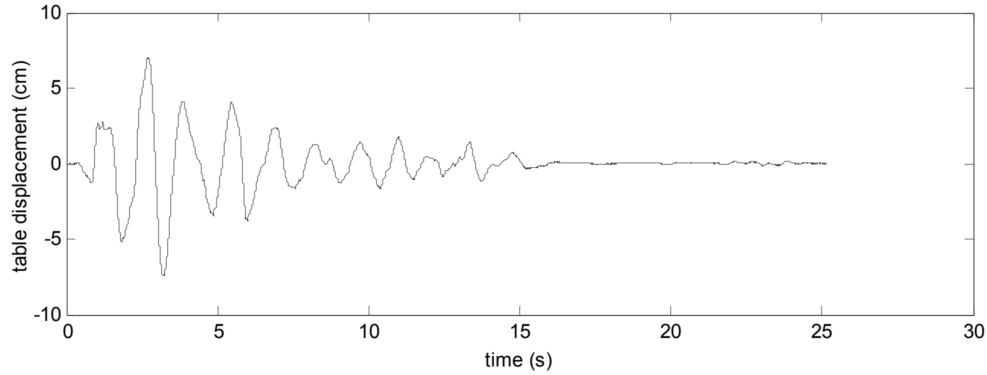

Figure 4.40. Shaking table displacement record for Test 7-12

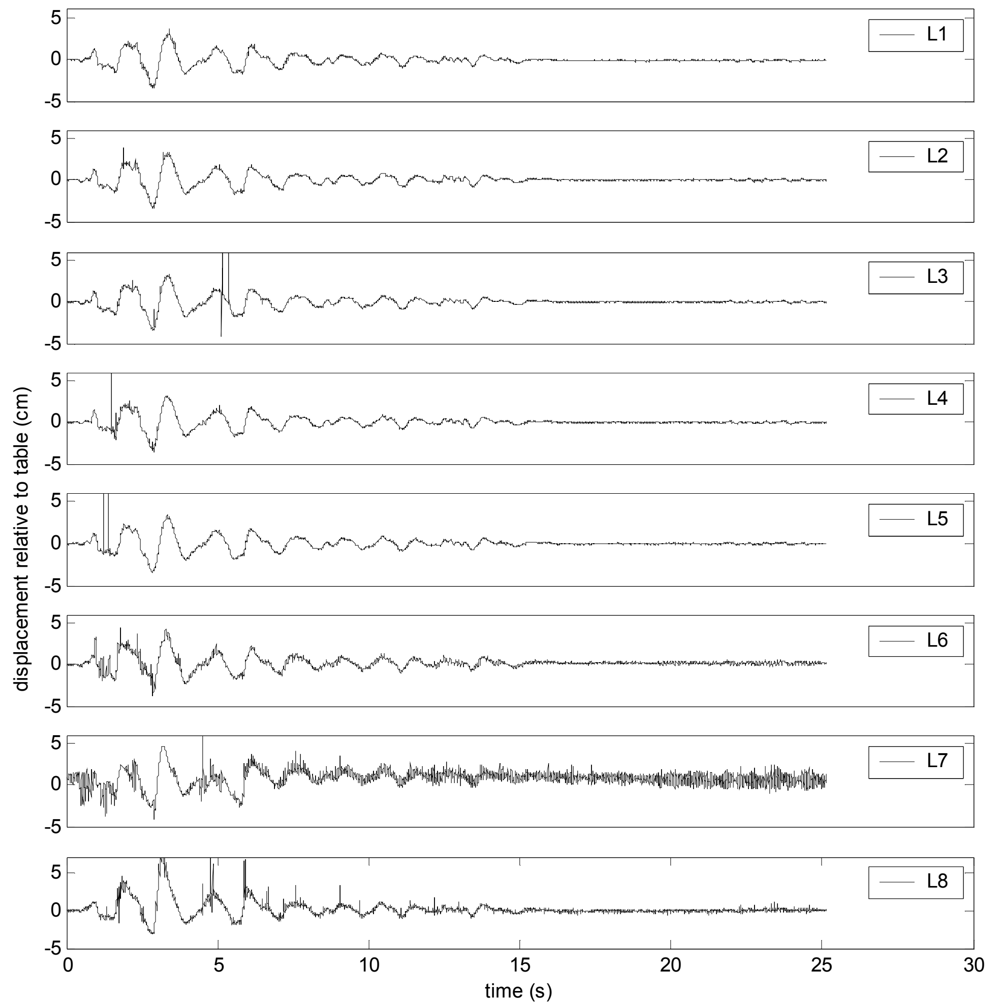

Figure 4.41. Record of relative displacements on wall face (bottom to top) for Test 7-12

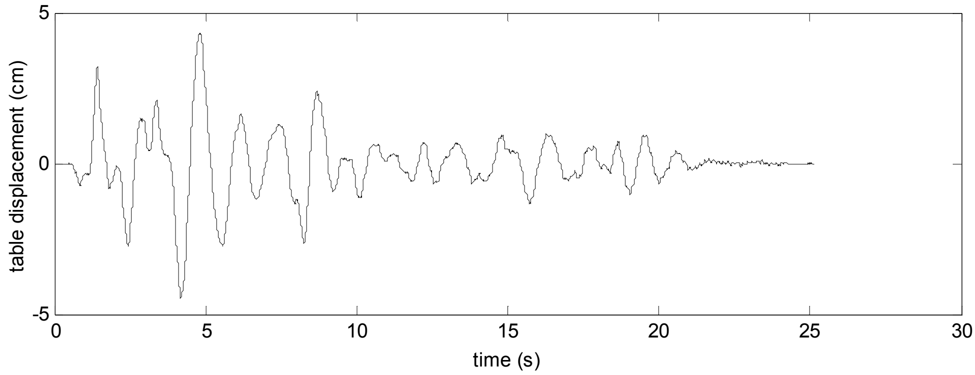

Figure 4.42. Shaking table displacement record for Test 8a-9

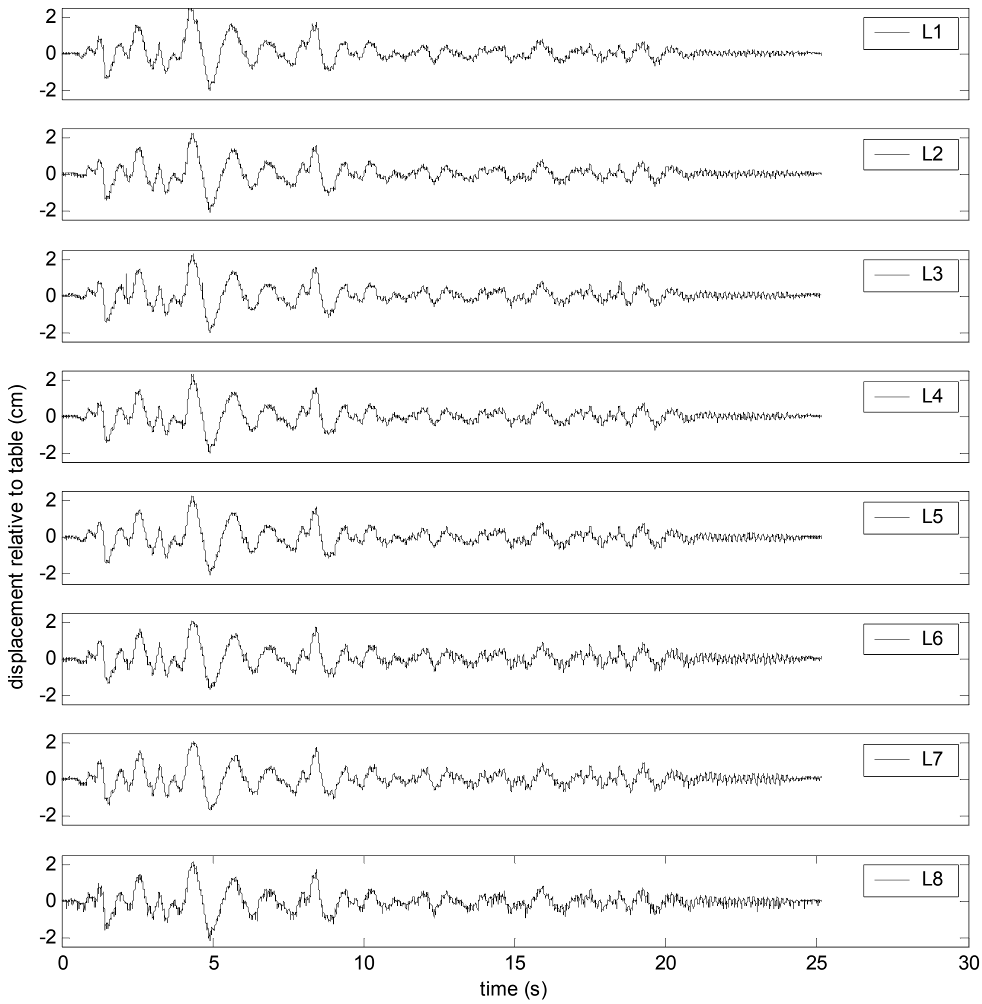

Figure 4.43. Record of relative displacements on wall face (bottom to top) for Test 8a-9

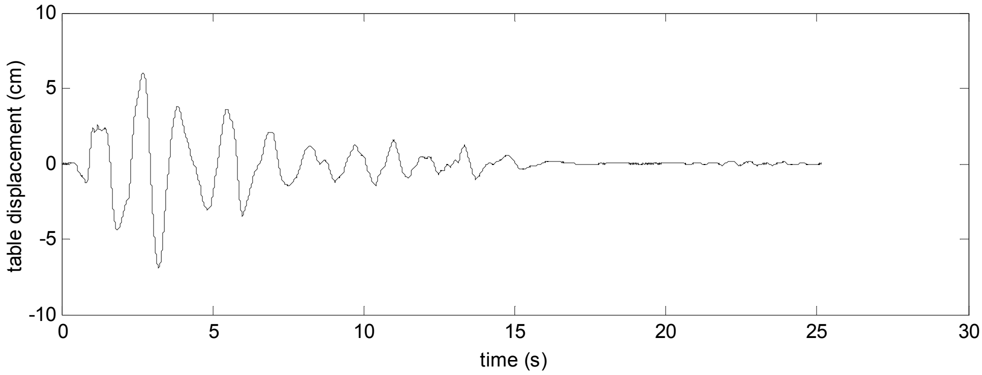

Figure 4.44. Shaking table displacement record for Test 8b-8

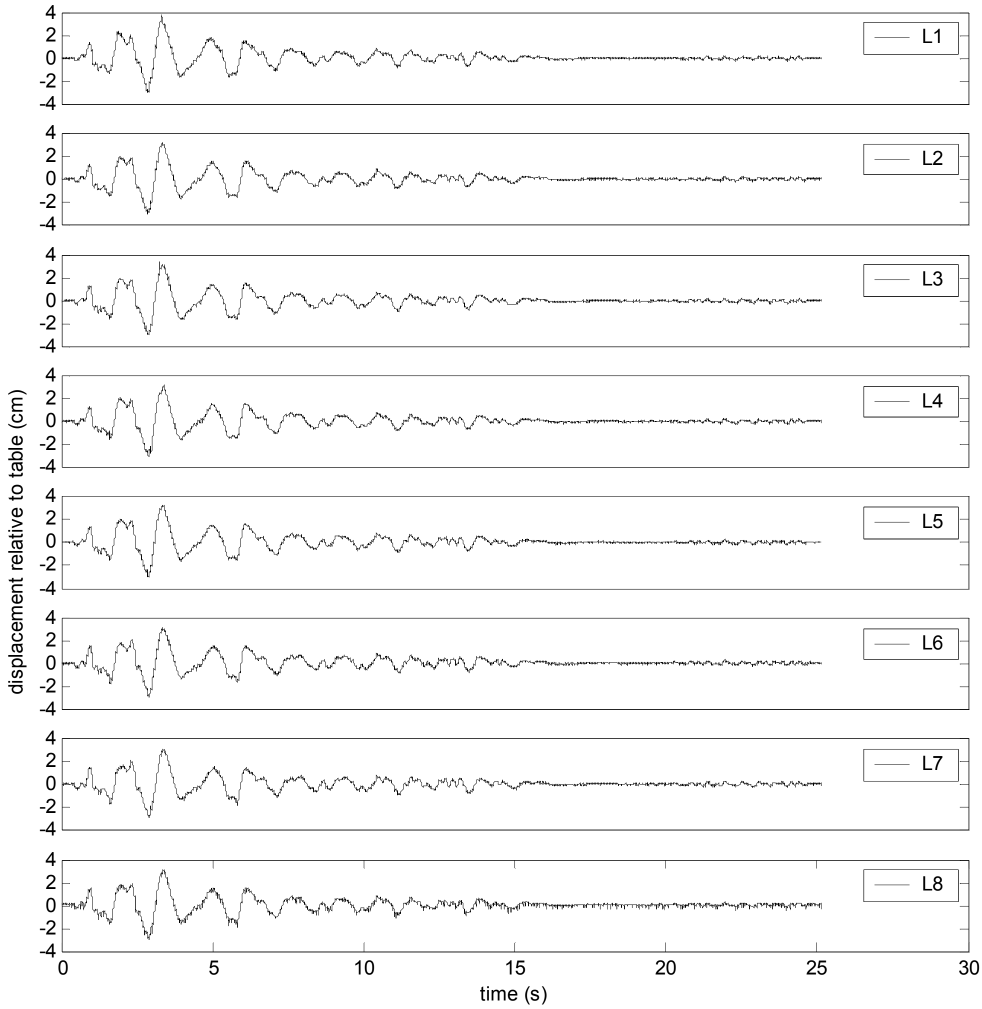

Figure 4.45. Record of relative displacements on wall face (bottom to top) for Test 8b-8

4.3.2. Displacement Records Calculated from Measured Acceleration Records

To check the consistency of acceleration data recorded with one system and displacement data recorded with the other system, acceleration data was used to calculate the expected displacements. Double numerical integration of the measured acceleration data without any corrections gives a very erroneous result for the displacement record due to the presence of low frequency components, integration of which gives very high amplitudes. This phenomenon is demonstrated in Figure 4.46. The ten Hz sine wave in this figure corresponds to the pure acceleration data (without the low frequency noise) of this study and the 0.5 Hz sine wave with a much smaller amplitude corresponds to the low frequency noise present in the recorded data. The summation of these two sine waves represents the recorded data, which has a low frequency noise. Integration of these three waves shows that the low frequency noise is dominant in determining the magnitudes achieved with integration. Therefore it was necessary to process the acceleration record in order to calculate a displacement record similar to the measured record.

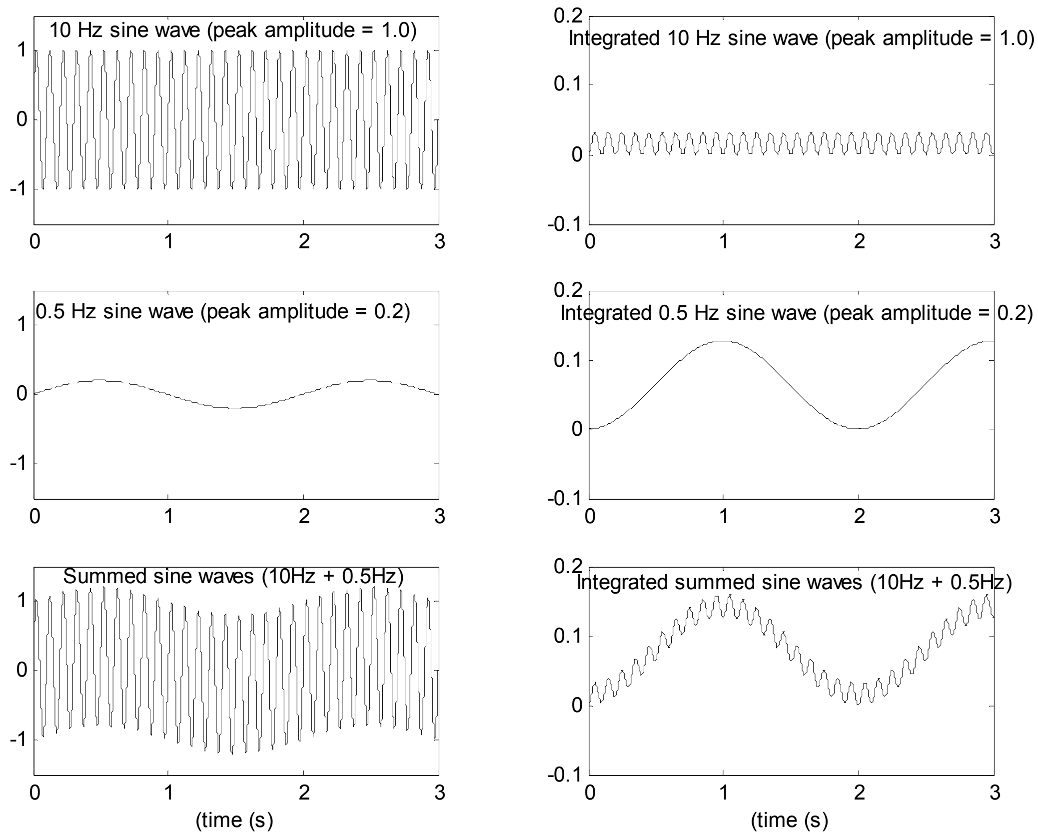

Figure 4.46. Demonstration of the effect of low frequency noise in numerical integration

For the correction and integration process, a Matlab code, AcctoDisp.m was written. This code removes the mean from the acceleration record, integrates to find the velocity using the cumulative trapezoidal numerical integration function cumtrapz, removes the mean from the calculated velocity record, and uses the function cumtrapz again to calculate displacement. Then a high degree polynomial is fitted using a least squares fit (polyfit function) and subtracted from this calculated displacement to remove the low frequency noise. Removing the low frequency noise from the measured acceleration record in the beginning gives the same results, so it is possible to use a corrected acceleration record for Newmark's sliding block analysis when there are permanent displacements.

Just as low frequency noise gives very high displacements in integration, high frequency data may give lower displacement magnitudes when integrated. When the sampling rate does not allow the recording of high frequency vibrations, displacements calculated from recorded acceleration data may be much larger than the actual displacements. This phenomenon is demonstrated in Figure 4.47. A 100 Hz sine wave is chosen to represent the acceleration data of a high frequency vibration and the data are sampled with the sampling rate of accelerometers used in this study, i.e. every 0.12 seconds. Integration of the sine wave itself and the sampled data show that the numerical integration of sampled data leads to erroneously large magnitudes when high frequency vibrations are present.

The displacement records were calculated at the levels for which both the measured acceleration records and the measured displacement data are available, i.e. at the shaking table, at 55 to 60 cm height (acceleration measured by M3, displacement measured by L2), and at 180 cm (acceleration measured by M7, displacement measured by L5), for all test runs. The calculated records superimposed on the measured records are given in the Figures 4.48 to 4.56 for the shaking with the highest maximum table acceleration in each of the eight tests.

It is noted that the calculated and measured shaking table displacements do not match perfectly. There is a time delay changing between 0.1 and 0.4 seconds between the two records. The calculated displacements are generally somewhat lower than the measured displacements, except for 180 cm height in some tests (Tests 4-18 and 6-7 are shown here) in which the amplification measured in acceleration is not reflected in the measured displacement record. The reason why the calculated displacements are mostly lower and in the remaining times higher may in fact be the same; the sampling interval of the acceleration recordings was nearly six times that of the displacement measurements. As shown in Table 3.8, the data acquisition system with the higher sampling rate measured higher table accelerations, so a lower sampling interval would have caught higher acceleration measurements and the displacements calculated from measured accelerations would have matched the measured displacement values. To confirm this, shaking table acceleration record measured by the VI Logger system was used to calculate the table displacements for Test 3-10, as shown in Figure 4.50. For the tests with calculated displacements much higher than measured values at 180 cm height, it is very probable that the accelerations increased to very high values at the top are the result of a high (i.e. higher than recording frequency) frequency phenomenon like vibration, and the real acceleration record jumped up and down several times between two consecutive recording points, as explained previously. This is the only possible explanation for the fact that displacement values observed were smaller than those calculated from acceleration data. In summary, the sampling frequency of the shaking table facility's own data acquisition system was not high enough to catch the real maxima and high frequency phenomena.

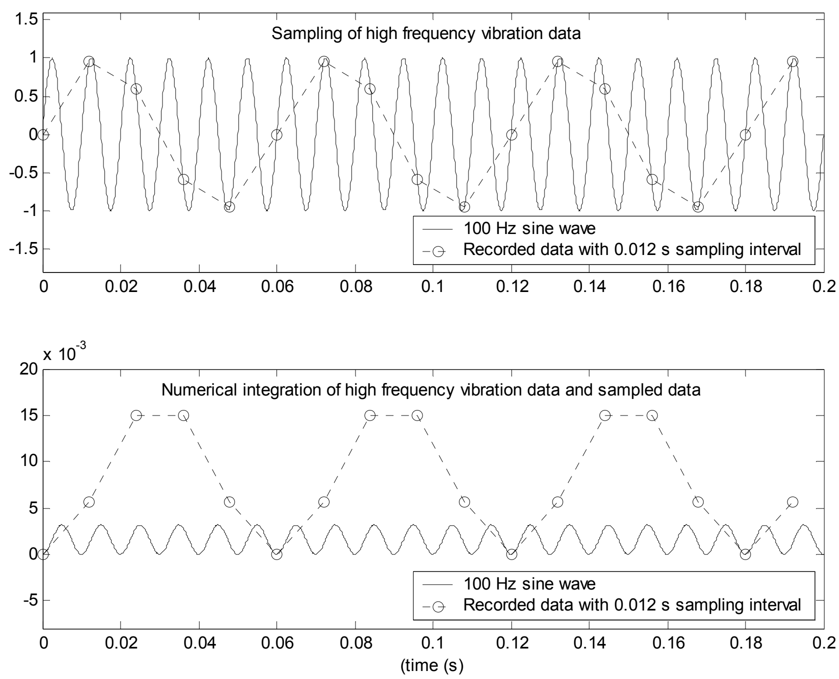

Figure 4.47. Demonstration of how the presence of high frequency vibrations lead to erroneously high values in displacement calculations

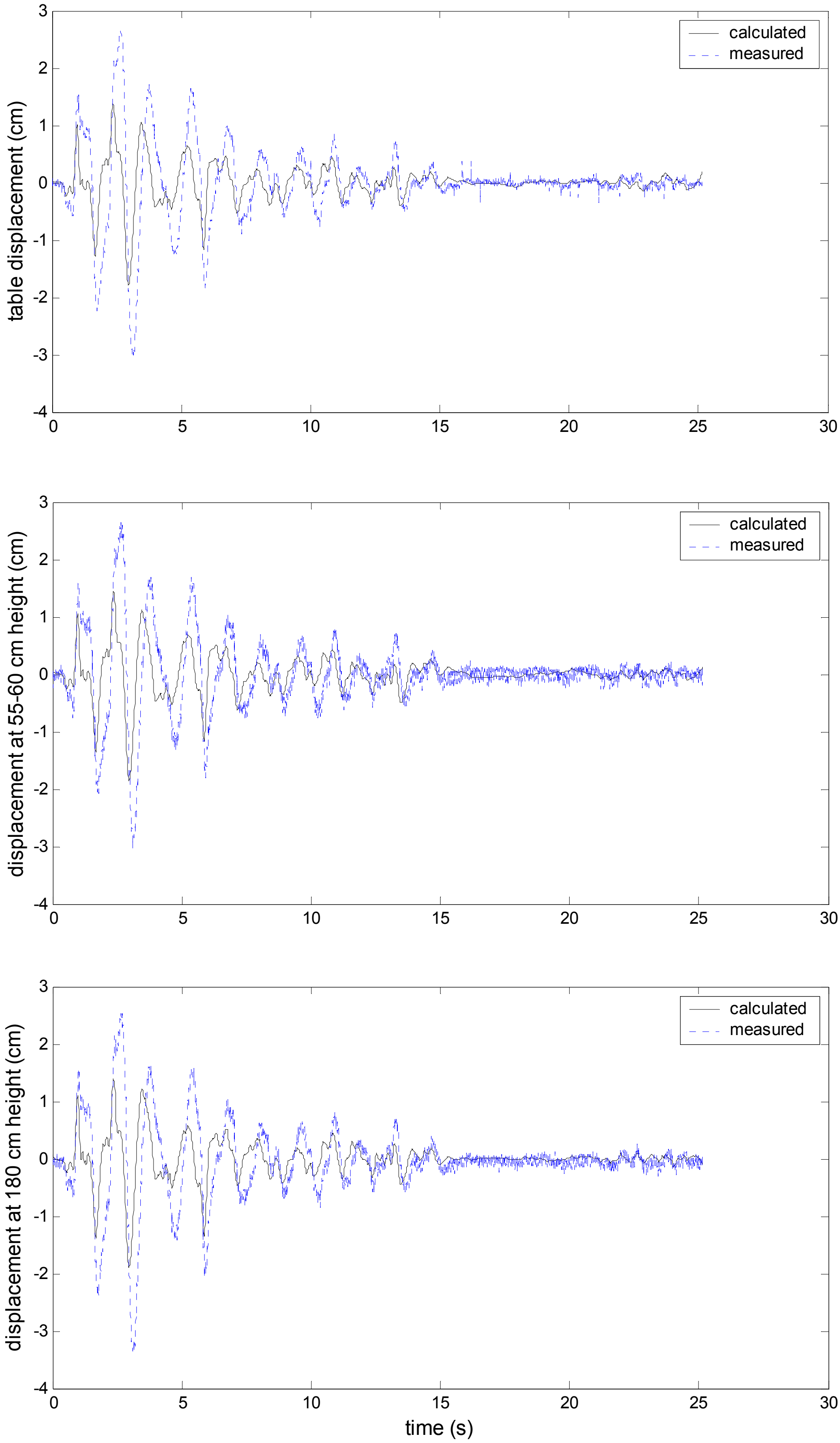

Figure 4.48. Calculated displacements compared to measured displacements for Test 1-10

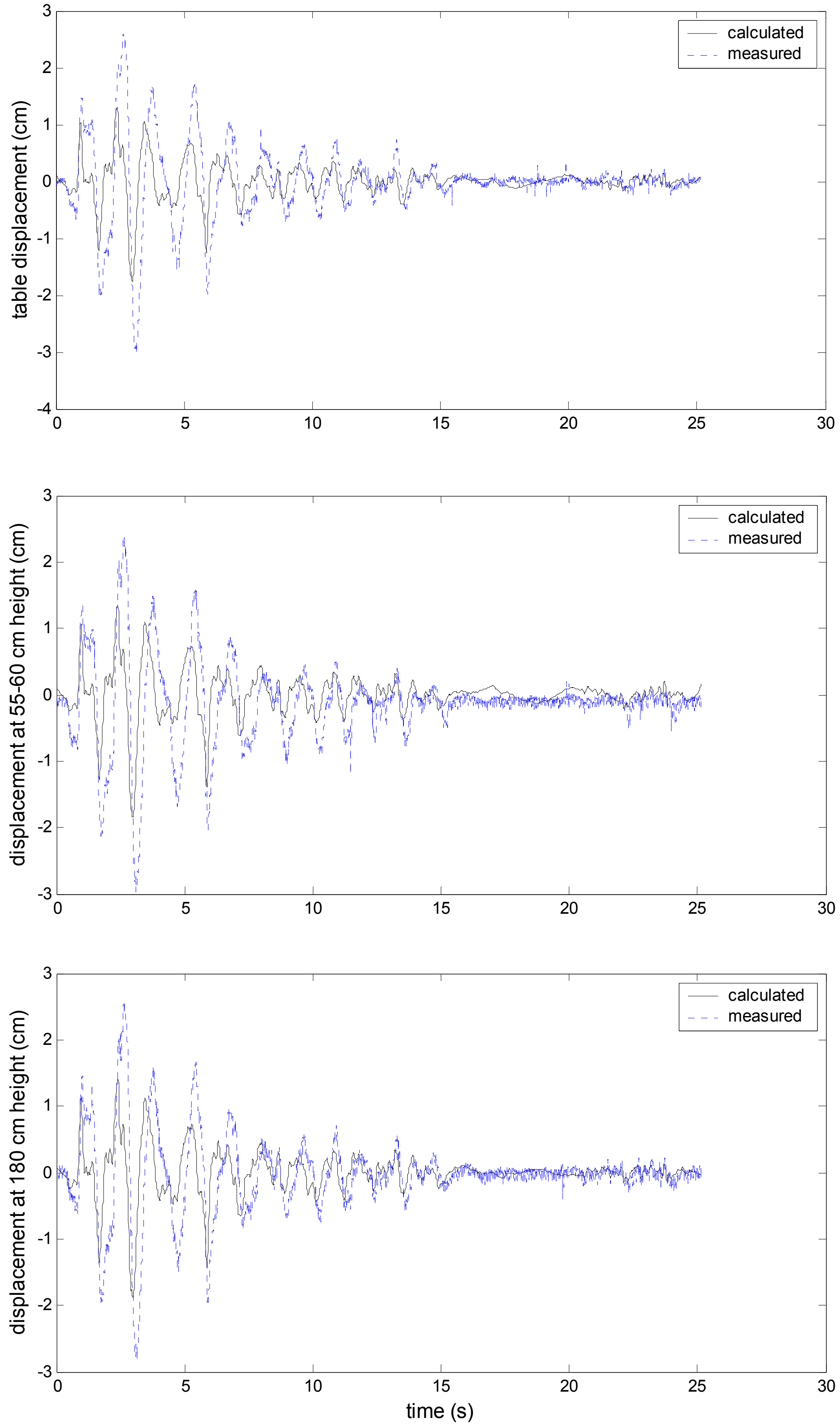

Figure 4.49. Calculated displacements compared to measured displacements for Test 2-6

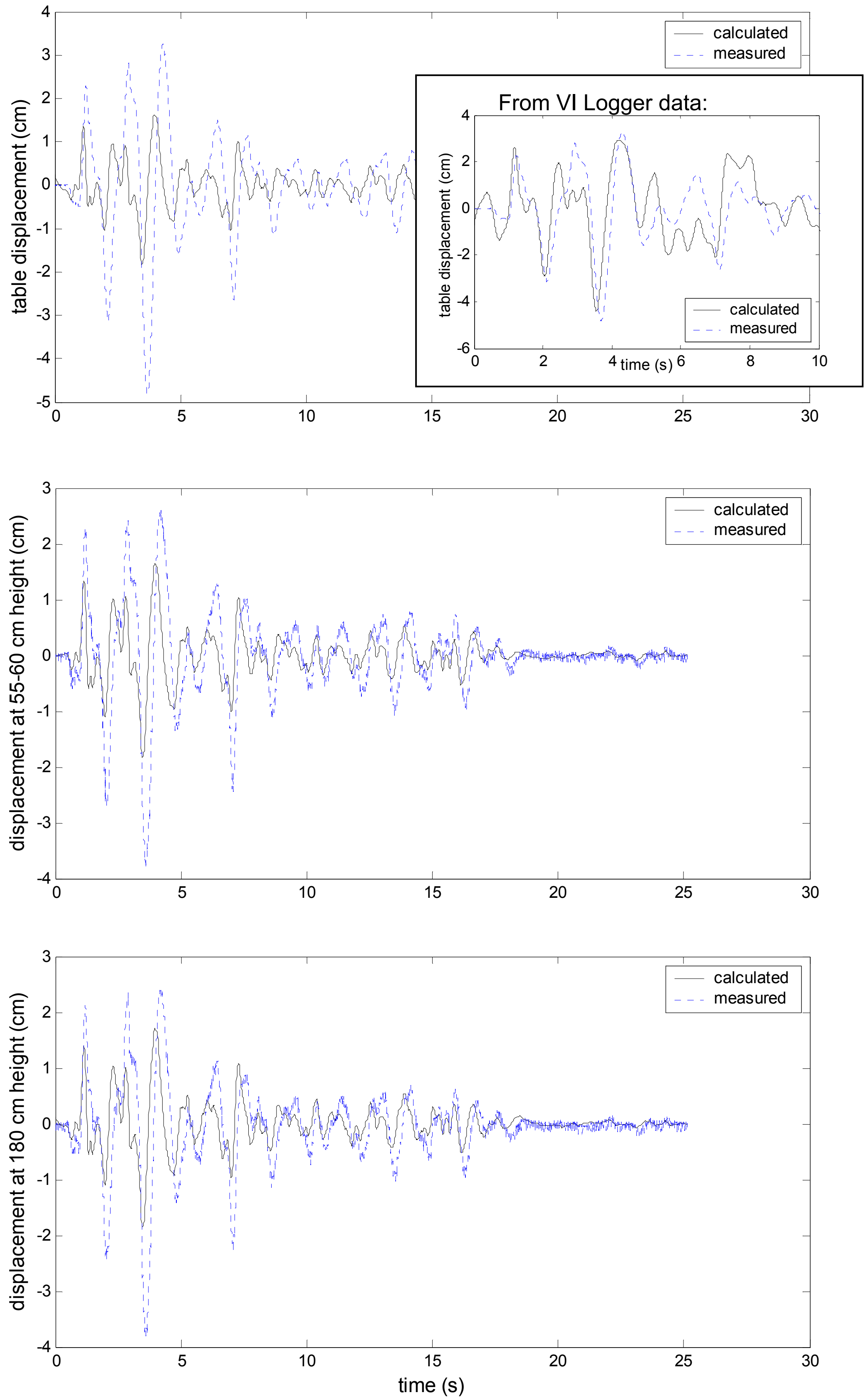

Figure 4.50. Calculated displacements compared to measured displacements for Test 3-10

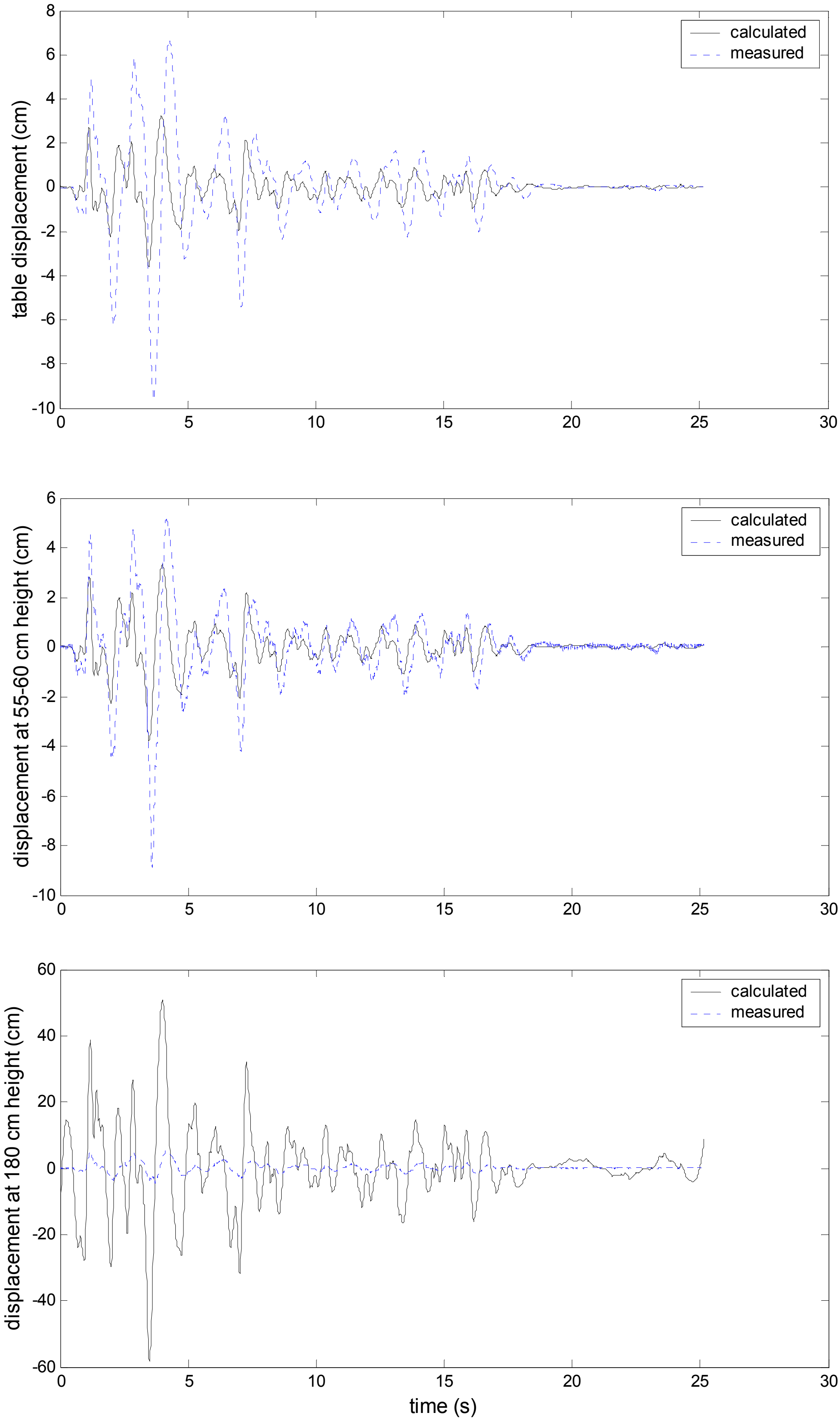

Figure 4.51. Calculated displacements compared to measured displacements for Test 4-18

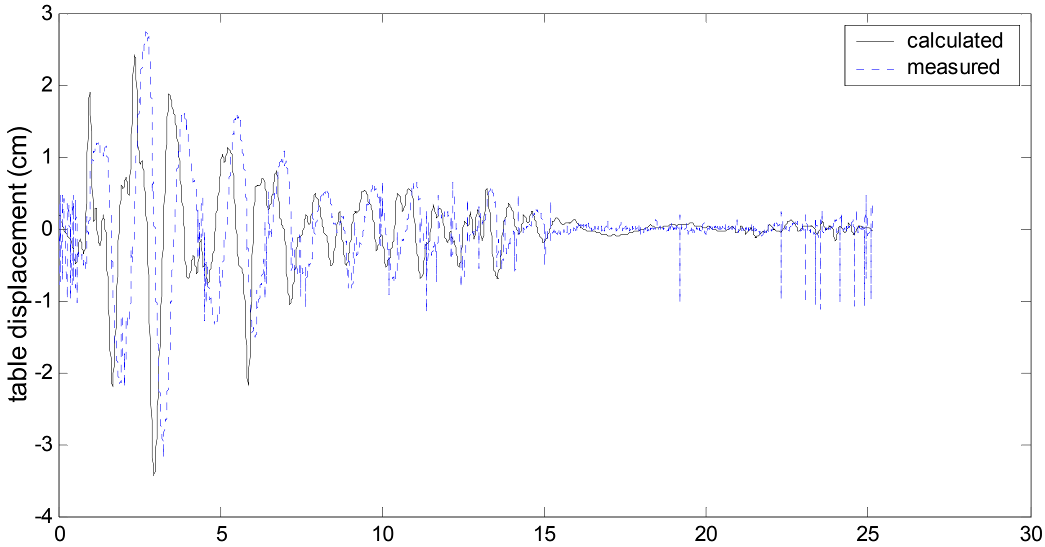

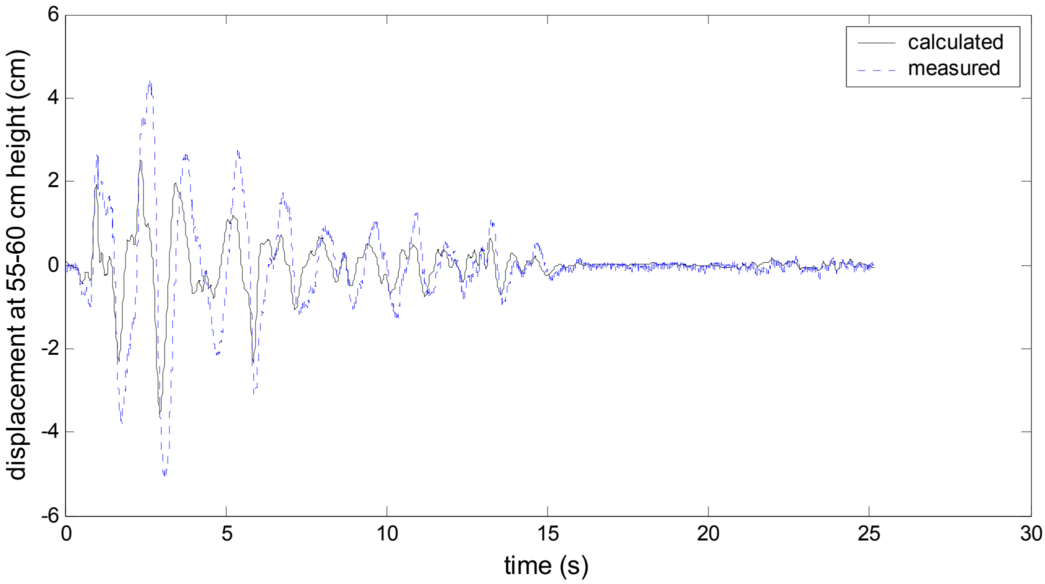

Figure 4.52. Calculated displacements compared to measured displacements for Test 5-8

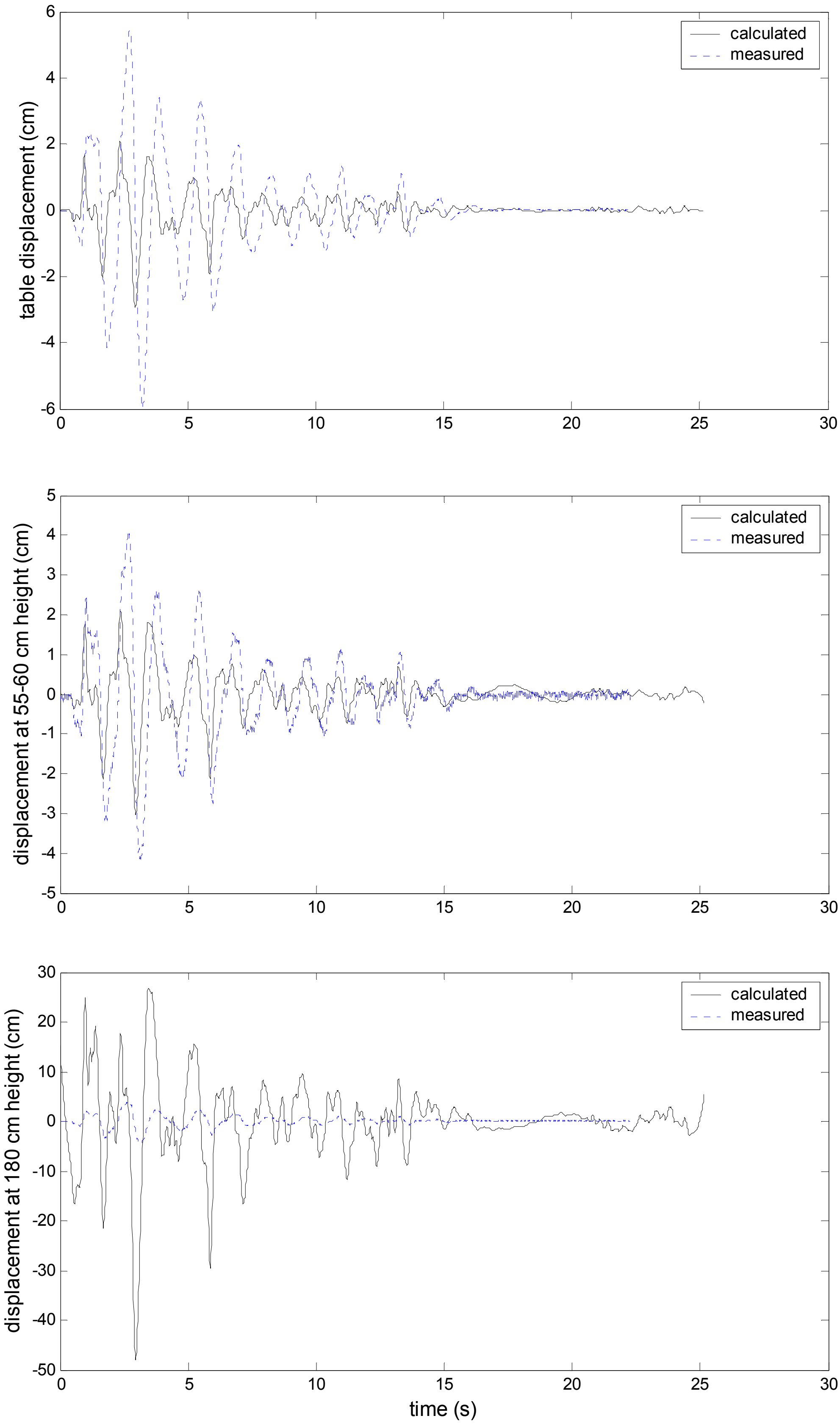

Figure 4.53. Calculated displacements compared to measured displacements for Test 6-7

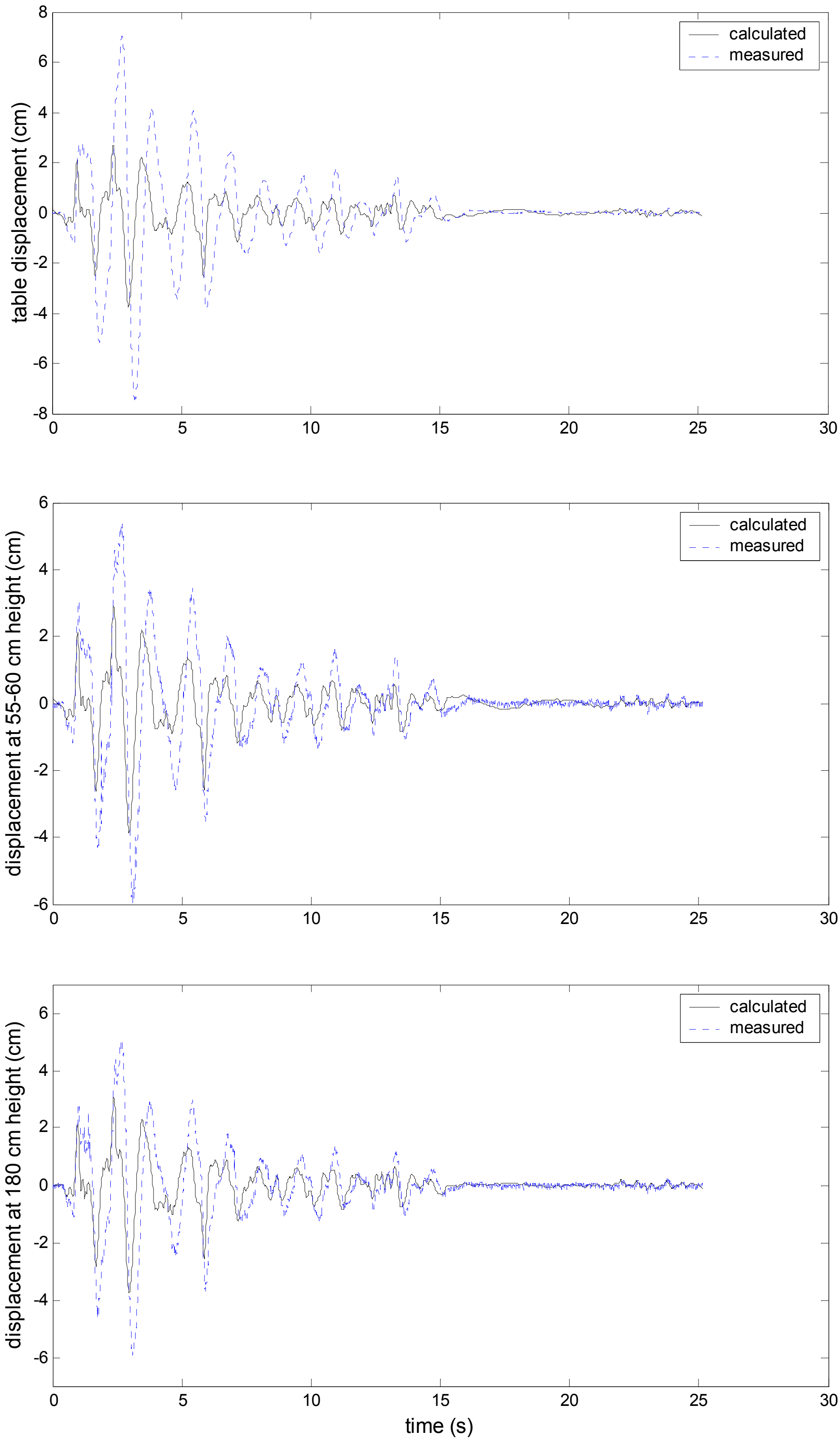

Figure 4.54. Calculated displacements compared to measured displacements for Test 7-12

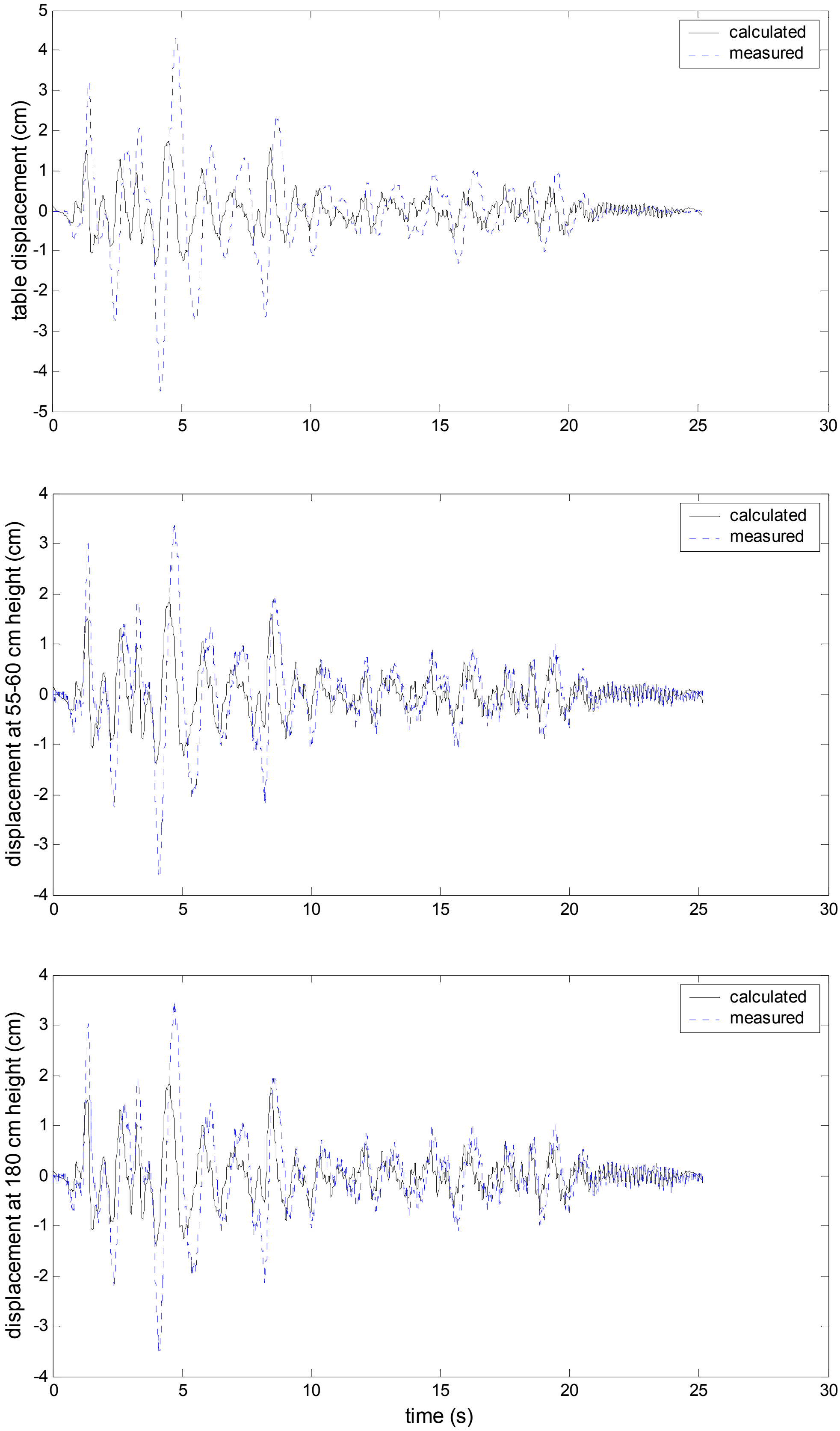

Figure 4.55. Calculated displacements compared to measured displacements for Test 8a-9

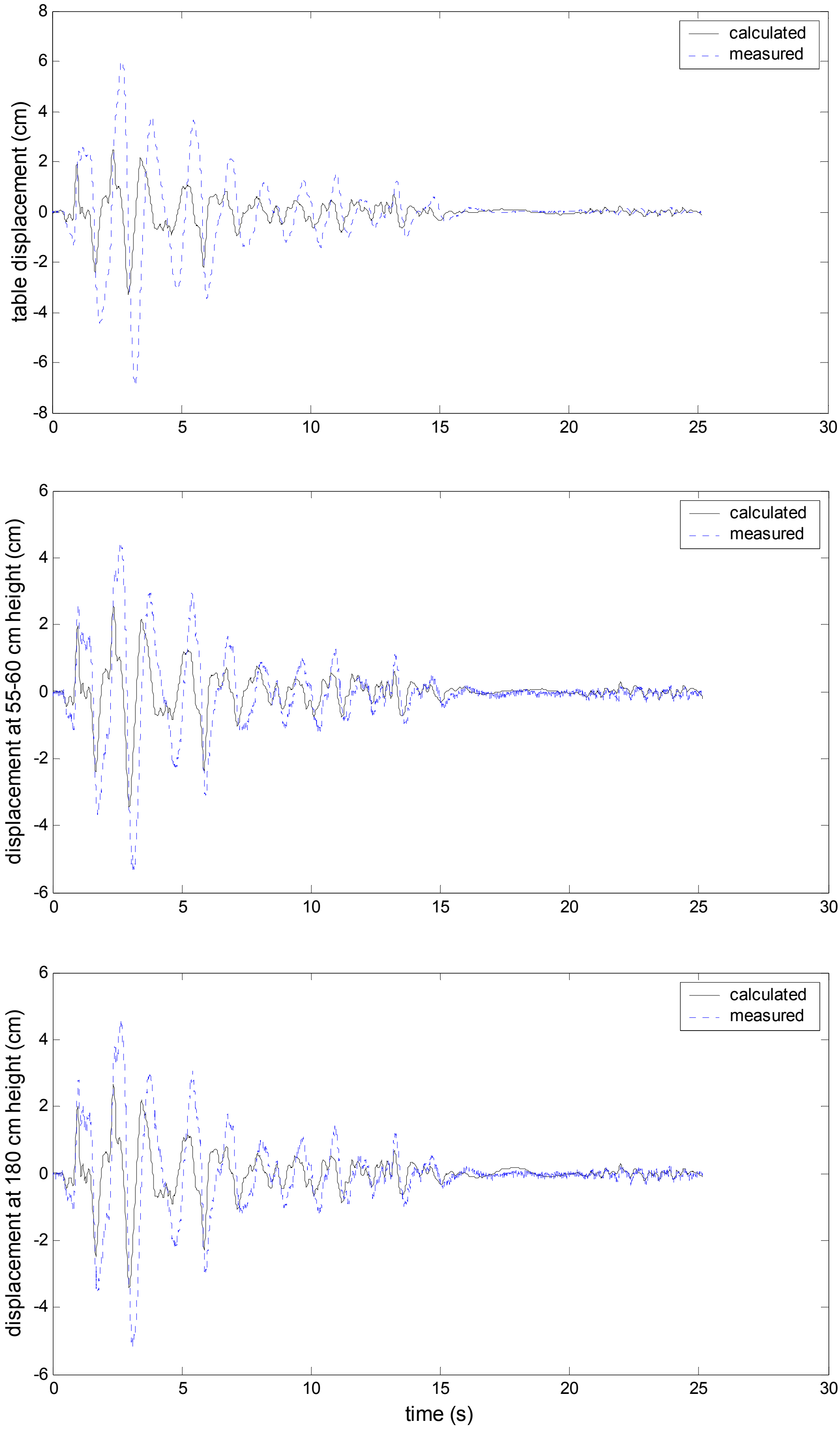

Figure 4.56. Calculated displacements compared to measured displacements for Test 8b-8

4.4. Geotextile Stress Records

The displacements measured by the transducers connected to the fishing lines are converted to strains and then to stresses for the instrumented geotextile regions by the Matlab code displacement.m. Negative values resulting from crumpling in geotextile are corrected as zero stress. Then the time records of calculated geotextile stresses are plotted. These plots reveal that there are instantaneous spikes, some of which even exceed the ultimate tensile strength of the geotextile reinforcement. However, no damage to the geotextile was observed while testing, so taking these extreme values into consideration in design would be too conservative. Therefore in order to filter these spikes, stress values were also averaged over 0.1 second intervals and records filtered in this way were plotted. The geotextile stress records plotted in both ways for the shakings with the highest maximum table acceleration in each of the eight tests are presented in Figures 4.57 to 4.74. Peak values obtained from these figures are used in Sections 4.5 to 4.10 in evaluating the effects of various parameters on maximum geotextile stresses during shaking.

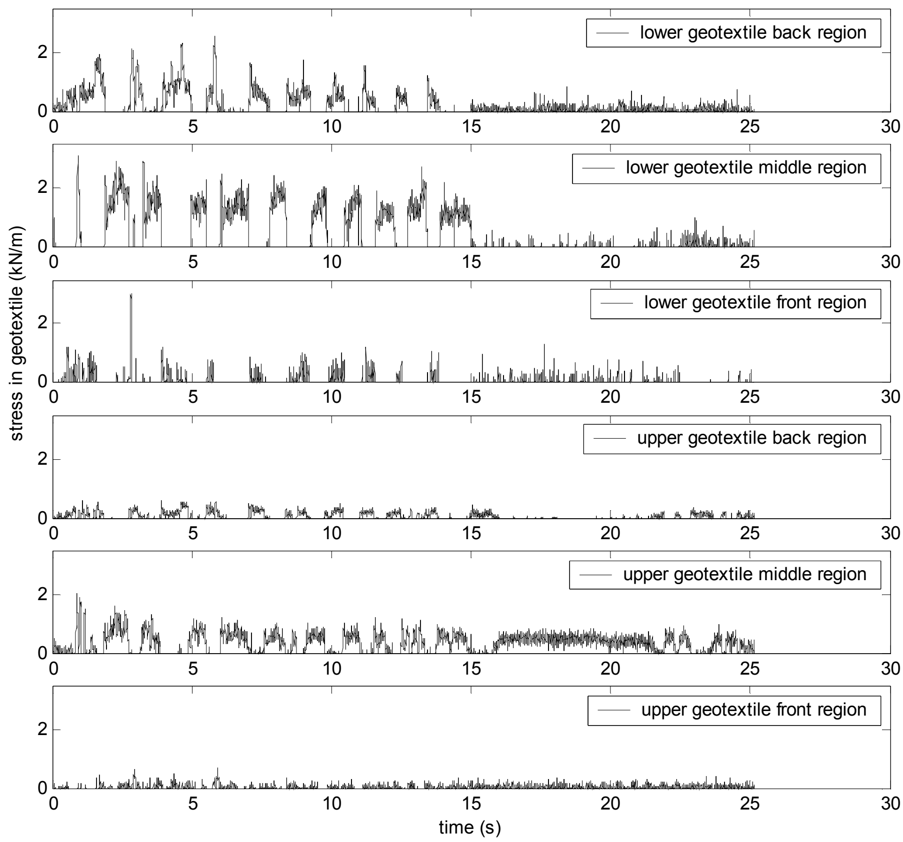

Figure 4.57. Stresses in instrumented geotextile layers for Test 1-10 (no filtering applied)

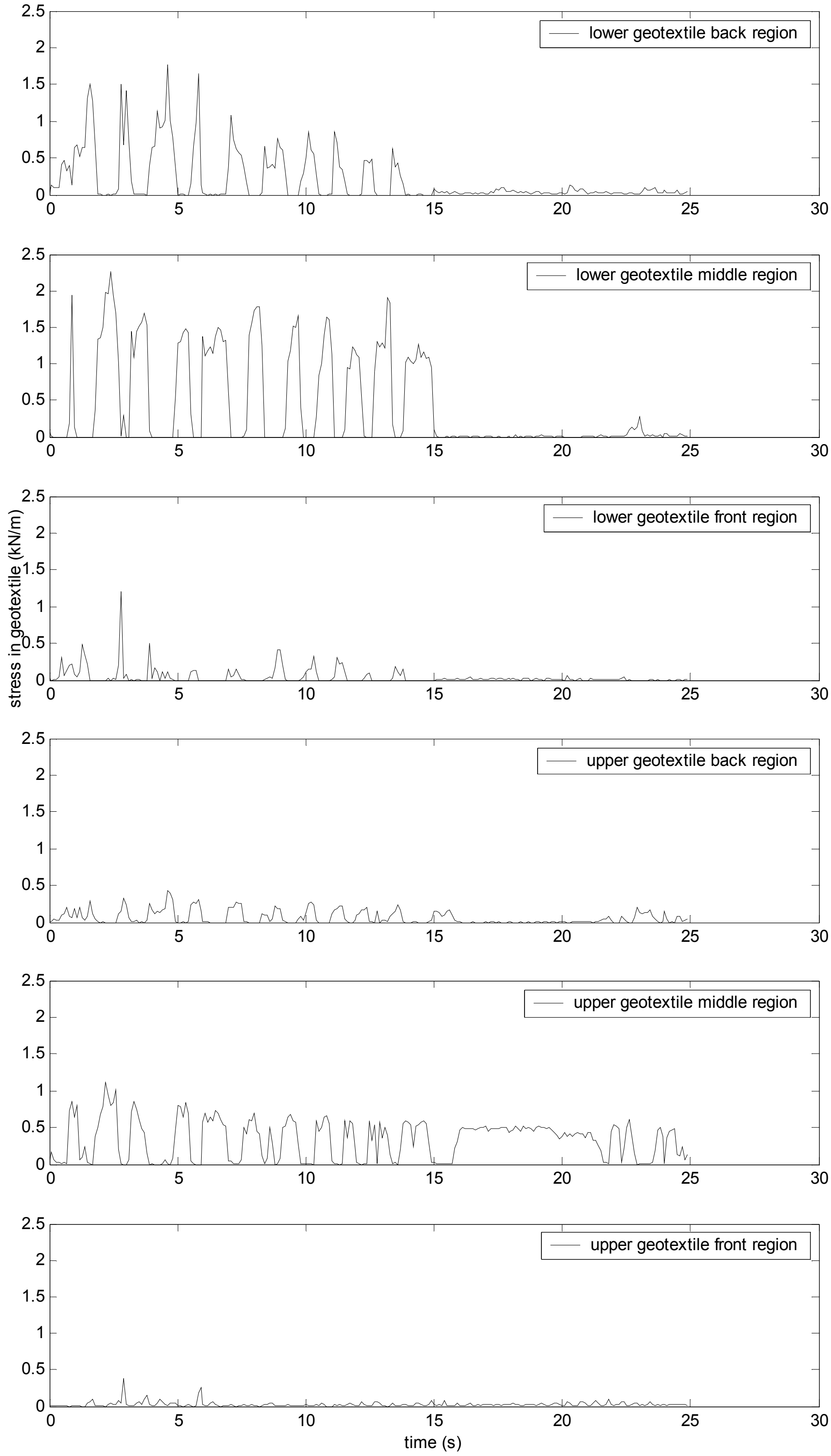

Figure 4.58. Stresses in instrumented geotextile layers for Test 1-10 (filtered by averaging for 0.1 s intervals)

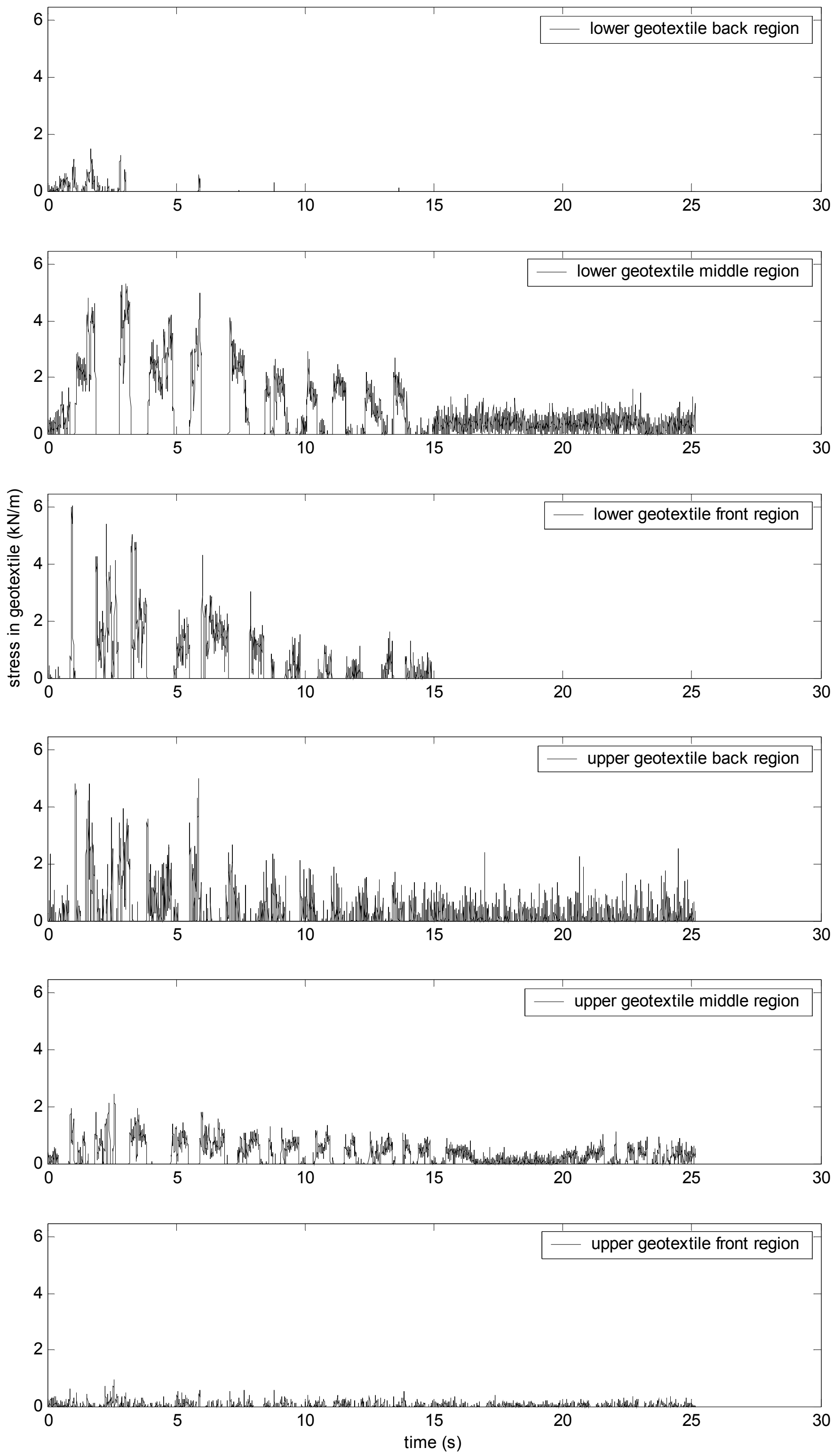

Figure 4.59. Stresses in instrumented geotextile layers for Test 2-6 (no filtering applied)

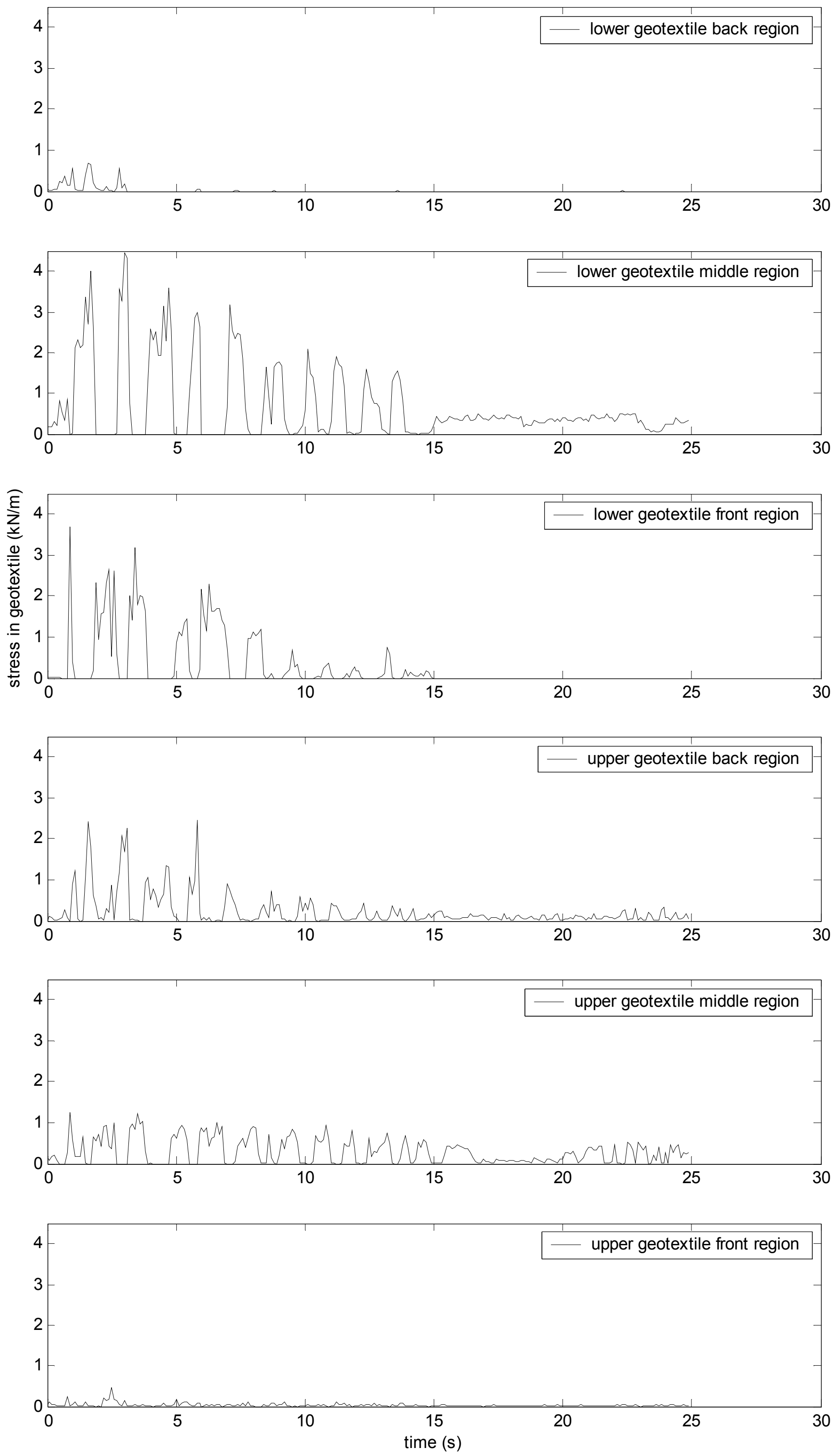

Figure 4.60. Stresses in instrumented geotextile layers for Test 2-6 (filtered by averaging for 0.1 s intervals)

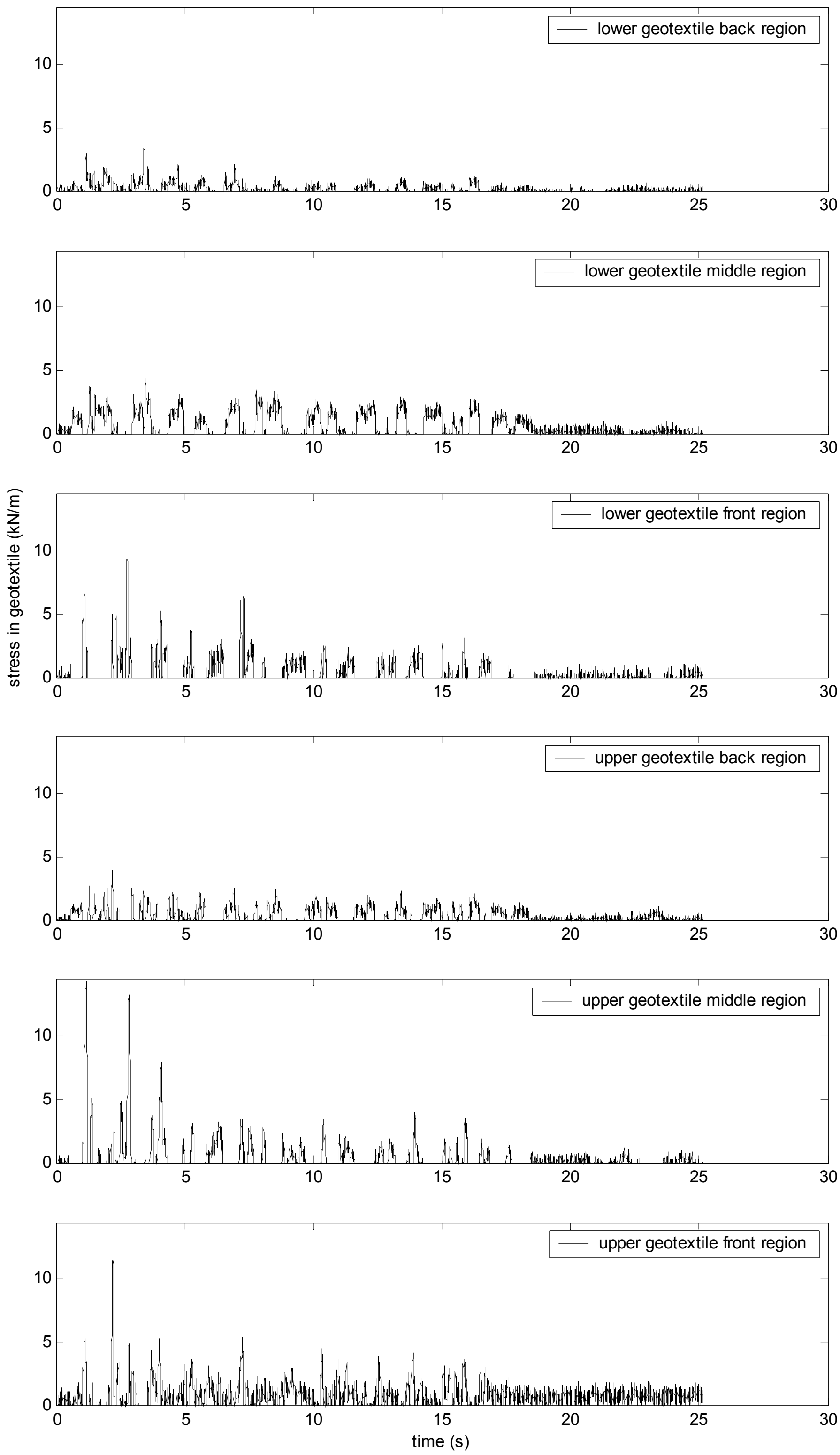

Figure 4.61. Stresses in instrumented geotextile layers for Test 3-10 (no filtering applied)

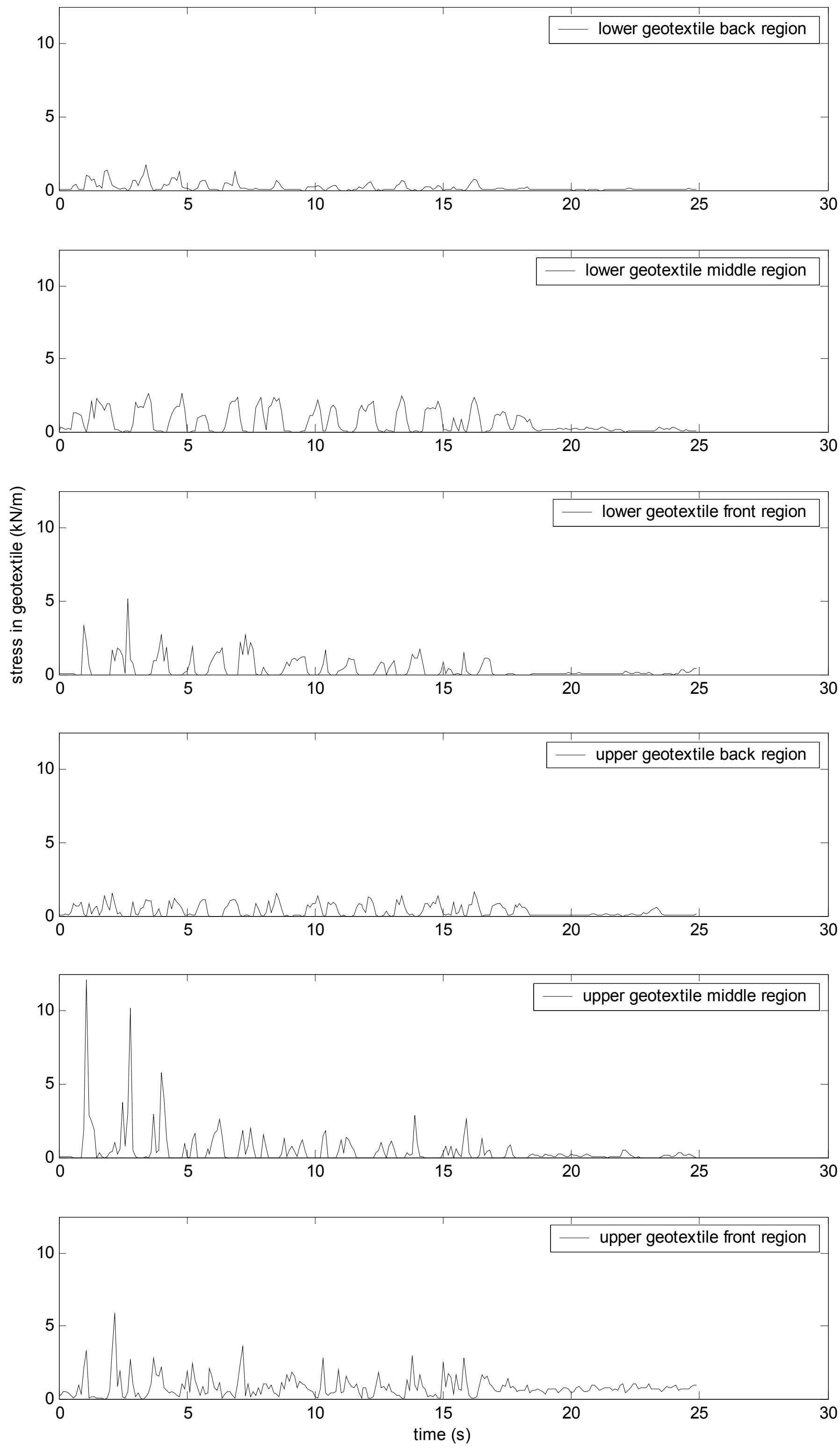

Figure 4.62. Stresses in instrumented geotextile layers for Test 3-10 (filtered by averaging for 0.1 s intervals)

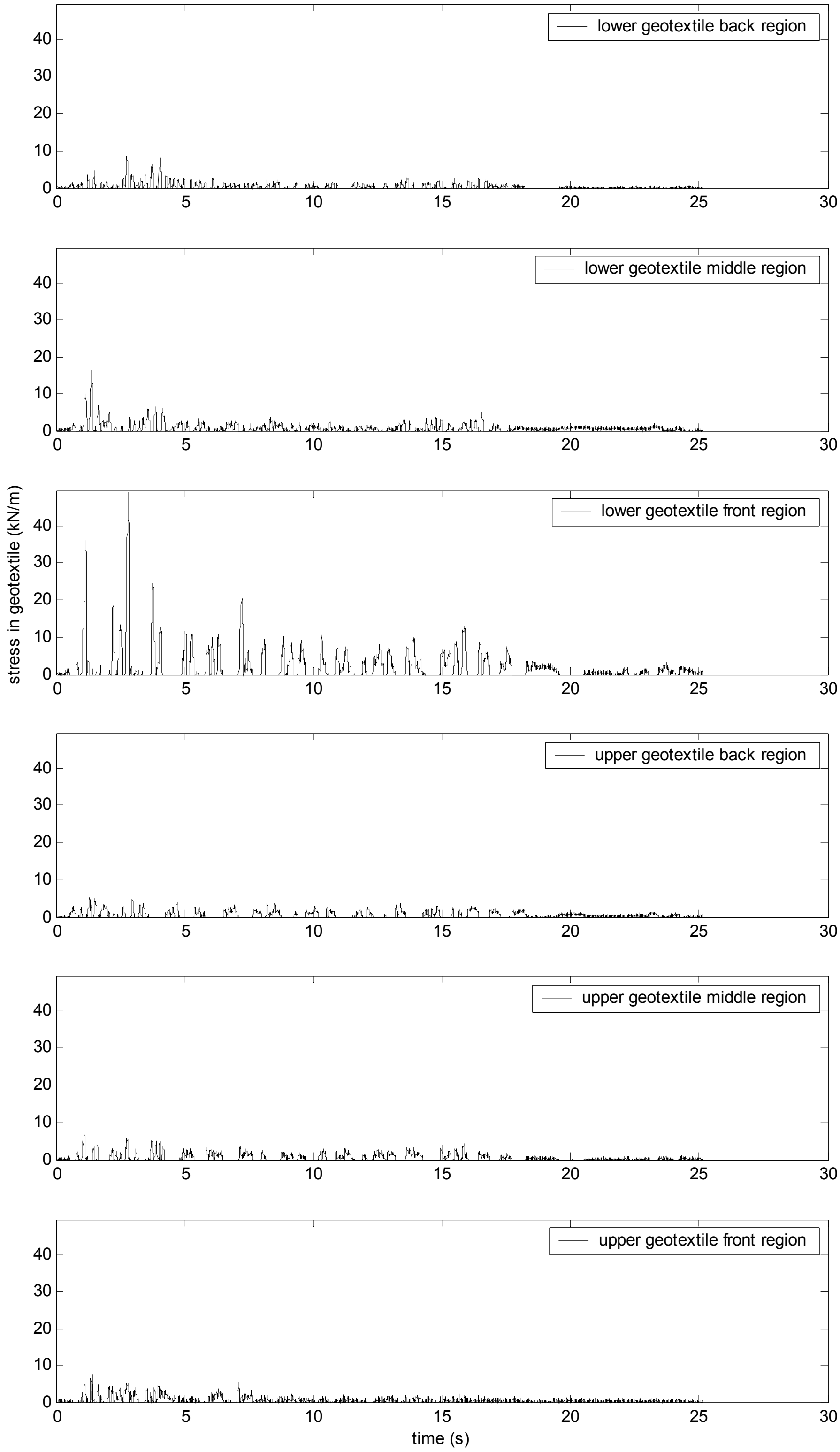

Figure 4.63. Stresses in instrumented geotextile layers for Test 4-18 (no filtering applied)

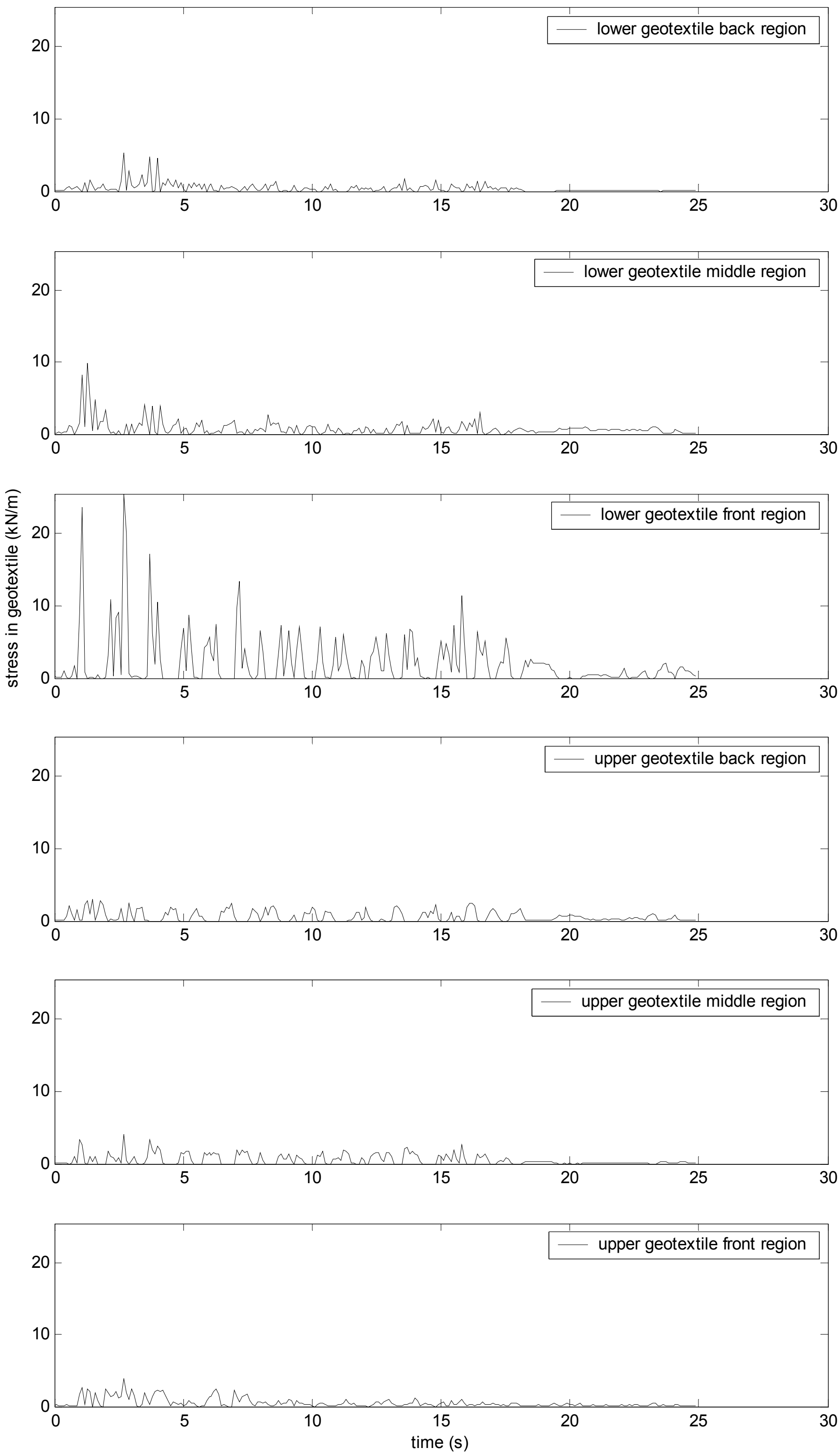

Figure 4.64. Stresses in instrumented geotextile layers for Test 4-18 (filtered by averaging for 0.1 s intervals)

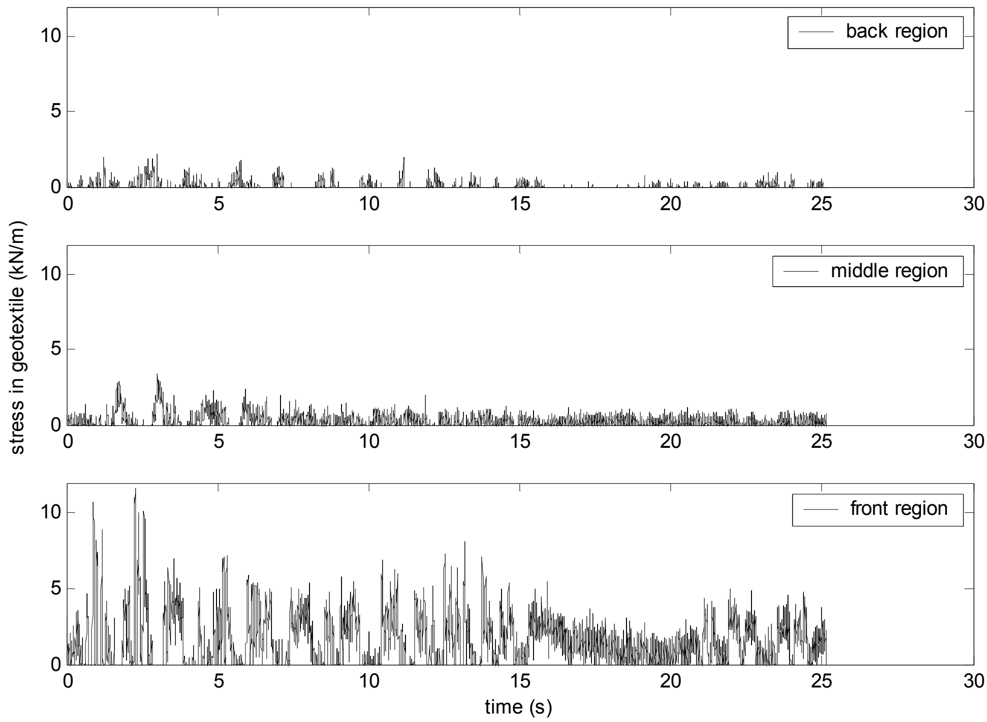

Figure 4.65. Stresses in instrumented geotextile layer for Test 5-8 (no filtering applied) (measurements for Test 5-9 are impaired by falling blocks)

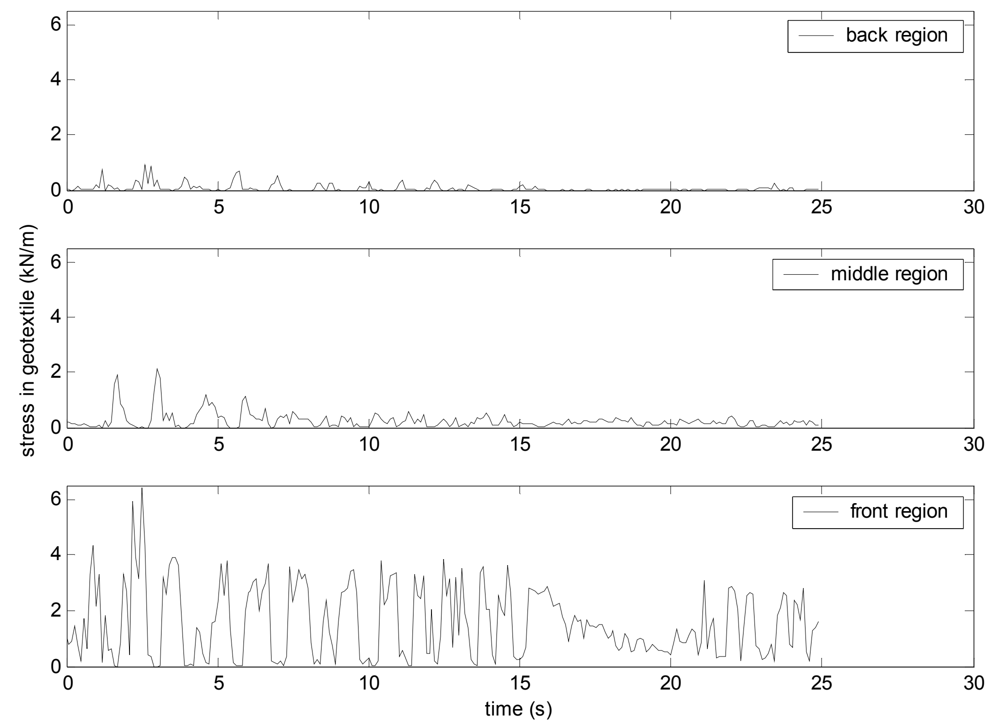

Figure 4.66. Stresses in instrumented geotextile layer for Test 5-8 (filtered by averaging for 0.1 s intervals)

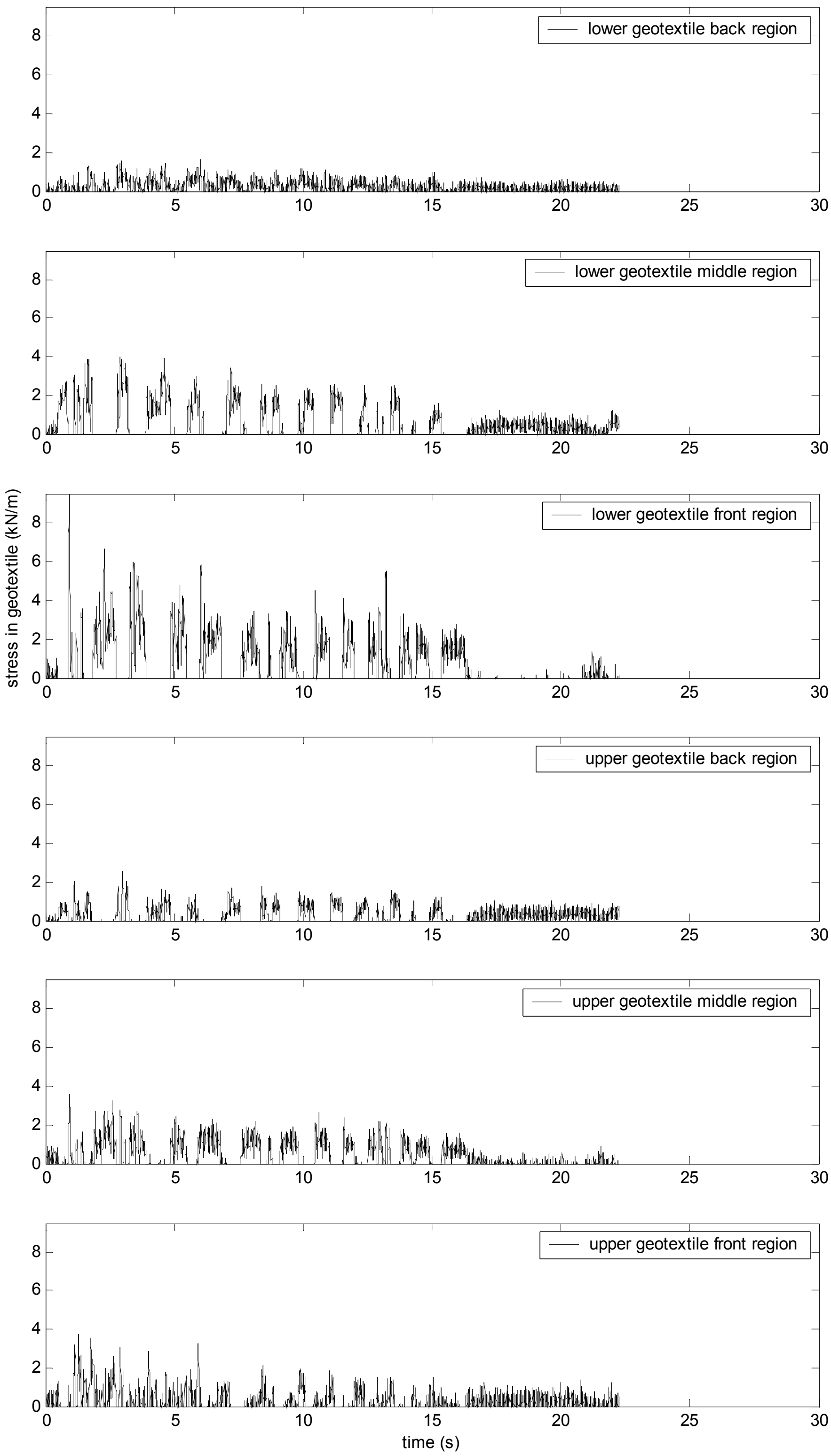

Figure 4.67. Stresses in instrumented geotextile layers for Test 6-7 (no filtering applied)

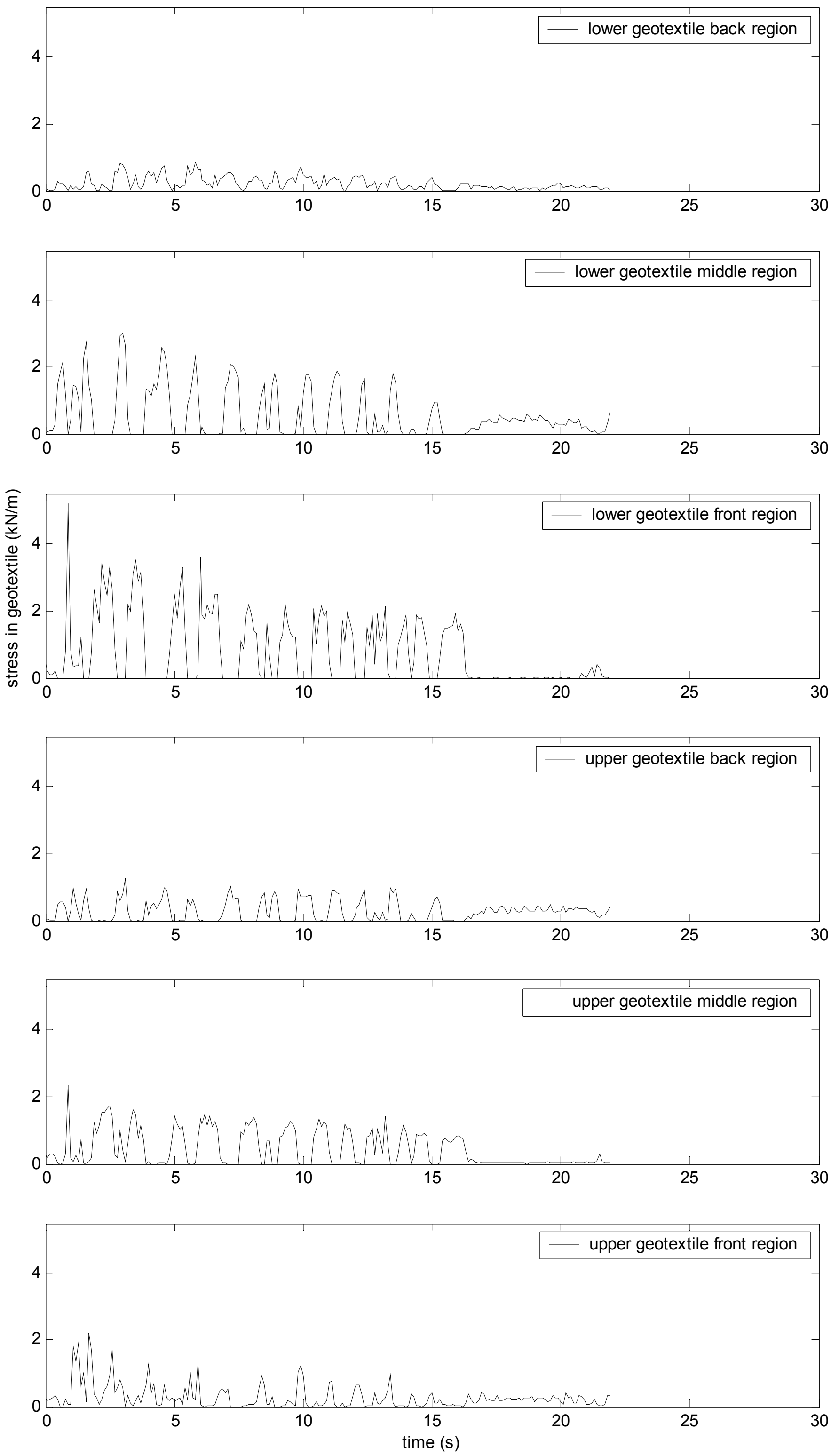

Figure 4.68. Stresses in instrumented geotextile layers for Test 6-7 (filtered by averaging for 0.1 s intervals)

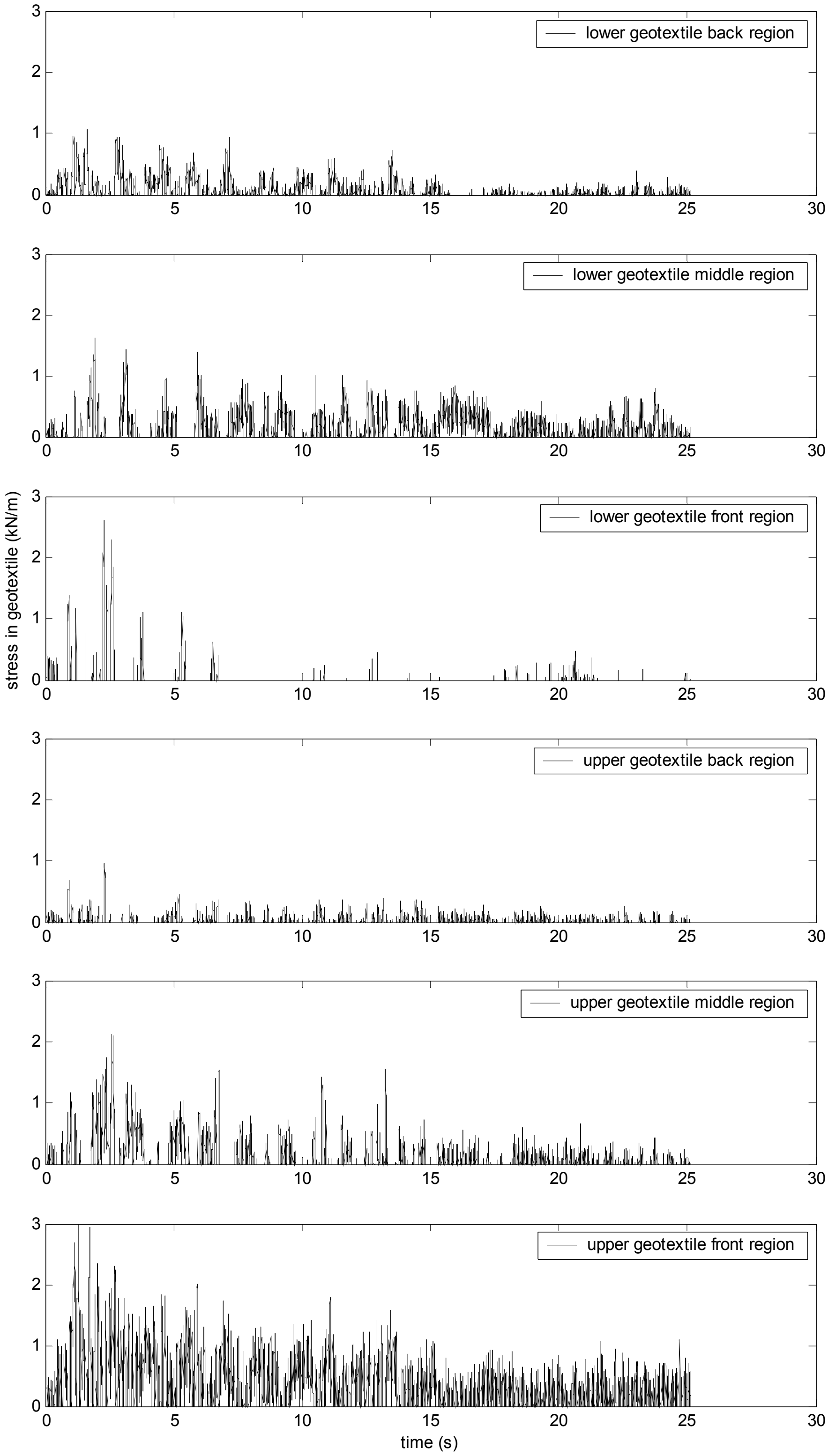

Figure 4.69. Stresses in instrumented geotextile layers for Test 7-12 (no filtering applied)

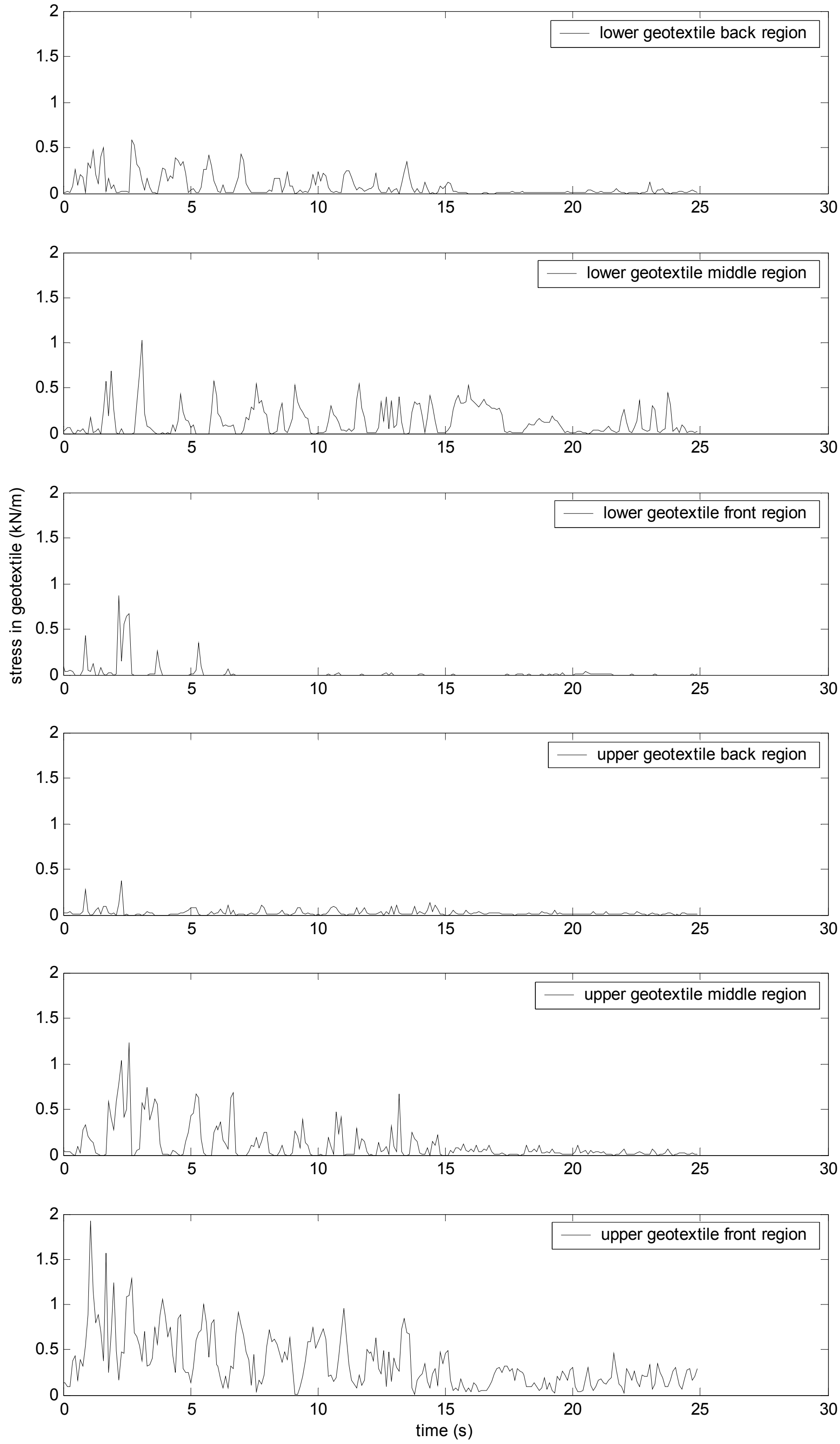

Figure 4.70. Stresses in instrumented geotextile layers for Test 7-12 (filtered by averaging for 0.1 s intervals)

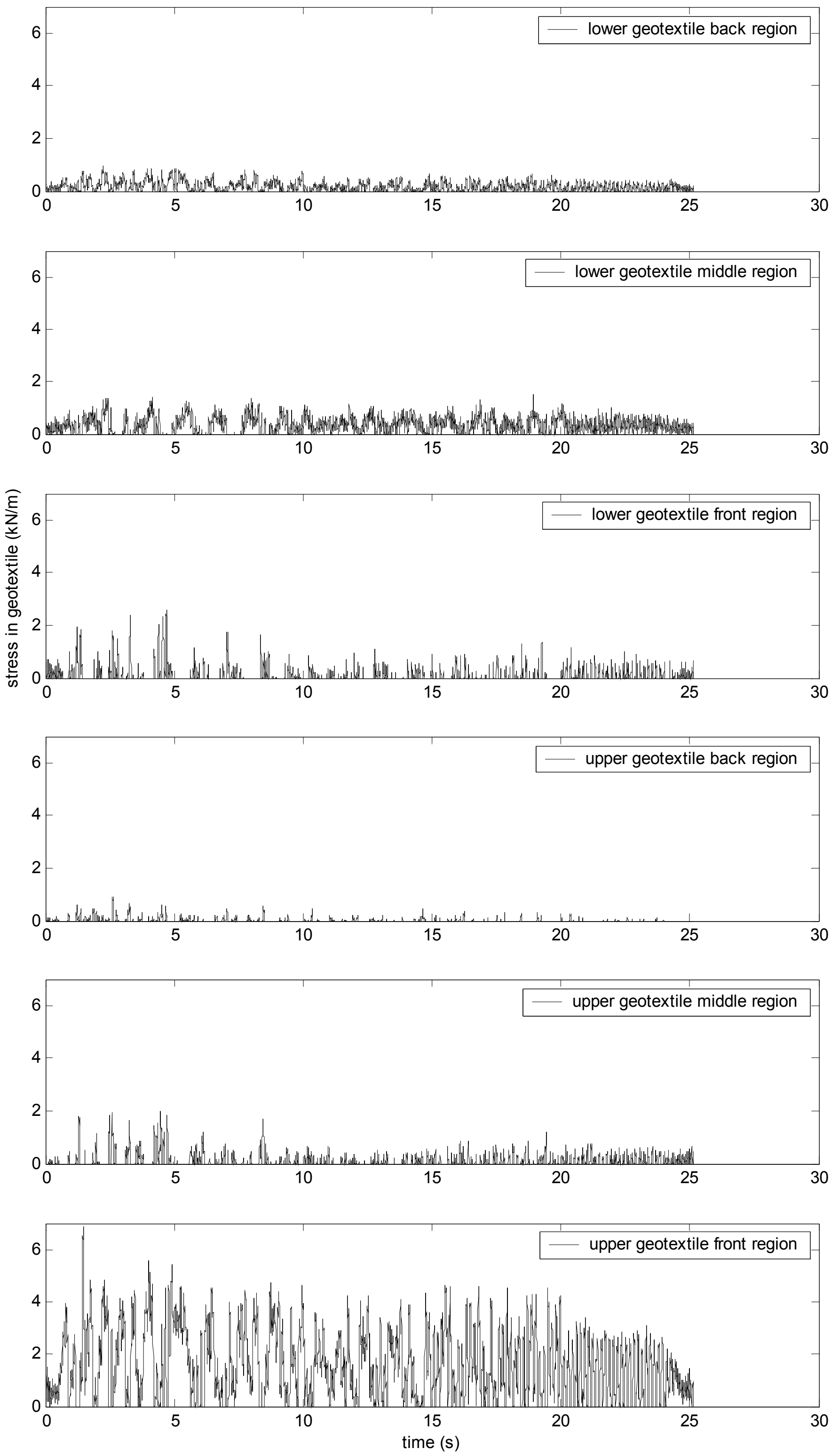

Figure 4.71. Stresses in instrumented geotextile layers for Test 8a-9 (no filtering applied)

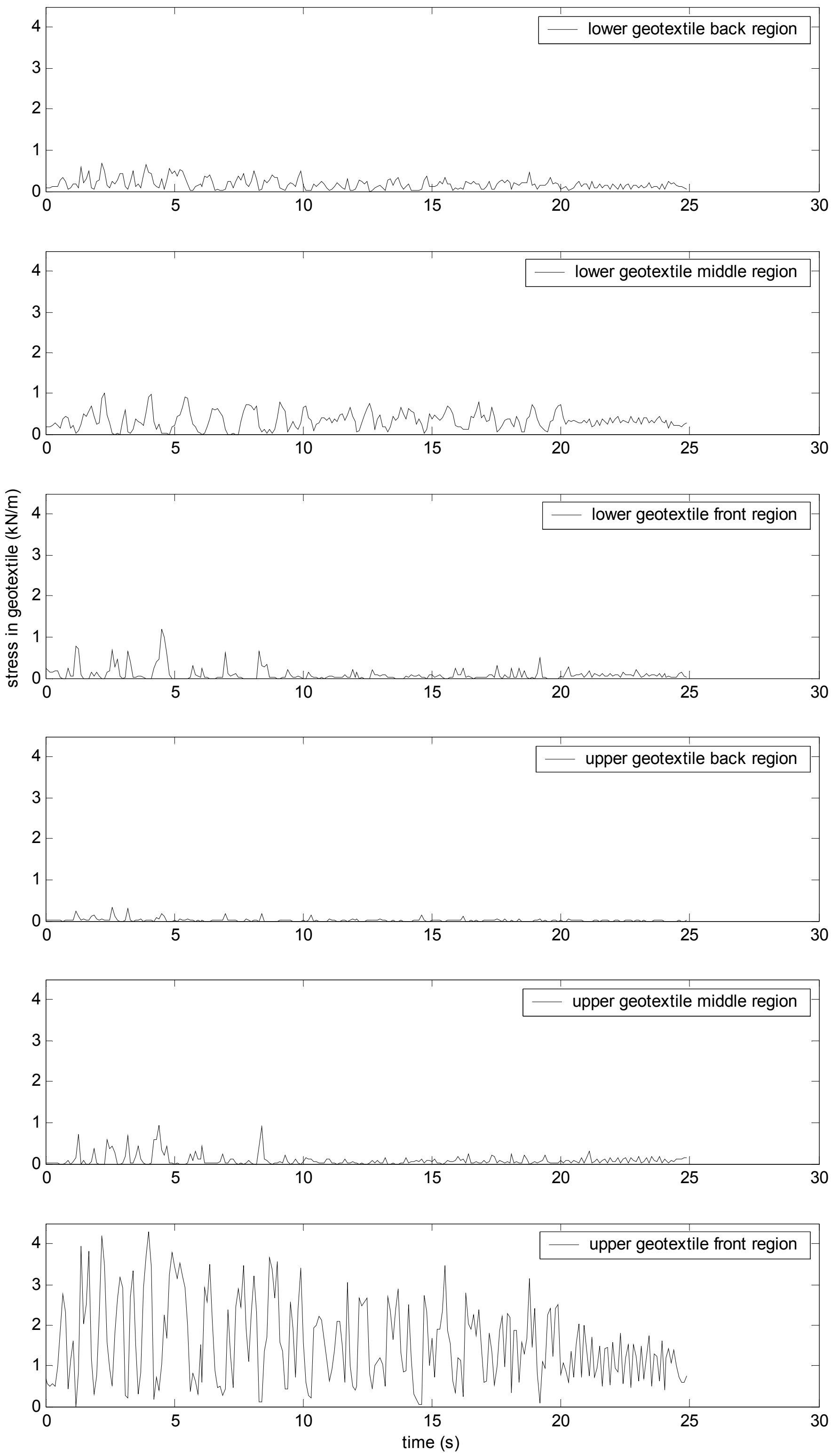

Figure 4.72. Stresses in instrumented geotextile layers for Test 8a-9 (filtered by averaging for 0.1 s intervals)

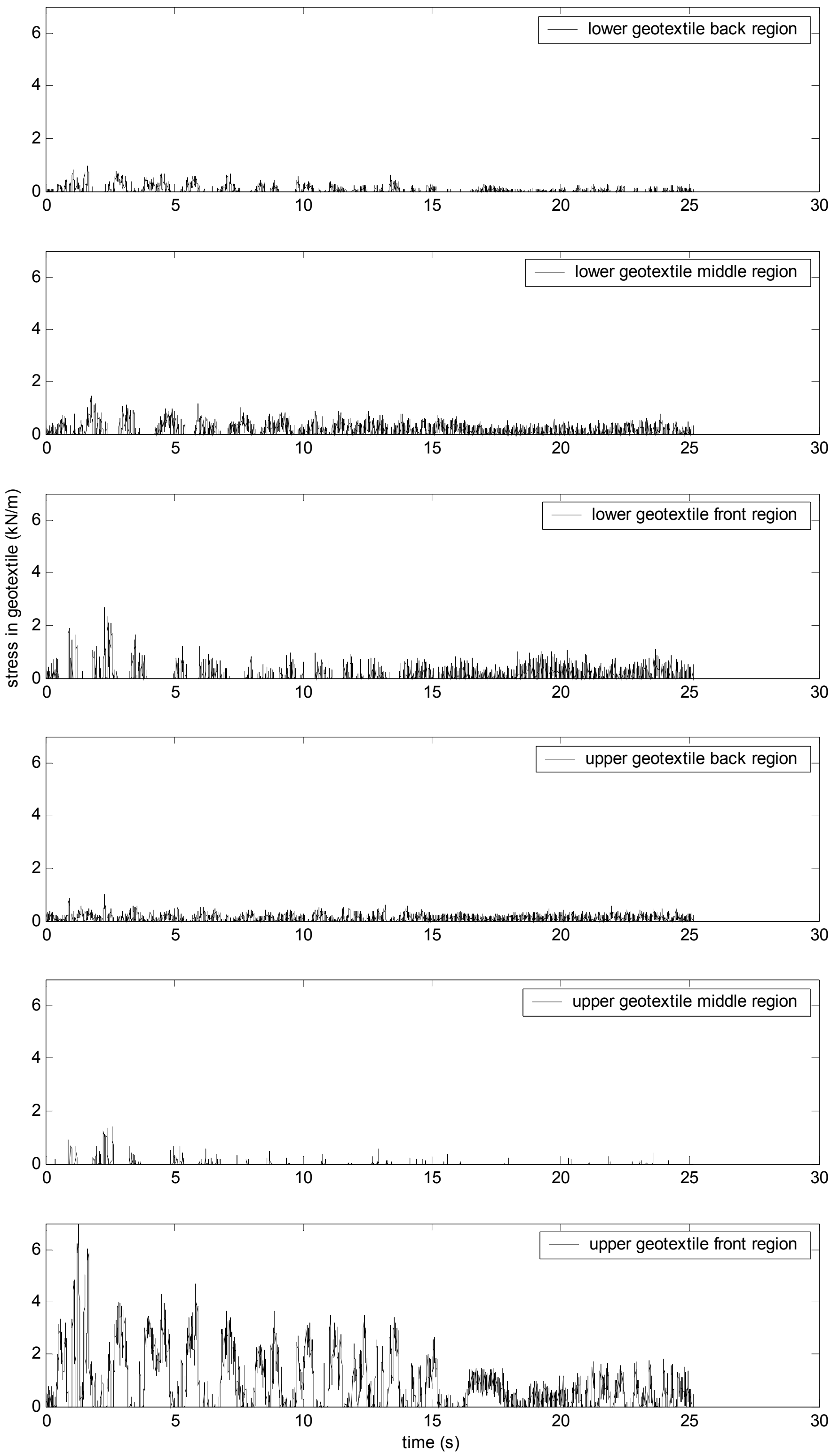

Figure 4.73. Stresses in instrumented geotextile layers for Test 8b-8 (no filtering applied)

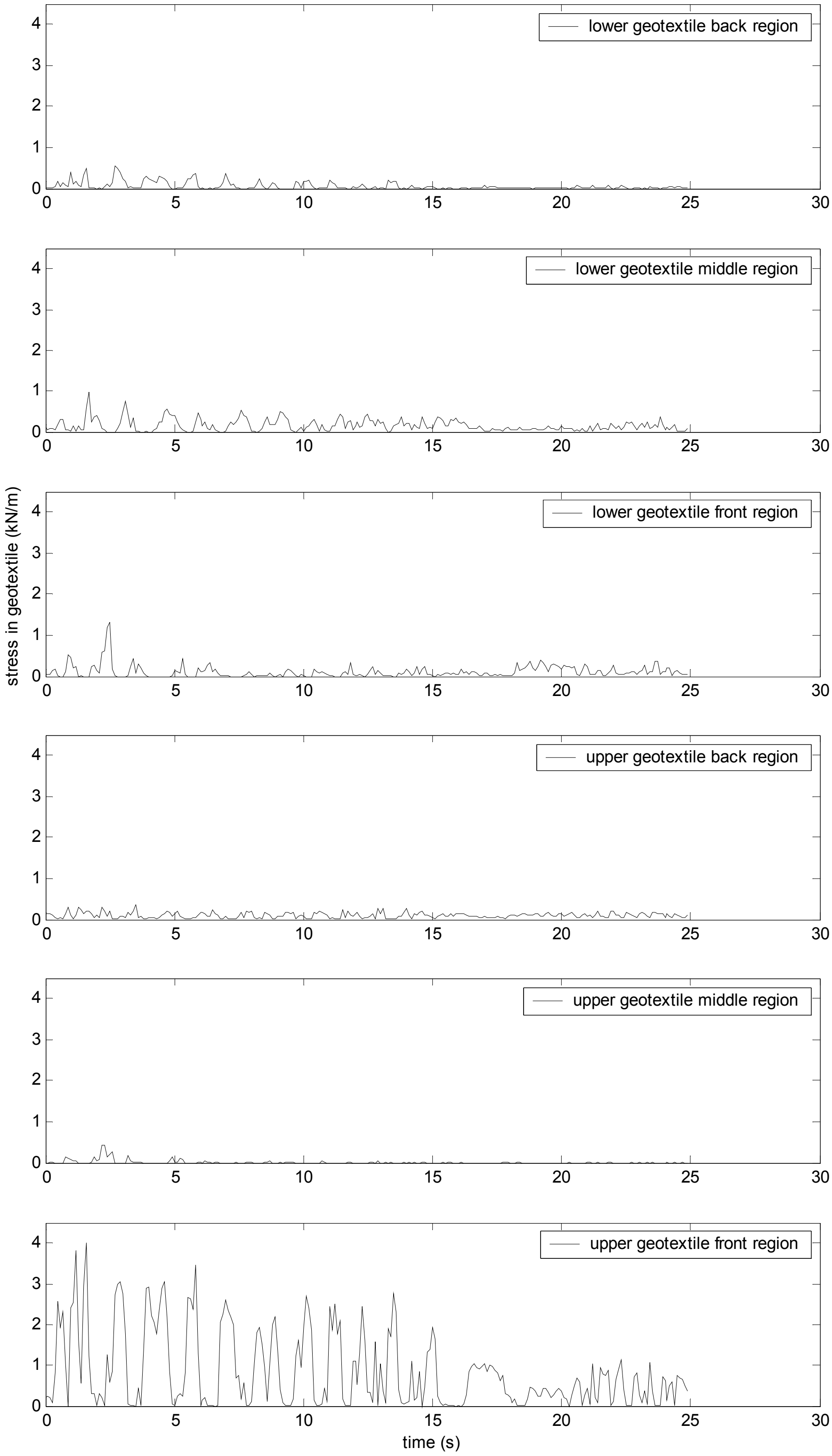

Figure 4.74. Stresses in instrumented geotextile layers for Test 8b-8 (filtered by averaging for 0.1 s intervals)

4.5. Effects of Increasing Shaking Table Acceleration

In all tests, the original El Centro earthquake record was scaled down in the beginning to ten or twenty per cent and this shaking was applied to the test configuration. Then the scale was increased and the configuration was shaken again, so the effect of increasing peak ground acceleration on the GRS wall was investigated.

4.5.1. Effects of Shaking Table Acceleration on Maximum Acceleration Measured on Wall Face and Top

It was observed from Figures 4.1 to 4.27 that measured accelerations increased from bottom to top on wall face and back to front on top and accelerations measured by M7 and M8, uppermost accelerometer on face and front accelerometer on top, respectively, were highest.

Table 4.1. Amplification of acceleration on face for Test 1

Accelerometer	Height from bottom (cm)	Equation of best fit line for		R^2 value for	
		Outward direction	Inward direction	Outward direction	Inward direction
M2	15	y=1.0326x+0.0007	y=1.0324x+0.0006	0.9993	0.9998
M3	55	y=1.1525x-0.0055	y=1.1101x-0.0053	0.9969	0.9952
M4	108	y=1.2529x-0.0073	y=1.3275x-0.0264	0.9965	0.9848
M6	160	y=1.3481x+0.0133	y=1.6222x-0.0446	0.9875	0.9625
M7	180	y=1.3682x+0.0297	y=1.6831x-0.0399	0.9519	0.9540

Table 4.2. Amplification of acceleration on top for Test 1

Accelerometer	Distance from wall face (cm)	Equation of best fit line for		R^2 value for	
		Outward direction	Inward direction	Outward direction	Inward direction
M8	30	y=1.2455x+0.0143	y=1.4995x+0.0341	0.9843	0.9611
M9	70	y=1.2277x-0.0029	y=1.4066x+0.0347	0.9803	0.9551
M10	110	y=1.2827x+0.0147	y=1.6030x+0.0441	0.9914	0.9616
M11	150	y=1.3041x+0.0177	y=1.6506x+0.0465	0.9904	0.9643
M12	190	y=1.2863x+0.0136	y=1.6100x-0.0461	0.9909	0.9608

The maximum outward (measured as positive) and inward (measured as negative) values measured during shaking by accelerometers located on the wall are plotted against the maximum acceleration recorded by the accelerometer located on the shaking table for each test in Figures 4.75 to 4.91. The values recorded are not necessarily concurrent. The plots reveal that the maximum accelerations on the wall face and top increase somewhat linearly with increasing maximum table acceleration. All measured accelerations on the wall face were higher than the table acceleration. The lowermost accelerometer on the wall face generally measured values very close to the table acceleration. Numerical figures defining the amplification of acceleration are shown in Tables 4.1 to 4.17.

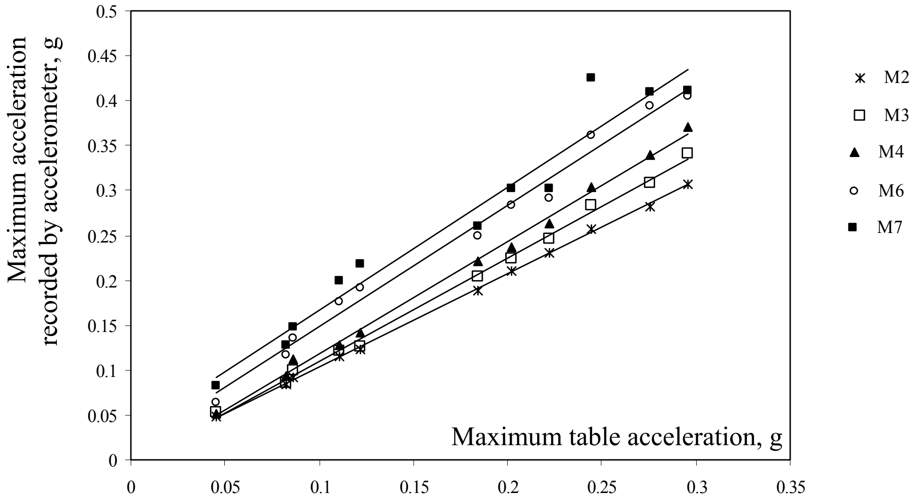

(a) Outward direction

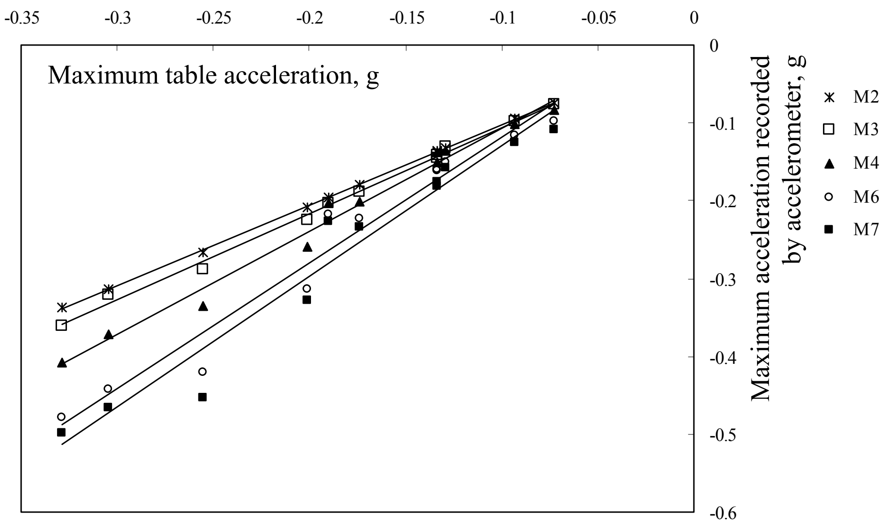

(b) Inward direction

Figure 4.75. Amplification of acceleration on face for Test 1

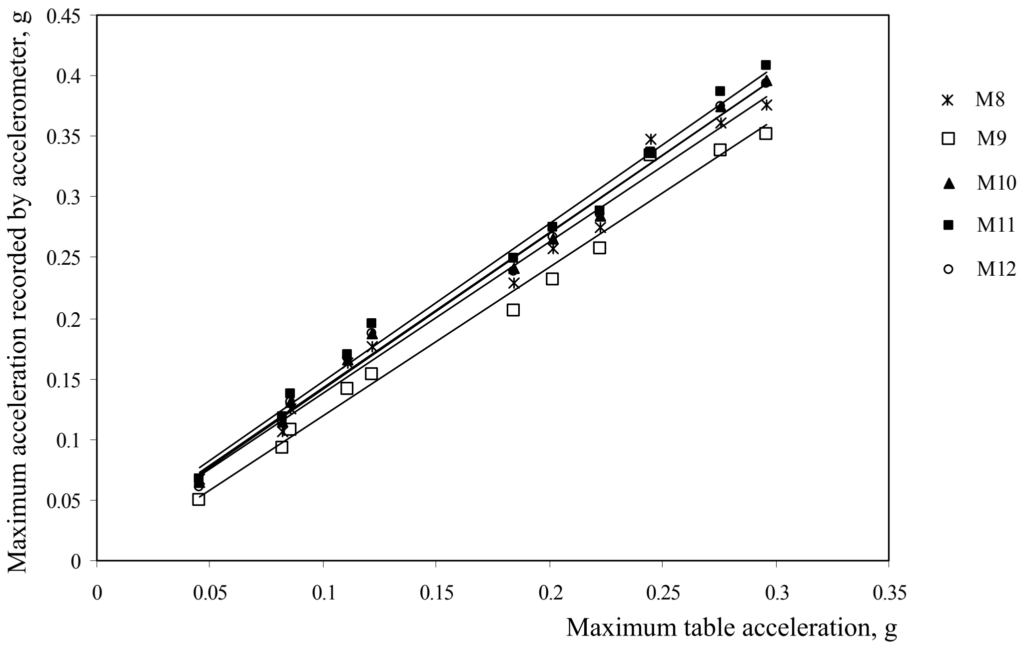

(a) Outward direction

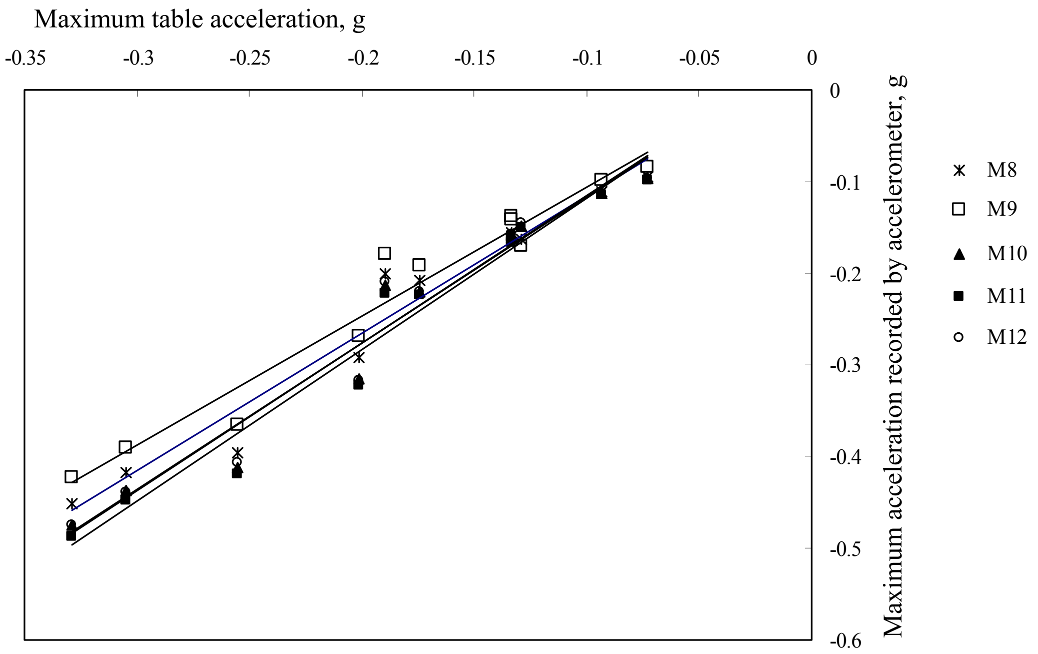

(b) Inward direction

Figure 4.76. Amplification of acceleration on top for Test 1

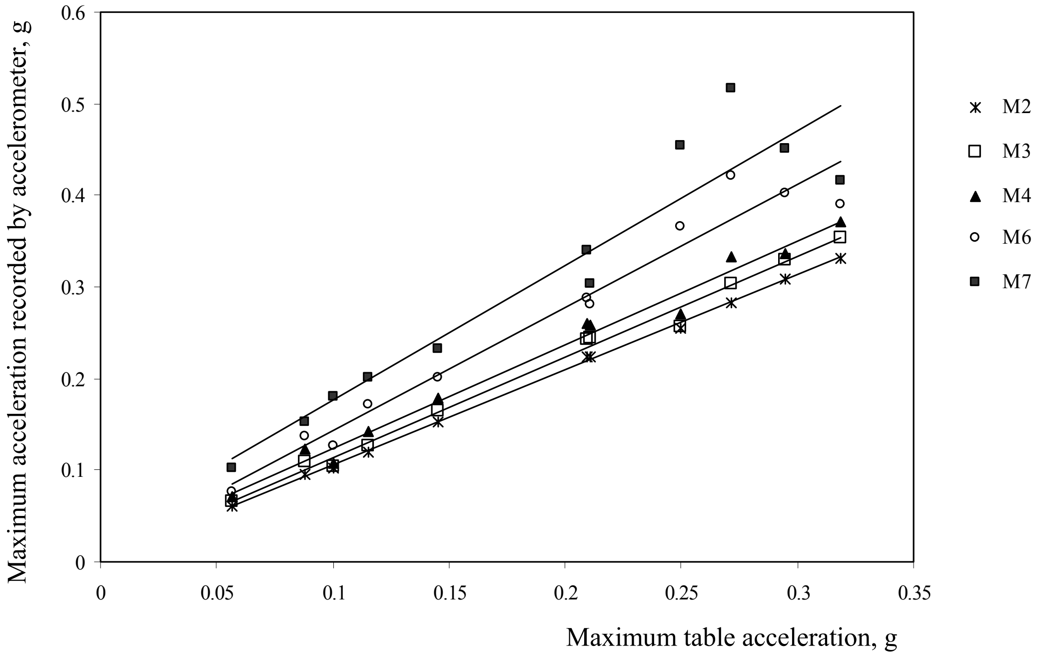

(a) Outward direction

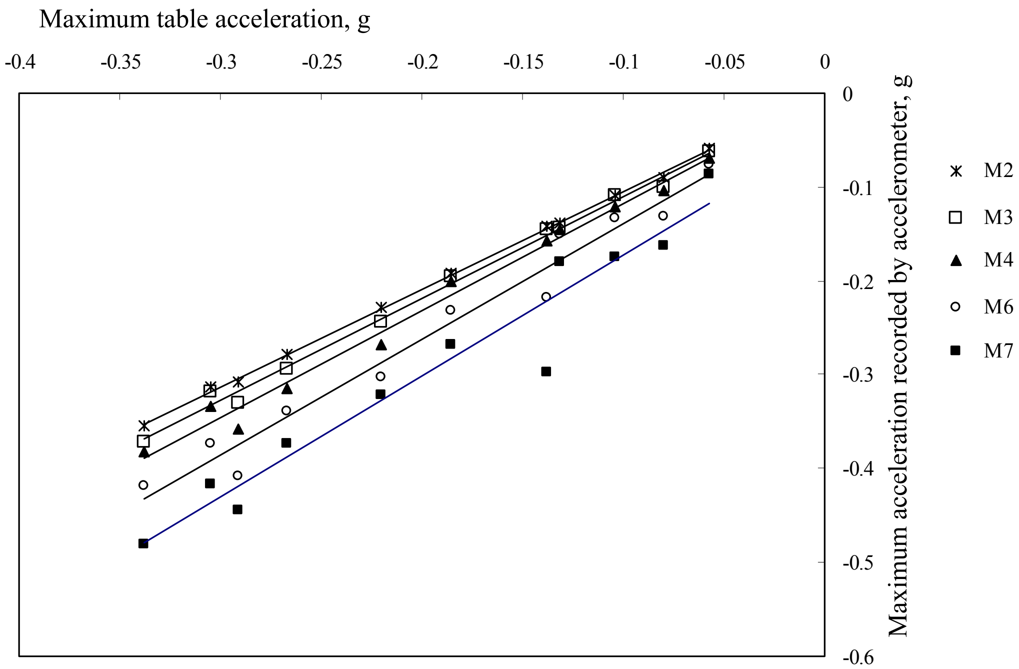

(b) Inward direction

Figure 4.77. Amplification of acceleration on face for Test 2

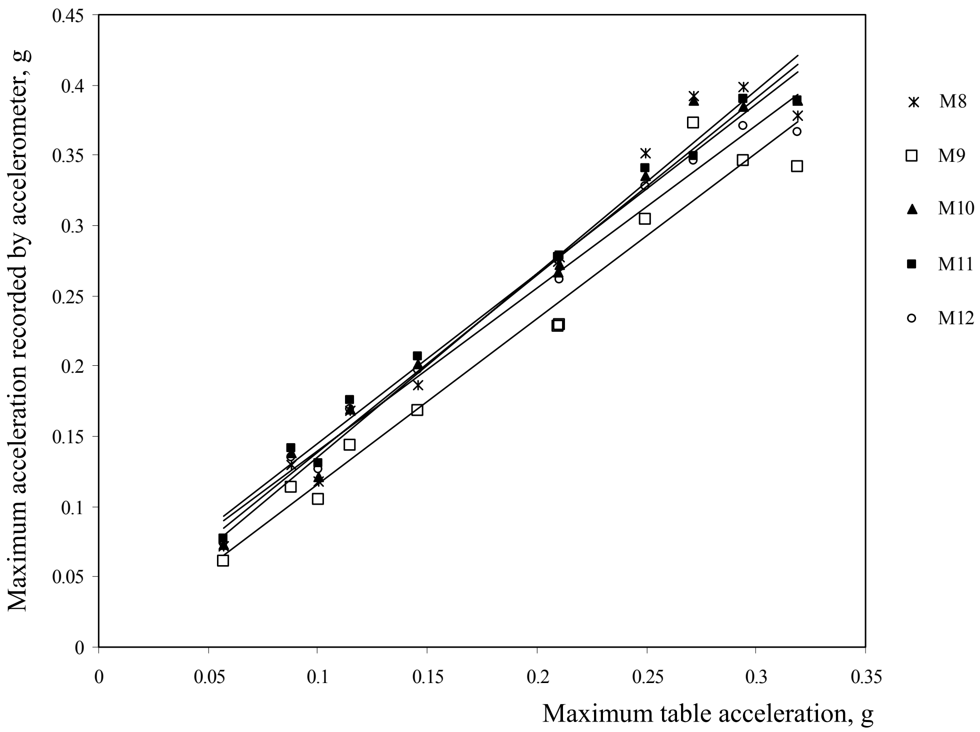

(a) Outward direction

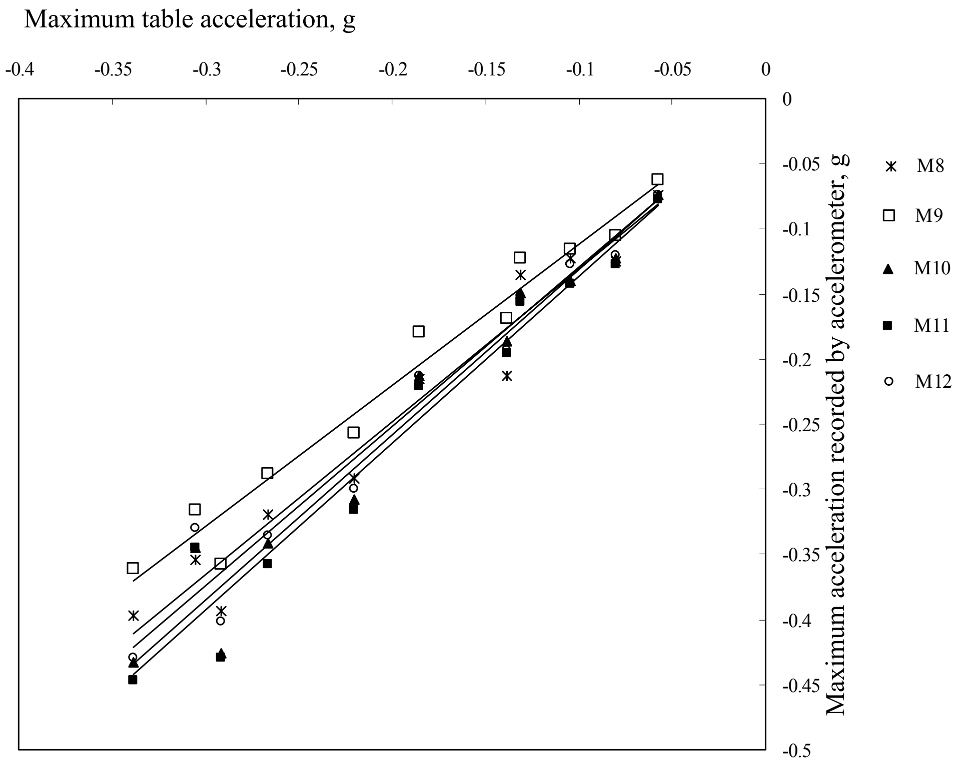

(b) Inward direction

Figure 4.78. Amplification of acceleration on top for Test 2

Table 4.3. Amplification of acceleration on face for Test 2

Accelerometer	Height from bottom (cm)	Equation of best fit line for		R^2 value for	
		Outward direction	Inward direction	Outward direction	Inward direction
M2	15	y=1.0357x+0.0002	y=1.0369x-0.0011	0.9990	0.9991
M3	55	y=1.0948x+0.0041	y=1.0844x-0.0015	0.9922	0.9944
M4	108	y=1.1297x+0.0111	y=1.1380x-0.0035	0.9866	0.9886
M6	160	y=1.3419x+0.0087	y=1.2290x-0.0162	0.9635	0.9707
M7	180	y=1.4740x+0.0284	y=1.2867x-0.0435	0.9024	0.9435

Table 4.4. Amplification of acceleration on top for Test 2

Accelerometer	Distance from wall face (cm)	Equation of best fit line for		R^2 value for	
		Outward direction	Inward direction	Outward direction	Inward direction
M8	30	y=1.3069x+0.0048	y=1.1723x-0.0143	0.9710	0.9595
M9	70	y=1.1794x-0.0017	y=1.0820x-0.0039	0.9578	0.9682
M10	110	y=1.2617x+0.0126	y=1.2662x-0.0052	0.9789	0.9567
M11	150	y=1.2071x+0.0244	y=1.2813x-0.0091	0.9874	0.9561
M12	190	y=1.1560x+0.0243	y=1.2203x-0.0081	0.9840	0.9605

Table 4.5. Amplification of acceleration on face for Test 3

Accelerometer	Height from bottom (cm)	Equation of best fit line for		R^2 value for	
		Outward direction	Inward direction	Outward direction	Inward direction
M2	15	y=1.0139x+0.0014	y=1.0212x+0.0010	0.9984	0.9987
M3	55	y=1.1141x-0.0057	y=1.0828x+0.0018	0.9912	0.9952
M4	108	y=1.2190x-0.0123	y=1.1036x-0.0003	0.9769	0.9896
M6	160	y=1.2786x-0.0048	y=1.0732x-0.0114	0.9757	0.9779
M7	180	y=1.2977x+0.0042	y=1.1566x-0.0147	0.9686	0.9758

Table 4.6. Amplification of acceleration on top for Test 3

Accelerometer	Distance from wall face (cm)	Equation of best fit line for		R^2 value for	
		Outward direction	Inward direction	Outward direction	Inward direction
M8	35	y=1.2288x+0.0079	y=1.0540x-0.0198	0.9707	0.9688
M9	110	y=1.1533x-0.0090	y=1.0755x-0.0083	0.9769	0.9803
M10	185	y=1.1503x-0.000005	y=1.0867x-0.0052	0.9832	0.9848
M11	260	y=1.0285x+0.0092	y=1.0002x-0.0046	0.9781	0.9837
M12	275 (inside rubber)	y=1.0379x+0.0151	y=1.0177x-0.0118	0.9818	0.9877

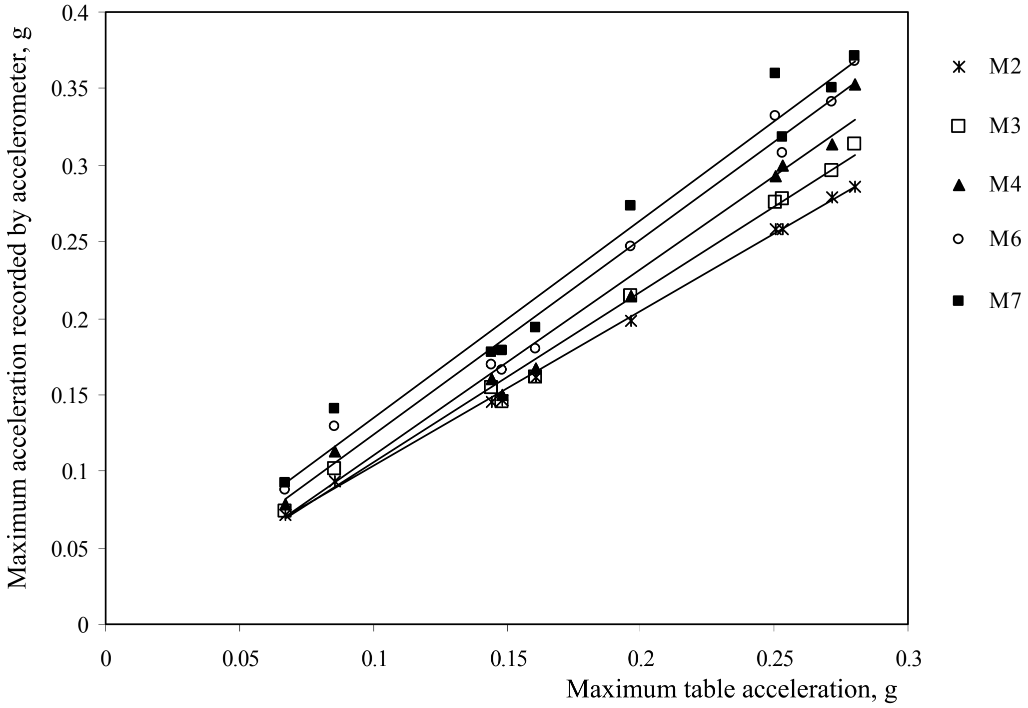

(a) Outward direction

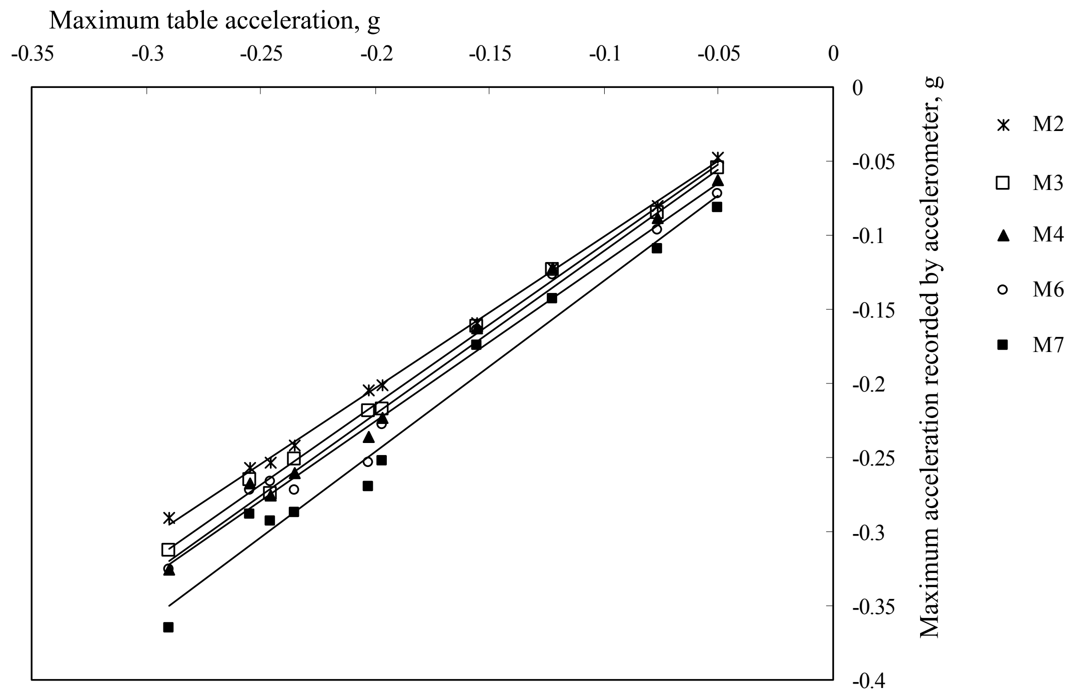

(b) Inward direction

Figure 4.79. Amplification of acceleration on face for Test 3

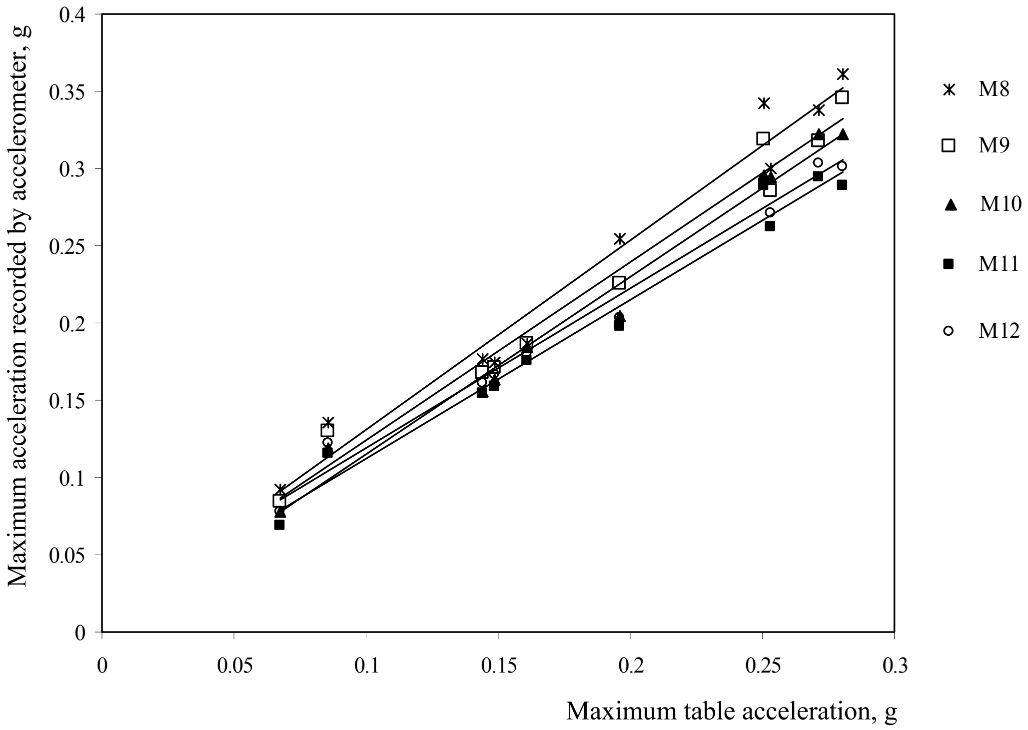

(a) Outward direction

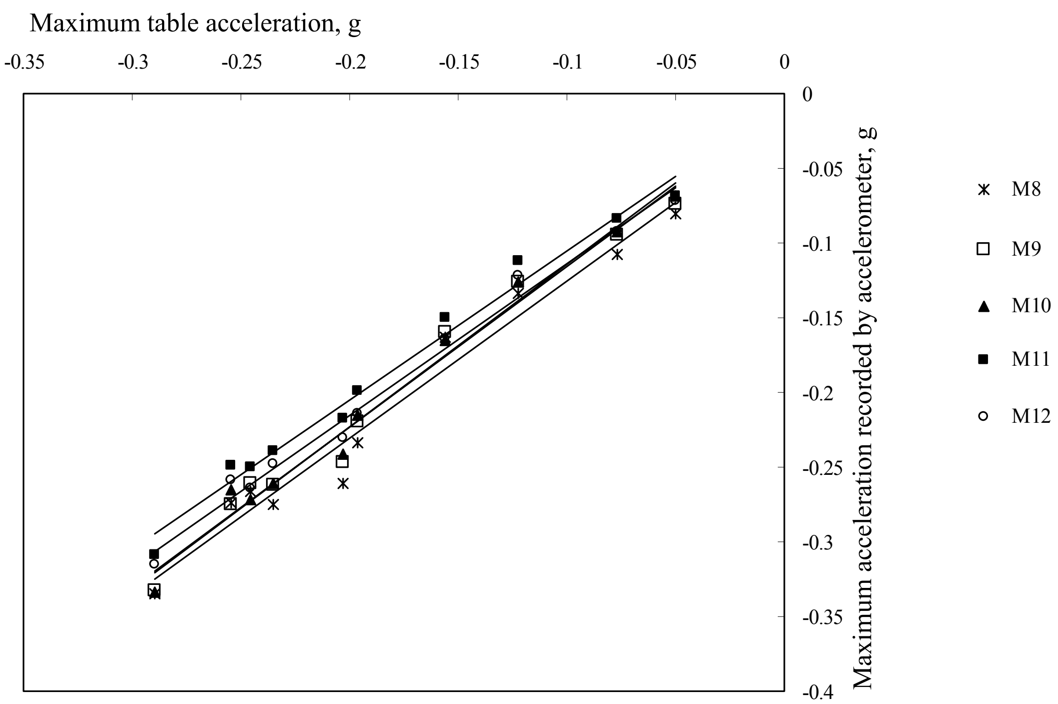

(b) Inward direction

Figure 4.80. Amplification of acceleration on top for Test 3

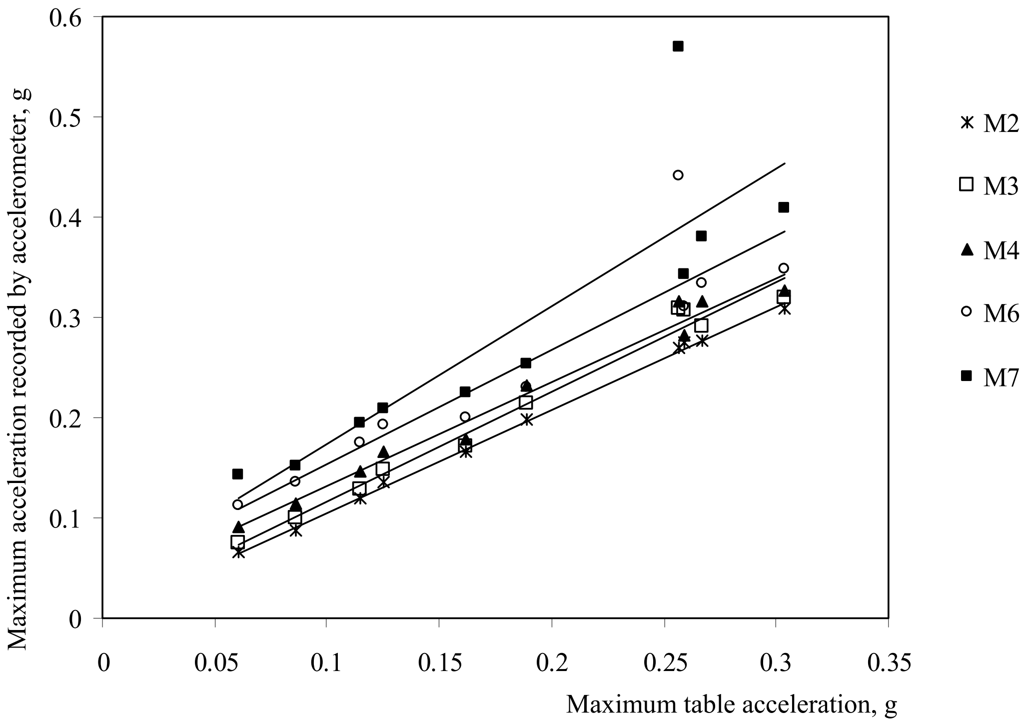

(a) Outward direction

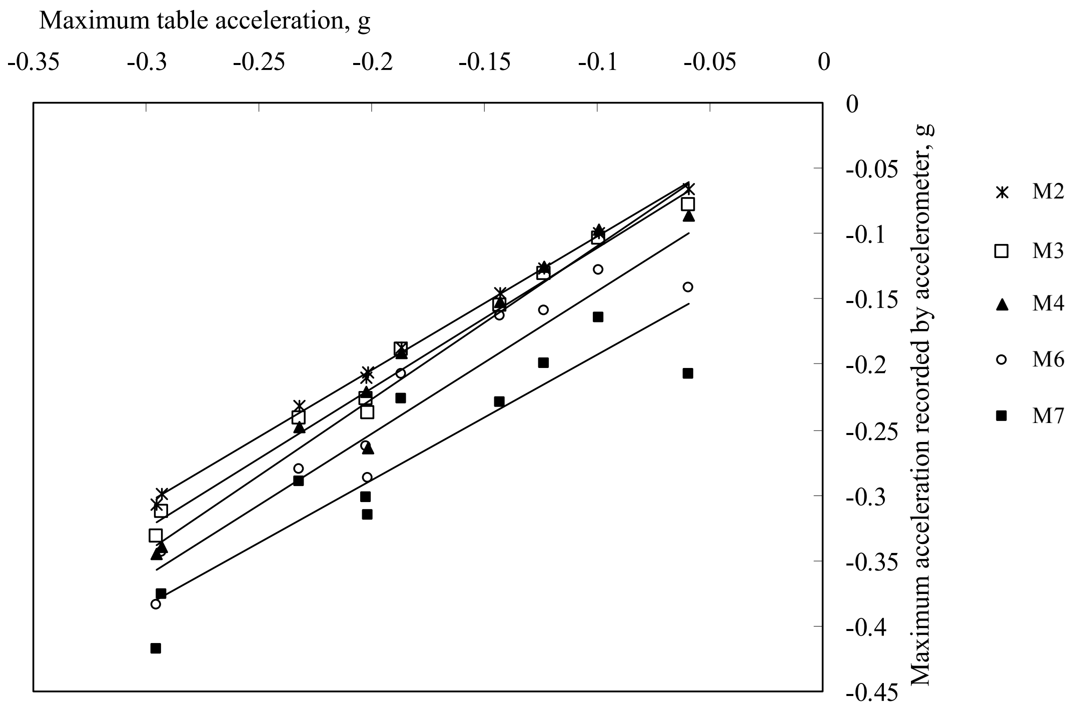

(b) Inward direction

Figure 4.81. Amplification of acceleration on face for Test 4 (Part 1)

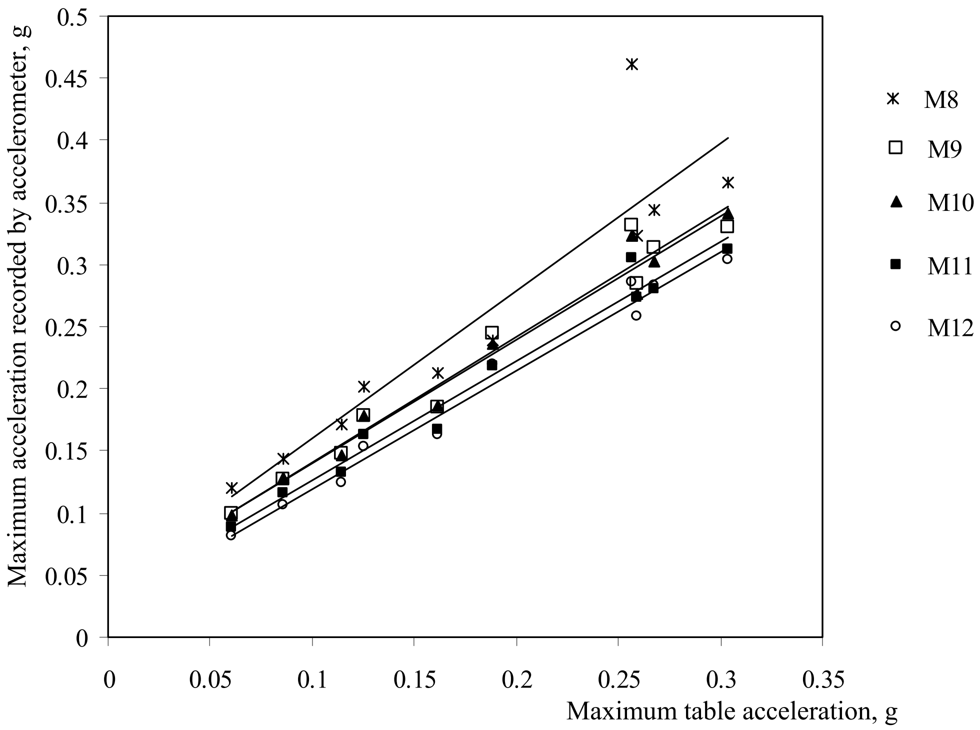

(a) Outward direction

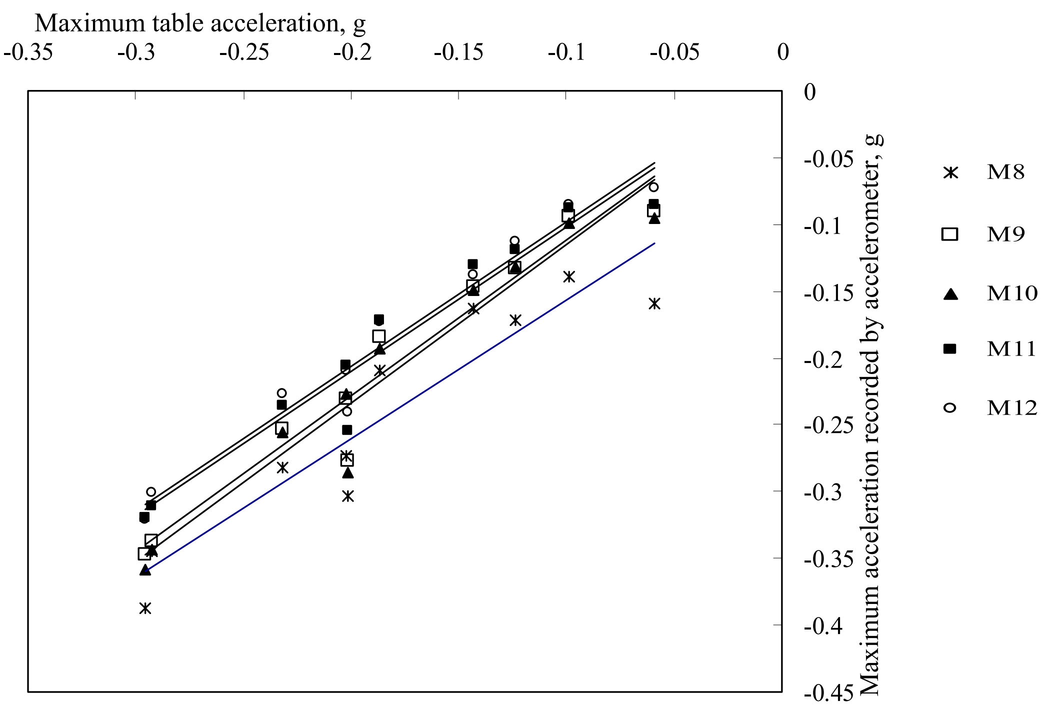

(b) Inward direction

Figure 4.82. Amplification of acceleration on top for Test 4 (Part 1)

Table 4.7. Amplification of acceleration on face for Test 4 (Part 1)

Accelerometer	Height from bottom (cm)	Equation of best fit line for		R^2 value for	
		Outward direction	Inward direction	Outward direction	Inward direction
M2	15	y=1.0307x+0.0020	y=1.0199x-0.0006	0.9983	0.9981
M3	55	y=1.0931x+0.0070	y=1.0747x-0.0032	0.9834	0.9839
M4	108	y=1.0365x+0.0276	y=1.1664x+0.0071	0.9785	0.9619
M6	160	y=1.1405x+0.0401	y=1.0926x-0.0348	0.8476	0.9183
M7	180	y=1.3764x+0.0367	y=0.9595x-0.0965	0.7539	0.8446

Table 4.8. Amplification of acceleration on top for Test 4 (Part 1)

Accelerometer	Distance from wall face (cm)	Equation of best fit line for		R^2 value for	
		Outward direction	Inward direction	Outward direction	Inward direction
M8	35	y=1.1900x+0.0413	y=1.0391x-0.0524	0.8481	0.8808
M9	110	y=1.0110x+0.0400	y=1.1695x+0.0054	0.9668	0.9440
M10	185	y=0.9977x+0.0398	y=1.1914x+0.0050	0.9741	0.9386
M11	260	y=0.9586x+0.0309	y=1.0802x+0.0063	0.9752	0.9445
M12	275 (inside rubber)	y=0.9534x+0.0238	y=1.0825x+0.0108	0.9800	0.9643

Table 4.9. Amplification of acceleration for Test 4 (Part 2)

Accelerometer	Location	Equation of best fit line for		R^2 value for	
		Outward direction	Inward direction	Outward direction	Inward direction
	Height from bottom (cm):				
M2	15	y=1.0167x+0.0041	y=0.9954x-0.0058	0.9992	0.9985
M3	55	y=1.0961x+0.0044	y=1.0851x+0.0070	0.9948	0.9983
M4	108	y=1.2271x-0.0094	y=1.1380x-0.0018	0.9906	0.9947
M6	160	y=1.7699x-0.0397	y=1.3540x+0.0194	0.8883	0.9918
M7	180	y=7.7745x+3.5044	y=9.2681x-2.4584	0.7534	0.8909
	Distance from wall face (cm):				
M8	35	y=7.6947x+3.1972	y=9.9970x-2.1222	0.7906	0.9293

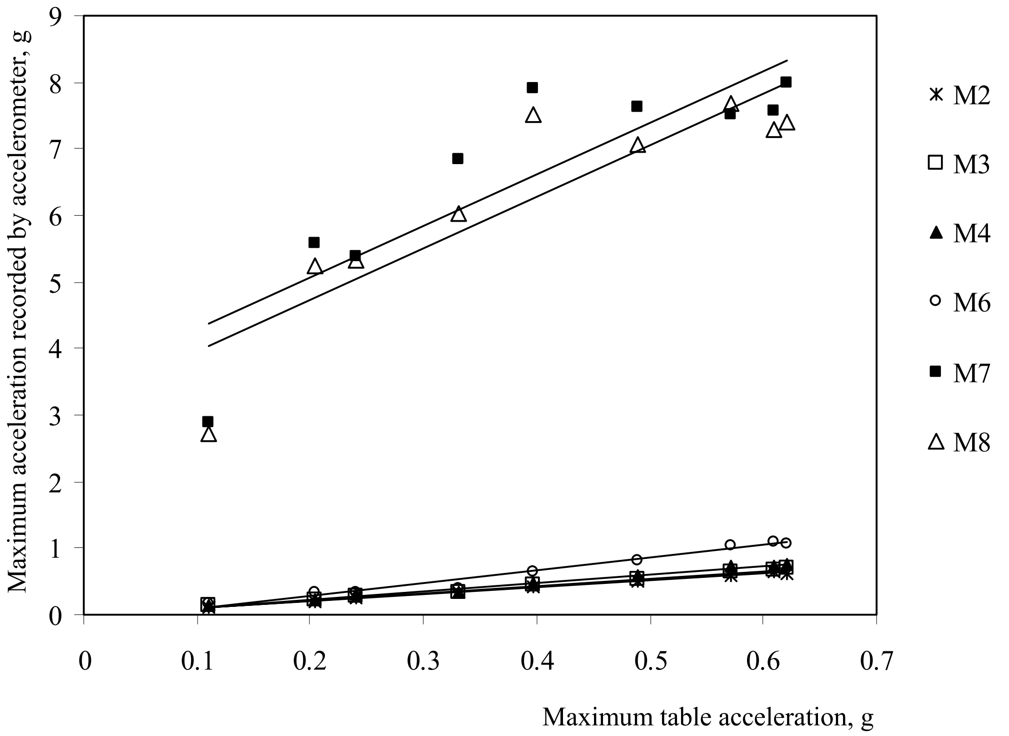

(a) Outward direction

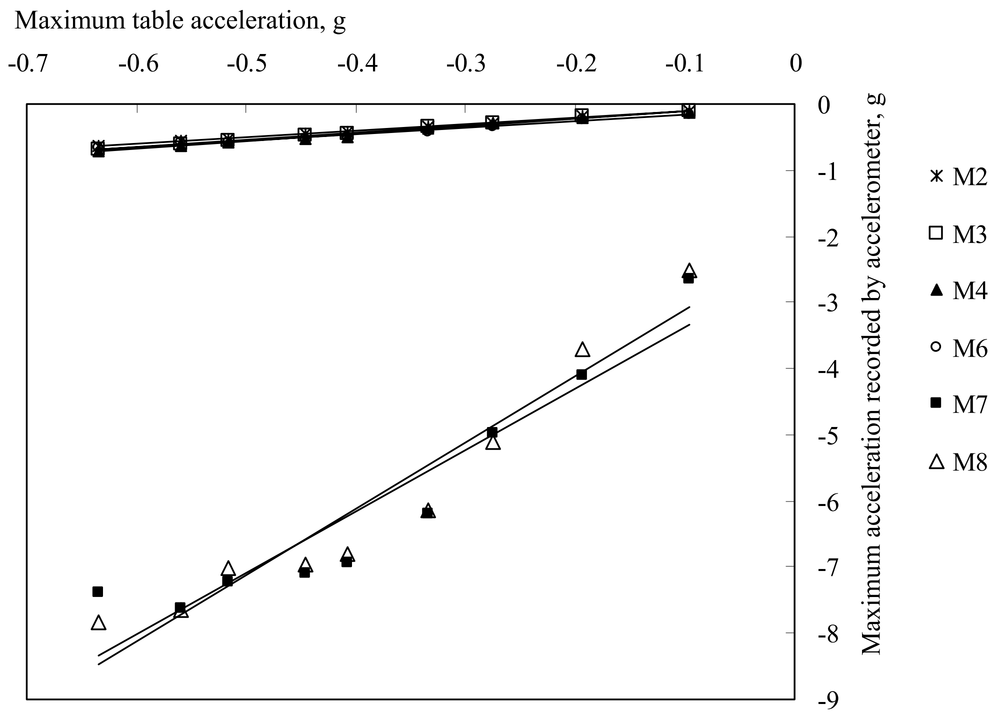

(b) Inward direction

Figure 4.83. Amplification of acceleration for Test 4 (Part2)

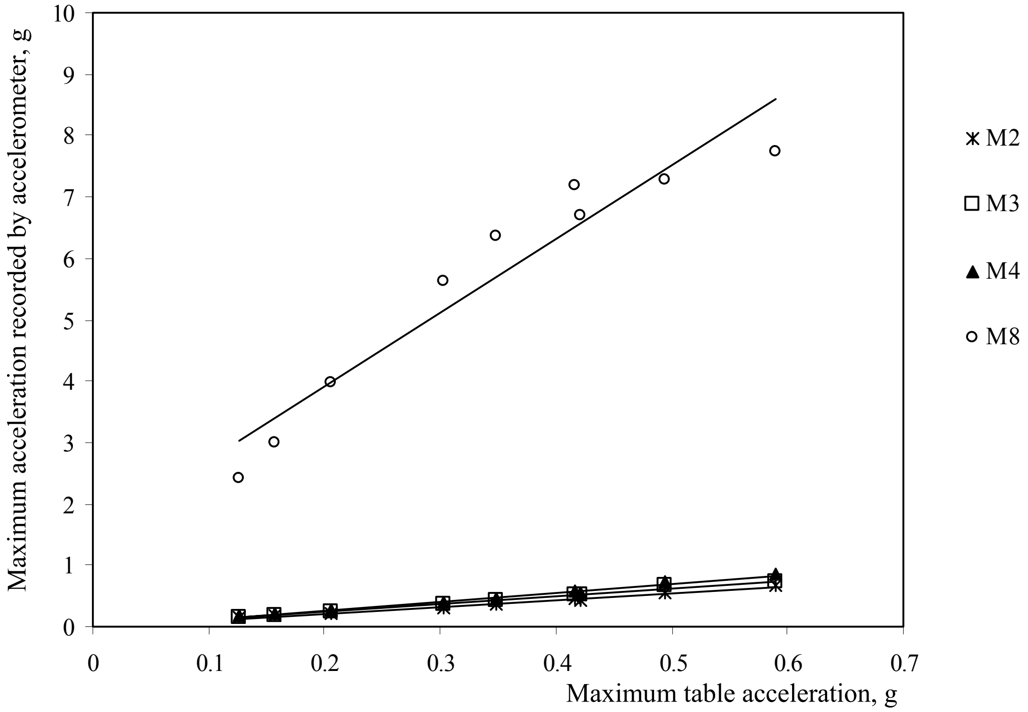

(a) Outward direction

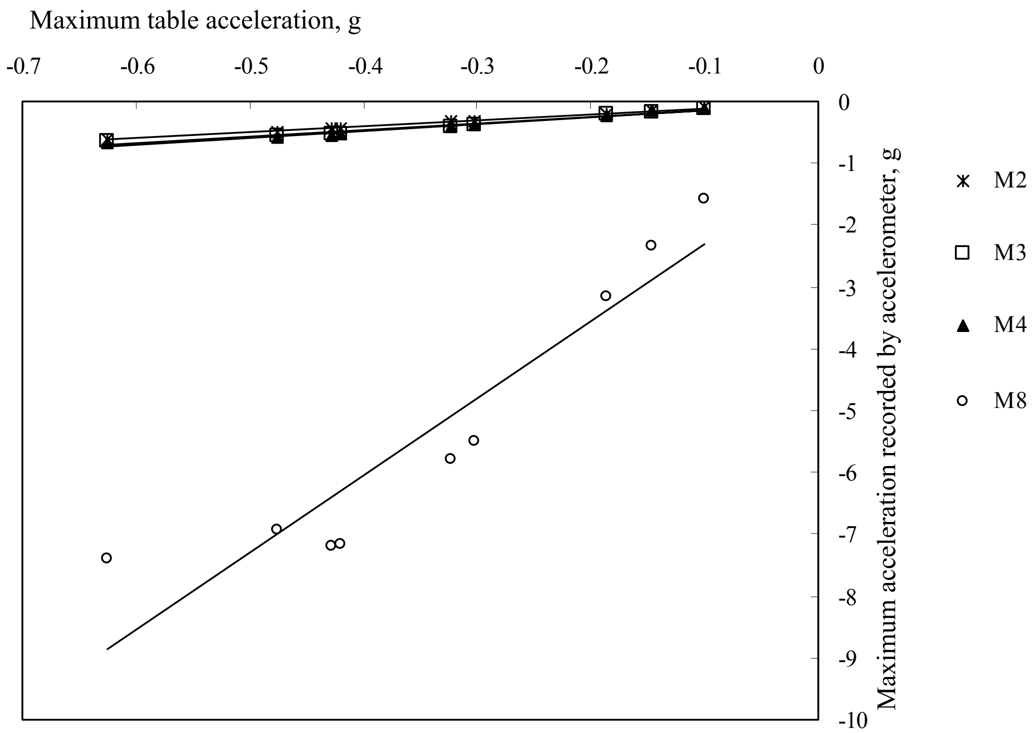

(b) Inward direction

Figure 4.84. Amplification of acceleration for Test 5

Figures 4.75 to 4.82 reveal comparatively small amplifications whereas in Figure 4.83, extremely large amplifications are measured by the uppermost accelerometer on face (M7) and front accelerometer on top (M8). This can be explained by the possibility that the connection between top two rows of blocks, which was fixed in the first part of Test 4, became loose and the uppermost blocks faced high frequency vibrations in the second part of the test.

Similarly, very high accelerations were measured at the top of the wall in Test 5, as seen in Figure 4.84. Again these high accelerations imply high frequency vibrations of the top blocks that were left free and the soil zone directly behind them.

Table 4.10. Amplification of acceleration for Test 5

Accelerometer	Location	Equation of best fit line for		R^2 value for	
		Outward direction	Inward direction	Outward direction	Inward direction
	Height from bottom (cm):				
M2	18	y=1.1181x-0.0132	y=0.9731x-0.0159	0.9960	0.9940
M3	59	y=1.2714x-0.0064	y=1.1005x-0.0241	0.9899	0.9622
M4	85	y=1.4810x-0.0340	y=1.1597x-0.0159	0.9843	0.9687
	Distance from wall face (cm):				
M8	35	y=12.082x+1.4795	y=12.435x-1.0700	0.9214	0.8708

Table 4.11. Amplification of acceleration for Test 6

Accelerometer	Location	Equation of best fit line for		R^2 value for	
		Outward direction	Inward direction	Outward direction	Inward direction
	Height from bottom (cm):				
M2	22	y=1.0097x+0.0087	y=1.0054x-0.0043	0.9987	0.9995
M3	59	y=1.0863x-0.0077	y=1.1570x+0.0138	0.9907	0.9972
M4	110	y=1.2689x+0.0019	y=1.2379x-0.0182	0.9641	0.9899
M6	161	y=1.7699x-0.0397	y=1.3540x+0.0194	0.8883	0.9918
M7	182	y=18.855x+0.8157	y=17.086x-0.4150	0.9060	0.9835
	Distance from wall face (cm):				
M8	35	y=18.340x+0.5920	y=15.519x-0.3856	0.9272	0.9810

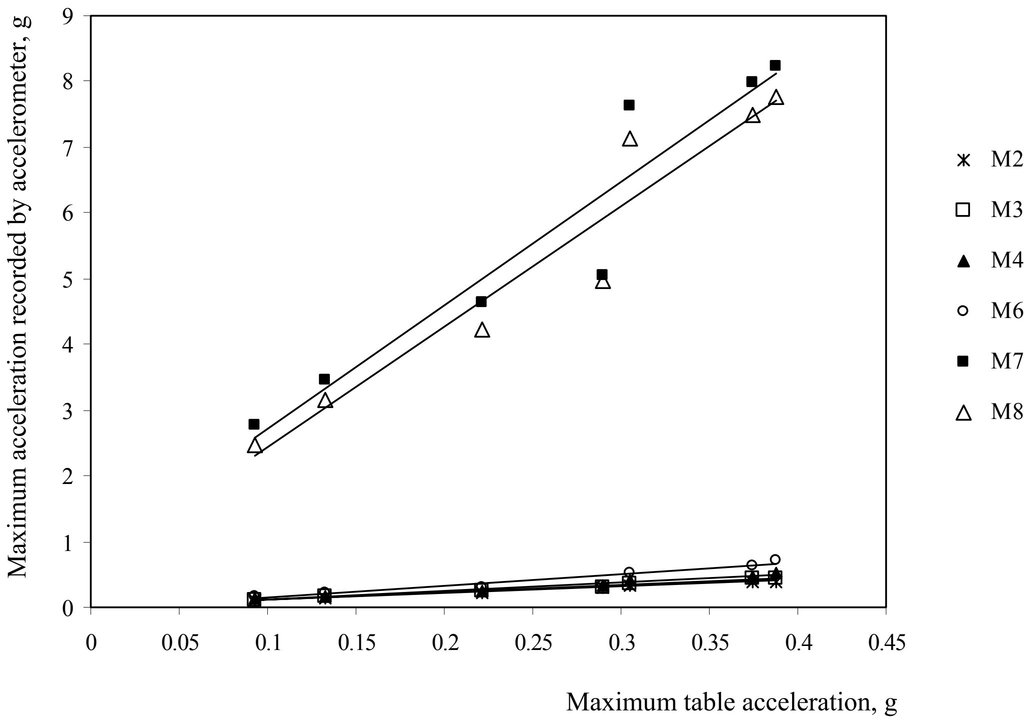

(a) Outward direction

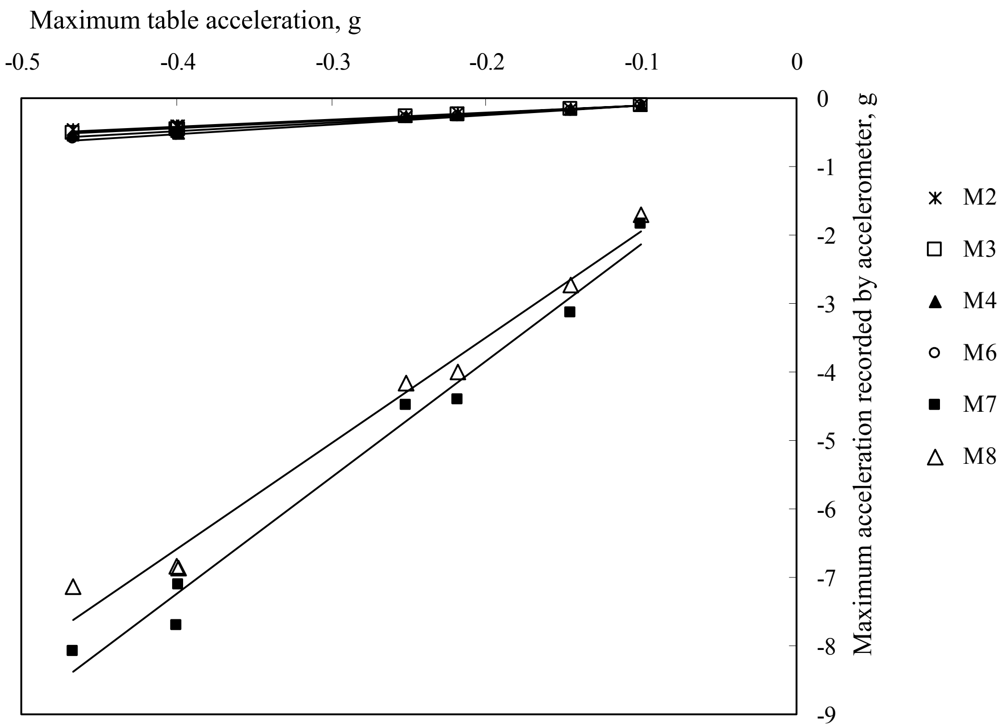

(b) Inward direction

Figure 4.85. Amplification of acceleration for Test 6

Figure 4.85 also implies vibration of the free top blocks in Test 6. In Test 7, which has a setup similar to Test 6 but a greater reinforcement length, the applied shaking table acceleration is higher. However the measured accelerations at the top of the wall remain much lower than those in Test 6, as seen in Figure 4.86. The increase in reinforcement length in Test 7 seems to have stopped the high frequency vibrations of the top layers of blocks.

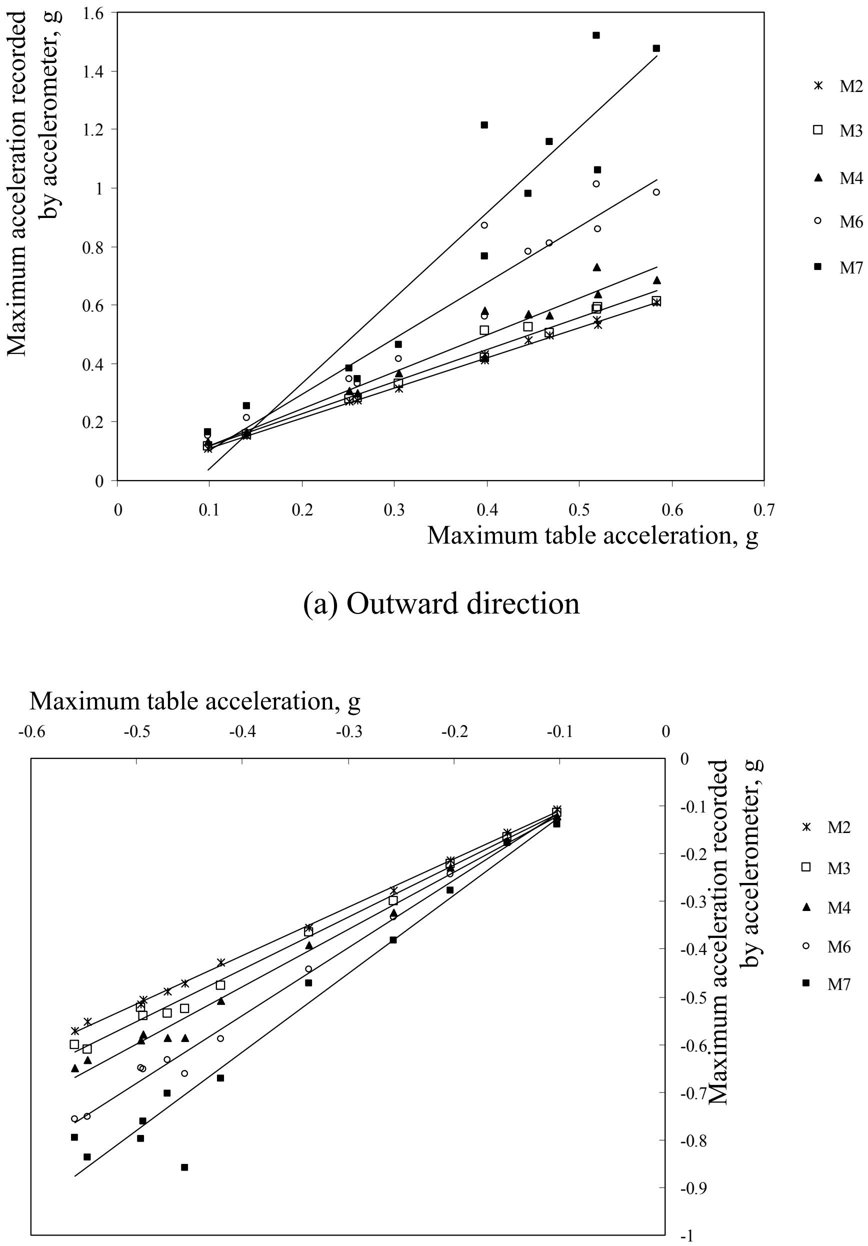

Figure 4.86. Amplification of acceleration on face for Test 7

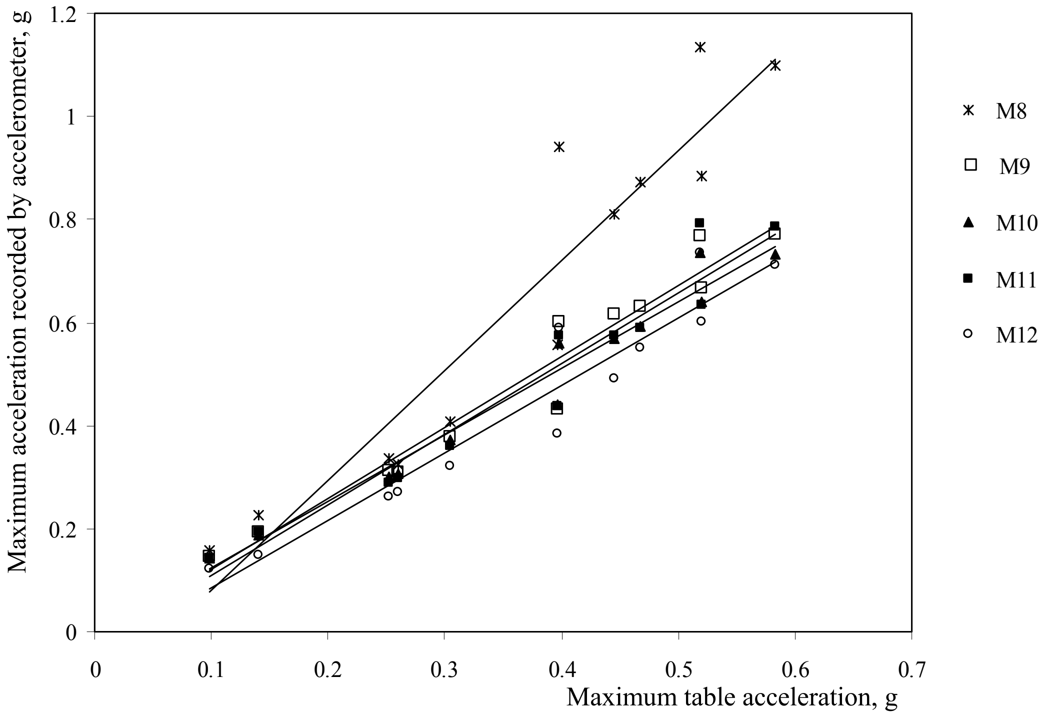

(a) Outward direction

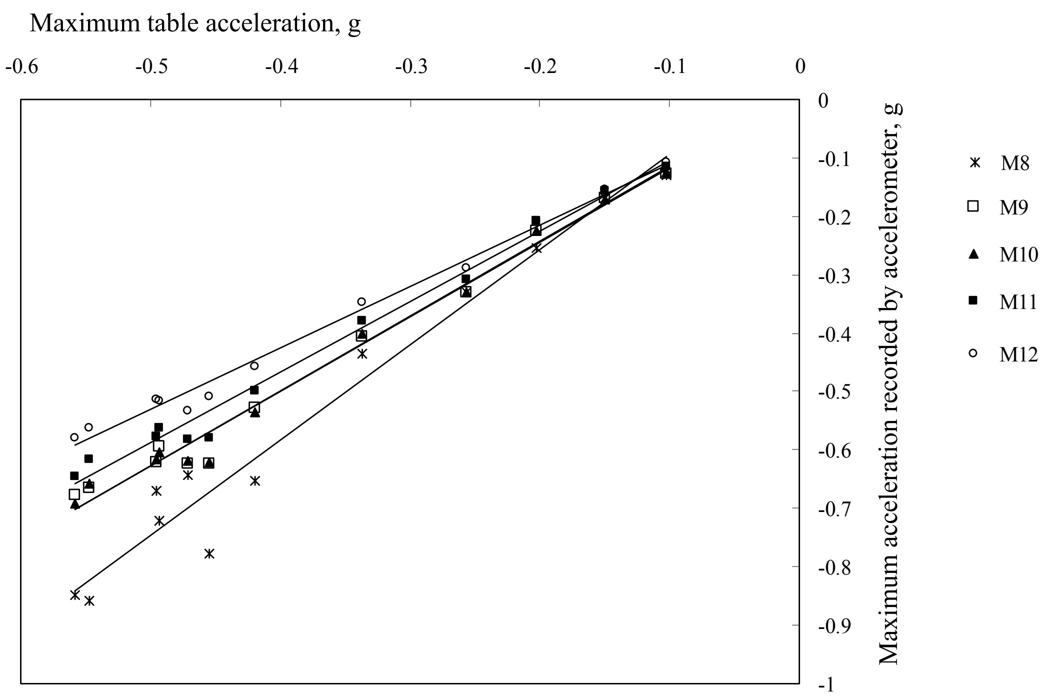

(b) Inward direction

Figure 4.87. Amplification of acceleration on top for Test 7

Table 4.12. Amplification of acceleration on face for Test 7

Accelerometer	Height from bottom (cm)	Equation of best fit line for		R^2 value for	
		Outward direction	Inward direction	Outward direction	Inward direction
M2	22	y=1.0348x+0.0065	y=1.0111x-0.0088	0.9976	0.9988
M3	59	y=1.0968x+0.0088	y=1.0955x-0.0051	0.9746	0.9938
M4	110	y=1.2658x-0.0081	y=1.1979x+0.0003	0.9481	0.9905
M6	161	y=1.9134x-0.0888	y=1.4179x+0.0286	0.9176	0.9921
M7	182	y=2.9191x-0.2529	y=1.6452x+0.0422	0.8750	0.9558

Table 4.13. Amplification of acceleration on top for Test 7

Accelerometer	Distance from wall face (cm)	Equation of best fit line for		R^2 value for	
		Outward direction	Inward direction	Outward direction	Inward direction
M8	35	y=2.1321x-0.1333	y=1.6285x+0.0680	0.8918	0.9664
M9	110	y=1.3767x-0.0179	y=1.2752x+0.0109	0.9524	0.9853
M10	185	y=1.2898x-0.0063	y=1.2817x+0.0133	0.9662	0.9873
M11	260	y=1.3718x-0.0290	y=1.2058x-0.0153	0.9444	0.9865
M12	275 (inside rubber)	y=1.3035x-0.0438	y=1.0547x-0.0037	0.9194	0.9903

Table 4.14. Amplification of acceleration on face for Test 8 (Part a)

Accelerometer	Height from bottom (cm)	Equation of best fit line for		R^2 value for	
		Outward direction	Inward direction	Outward direction	Inward direction
M2	22	y=1.0424x-0.00008	y=1.0322x-0.0025	0.9988	0.9993
M3	59	y=1.0889x-0.0016	y=1.0310x-0.0116	0.9935	0.9962
M4	110	y=1.1239x+0.0045	y=1.0075x-0.0283	0.9903	0.9852
M6	161	y=1.2168x+0.0131	y=1.0078x-0.0625	0.9665	0.9802
M7	182	y=1.2480x+0.0246	y=0.9832x-0.0893	0.9320	0.9777

Table 4.15. Amplification of acceleration on top for Test 8 (Part a)

Accelerometer	Distance from wall face (cm)	Equation of best fit line for		R^2 value for	
		Outward direction	Inward direction	Outward direction	Inward direction
M8	35	y=1.2338x+0.0199	y=0.9488x-0.0887	0.9284	0.9760
M9	110	y=1.1224x+0.0122	y=0.9473x-0.0514	0.9813	0.9768
M10	185	y=1.1328x+0.0074	y=0.9646x-0.0472	0.9813	0.9811
M11	260	y=1.1315x-0.0004	y=0.9303x-0.0411	0.9779	0.9827
M12	275 (inside rubber)	y=1.0466x-0.0024	y=0.9424x-0.0205	0.9856	0.9867

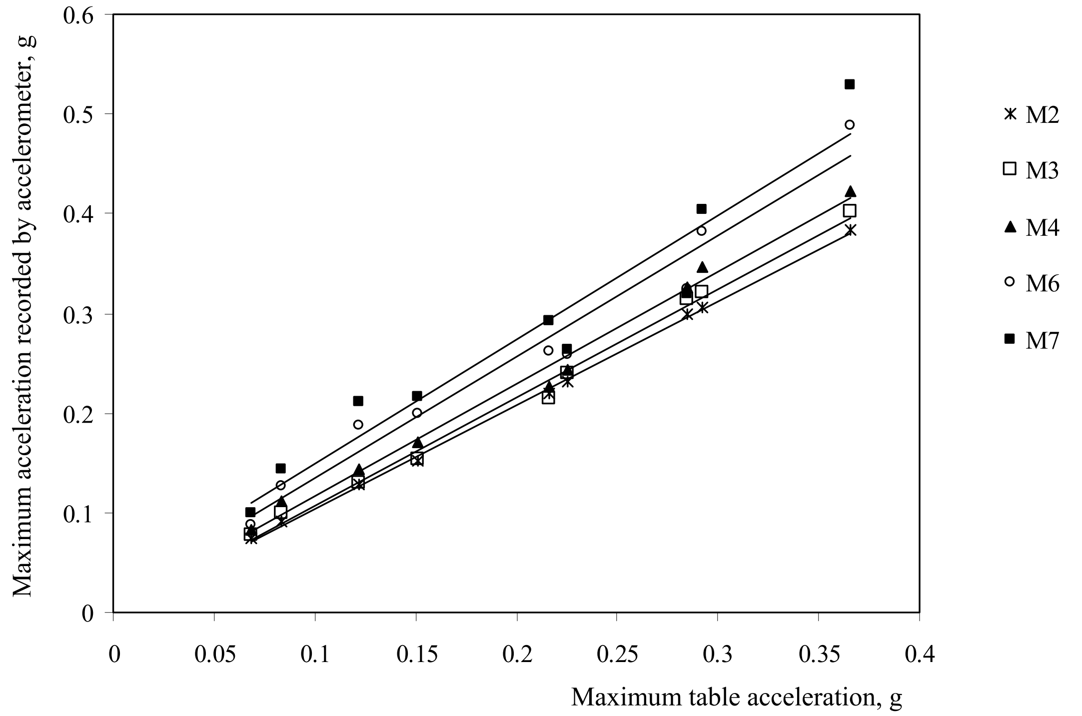

(a) Outward direction

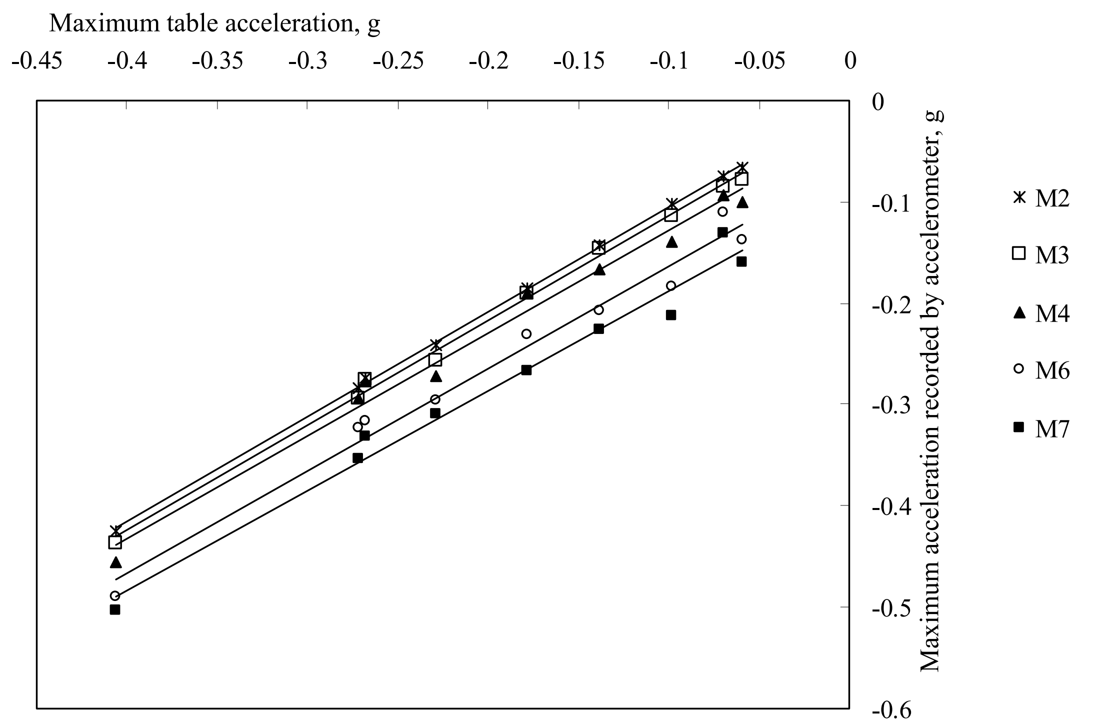

(b) Inward direction

Figure 4.88. Amplification of acceleration on face for Test 8 (Part a)

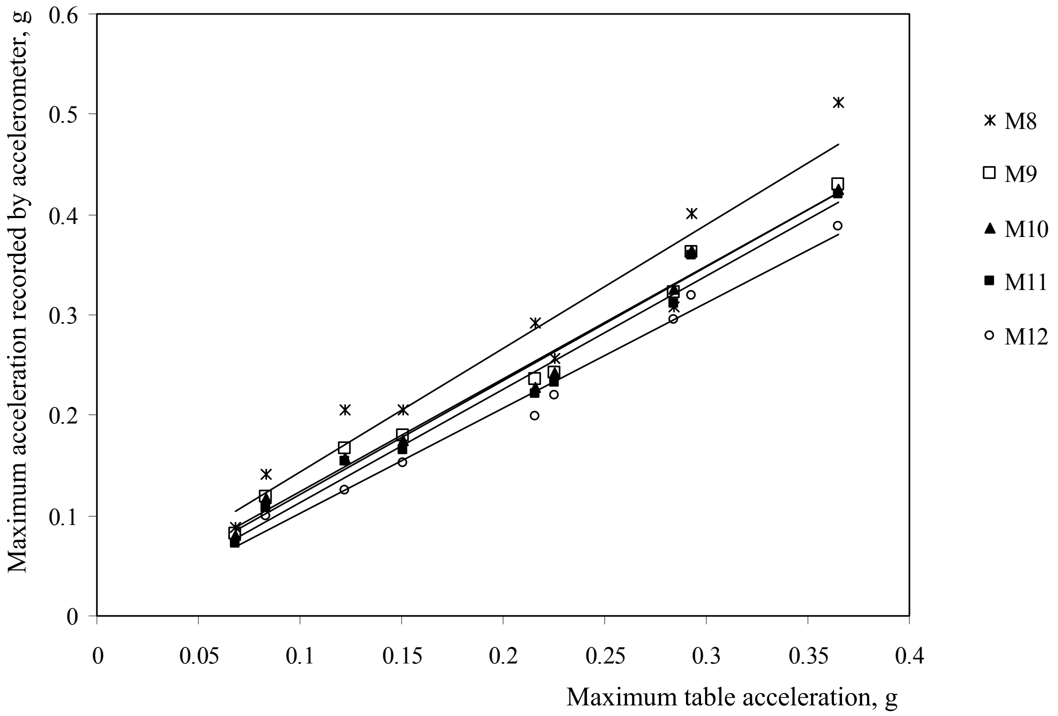

(a) Outward direction

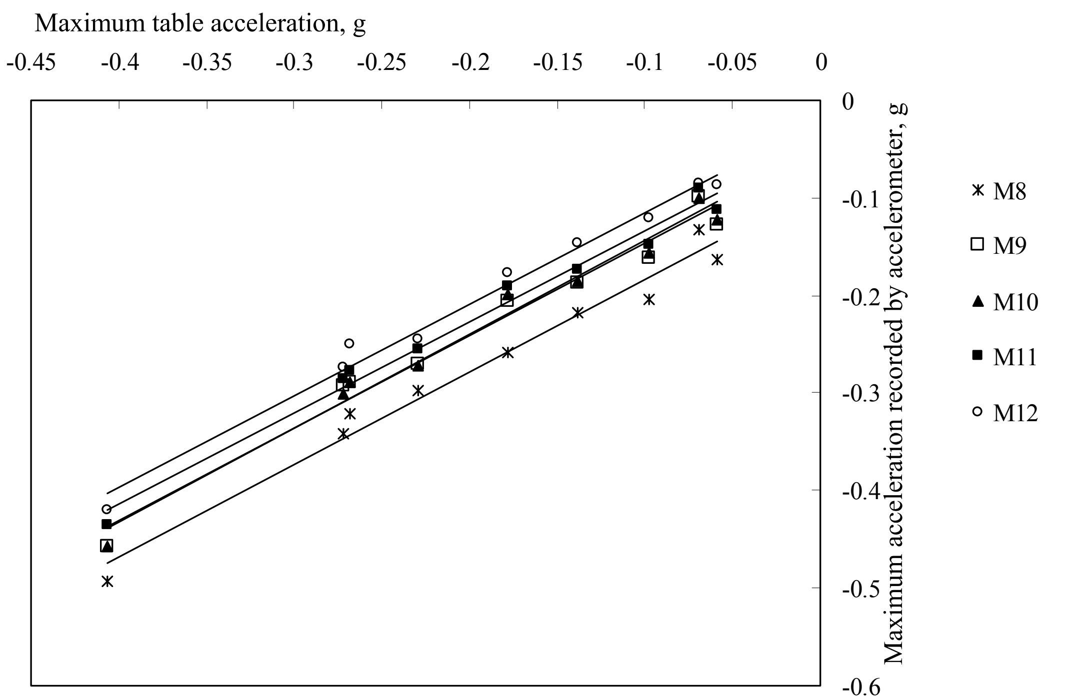

(b) Inward direction

Figure 4.89. Amplification of acceleration on top for Test 8 (Part a)

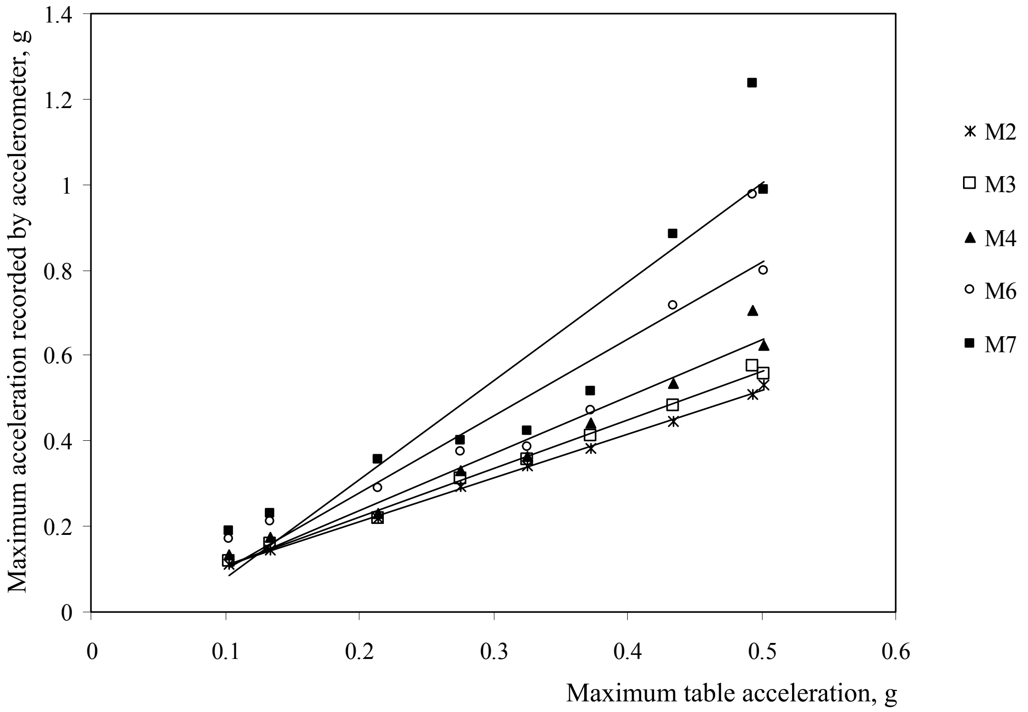

(a) Outward direction

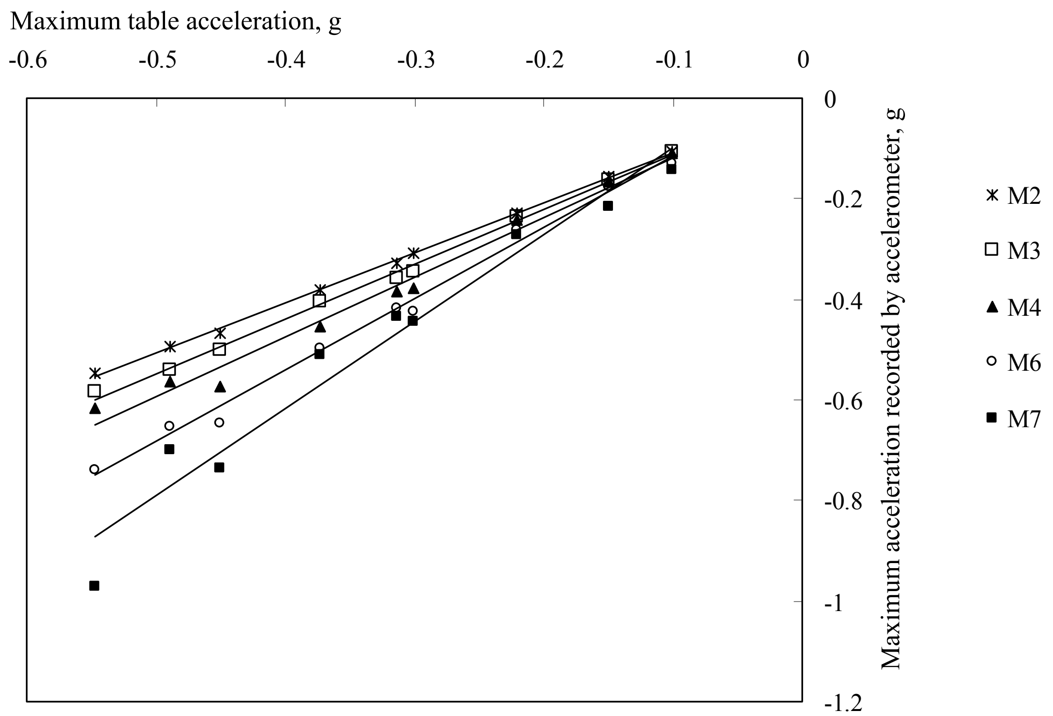

(b) Inward direction

Figure 4.90. Amplification of acceleration on face for Test 8 (Part b)

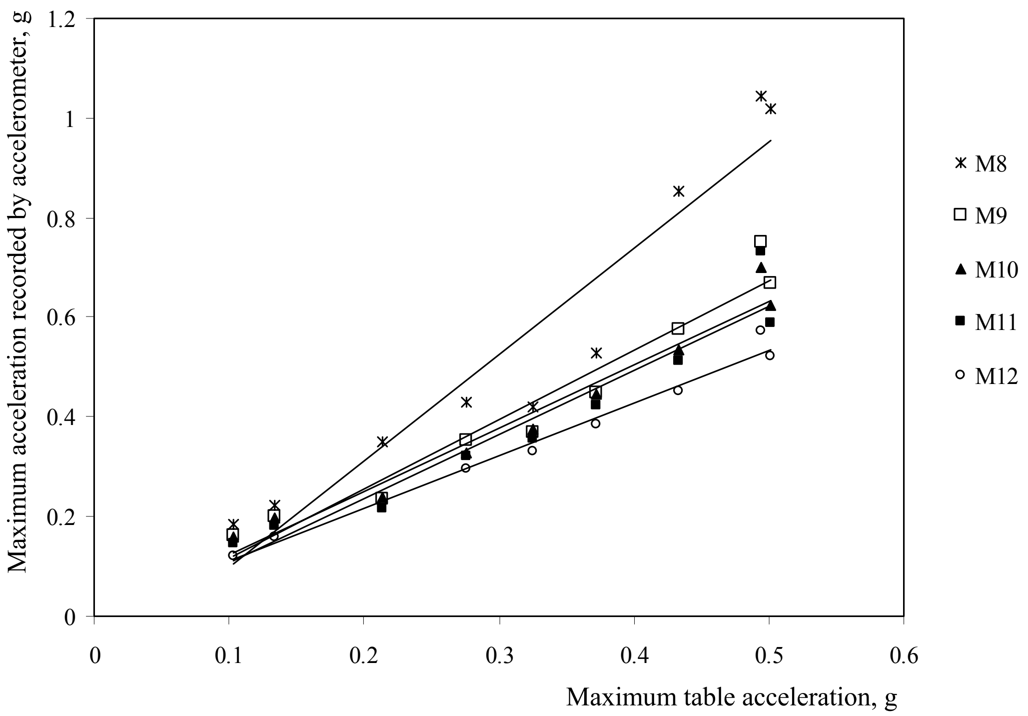

(a) Outward direction

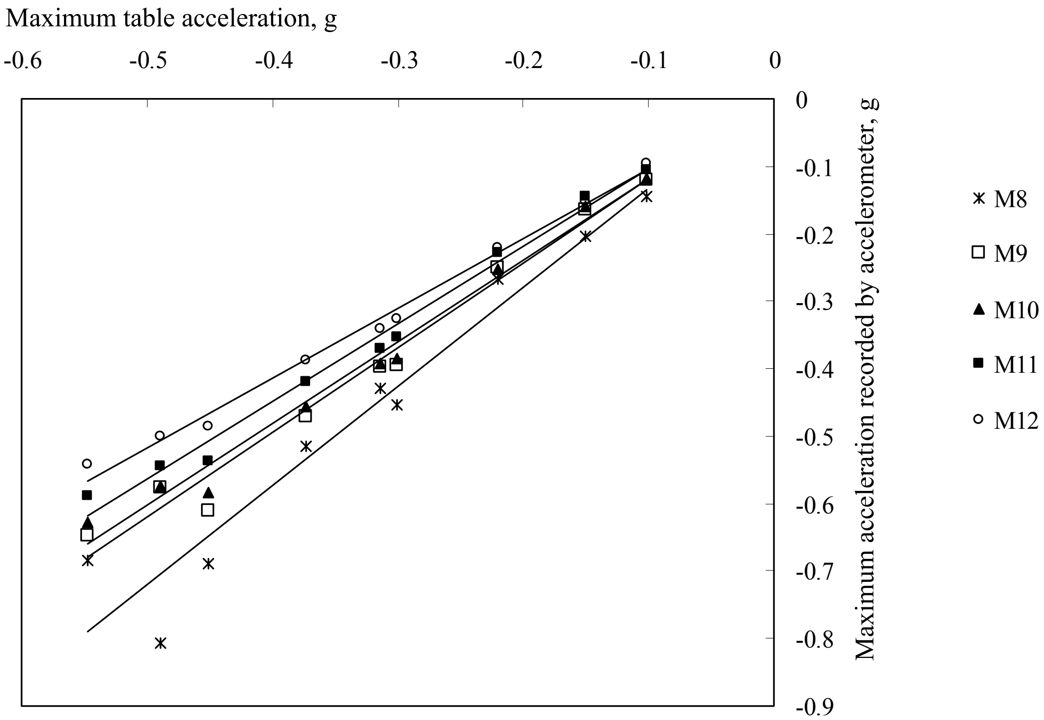

(b) Inward direction

Figure 4.91. Amplification of acceleration on top for Test 8 (Part b)

Table 4.16. Amplification of acceleration on face for Test 8 (Part b)

Accelerometer	Height from bottom (cm)	Equation of best fit line for		R^2 value for	
		Outward direction	Inward direction	Outward direction	Inward direction
M2	22	y=1.0276x+0.0053	y=0.9958x-0.0091	0.9983	0.9987
M3	59	y=1.1320x-0.0048	y=1.0945x-0.0017	0.9944	0.9965
M4	110	y=1.3301x-0.0285	y=1.1923x+0.0026	0.9671	0.9839
M6	161	y=1.8006x-0.0828	y=1.4186x+0.0264	0.8953	0.9922
M7	182	y=2.3090x-0.1520	y=1.7329x+0.0751	0.8589	0.9576

Table 4.17. Amplification of acceleration on top for Test 8 (Part b)

Accelerometer	Distance from wall face (cm)	Equation of best fit line for		R^2 value for	
		Outward direction	Inward direction	Outward direction	Inward direction
M8	35	y=2.1319x-0.1151	y=1.4704x+0.0148	0.9114	0.9389
M9	110	y=1.3906x-0.0225	y=1.2530x+0.0062	0.9493	0.9791
M10	185	y=1.2713x-0.0031	y=1.2106x+0.0022	0.9622	0.9848
M11	260	y=1.2917x-0.0229	y=1.1490x+0.0103	0.9270	0.9879
M12	275 (inside rubber)	y=1.0574x+0.0058	y=1.0314x-0.0016	0.9839	0.9918

4.5.2. Effects of Shaking Table Acceleration on Maximum Face Displacements During Shaking

Shaking table displacement records and records of wall face displacements relative to the shaking table were presented in the Figures 4.28 to 4.45 for the shaking with the highest maximum table acceleration in each of the eight tests. Initial positions of the shaking table and the wall face were equated to zero, the change in position from the initial position were the global displacements, and relative displacements during shaking were calculated by finding the difference between the global displacement of the shaking table and the global displacements of assessed points on face at every recorded point in time. Mostly, the global displacements undergone by the shaking table and the face match in terms of magnitude. A few examples showing this match are given in Figures 4.92 to 4.96. From these figures it is also seen that sometimes a shift in the phase occurs. In Test 1 and Test 2, the table and the wall move simultaneously. However in Tests 3, 6 and 8, there is a phase shift, causing the difference between the positions of the table and the wall face to increase, i.e. causing the relative displacement of the wall to increase.

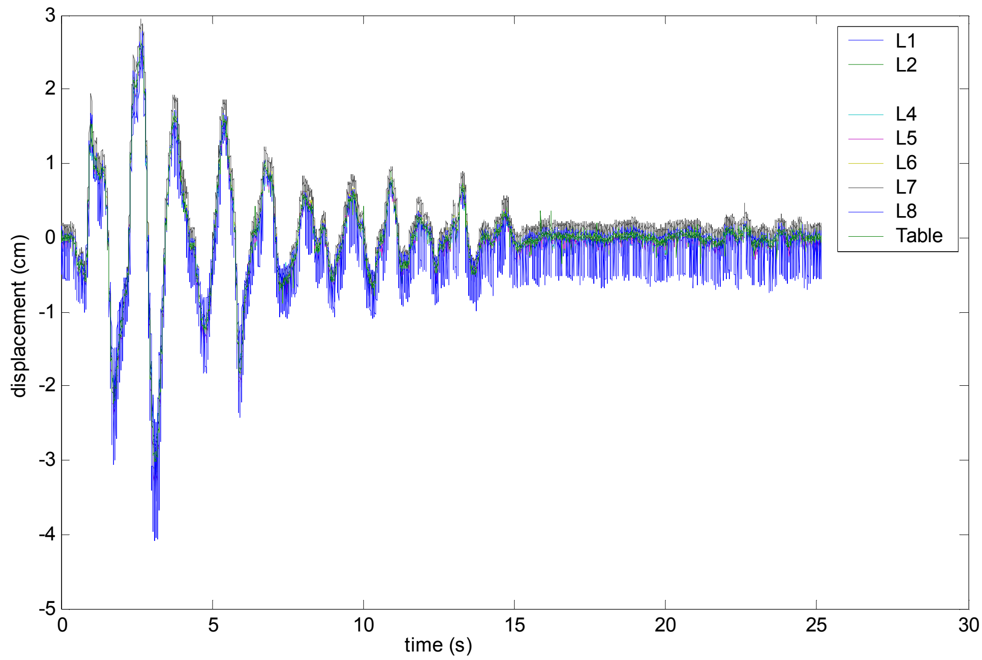

Figure 4.92. Record of global displacements of shaking table and wall face for Test 1-10

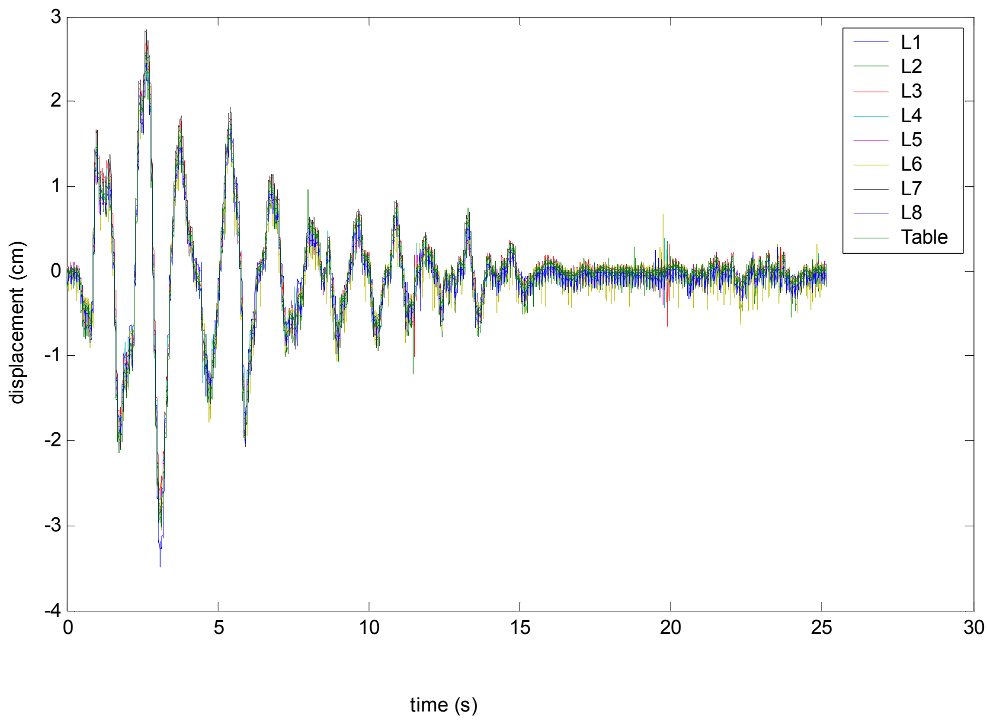

Figure 4.93. Record of global displacements of shaking table and wall face for Test 2-6

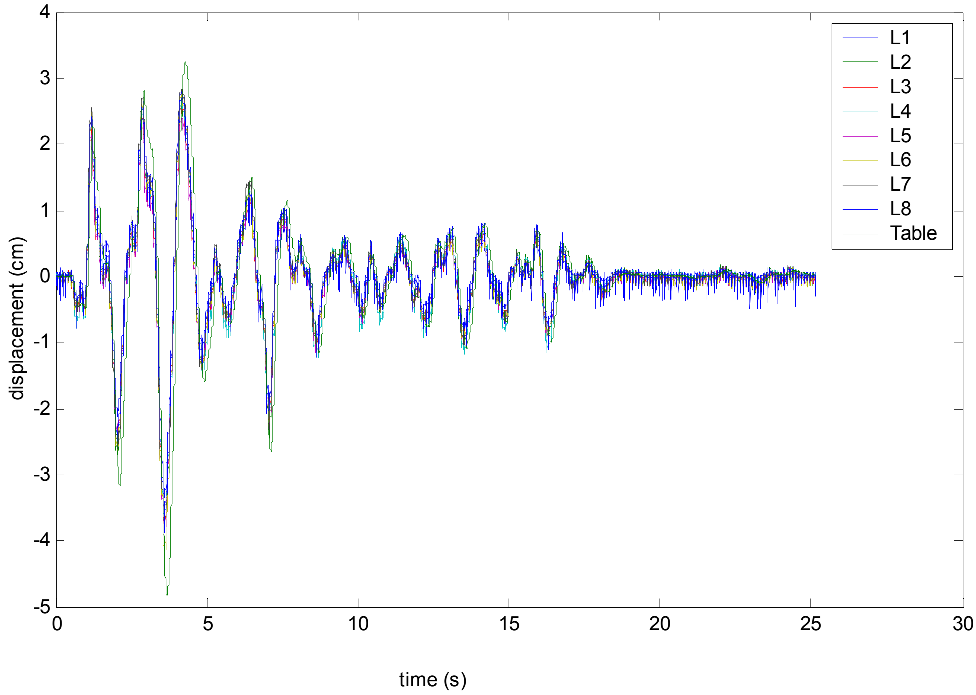

Figure 4.94. Record of global displacements of shaking table and wall face for Test 3-10

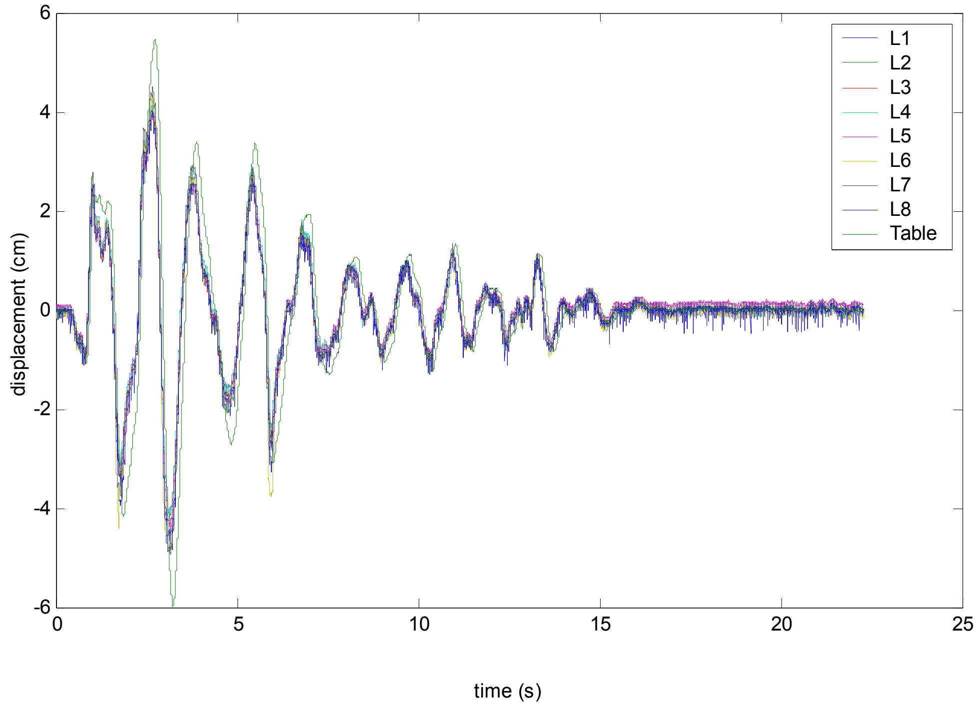

Figure 4.95. Record of global displacements of shaking table and wall face for Test 6-7

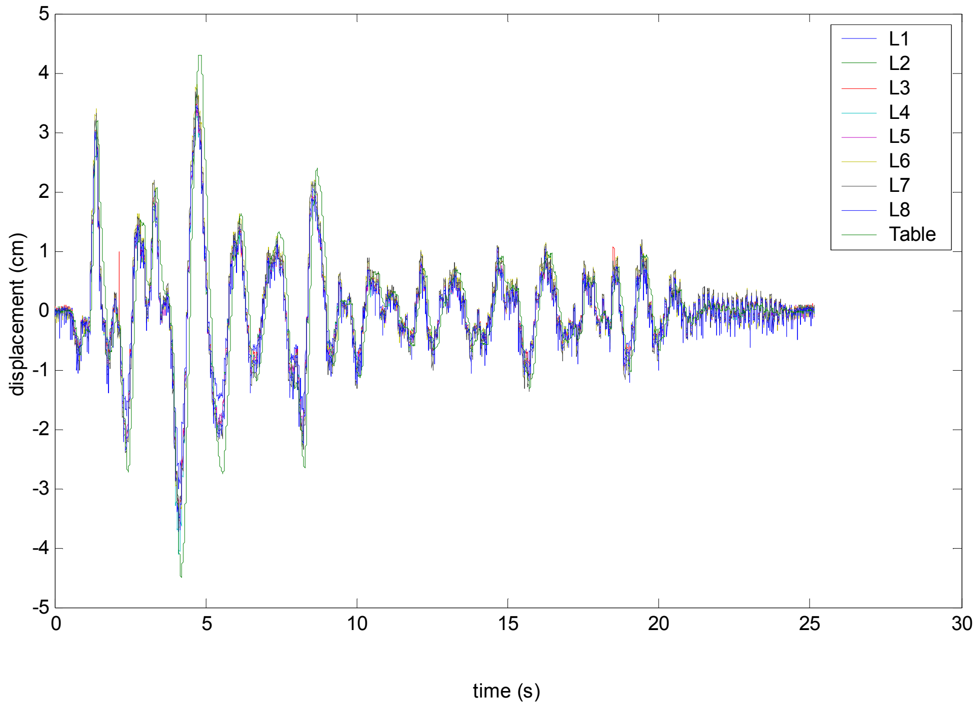

Figure 4.96. Record of global displacements of shaking table and wall face for Test 8a-9

Figures 4.97 to 4.106 show how the maximum relative face displacements during shaking change with increasing maximum acceleration. The maximum relative face displacements generally increase with increasing maximum table acceleration, but as seen in Figures 4.92 to 4.96, as explained previously this does not mean that the wall on the shaking table moves more than the shaking table relative to the ground. The movement of the wall face is not concurrent with the movement of the shaking table, so the maximum relative displacements shown in Figures 4.97 to 4.106 are observed. The location on face where the relative displacement is highest is not necessarily at the top. In fact this location changes for each test configuration. This can be seen in Figures 4.107 to 4.116, in which maximum relative wall face displacements throughout height of wall are illustrated for chosen table shakings.

In Figure 4.98 (Test 2), the outlying data points belong to a test run with a much higher table acceleration recorded with the other data acquisition system, which could not be caught with the shaking table facility's own system.

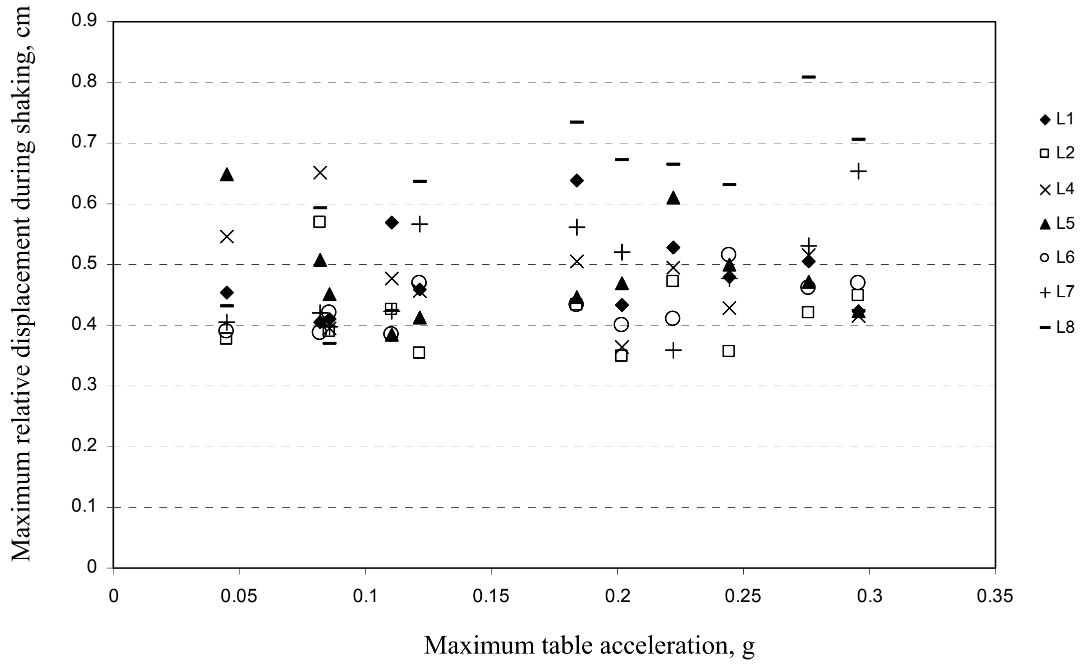

Figure 4.97. Effect of increase in acceleration on maximum wall face displacement relative to shaking table measured by L1-L8 (bottom to top) for Test 1 (L3 measurements were erroneous and discarded)

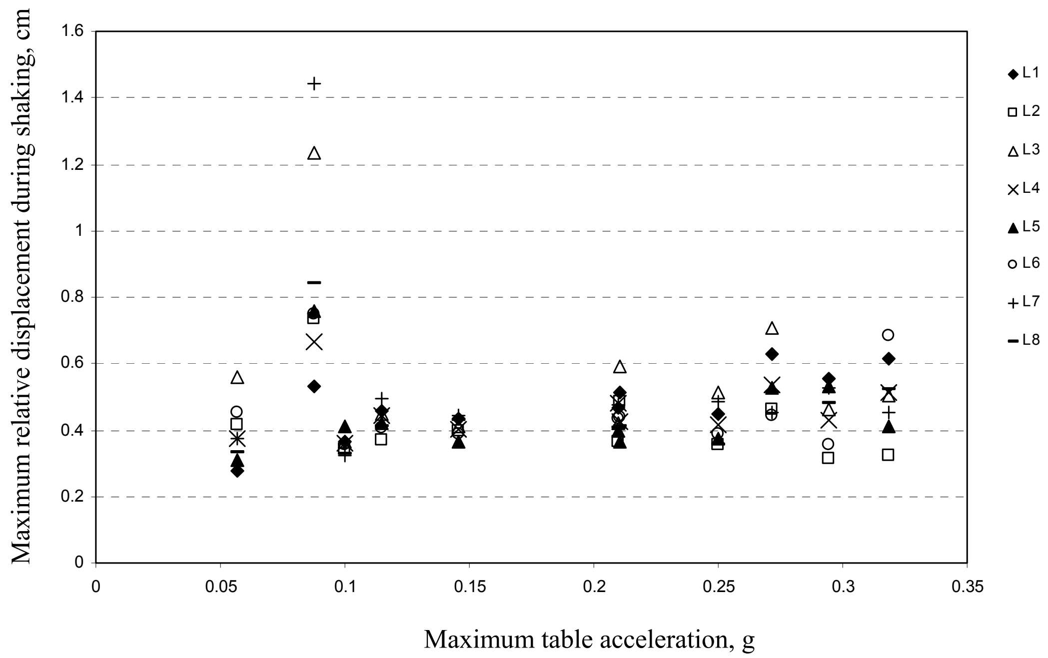

Figure 4.98. Effect of increase in acceleration on maximum wall face displacement relative to shaking table measured by L1-L8 (bottom to top) for Test 2

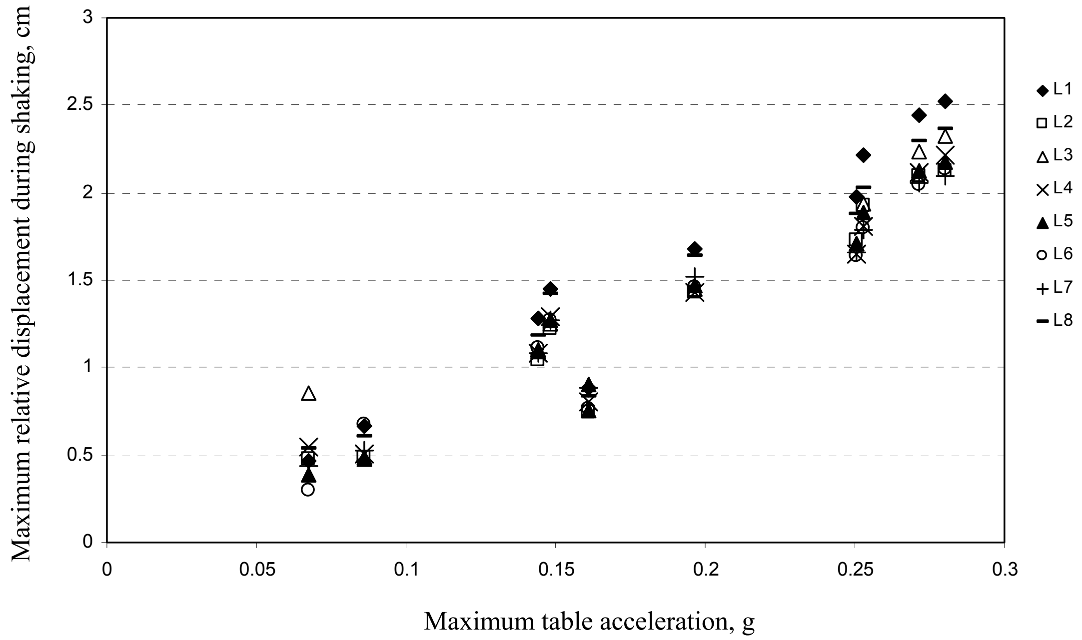

Figure 4.99. Effect of increase in acceleration on maximum wall face displacement relative to shaking table measured by L1-L8 (bottom to top) for Test 3

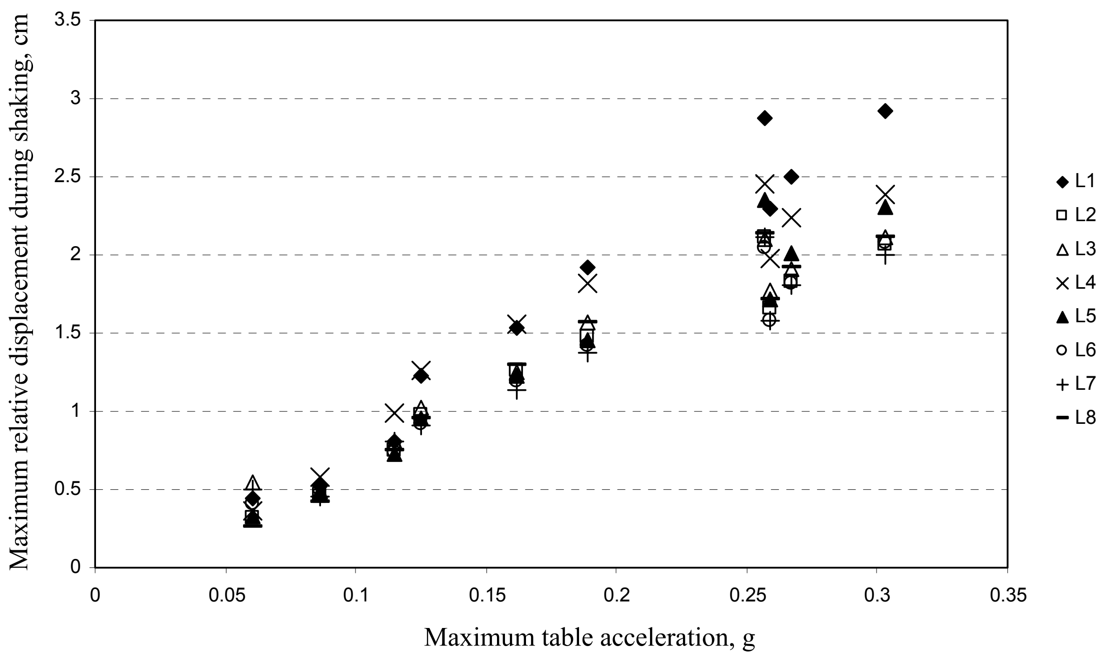

Figure 4.100. Effect of increase in acceleration on maximum wall face displacement relative to shaking table measured by L1-L8 (bottom to top) for Test 4 Part 1 (Runs 4-1 to 4-10)

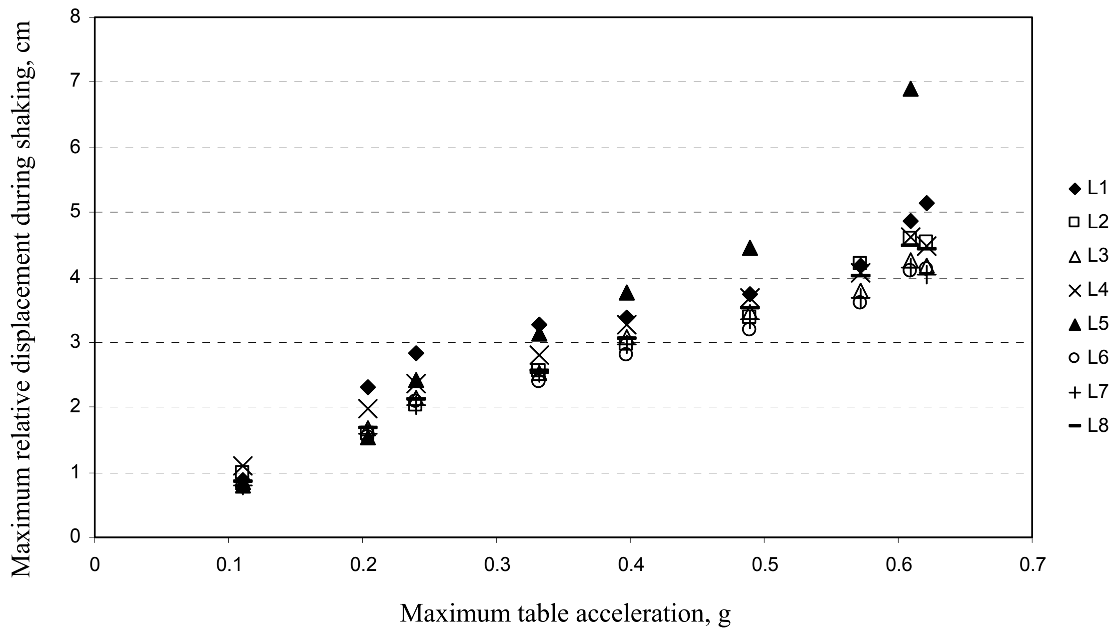

Figure 4.101. Effect of increase in acceleration on maximum wall face displacement relative to shaking table measured by L1-L8 (bottom to top) for Test 4 Part 2 (Runs 4-11 to 4-19)

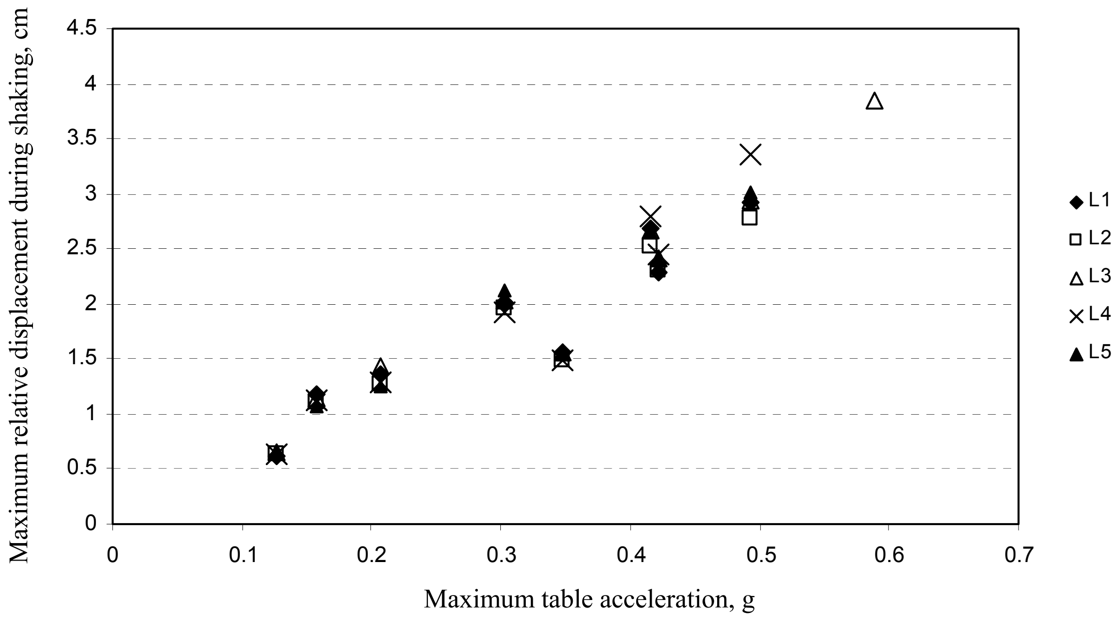

Figure 4.102. Effect of increase in acceleration on maximum wall face displacement relative to shaking table measured by L1-L5 (bottom to top) for Test 5

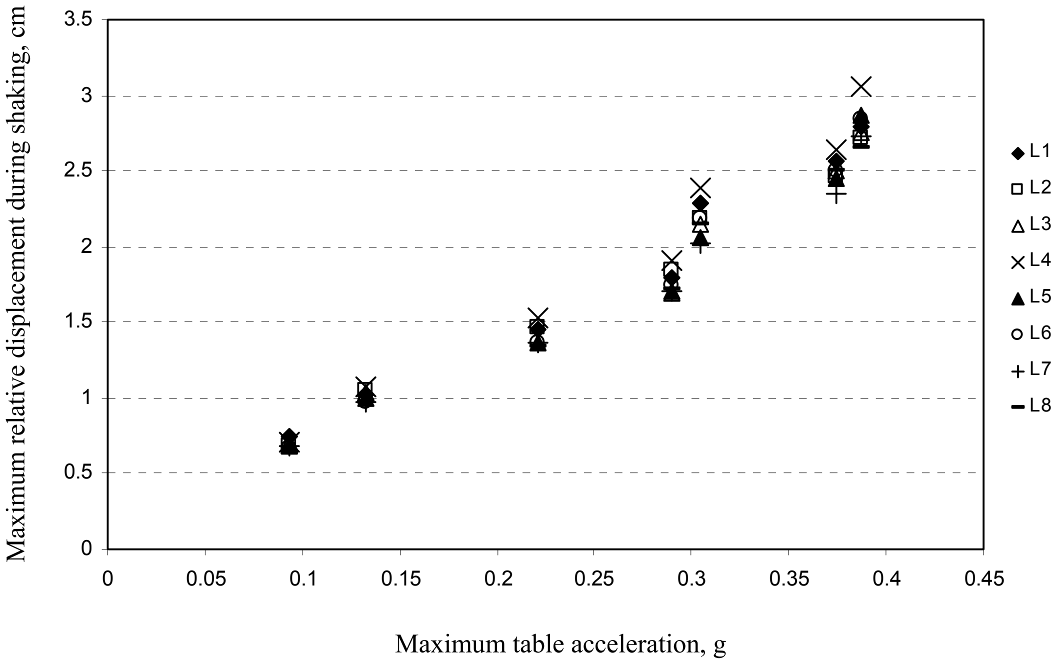

Figure 4.103. Effect of increase in acceleration on maximum wall face displacement relative to shaking table measured by L1-L8 (bottom to top) for Test 6

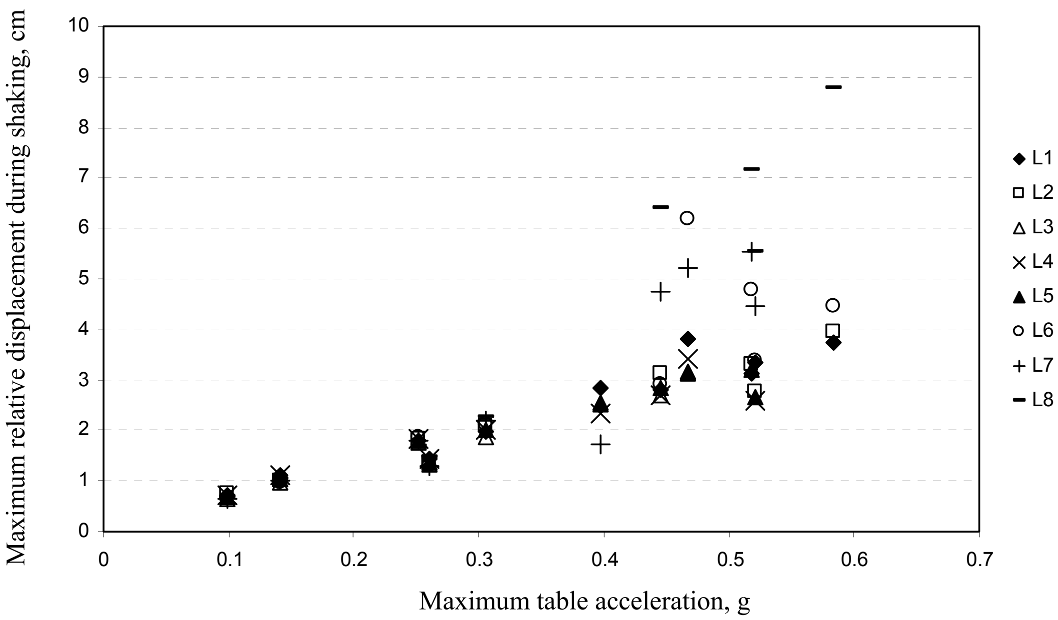

Figure 4.104. Effect of increase in acceleration on maximum wall face displacement relative to shaking table measured by L1-L8 (bottom to top) for Test 7

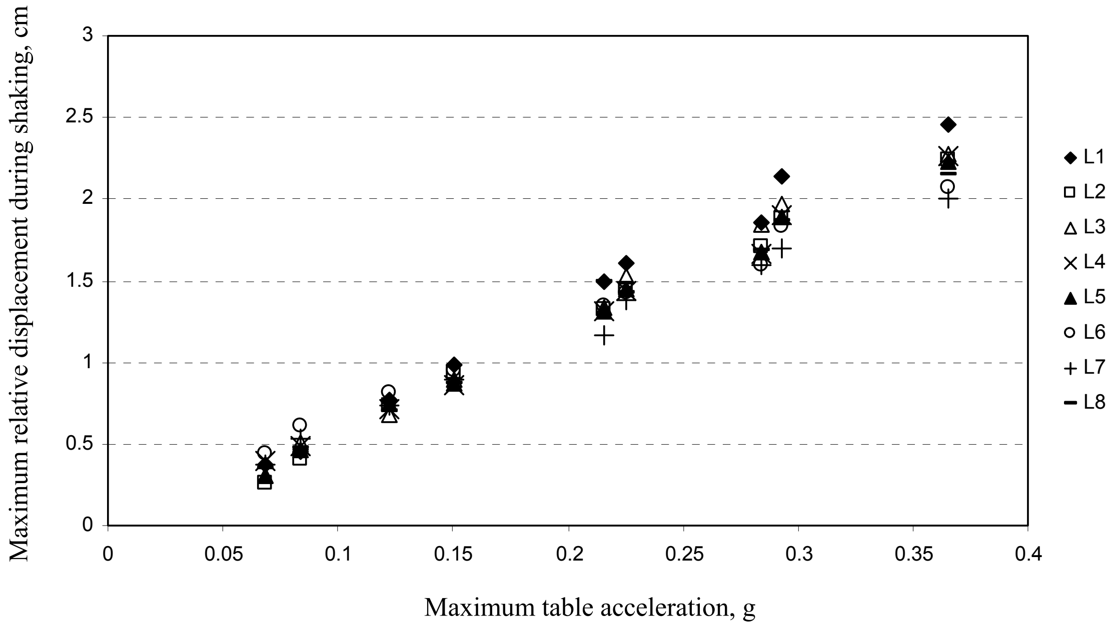

Figure 4.105. Effect of increase in acceleration on maximum wall face displacement relative to shaking table measured by L1-L8 (bottom to top) for Test 8 Part a

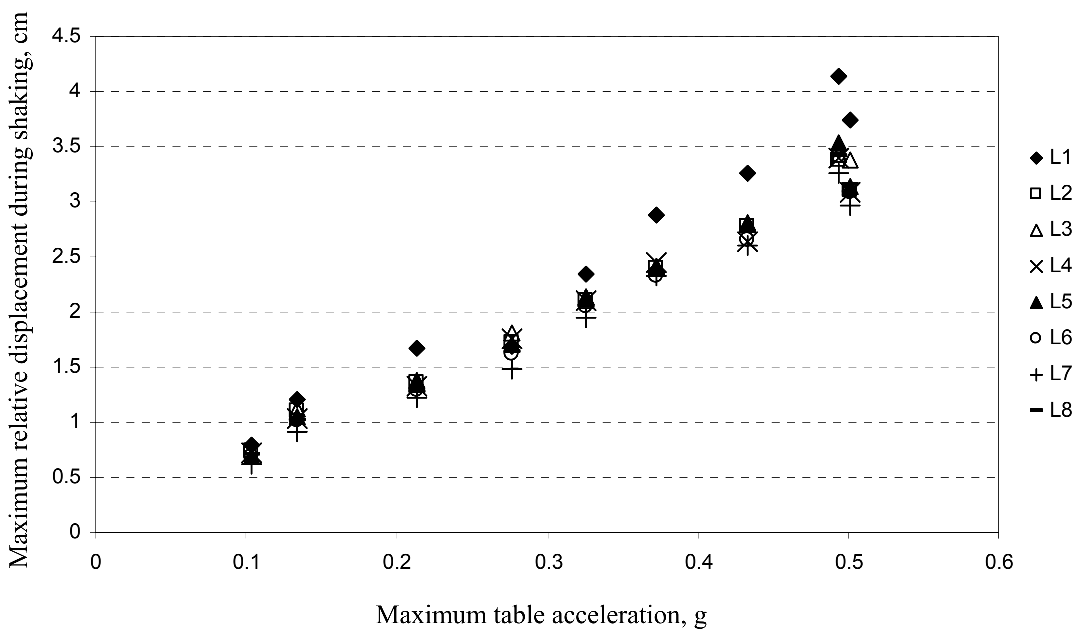

Figure 4.106. Effect of increase in acceleration on maximum wall face displacement relative to shaking table measured by L1-L8 (bottom to top) for Test 8 Part b

It is observed from Figures 4.107 to 4.116 that in the tests with relatively long reinforcements, the maximum relative face displacements during shaking are similar in magnitude for inward and outward directions. For the tests with shorter reinforcements, relative face displacements in the outward direction exceed the backward displacements and the difference becomes more pronounced as the shaking table acceleration is increased.

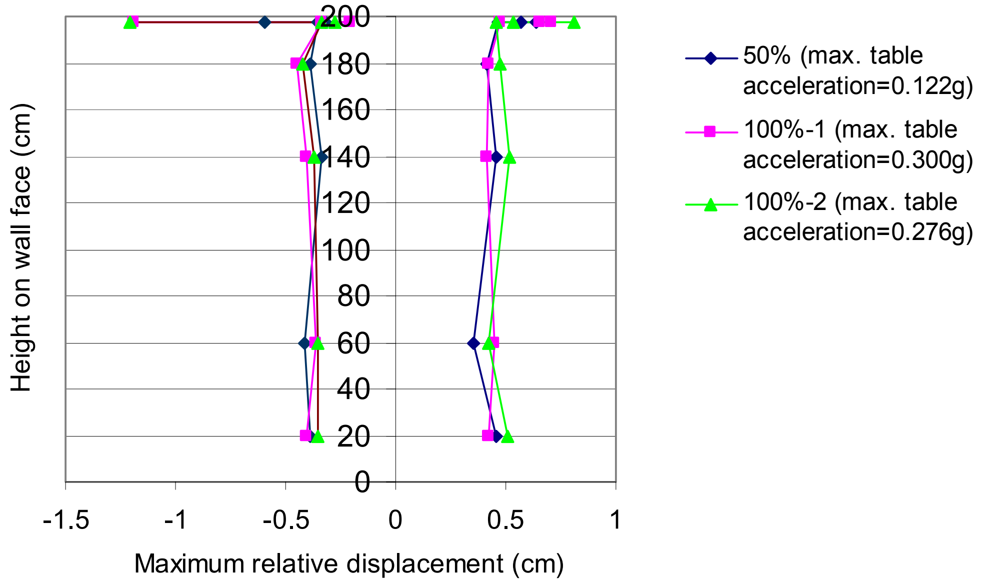

Figure 4.107. Effect of increase in acceleration on maximum relative wall face displacement throughout height of wall for Test 1

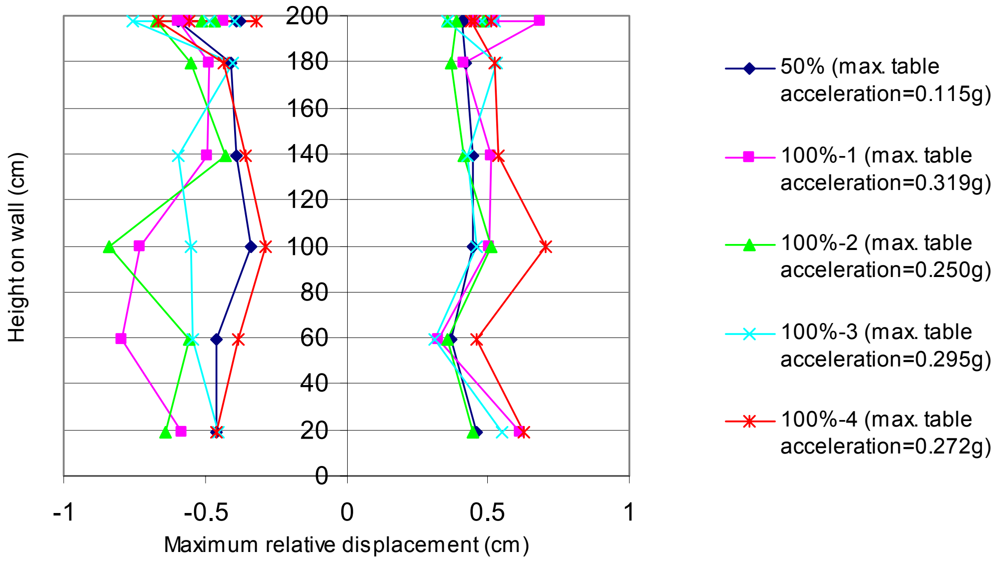

Figure 4.108. Effect of increase in acceleration on maximum relative wall face displacement throughout height of wall for Test 2

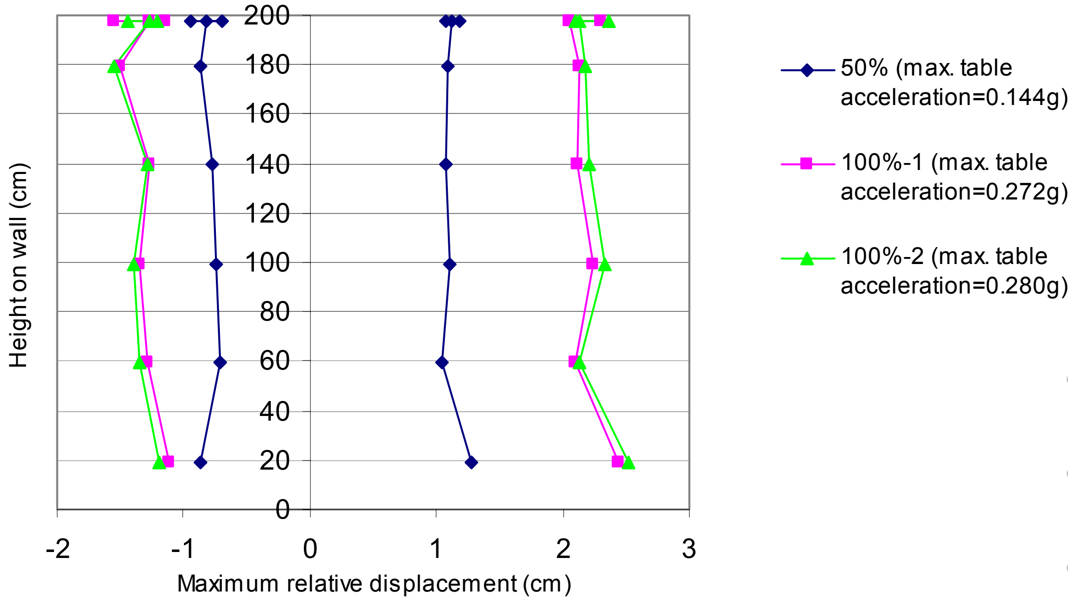

Figure 4.109. Effect of increase in acceleration on maximum relative wall face displacement throughout height of wall for Test 3

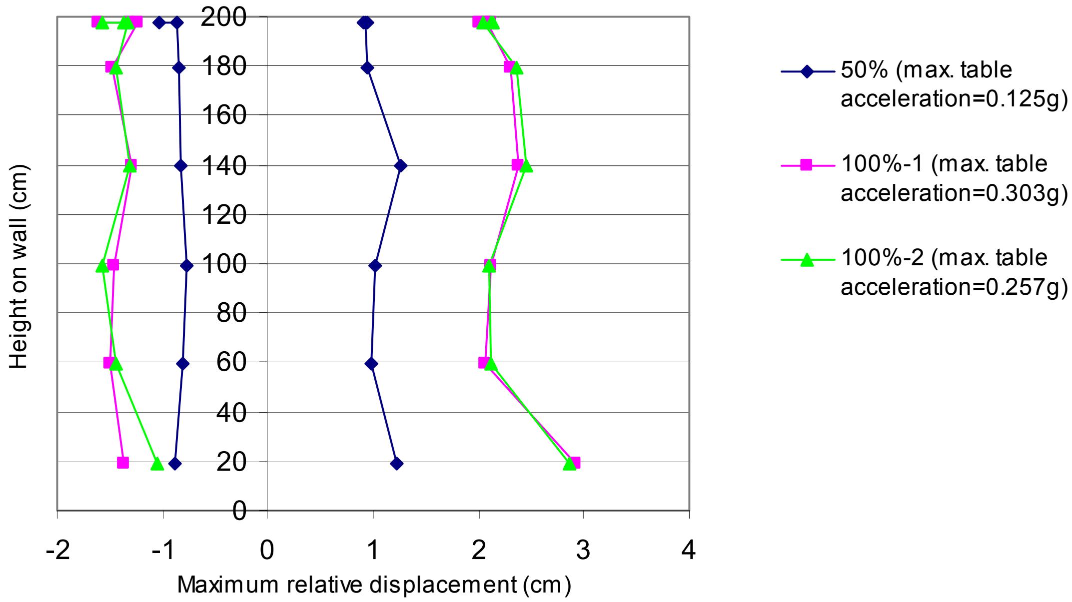

Figure 4.110. Effect of increase in acceleration on maximum relative wall face displacement throughout height of wall for Test 4 Part 1

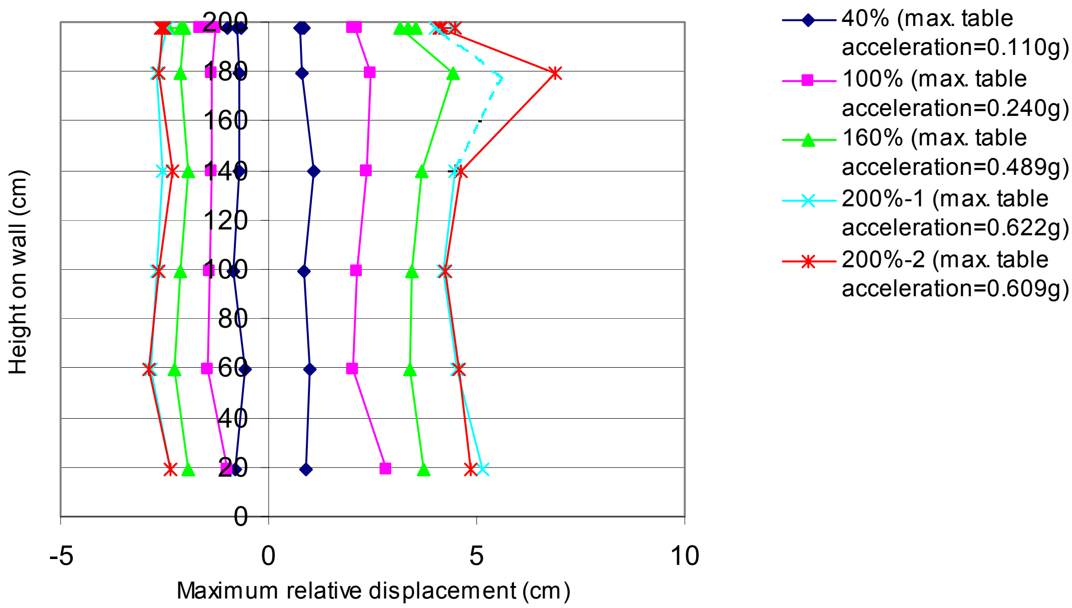

Figure 4.111. Effect of increase in acceleration on maximum relative wall face displacement throughout height of wall for Test 4 Part 2

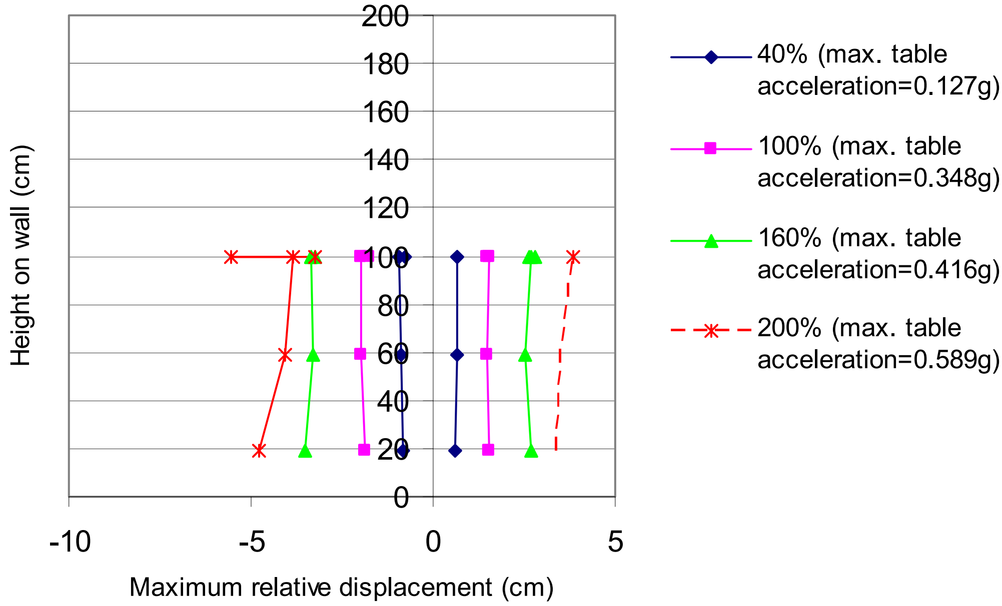

Figure 4.112. Effect of increase in acceleration on maximum relative wall face displacement throughout height of wall for Test 5

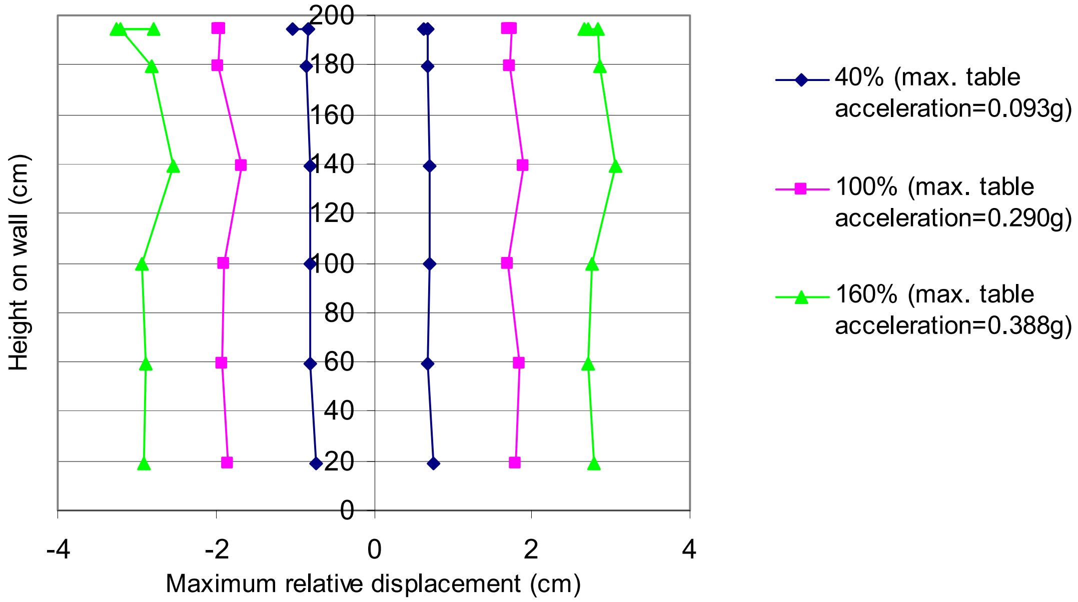

Figure 4.113. Effect of increase in acceleration on maximum relative wall face displacement throughout height of wall for Test 6

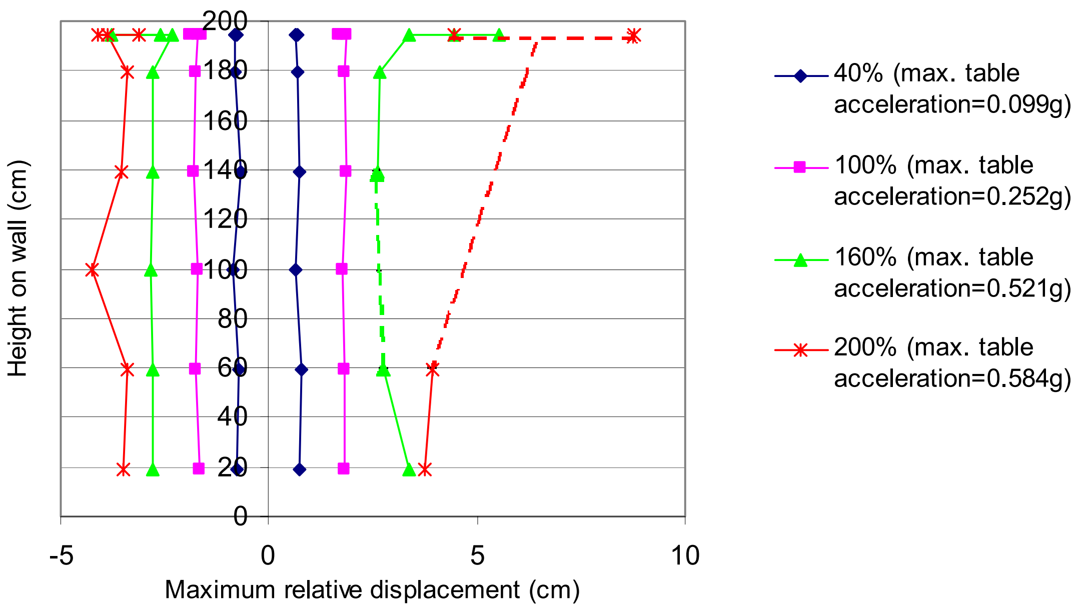

Figure 4.114. Effect of increase in acceleration on maximum relative wall face displacement throughout height of wall for Test 7

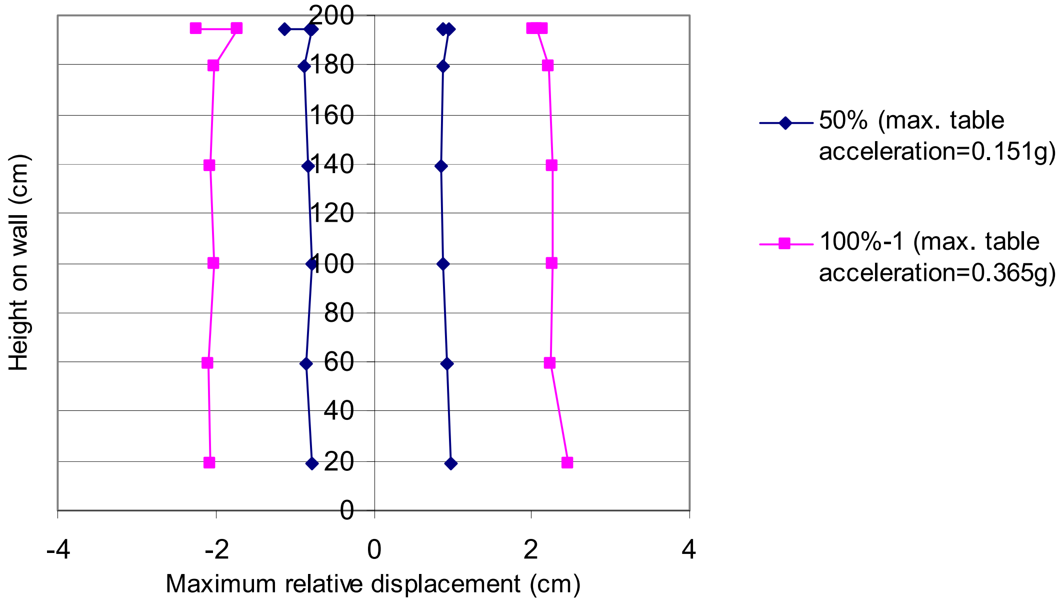

Figure 4.115. Effect of increase in acceleration on maximum relative wall face displacement throughout height of wall for Test 8 Part a

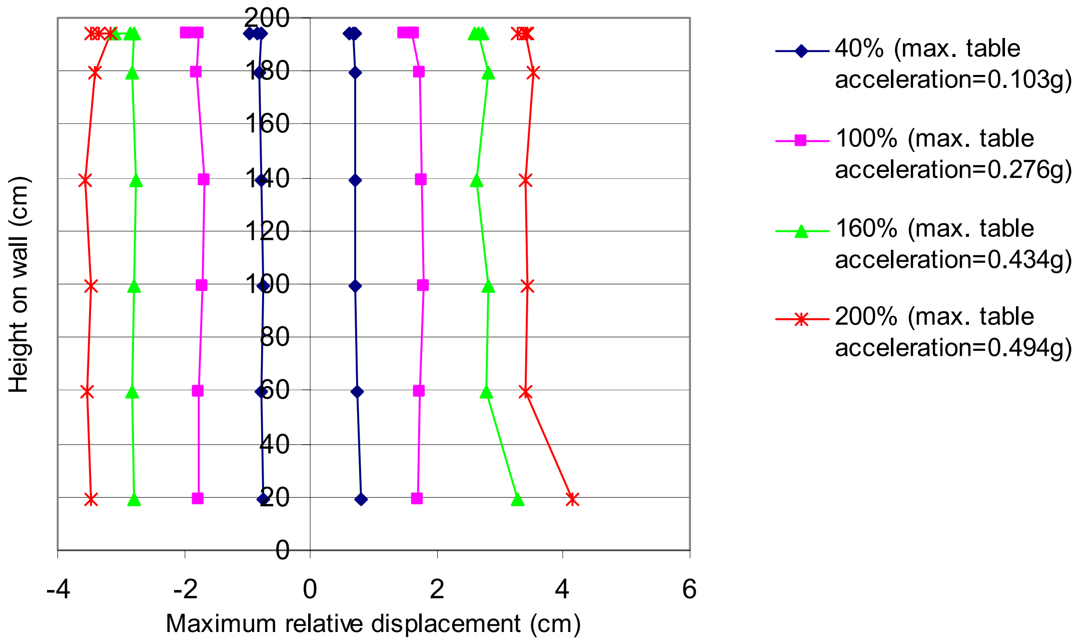

Figure 4.116. Effect of increase in acceleration on maximum relative wall face displacement throughout height of wall for Test 8 Part b

4.5.3. Effects of Shaking Table Acceleration on Permanent Face Displacements

Figures 4.117 to 4.126 show the effect of increase in maximum table acceleration on permanent displacements of wall face for each test. Permanent displacements remain in the range of ±0.1 cm with a few exceptions that are still a few millimeters and may be considered insignificant. No tendency of increase in permanent displacements with increasing maximum table acceleration was observed.

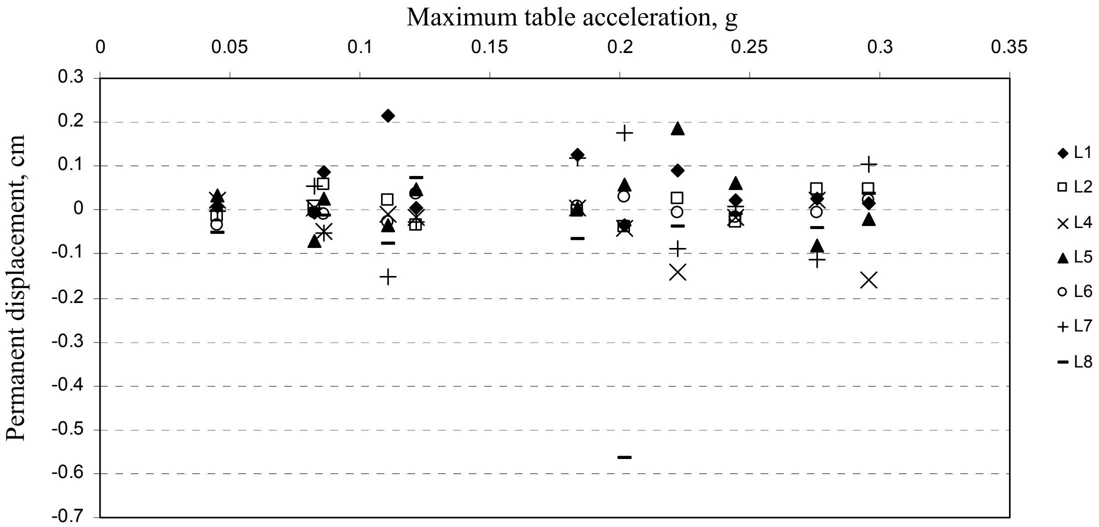

Figure 4.117. Effect of increase in acceleration on permanent displacement measured by L1-L8 (bottom to top) for Test 1

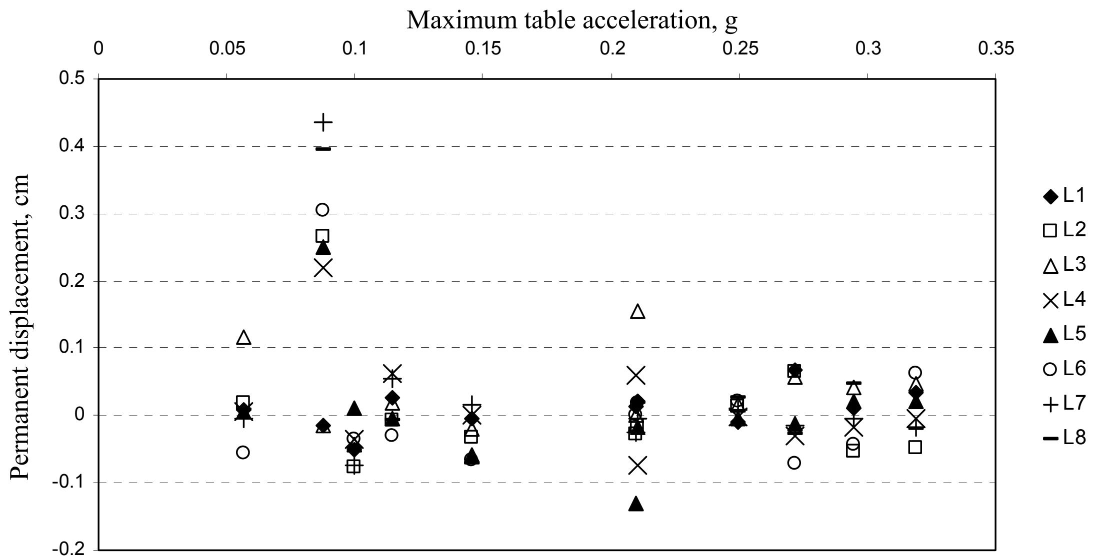

Figure 4.118. Effect of increase in acceleration on permanent displacement measured by L1-L8 (bottom to top) for Test 2

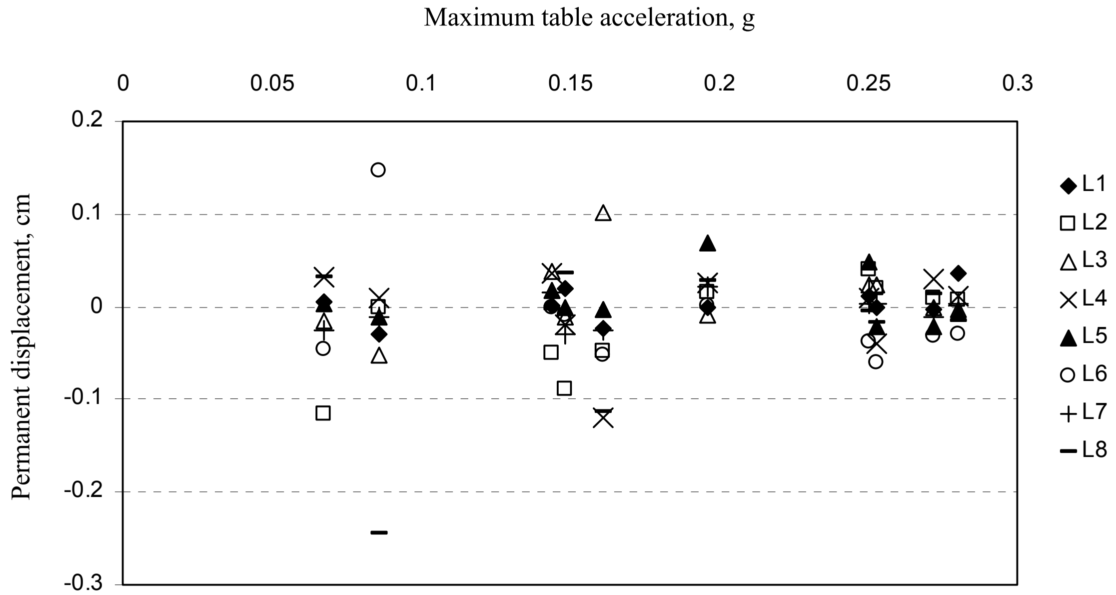

Figure 4.119. Effect of increase in acceleration on permanent displacement measured by L1-L8 (bottom to top) for Test 3

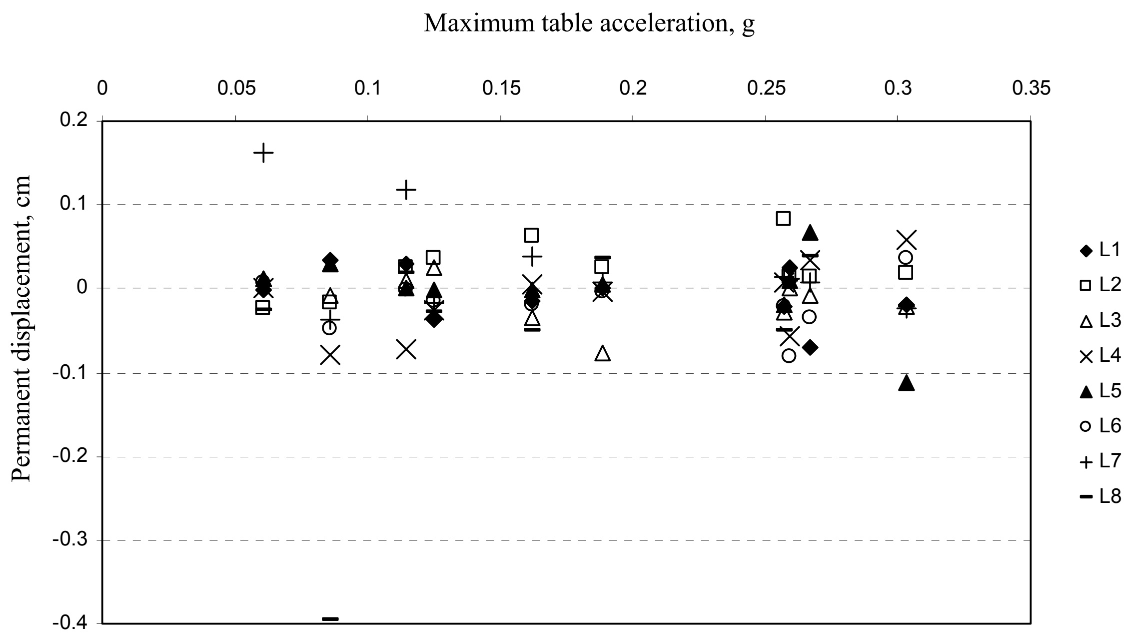

Figure 4.120. Effect of increase in acceleration on permanent displacement measured by L1-L8 (bottom to top) for Test 4 Part 1 (Runs 4-1 to 4-10)

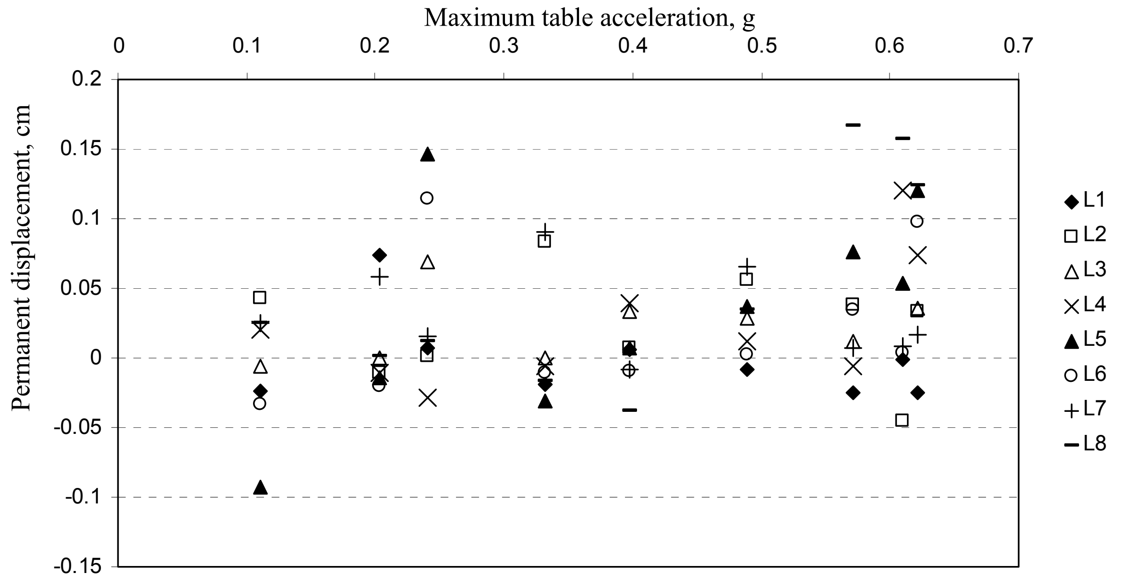

Figure 4.121. Effect of increase in acceleration on permanent displacement measured by L1-L8 (bottom to top) for Test 4 Part 2 (Runs 4-11 to 4-19)

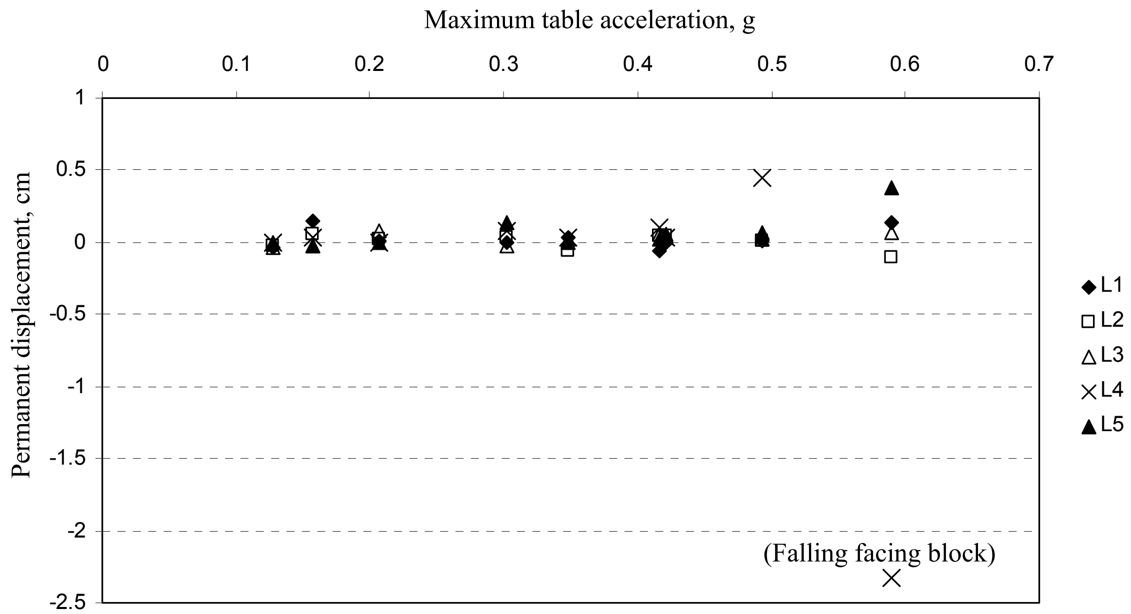

Figure 4.122. Effect of increase in acceleration on permanent displacement measured by L1-L5 (bottom to top) for Test 5

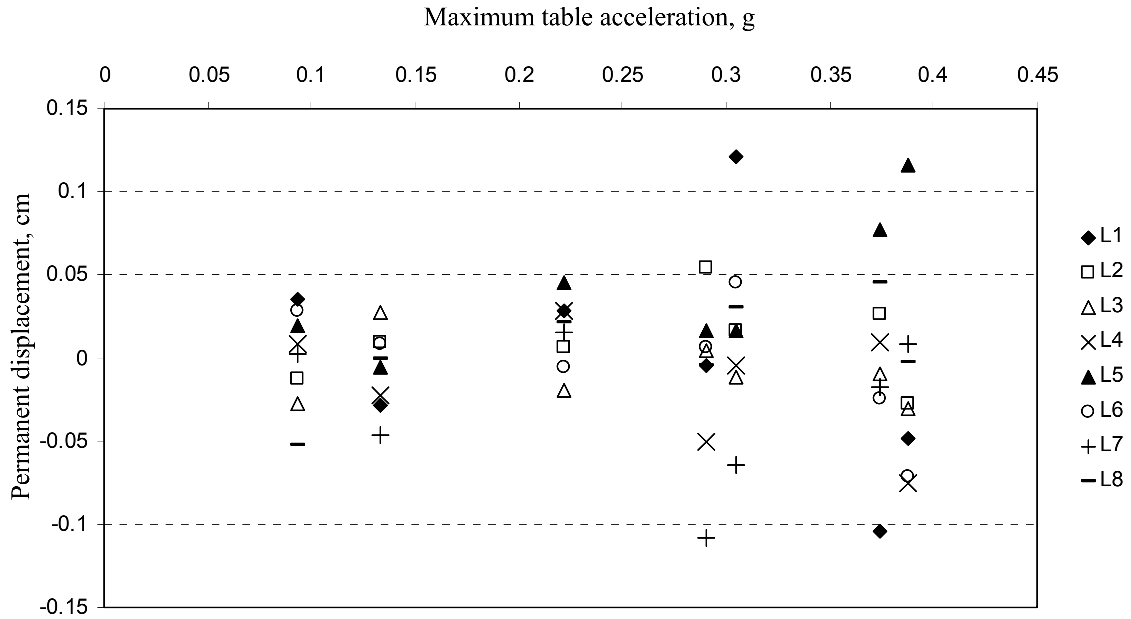

Figure 4.123. Effect of increase in acceleration on permanent displacement measured by L1-L8 (bottom to top) for Test 6

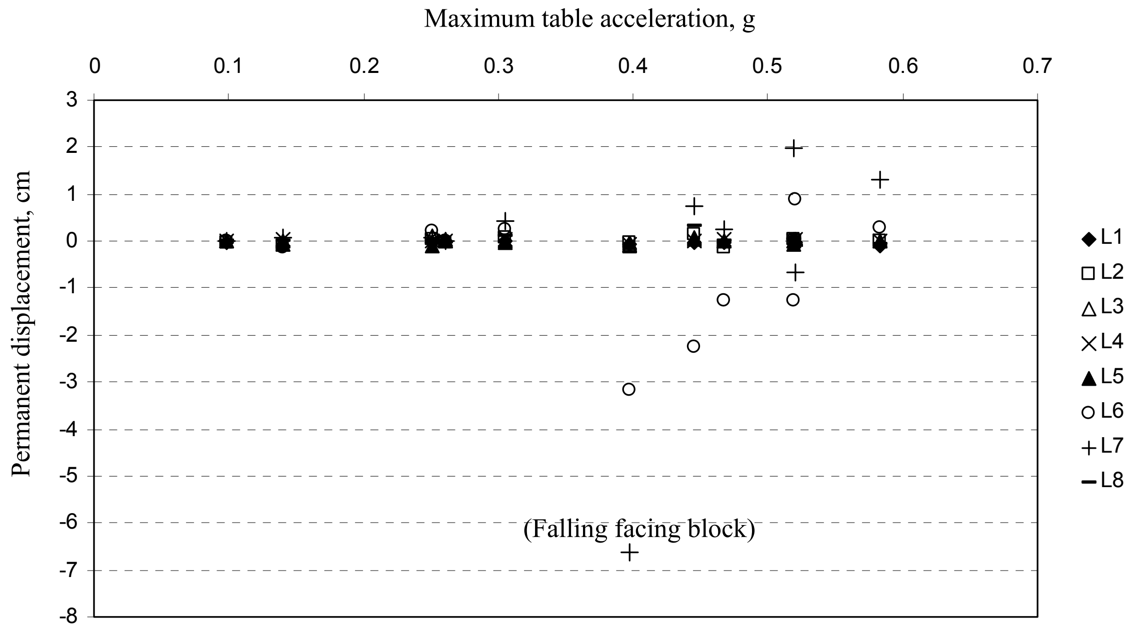

Figure 4.124. Effect of increase in acceleration on permanent displacement measured by L1-L8 (bottom to top) for Test 7

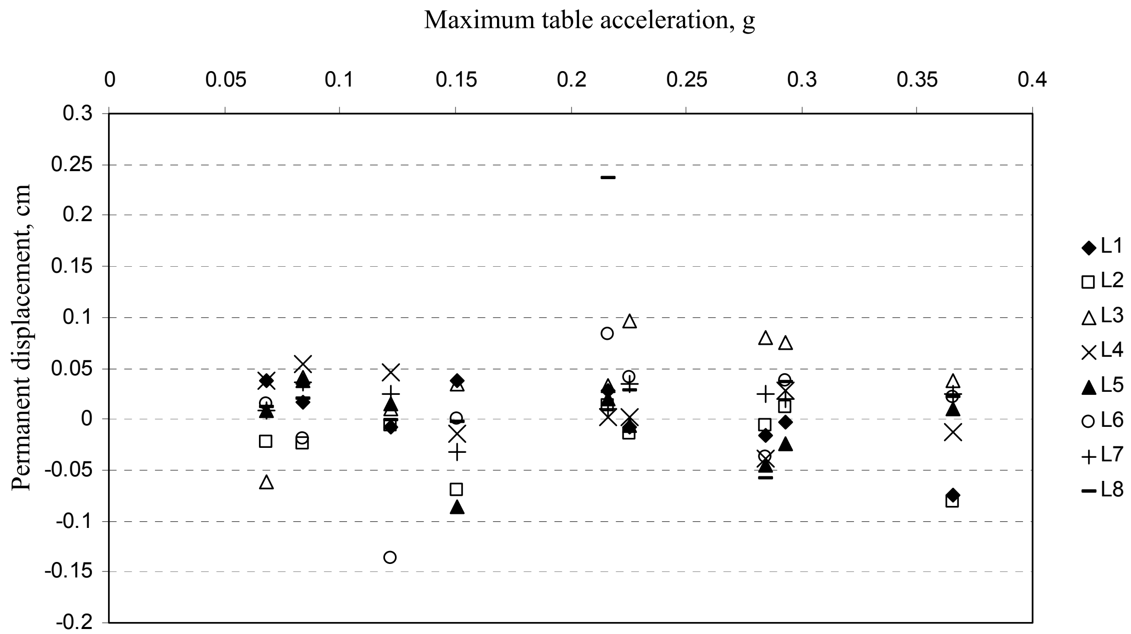

Figure 4.125. Effect of increase in acceleration on permanent displacement measured by L1-L8 (bottom to top) for Test 8 Part a

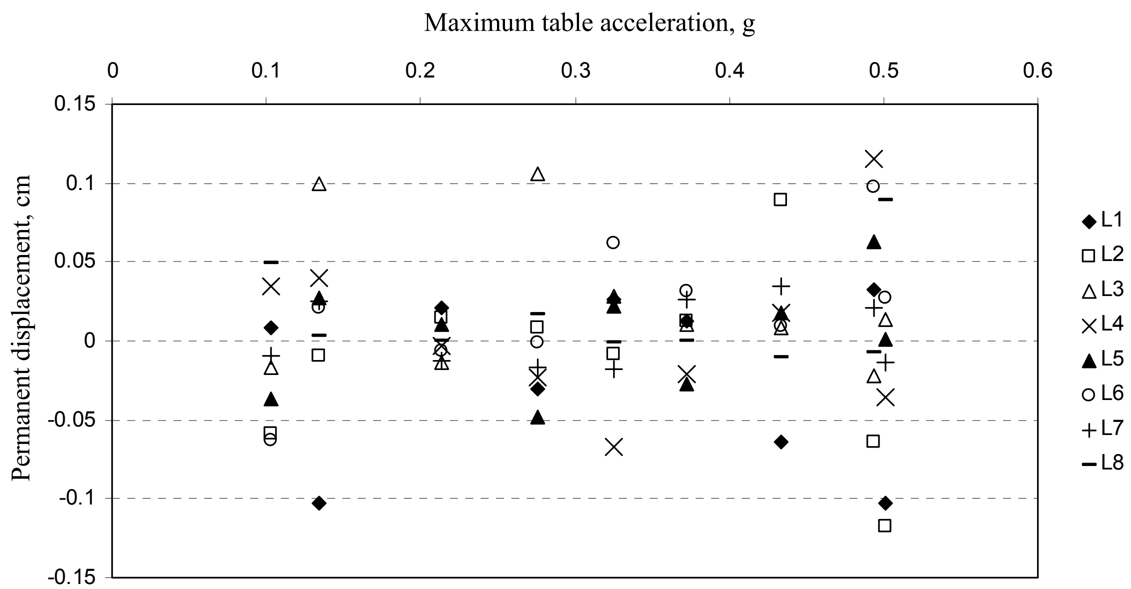

Figure 4.126. Effect of increase in acceleration on permanent displacement measured by L1-L8 (bottom to top) for Test 8 Part b

4.5.4. Effects of Shaking Table Acceleration on Stresses in Geotextile Reinforcement

Figures 4.127 to 4.136 show how the maximum geotextile stresses measured during shaking (without filtering) change with increasing maximum shaking table acceleration. A region with relatively high stresses and a trend to increase with increasing maximum table acceleration is inferred to be a region of potential failure. For example in Figure 4.127 (Test 1), the middle regions of both lower and upper geotextile reinforcements are the regions with highest stresses, and they both show a trend of increase with increasing acceleration. Solid lines in the figure demonstrate this trend. A plane passing through these regions may be considered as a critical surface. The critical surfaces deduced in this way are illustrated and compared to Rankine potential failure plane in Section 4.12.

Inspection of Figures 4.130 and 4.131 show that in Test 4, in which the reinforcements were comparatively very short, high stresses were developed only at the lower geotextile. Although reinforcement length was the same in Test 3, Figure 4.129 shows that the upper geotextile middle region was the region with the highest stress. The small geotextile spacing in Test 3 appears to have resulted in redistribution of stress and a critical failure surface different from that in Test 4.

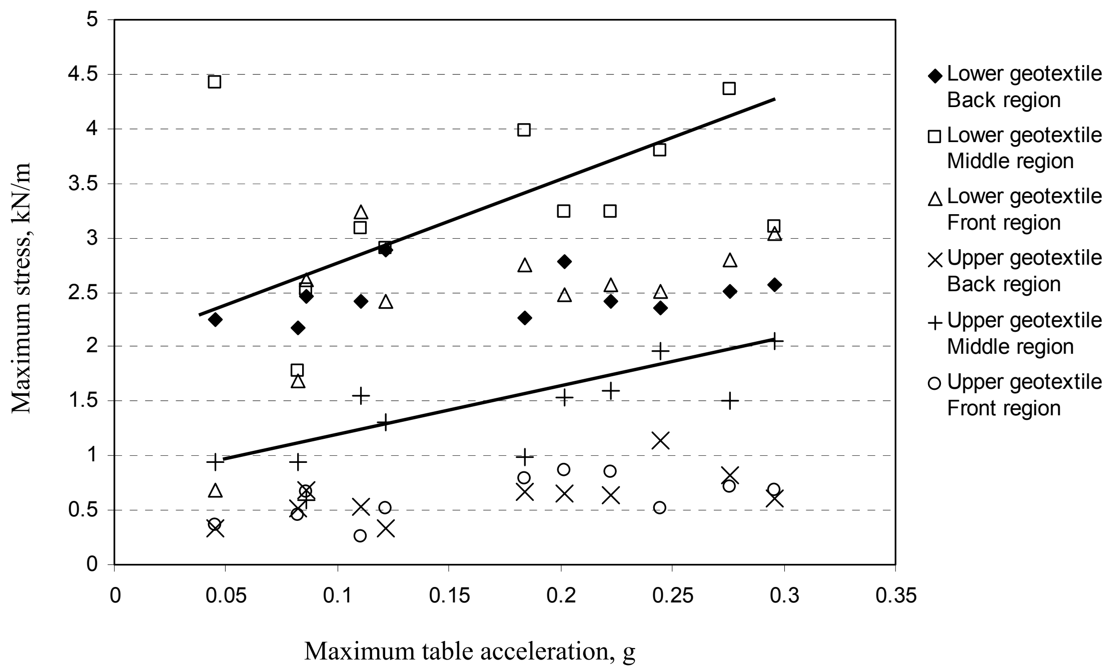

Figure 4.127. Effect of increase in acceleration on geotextile stresses for Test 1

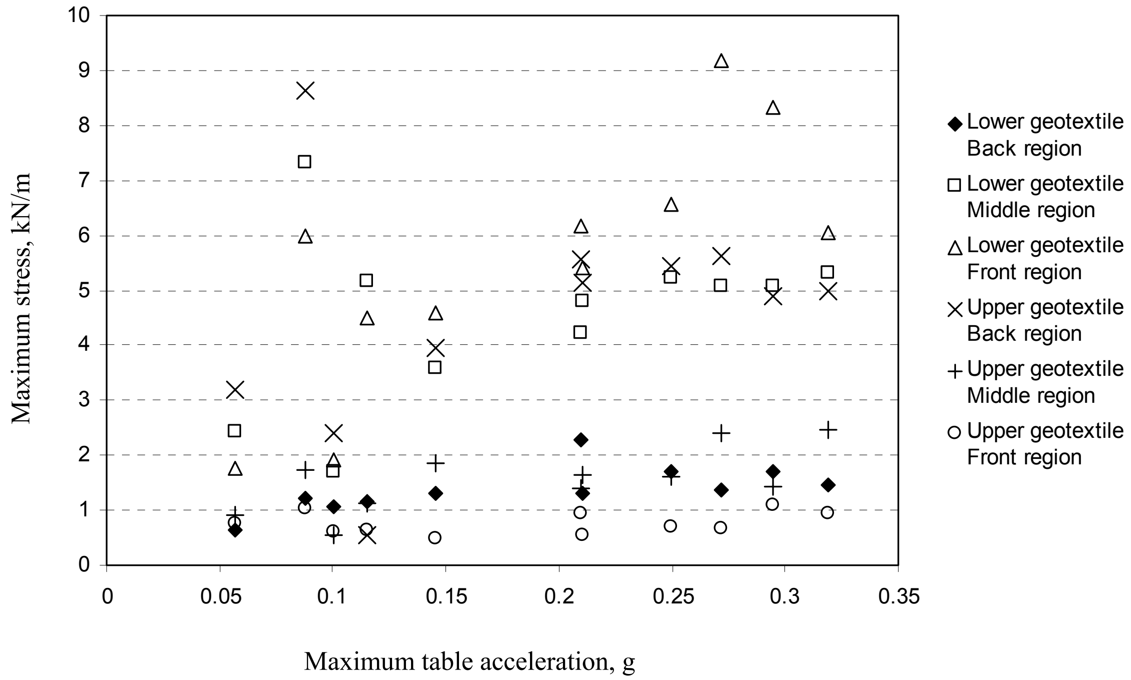

Figure 4.128. Effect of increase in acceleration on geotextile stresses for Test 2

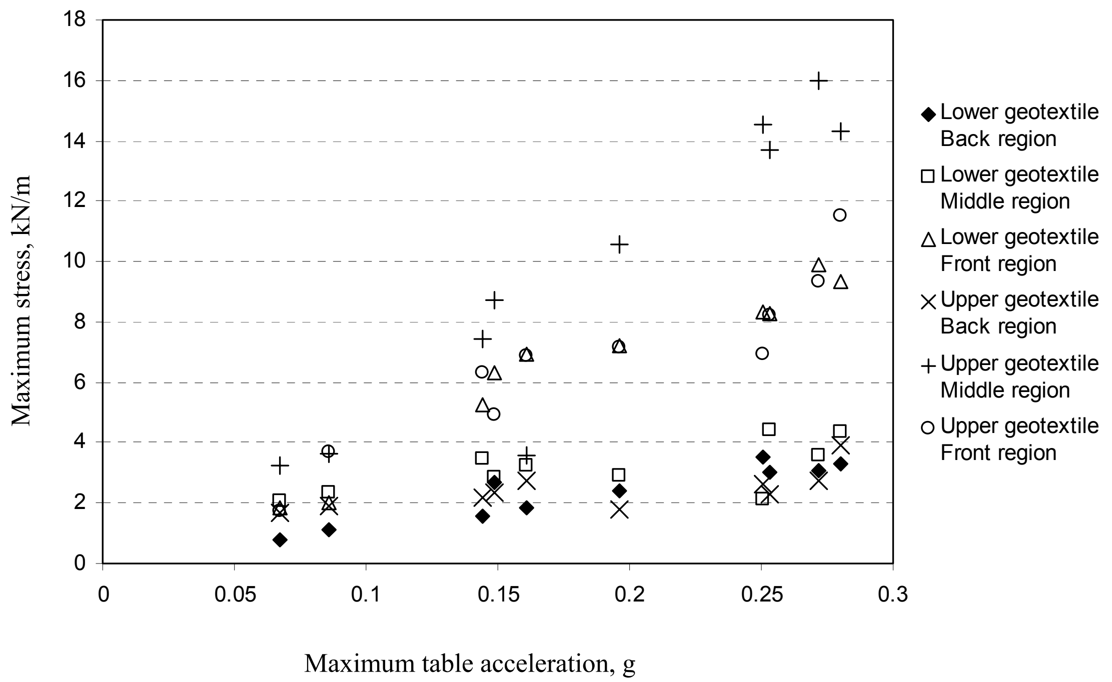

Figure 4.129. Effect of increase in acceleration on geotextile stresses for Test 3

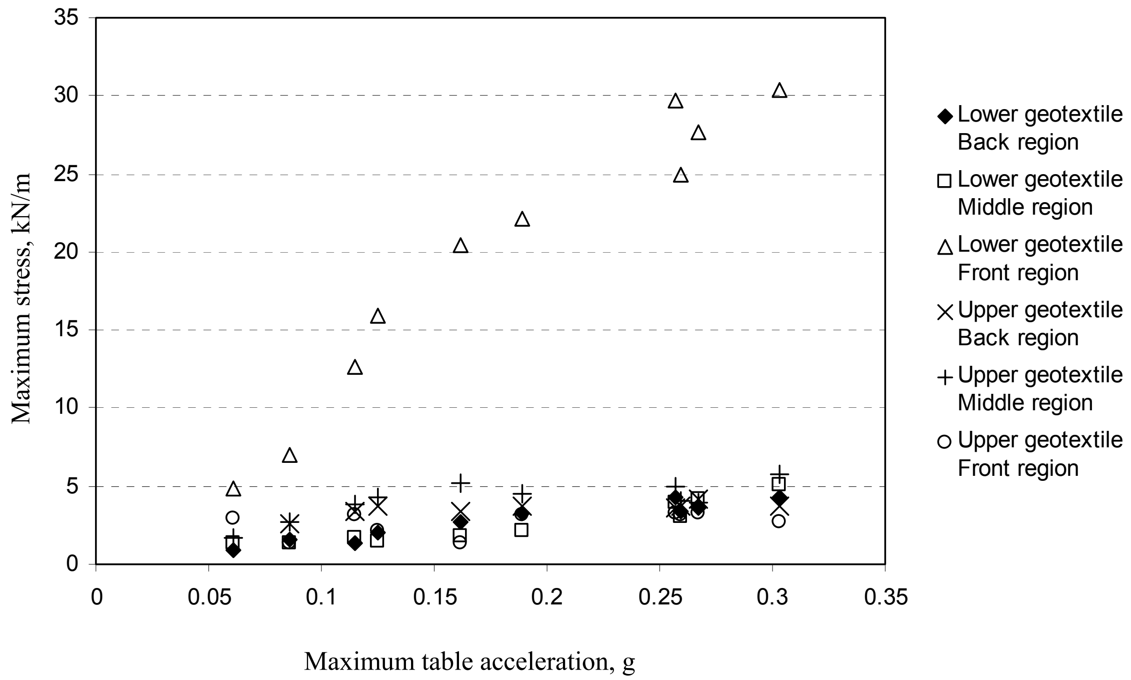

Figure 4.130. Effect of increase in acceleration on geotextile stresses for Test 4 Part 1 (Runs 4-1 to 4-10)

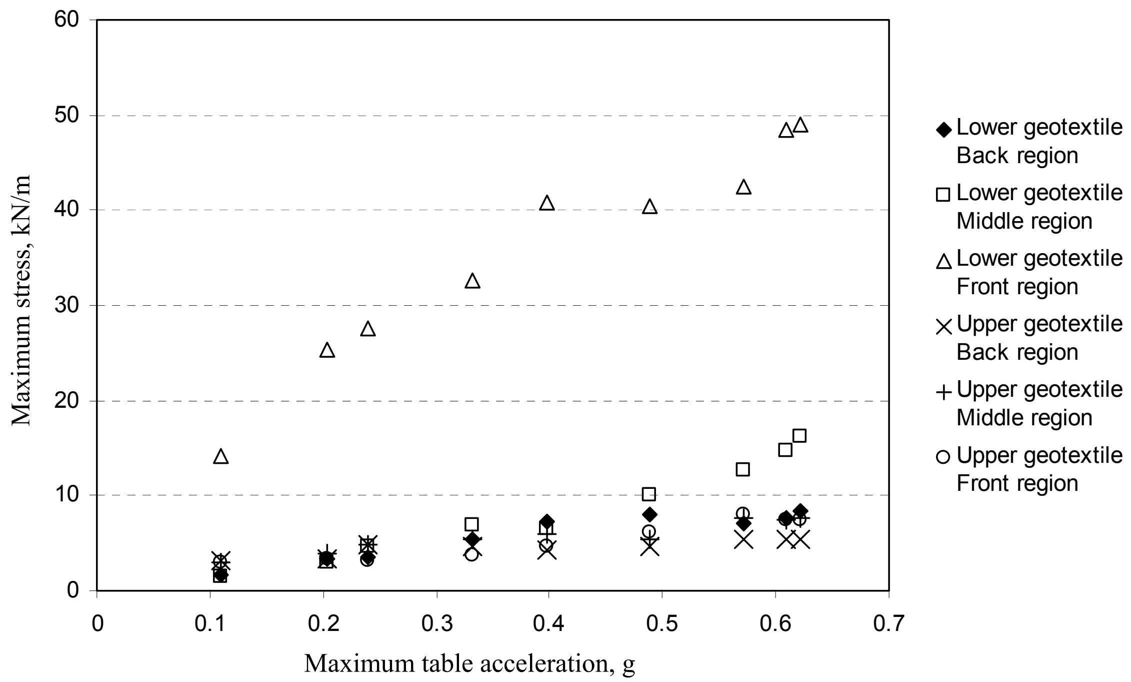

Figure 4.131. Effect of increase in acceleration on geotextile stresses for Test 4 Part 2 (Runs 4-11 to 4-19)

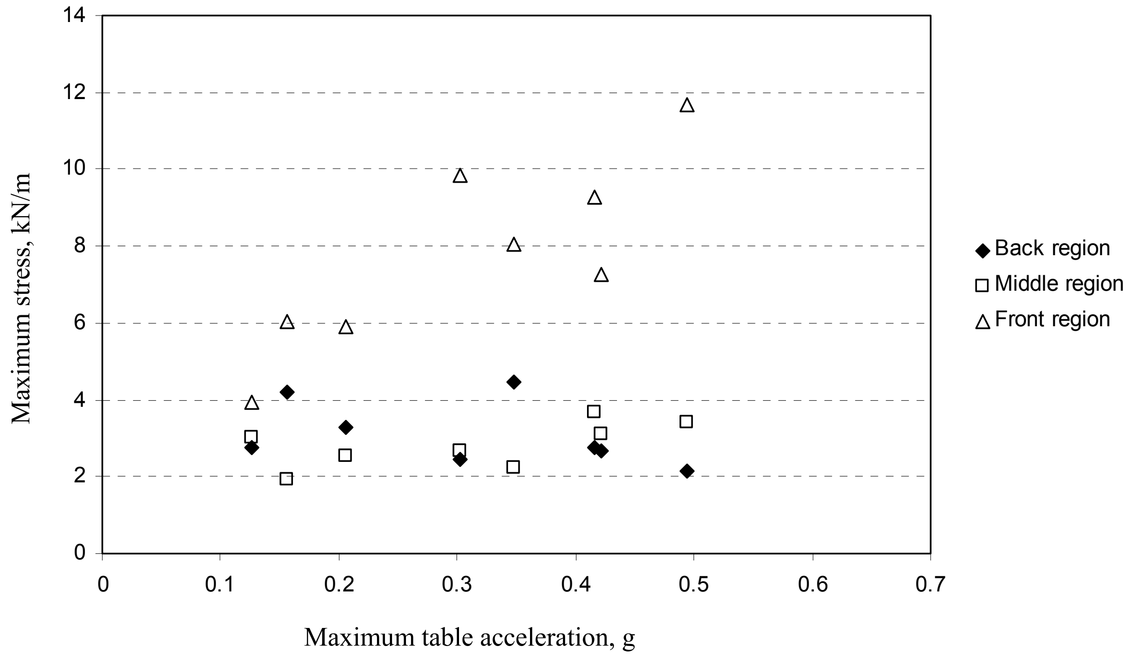

Figure 4.132. Effect of increase in acceleration on geotextile stresses for Test 5

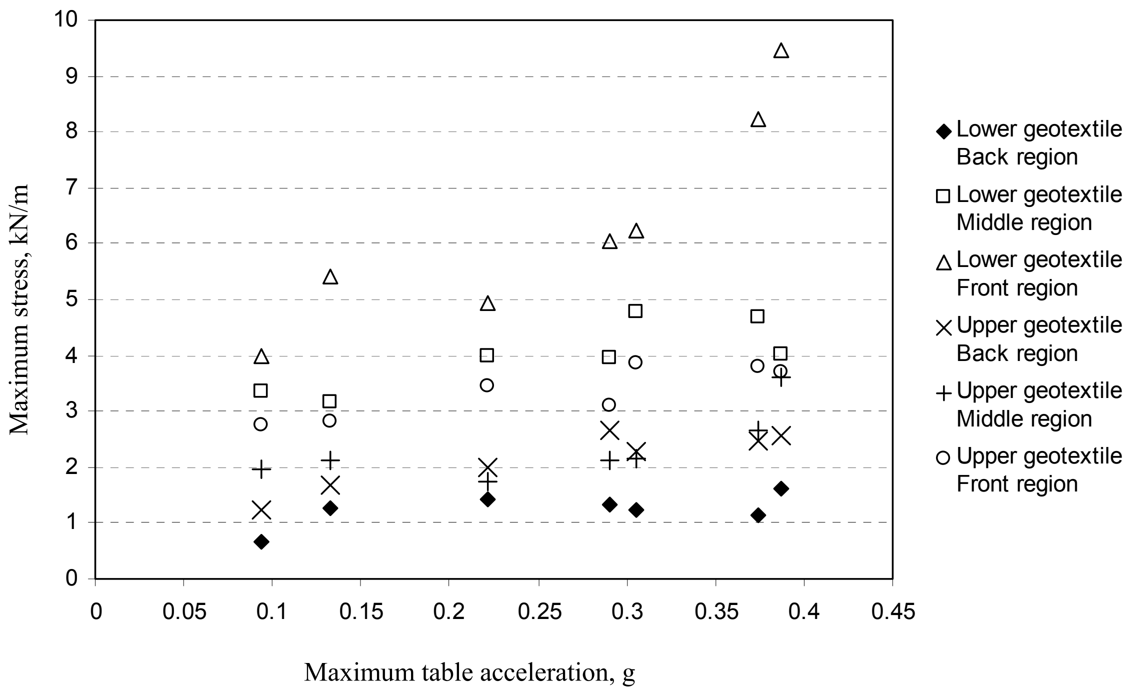

Figure 4.133. Effect of increase in acceleration on geotextile stresses for Test 6

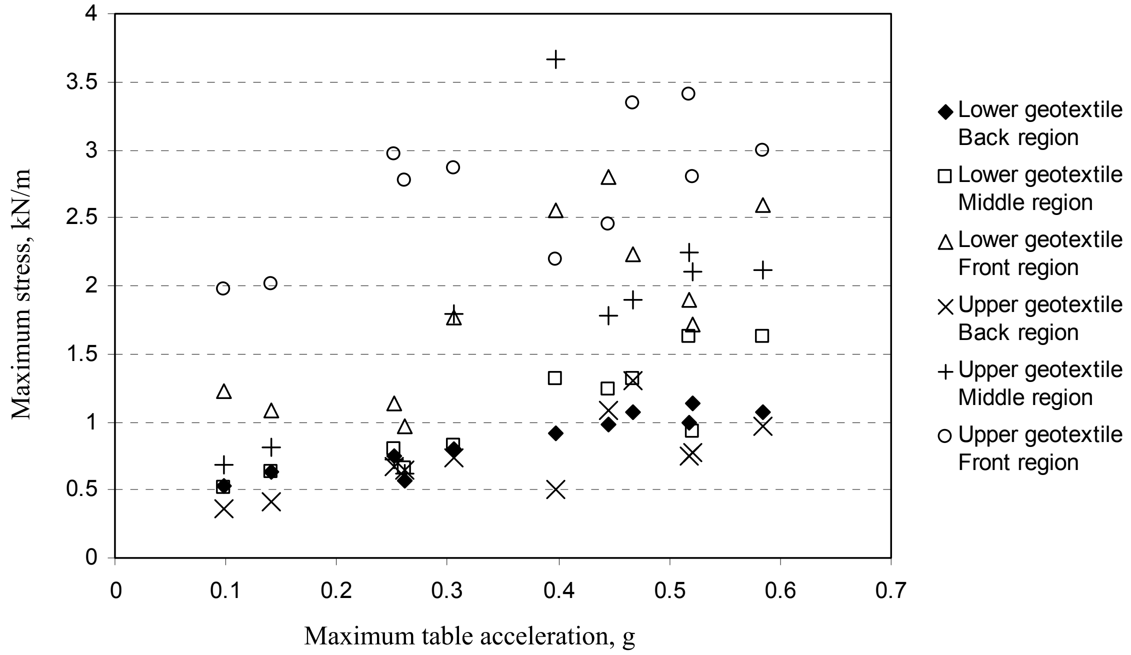

Figure 4.134. Effect of increase in acceleration on geotextile stresses for Test 7

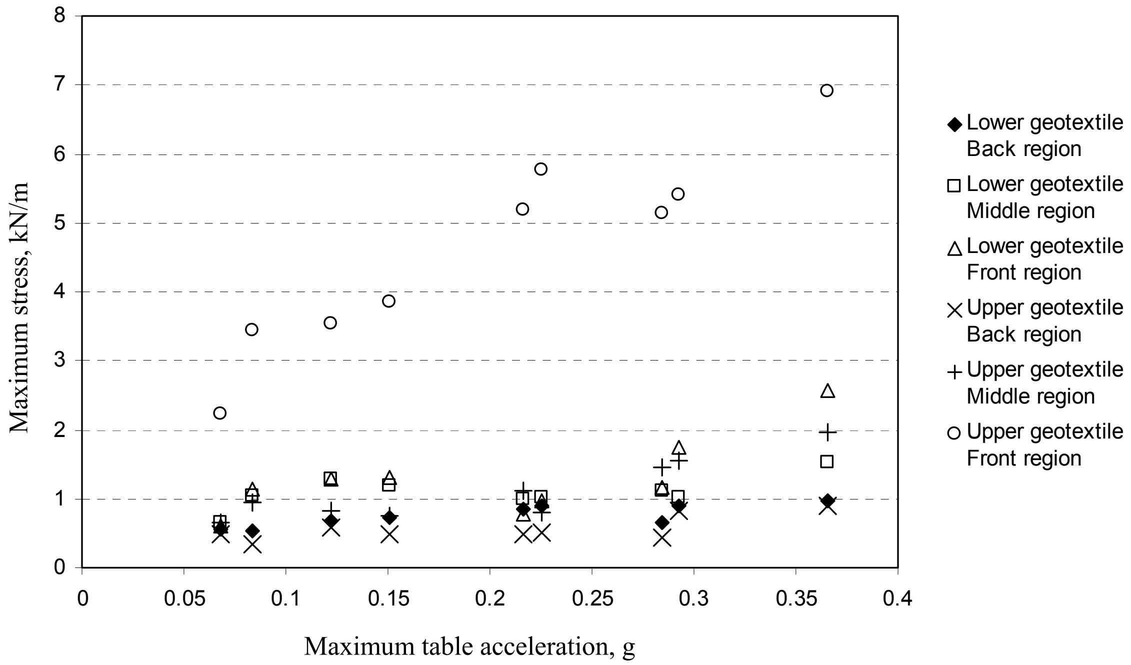

Figure 4.135. Effect of increase in acceleration on geotextile stresses for Test 8a

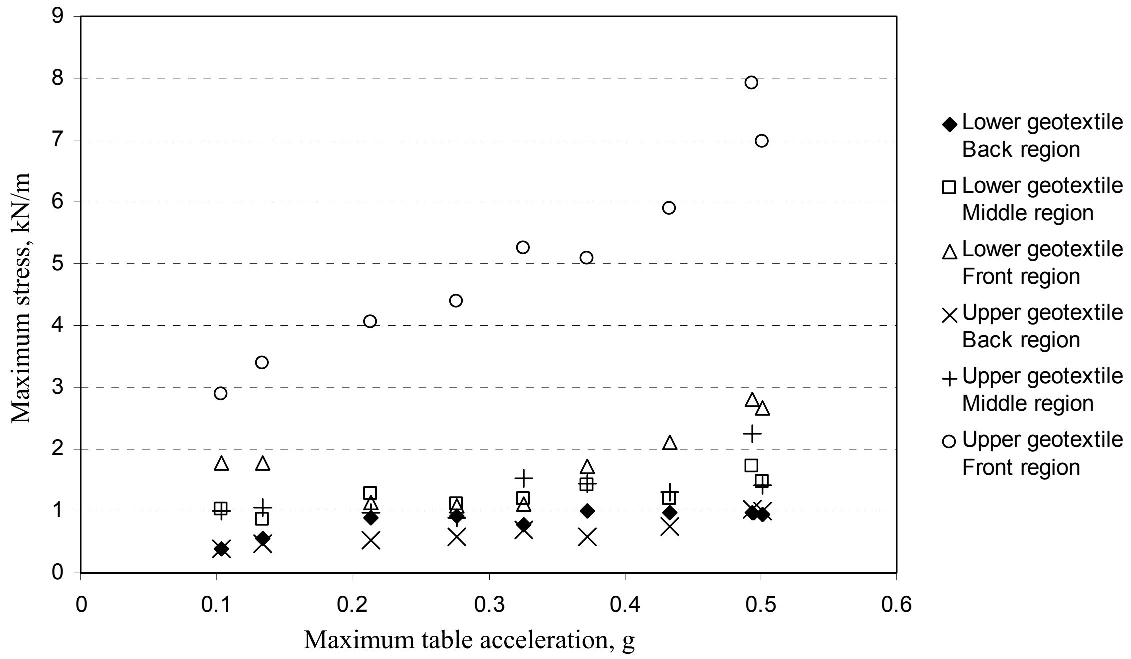

Figure 4.136. Effect of increase in acceleration on geotextile stresses for Test 8b

4.6. Effects of L/H (Reinforcement Length to Wall Height Ratio)

To enable comparisons among different test configurations, the values of parameters under investigation were calculated for the prototype walls. To evaluate the effects of reinforcement length to wall height ratio (L/H) on seismic performance, tests with configurations having only L/H as the changing parameter were chosen and compared. Tests 1, 2, and 4 (model scale 1:2) constitute the first investigated group and Tests 6 and 7 (model scale 1:4) constitute the second group.

The prototype walls for Tests 1, 2, and 4 have a height of four meters (396 cm to be accurate). The frequency of the earthquake applied on the prototype wall is the same as the original El Centro frequency, the reinforcement spacing is 40 cm in the prototype wall, and the top two layers of blocks are fixed for all these three tests with 1:2 model scale. The investigated parameter, L/H, is 0.8, 0.52, and 0.375 for Test 1, Test 2, and Test 4, respectively. Tail geotextiles (short geotextiles used between the blocks where no reinforcement geotextile is placed) were used in Tests 1 and 2.

The prototype walls for Tests 6 and 7 have a height of 780 cm. For both tests, the model scale is 1:4, the frequency of the earthquake applied on the prototype wall is the same as the original El Centro frequency, the geotextile spacing is 40 cm and the top two layers of facing blocks are free. The only variable is L/H, which is 0.4 for Test 6 and 0.7 for Test 7.

4.6.1. Effects of L/H on Maximum Acceleration Measured on Wall

In the second part of Test 4, the readings by accelerometers M7 and M8 (front top and top front accelerometers, respectively) were much higher than the readings in the first part (Figure 4.137). In fact, in the first run of the test where the maximum shaking table acceleration was 0.11g, maximum acceleration readings by M7 and M8 were 2.9g and 2.7g. These values increased greatly with increasing maximum table acceleration. This tremendous increase in measured accelerations was not reflected in the displacement measurements. Top two block layers were fixed in this test, but there may have been a loosening that caused extreme accelerations which were very high frequency vibrations and the sampling frequency of the accelerometers did not allow all fluctuations to be recorded, as demonstrated previously in Section 4.3.2.

Comparison of Tests 1, 2, and 4 revealed that the increase in acceleration on wall face was not dependent on L/H for configurations with top blocks fixed (Figure 4.138). In Tests 1, 2, and 7 the geotextile at the top was extended beyond Rankine failure plane. In Tests 4 and 6, the geotextile at the top ended at Rankine plane. Considering there was a loosening in top blocks in the second part of Test 4, it may be deduced that for the top blocks left free, acceleration at top increased largely for configurations with geotextile length not extended sufficiently beyond Rankine failure surface (Figures 4.137 and 4.139). Accelerations at the levels below were not affected by geotextile length.

It can be concluded that as long as the reinforcement is sufficiently extended beyond the Rankine surface, the change in L/H ratio does not significantly affect the amplification in acceleration.

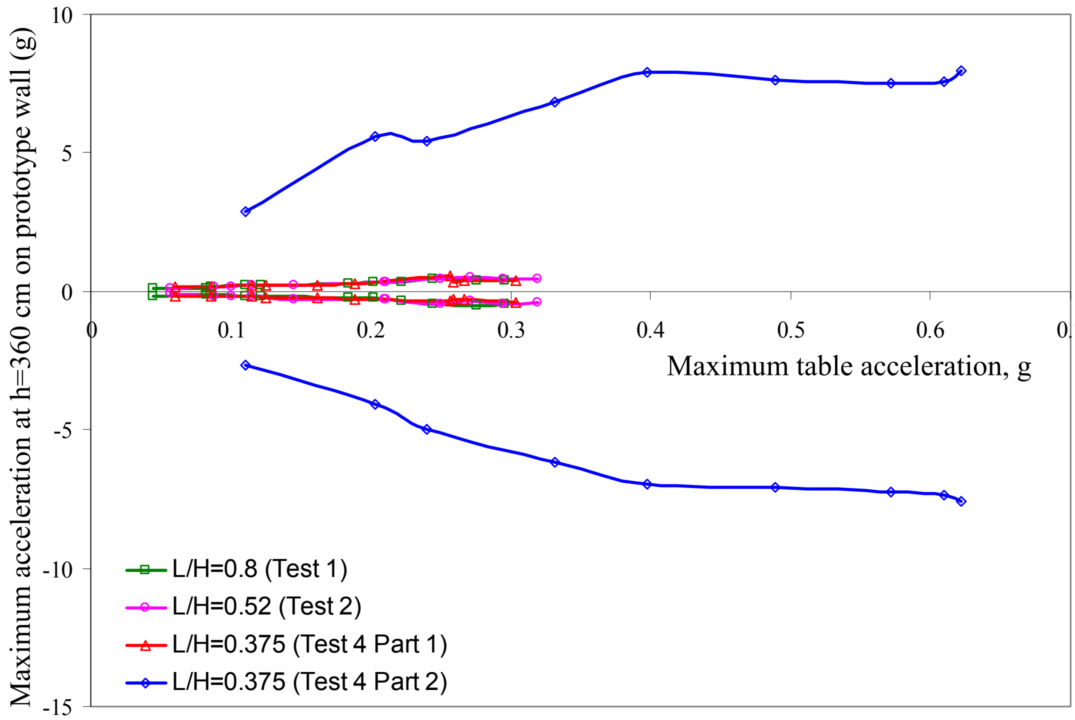

Figure 4.137. Comparison of maximum accelerations measured by accelerometer M7 for Tests 1, 2, and 4

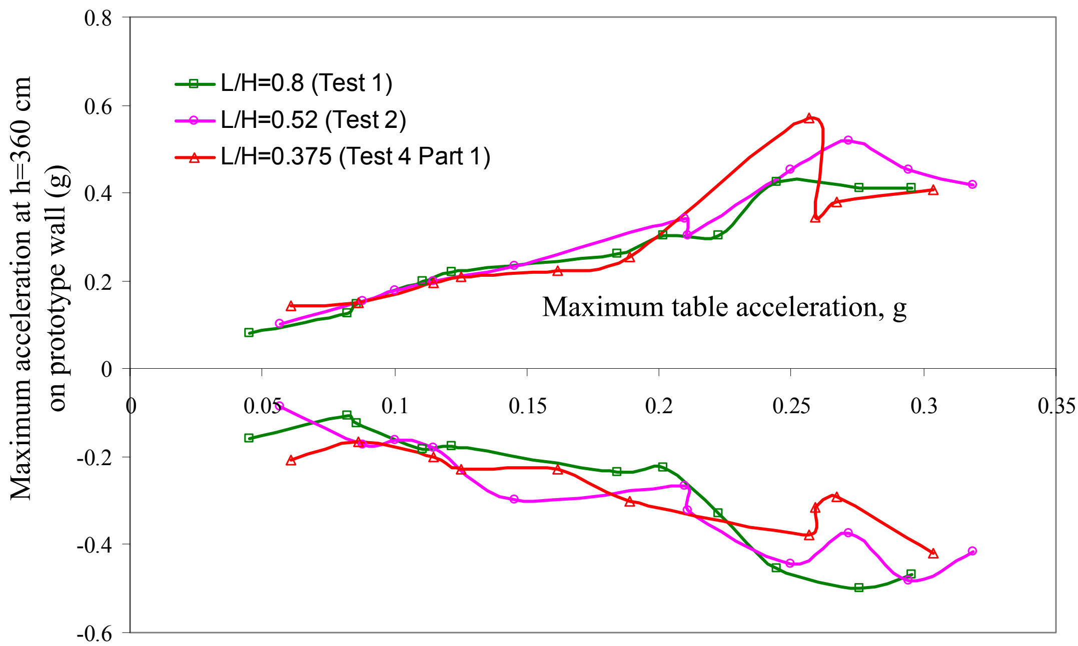

Figure 4.138. Comparison of maximum accelerations measured by accelerometer M7 for Tests 1, 2, and 4 (Test 4 Part 2 is excluded.)

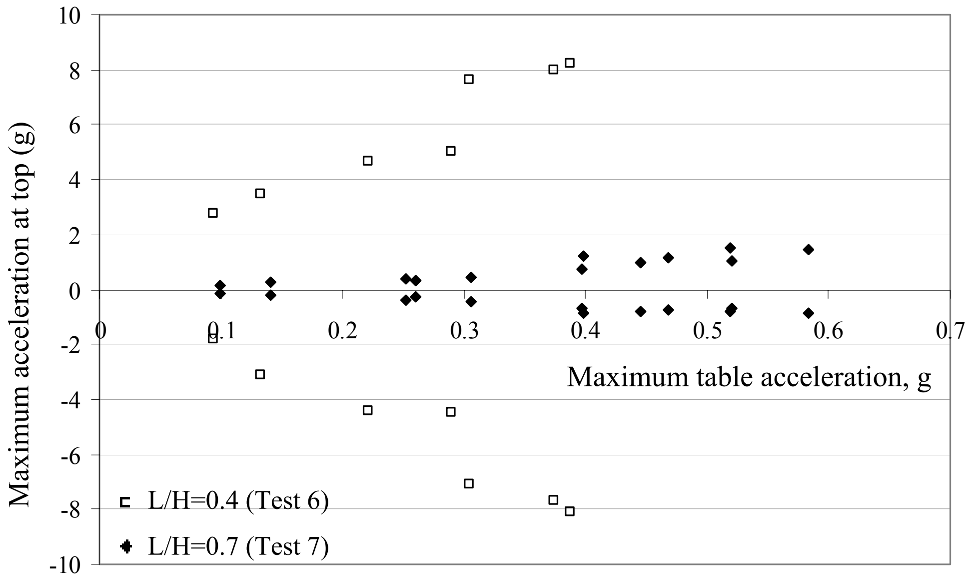

Figure 4.139. Comparison of maximum accelerations measured by accelerometer M7 (height 728 cm on prototype wall) for Tests 6 and 7

4.6.2. Effects of L/H on Maximum Face Displacements During Shaking

Maximum global displacements on the wall face during shaking were only slightly affected by geotextile length, as seen in Figures 140 to 144.

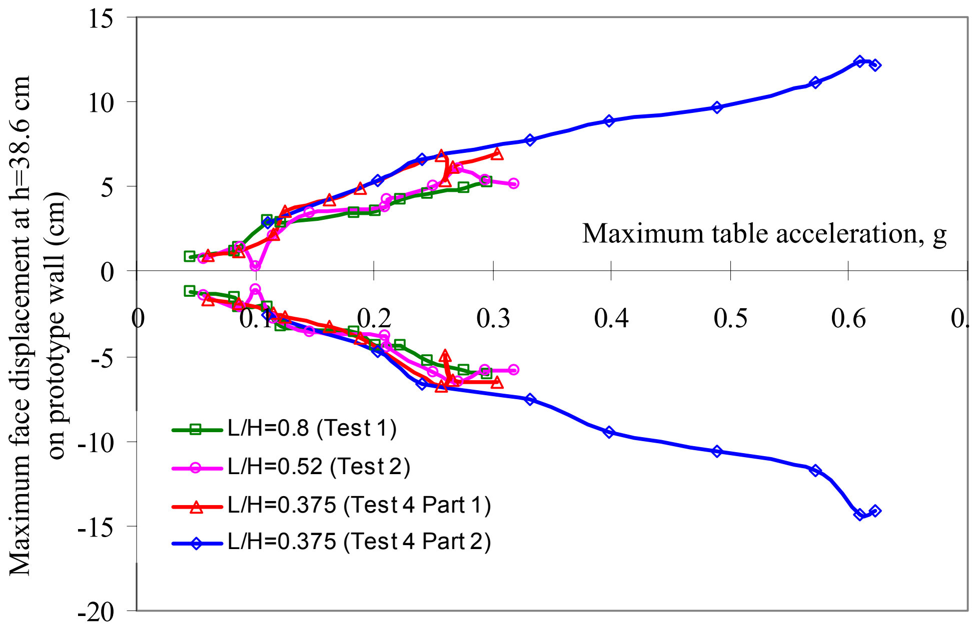

Figure 4.140. Comparison of maximum face displacements measured by optical laser distance sensor L1 for Tests 1, 2 and 4

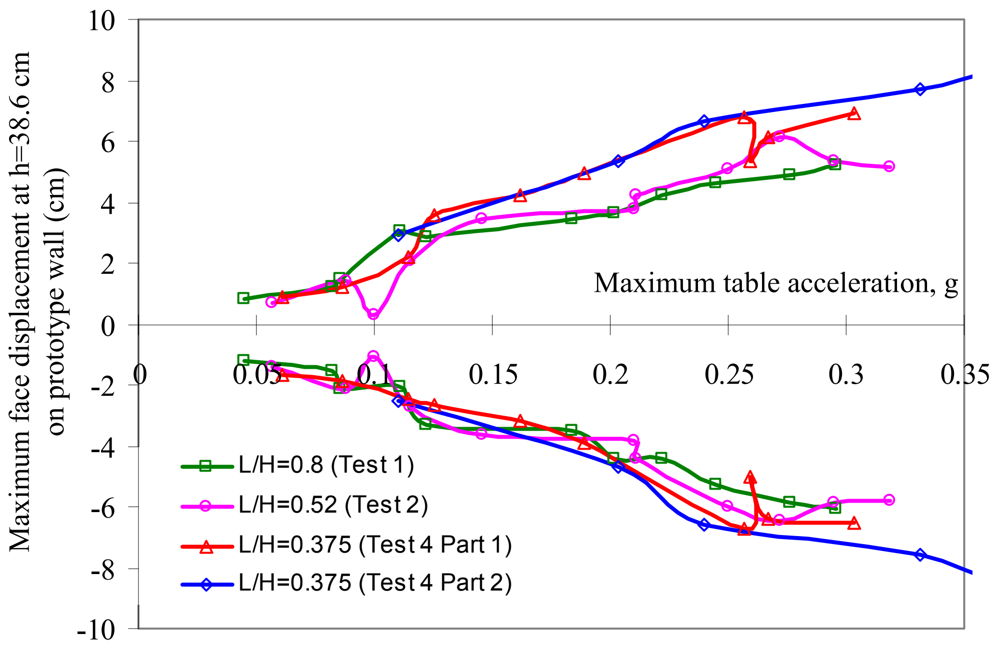

Figure 4.141. Comparison of maximum face displacements measured by optical laser distance sensor L1 for Tests 1, 2, and 4 (close-up of the initial section)

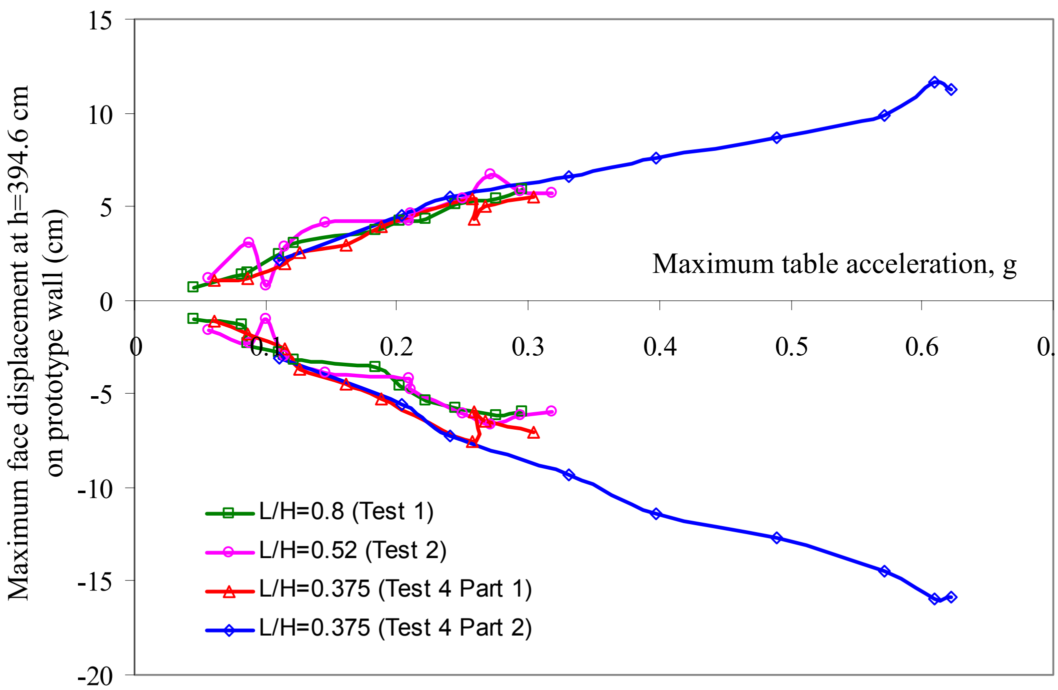

Figure 4.142. Comparison of maximum face displacements measured by optical laser distance sensor L7 for Tests 1, 2, and 4

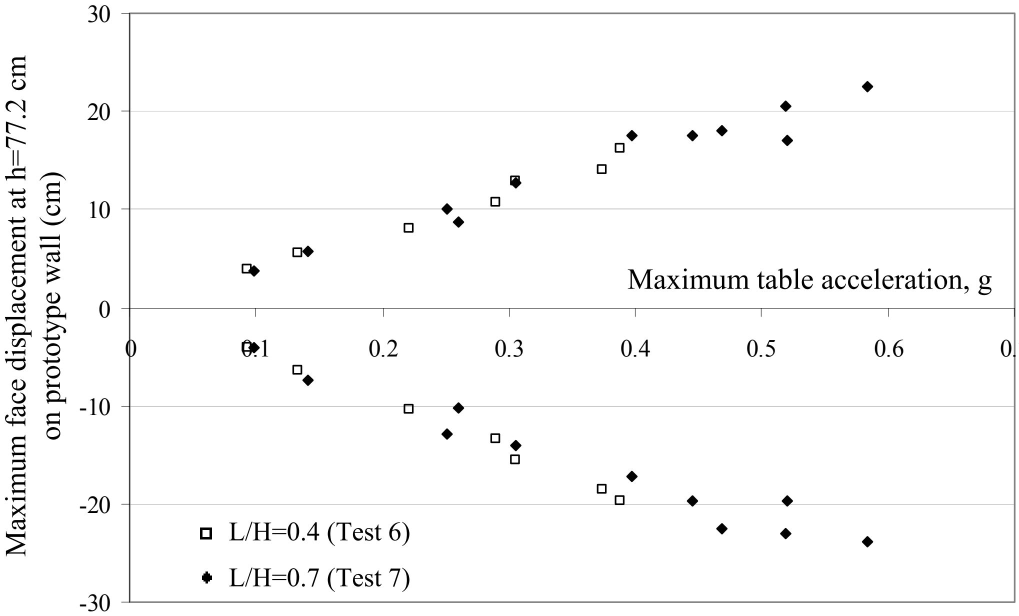

Figure 4.143. Comparison of maximum face displacements measured by optical laser distance sensor L1 for tests 6 and 7

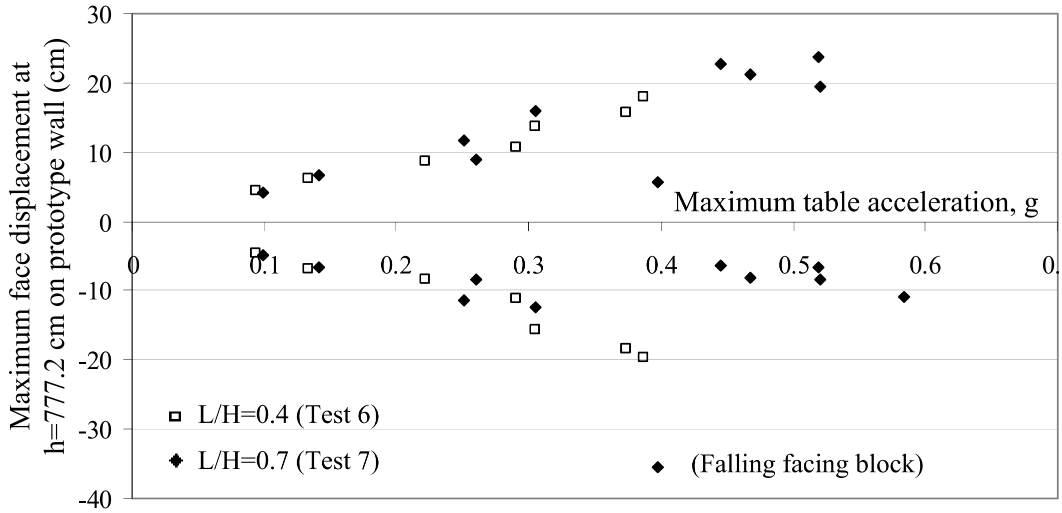

Figure 4.144. Comparison of maximum face displacements measured by optical laser distance sensor L7 for tests 6 and 7

4.6.3. Effects of L/H on Permanent Face Displacements

In Test 4, a configuration with design factor of safety very close to one was tested and all permanent displacements were below two millimeters. Therefore, it can be inferred that performance (in terms of permanent displacements) of geosynthetic-reinforced soil retaining walls with facing consisting of concrete blocks under earthquake loading is not dependent on L/H for the tested configurations as long as the design factor of safety is above one for that specific peak ground acceleration.

4.6.4. Effects of L/H on Stresses in Geotextile Reinforcement

In Test 1, the geotextile stresses were generally higher in the lower geotextile. The highest stresses were in the middle for both geotextiles. There was a trend of increase in stress at these regions with increasing maximum table acceleration. This trend was not observed for the other regions, suggesting that the most critical surface passes through these middle regions.

In Test 2, the geotextile stresses were considerably higher in lower geotextile front and middle regions and upper geotextile back region. There was a trend of increase in stress at these regions with increasing maximum table acceleration. This trend was not observed for the other regions.

In Test 4, geotextile stresses were higher and increased with increasing maximum table acceleration in lower geotextile front region. Stresses in the upper geotextile remained low compared to the stress in lower geotextile front region. It is possible that the critical surface passed through the front region of the lower geotextile and through the unreinforced area behind the upper geotextile.

The maximum stresses in these tests (Tests 1, 2, and 4) measured during shaking in the critical regions of the lower geotextile are compared in Figure 4.145. This figure shows that the stresses in the reinforcement increase as the reinforcement length decreases. In Figure 4.146, a similar comparison for the upper geotextile critical region is given. In this figure, measurements for Test 1 and Test 2 exhibit a trend similar to Figure 4.145, i.e. stress increases with decreasing reinforcement length. Although the reinforcement length was much lower in Test 4, the stress in reinforcement is not increased because the reinforcement does not provide anchorage beyond the Rankine plane. Therefore it may be concluded that geotextile stress increases with decreasing L/H as long as the reinforcement is extended sufficiently beyond the critical surface.

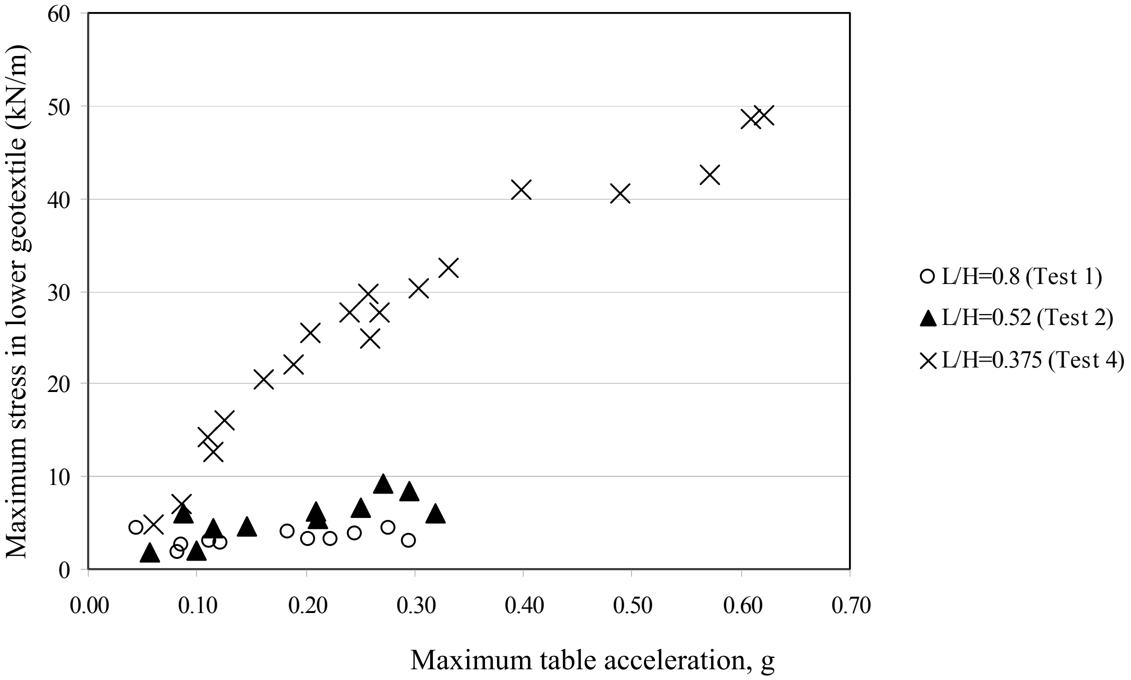

Figure 4.145. Comparison of maximum stresses in lower geotextile for Tests 1, 2, and 4

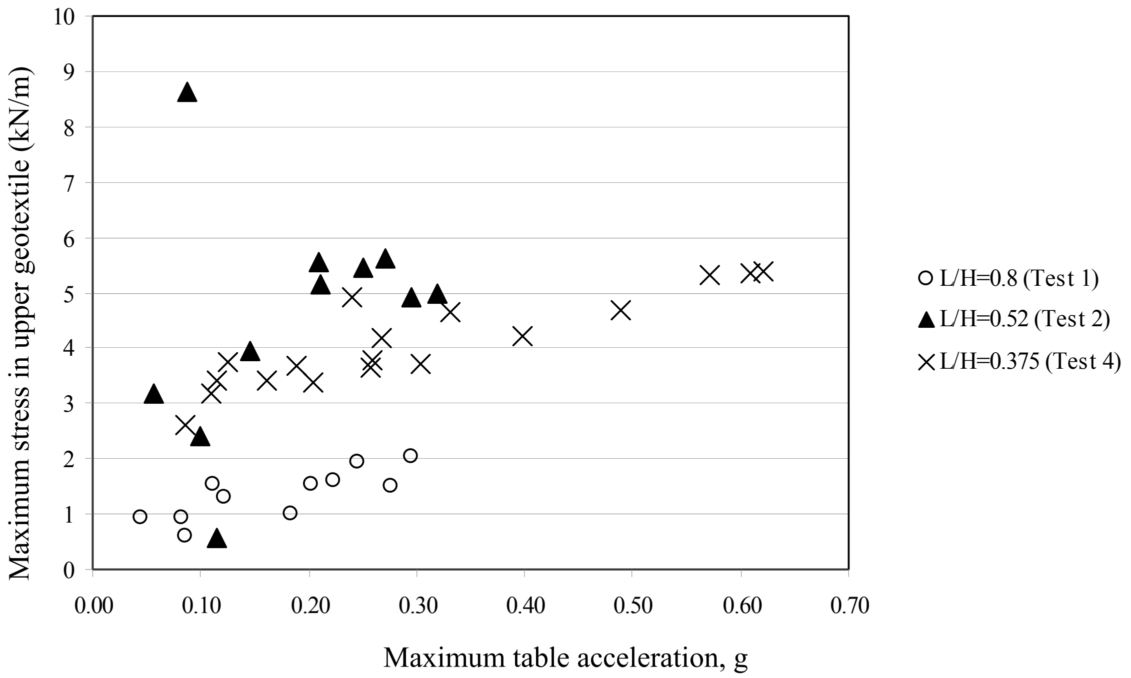

Figure 4.146. Comparison of maximum stresses in upper geotextile for Tests 1, 2, and 4

A similar comparison can be made for Test 6 and Test 7. In Test 6, geotextile stresses were highest in the front region of the lower geotextile and tended to increase with increasing table acceleration at this region. The other regions did not show this trend. In Test 7, geotextile stresses were highest in the front and middle regions of the upper geotextile and in the front region of the lower geotextile. The stresses increased with increasing table acceleration. Maximum stresses measured during shaking in the critical regions of the lower and upper geotextiles of Tests 6 and 7 are compared in Figures 4.147 and 4.148. Similar to the conclusion drawn from comparison of Tests 1, 2, and 4, the stress in lower reinforcement increases as L/H decreases, but this is not the case in the upper reinforcement since the upper reinforcement does not pass the Rankine plane in Test 6.

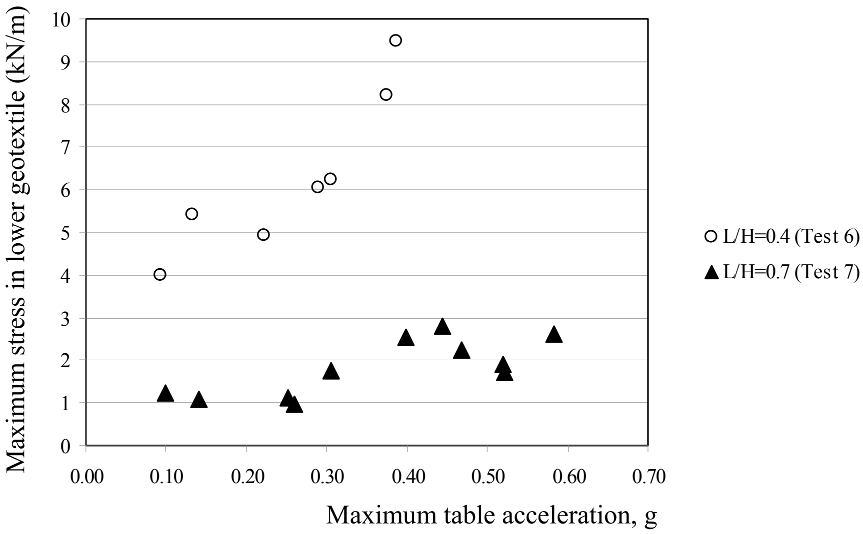

Figure 4.147. Comparison of maximum stresses in lower geotextile for Tests 6 and 7

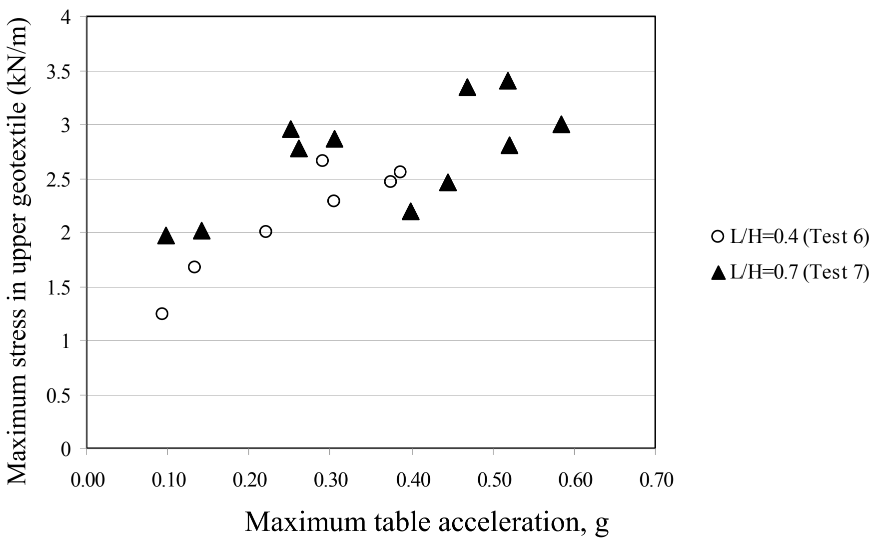

Figure 4.148. Comparison of maximum stresses in upper geotextile for Tests 6 and 7

4.7. Effects of Reinforcement Spacing

To evaluate the effects of reinforcement spacing, s_v, on seismic performance, Test 3 and the first part of Test 4 were compared. These tests were the only test group with only s_v as the changing parameter. The prototype walls for Test 3 and Test 4 have a height of four meters (396 cm to be accurate). The frequency of the earthquake applied on the prototype wall is the same as the original El Centro frequency, L/H is 0.375, and the top two layers of blocks are fixed for these two tests with 1:2 model scale. The investigated parameter, s_v, is 20 cm in Test 3 and 40 cm in Test 4 for the prototype wall.

4.7.1. Effects of s_v on Maximum Acceleration Measured on Wall

Maximum accelerations measured at the top of wall for Test 3 and for the first part of Test 4 are compared in Figure 4.149. The figure shows that there is a tendency of increase in face accelerations with increasing reinforcement spacing.

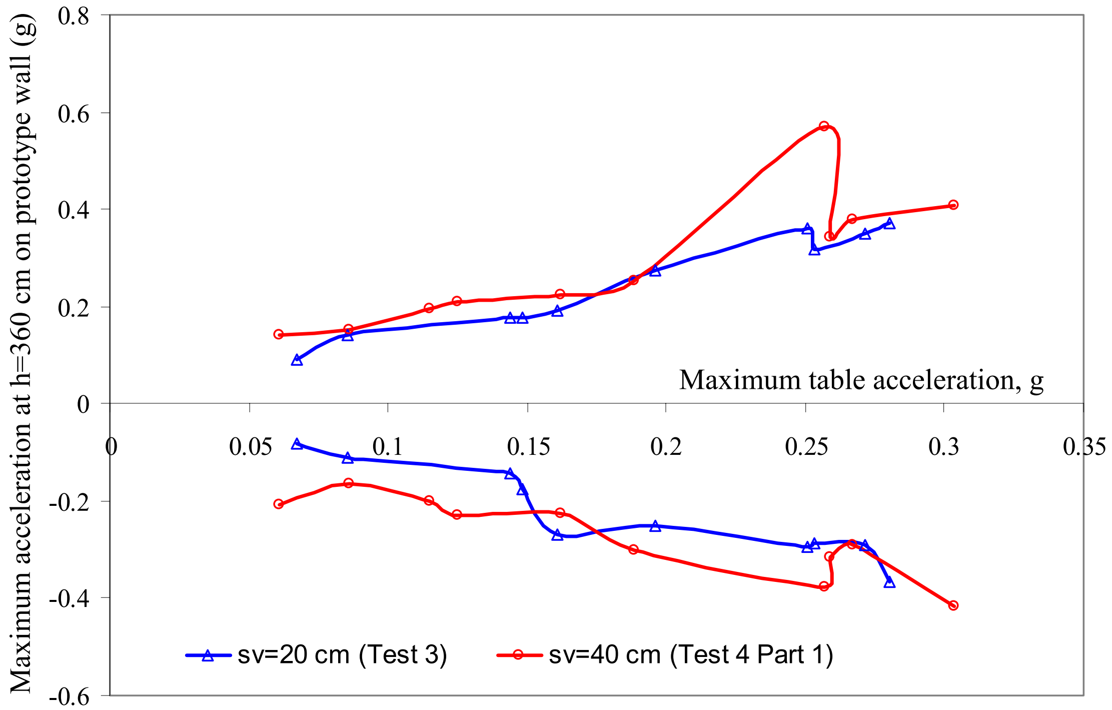

Figure 4.149. Comparison of maximum accelerations measured by accelerometer M7 for Test 3 and Test 4 Part 1

4.7.2. Effects of s_v on Maximum Face Displacements During Shaking

Maximum global face displacements (displacements relative to the ground) measured at the bottom and top of the wall for Test 3 and for the first part of Test 4 are compared in Figures 4.150 and 4.151. The figures show that maximum displacements on the wall face during shaking tended to increase with decreasing reinforcement spacing.

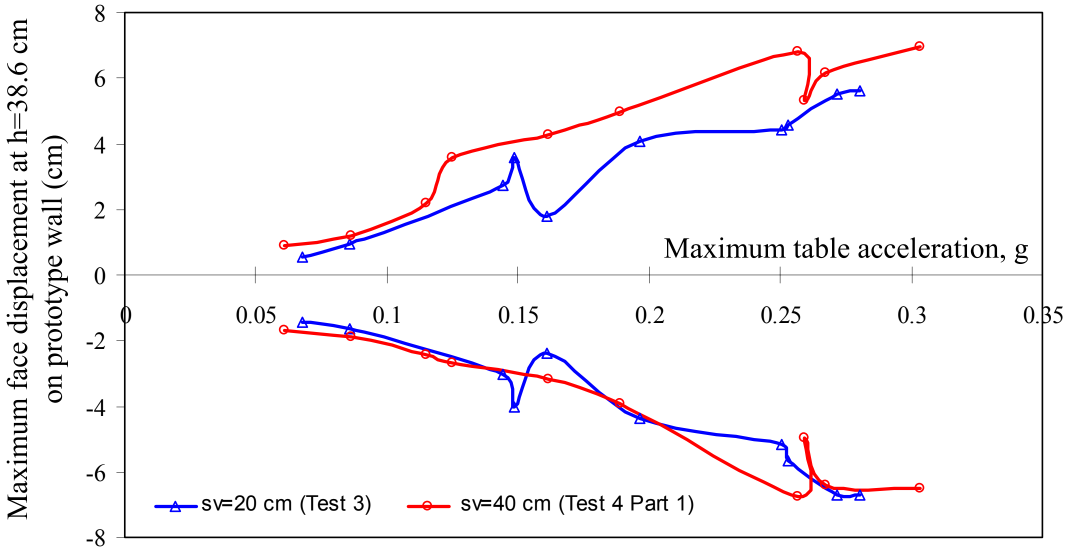

Figure 4.150. Comparison of maximum face displacements measured by optical laser distance sensor L1 for Test 3 and Test 4 Part 1

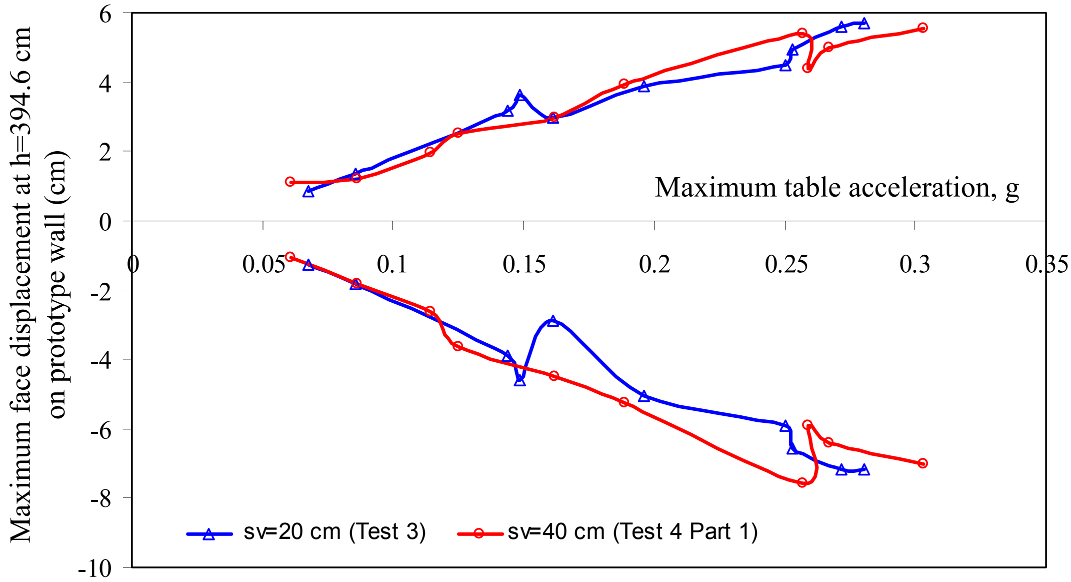

Figure 4.151. Comparison of maximum face displacements measured by optical laser distance sensor L7 for Test 3 and Test 4 Part 1

4.7.3. Effects of s_v on Permanent Face Displacements

Since no significant permanent displacements were observed in the compared tests, it was not possible to comment on the effect of reinforcement spacing on permanent wall displacements.

4.7.4. Effects of s_v on Stresses in Geotextile Reinforcement

As explained in Section 4.6.4, in Test 4, geotextile stresses were higher and increased with increasing maximum table acceleration in lower geotextile front region. Stresses in the upper geotextile remained low compared to the stress in lower geotextile front region. Therefore it was assumed that the critical surface passed through the front region of the lower geotextile and through the unreinforced area behind the upper geotextile. In Test 3, geotextile stresses were considerably higher in lower geotextile front region and upper geotextile front and middle regions compared to the remaining regions. There was a trend of increase in geotextile stresses, which was more obvious in the regions with higher stresses.

In Figure 4.152, maximum stresses measured during shaking in the critical regions of the lower geotextile (determined above) of Test 3 and the first part of Test 4 are compared. For the lower geotextile, the critical regions determined above are also the regions where the Rankine plane intersects the reinforcements. The lower geotextile is extended sufficiently beyond the Rankine plane in both tests. Under this condition, it is observed that the maximum stress in geotextile is more than doubled when the geotextile spacing is doubled.

In Figure 4.153, a similar comparison for the upper geotextile critical region is given. The upper geotextile ends at the Rankine plane in both tests. In Test 4, where the geotextile spacing is 40 cm in the prototype wall, geotextile stresses remain close to five kN/m throughout the geotextile; this is not surprising since the geotextile cannot fulfill the anchoring function beyond the Rankine plane. In Test 3, where the geotextile spacing is 20 cm in the prototype wall, the geotextile stress in the middle region is much higher. It may be stated that decreasing the reinforcement spacing effected the distribution of stress in the reinforcement layers. Smaller reinforcement spacing reduced the maximum stress in lower reinforcement and increased the maximum stress in the upper reinforcement, leading to a more uniform stress distribution.

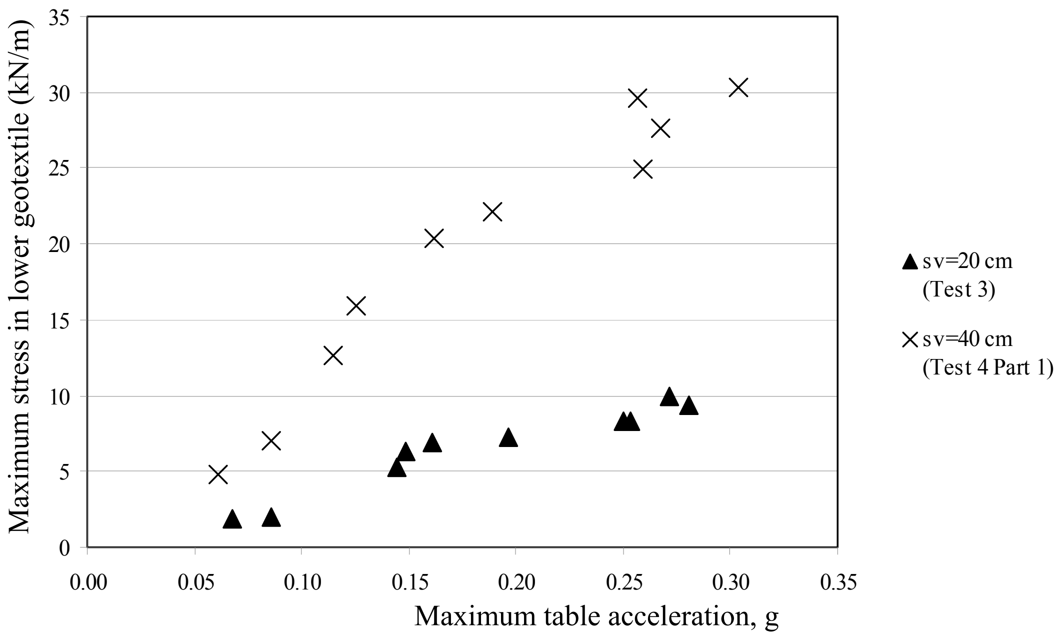

Figure 4.152. Comparison of maximum stresses in lower geotextile for Test 3 and Test 4 Part 1

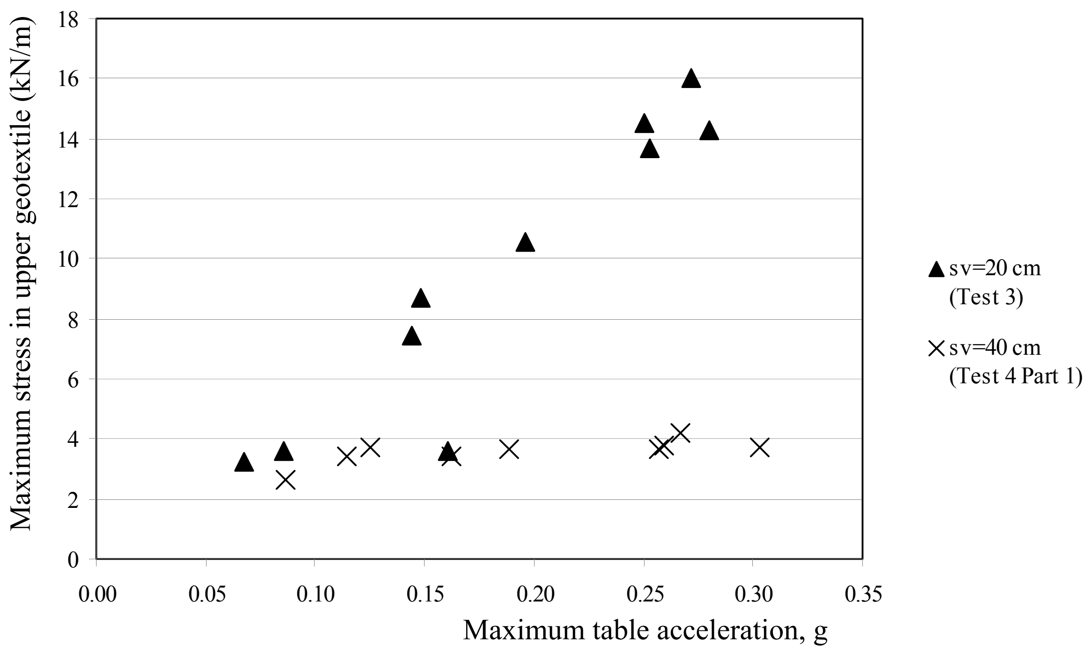

Figure 4.153. Comparison of maximum stresses in upper geotextile for Test 3 and Test 4 Part 1

4.8. Effects of Model Scale

To evaluate the effects of model scale, Test 4 and Test 5 were compared. The prototype walls for these tests have a height of four meters. Test 4 has a model scale of 1:2 and Test 5 has a model scale of 1:4. For both tests, the frequency of the earthquake applied on the prototype wall is the same as the original El Centro frequency, the geotextile spacing is 40 cm and L/H is 0.375 in the prototype wall.

The top two layers of blocks are fixed for Test 4, but as explained previously, it is deduced that the top blocks loosened and lost this feature in the second part of the test. In Test 5, top two layers of facing blocks were not fixed to each other, they were stacked just like the lower blocks. A total of five blocks fell off from these layers during the last four runs of the test. Figure 4.154 shows the wall face after Test 5 is completed. Measurements impaired by the falling blocks were discarded in the analysis.

Figure 4.154. Top of wall face at the end of Test 5

4.8.1. Effects of Model Scale on Maximum Acceleration Measured on Wall

In Test 5, the accelerations measured by accelerometer at the top of face (M4, seen in Figure 4.154) showed an amplification factor of 1.481, but M8 (front accelerometer on top) measurements showed an amplification factor of 12.082 (Table 4.10). Review of Figure 4.84 shows that the maximum acceleration measured by M8 versus maximum table acceleration tends to flatten at the point where the blocks start to fall. The reason may be related to the explanation given for the second part of Test 4; vibration of the free blocks may have caused the extreme acceleration values.

To assess the acceleration on the top of wall face, M6 and M7 accelerometer readings (corresponding to 320 cm and 360 cm heights in the prototype) of Test 4 are compared to M4 accelerometer readings (corresponding to 340 cm height) of Test 5 in Figures 4.155 and 4.156. Figure 4.156 also includes the measurements by M8 in Test 5. The accelerations measured at 340 cm height for Test 5 are consistent with the accelerations measured at 320 cm and 360 cm heights of Test 4 Part 1 and 320 cm height of Test 4 Part 2. Although it was not possible to measure the acceleration at 360 cm height of prototype wall in Test 5, measurements of the accelerometer buried in the top front coincide with the measurements at 360 cm height in Test 4 Part 2. This means top blocks when left free underwent similar vibrations at same shaking table accelerations in these tests. These vibrations are the reason for falling blocks in Test 5. The figures show that model scale did not effect maximum accelerations measured on the wall.

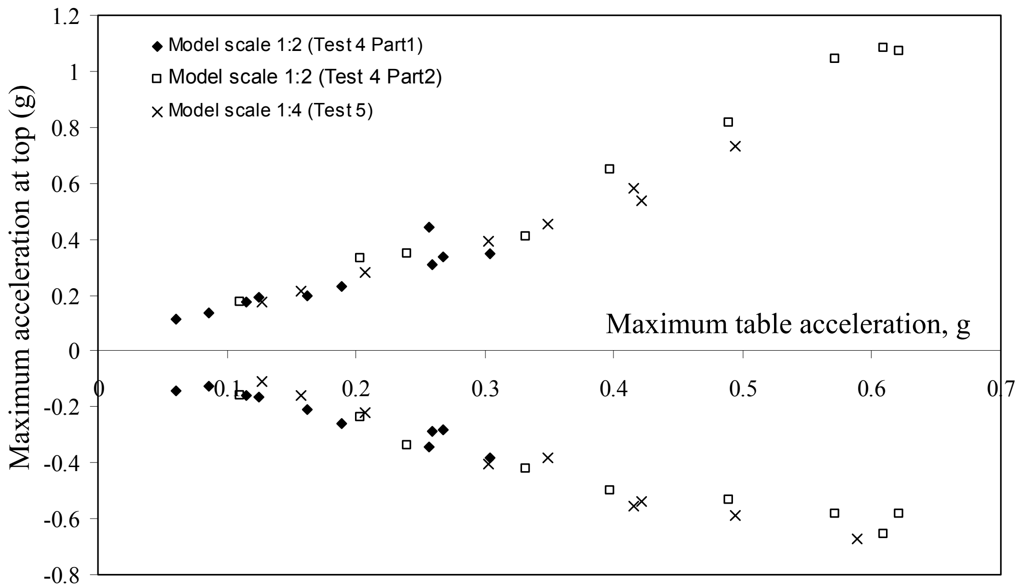

Figure 4.155. Comparison of maximum accelerations measured by accelerometer M6 (height 320 cm in prototype wall) for Test 4 and accelerometer M4 (height 340 cm in prototype wall) for Test 5

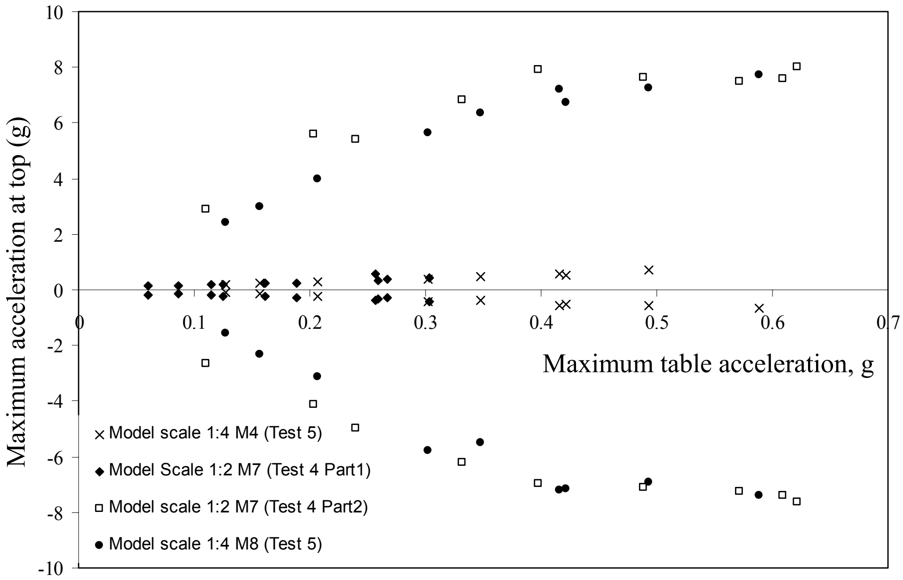

Figure 4.156. Comparison of maximum accelerations measured by accelerometer M7 (height 360 cm in prototype wall) for Test 4 and accelerometer M4 (height 340 cm in prototype wall) and accelerometer M8 (top front) for Test 5

4.8.2. Effects of Model Scale on Maximum Face Displacements During Shaking

Maximum global face displacements measured at the top of the wall for Tests 4 and 5 are compared in Figure 4.157. The figure shows that maximum face displacements observed during shaking were higher for the 1:4 scale test. The heights of laser distance sensors placed on the lower levels are not equivalent in the prototype for 1:4 and 1:2 scale tests, but measurements of L2 in Test 5 (corresponding to a height of 237 cm) and L4 in Test 4 (corresponding to a height of 279 cm) are compared in Figure 4.158 to confirm that the difference in face displacements between the two tests is not due completely to the difference in the treatment of top two rows. The figure shows that in the 1:2 scale model, even the face displacements at a slightly higher level are lower than those in the 1:4 scale model. Therefore, it is inferred that as the model size decreases, the displacements measured increase, which is a conservative error.

4.8.3. Effects of Model Scale on Permanent Face Displacements

Since no significant permanent displacements were observed in the compared tests, it is not possible to comment on the effect of model scale on permanent displacements.

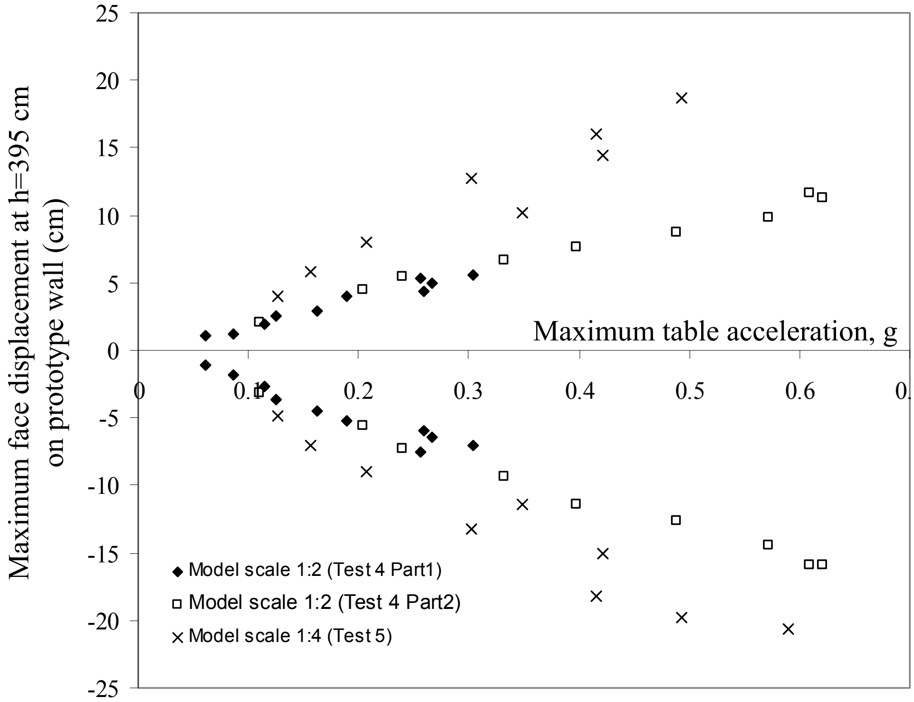

Figure 4.157. Comparison of maximum face displacements measured by optical laser distance sensor L7 in Test 4 and L5 in Test 5, which are the uppermost middle distance sensors in these tests

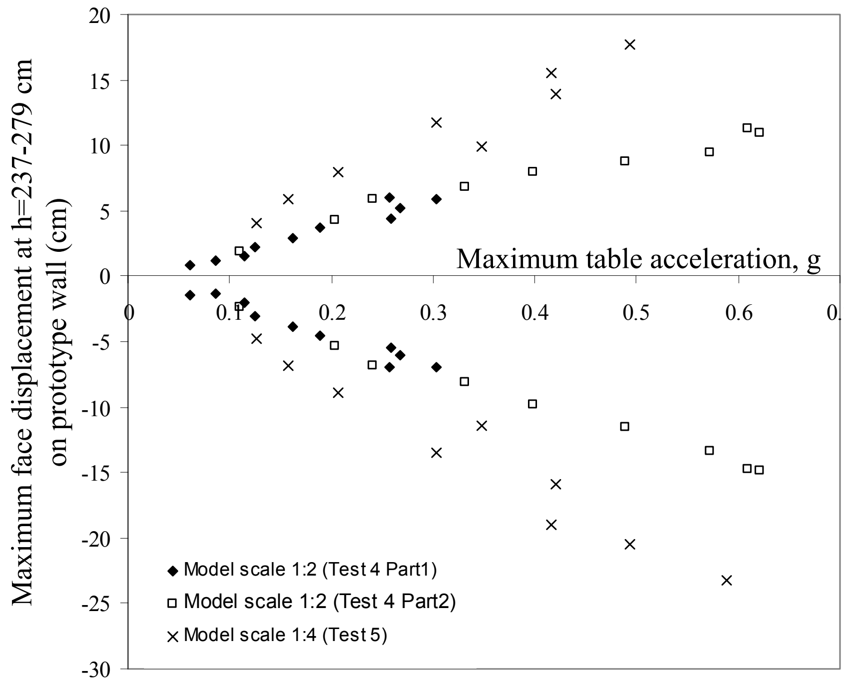

Figure 4.158. Comparison of maximum face displacements measured by optical laser distance sensor L4 in Test 4 (height 279 cm in prototype wall) and L2 in Test 5 (height 237 cm in prototype wall)

4.8.4. Effects of Model Scale on Stresses in Geotextile Reinforcement

In Test 5, only one geotextile layer could be instrumented due to model wall height limitations. The height of instrumented reinforcement corresponds to 160 cm in prototype. The heights of instrumented reinforcement layers in Test 4 correspond to 80 cm and 320 cm in prototype.

As explained previously, in Test 4, geotextile stresses were higher and increased with increasing maximum table acceleration in lower geotextile front region. Stresses in the upper geotextile remained low. In Test 5, geotextile stresses were highest in the front region and tended to increase with increasing table acceleration at this region. The other two regions did not show this trend. Since the instrumented geotextile layers are not at the same heights, it is not possible to compare the two tests directly. Maximum stresses measured during shaking in the critical regions of all three geotextiles in question are plotted in Figure 4.159.

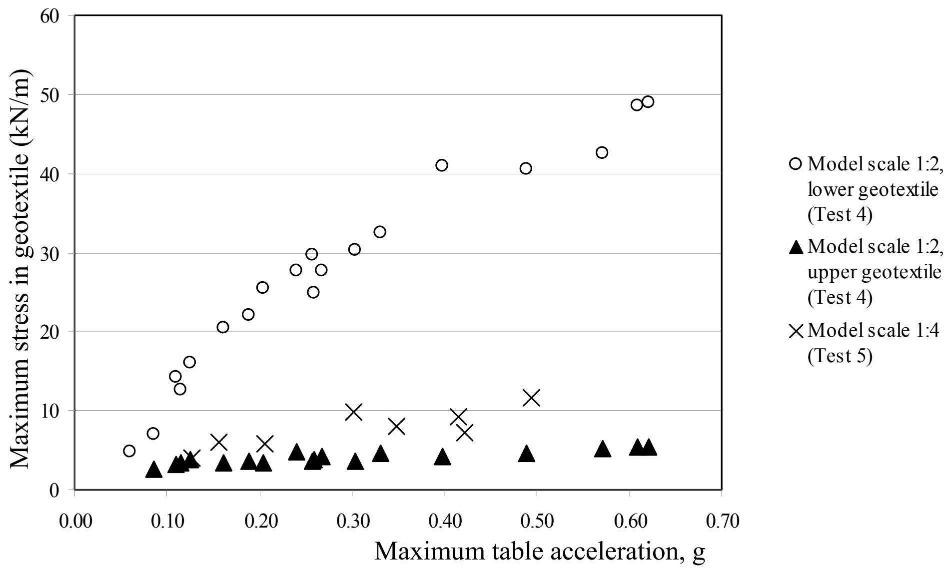

Figure 4.159. Comparison of maximum stresses in geotextile reinforcements for Test 4 and Test 5

4.9. Effects of Treatment of Top Two Block Rows

Comparisons with Test 4, Test 5, and Test 6 explained previously showed that when the geotextile reinforcements at the top are not extended beyond the Rankine plane, blocks that are not fixed adequately undergo vibrations and fall down when the shaking table acceleration is high enough. This section investigates what happens when the top block rows are not fixed but the geotextile reinforcements at the top are extended beyond the Rankine plane by comparing Test 7 and Test 8 Part b.

The test setups for Test 7 and Test 8 are the same except for the condition of top two rows. The prototype walls for these tests have a height of 780 cm. For both tests, the model scale is 1:4, the geotextile spacing is 40 cm and the L/H is 0.7. In Test 7 the top two rows are free, i.e. there is no connection between the two rows. In Test 8, top two rows are fixed to each other by pins as shown in Figure 3.20. The frequency of the earthquake applied on the prototype wall is the same as the original El Centro frequency for Test 7 and Test 8 Part b.

4.9.1. Effects of Treatment of Top Two Block Rows on Maximum Acceleration Measured on Wall

Figure 4.160 shows the accelerations measured by the accelerometer on the top of wall face for Test 7 and Test 8 Part b. Although the top blocks are free in Test 7, the maximum accelerations measured at the top are similar to the fixed case. This may be explained by the sufficient length of geotextile, which prevents vibrations of facing blocks.

4.9.2. Effects of Treatment of Top Two Block Rows on Maximum Face Displacements During Shaking

Maximum face displacements measured at the bottom and at the top of the wall for Test 7 and Test 8 Part b are compared in Figures 4.161 and 4.162. Maximum face displacements observed during shaking were similar, but at the sixth run of Test 7, a few blocks fell from the top two rows and in the runs after this, L7 measured the displacement of the soil directly. The backward movement of the soil was smaller without the facing blocks, as seen in Figure 4.162. In summary, the wall with top two block layers free did not move more than the wall with top two block layers fixed during shaking, but when the loads on the free blocks exceeded the available friction, the blocks fell down.

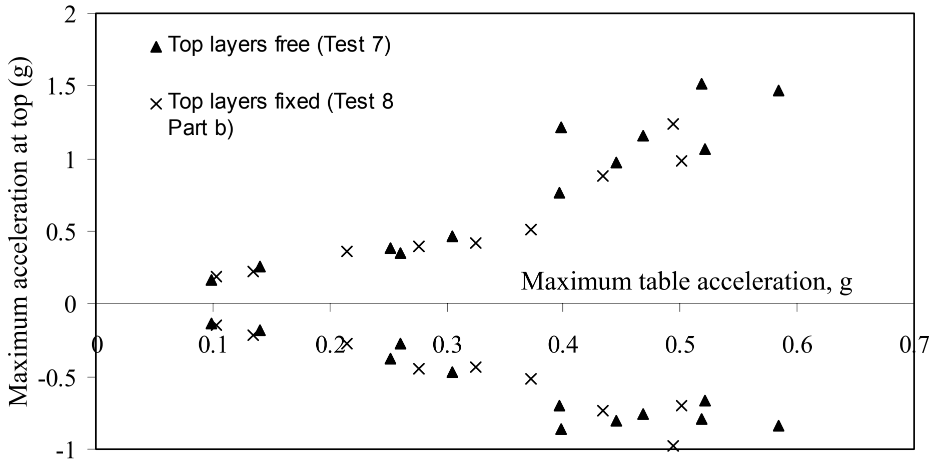

Figure 4.160. Comparison of maximum accelerations measured by accelerometer M7 (height 728 cm in prototype) for Test 7 and Test 8 Part b

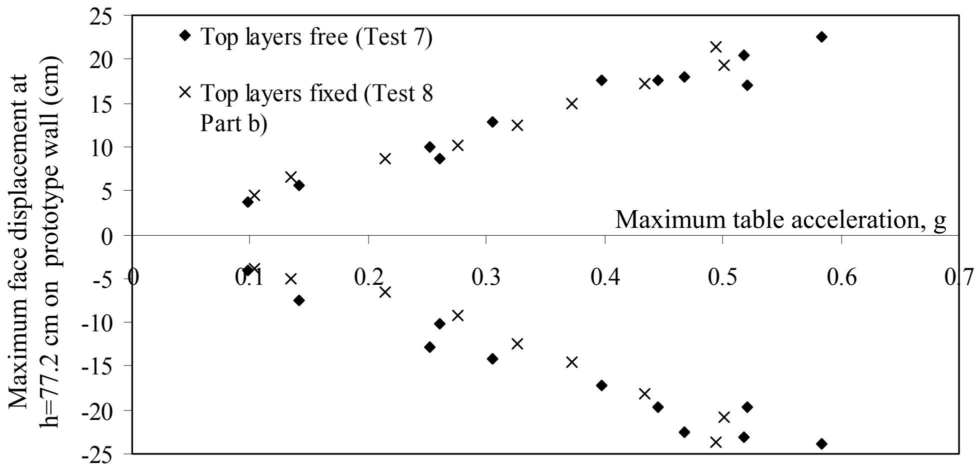

Figure 4.161. Comparison of maximum face displacements measured by optical laser distance sensor L1 for Tests 7 and Test 8 Part b

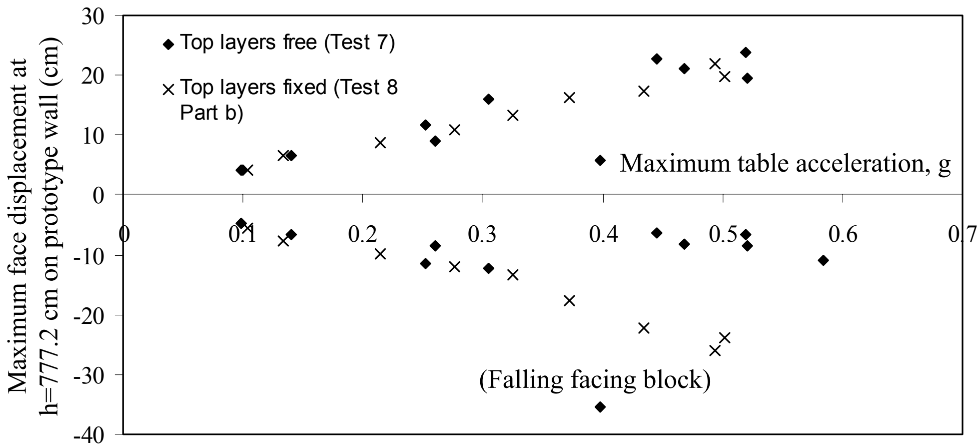

Figure 4.162. Comparison of maximum face displacements measured by optical laser distance sensor L7 for Test 7 and Test 8 Part b

4.9.3. Effects of Treatment of Top Two Block Rows on Permanent Face Displacements

No significant permanent displacements were observed in Test 8, where the top two block layers were fixed. In Test 7, where the top two block layers were free, there were no significant permanent displacements until the run in which a few blocks fell down. Afterwards, there are permanent displacements due to falling blocks and the soil at the back moving freely forward (Figure 4.124).

4.9.4. Effects of Treatment of Top Two Block Rows on Stresses in Geotextile Reinforcement

In both Test 7 and Test 8, the regions with the maximum geotextile stresses were the front regions of lower and upper geotextiles. In Figure 4.163, maximum stresses measured during shaking in the critical (front) regions of the lower geotextile of Test 7 and Test 8 Part b are compared. The stresses in the two tests are similar in magnitude.

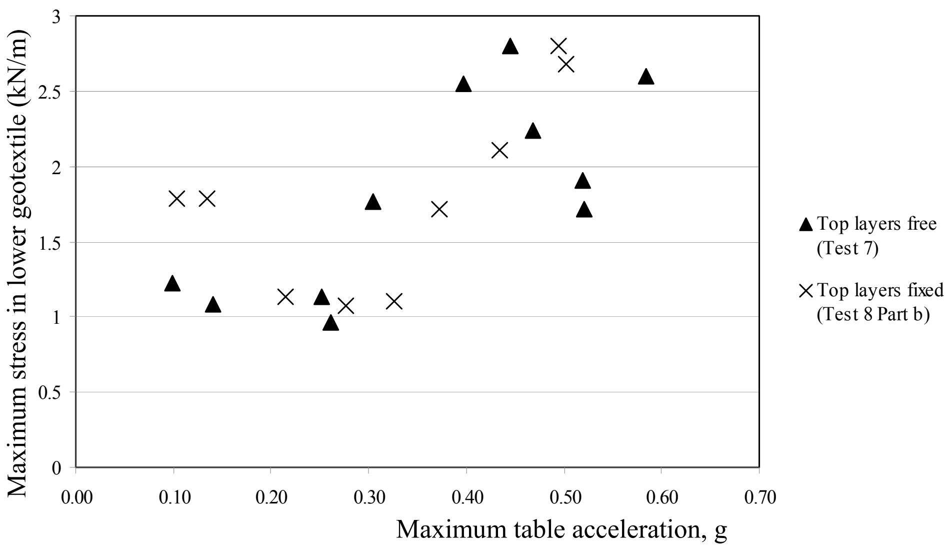

Figure 4.163. Comparison of maximum stresses in lower geotextile for Test 7 and Test 8 Part b

In Figure 4.164, a similar comparison for the upper geotextile critical (front) region is given. The figure shows that the configuration with the top two layers of facing blocks fixed faced higher stresses in the upper geotextile. The stress in the front region of upper geotextile in the test with free top blocks did not increase with increasing maximum table acceleration.

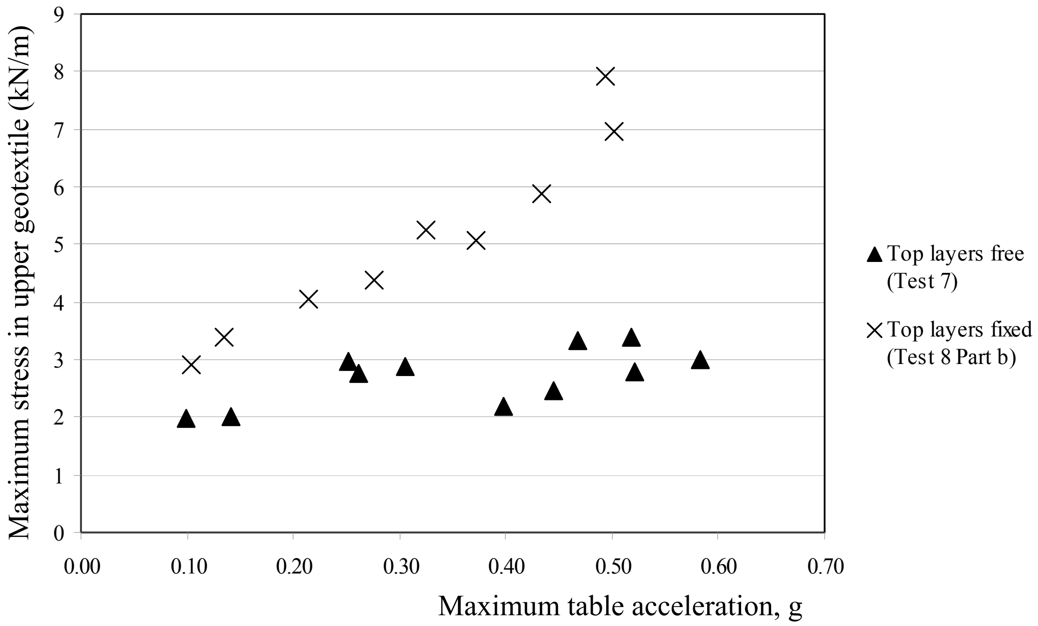

Figure 4.164. Comparison of maximum stresses in upper geotextile for Test 7 and Test 8 Part b

4.10. Effects of Applied Earthquake Frequency

In Test 8, two different frequencies for the El Centro input earthquake record was used. In Test 8 Part a, the frequency of the earthquake applied corresponds to 0.7 times the original El Centro frequency. In Test 8 Part b, the frequency of the earthquake applied corresponds to the original El Centro frequency.

4.10.1. Effects of Applied Earthquake Frequency on Maximum Acceleration Measured on Wall

Figure 4.165 shows the accelerations measured by the accelerometer on the top of wall face for Test 8 Part a and Test 8 Part b. Changing the earthquake frequency in this range did not effect the maximum accelerations during shaking in this configuration.

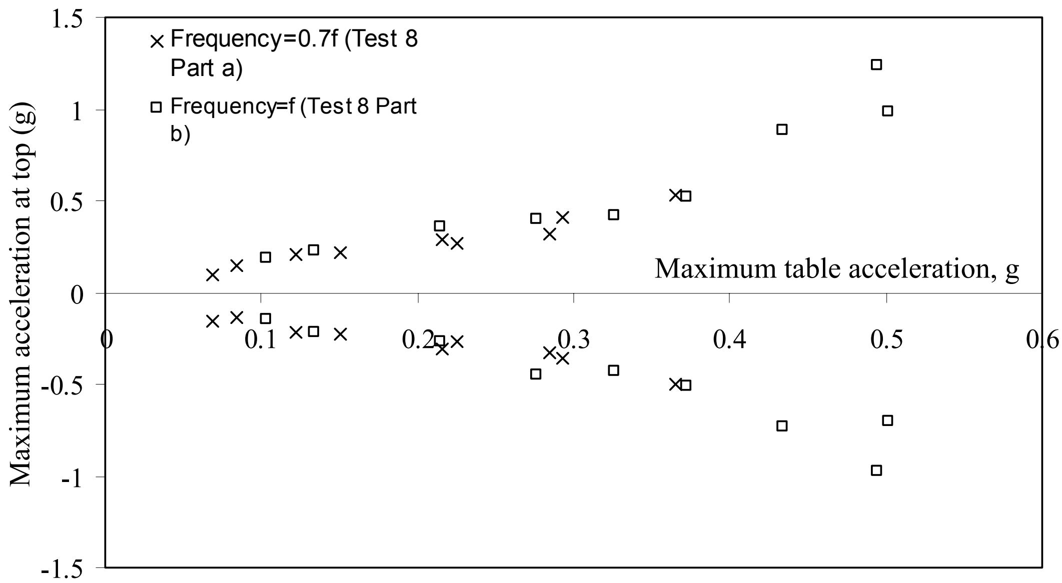

Figure 4.165. Comparison of maximum accelerations measured by accelerometer M7 (height 728 cm in prototype) for Test 8 Part a and Test 8 Part b

4.10.2. Effects of Applied Earthquake Frequency on Maximum Face Displacements During Shaking

Maximum face displacements measured at the bottom and at the top of the wall for Test 8 Part a and Test 8 Part b are compared in Figures 4.166 and 4.167. Maximum face displacements observed during shaking were similar.

4.10.3. Effects of Applied Earthquake Frequency on Permanent Face Displacements

No significant permanent displacements were observed in Test 8, so no conclusions on the effect of applied earthquake frequency on permanent face displacements could be drawn.

4.10.4. Effects of Applied Earthquake Frequency on Stresses in Geotextile Reinforcement

In both parts of Test 8, the regions with the maximum geotextile stresses were the front regions of lower and upper geotextiles. In Figure 4.168, maximum stresses measured during shaking in the critical (front) regions of the lower geotextile of Test 8 Part a and Test 8 Part b are compared. The stresses in the two tests are close in magnitude.

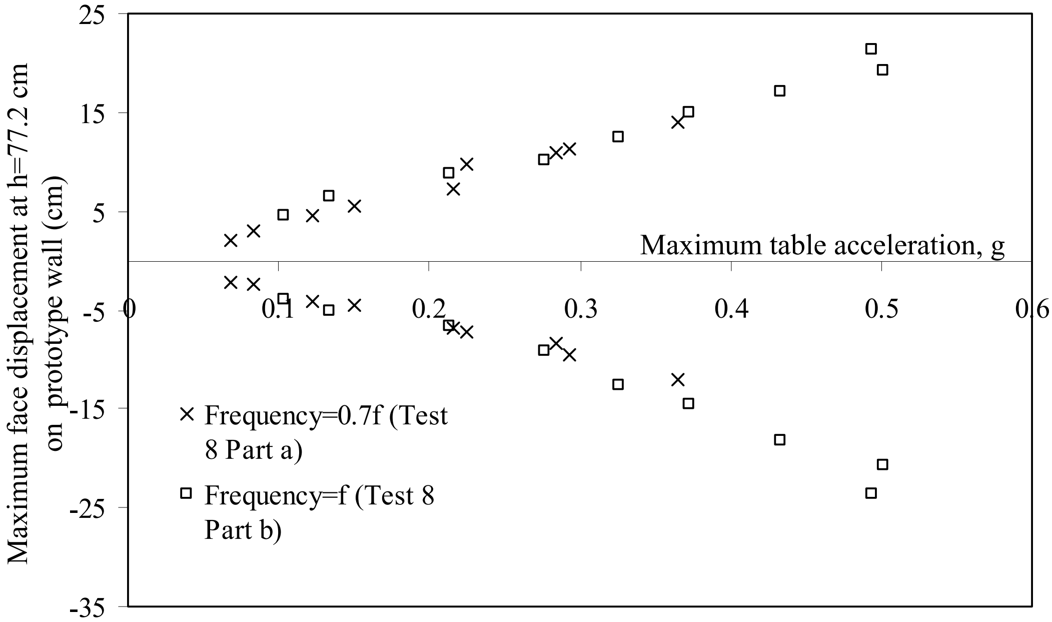

Figure 4.166. Comparison of maximum face displacements measured by optical laser distance sensor L1 for Test 8 Part a and Test 8 Part b

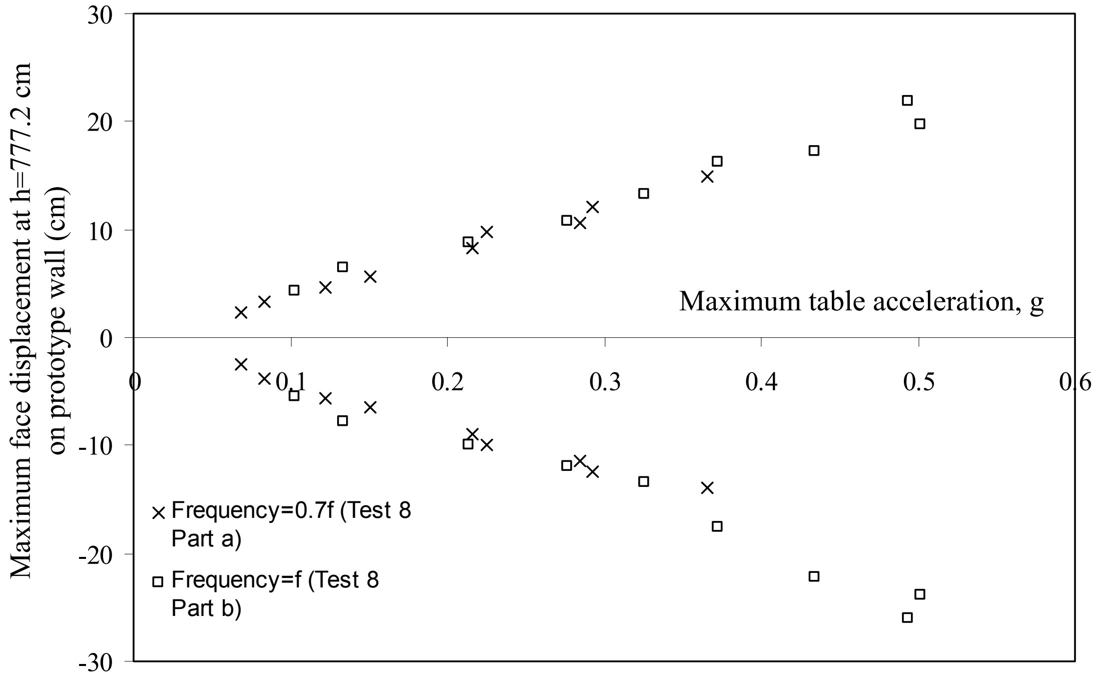

Figure 4.167. Comparison of maximum face displacements measured by optical laser distance sensor L7 for Test 8 Part a and Test 8 Part b

In Figure 4.169, a similar comparison for the upper geotextile critical (front) region is given. The stresses are again close in magnitude.

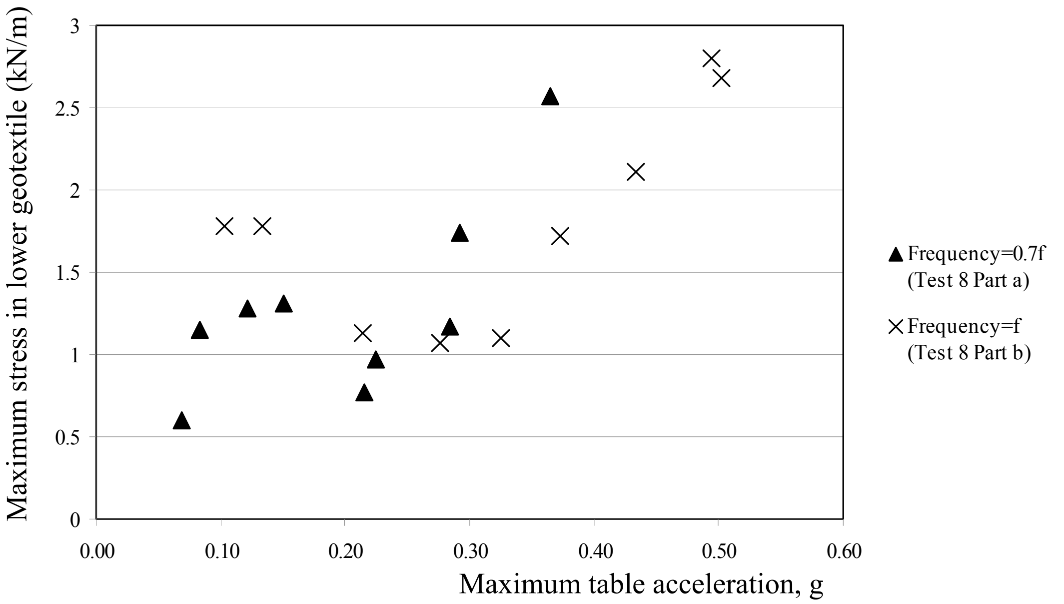

Figure 4.168. Comparison of maximum stresses in lower geotextile for Test 8 Part a and Test 8 Part b

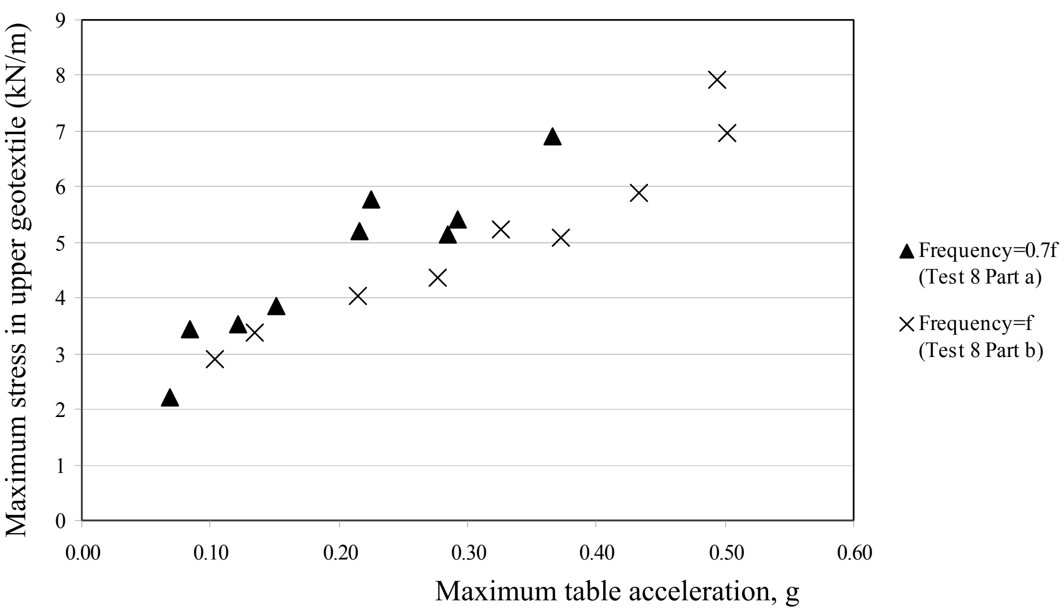

Figure 4.169. Comparison of maximum stresses in upper geotextile for Test 8 Part a and Test 8 Part b

4.11. Comparison of Measured Stresses in Geotextile with Stresses Used in Design

Spreadsheets given in Appendix C were used to calculate the additional geotextile stresses due to earthquake loading assumed in the design specifications of FHWA and NCMA for the instrumented geotextile layers. Calculations are in accordance with the design principles explained in Sections 2.3.1, 2.3.2, and 2.3.3. The values recommended in design are compared to the measured values at the most stressed region of the geotextile in Figures 4.170 to 4.186. Both the measured peak values and maxima from stress records smoothed by averaging for 0.1 second intervals are used in comparison.

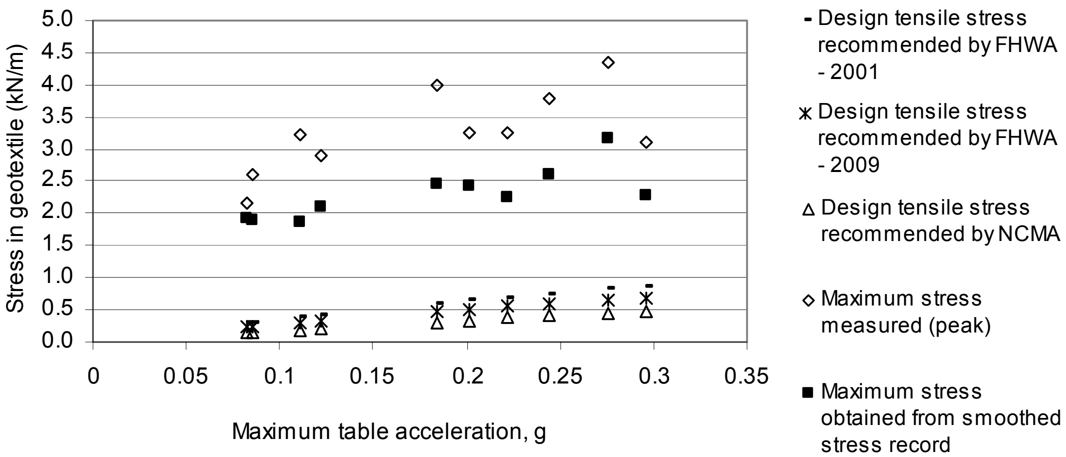

Figure 4.170. Comparison of seismic-induced design stresses and measured stresses in lower geotextile for Test 1 (L/H=0.8)

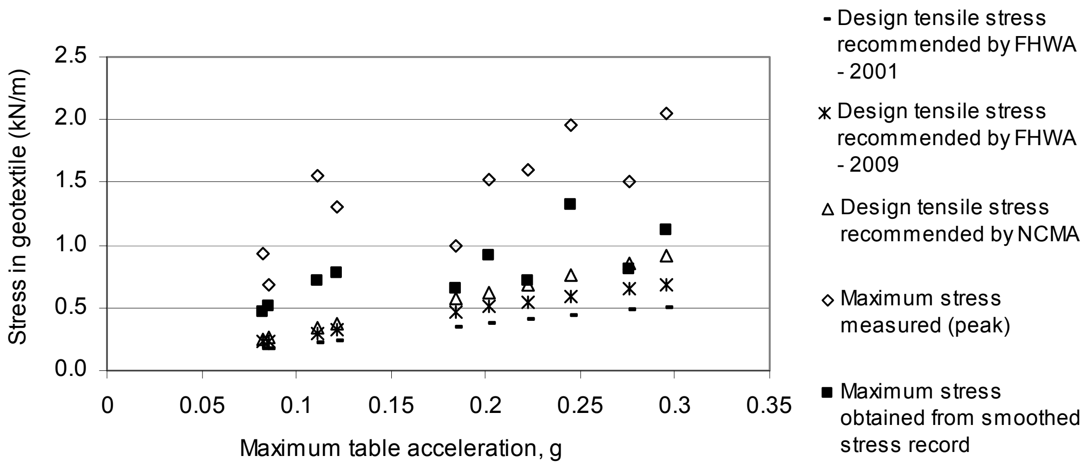

Figure 4.171. Comparison of seismic-induced design stresses and measured stresses in upper geotextile for Test 1 (L/H=0.8)

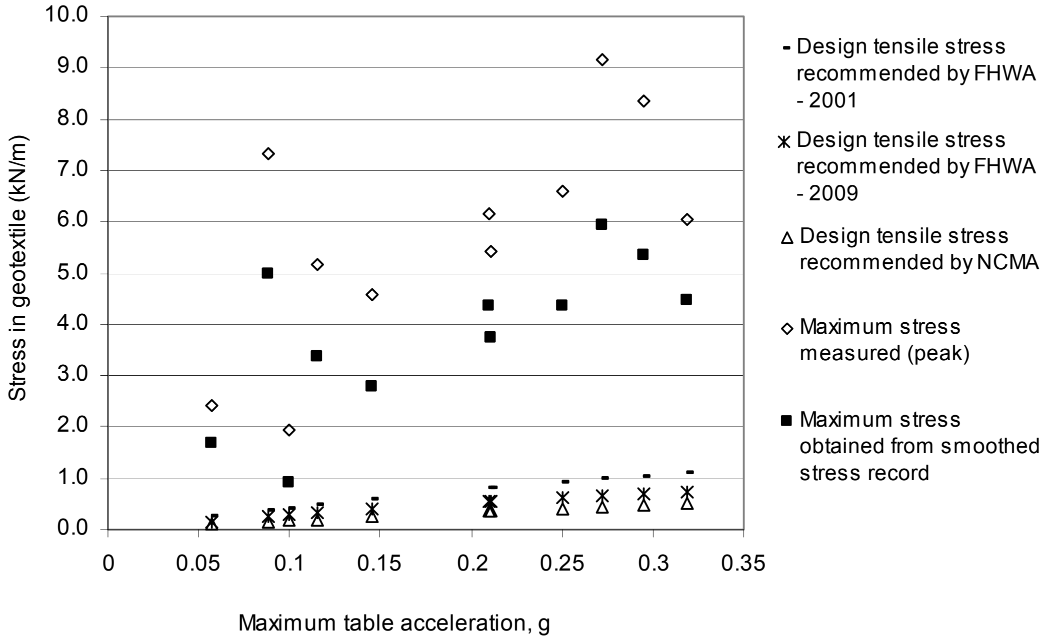

Figure 4.172. Comparison of seismic-induced design stresses and measured stresses in lower geotextile for Test 2 (L/H=0.52)

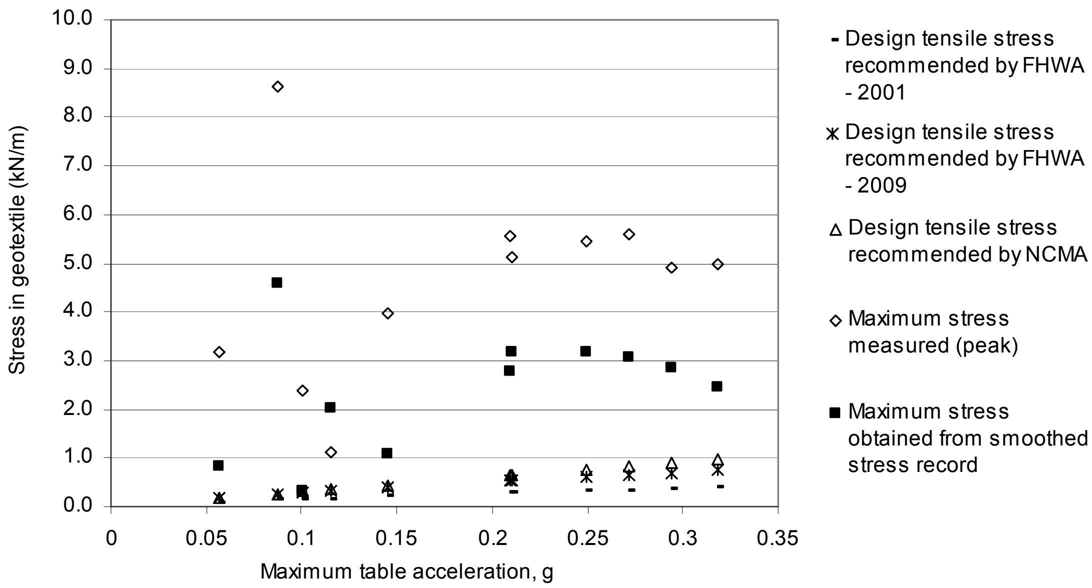

Figure 4.173. Comparison of seismic-induced design stresses and measured stresses in upper geotextile for Test 2 (L/H=0.52)

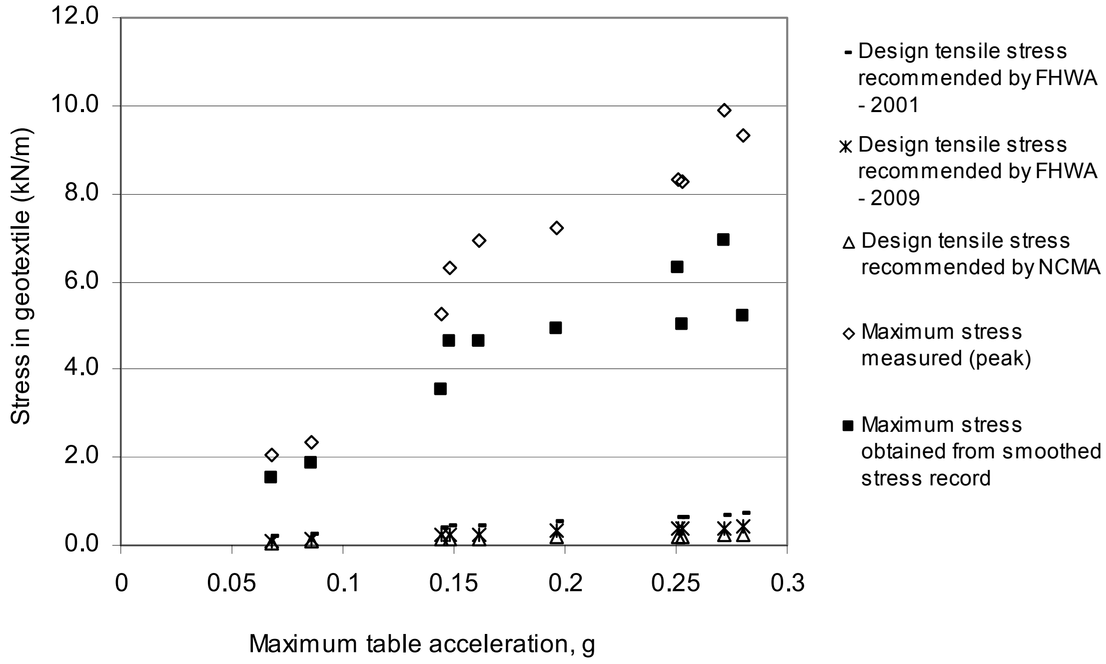

Figure 4.174. Comparison of seismic-induced design stresses and measured stresses in lower geotextile for Test 3 (L/H=0.375)

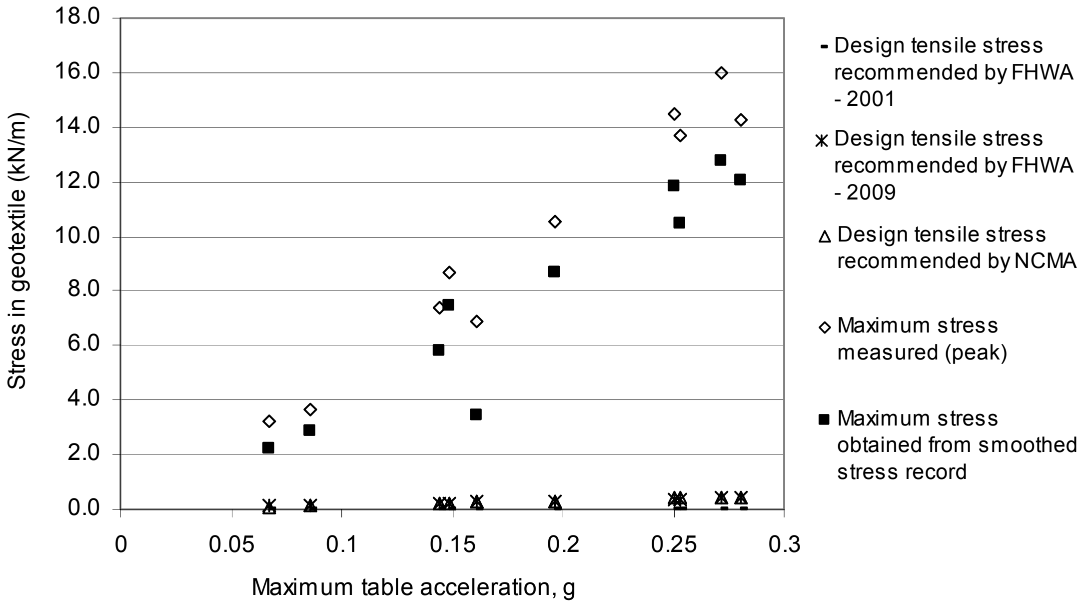

Figure 4.175. Comparison of seismic-induced design stresses and measured stresses in upper geotextile for Test 3 (L/H=0.375)

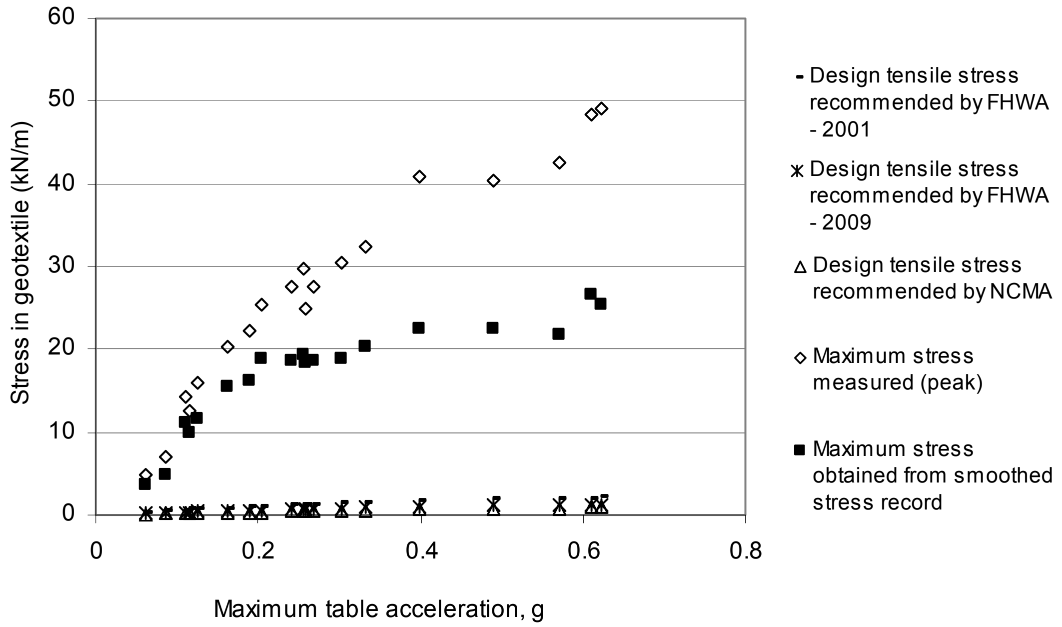

Figure 4.176. Comparison of seismic-induced design stresses and measured stresses in lower geotextile for Test 4 (L/H=0.375)

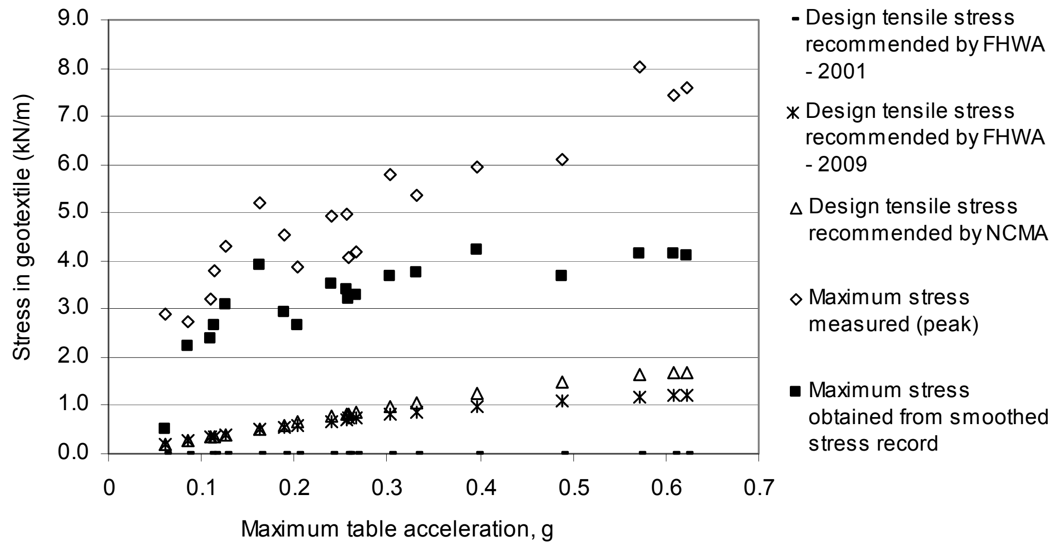

Figure 4.177. Comparison of seismic-induced design stresses and measured stresses in upper geotextile for Test 4 (L/H=0.375)

The figures for the first four tests show that the design stresses assumed to be induced from seismic loading are inadequate in representing the actual stresses that the reinforcements experience. Even smoothed measured stresses remain much higher than design stresses. In some tests, smoothed measured stresses in the upper reinforcements are low (as in Figures 4.171 and 4.173), and these are the only instances where design stresses and measured stresses get close. Considering the first four tests, the gap between measured and design stresses tend to increase as the design of tested wall configuration gets less conservative, i.e. L/H decreases.

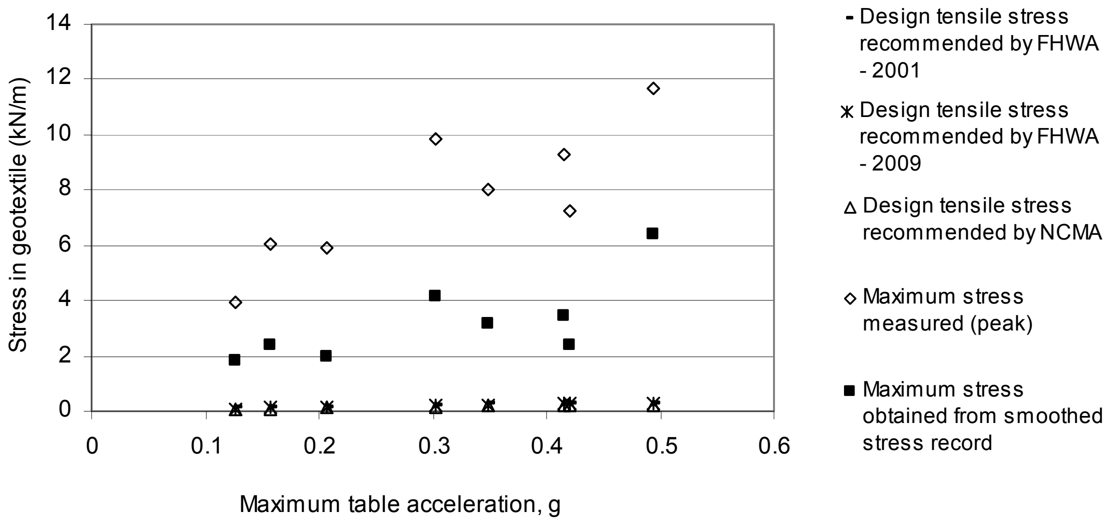

Figure 4.178. Comparison of seismic-induced design stresses and measured stresses in geotextile for Test 5 (L/H=0.375)

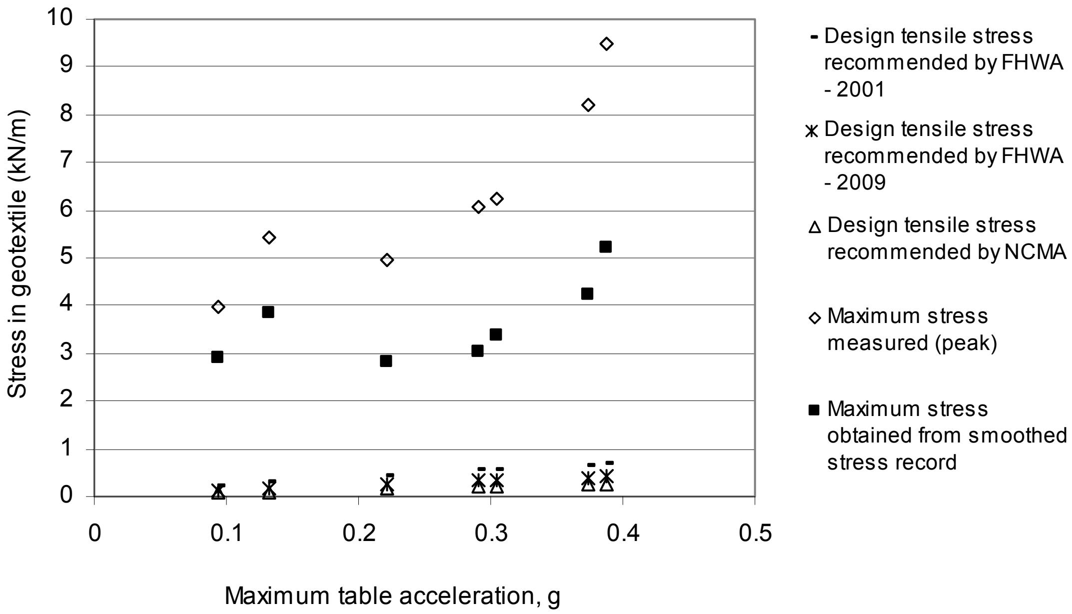

Figure 4.179. Comparison of seismic-induced design stresses and measured stresses in lower geotextile for Test 6 (L/H=0.4)

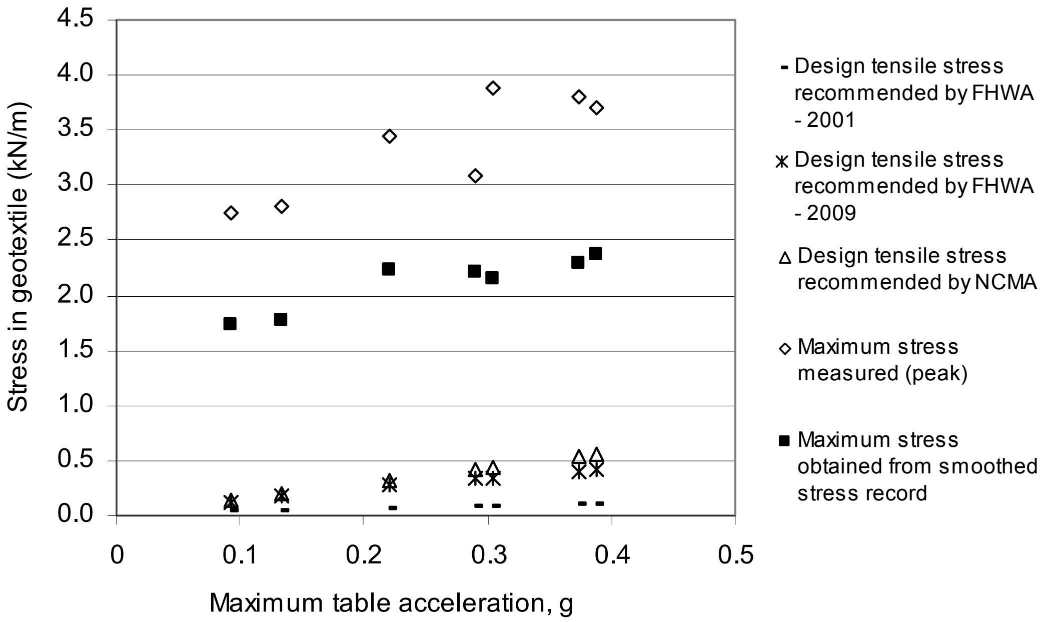

Figure 4.180. Comparison of seismic-induced design stresses and measured stresses in upper geotextile for Test 6 (L/H=0.4)

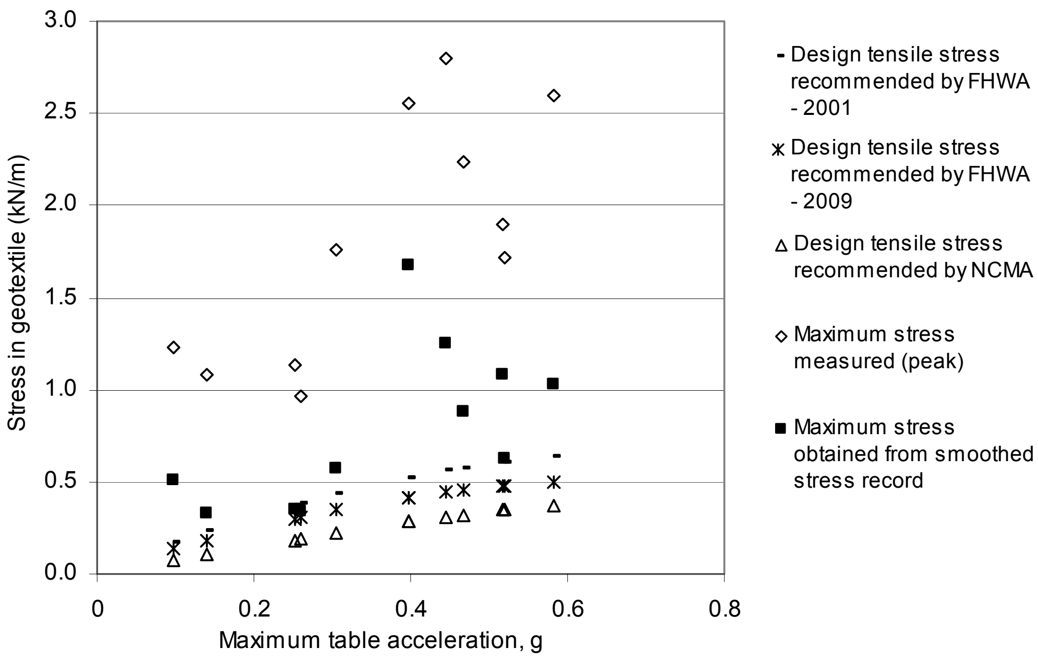

Figure 4.181. Comparison of seismic-induced design stresses and measured stresses in lower geotextile for Test 7 (L/H=0.7)

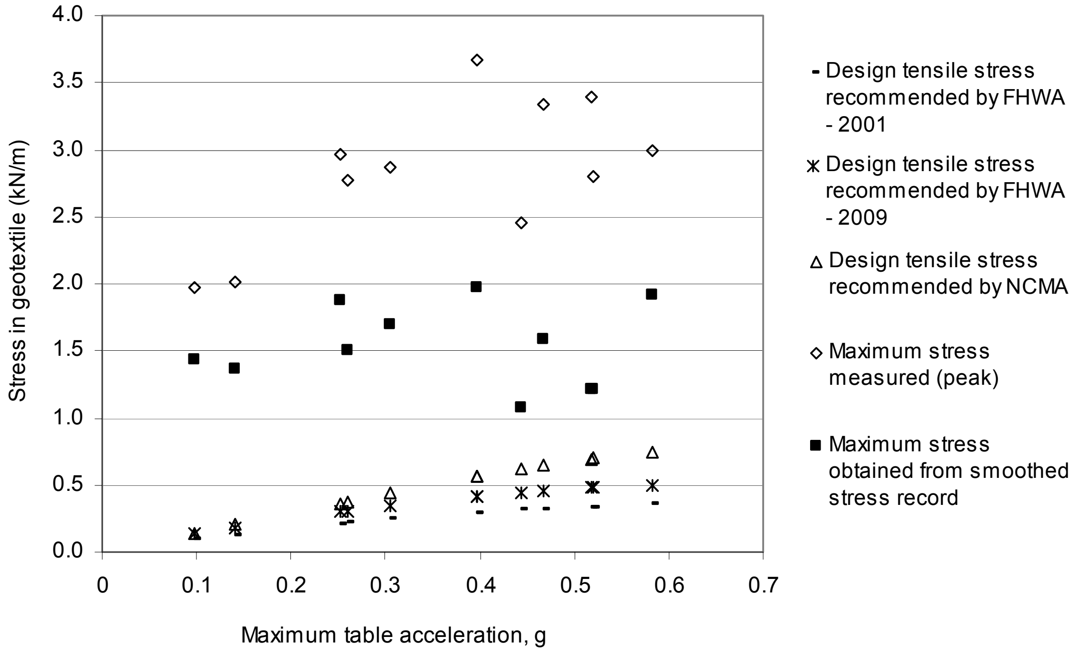

Figure 4.182. Comparison of seismic-induced design stresses and measured stresses in upper geotextile for Test 7 (L/H=0.7)

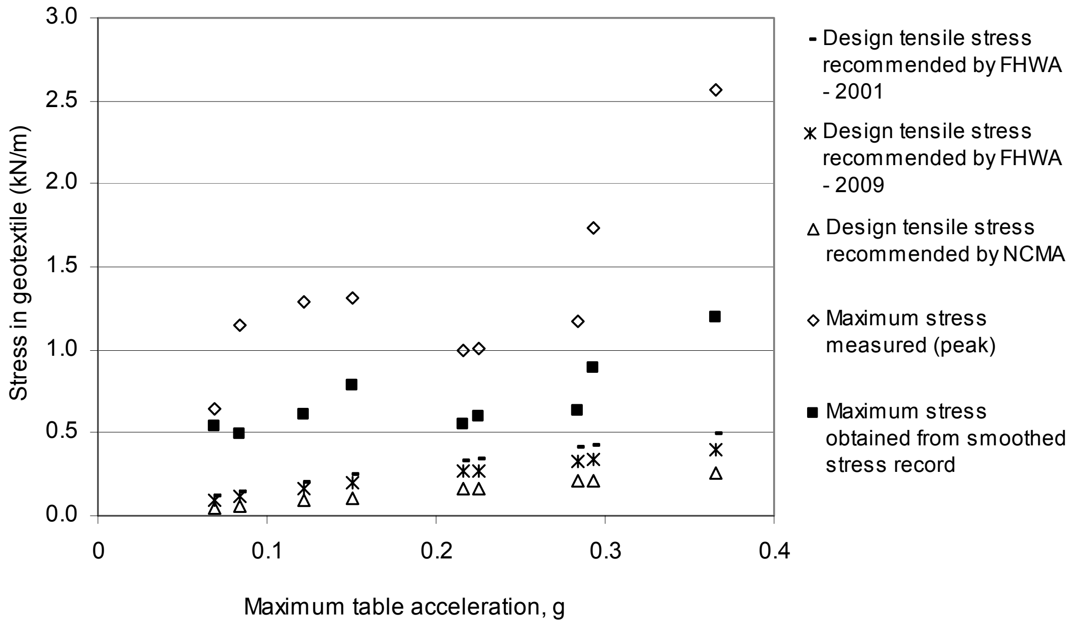

Figure 4.183. Comparison of seismic-induced design stresses and measured stresses in lower geotextile for Test 8 Part a (L/H=0.7)

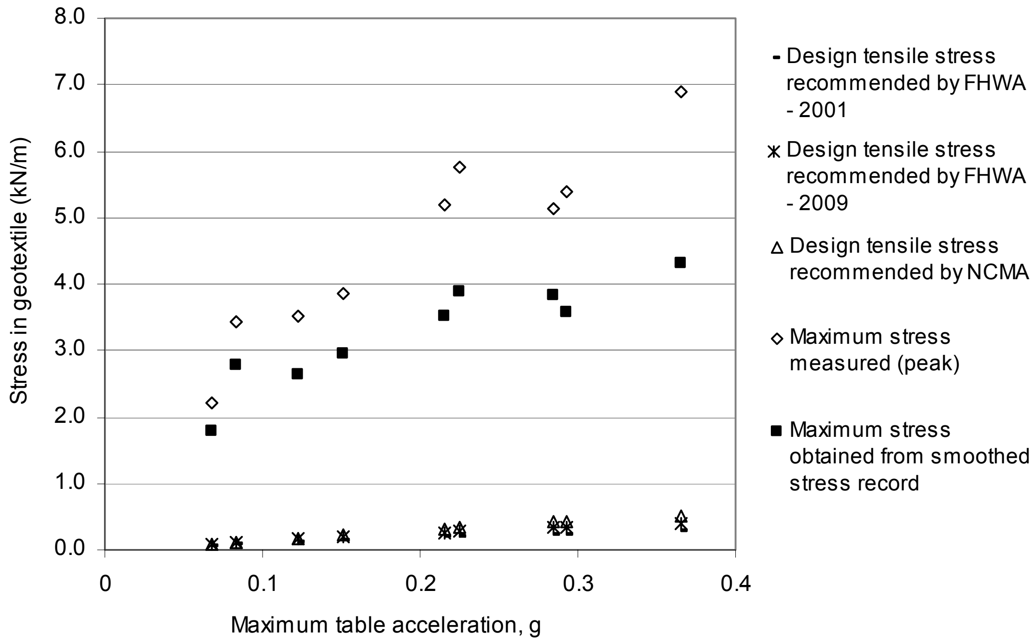

Figure 4.184. Comparison of seismic-induced design stresses and measured stresses in upper geotextile for Test 8 Part a (L/H=0.7)

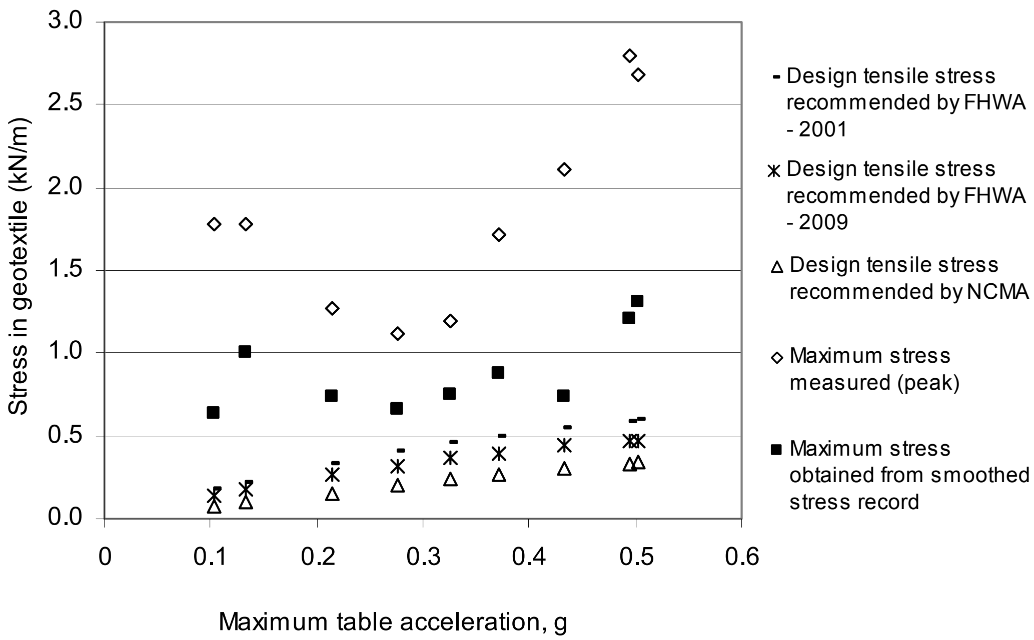

Figure 4.185. Comparison of seismic-induced design stresses and measured stresses in lower geotextile for Test 8 Part b (L/H=0.7)

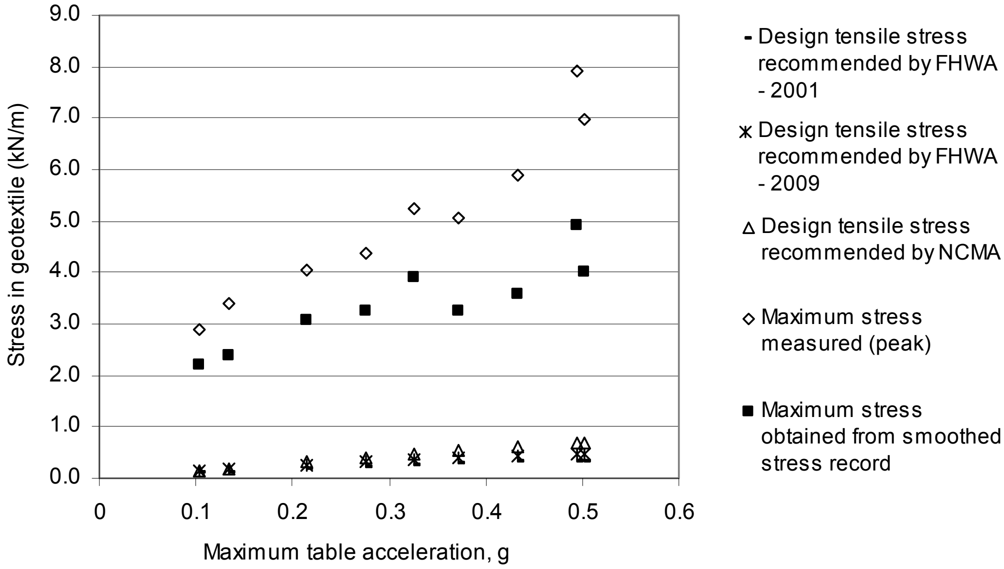

Figure 4.186. Comparison of seismic-induced design stresses and measured stresses in upper geotextile for Test 8 Part b (L/H=0.7)

Comparing the last four tests which have a model scale of 1:4, in the tests with safer setups (Tests 7 and 8), measured reinforcement stresses are generally closer to design values in the lower part of the wall, indicating that if the design recommendations about reinforcement length are complied with, reinforcement stresses will not be critical in properly designed structures. However, for the upper part of the wall, design recommendations are not sufficient in predicting the reinforcement stresses even for walls complying with the recommendations in terms of wall geometry.

4.12. Geometry of Maximum Geotextile Stresses and Assumed Failure Surfaces

The geotextile stresses are illustrated on the prototype walls in this section. To give an idea of the geotextile regions at which there are increased stresses, maximum stresses measured throughout each test is averaged and shown in Figures 4.187 to 4.196. The stresses on lower geotextile are shown downwards just for convenience. The Rankine potential failure plane assumed in design and the plane of highest geotextile stresses determined in this study are shown on these figures. Then a specific run (namely the shaking with the highest maximum table acceleration) is chosen and illustrated for each test (Figures 4.197 to 4.206). Both the geotextile stress scale and the geometrical scale are consistent in Figures 4.187 to 4.206.

For Tests 1, 2, 3, 5, 7, and 8 (Figures 4.187, 4.188, 4.189, 4.192, 4.194, 4.195, and 4.196), the critical surface line determined in this study was drawn by connecting the toe to the center points of the regions with the highest stresses. For Test 4 (Figures 4.190 and 4.191), the stresses in the upper geotextile were much lower than those in the lower geotextile, so the critical surface was considered to pass at a point beyond the instrumented regions at the upper geotextile level. The critical surface line was drawn by connecting the toe to the highly stressed region of the lower geotextile and extending linearly to the surface of backfill. Although the difference in stresses is not as pronounced in Test 6 (Figure 4.193), the same approach was adopted since the physically observed failure location was behind the tip of upper geotextile.

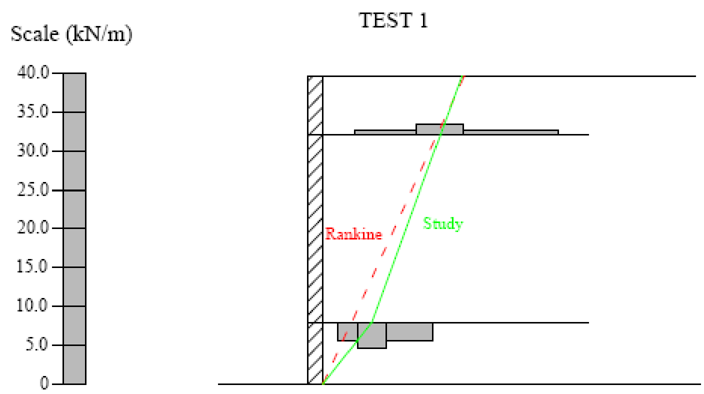

Figure 4.187. Illustration of prototype wall cross-section for Test 1 showing the average maximum geotextile stresses in all instrumented regions

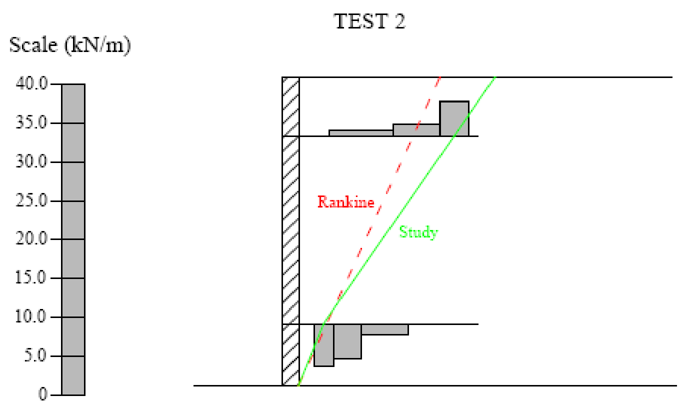

Figure 4.188. Illustration of prototype wall cross-section for Test 2 showing the average maximum geotextile stresses in all instrumented regions

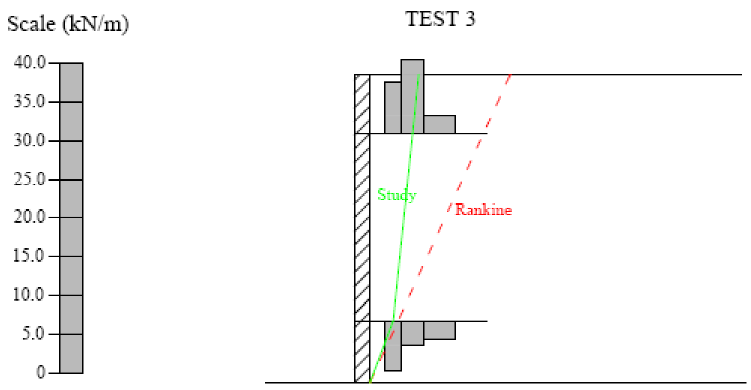

Figure 4.189. Illustration of prototype wall cross-section for Test 3 showing the average maximum geotextile stresses in all instrumented regions

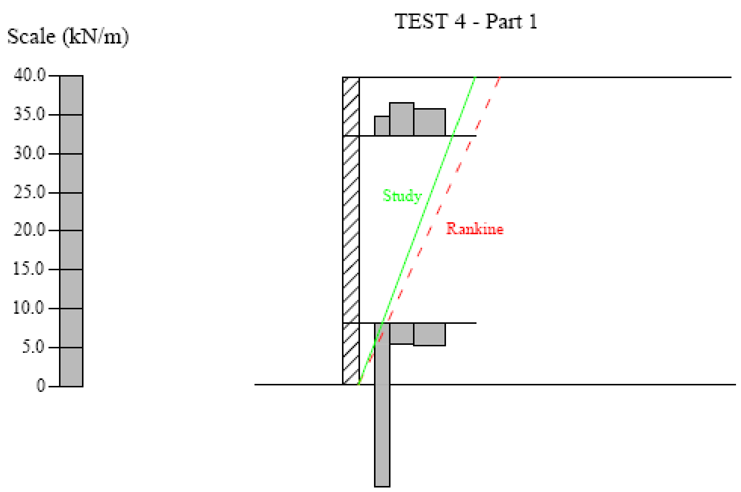

Figure 4.190. Illustration of prototype wall cross-section for Test 4 Part 1 showing the average maximum geotextile stresses in all instrumented regions

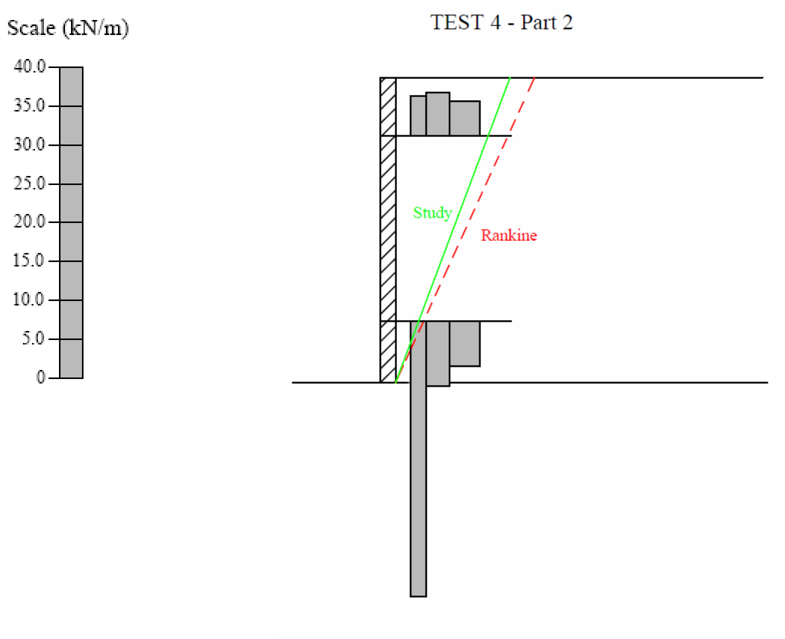

Figure 4.191. Illustration of prototype wall cross-section for Test 4 Part 2 showing the average maximum geotextile stresses in all instrumented regions

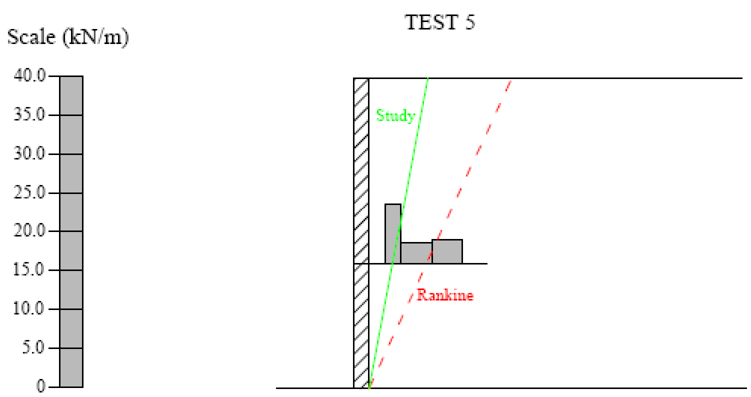

Figure 4.192. Illustration of prototype wall cross-section for Test 5 showing the average maximum geotextile stresses in all instrumented regions

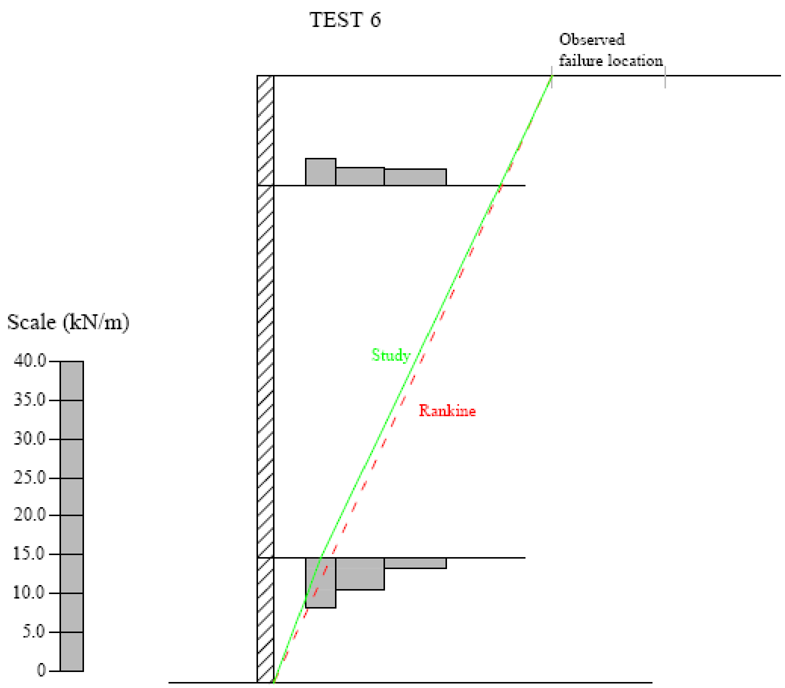

Figure 4.193. Illustration of prototype wall cross-section for Test 6 showing the average maximum geotextile stresses in all instrumented regions

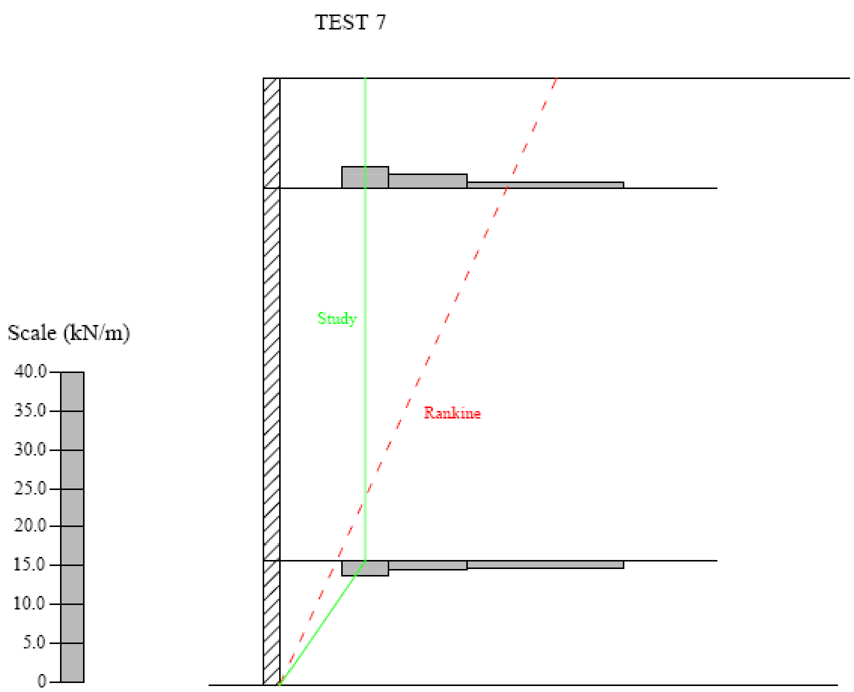

Figure 4.194. Illustration of prototype wall cross-section for Test 7 showing the average maximum geotextile stresses in all instrumented regions

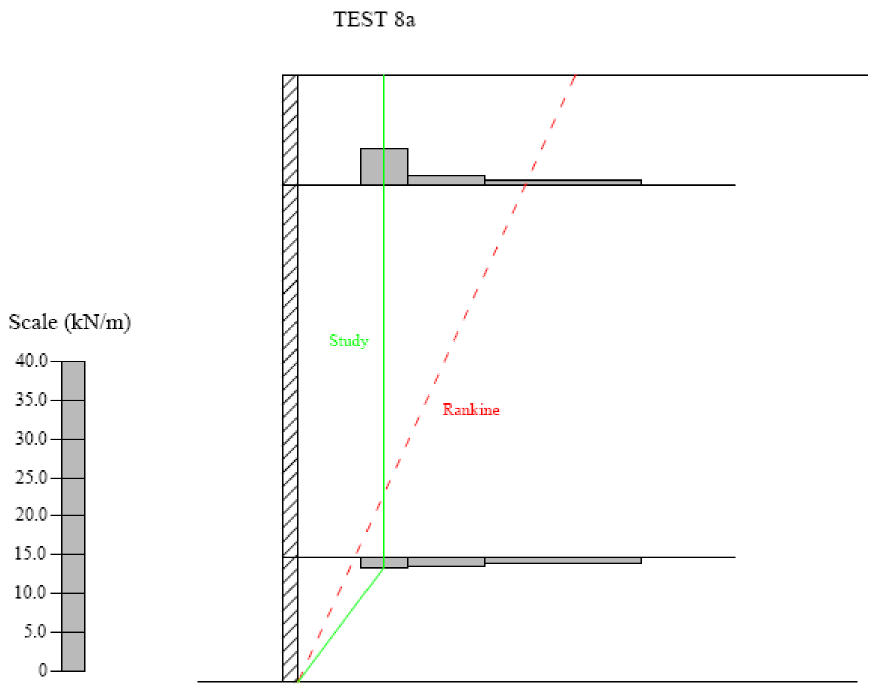

Figure 4.195. Illustration of prototype wall cross-section for Test 8a showing the average maximum geotextile stresses in all instrumented regions

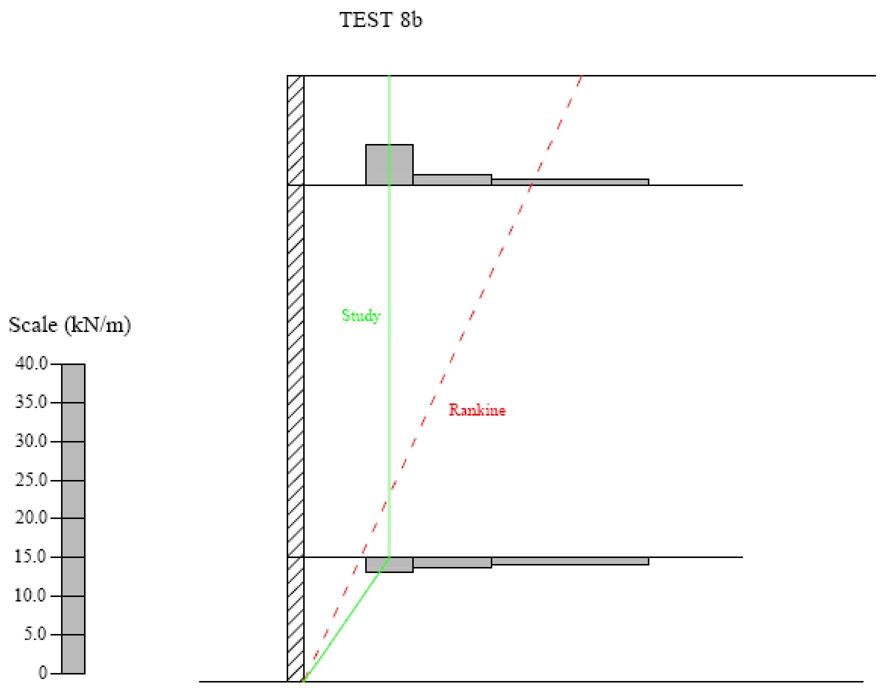

Figure 4.196. Illustration of prototype wall cross-section for Test 8b showing the average maximum geotextile stresses in all instrumented regions

The following figures illustrating the geotextile stresses for the test runs with the highest shaking table acceleration in each test show stress distributions similar to the previous figures. The previously explained approach for determining the critical surface can be applied on Figures 4.197 to 4.206 to give the same critical surfaces illustrated in Figures 4.187 to 4.196.

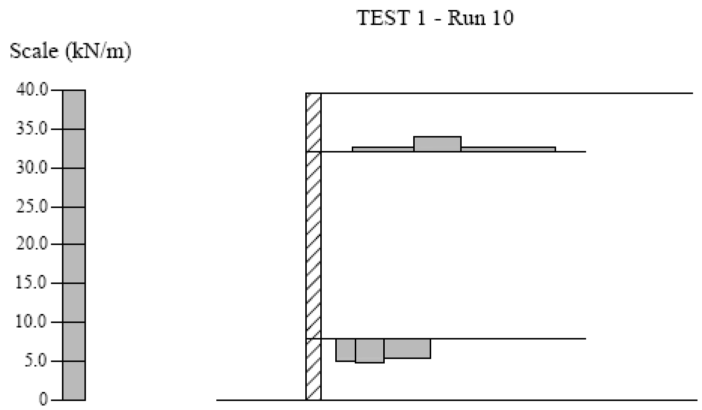

Figure 4.197. Illustration of prototype wall cross-section showing the maximum geotextile stresses in all instrumented regions for Test 1 run with the maximum table acceleration (0.296 g)

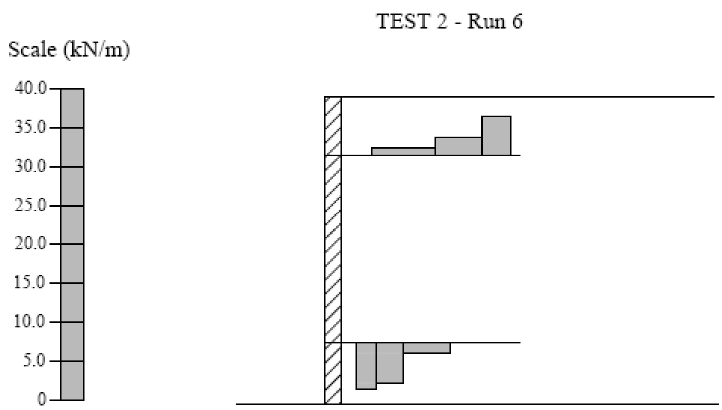

Figure 4.198. Illustration of prototype wall cross-section showing the maximum geotextile stresses in all instrumented regions for Test 2 run with the maximum table acceleration (0.319g)

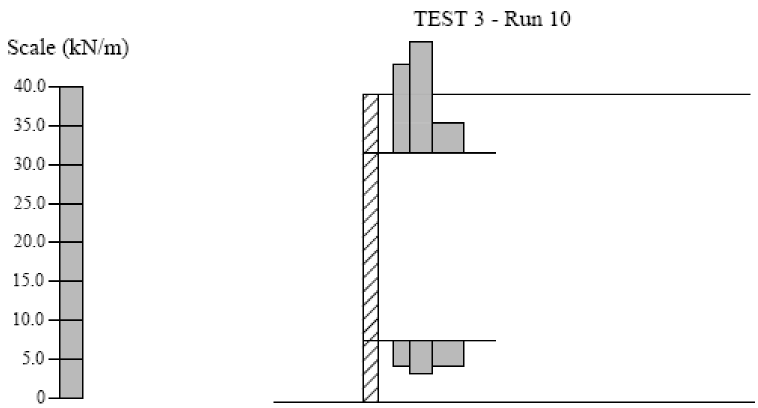

Figure 4.199. Illustration of prototype wall cross-section showing the maximum geotextile stresses in all instrumented regions for Test 3 run with the maximum table acceleration (0.280g)

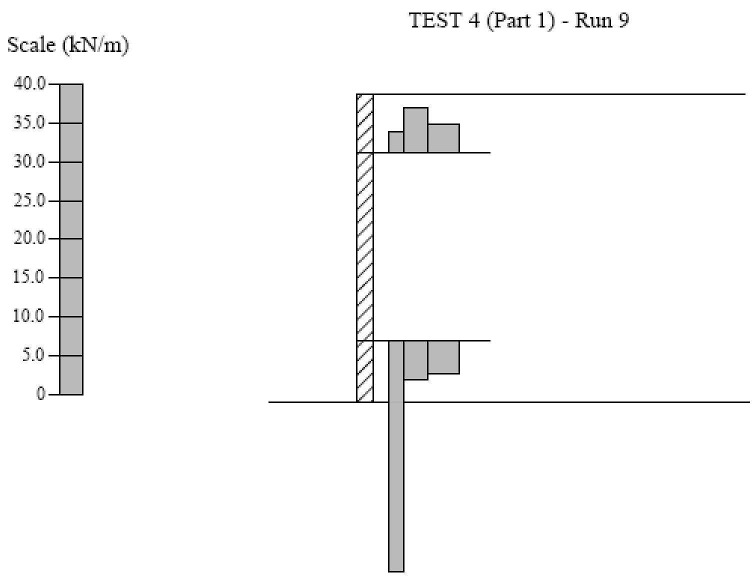

Figure 4.200. Illustration of prototype wall cross-section showing the maximum geotextile stresses in all instrumented regions for Test 4 (Part 1) run with the maximum table acceleration (0.303g)

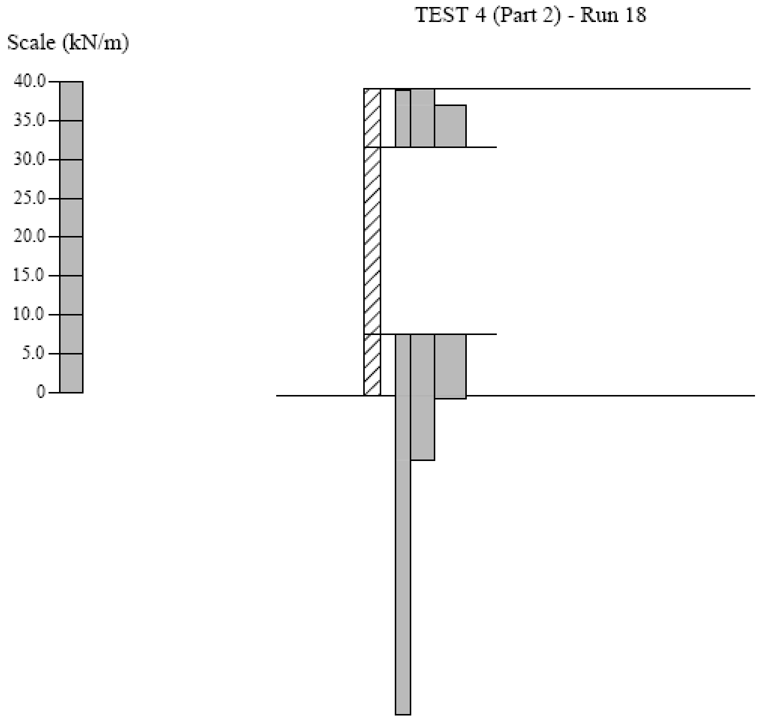

Figure 4.201. Illustration of prototype wall cross-section showing the maximum geotextile stresses in all instrumented regions for Test 4 (Part 2) run with the maximum table acceleration (0.622g)

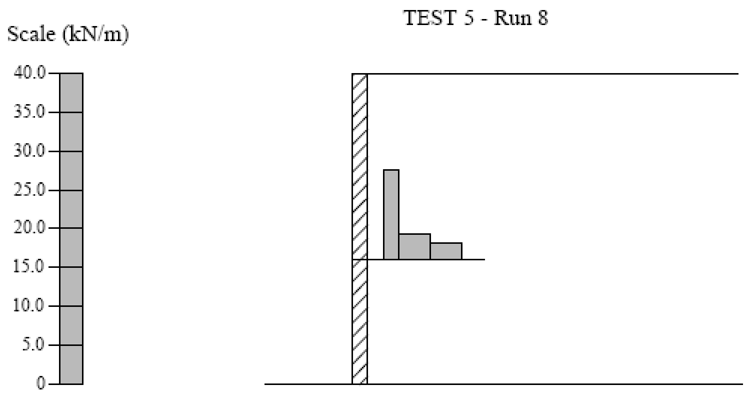

Figure 4.202. Illustration of prototype wall cross-section showing the maximum geotextile stresses in all instrumented regions for Test 5 run with the maximum table acceleration (0.494g)

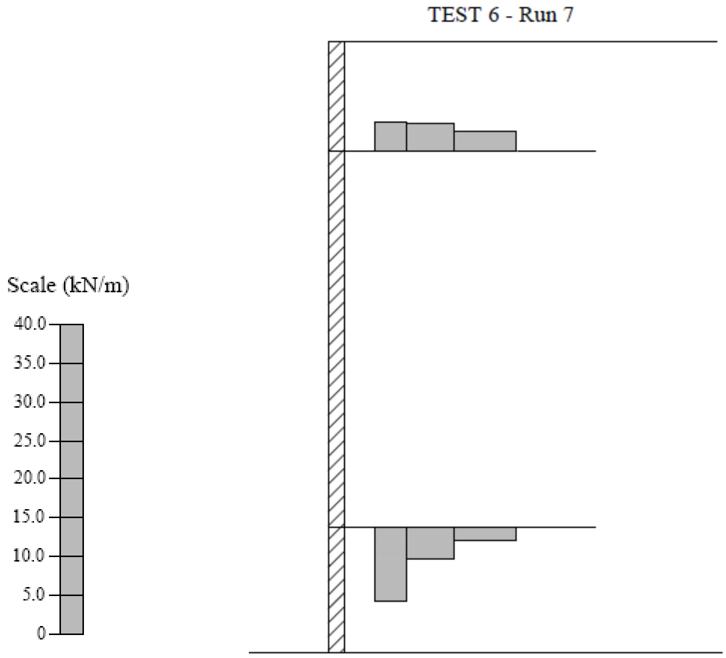

Figure 4.203. Illustration of prototype wall cross-section showing the maximum geotextile stresses in all instrumented regions for Test 6 run with the maximum table acceleration (0.388g)

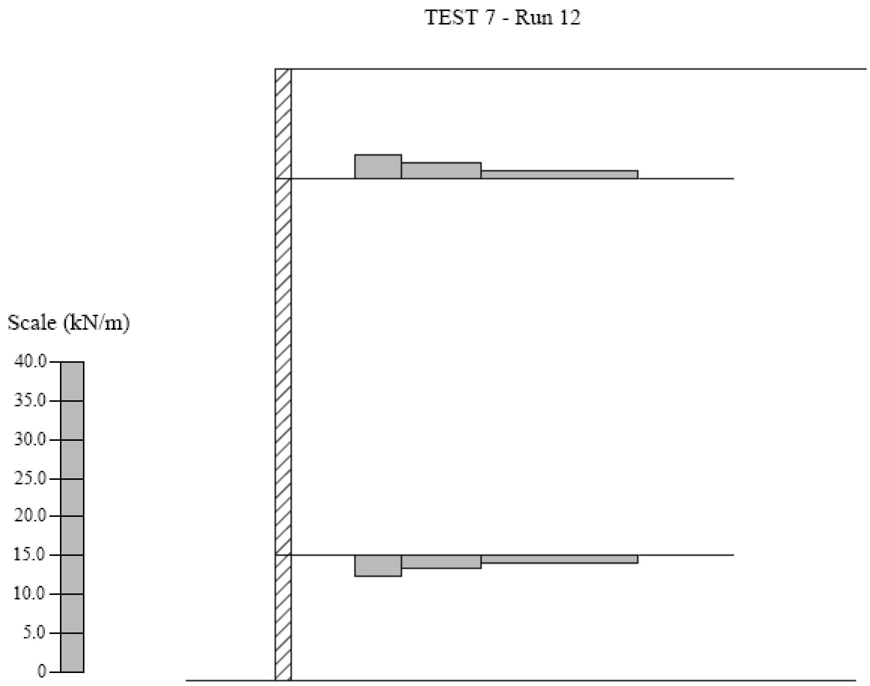

Figure 4.204. Illustration of prototype wall cross-section showing the maximum geotextile stresses in all instrumented regions for Test 7 run with the maximum table acceleration (0.584g)

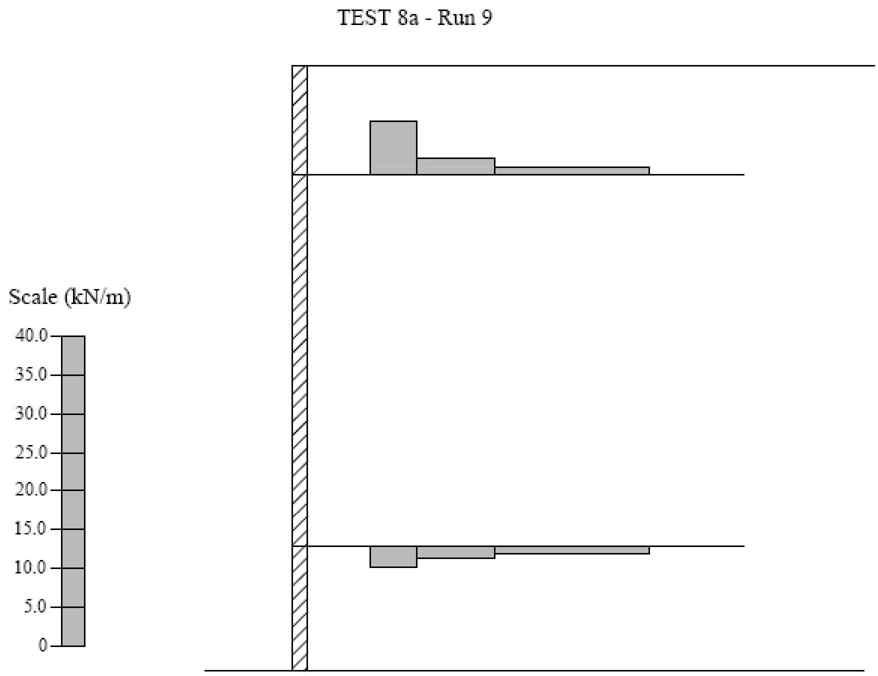

Figure 4.205. Illustration of prototype wall cross-section showing the maximum geotextile stresses in all instrumented regions for Test 8a run with the maximum table acceleration (0.365g)

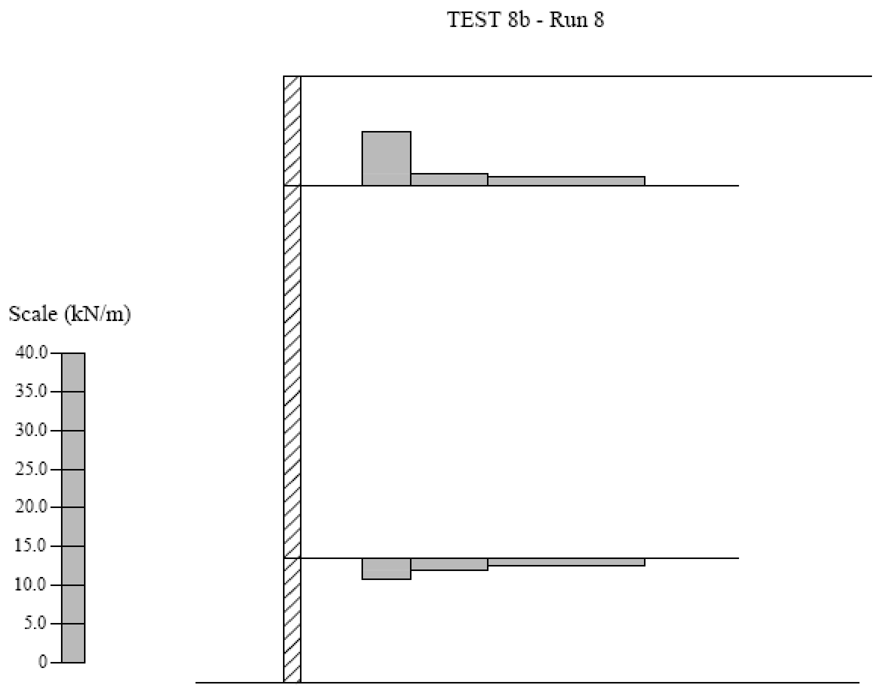

Figure 4.206. Illustration of prototype wall cross-section showing the maximum geotextile stresses in all instrumented regions for Test 8b run with the maximum table acceleration (0.502g)

4.13. Note on Wall Failure in Test 6 Run 8

In Test 6, the model scale was 1:4 and L/H was 0.4. No tail geotextile was used and top two layers of facing blocks were not fixed to each other. No extreme occurrences took place until the eighth run of the test. At the eighth run, the shaking table system failed to stay close to the applied earthquake record and the table acceleration record shown in Figure 4.207 was applied. This resulted in failure of the wall (Figure 4.208) and the test was stopped. Accelerometer readings are not available for this test run since the shaking table facility's own recording system failed. Photographs in Figure 4.208 show that the wall faced remained linear and the facing blocks did not slide relative to each other. Overturning was the evident mode of failure. Observation of the top of wall after failure is illustrated and dimensioned in Figure 4.209. The major failure location shown in this figure coincides with the intersection of Rankine plane with the top of GRS wall. The reinforced zone in front remained relatively intact.

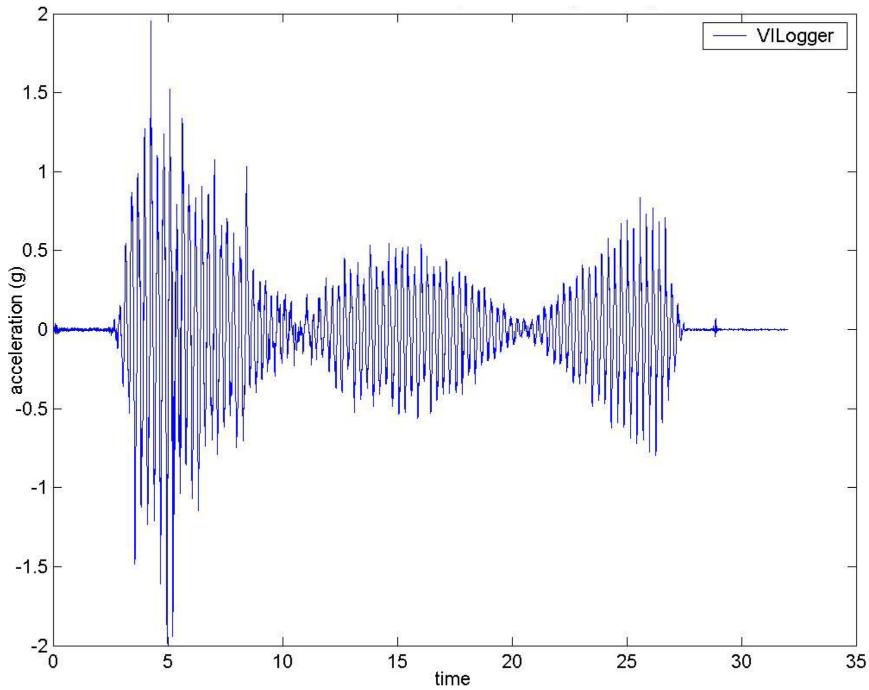

Figure 4.207. Table acceleration record for Test 6-8

Figure 4.208. Photographs of the failed wall (Test 6-8)

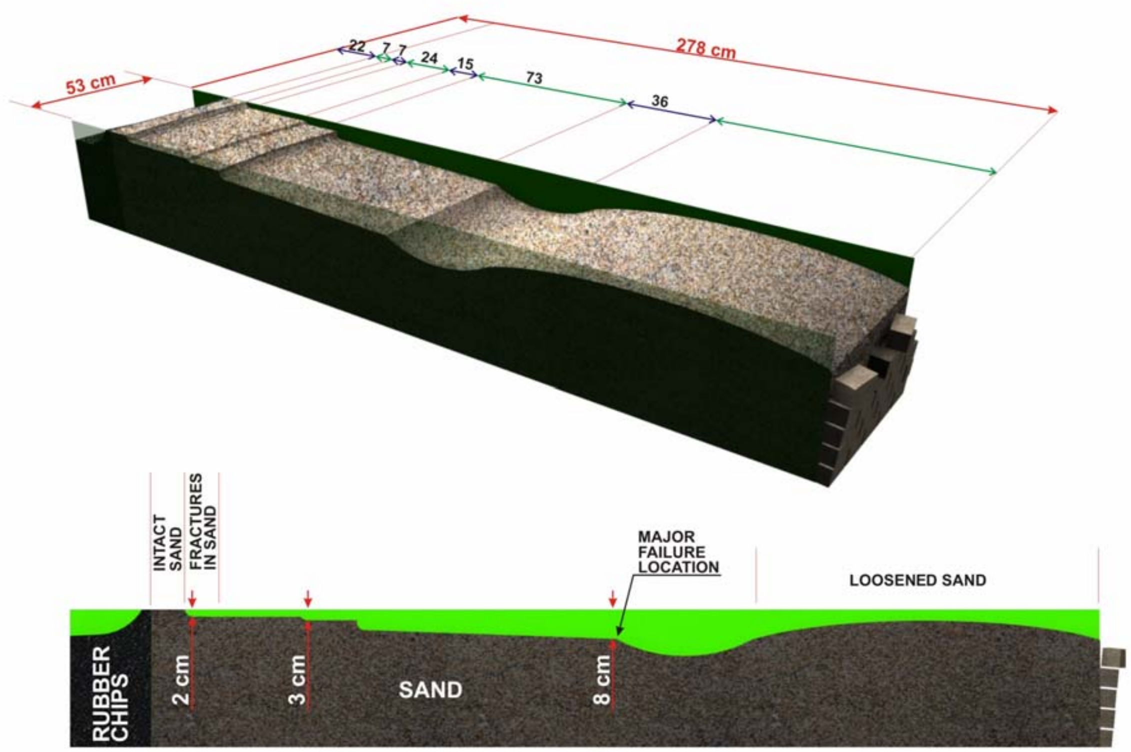

Figure 4.209. Illustration of top of wall after Test 6-8

5. CONCLUSIONS

Maximum accelerations observed during shaking on the wall face increased from bottom to top, in accordance with that reported in literature. For all tests, the maximum acceleration at a certain point on face increased rather linearly with increasing maximum table acceleration, implying constant amplification factors determined by the wall configuration.

No correlation between amplification of acceleration on face and reinforcement length could be established for configurations with the top two layers of blocks fixed to each other.

The condition of top two layers of blocks combined with reinforcement length had an important effect on amplification factors. Free blocks on shorter reinforcements resulted in high amplification factors on top of wall face. When the reinforcement length was increased sufficiently beyond the potential failure plane, no radical rise in top accelerations was observed. This observation can be explained by high frequency vibrations in the free blocks (and the soil directly behind it) over short reinforcements that did not cause additional face displacements when the forces in the failure zone are not high enough to cause failure.

Accelerometers placed on top of the fill also measured maximum accelerations increasing with increasing maximum table acceleration, and this increase may be considered linear, so constant amplification factors can be assumed. For individual test runs, accelerometer readings above the reinforced zone remained somewhat constant and decreased towards the back in the backfill. This indicates that the reinforced zone remained as a monolithic block.

Backward accelerations measured on the facing were nearly symmetrical with the outward accelerations. This is in accordance with the observation of zero permanent displacements at all levels. This can be interpreted as an indication of the movements remaining in the elastic range.

Model scales used in this study did not have a significant effect on the accelerations measured. The only remarkable difference resulting from using a 1:4 model scale was the observation of larger maximum face displacements during shaking compared to a 1:2 scale model. Earthquake frequencies applied in this study did not have a significant effect on the investigated parameters.

Maximum displacements relative to shaking table during shaking did not have a clear trend of increasing towards the top.

Face displacements during shaking varied only slightly with reinforcement length and spacing. No significant permanent displacements were observed. Decreasing the reinforcement spacing changed the distribution of stress in geotextile layers and led to a more uniform stress distribution.

Investigation of the geotextile stresses showed that the additional stresses induced by seismic loading are generally higher than design stresses recommended by FHWA and NCMA. For the model walls complying with the design recommendations in terms of reinforcement length, measured stresses in the lower reinforcement were closer to the design stresses.

Measured geotextile stresses increased with decreasing geotextile length and increasing geotextile spacing.

All these conclusions indicate that pseudo-static design approach is sufficient in determining the length and spacing of geotextile reinforcement in geosynthetic reinforced soil retaining walls with concrete block facing, in which the reinforced fill and backfill soils are granular. As long as the reinforcements are extended sufficiently beyond the potential failure surface and the design factor of safety is kept above unity for the specific peak ground acceleration, displacements and accelerations during shaking will be similar, and no significant permanent displacements will be observed. To minimize the effects of maximum relative displacements or accelerations during shaking on the above structures, other parameters like toe condition and properties of facing can be modified. In design, it should be considered that reinforcement stresses under seismic loading can be higher than those recommended by current design recommendations and the reinforcement should be selected accordingly. This study also confirms that purely frictional bonding between facing blocks and geotextiles shows a good performance under seismic loading as long as the top two block layers are fixed to each other.

APPENDIX A: SHAKING TABLE RESPONSE TO APPLIED EARTHQUAKE RECORD

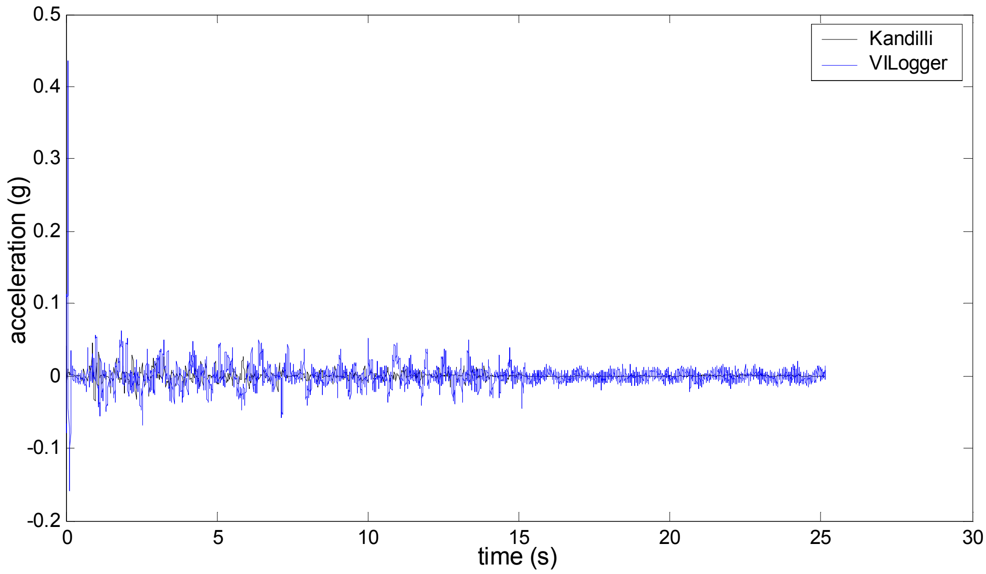

Figure A.1. Measured table acceleration for Test 1 Run 1-1

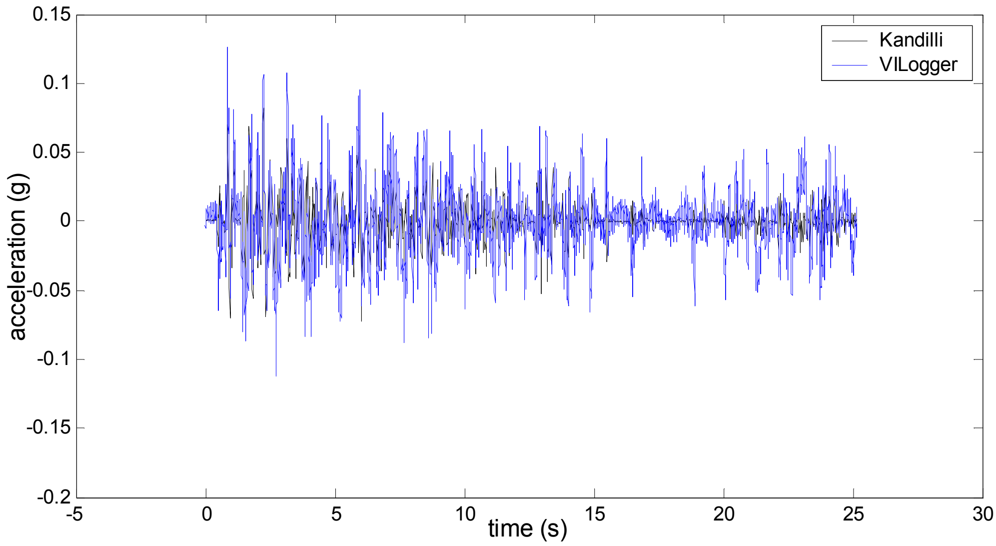

Figure A.2. Measured table acceleration for Test 1 Run 1-2

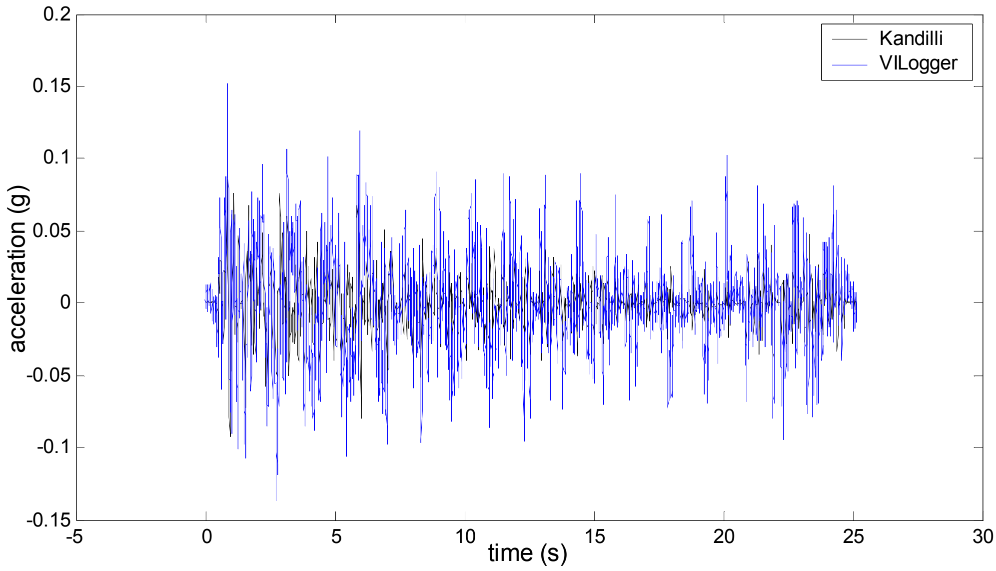

Figure A.3. Measured table acceleration for Test 1 Run 1-3

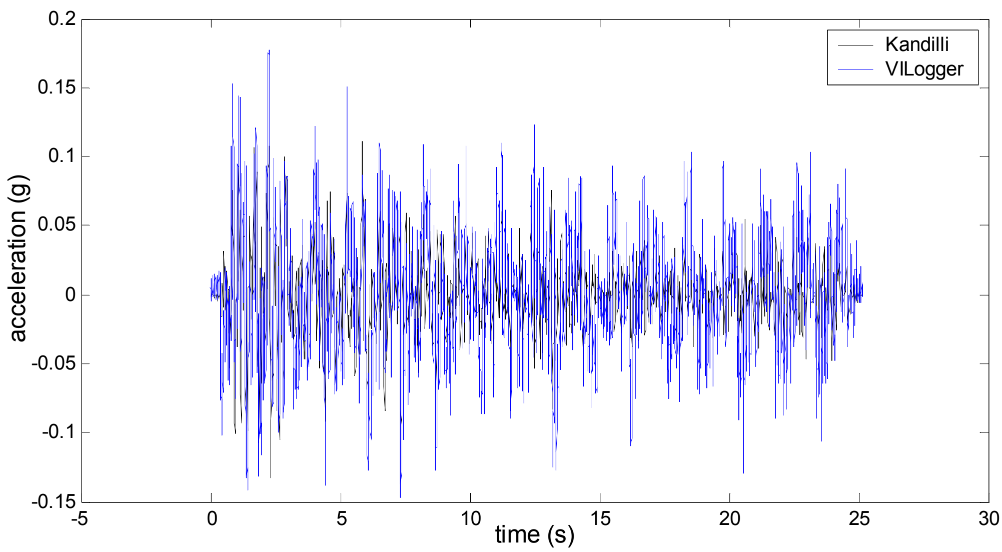

Figure A.4. Measured table acceleration for Test 1 Run 1-4

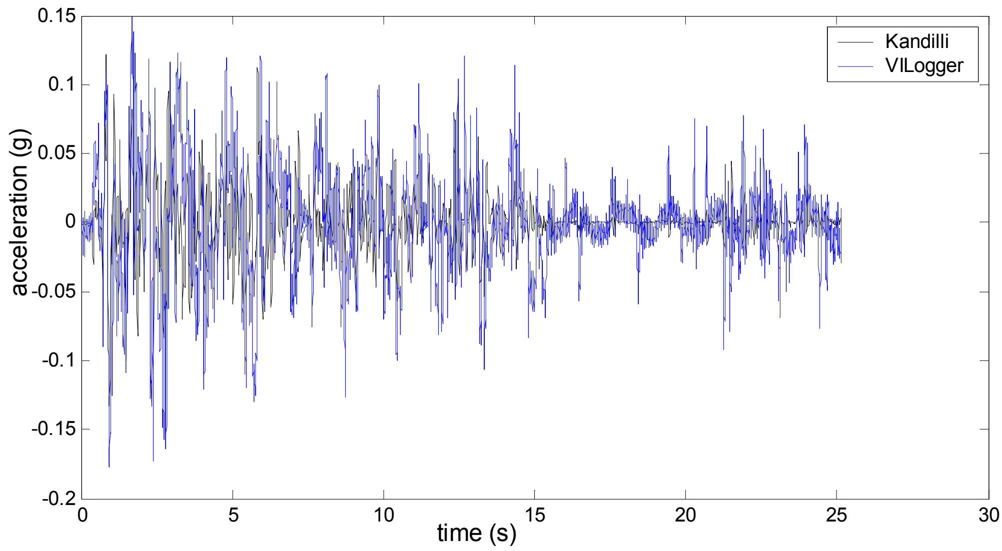

Figure A.5. Measured table acceleration for Test 1 Run 1-5

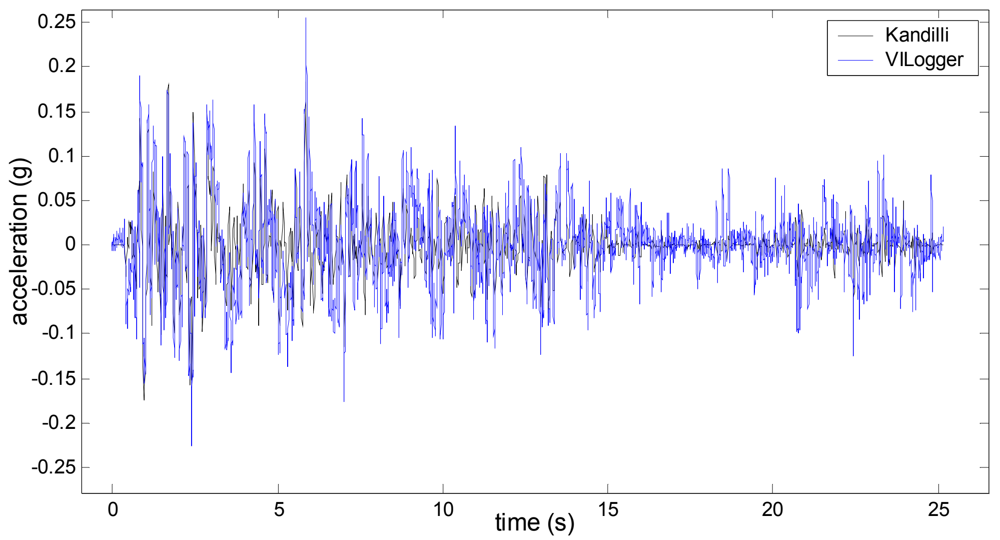

Figure A.6. Measured table acceleration for Test 1 Run 1-6

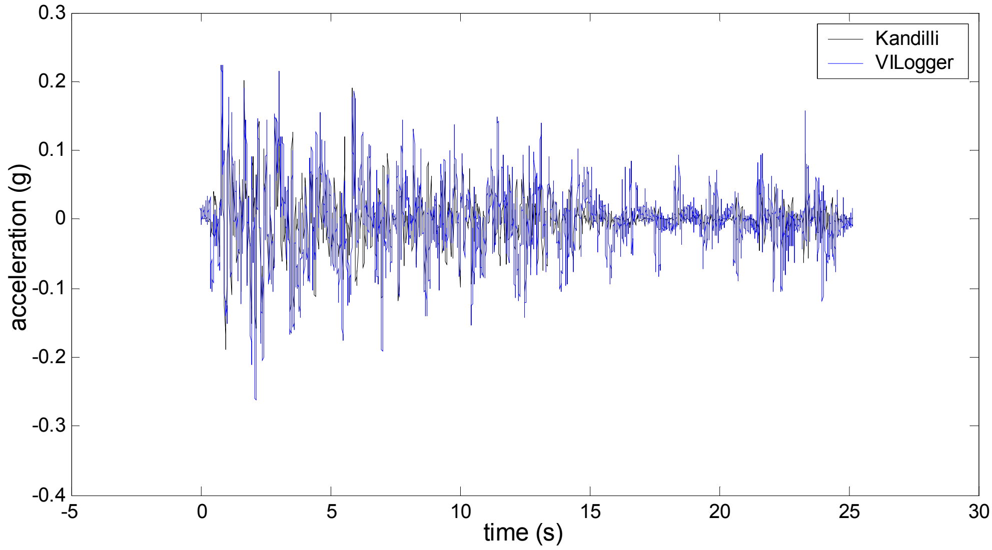

Figure A.7. Measured table acceleration for Test 1 Run 1-7

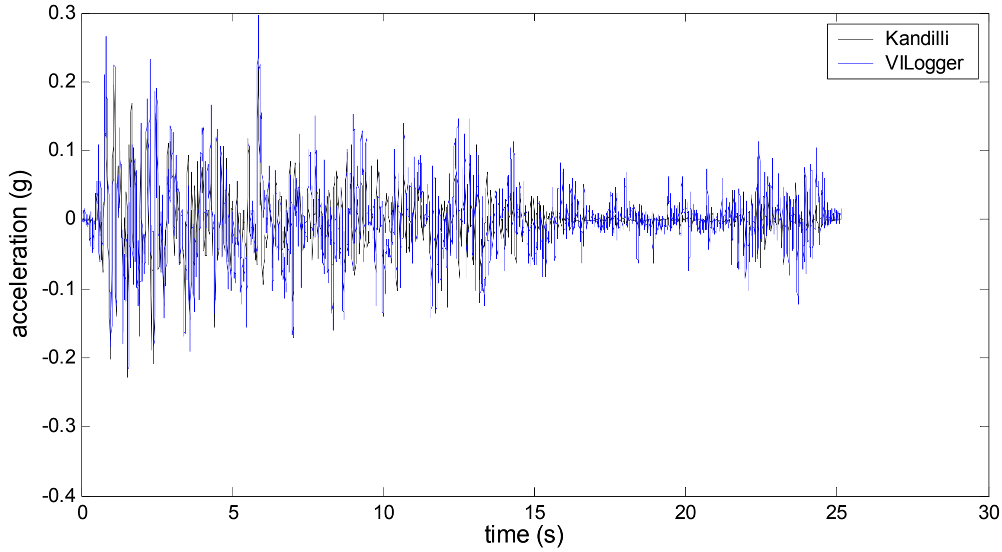

Figure A.8. Measured table acceleration for Test 1 Run 1-8

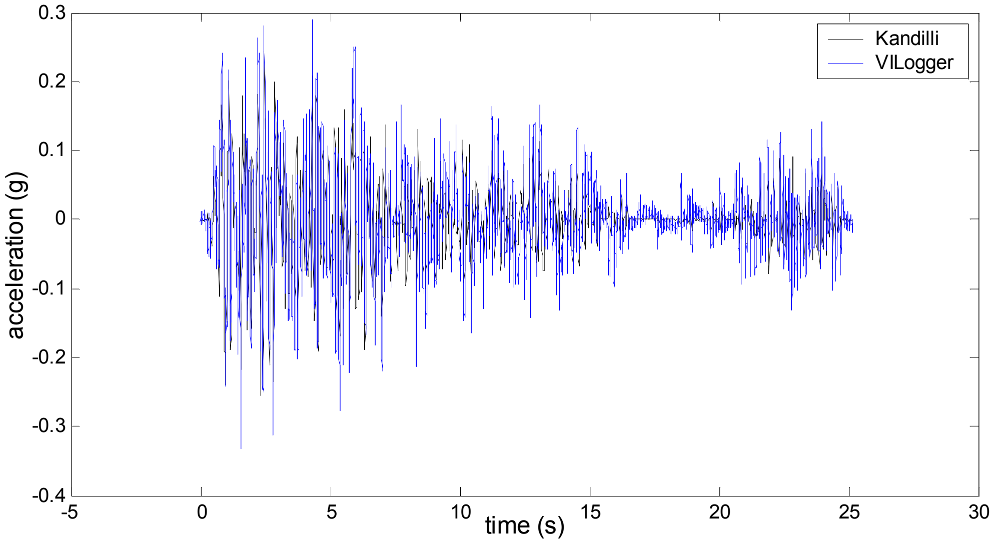

Figure A.9. Measured table acceleration for Test 1 Run 1-9

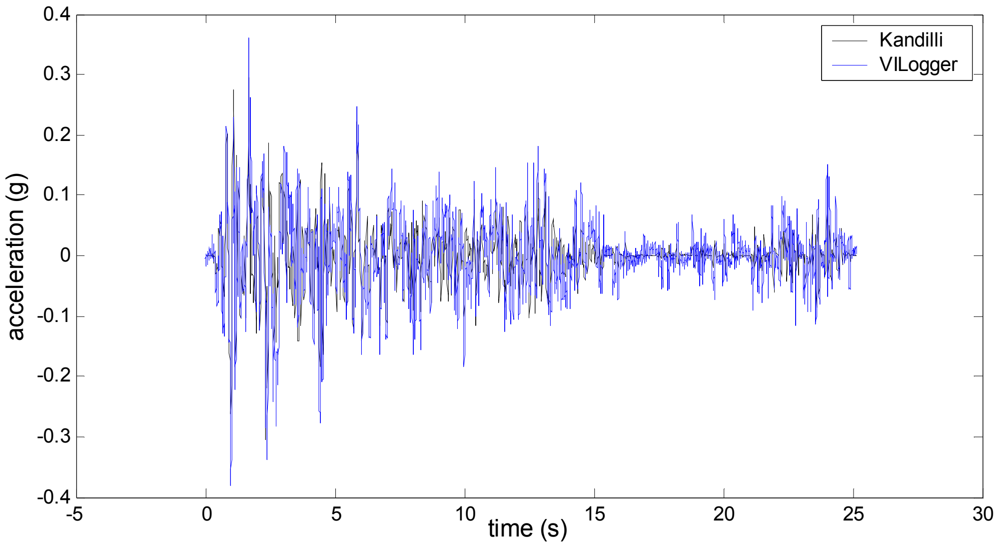

Figure A.10. Measured table acceleration for Test 1 Run 1-10

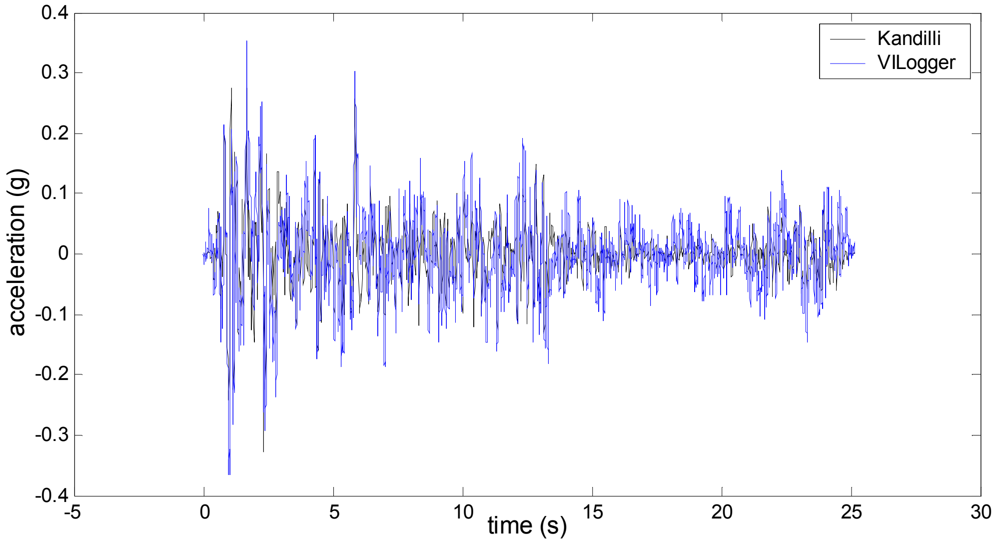

Figure A.11. Measured table acceleration for Test 1 Run 1-11

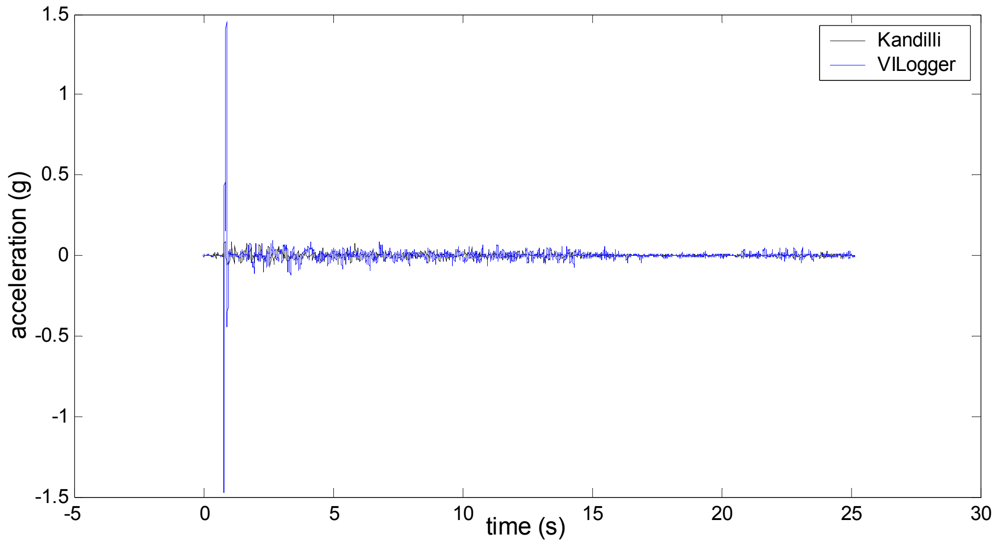

Figure A.12. Measured table acceleration for Test 2 Run 2-1

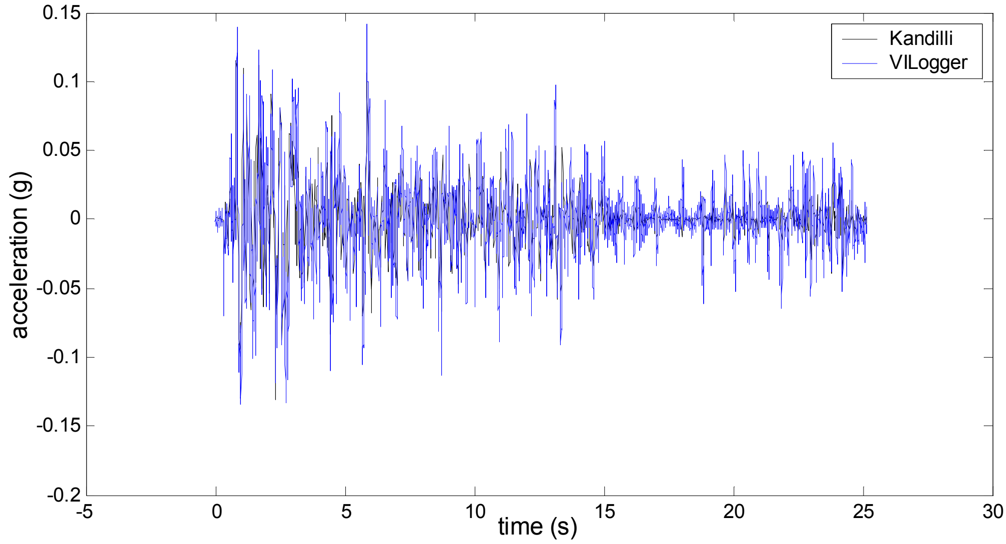

Figure A.13. Measured table acceleration for Test 2 Run 2-2

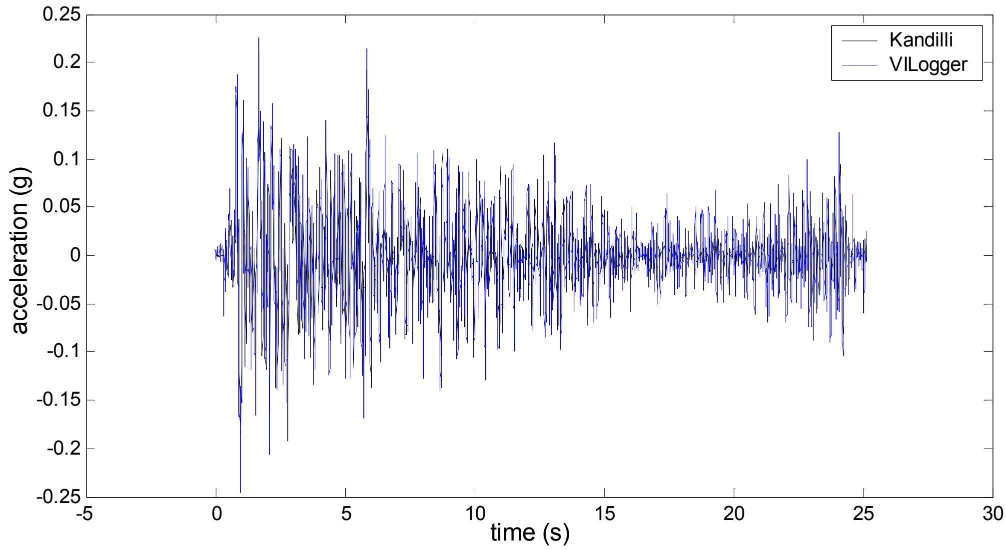

Figure A.14. Measured table acceleration for Test 2 Run 2-3

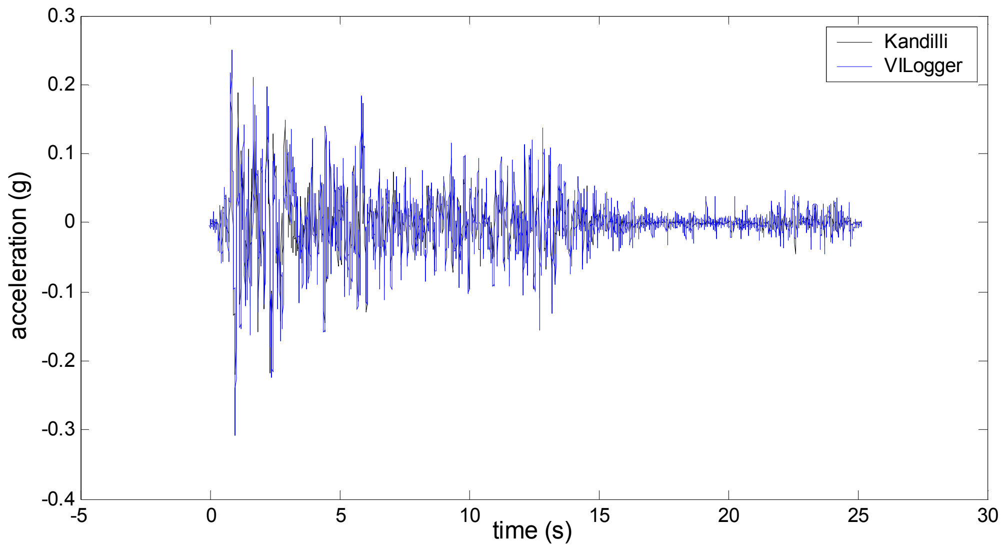

Figure A.15. Measured table acceleration for Test 2 Run 2-4

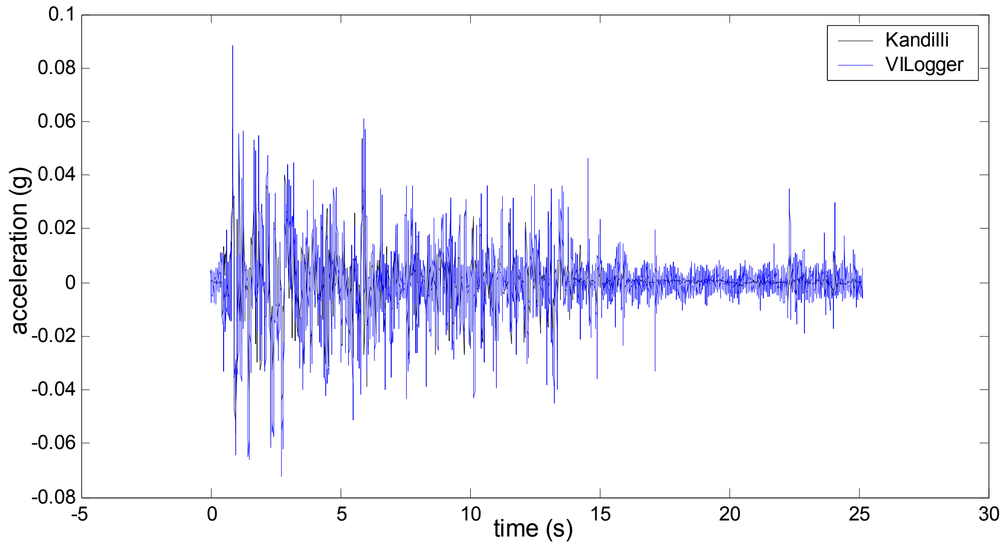

Figure A.16. Measured table acceleration for Test 2 Run 2-5

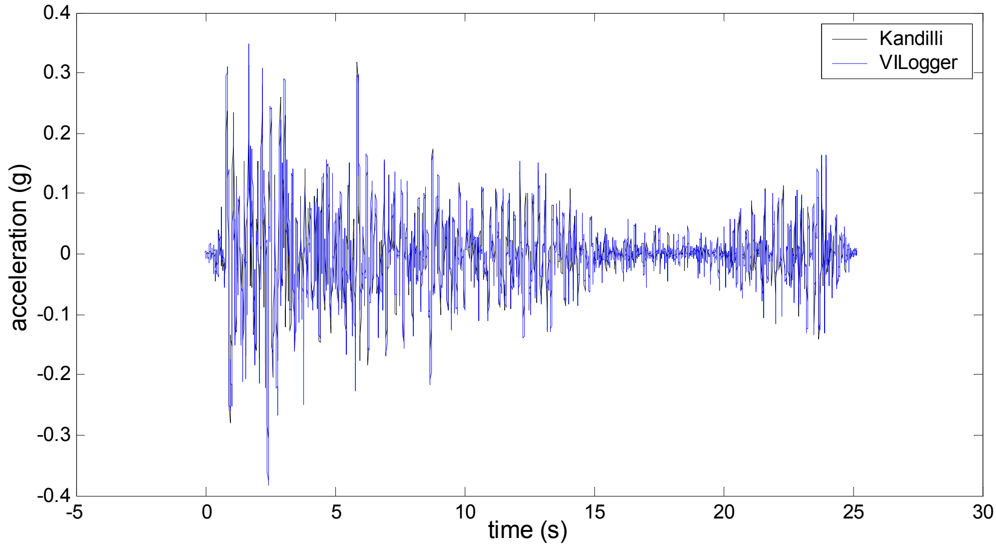

Figure A.17. Measured table acceleration for Test 2 Run 2-6

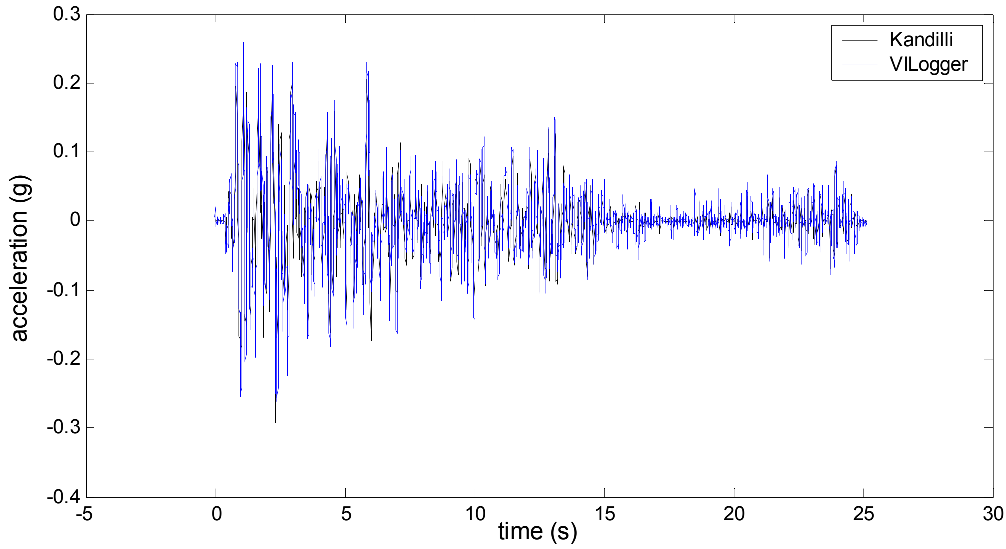

Figure A.18. Measured table acceleration for Test 2 Run 2-7

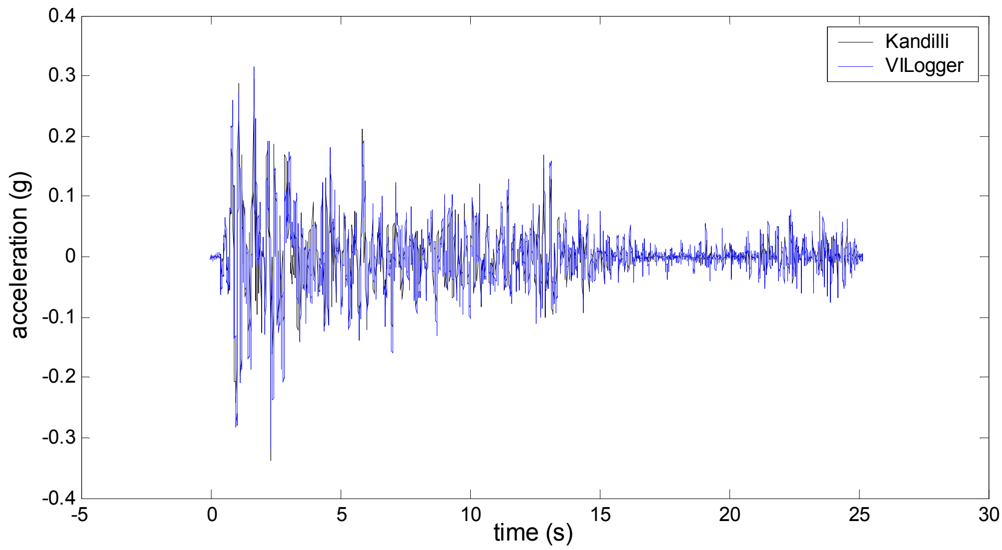

Figure A.19. Measured table acceleration for Test 2 Run 2-8

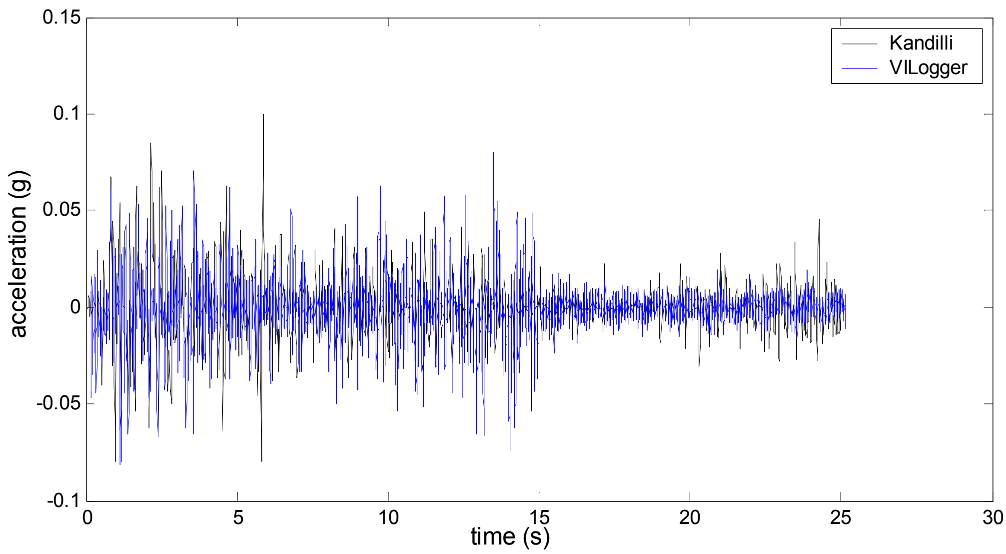

Figure A.20. Measured table acceleration for Test 2 Run 2-9

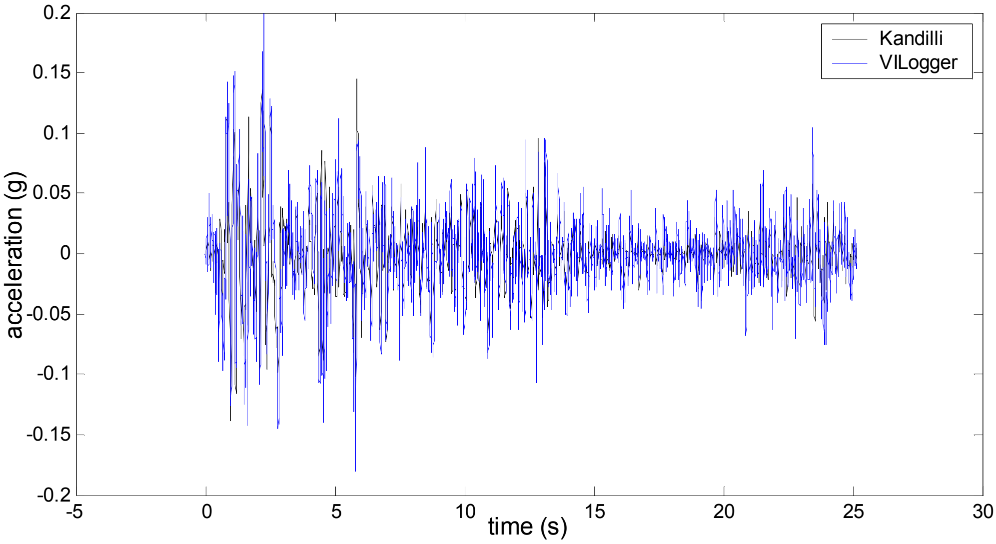

Figure A.21. Measured table acceleration for Test 2 Run 2-10

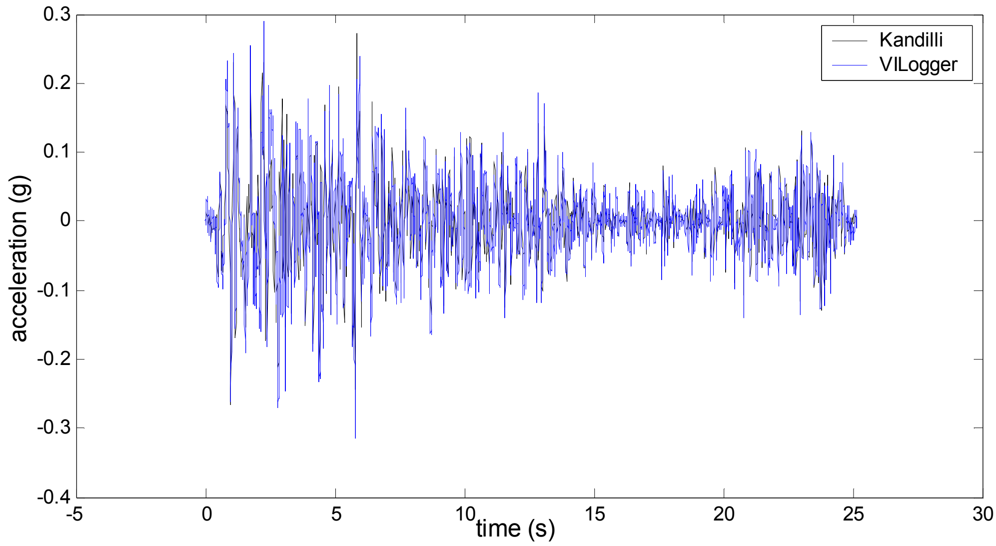

Figure A.22. Measured table acceleration for Test 2 Run 2-11

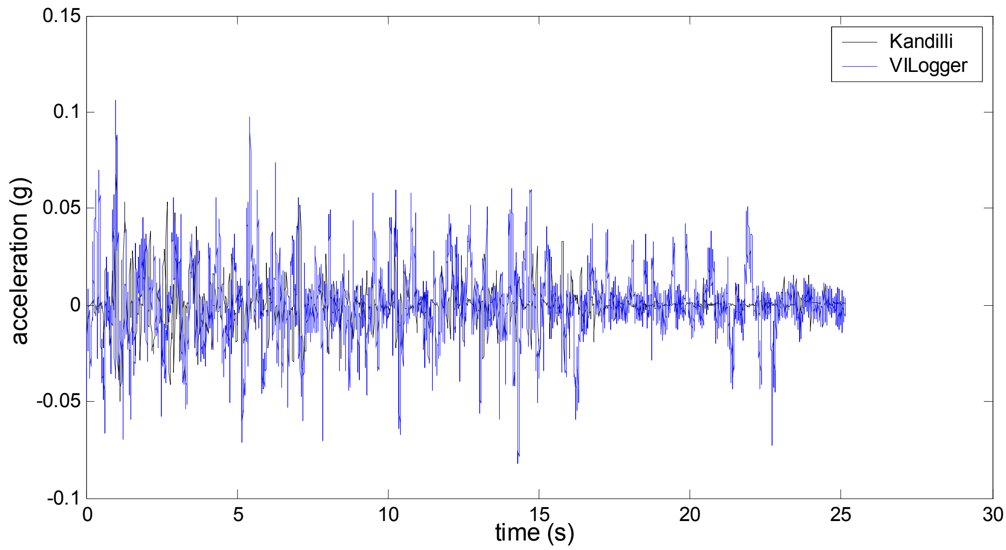

Figure A.23. Measured table acceleration for Test 3 Run 3-1

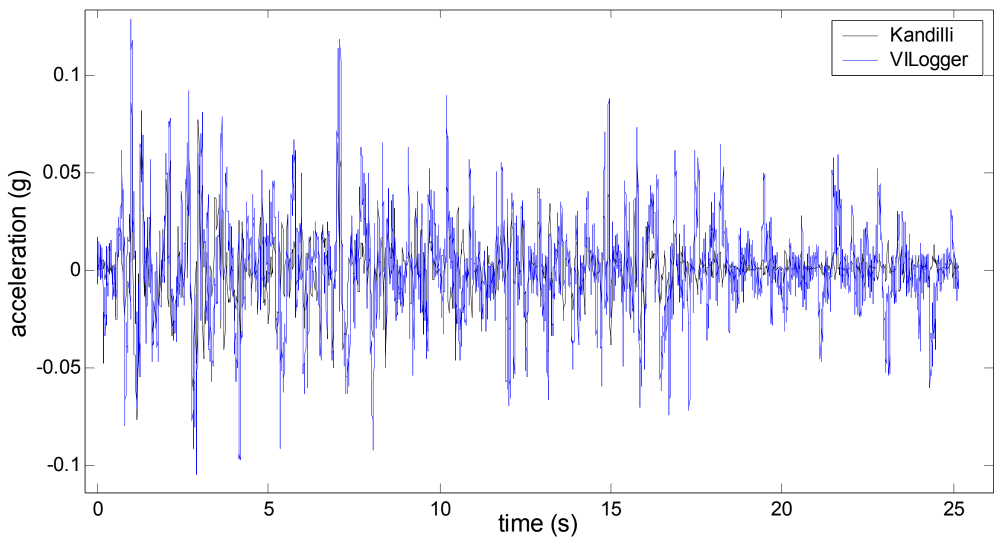

Figure A.24. Measured table acceleration for Test 3 Run 3-2

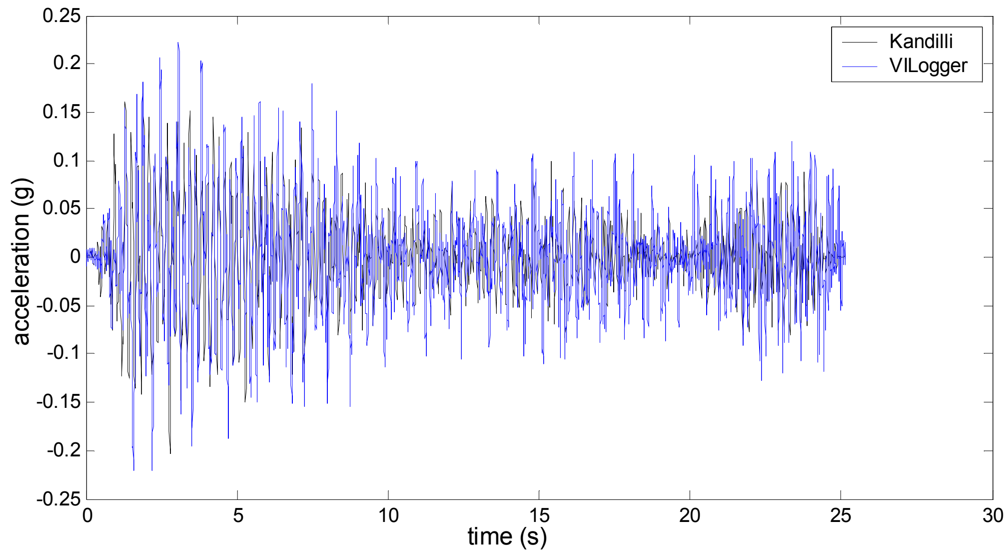

Figure A.25. Measured table acceleration for Test 3 Run 3-3

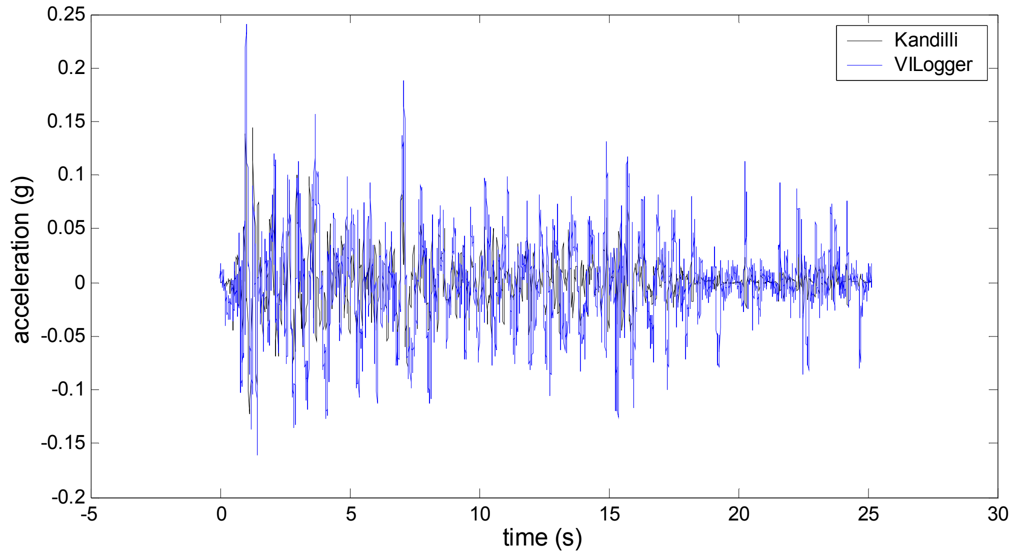

Figure A.26. Measured table acceleration for Test 3 Run 3-4

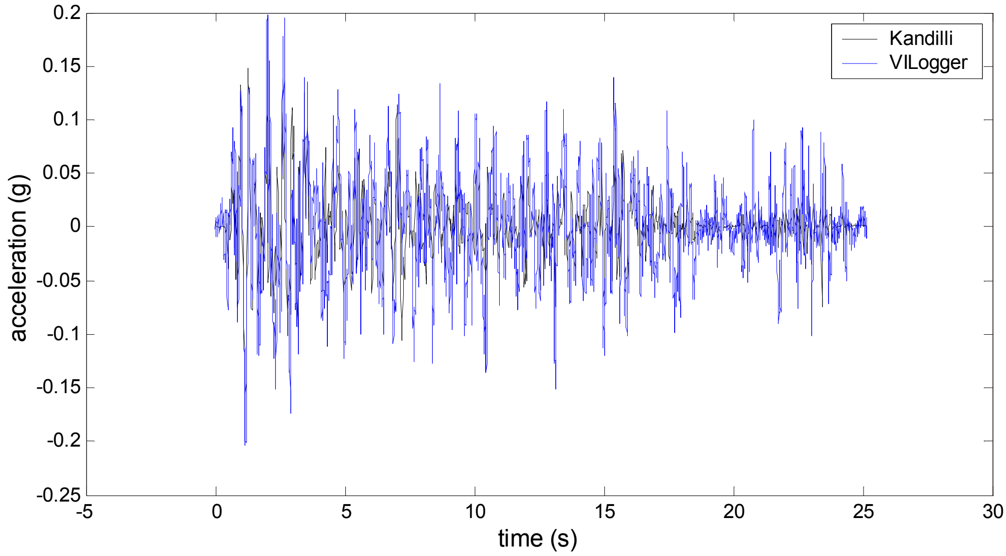

Figure A.27. Measured table acceleration for Test 3 Run 3-5

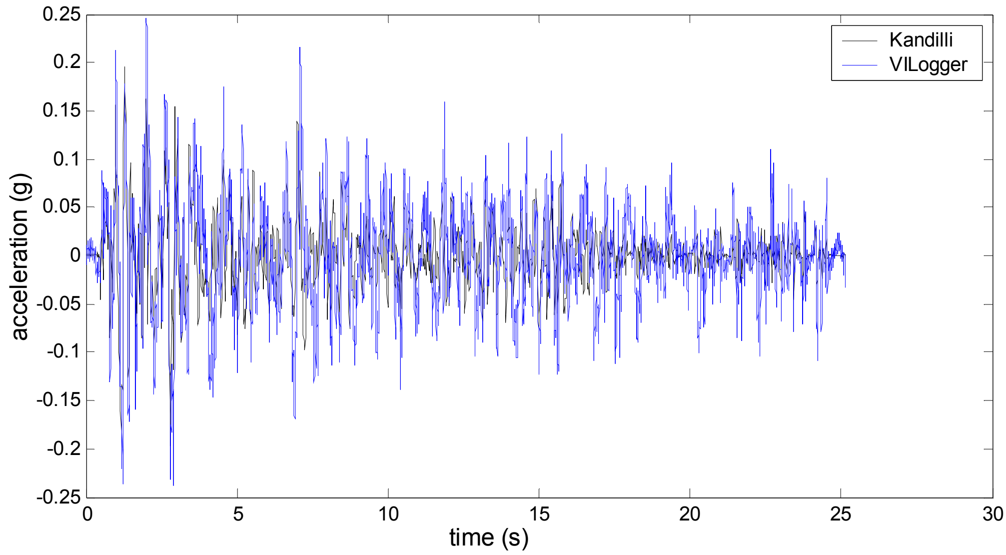

Figure A.28. Measured table acceleration for Test 3 Run 3-6

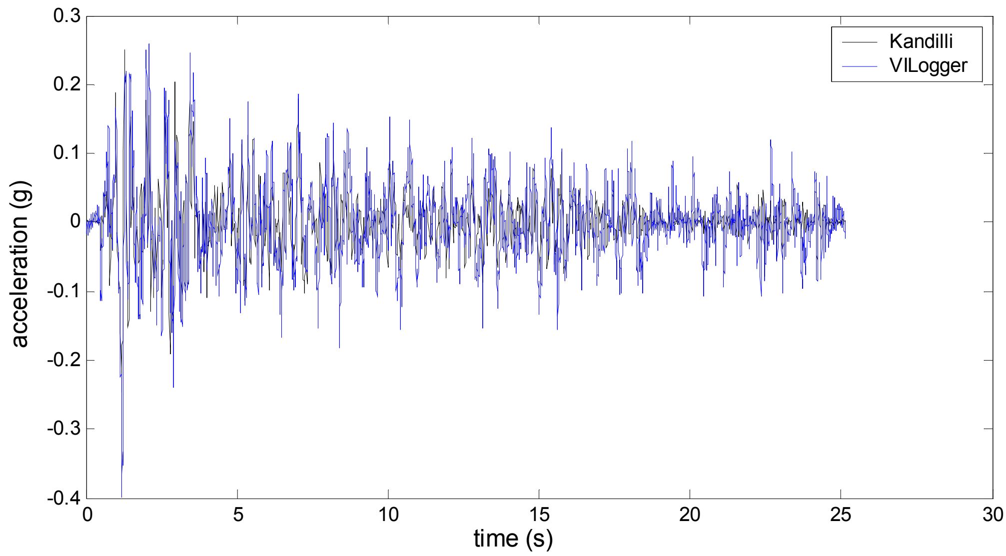

Figure A.29. Measured table acceleration for Test 3 Run 3-7

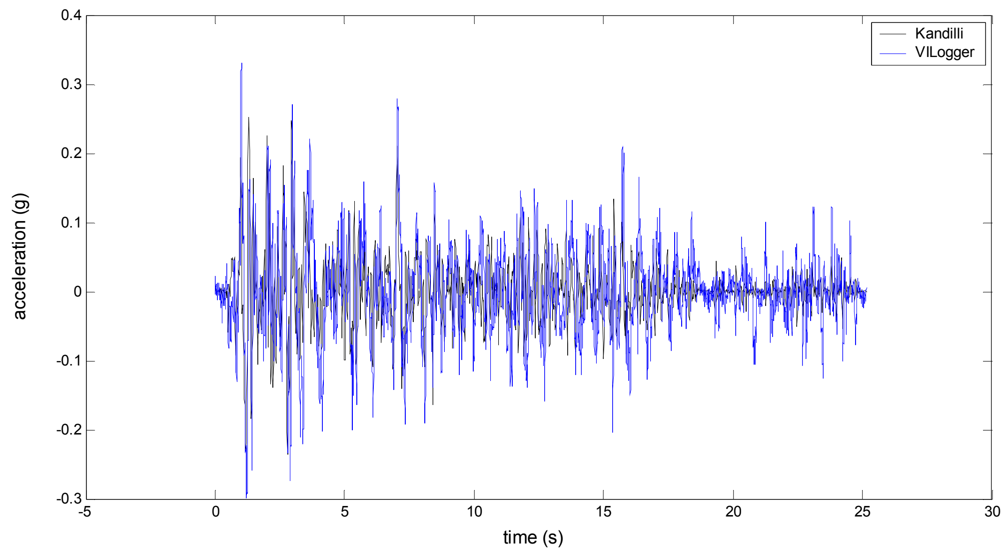

Figure A.30. Measured table acceleration for Test 3 Run 3-8

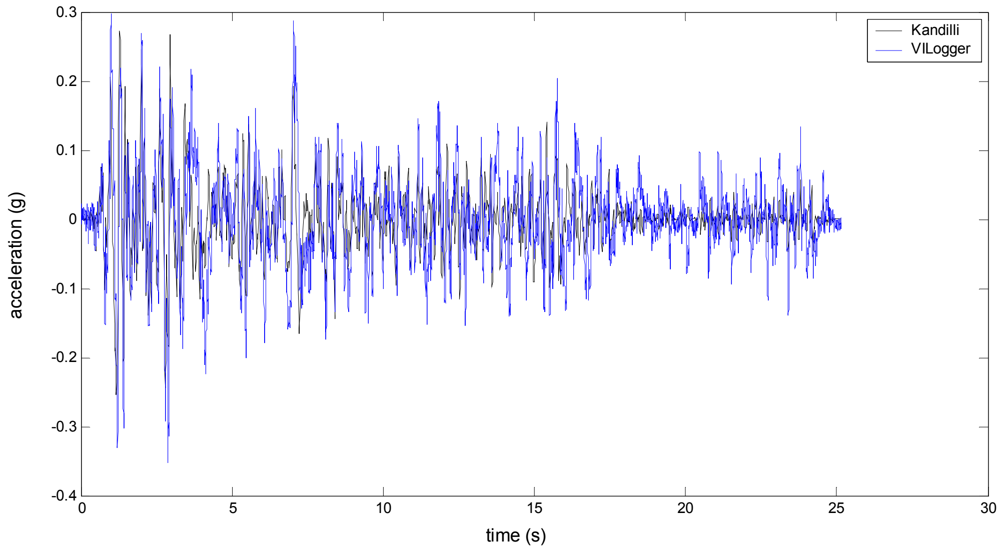

Figure A.31. Measured table acceleration for Test 3 Run 3-9

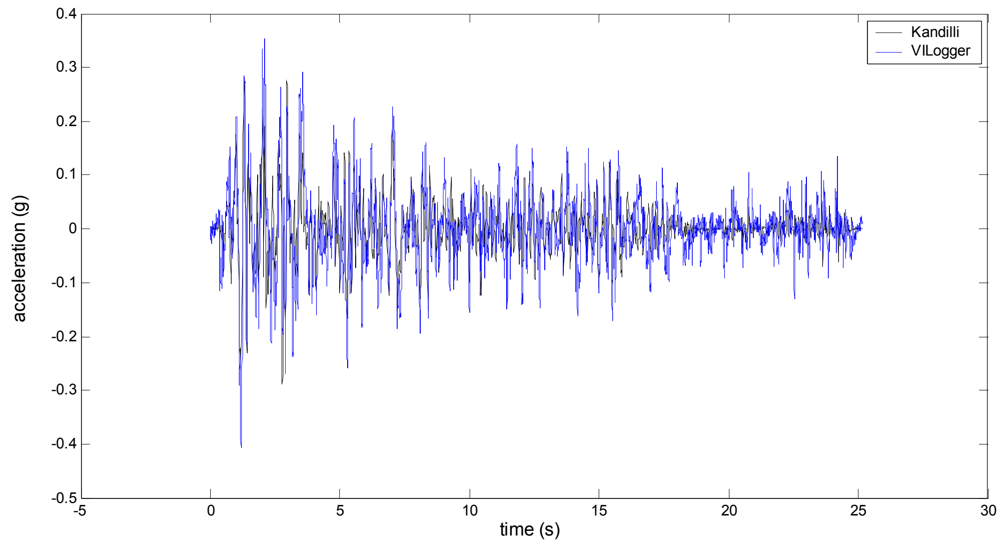

Figure A.32. Measured table acceleration for Test 3 Run 3-10

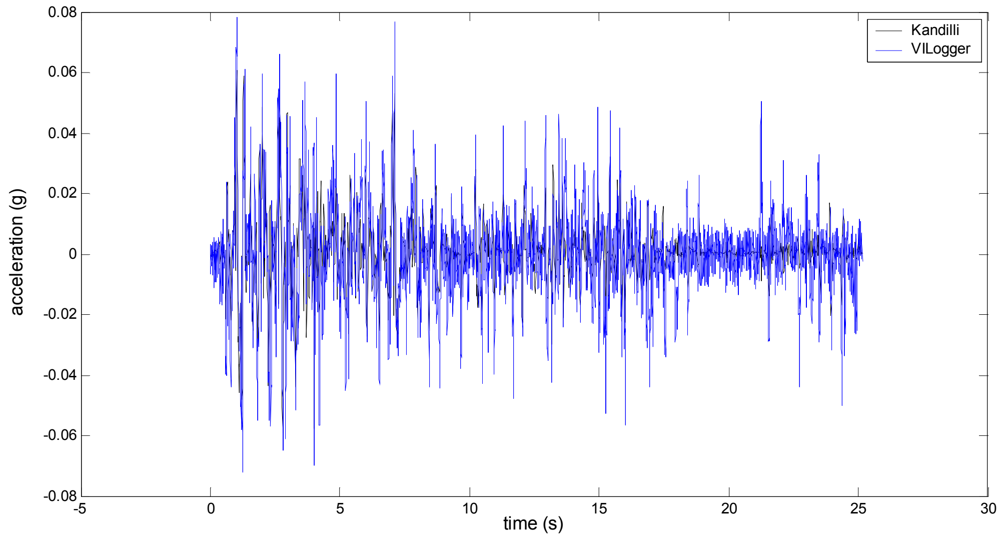

Figure A.33. Measured table acceleration for Test 4 Run 4-1

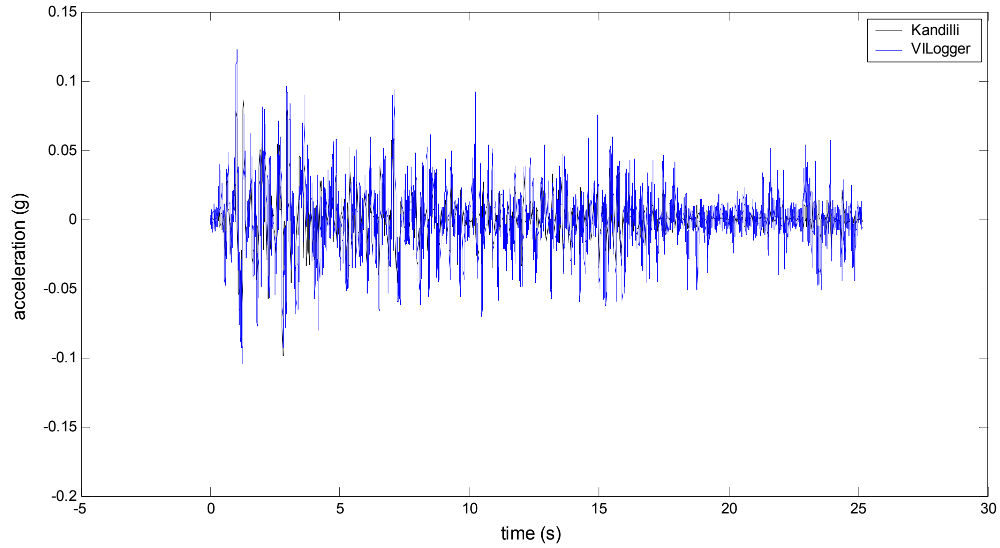

Figure A.34. Measured table acceleration for Test 4 Run 4-2

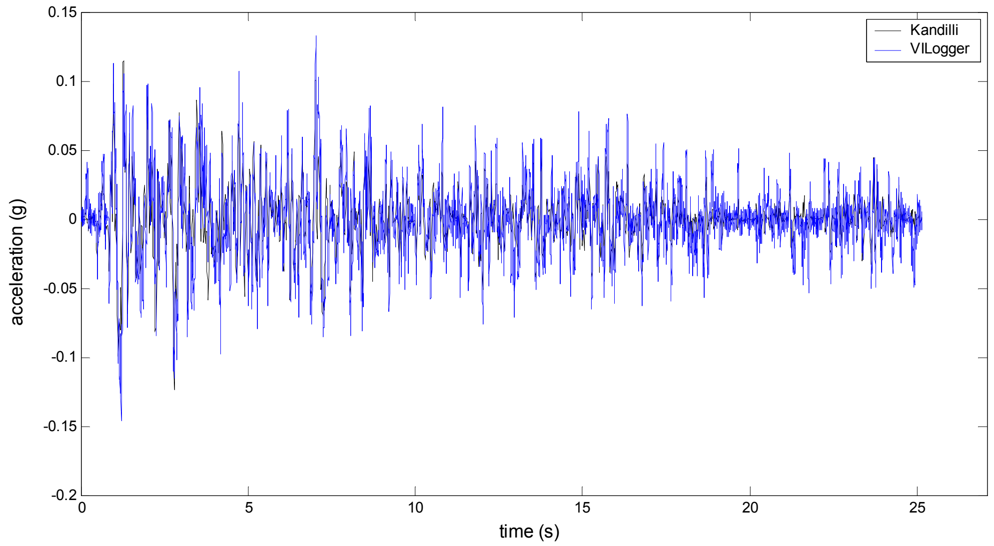

Figure A.35. Measured table acceleration for Test 4 Run 4-3

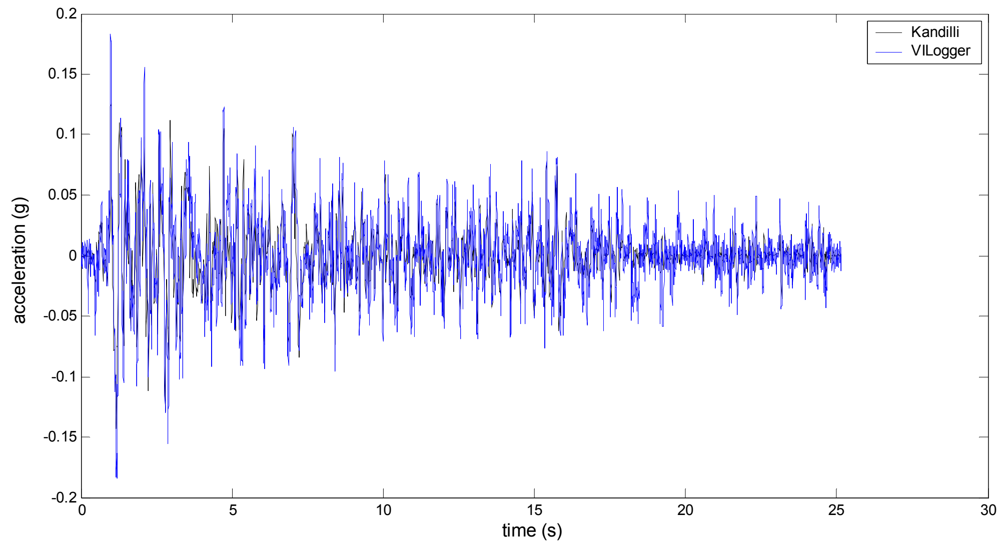

Figure A.36. Measured table acceleration for Test 4 Run 4-4

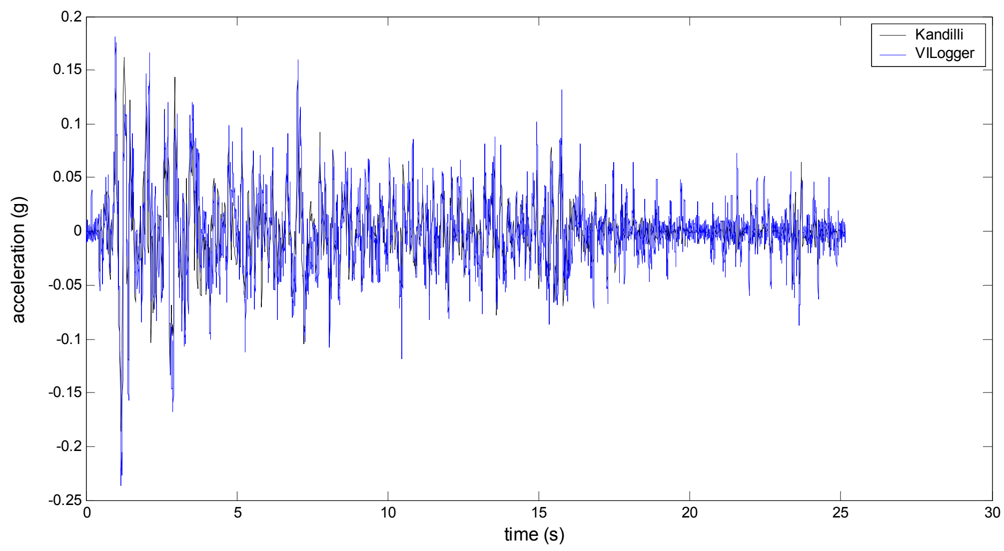

Figure A.37. Measured table acceleration for Test 4 Run 4-5

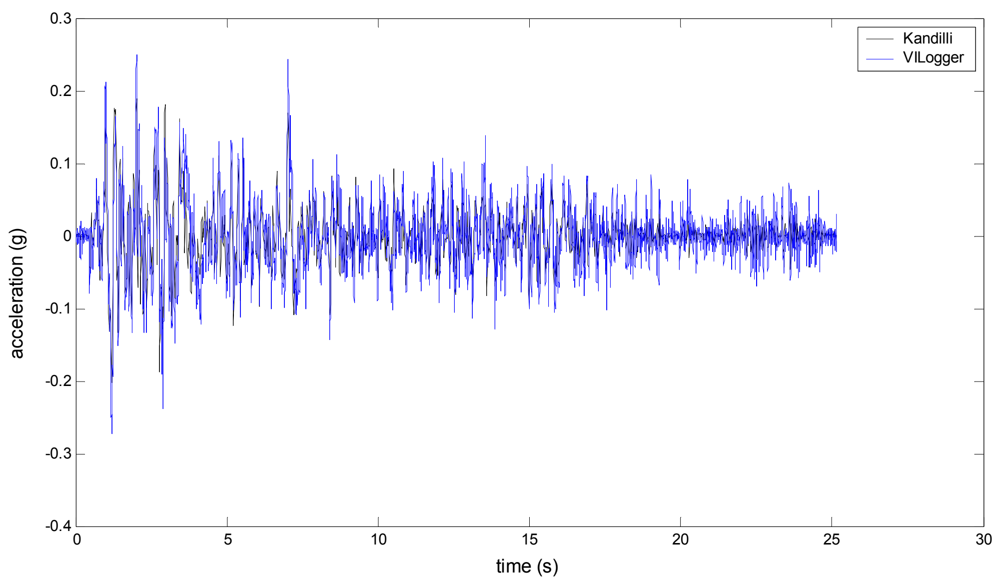

Figure A.38. Measured table acceleration for Test 4 Run 4-6

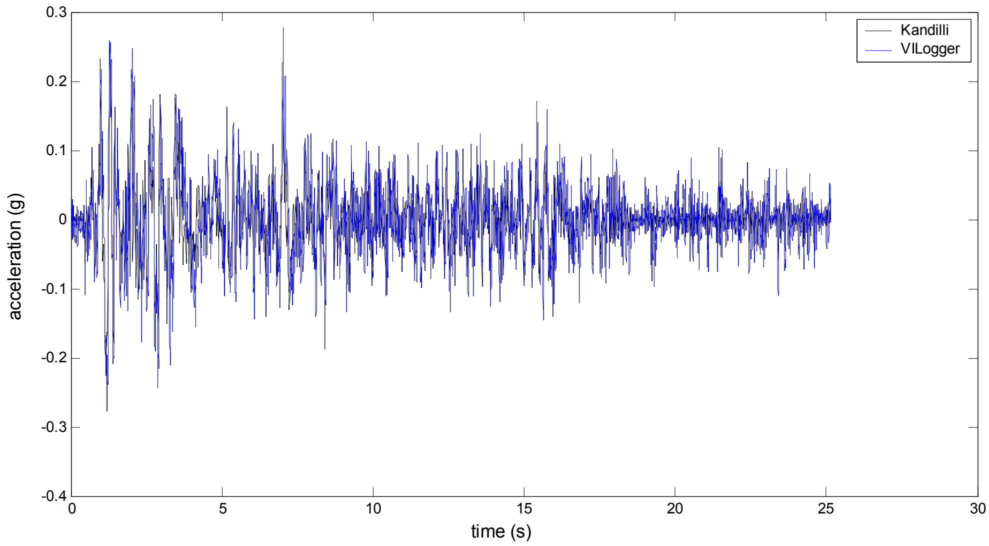

Figure A.39. Measured table acceleration for Test 4 Run 4-7

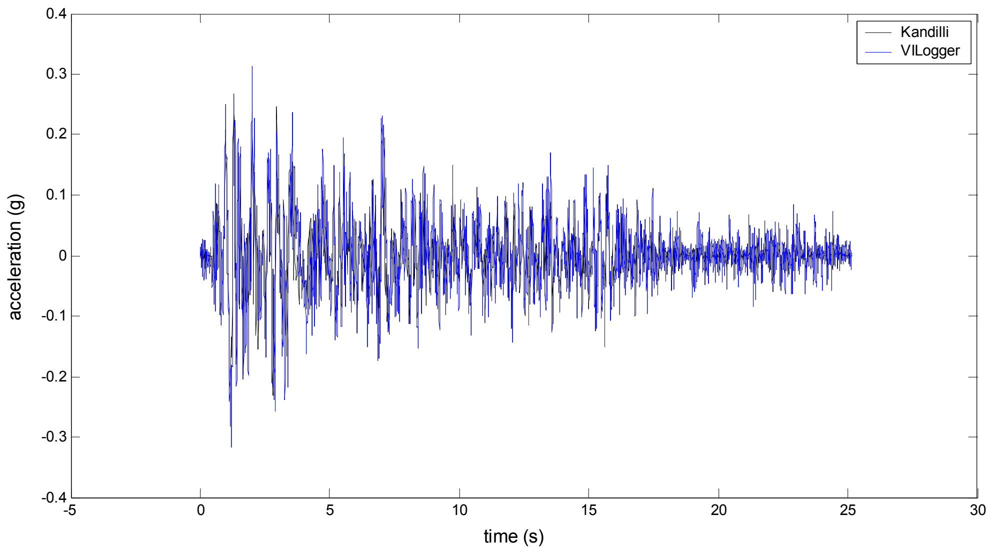

Figure A.40. Measured table acceleration for Test 4 Run 4-8

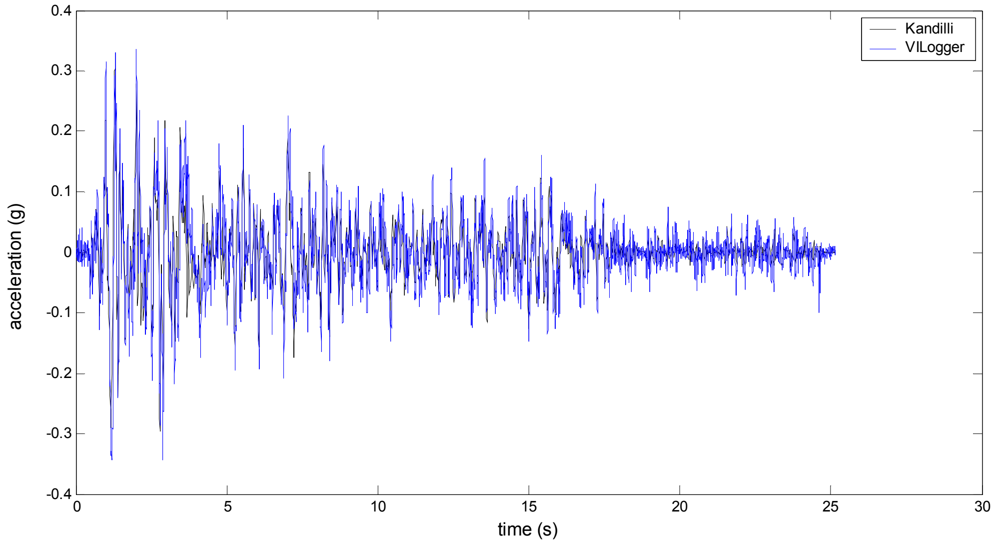

Figure A.41. Measured table acceleration for Test 4 Run 4-9

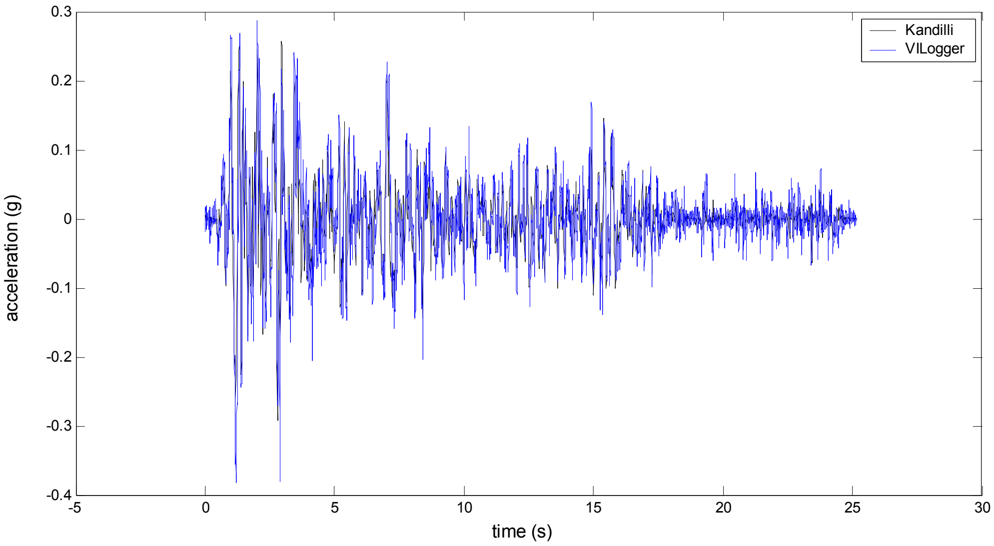

Figure A.42. Measured table acceleration for Test 4 Run 4-10

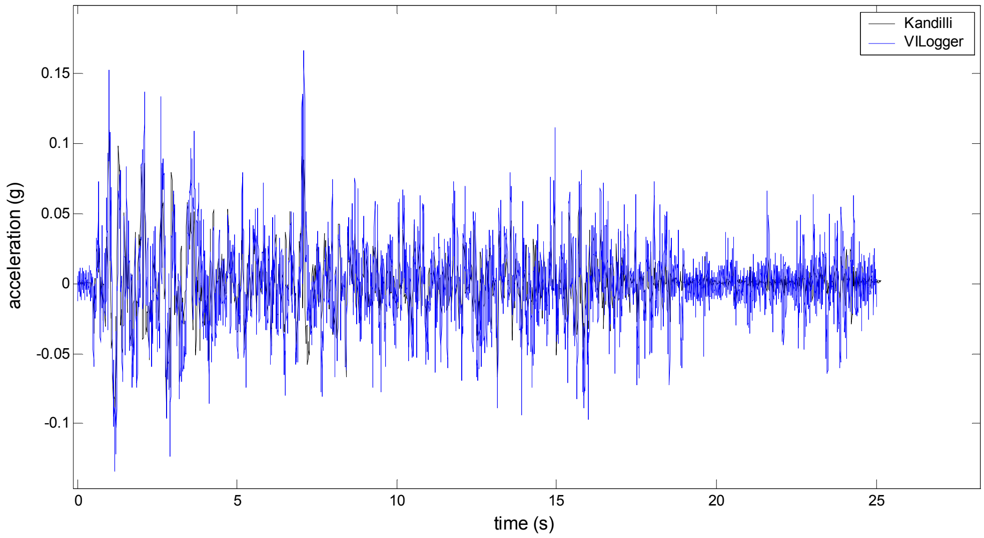

Figure A.43. Measured table acceleration for Test 4 Run 4-11

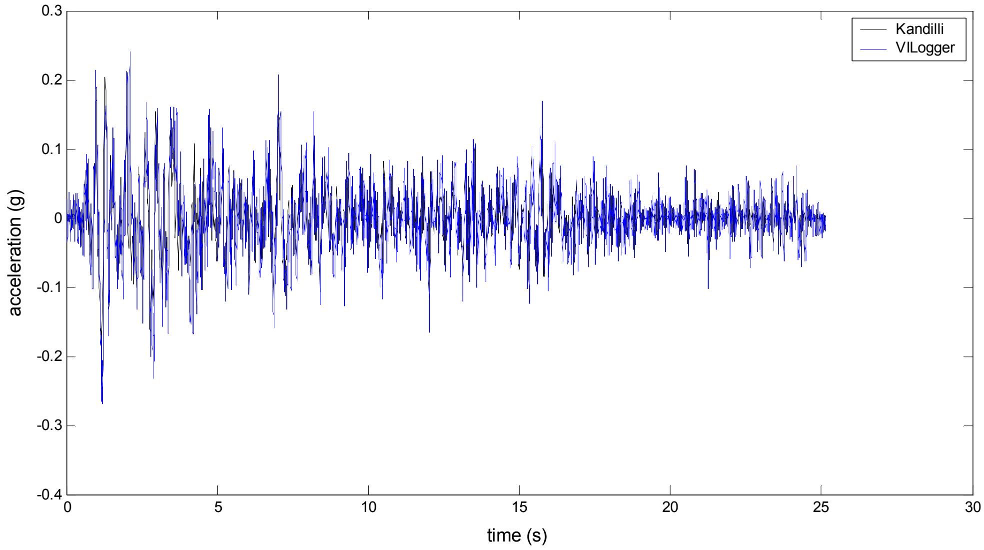

Figure A.44. Measured table acceleration for Test 4 Run 4-12

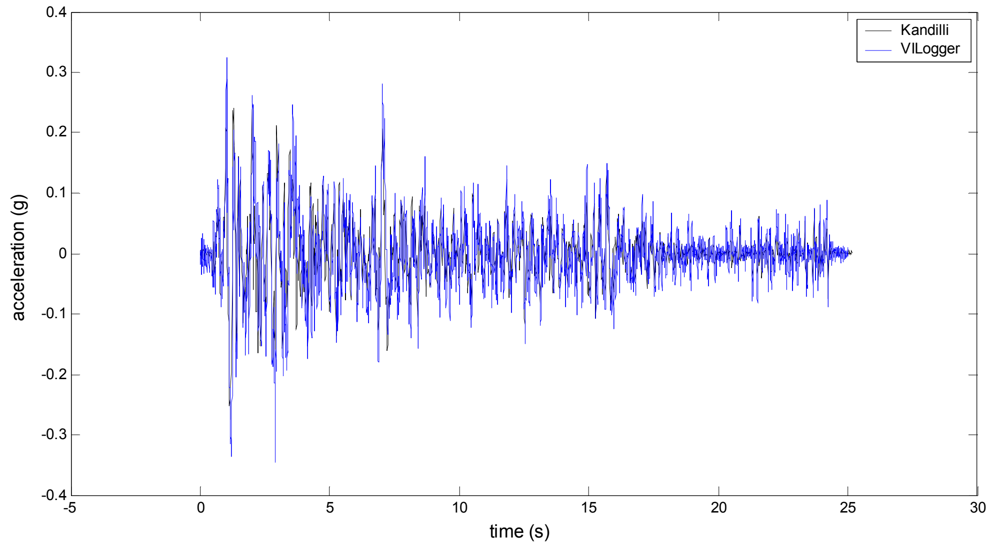

Figure A.45. Measured table acceleration for Test 4 Run 4-13

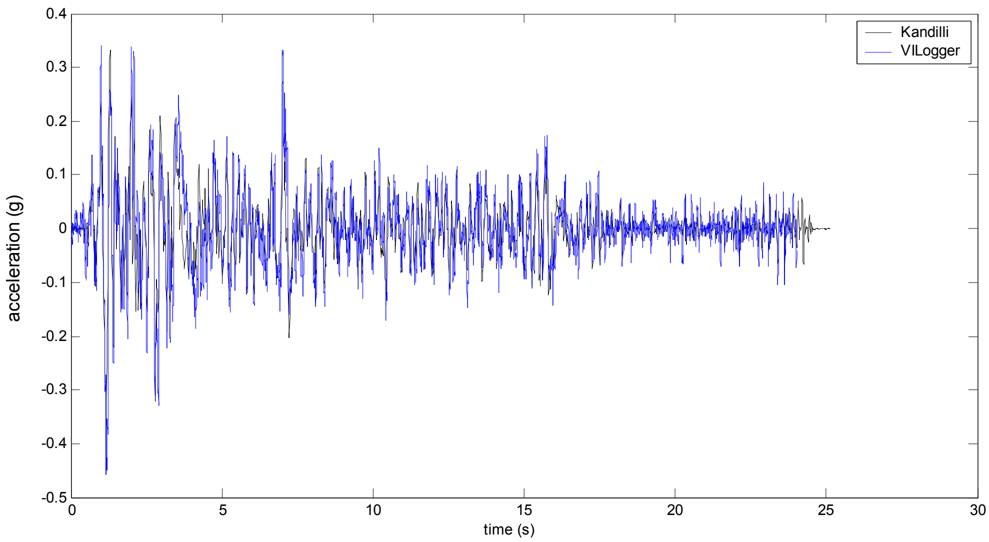

Figure A.46. Measured table acceleration for Test 4 Run 4-14

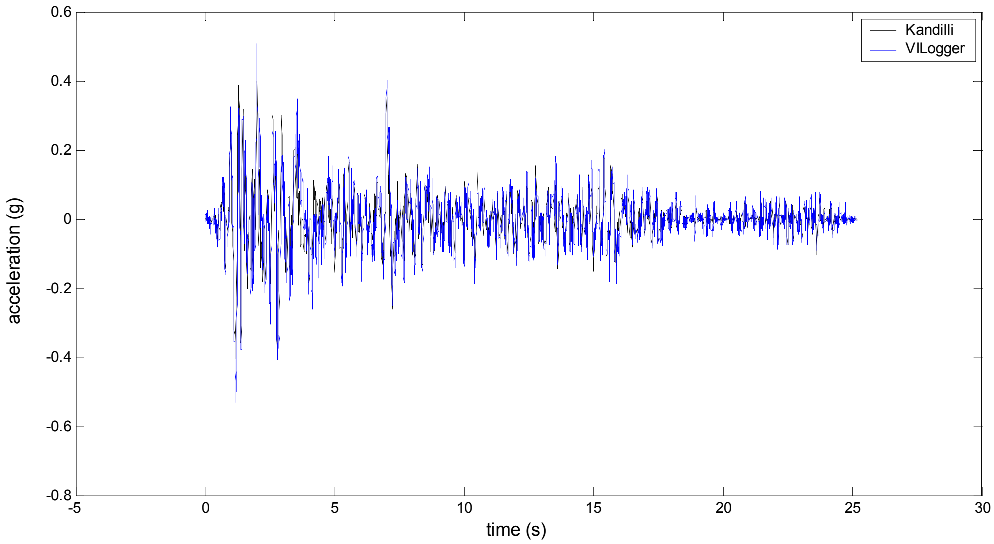

Figure A.47. Measured table acceleration for Test 4 Run 4-15

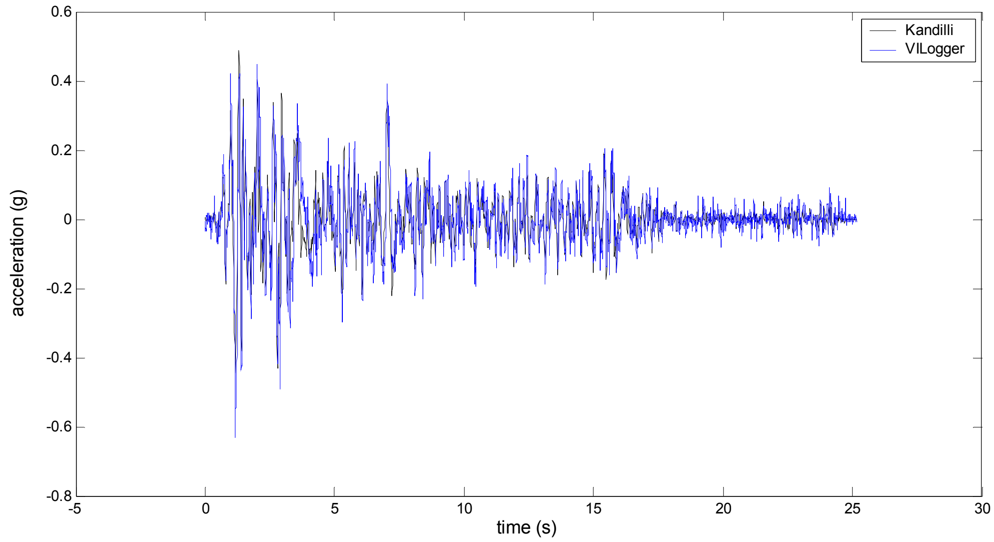

Figure A.48. Measured table acceleration for Test 4 Run 4-16

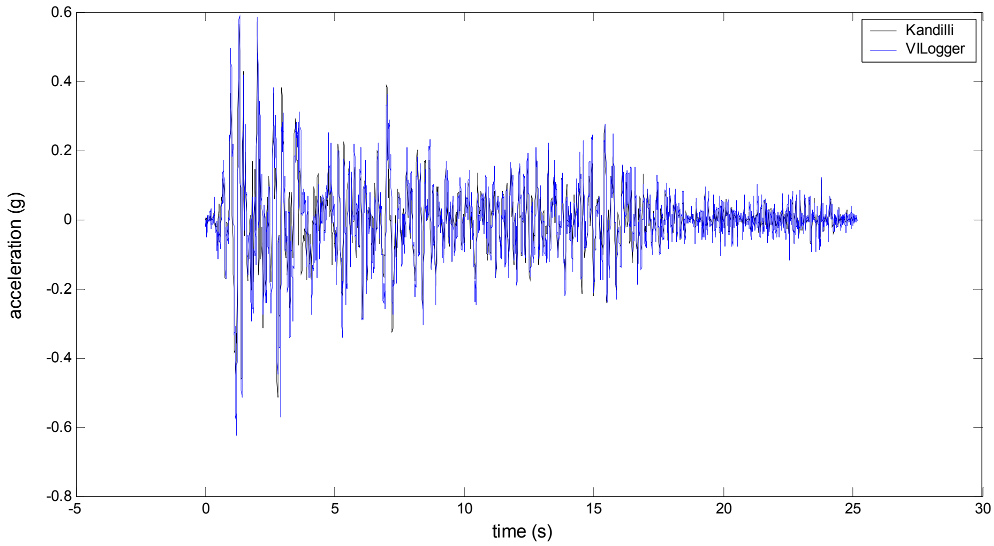

Figure A.49. Measured table acceleration for Test 4 Run 4-17

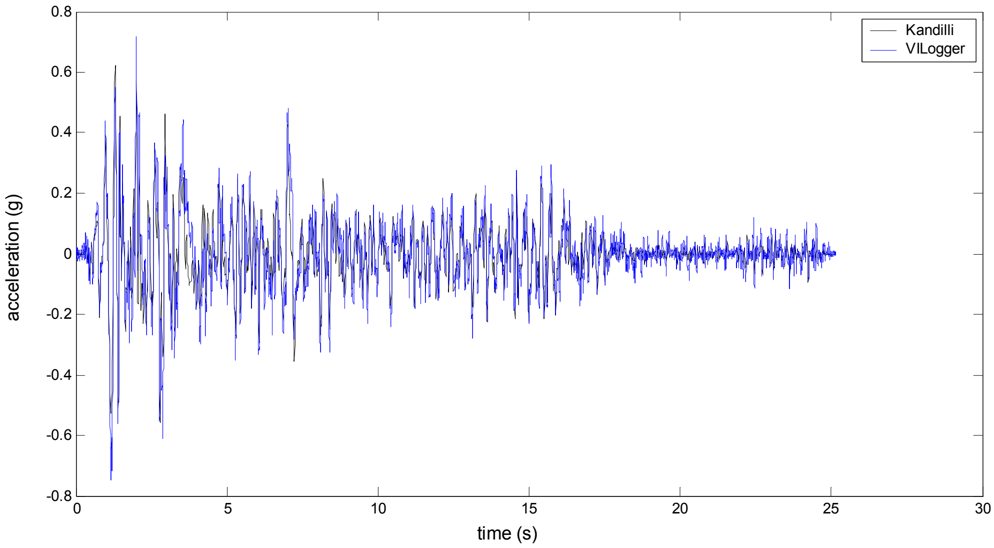

Figure A.50. Measured table acceleration for Test 4 Run 4-18

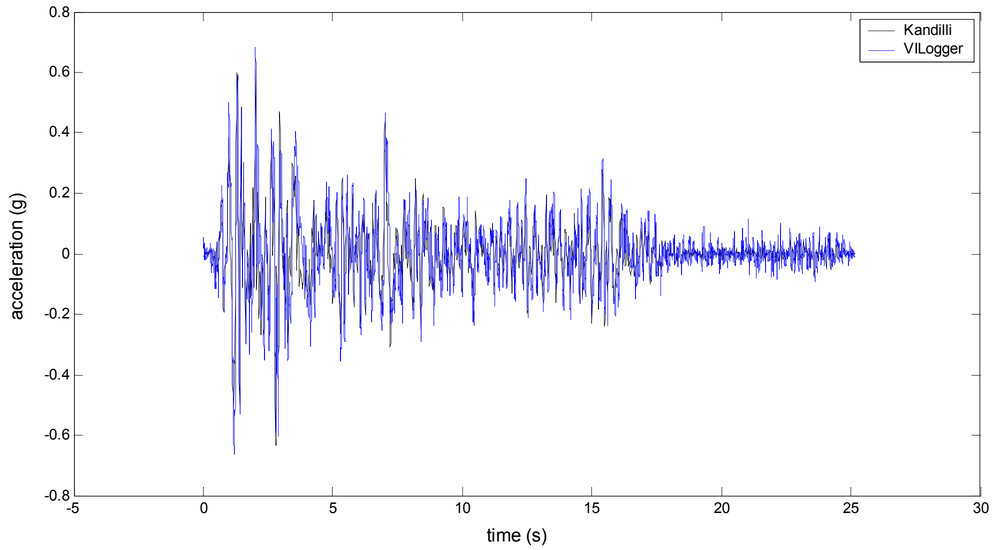

Figure A.51. Measured table acceleration for Test 4 Run 4-19

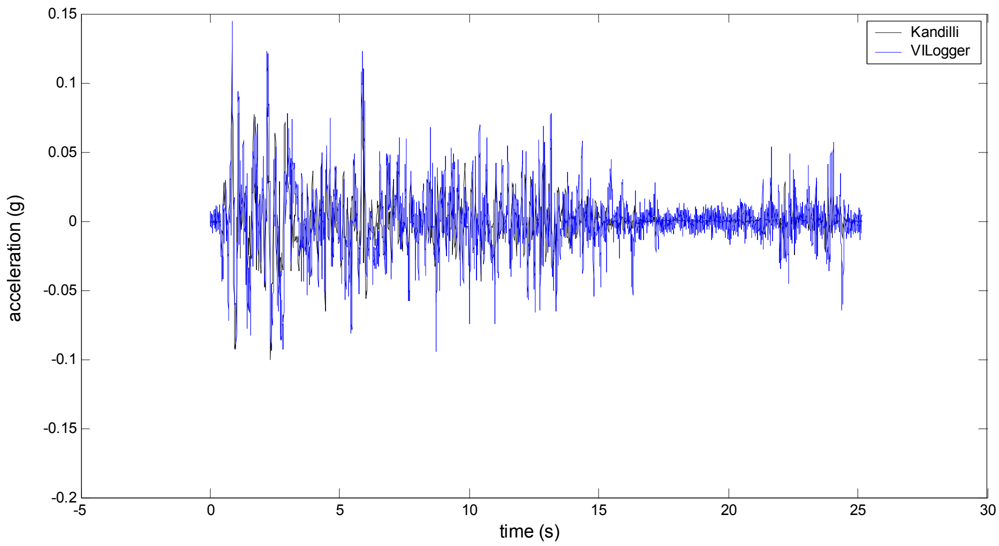

Figure A.52. Measured table acceleration for Test 5 Run 5-1

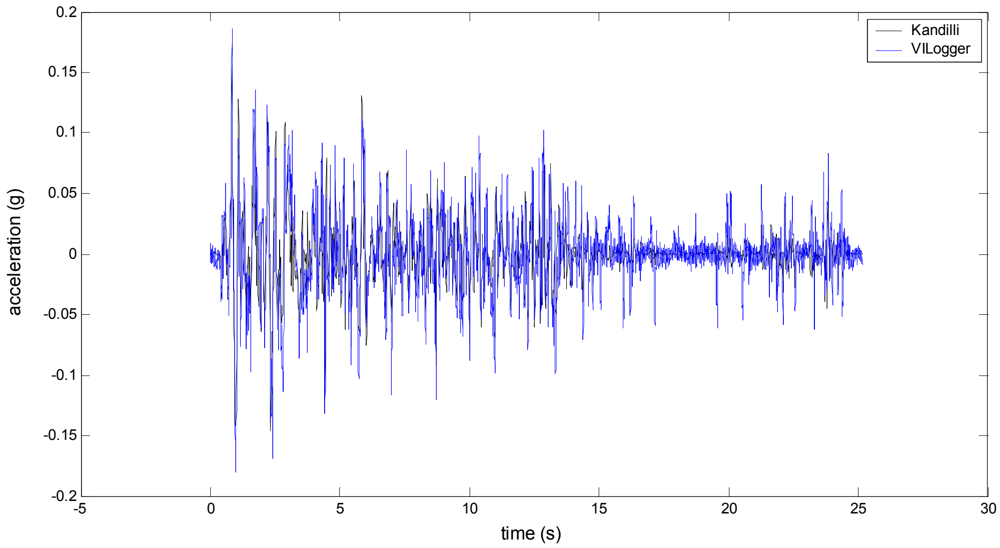

Figure A.53. Measured table acceleration for Test 5 Run 5-2

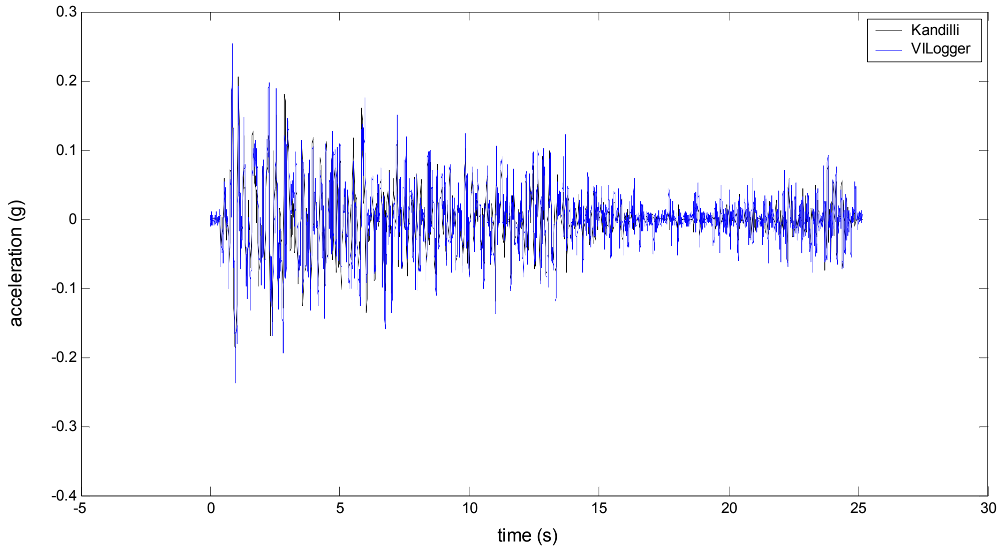

Figure A.54. Measured table acceleration for Test 5 Run 5-3

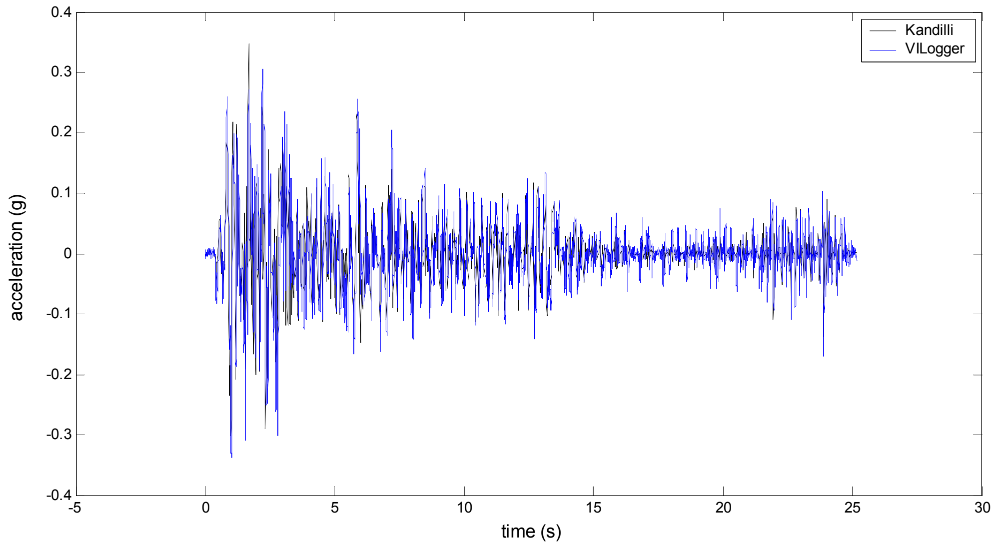

Figure A.55. Measured table acceleration for Test 5 Run 5-4

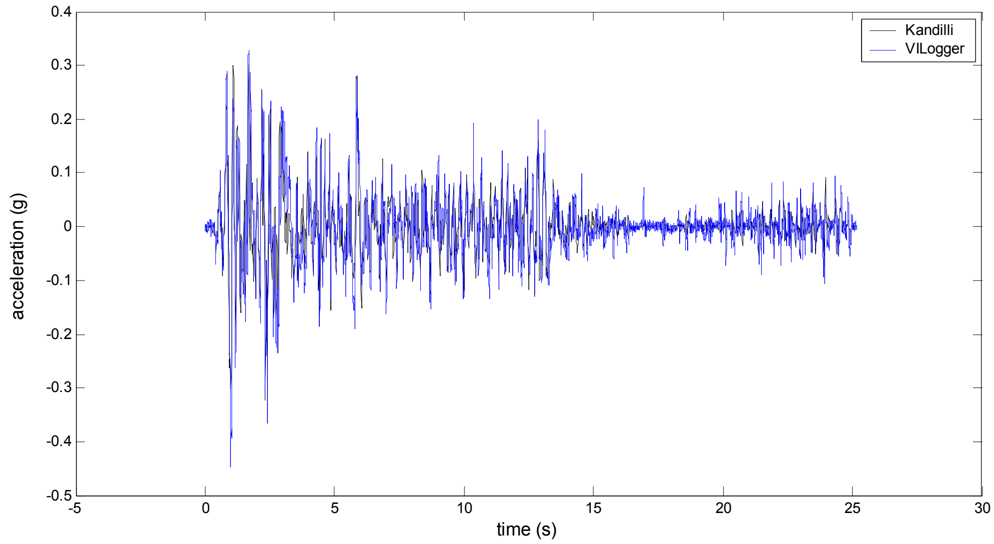

Figure A.56. Measured table acceleration for Test 5 Run 5-5

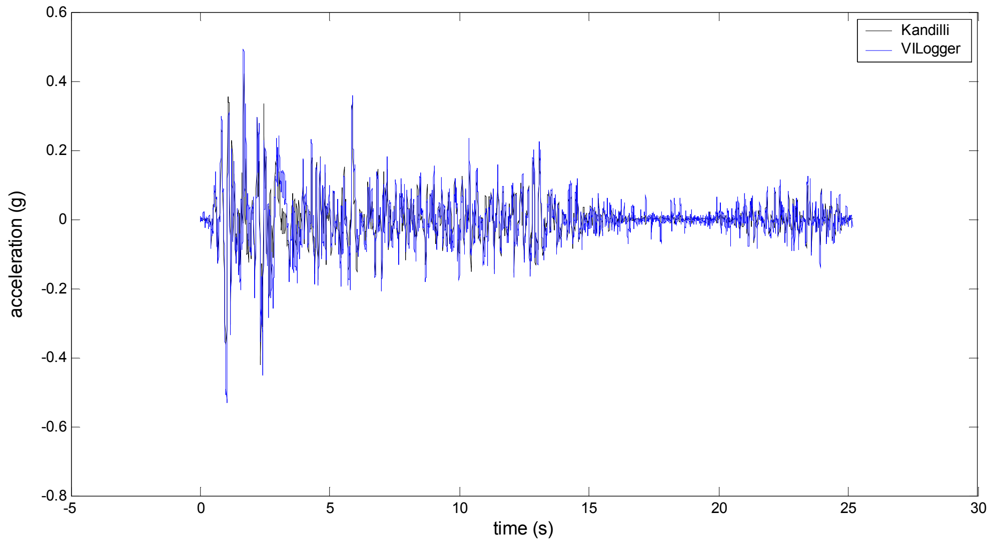

Figure A.57. Measured table acceleration for Test 5 Run 5-6

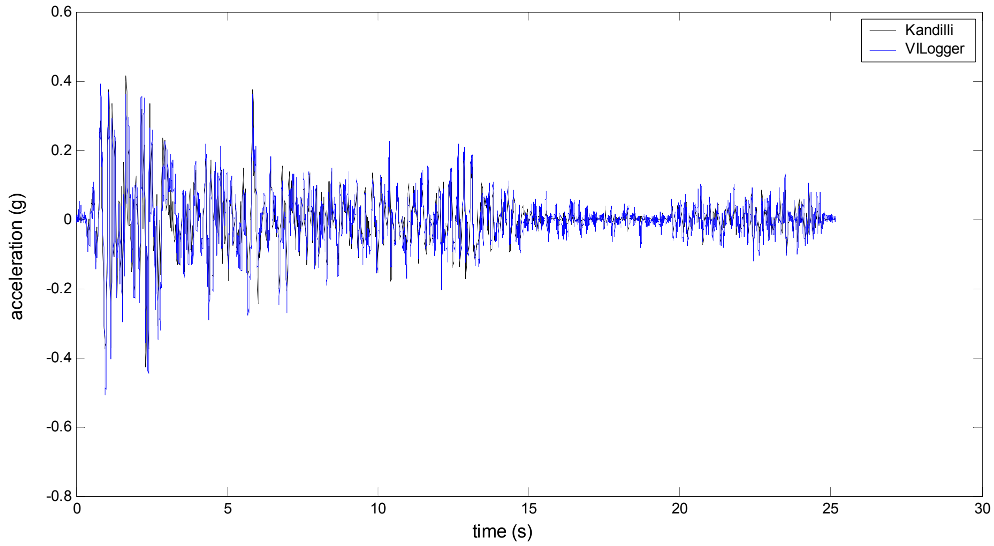

Figure A.58. Measured table acceleration for Test 5 Run 5-7

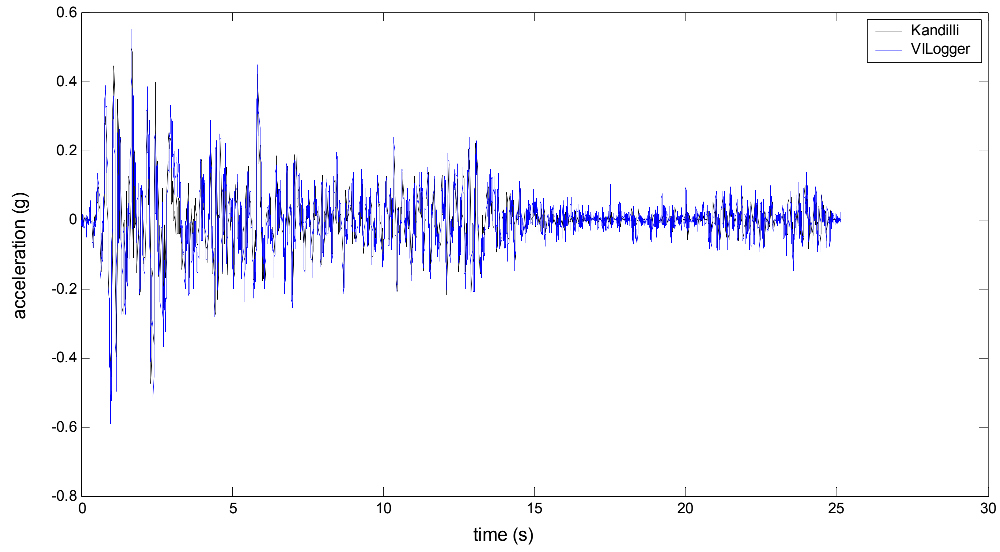

Figure A.59. Measured table acceleration for Test 5 Run 5-8

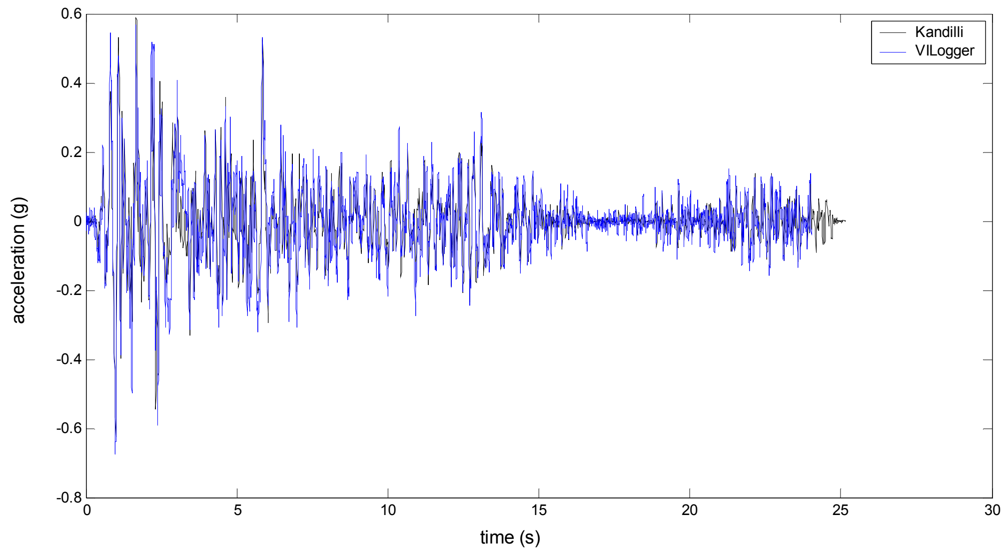

Figure A.60. Measured table acceleration for Test 5 Run 5-9

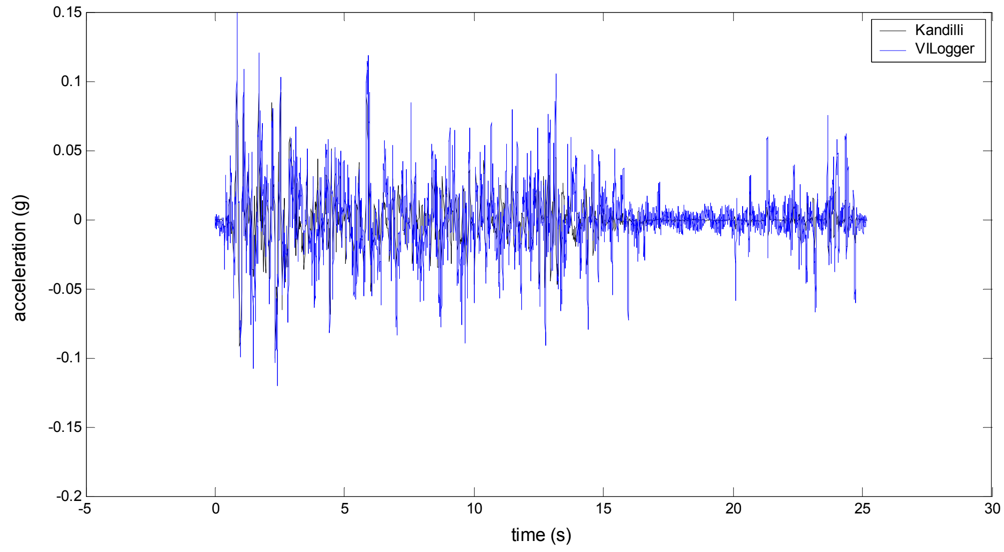

Figure A.61. Measured table acceleration for Test 6 Run 6-1

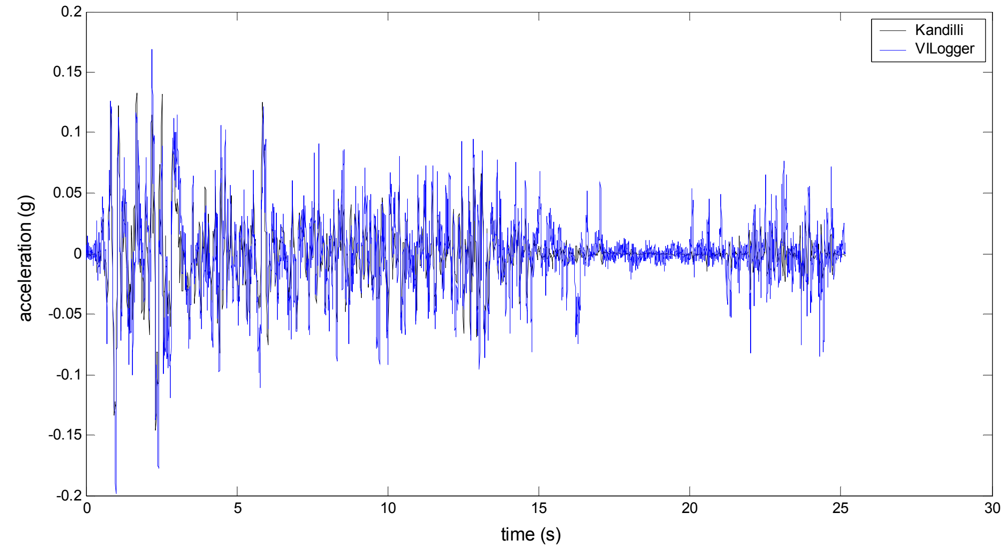

Figure A.62. Measured table acceleration for Test 6 Run 6-2

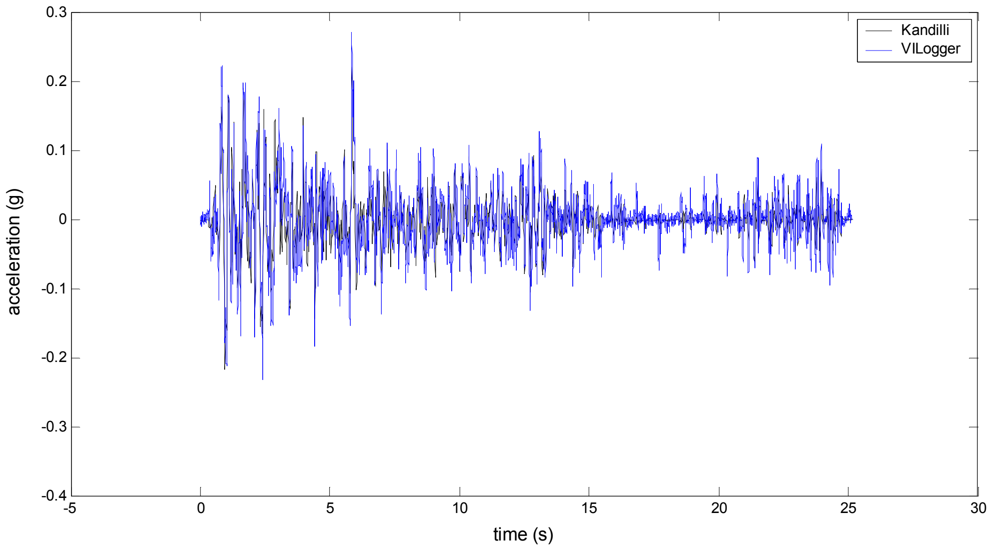

Figure A.63. Measured table acceleration for Test 6 Run 6-3

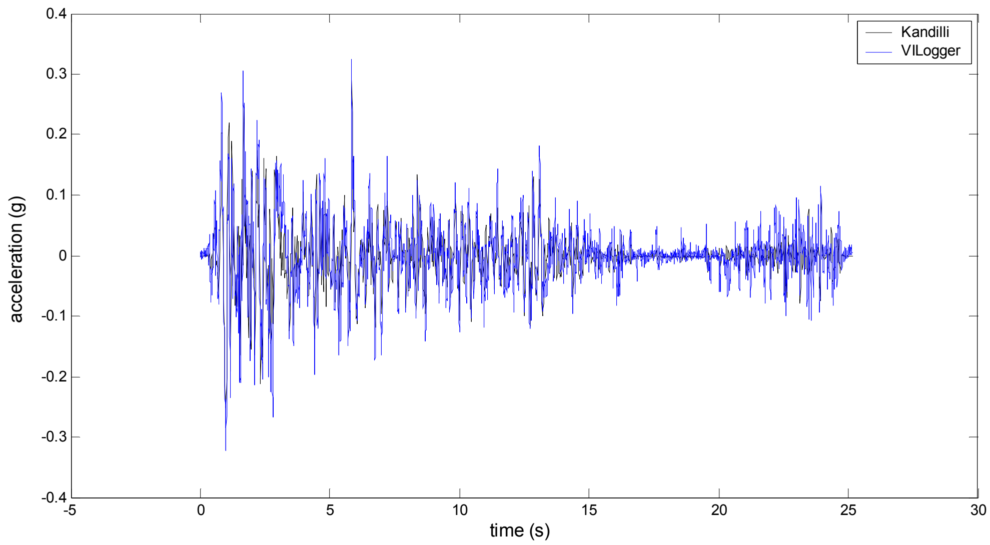

Figure A.64. Measured table acceleration for Test 6 Run 6-4

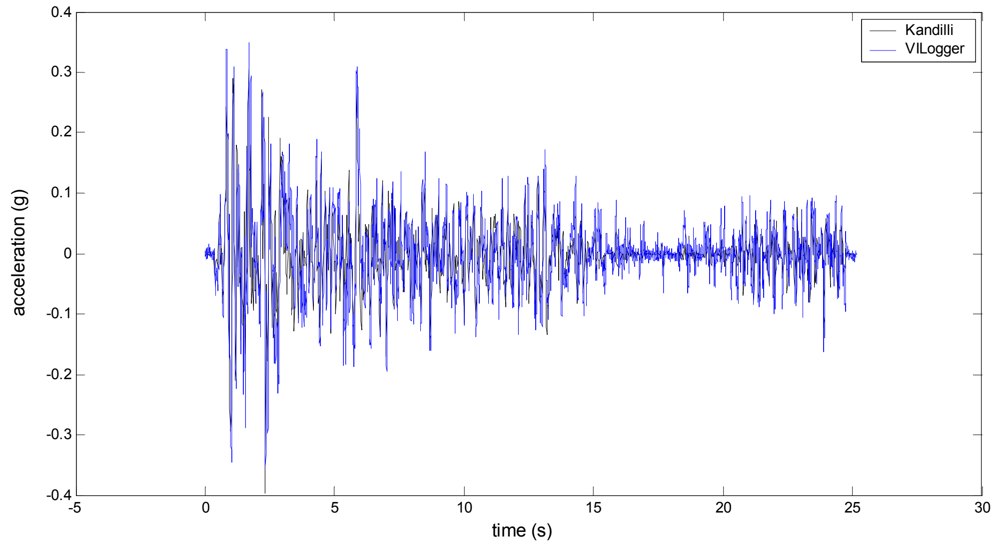

Figure A.65. Measured table acceleration for Test 6 Run 6-5

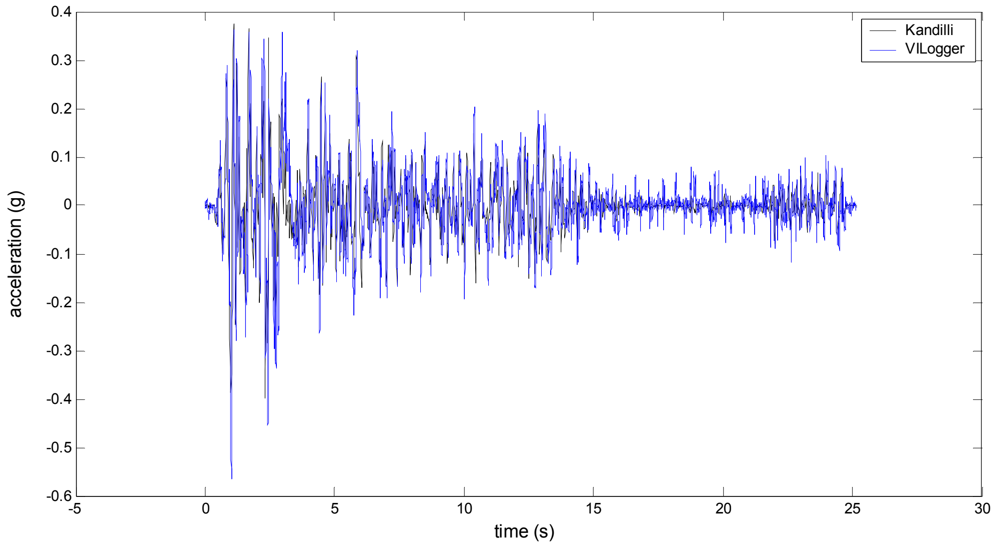

Figure A.66. Measured table acceleration for Test 6 Run 6-6

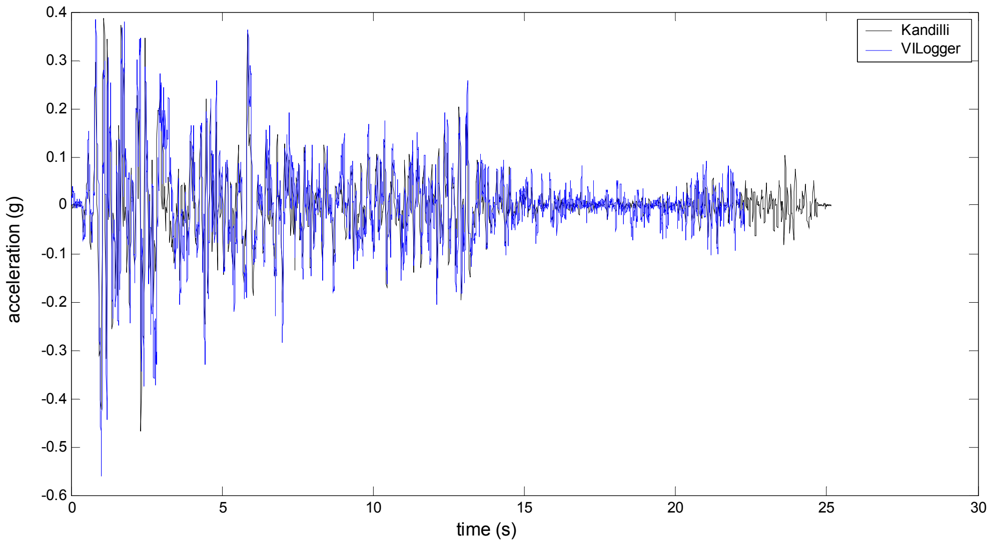

Figure A.67. Measured table acceleration for Test 6 Run 6-7

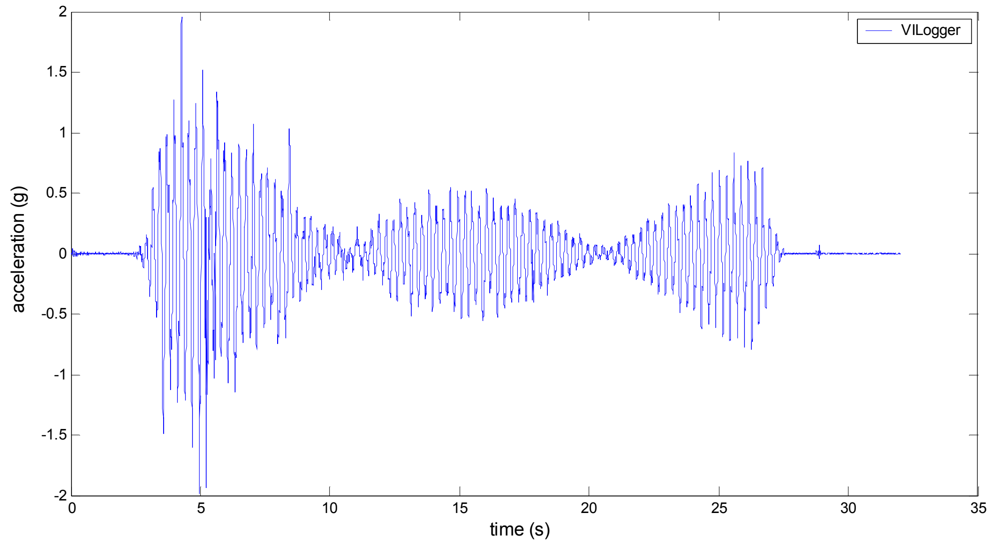

Figure A.68. Measured table acceleration for Test 6 Run 6-8

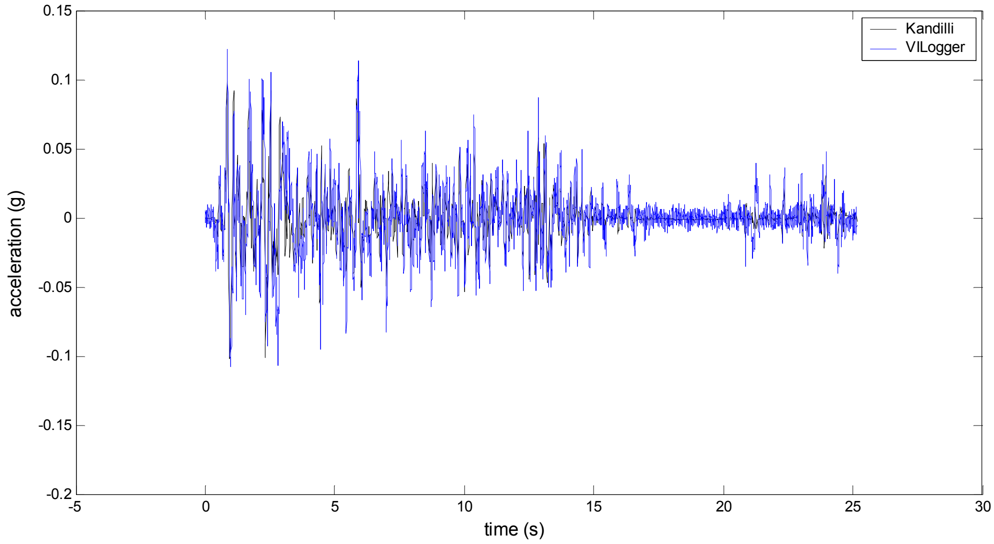

Figure A.69. Measured table acceleration for Test 7 Run 7-1

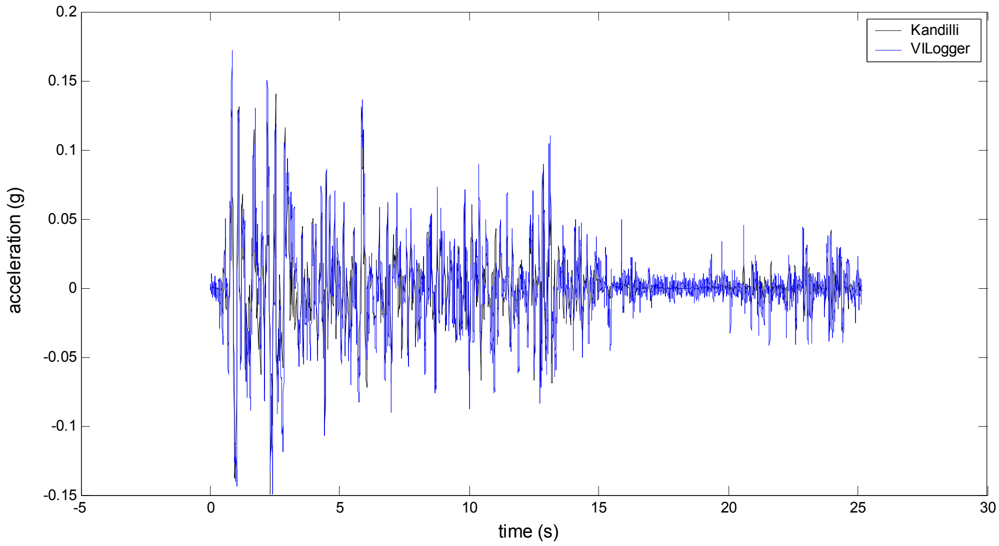

Figure A.70. Measured table acceleration for Test 7 Run 7-2

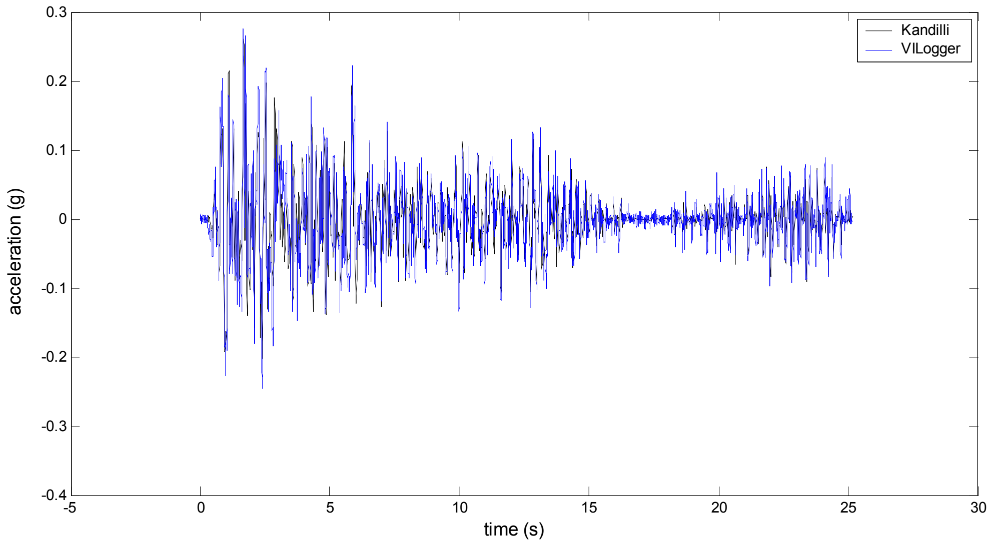

Figure A.71. Measured table acceleration for Test 7 Run 7-3

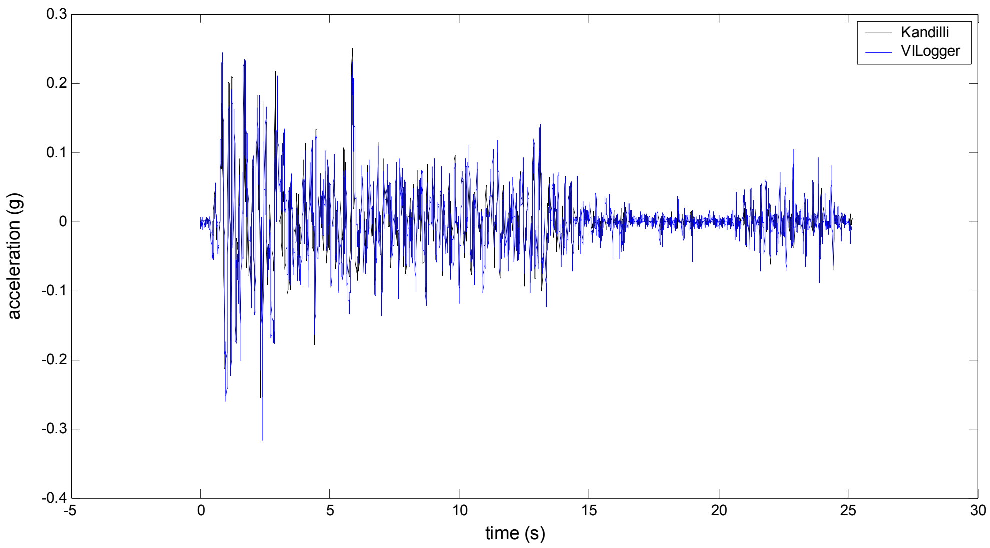

Figure A.72. Measured table acceleration for Test 7 Run 7-4

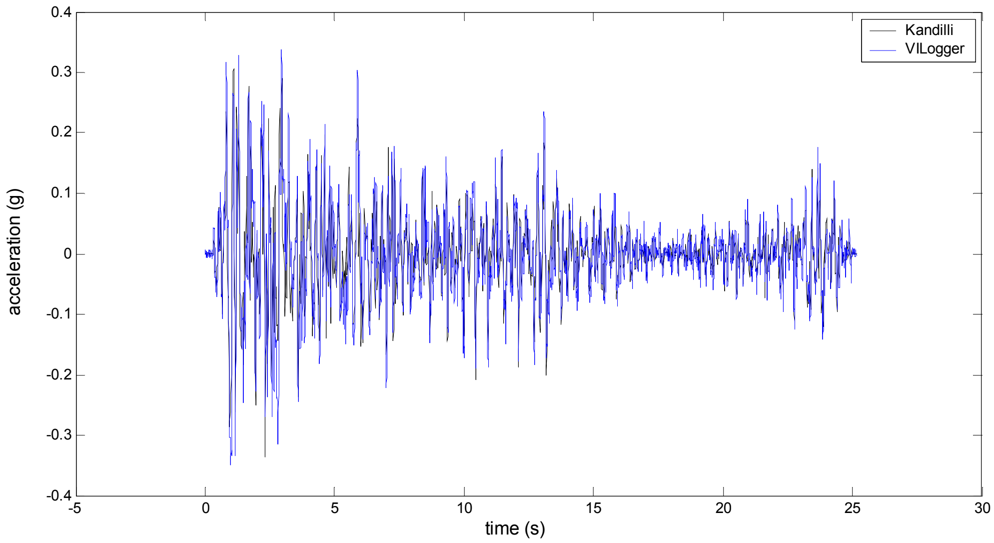

Figure A.73. Measured table acceleration for Test 7 Run 7-5

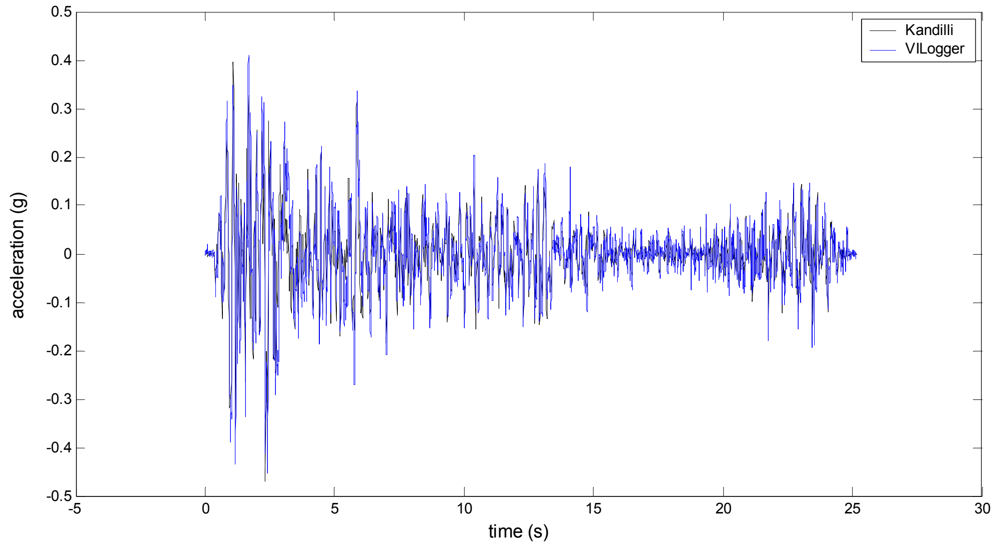

Figure A.74. Measured table acceleration for Test 7 Run 7-6

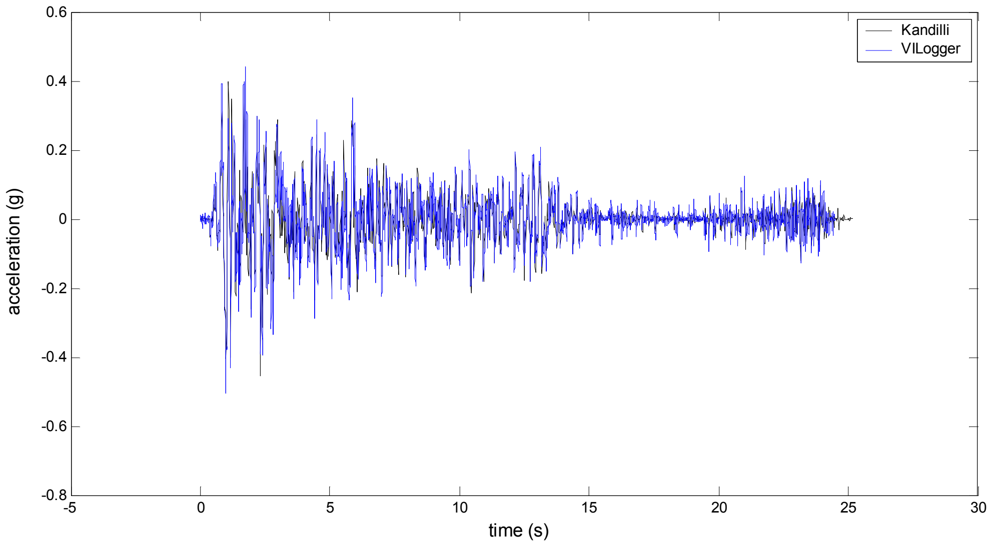

Figure A.75. Measured table acceleration for Test 7 Run 7-7

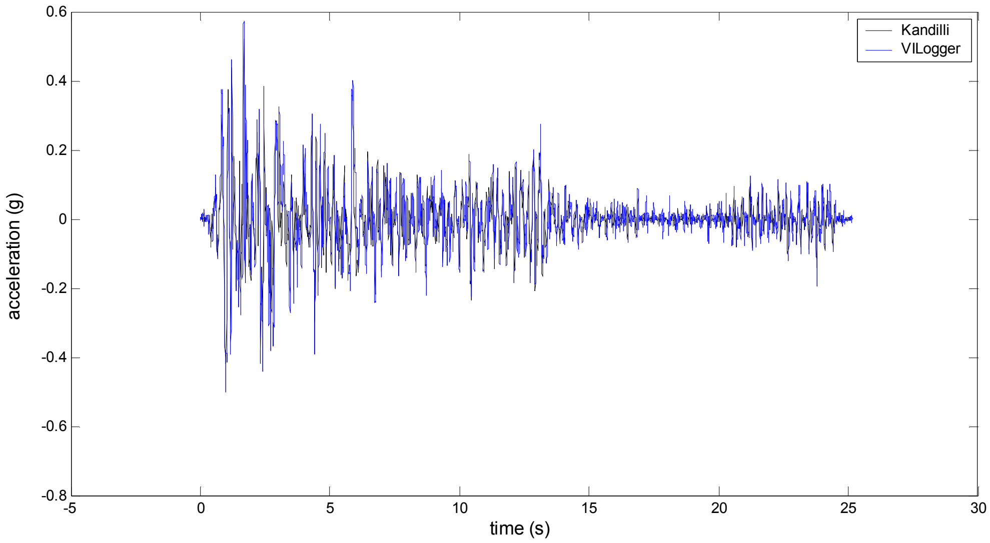

Figure A.76. Measured table acceleration for Test 7 Run 7-8

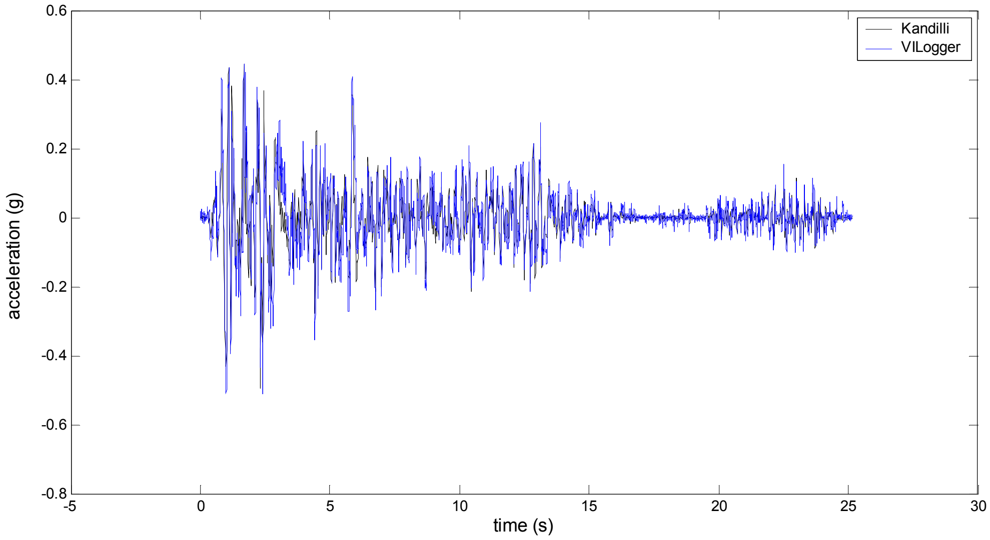

Figure A.77. Measured table acceleration for Test 7 Run 7-9

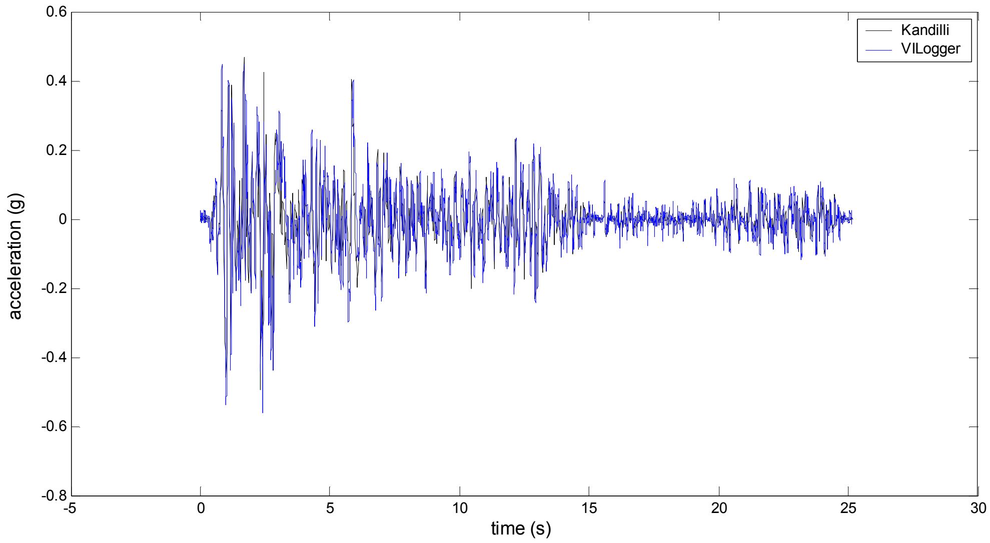

Figure A.78. Measured table acceleration for Test 7 Run 7-10

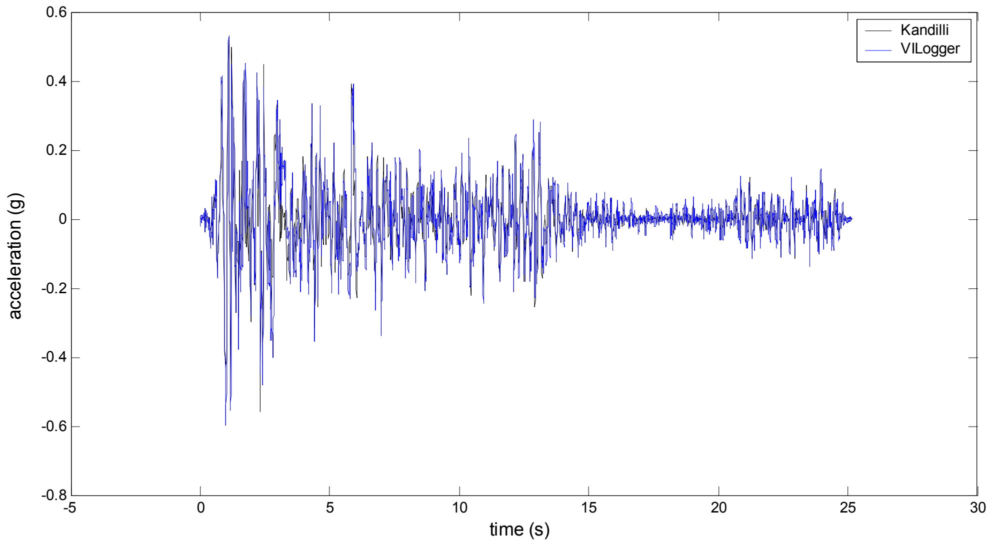

Figure A.79. Measured table acceleration for Test 7 Run 7-11

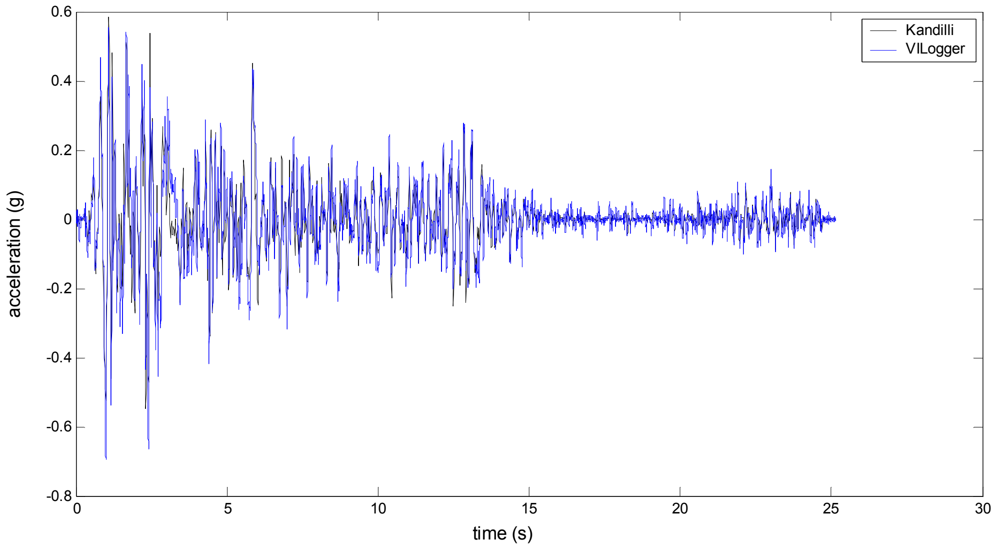

Figure A.80. Measured table acceleration for Test 7 Run 7-12

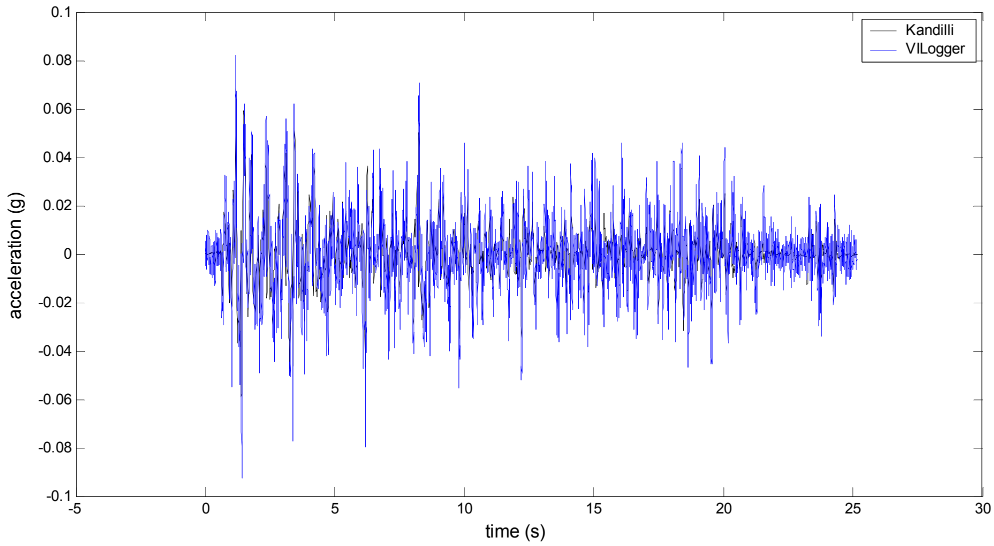

Figure A.81. Measured table acceleration for Test 8 Run 8a-1

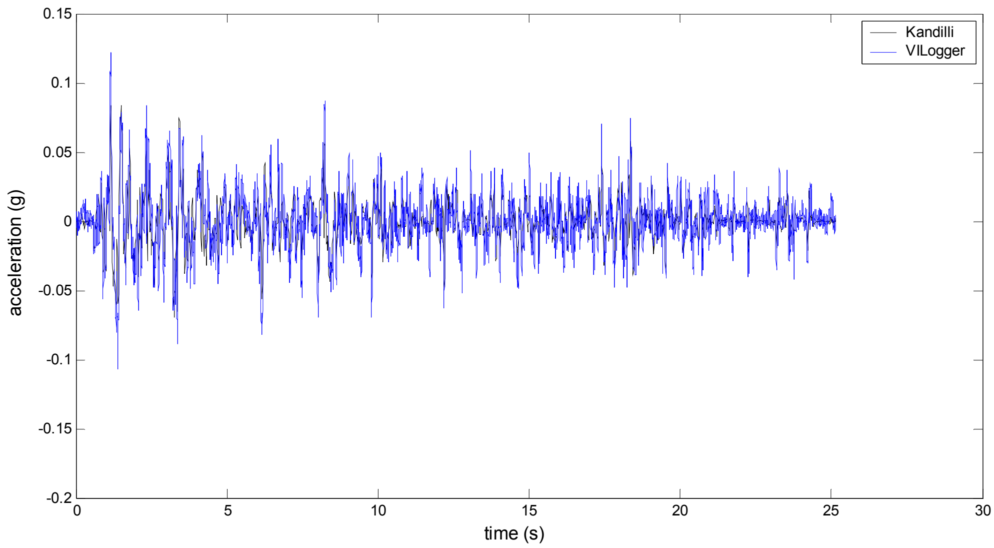

Figure A.82. Measured table acceleration for Test 8 Run 8a-2

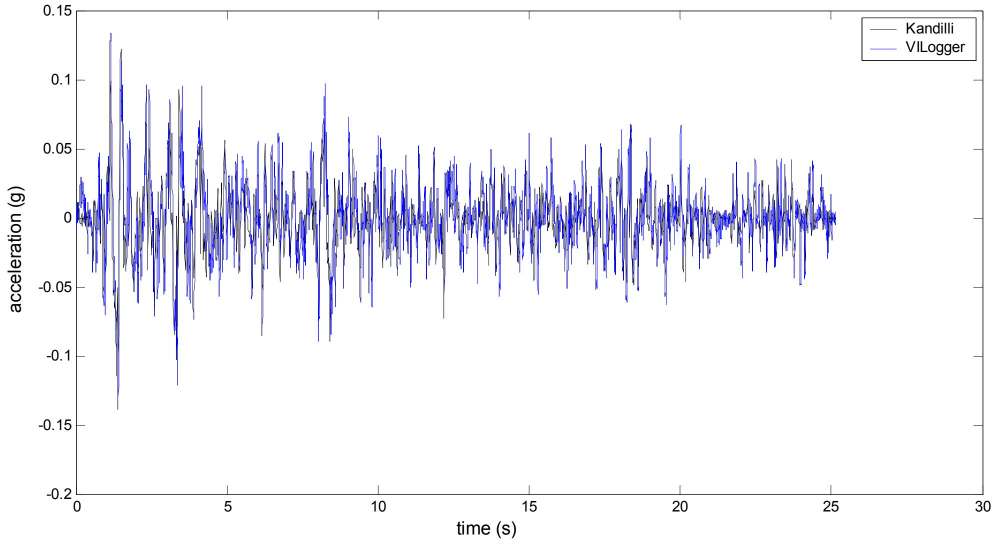

Figure A.83. Measured table acceleration for Test 8 Run 8a-3

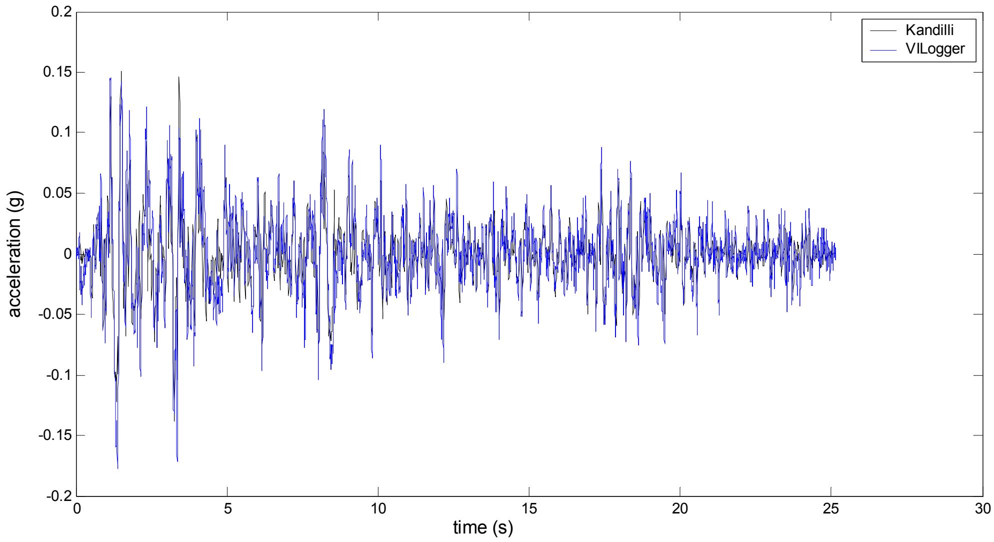

Figure A.84. Measured table acceleration for Test 8 Run 8a-4

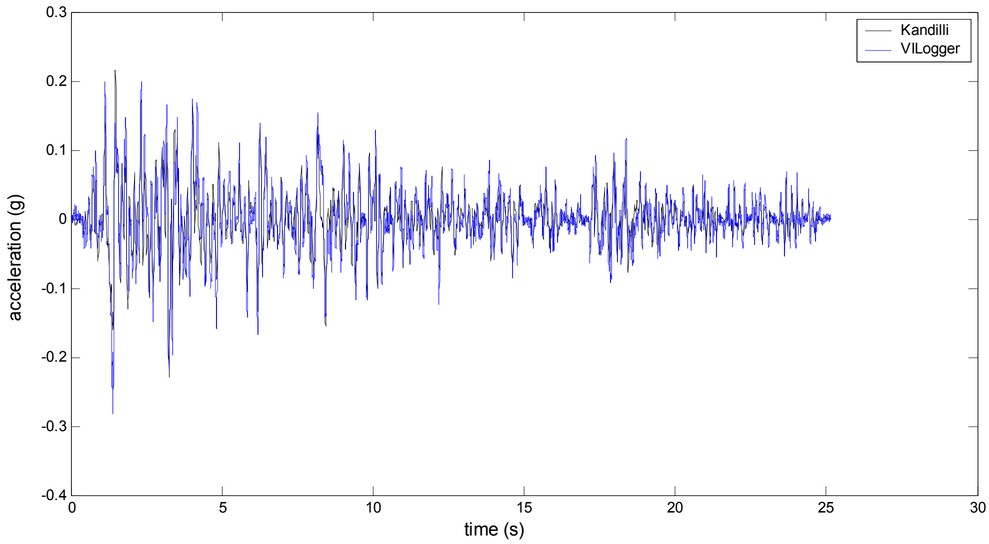

Figure A.85. Measured table acceleration for Test 8 Run 8a-5

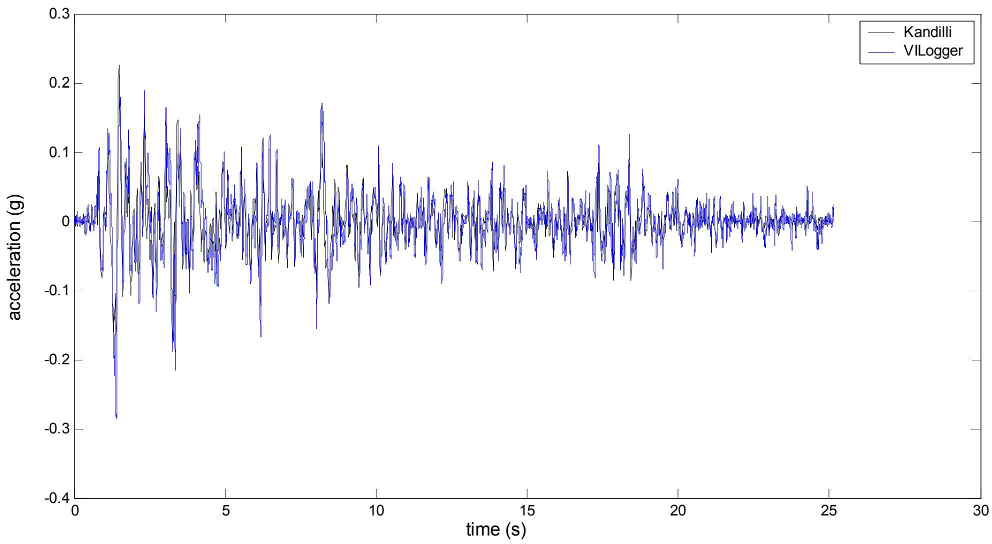

Figure A.86. Measured table acceleration for Test 8 Run 8a-6

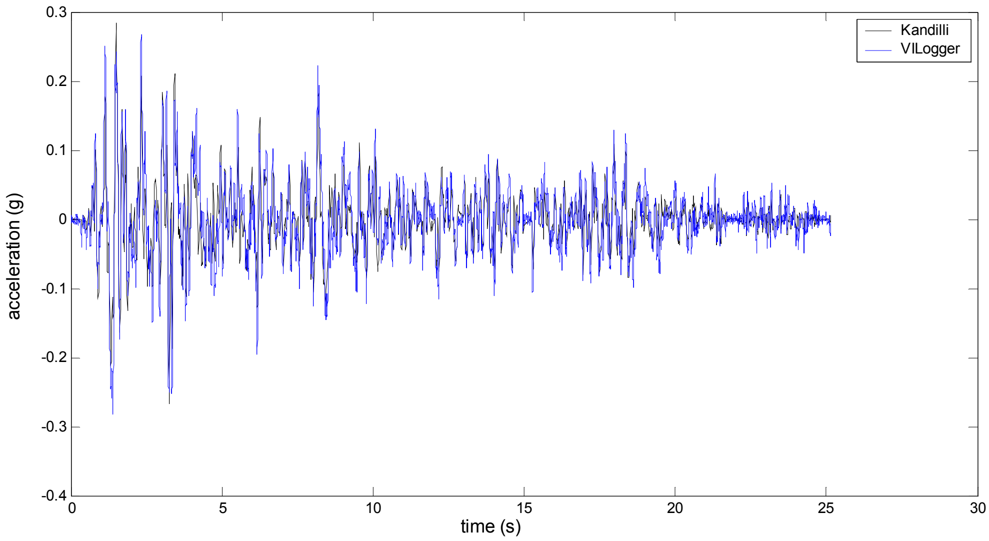

Figure A.87. Measured table acceleration for Test 8 Run 8a-7

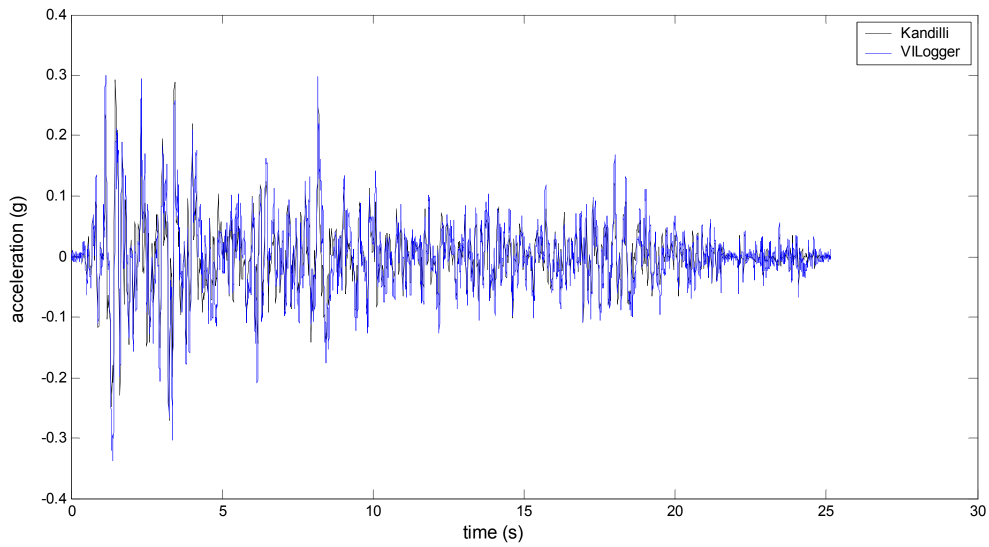

Figure A.88. Measured table acceleration for Test 8 Run 8a-8

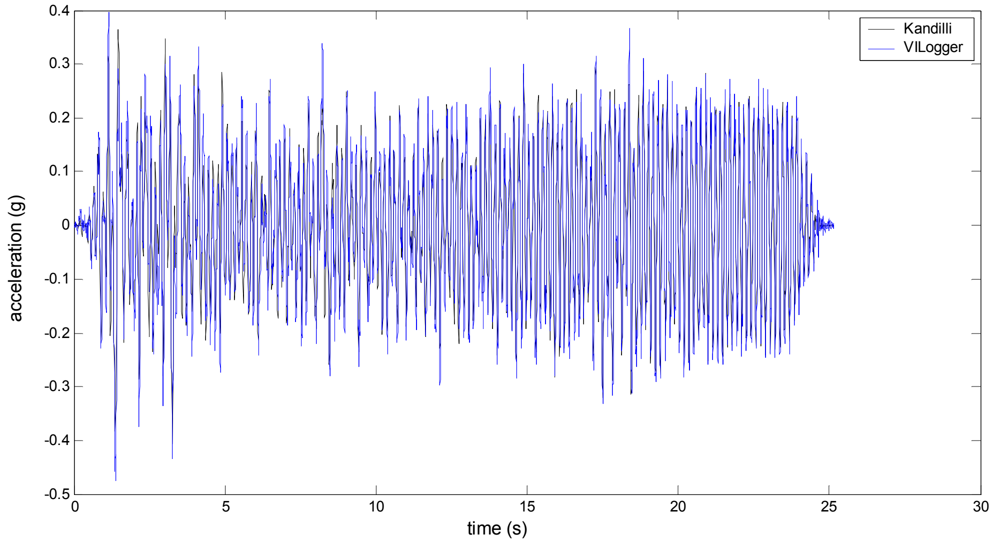

Figure A.89. Measured table acceleration for Test 8 Run 8a-9

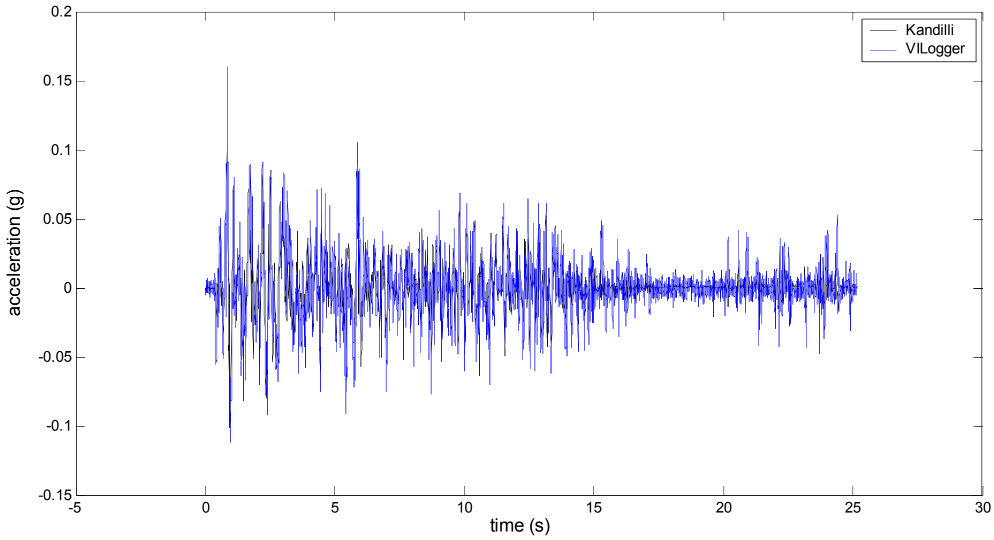

Figure A.90. Measured table acceleration for Test 8 Run 8b-1

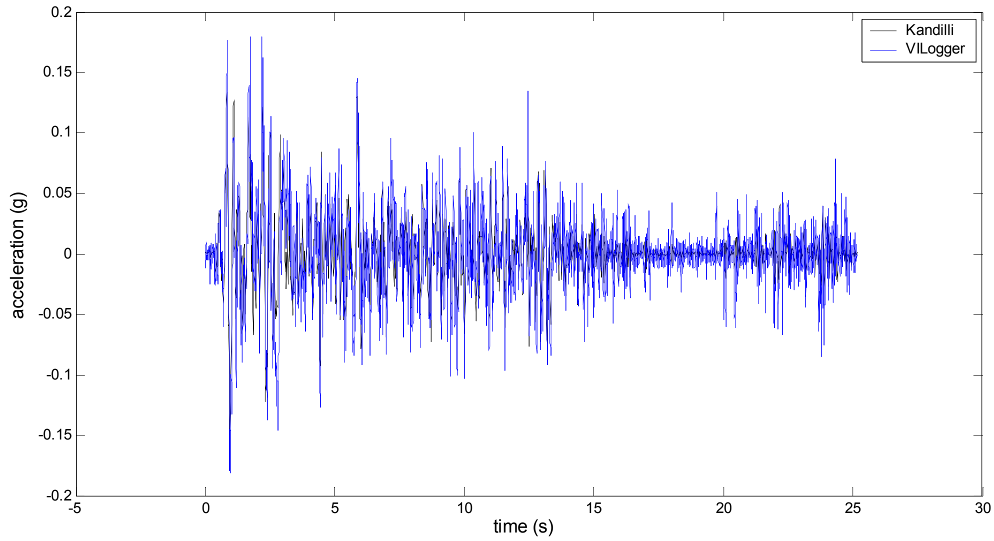

Figure A.91. Measured table acceleration for Test 8 Run 8b-2

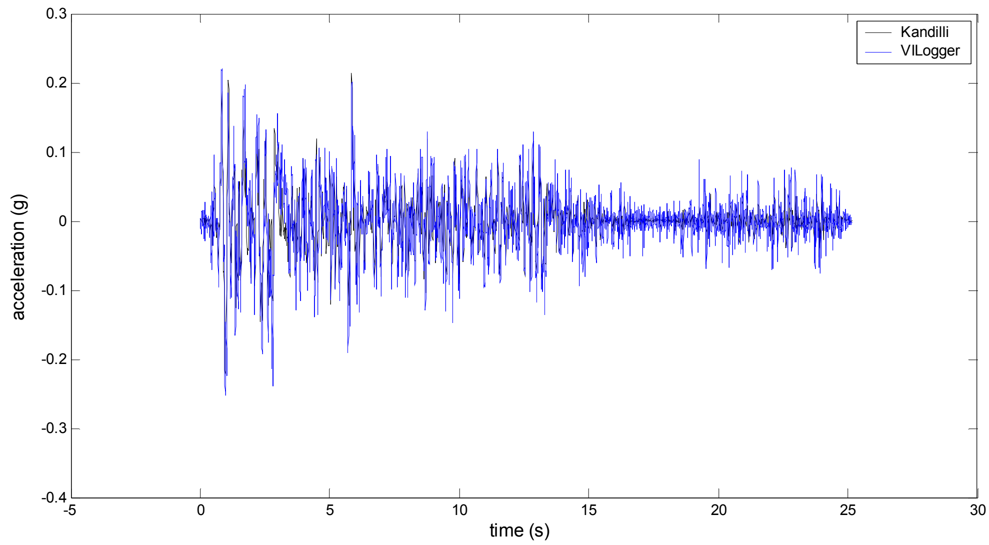

Figure A.92. Measured table acceleration for Test 8 Run 8b-3

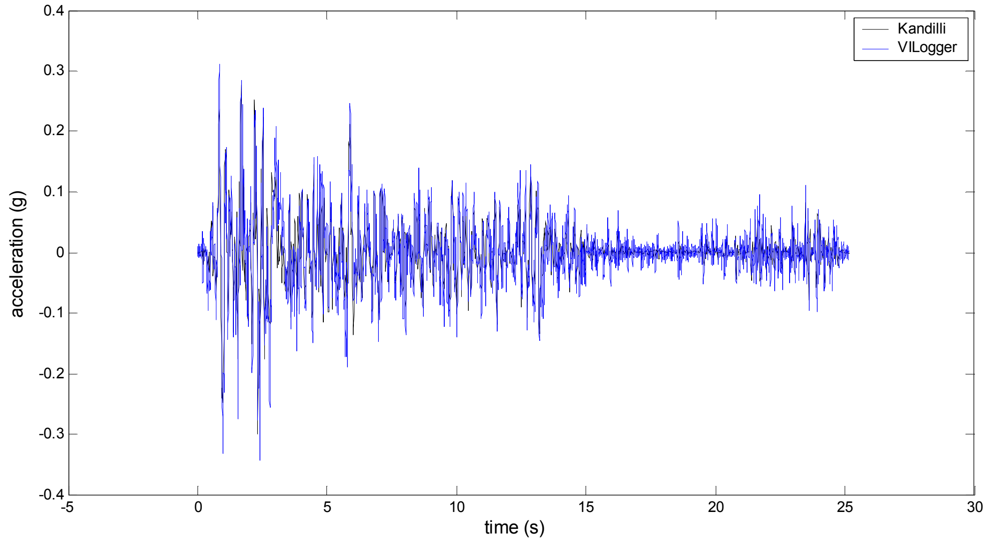

Figure A.93. Measured table acceleration for Test 8 Run 8b-4

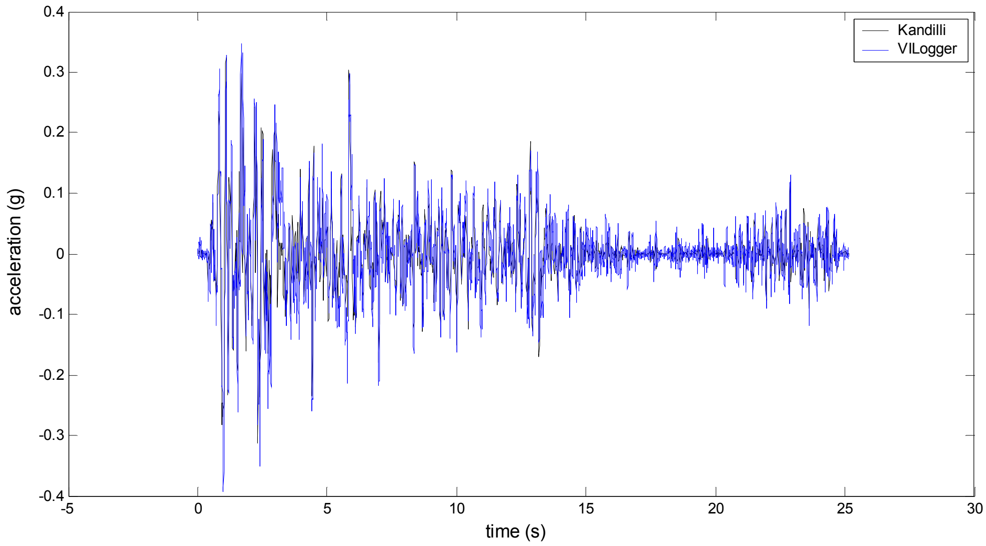

Figure A.94. Measured table acceleration for Test 8 Run 8b-5

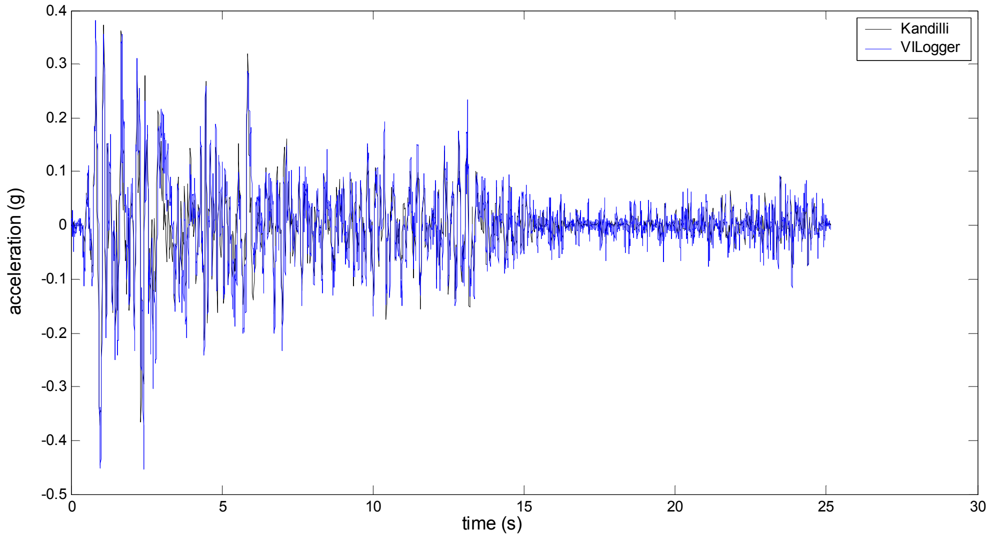

Figure A.95. Measured table acceleration for Test 8 Run 8b-6

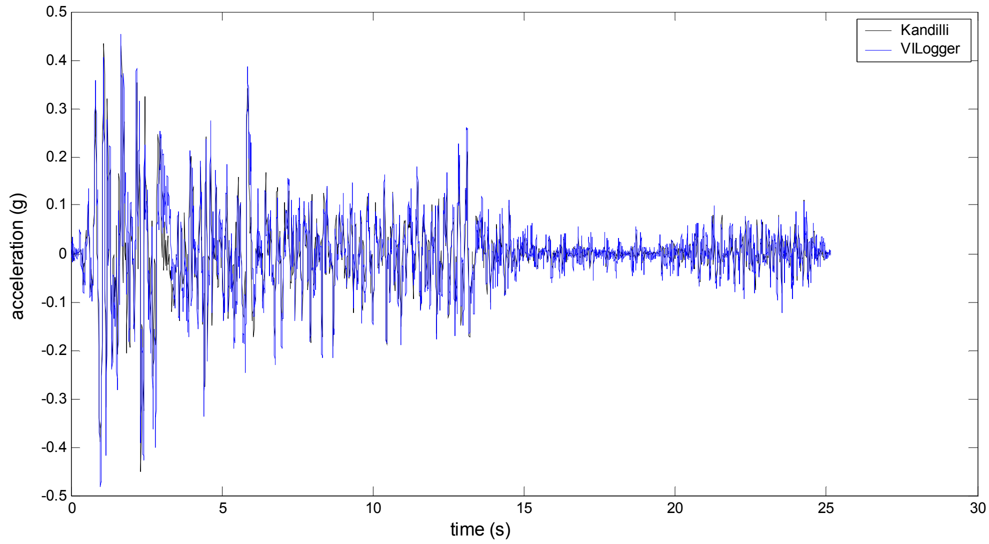

Figure A.96. Measured table acceleration for Test 8 Run 8b-7

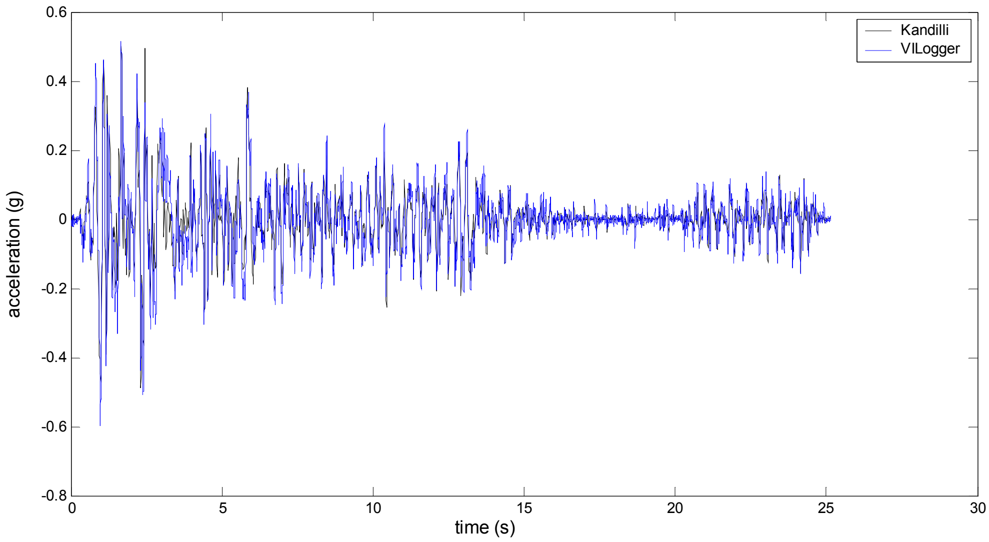

Figure A.97. Measured table acceleration for Test 8 Run 8b-8

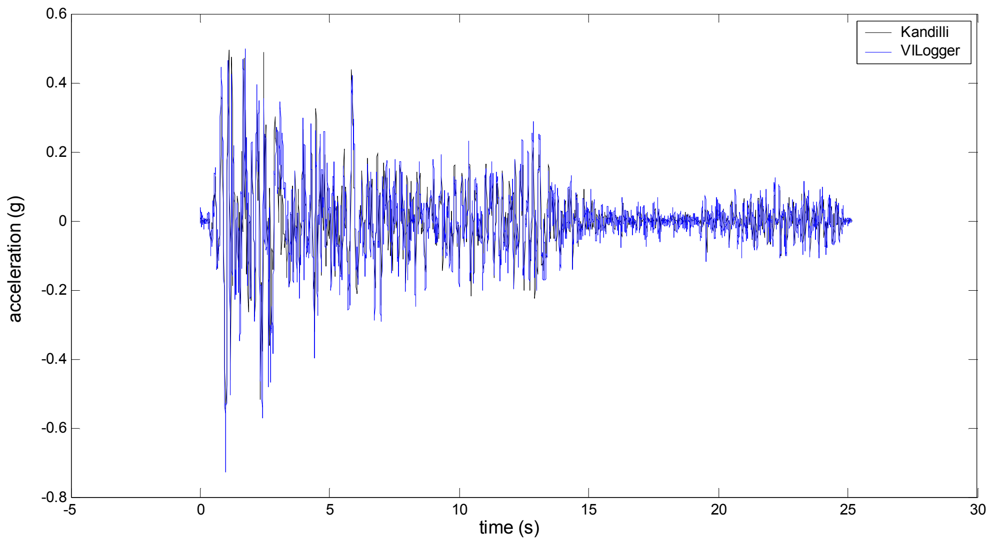

Figure A.98. Measured table acceleration for Test 8 Run 8b-9

APPENDIX B: MEASURED TABLE DISPLACEMENTS

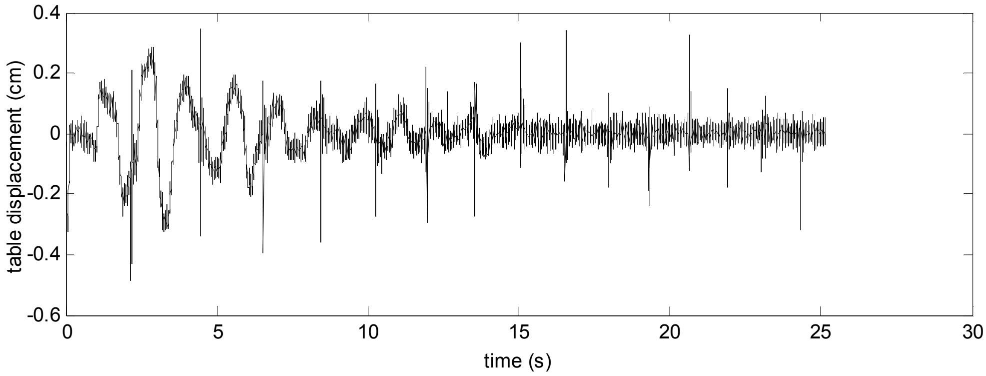

Figure B.1. Measured table displacement for Test 1 Run 1-1

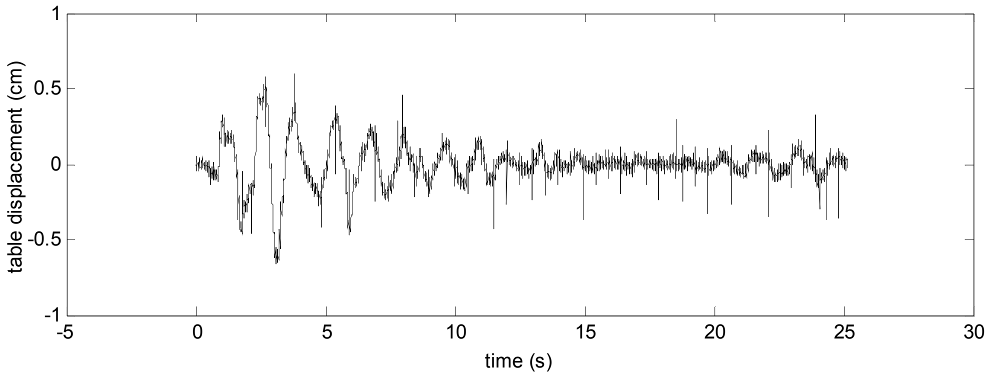

Figure B.2. Measured table displacement for Test 1 Run 1-2

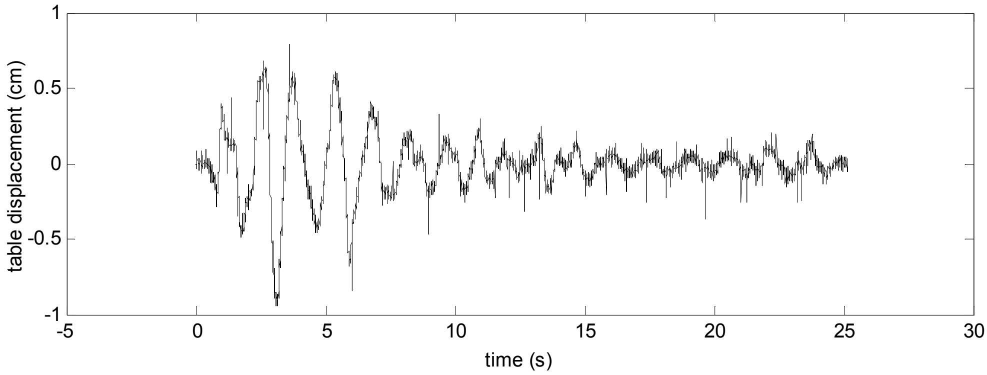

Figure B.3. Measured table displacement for Test 1 Run 1-3

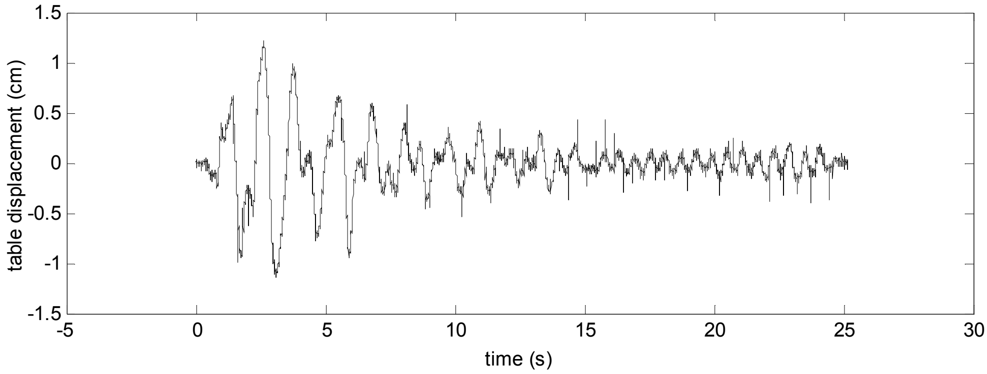

Figure B.4. Measured table displacement for Test 1 Run 1-4

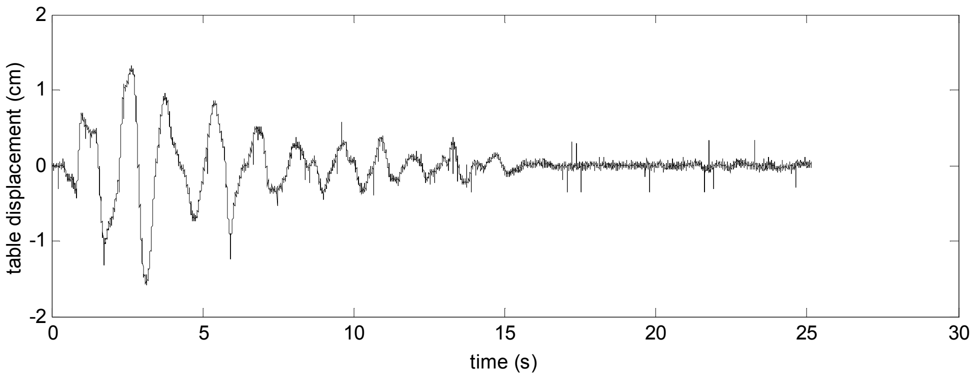

Figure B.5. Measured table displacement for Test 1 Run 1-5

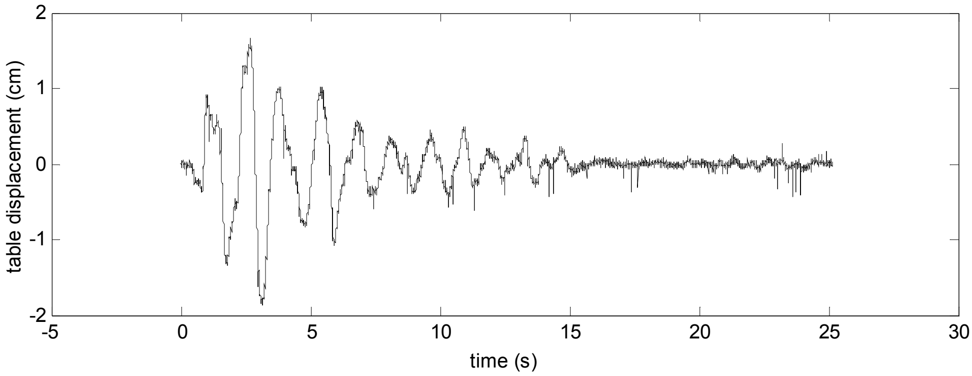

Figure B.6. Measured table displacement for Test 1 Run 1-6

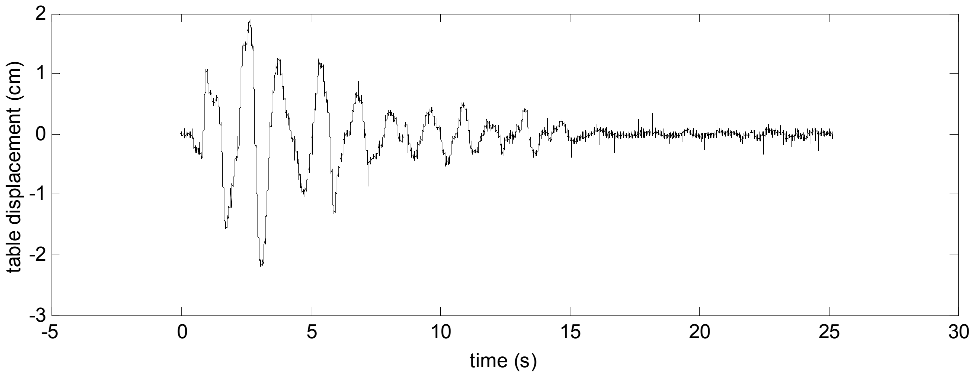

Figure B.7. Measured table displacement for Test 1 Run 1-7

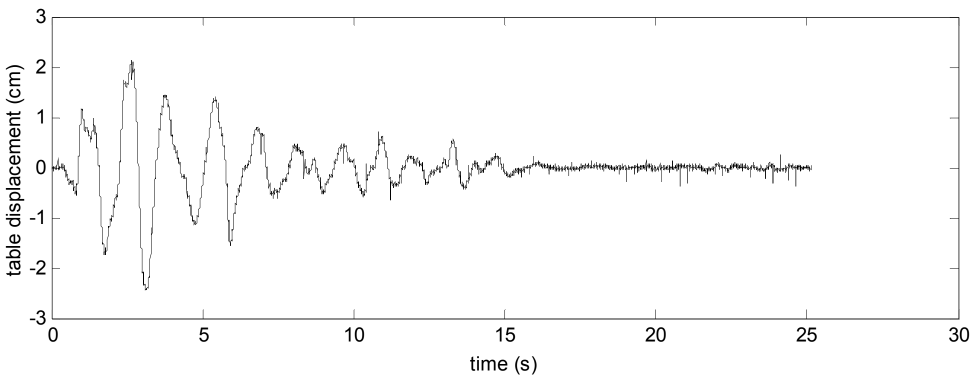

Figure B.8. Measured table displacement for Test 1 Run 1-8

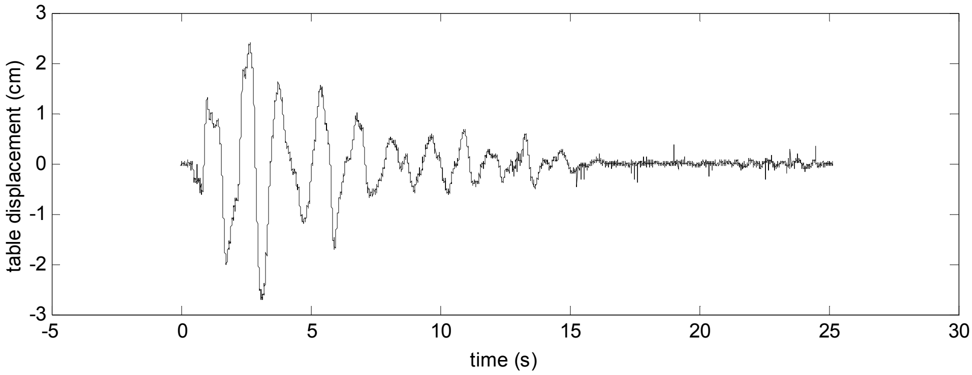

Figure B.9. Measured table displacement for Test 1 Run 1-9

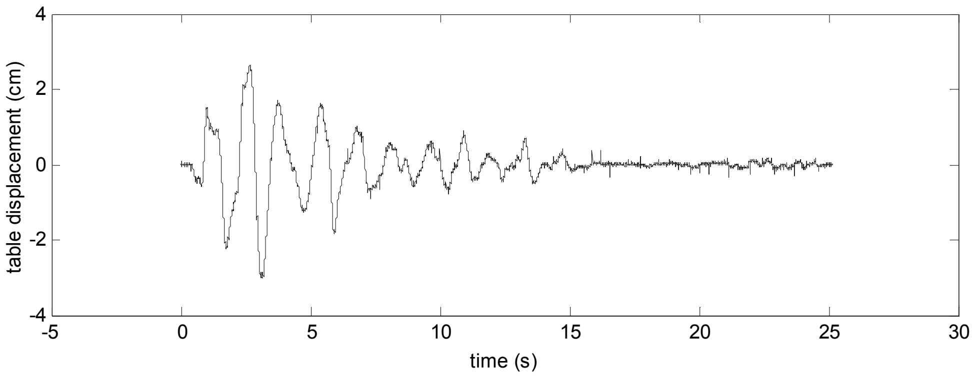

Figure B.10. Measured table displacement for Test 1 Run 1-10

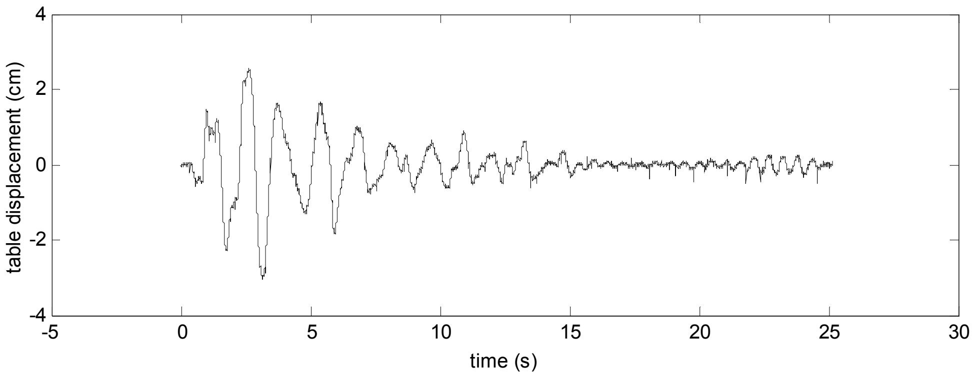

Figure B.11. Measured table displacement for Test 1 Run 1-11

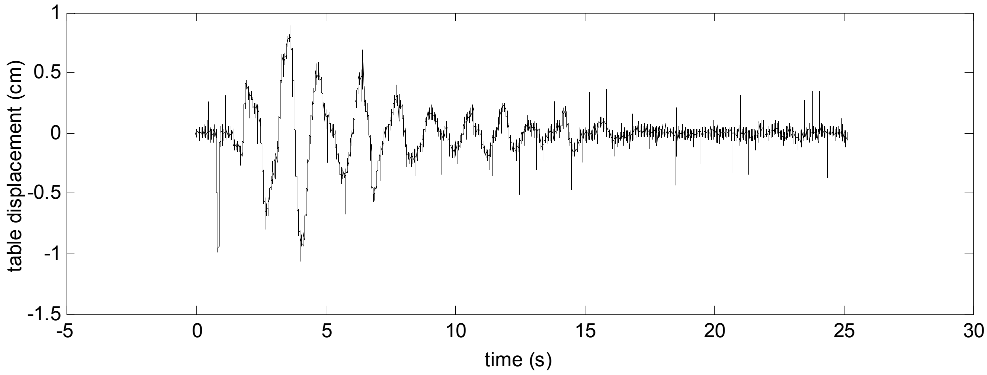

Figure B.12. Measured table displacement for Test 2 Run 2-1

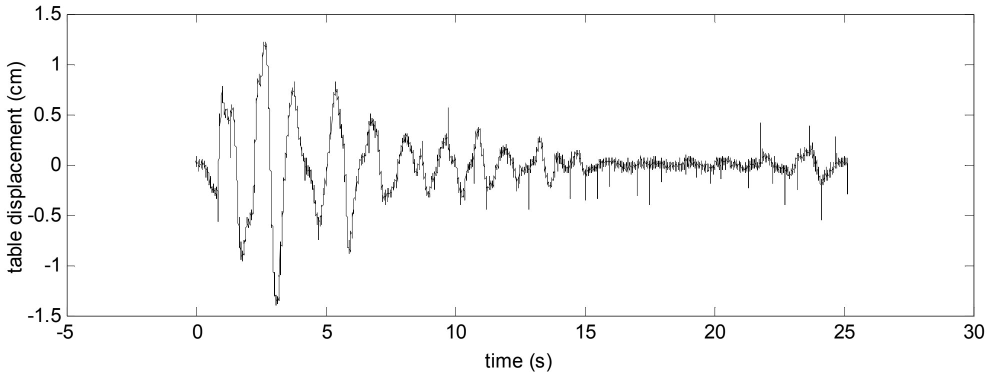

Figure B.13. Measured table displacement for Test 2 Run 2-2

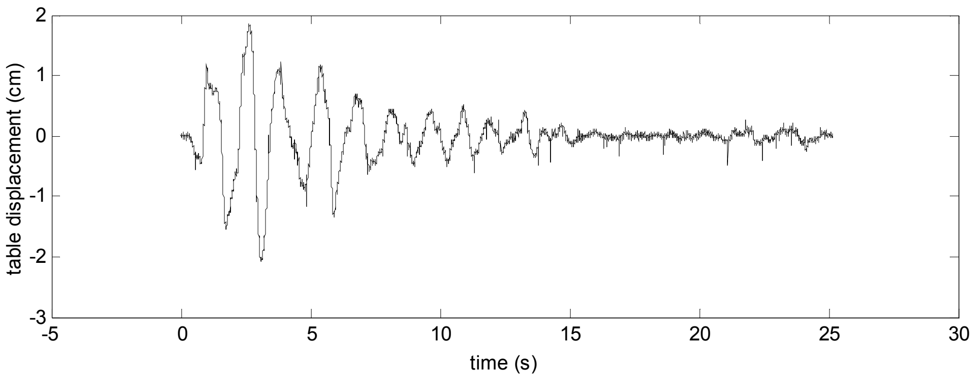

Figure B.14. Measured table displacement for Test 2 Run 2-3

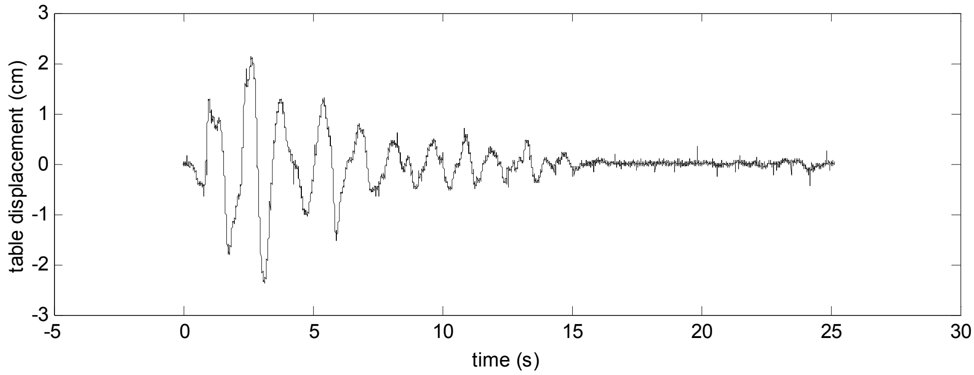

Figure B.15. Measured table displacement for Test 2 Run 2-4

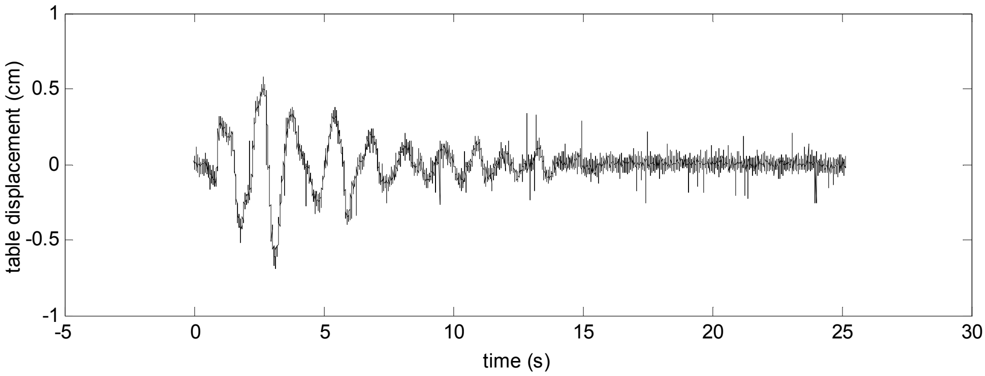

Figure B.16. Measured table displacement for Test 2 Run 2-5

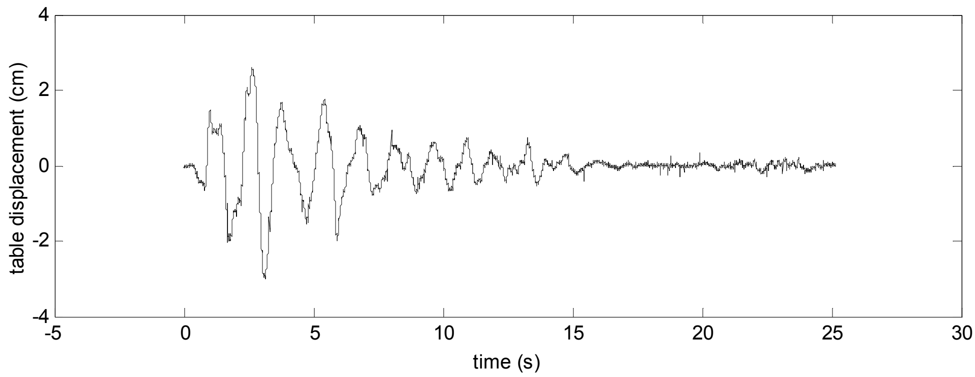

Figure B.17. Measured table displacement for Test 2 Run 2-6

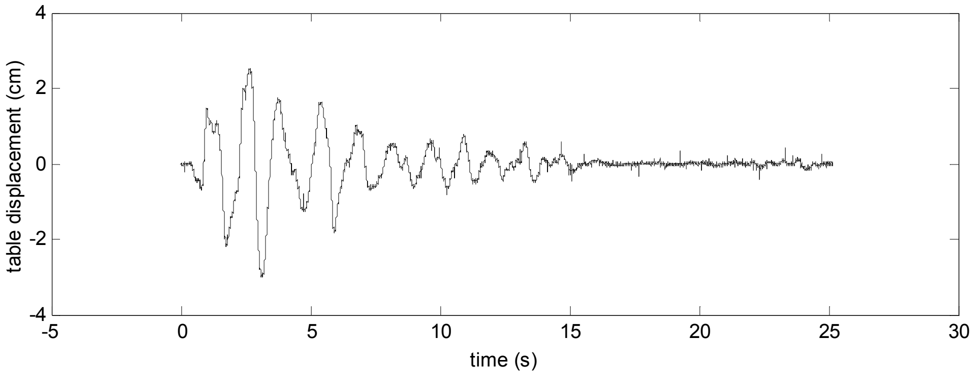

Figure B.18. Measured table displacement for Test 2 Run 2-7

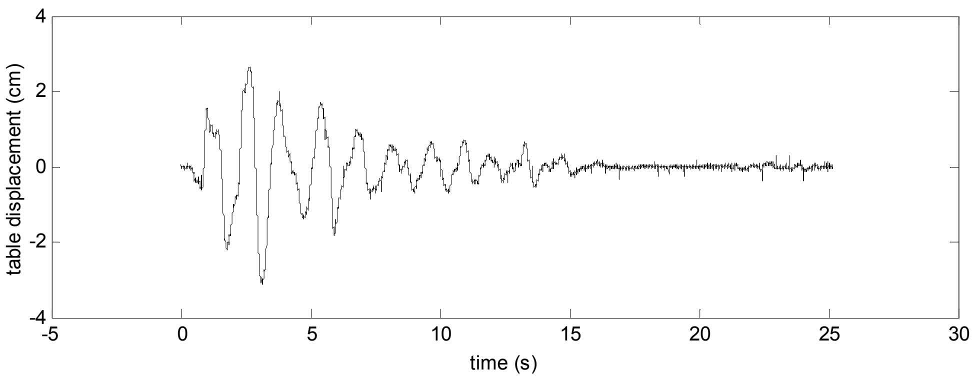

Figure B.19. Measured table displacement for Test 2 Run 2-8

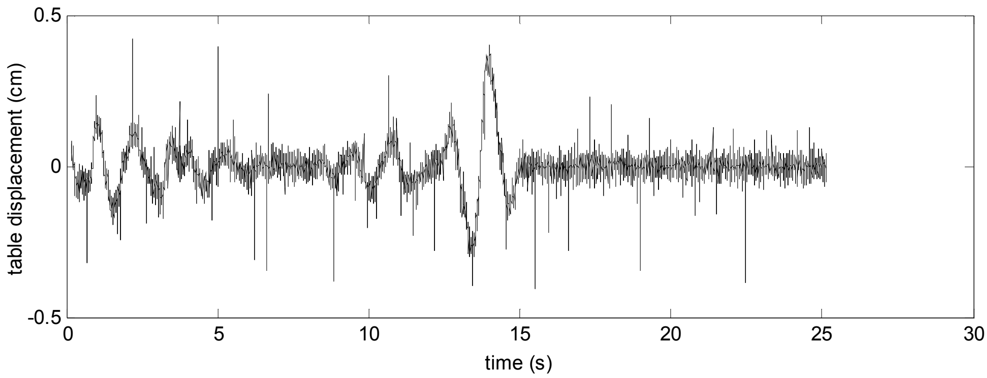

Figure B.20. Measured table displacement for Test 2 Run 2-9

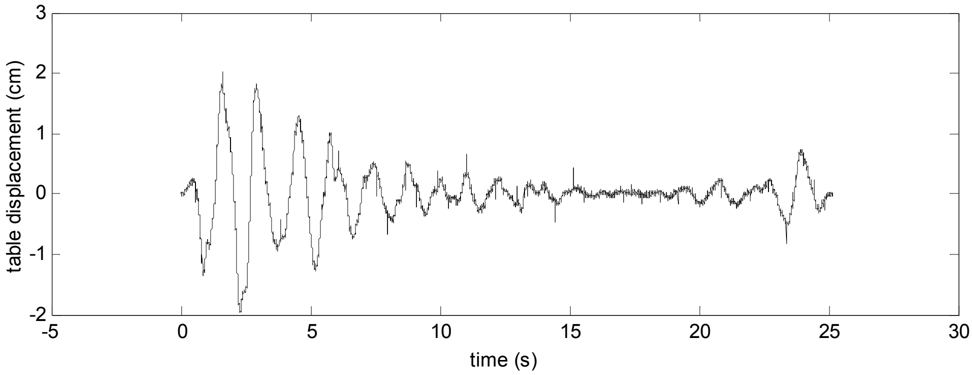

Figure B.21. Measured table displacement for Test 2 Run 2-10

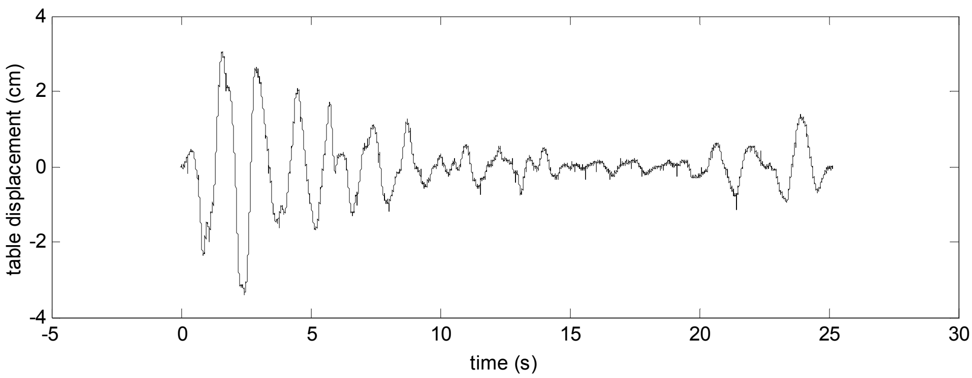

Figure B.22. Measured table displacement for Test 2 Run 2-11

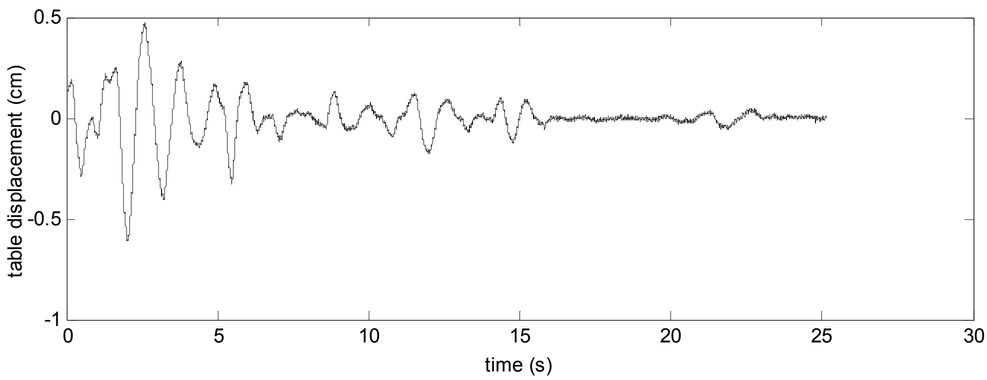

Figure B.23. Measured table displacement for Test 3 Run 3-1

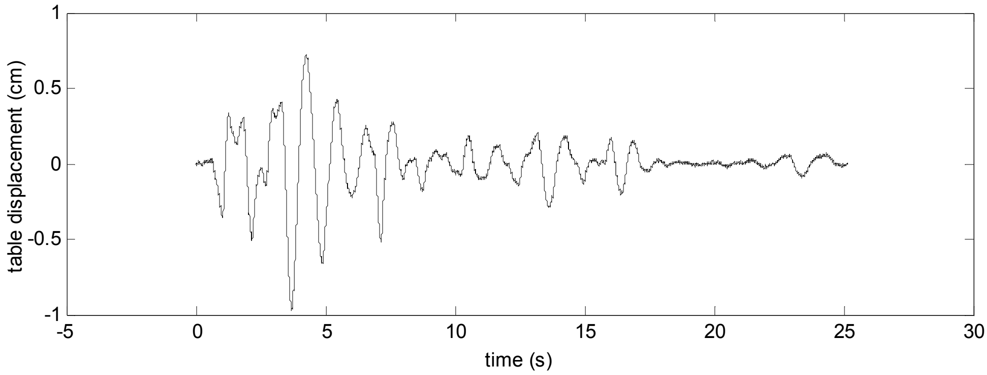

Figure B.24. Measured table displacement for Test 3 Run 3-2

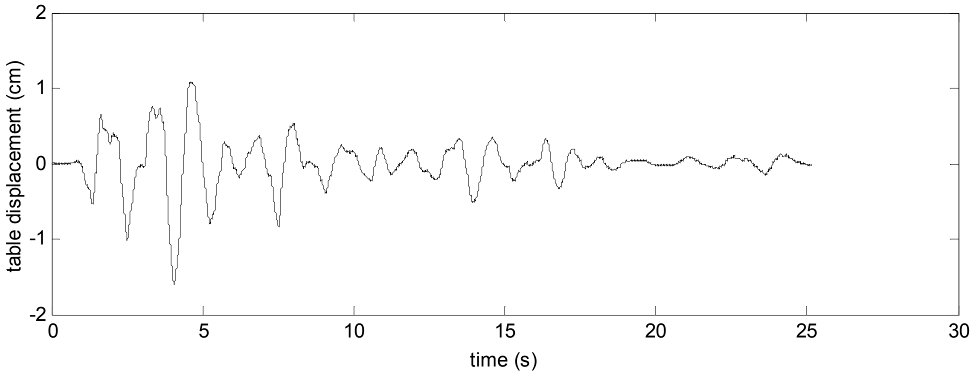

Figure B.25. Measured table displacement for Test 3 Run 3-3

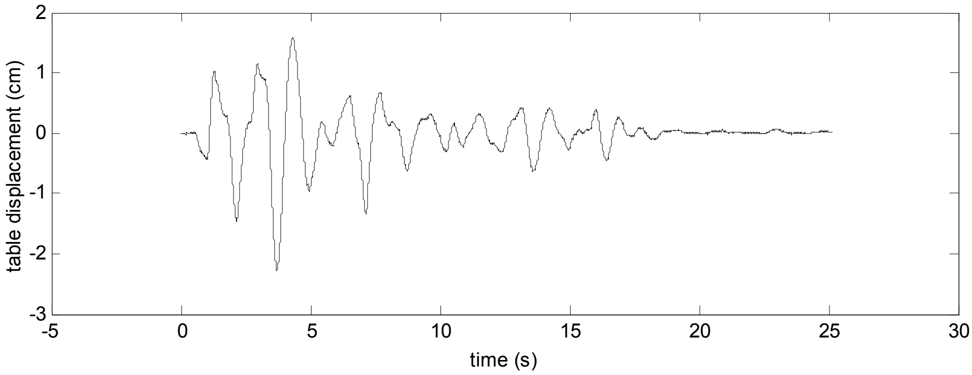

Figure B.26. Measured table displacement for Test 3 Run 3-4

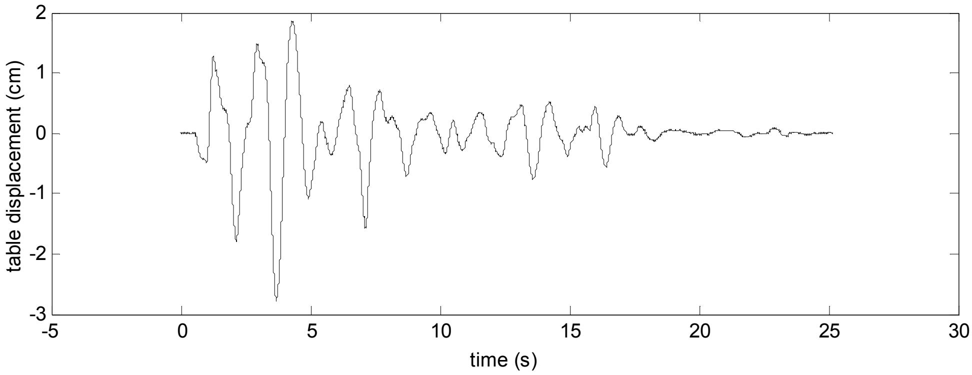

Figure B.27. Measured table displacement for Test 3 Run 3-5

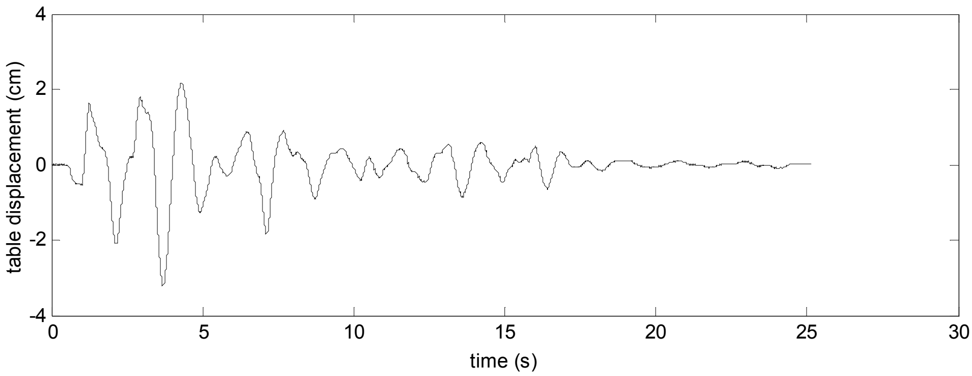

Figure B.28. Measured table displacement for Test 3 Run 3-6

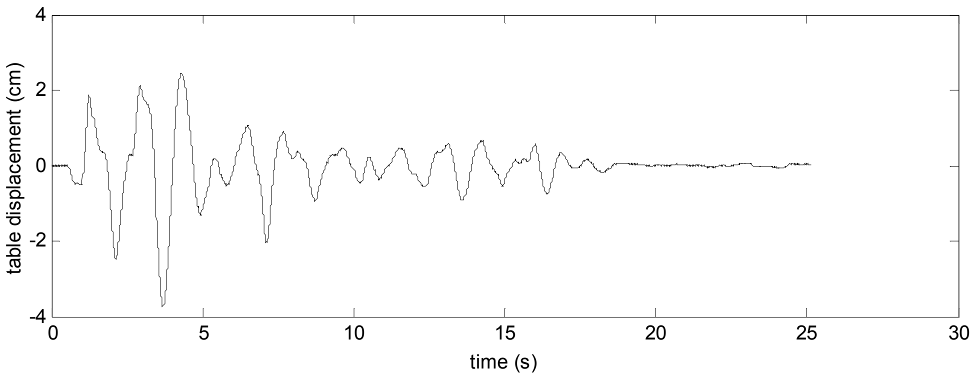

Figure B.29. Measured table displacement for Test 3 Run 3-7

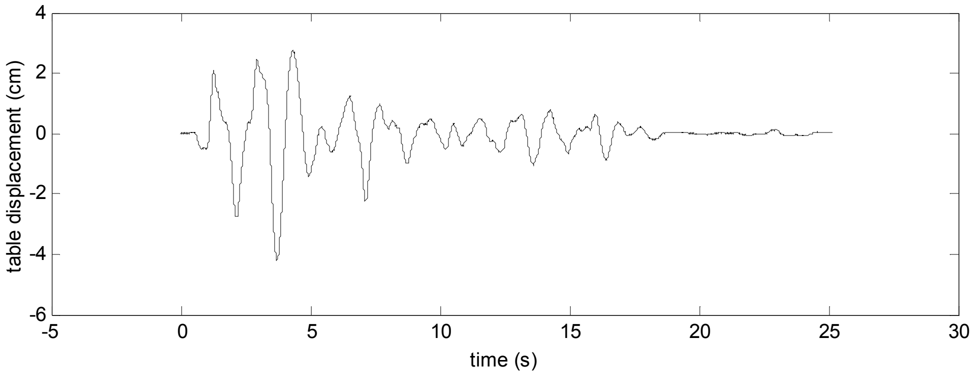

Figure B.30. Measured table displacement for Test 3 Run 3-8

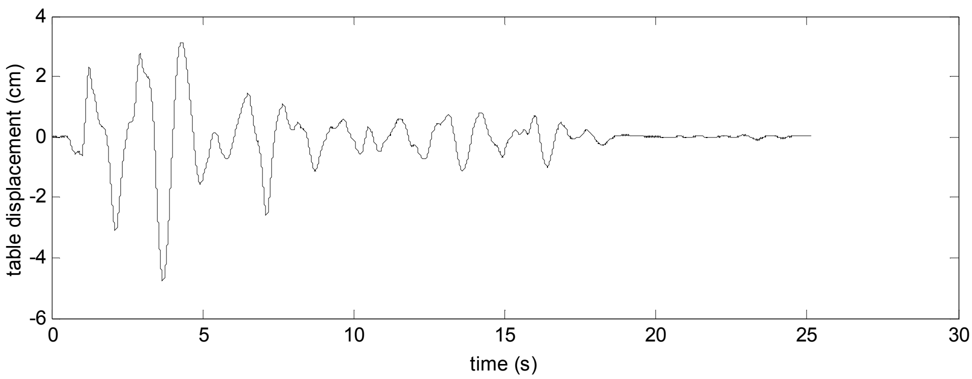

Figure B.31. Measured table displacement for Test 3 Run 3-9

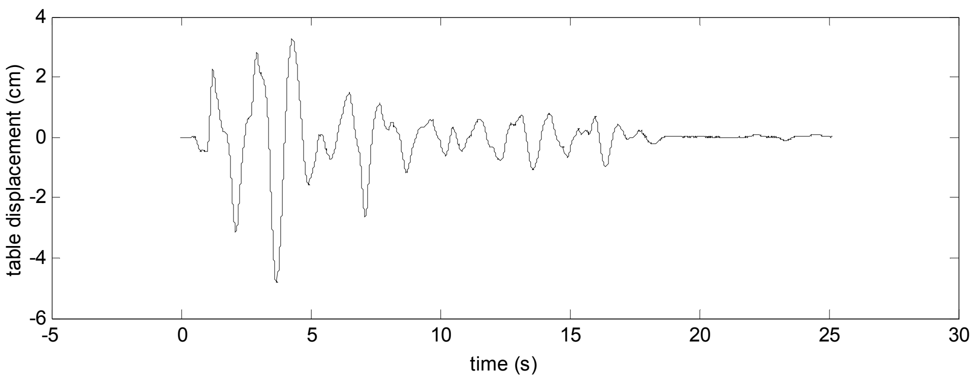

Figure B.32. Measured table displacement for Test 3 Run 3-10

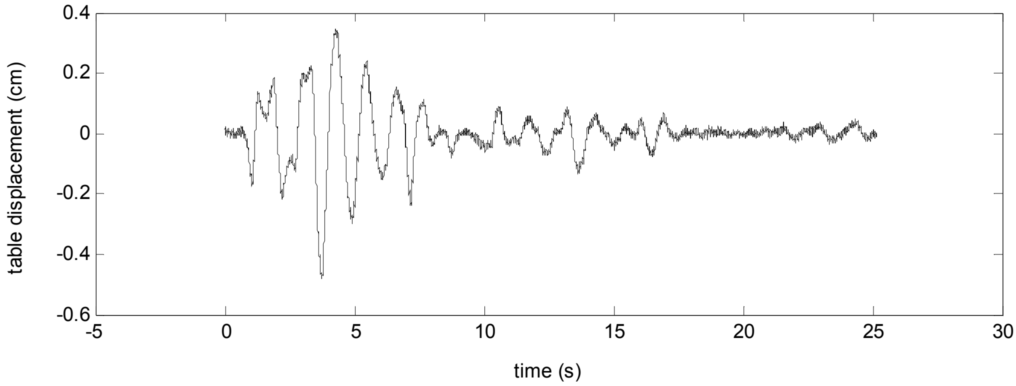

Figure B.33. Measured table displacement for Test 4 Run 4-1

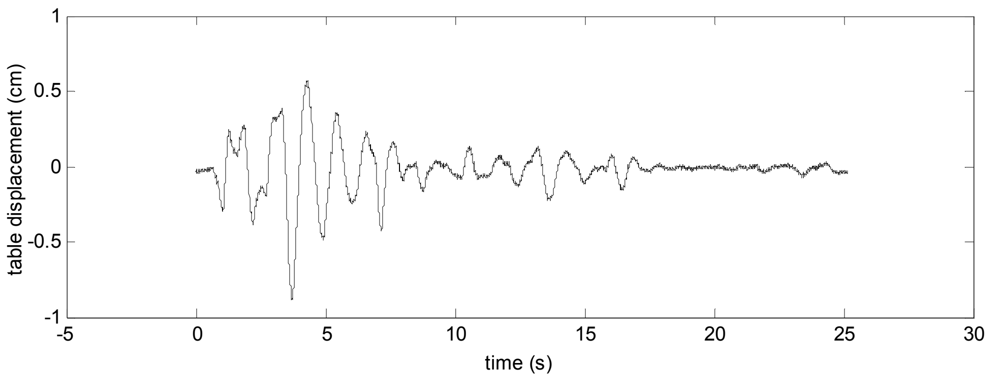

Figure B.34. Measured table displacement for Test 4 Run 4-2

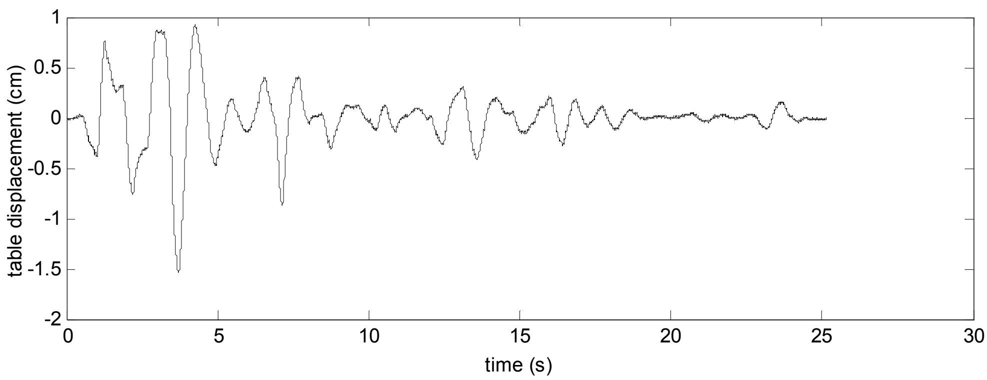

Figure B.35. Measured table displacement for Test 4 Run 4-3

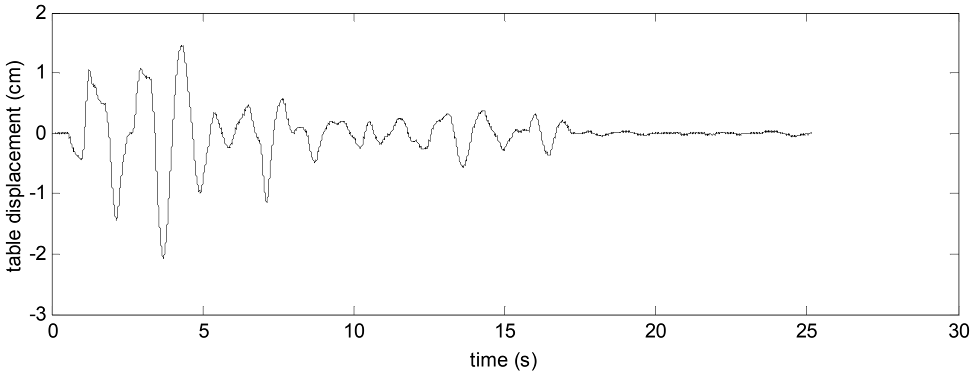

Figure B.36. Measured table displacement for Test 4 Run 4-4

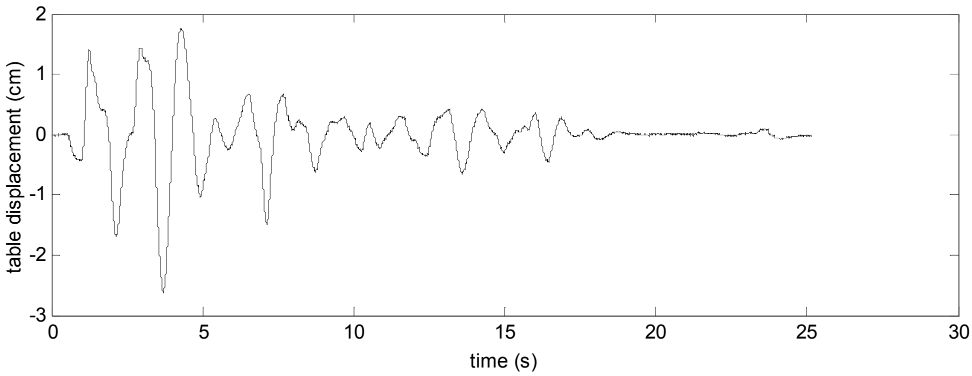

Figure B.37. Measured table displacement for Test 4 Run 4-5

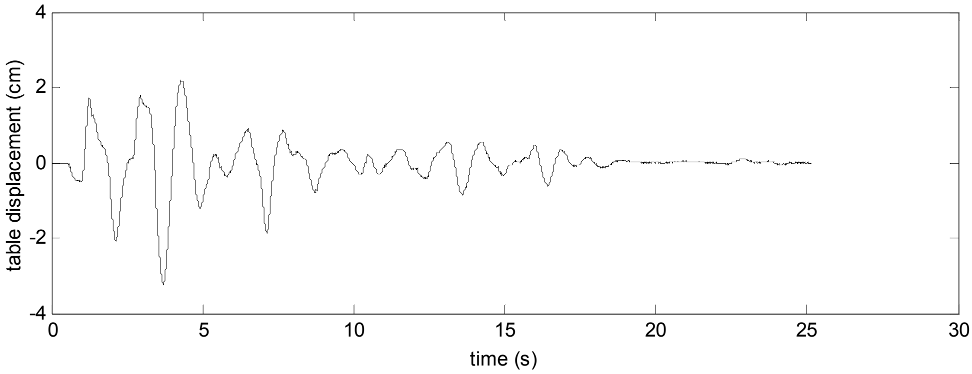

Figure B.38. Measured table displacement for Test 4 Run 4-6

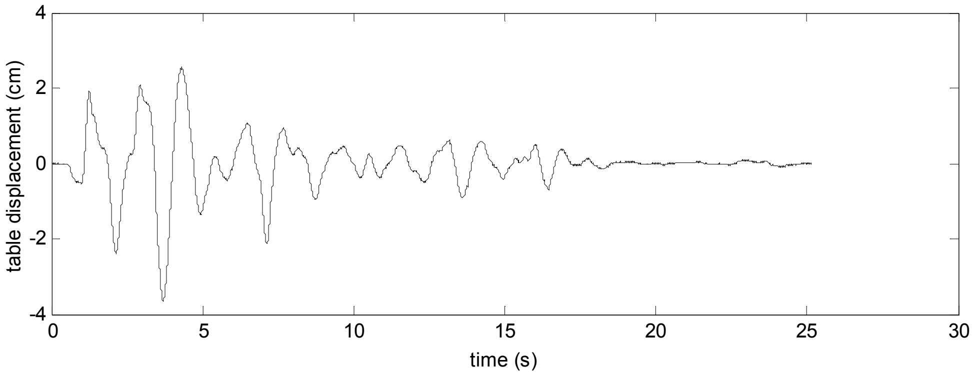

Figure B.39. Measured table displacement for Test 4 Run 4-7

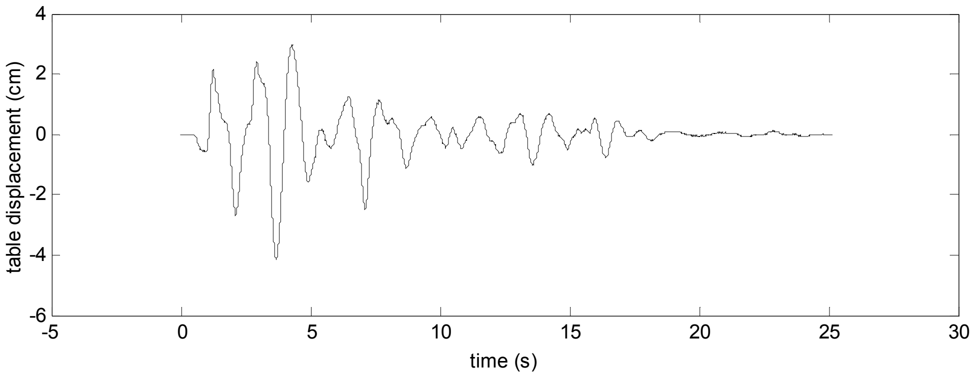

Figure B.40. Measured table displacement for Test 4 Run 4-8

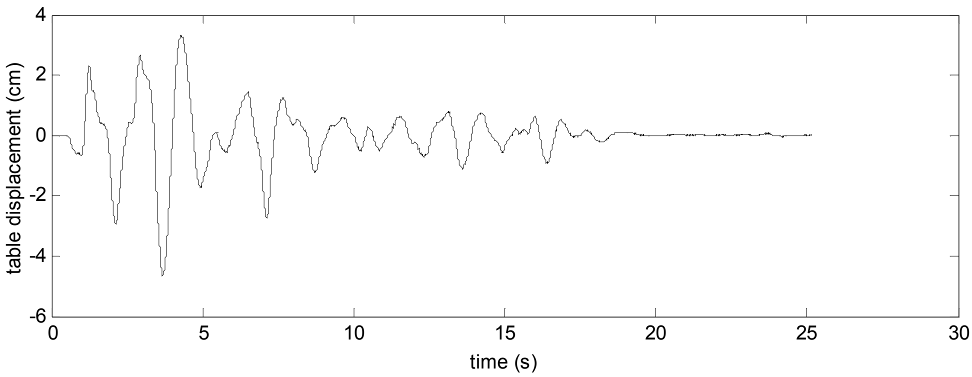

Figure B.41. Measured table displacement for Test 4 Run 4-9

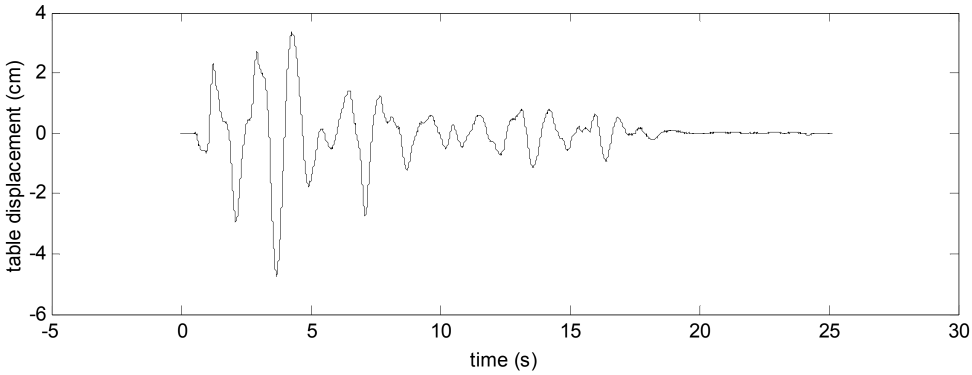

Figure B.42. Measured table displacement for Test 4 Run 4-10

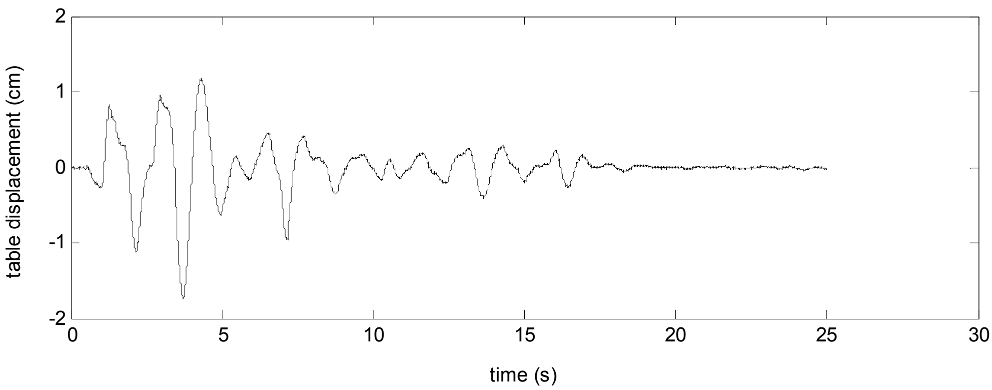

Figure B.43. Measured table displacement for Test 4 Run 4-11

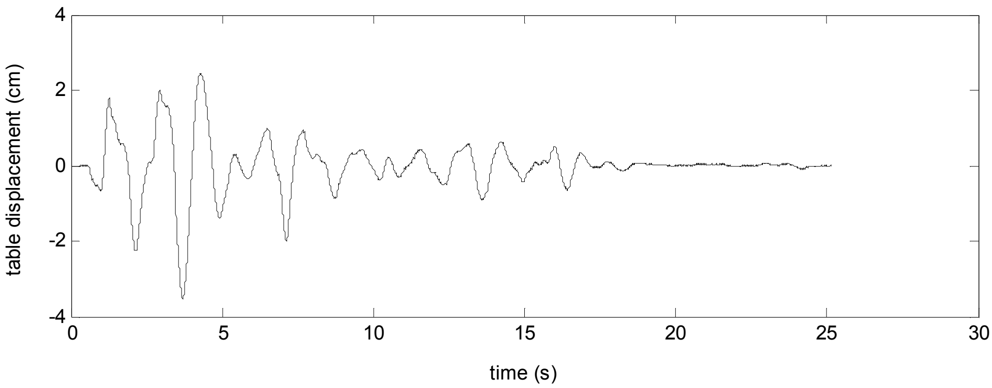

Figure B.44. Measured table displacement for Test 4 Run 4-12

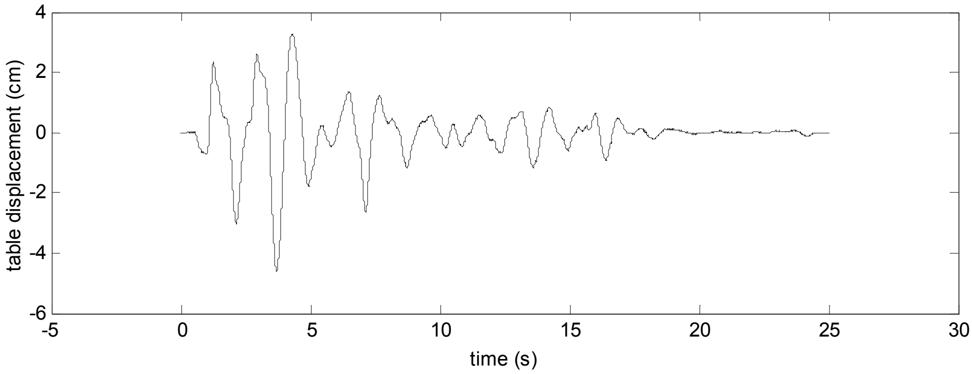

Figure B.45. Measured table displacement for Test 4 Run 4-13

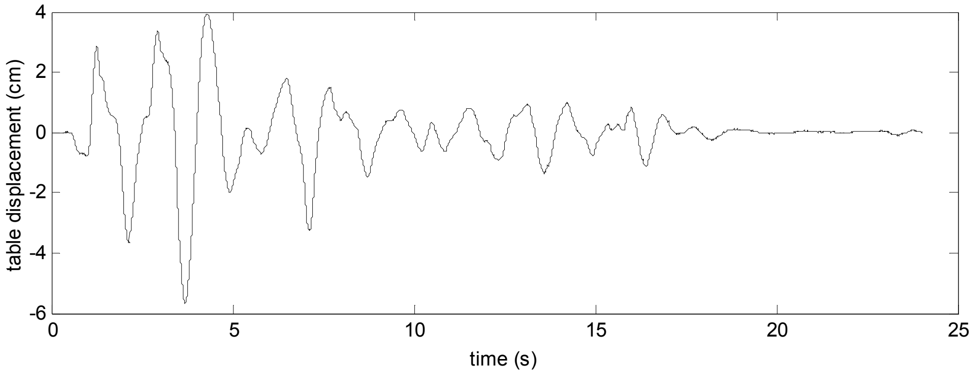

Figure B.46. Measured table displacement for Test 4 Run 4-14

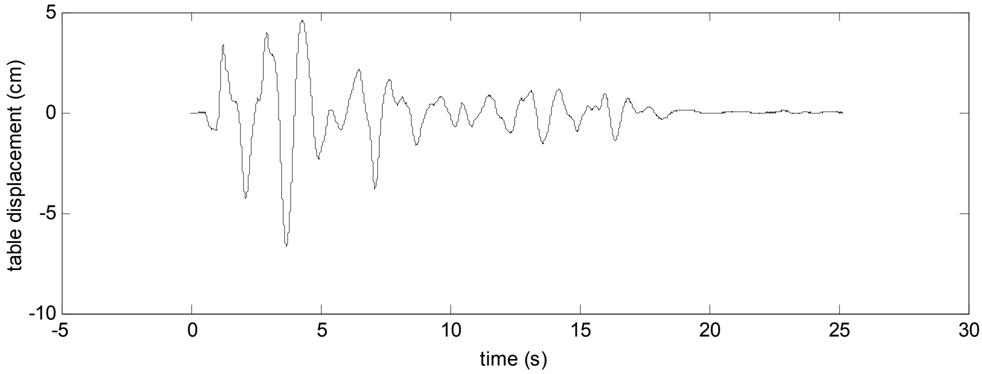

Figure B.47. Measured table displacement for Test 4 Run 4-15

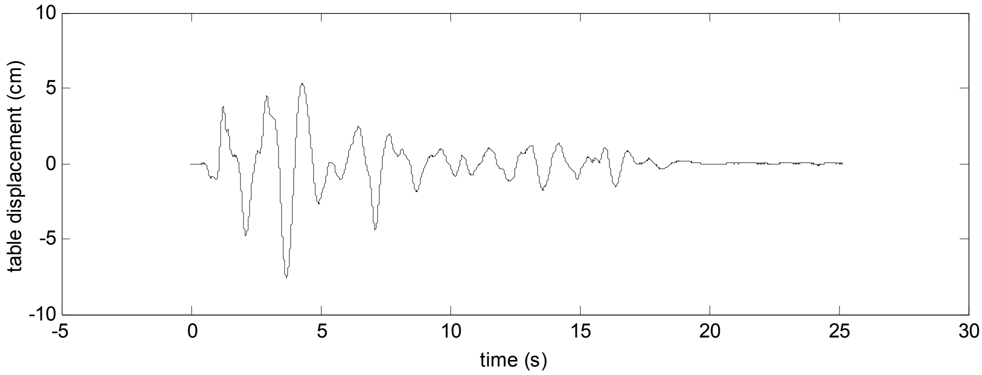

Figure B.48. Measured table displacement for Test 4 Run 4-16

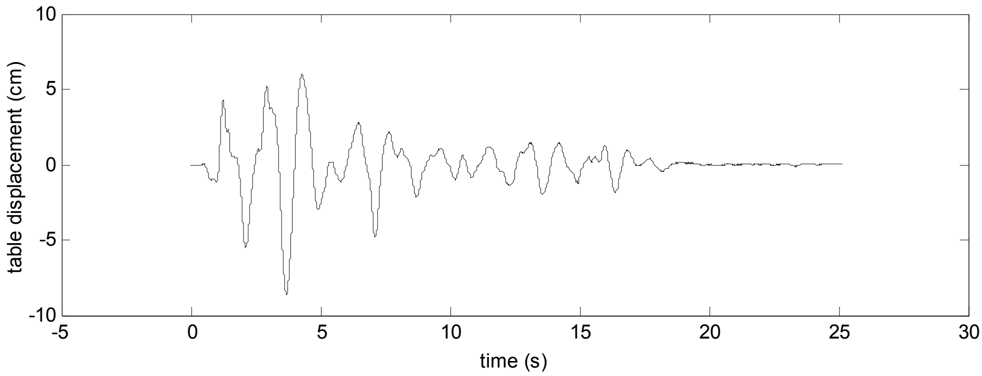

Figure B.49. Measured table displacement for Test 4 Run 4-17

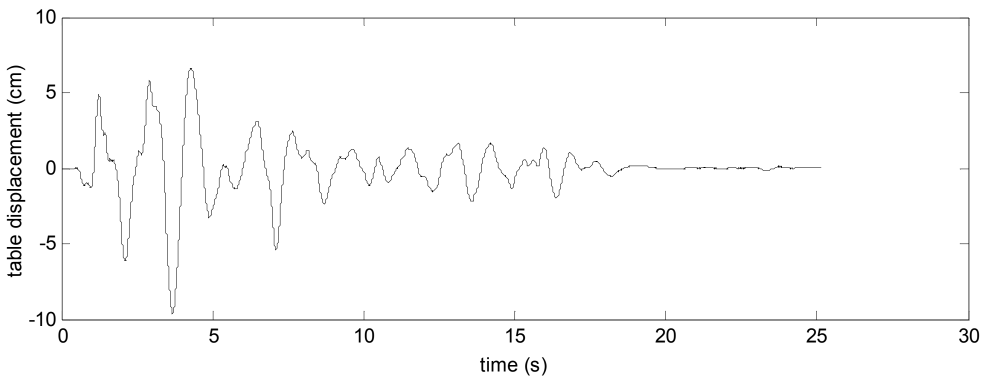

Figure B.50. Measured table displacement for Test 4 Run 4-18

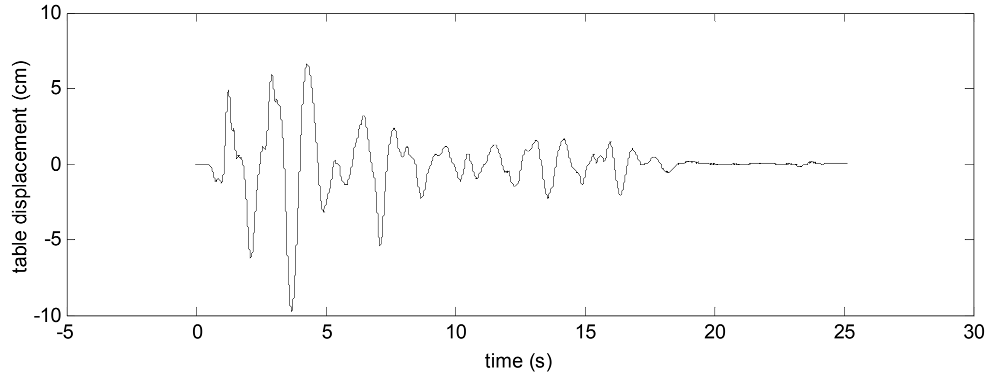

Figure B.51. Measured table displacement for Test 4 Run 4-19

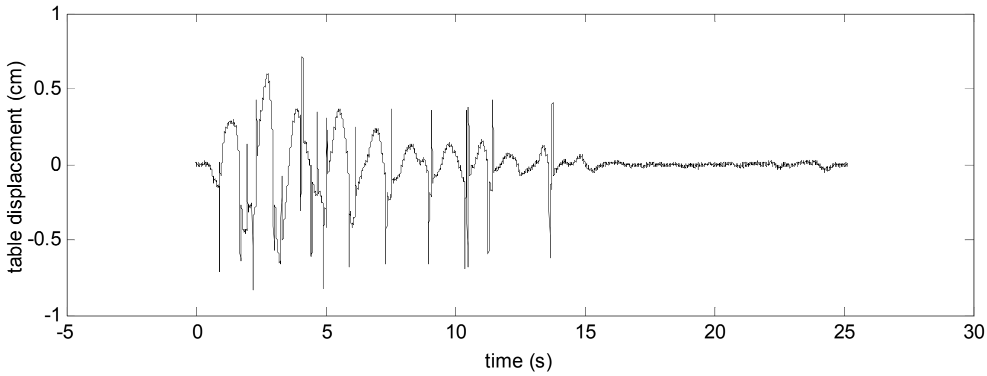

Figure B.52. Measured table displacement for Test 5 Run 5-1

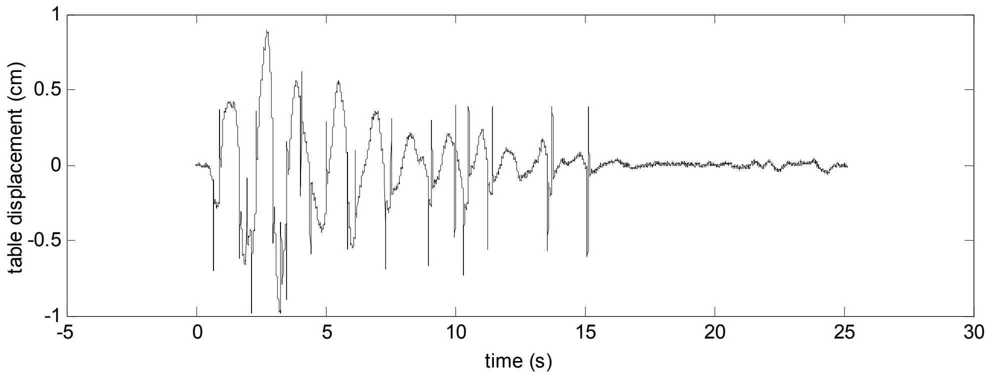

Figure B.53. Measured table displacement for Test 5 Run 5-2

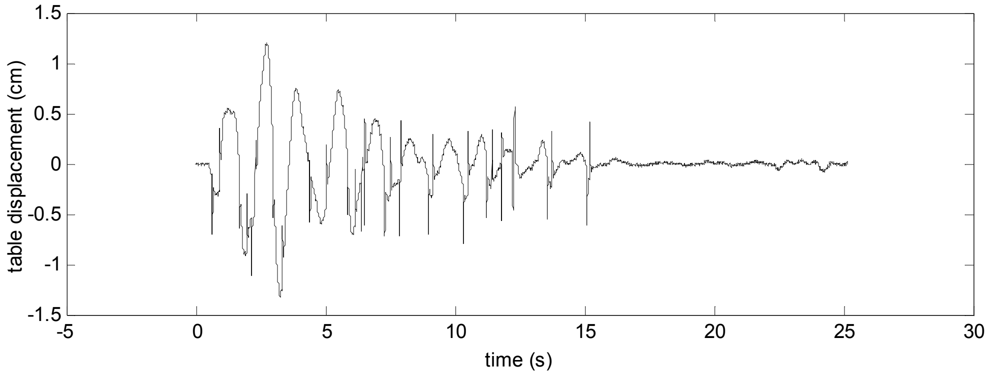

Figure B.54. Measured table displacement for Test 5 Run 5-3

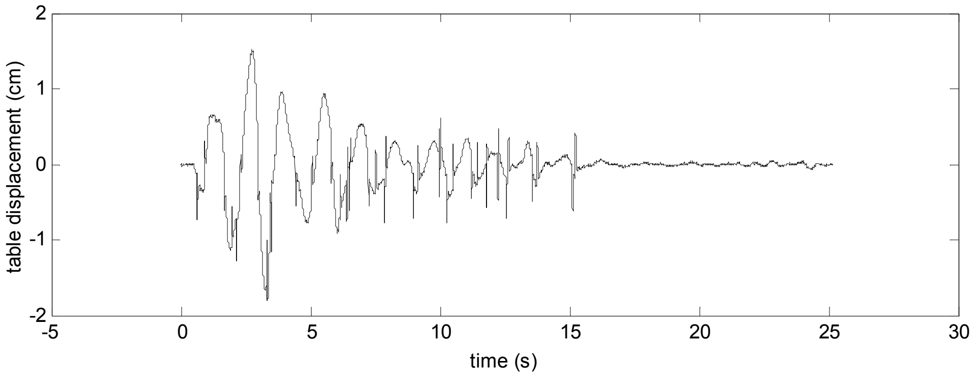

Figure B.55. Measured table displacement for Test 5 Run 5-4

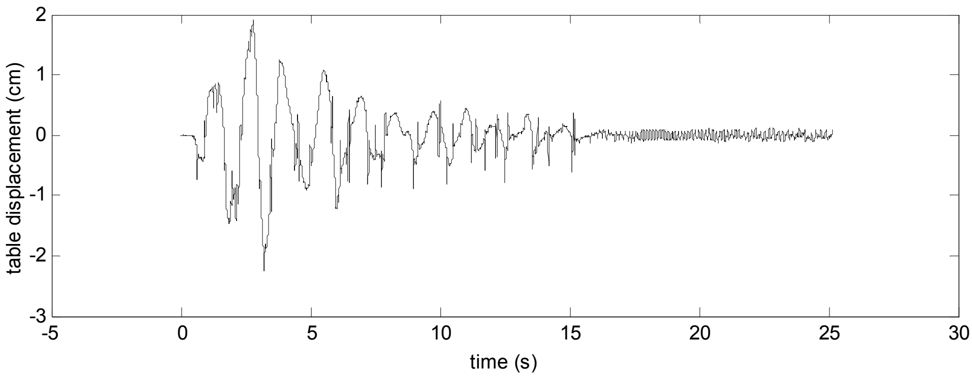

Figure B.56. Measured table displacement for Test 5 Run 5-5

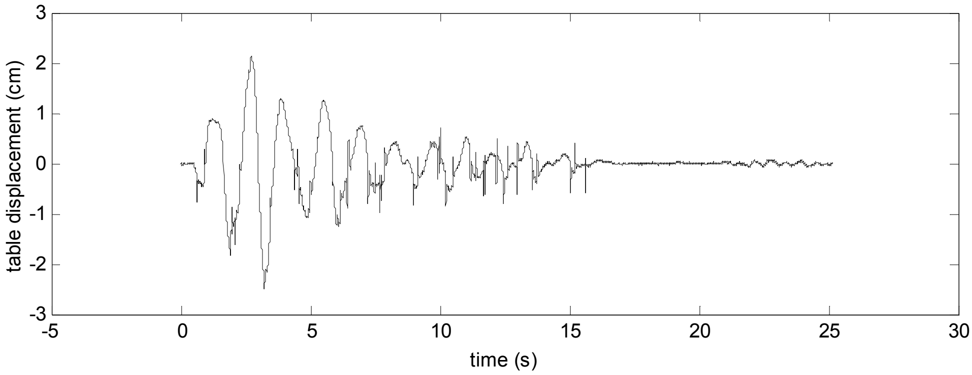

Figure B.57. Measured table displacement for Test 5 Run 5-6

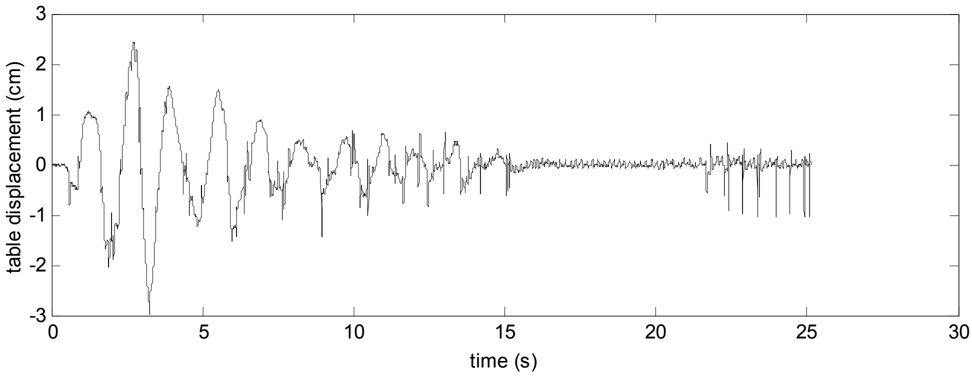

Figure B.58. Measured table displacement for Test 5 Run 5-7

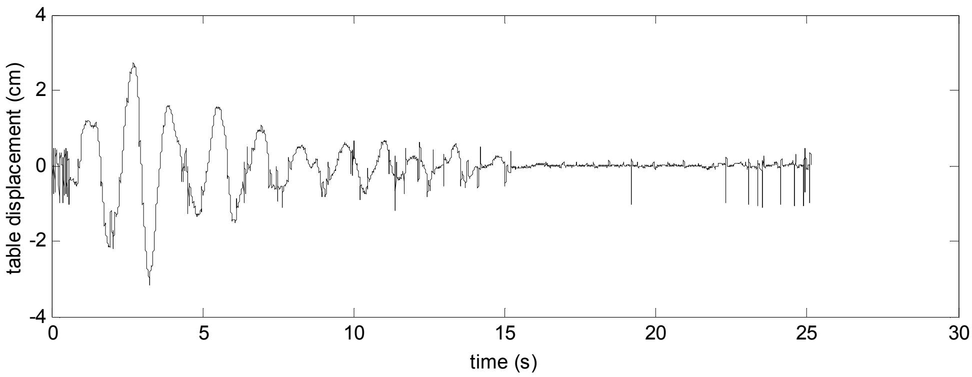

Figure B.59. Measured table displacement for Test 5 Run 5-8

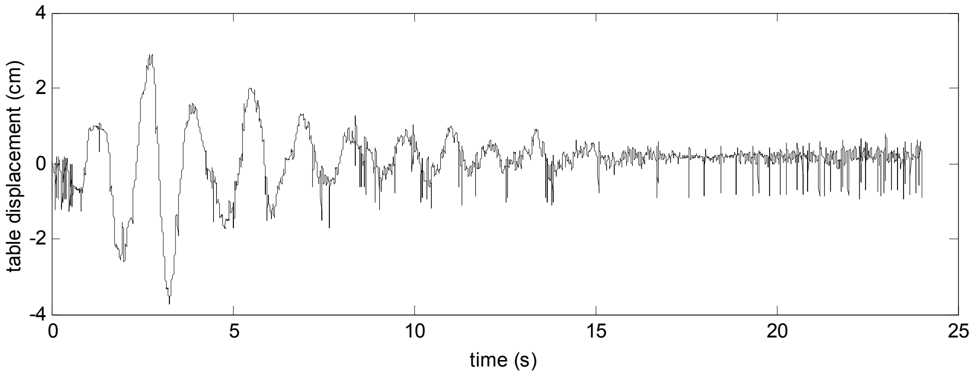

Figure B.60. Measured table displacement for Test 5 Run 5-9

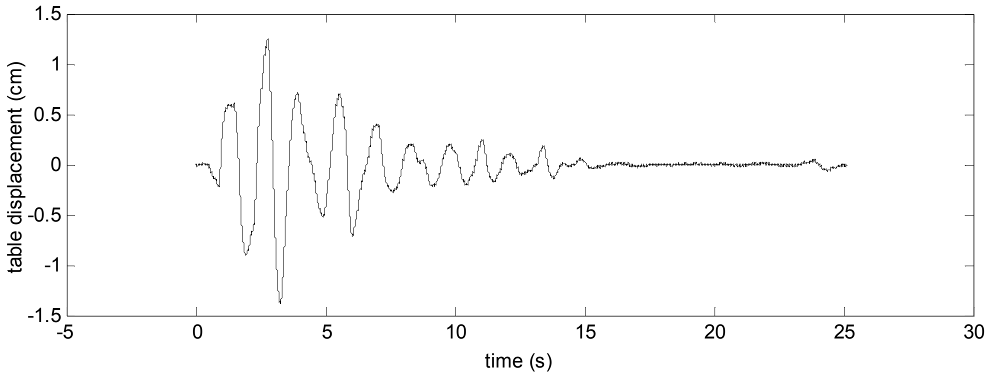

Figure B.61. Measured table displacement for Test 6 Run 6-1

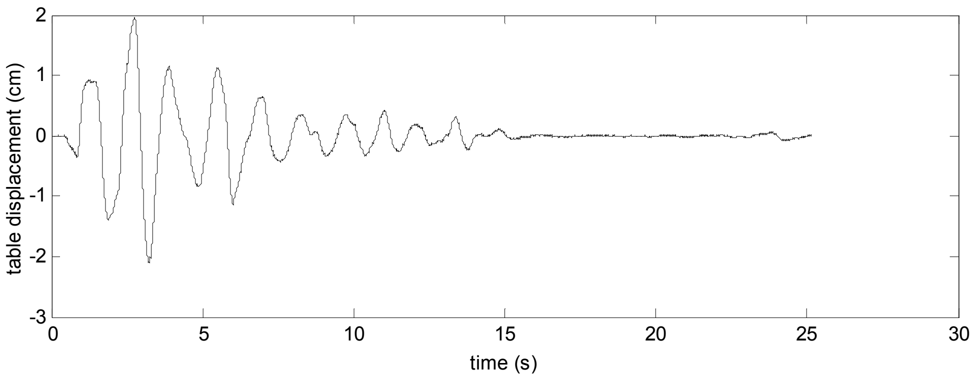

Figure B.62. Measured table displacement for Test 6 Run 6-2

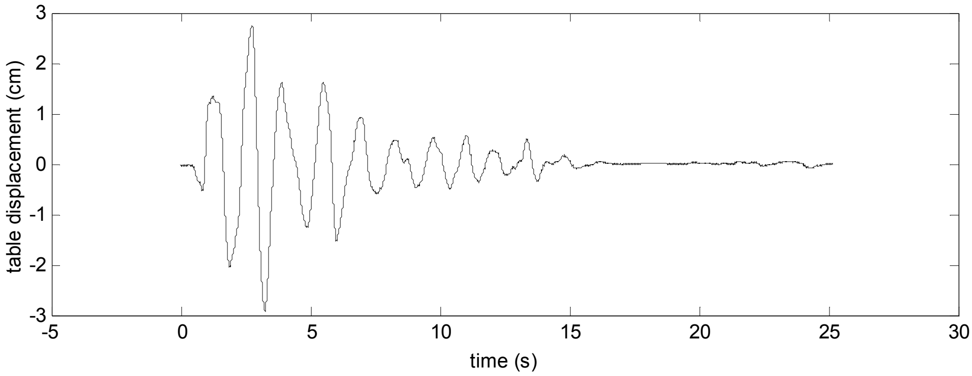

Figure B.63. Measured table displacement for Test 6 Run 6-3

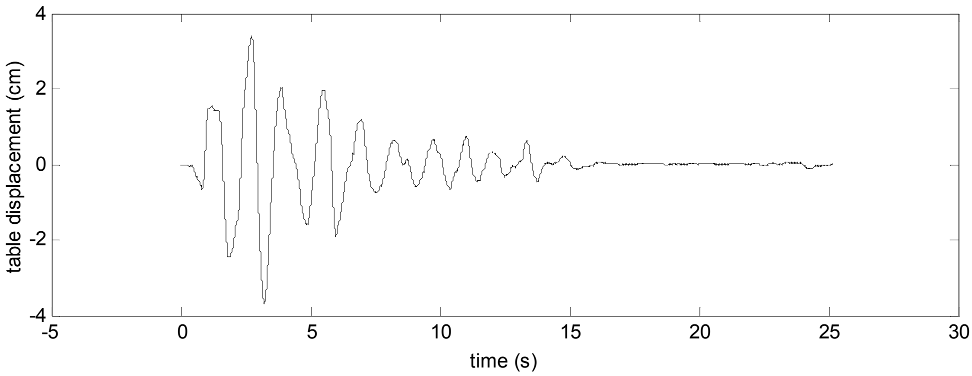

Figure B.64. Measured table displacement for Test 6 Run 6-4

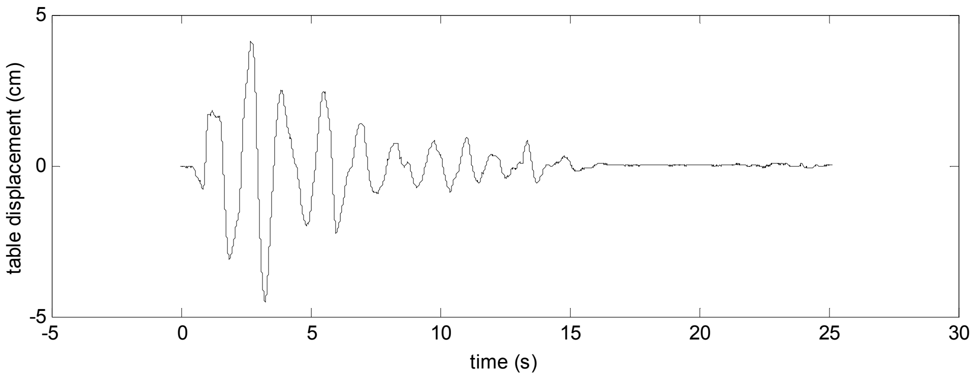

Figure B.65. Measured table displacement for Test 6 Run 6-5

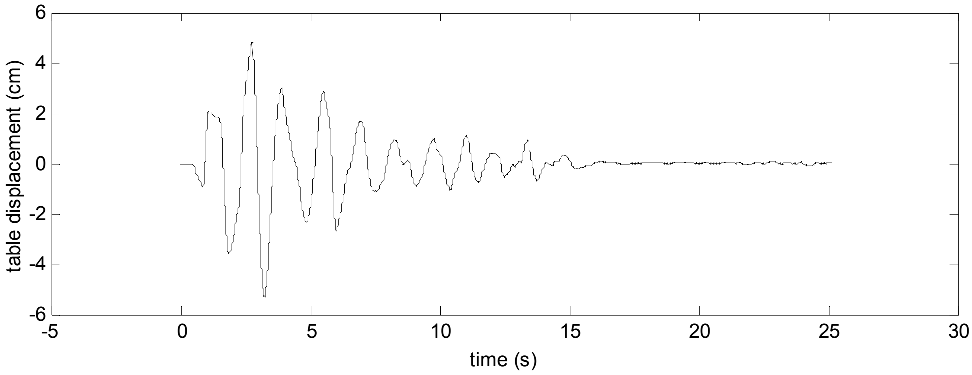

Figure B.66. Measured table displacement for Test 6 Run 6-6

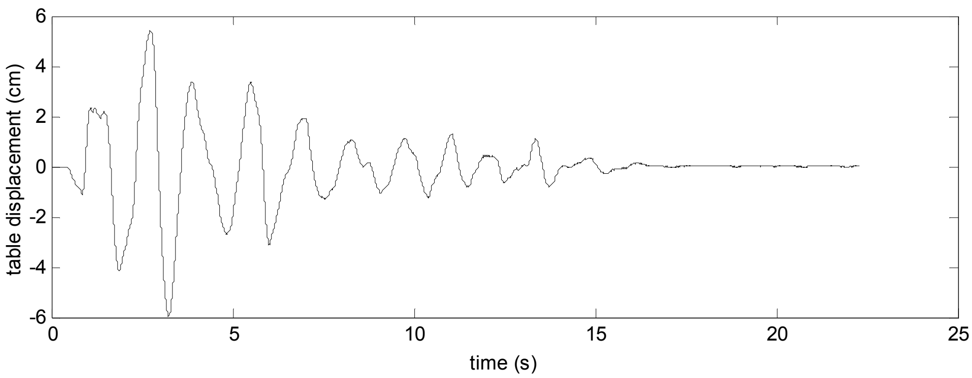

Figure B.67. Measured table displacement for Test 6 Run 6-7

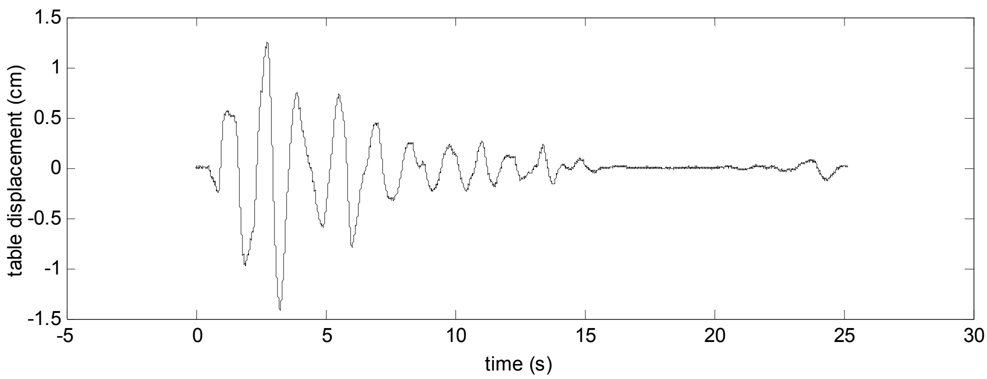

Figure B.68. Measured table displacement for Test 7 Run 7-1

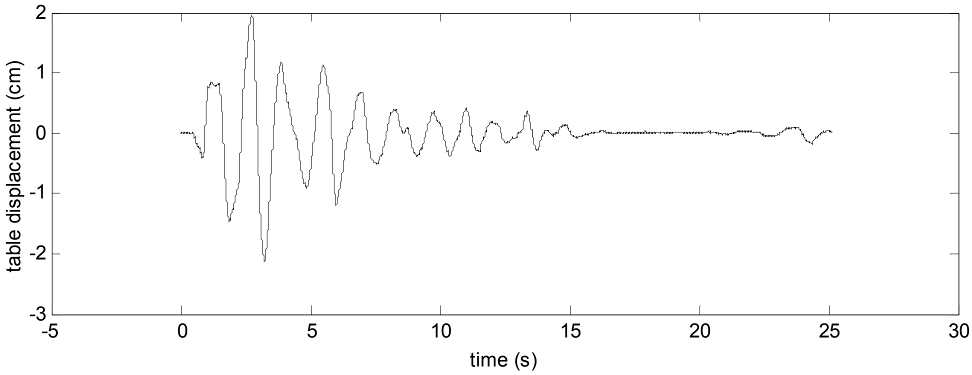

Figure B.69. Measured table displacement for Test 7 Run 7-2

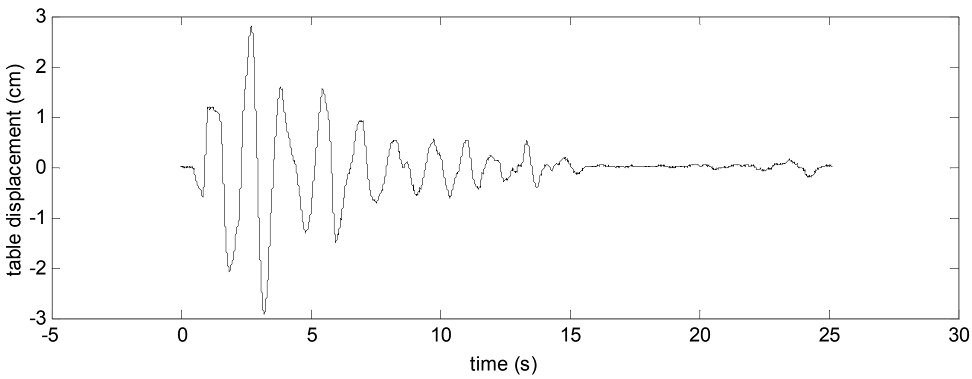

Figure B.70. Measured table displacement for Test 7 Run 7-3

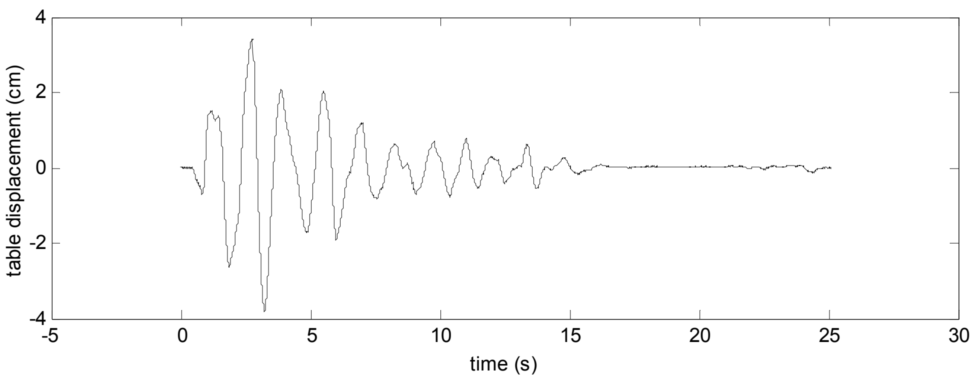

Figure B.71. Measured table displacement for Test 7 Run 7-4

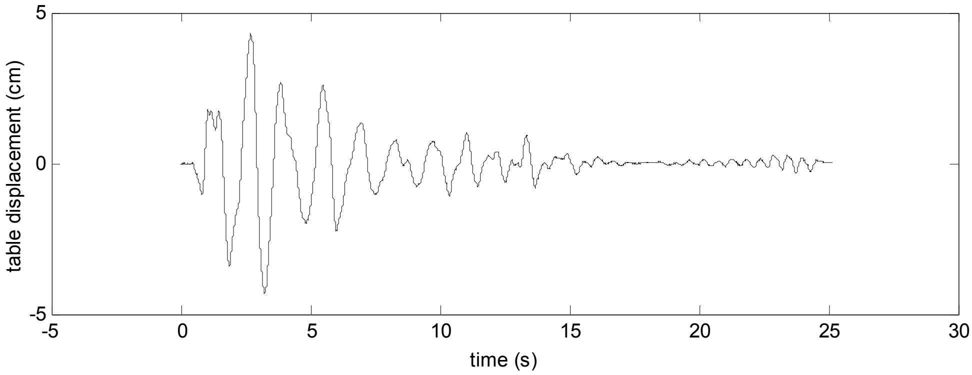

Figure B.72. Measured table displacement for Test 7 Run 7-5

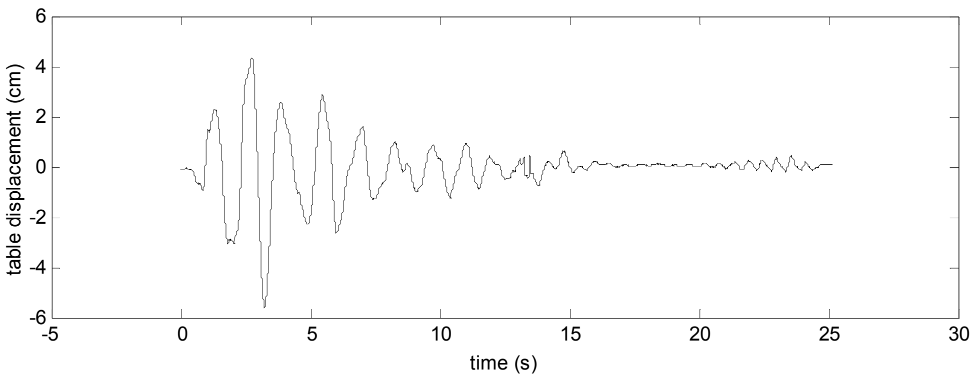

Figure B.73. Measured table displacement for Test 7 Run 7-6

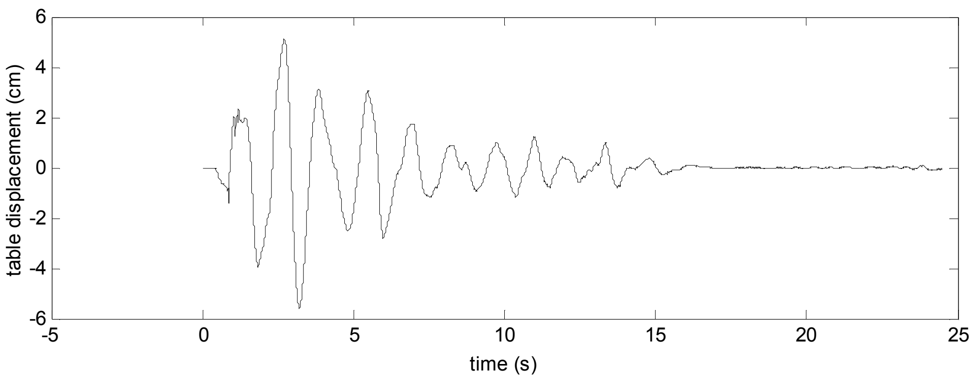

Figure B.74. Measured table displacement for Test 7 Run 7-7

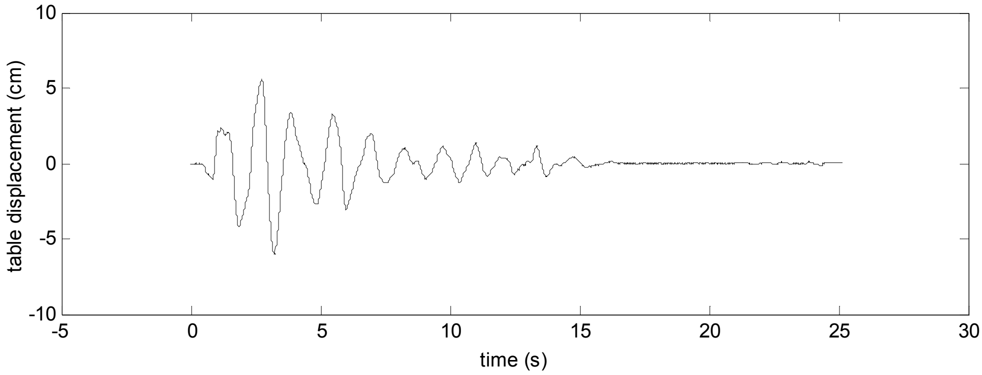

Figure B.75. Measured table displacement for Test 7 Run 7-8

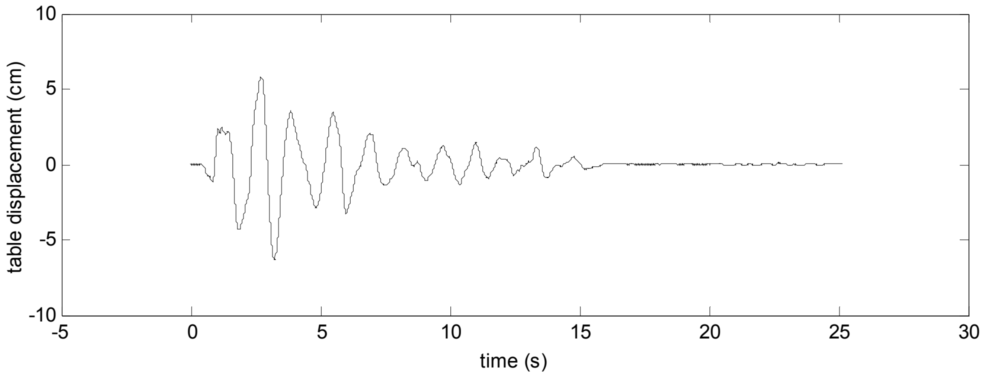

Figure B.76. Measured table displacement for Test 7 Run 7-9

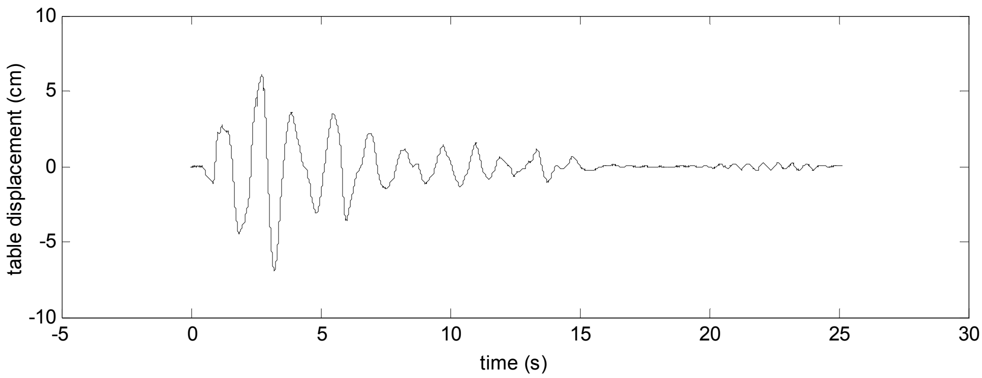

Figure B.77. Measured table displacement for Test 7 Run 7-10

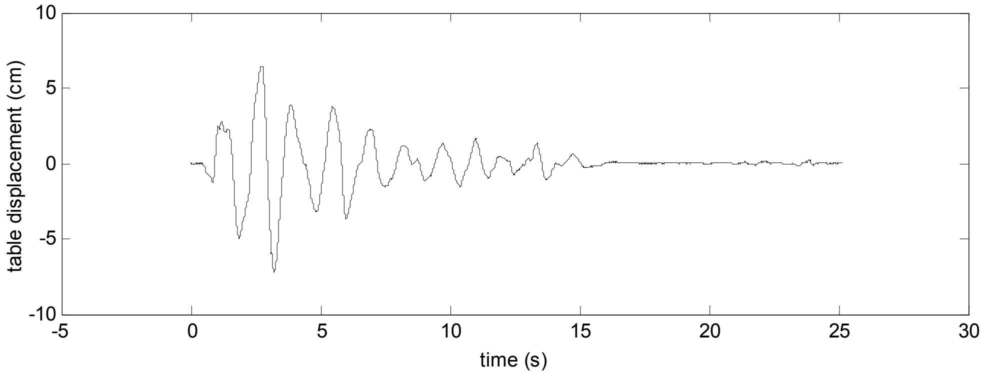

Figure B.78. Measured table displacement for Test 7 Run 7-11

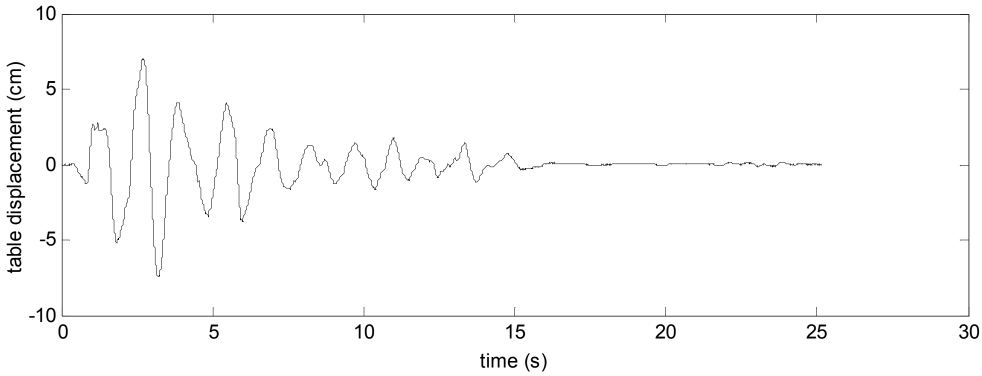

Figure B.79. Measured table displacement for Test 7 Run 7-12

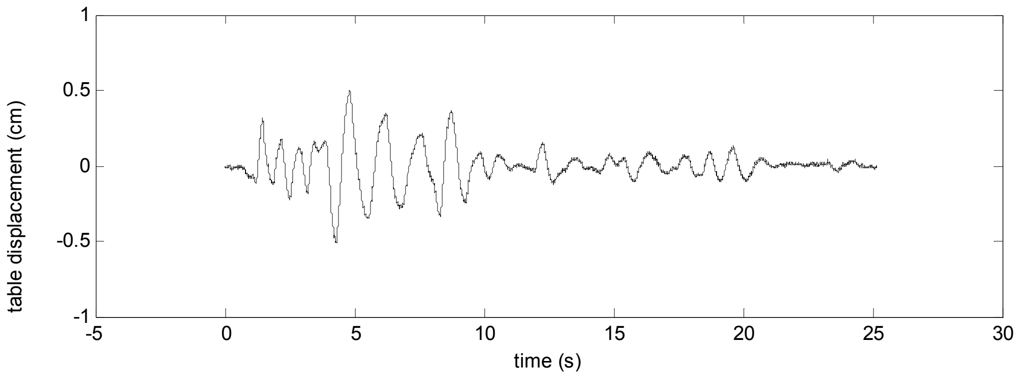

Figure B.80. Measured table displacement for Test 8 Run 8a-1

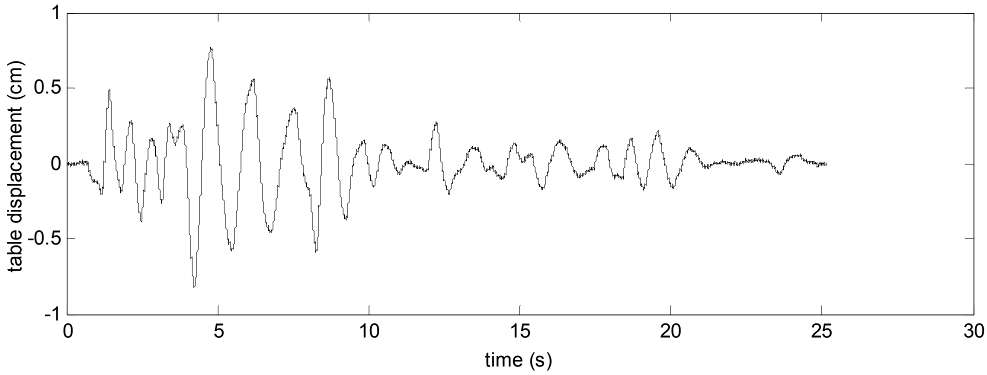

Figure B.81. Measured table displacement for Test 8 Run 8a-2

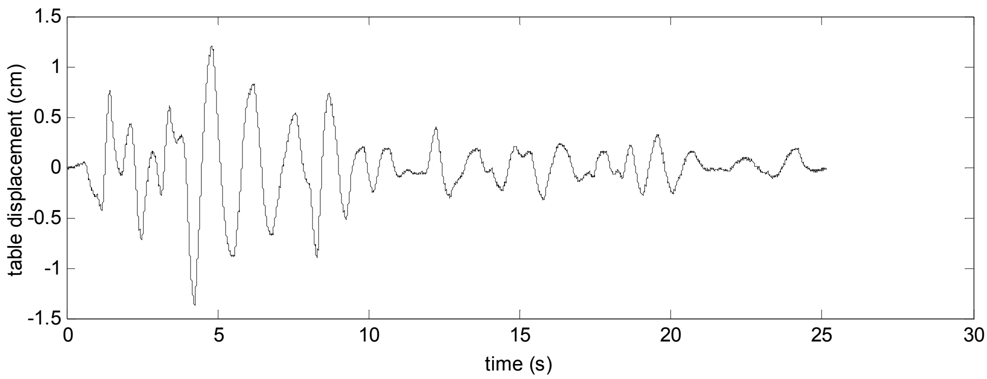

Figure B.82. Measured table displacement for Test 8 Run 8a-3

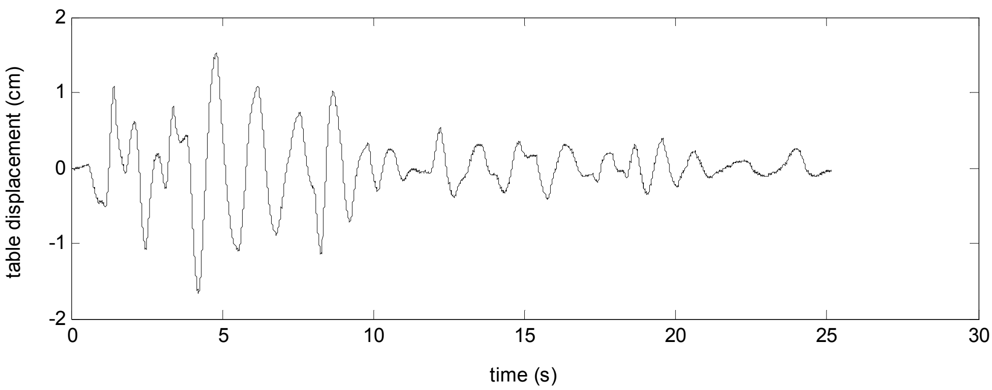

Figure B.83. Measured table displacement for Test 8 Run 8a-4

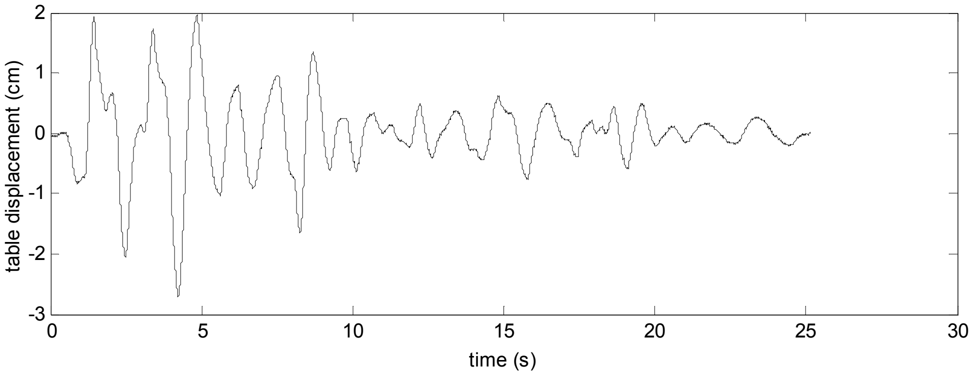

Figure B.84. Measured table displacement for Test 8 Run 8a-5

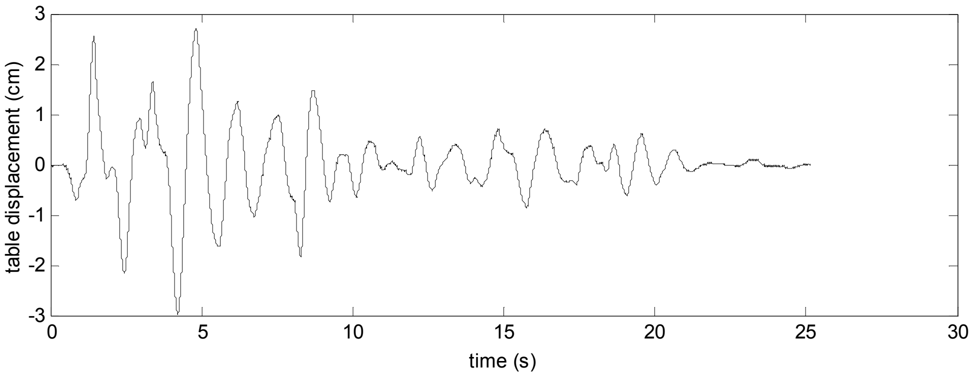

Figure B.85. Measured table displacement for Test 8 Run 8a-6

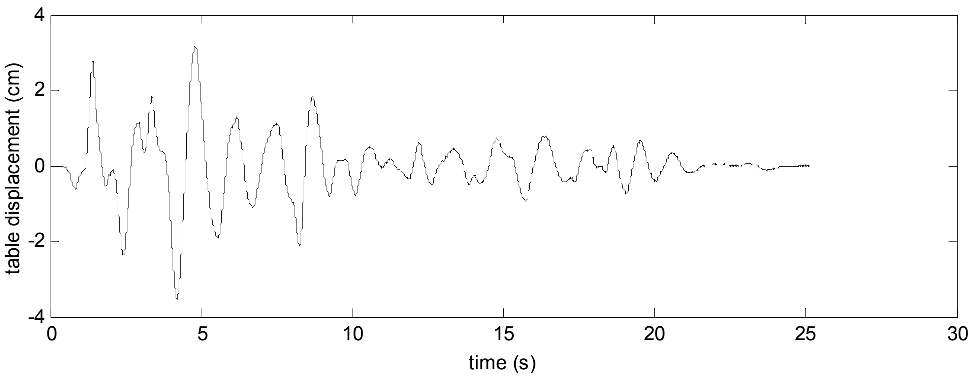

Figure B.86. Measured table displacement for Test 8 Run 8a-7

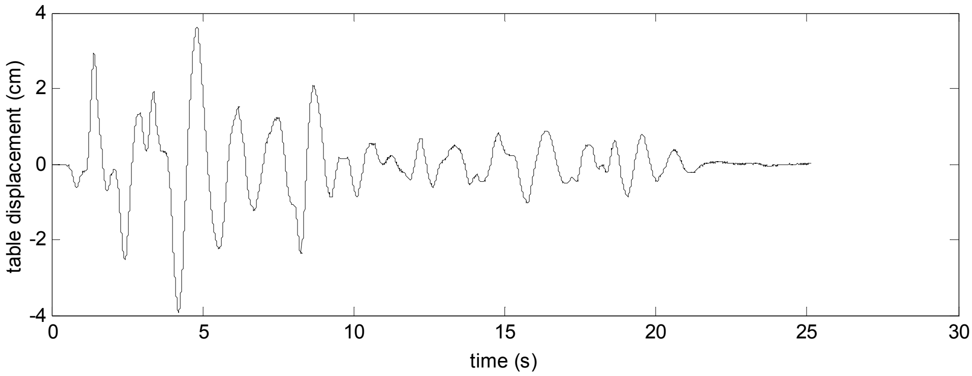

Figure B.87. Measured table displacement for Test 8 Run 8a-8

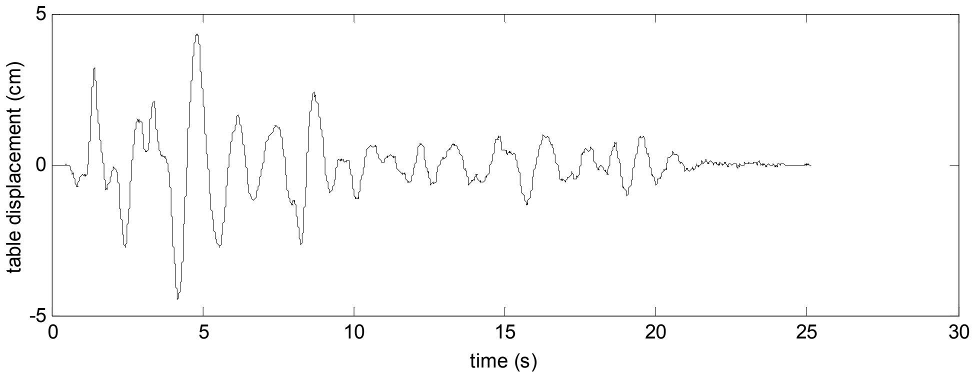

Figure B.88. Measured table displacement for Test 8 Run 8a-9

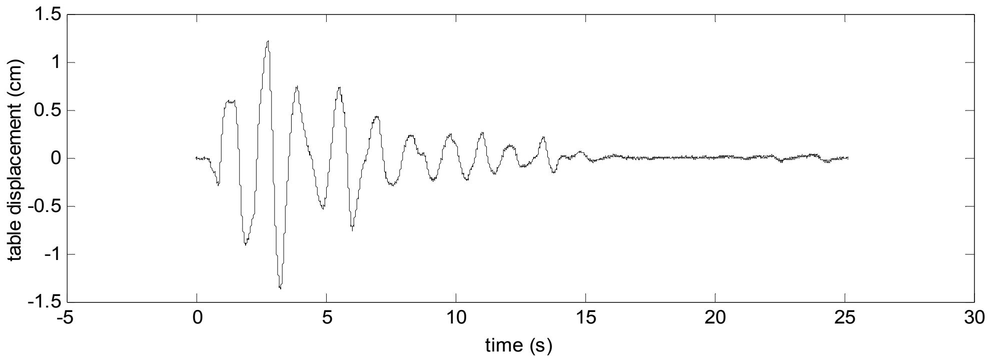

Figure B.89. Measured table displacement for Test 8 Run 8b-1

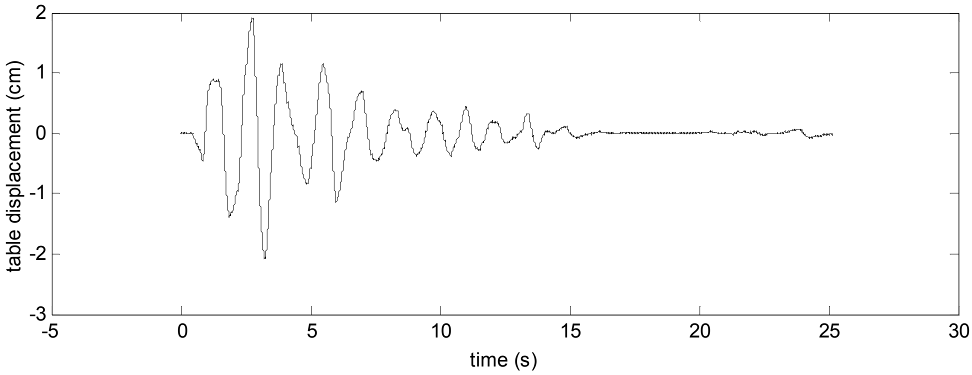

Figure B.90. Measured table displacement for Test 8 Run 8b-2

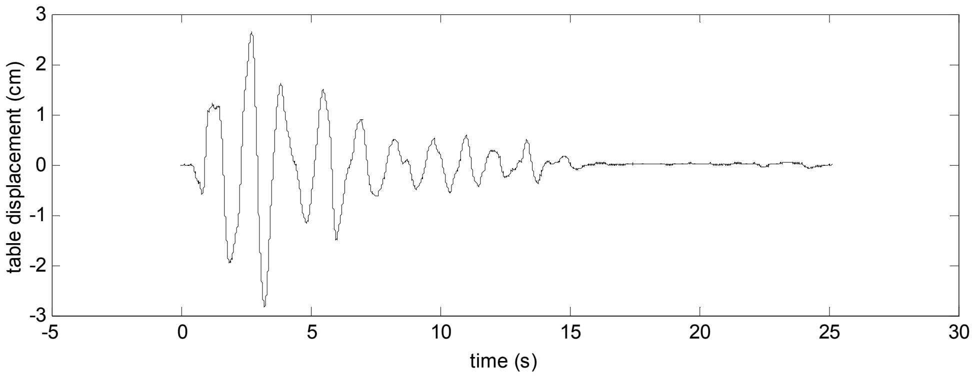

Figure B.91. Measured table displacement for Test 8 Run 8b-3

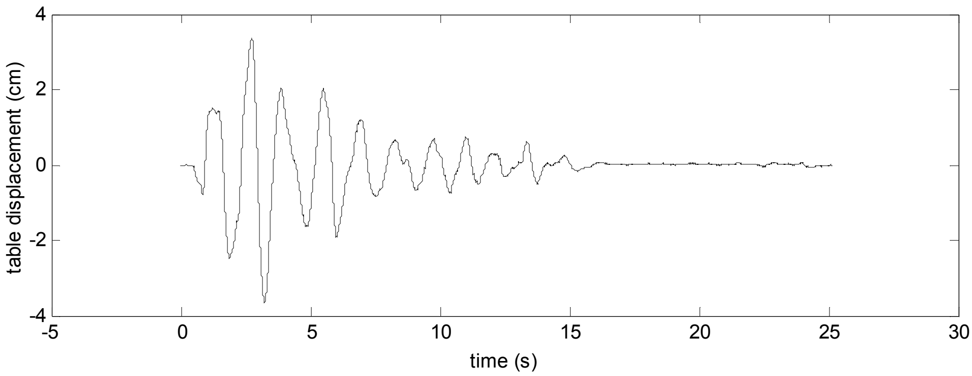

Figure B.92. Measured table displacement for Test 8 Run 8b-4

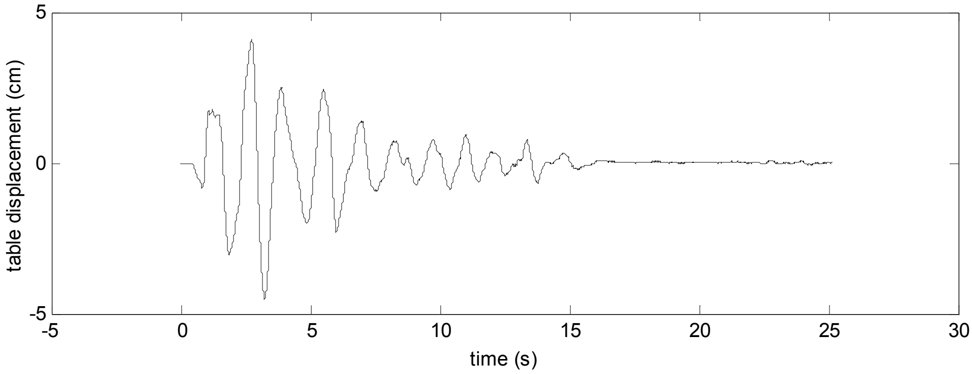

Figure B.93. Measured table displacement for Test 8 Run 8b-5

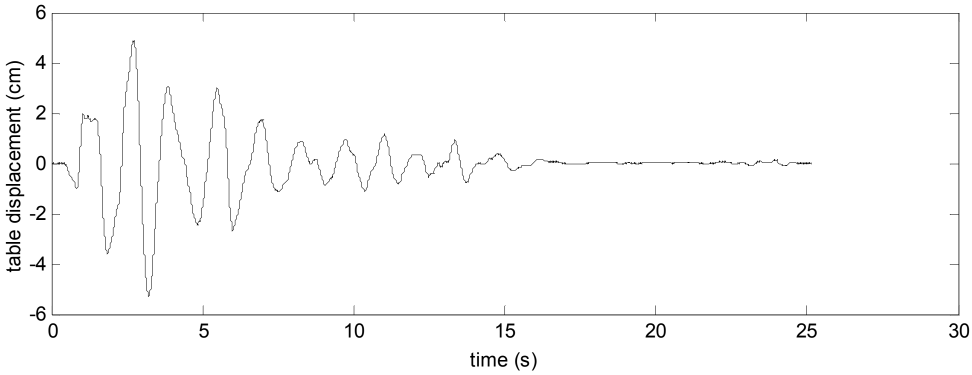

Figure B.94. Measured table displacement for Test 8 Run 8b-6

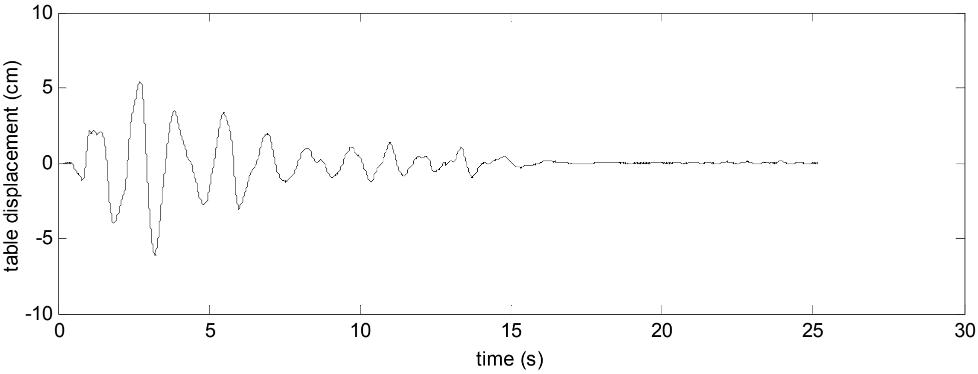

Figure B.95. Measured table displacement for Test 8 Run 8b-7

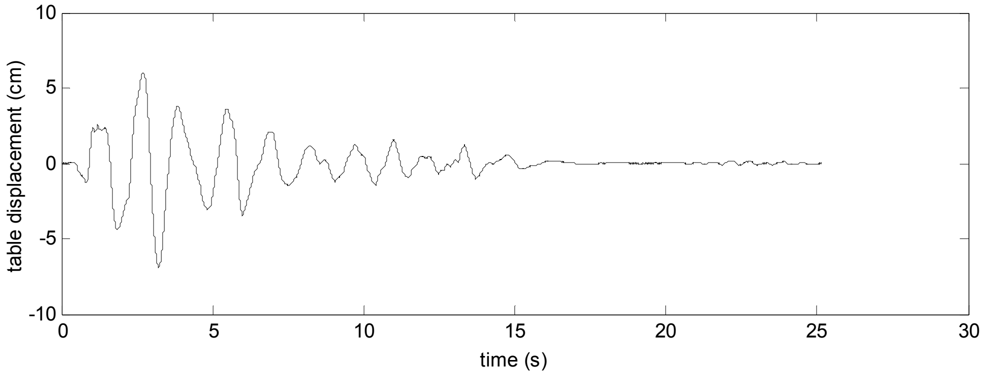

Figure B.96. Measured table displacement for Test 8 Run 8b-8

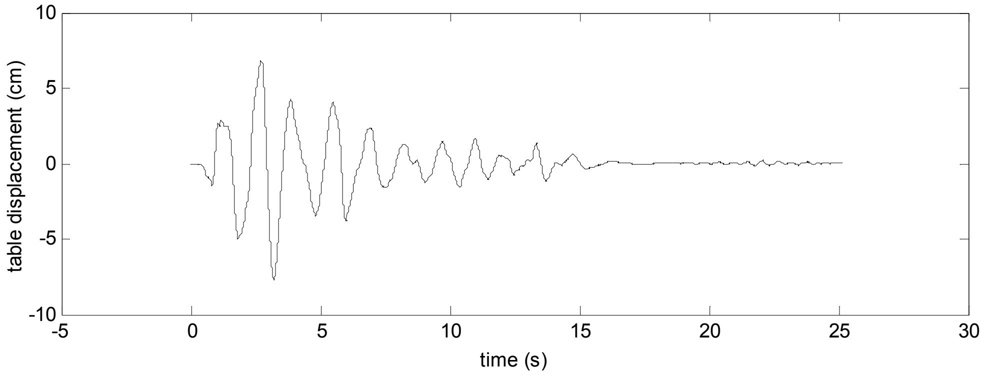

Figure B.97. Measured table displacement for Test 8 Run 8b-9

APPENDIX C: SAMPLE DESIGN GEOTEXTILE STRESS CALCULATION TABLES

Table C.1. Calculation of design tensile stresses due to seismic loads in geotextile reinforcements for Test 1-10 using FHWA method

Calculation of Tensile Load in Geotextiles for TEST 1 using FHWA Recommendations

$a_{max(table)}/g$	0.2957208
A_m	0.341
θ	18.85
K_A	0.260
K_{AE}	0.500
ΔK_{dyn}	0.24

H	1.88
L	1.70
K_{AH}	0.21
K_{AEH}	0.40
ΔK_{dynH}	0.19

Φ	(backfill)	36.00
γ	(backfill)	15.25
Mobilized interface friction angle	(backfill)	36.00
Φ	(reinforced soil)	36.00
γ	(reinforced soil)	15.25

W_w	4.32
W_i	45.87
W_r	50.20

W_i'	24.08
W_A	18.06

Block depth	0.10
Block unit weight	23.00

R_S	36.47
P_{IR}	9.70
P_{AEH}	8.28
FS_{sl}	2.03

P_I	6.16

Tensile stresses in geotextiles

									2001	2009
Layer Number	Elevation	Z_{vi}	S_{vi}	L_i	H	$K\ \sigma_{vi}$	L_a	Le	T_{md}	T_{md}
1	0.10	1.78	0.20	1.60	1.88	5.70	0.05	1.55	0.93	0.685
2	0.30	1.58	0.20	1.60	1.88	5.06	0.15	1.45	0.87	0.685
3	0.50	1.38	0.20	1.60	1.88	4.42	0.25	1.35	0.81	0.685
4	0.70	1.18	0.20	1.60	1.88	3.78	0.36	1.24	0.75	0.685
5	0.90	0.98	0.20	1.60	1.88	3.14	0.46	1.14	0.68	0.685
6	1.10	0.78	0.20	1.60	1.88	2.50	0.56	1.04	0.62	0.685
7	1.30	0.58	0.20	1.60	1.88	1.86	0.66	0.94	0.56	0.685
8	1.50	0.38	0.20	1.60	1.88	1.22	0.76	0.84	0.50	0.685
9	1.70	0.18	0.28	1.60	1.88	0.58	0.87	0.73	0.44	0.685
							Sum	10.27	6.16	6.16

Table C.2. Calculation of design tensile stresses due to seismic loads in geotextile reinforcements for Test 1-10 using NCMA method

Calculation of Tensile Load in Geotextiles for TEST 1 using NCMA Segmental Retaining Walls Seismic Design Manual

$A=a_{max(table)}/g$	0.2957208
k_h (int)	0.341
θ (int)	18.85
k_h (ext)	0.15
θ (ext)	8.41
K_A	0.260
K_{AE} (int)	0.500
$\Delta K_{dyn\ (int)}$	0.24
K_{AE} (ext)	0.345
$\Delta K_{dyn\ (ext)}$	0.09

H	1.88
L	1.70
K_{AH}	0.21
$K_{AEH\ (int)}$	0.40
$\Delta K_{dynH\ (int)}$	0.19
$K_{AEH\ (ext)}$	0.28
$\Delta K_{dynH\ (ext)}$	0.07

Φ	(backfill)	36.00
γ	(backfill)	15.25
Mobilized interface friction angle, δ	(backfill)	36.00
Φ	(reinforced soil)	36.00
γ	(reinforced soil)	15.25

Block depth	0.10
Block unit weight	23.00

W_w	4.32
W_i	45.87
W_r	50.20

W_i'	24.08

R_S	36.47
P_{IR}	4.20
P_{AEH}	6.59
$FS_{sliding}$	3.38
$FS_{overturning}$	4.85

Reinforcement loads

Layer Number	Elevation	Z_{vi}	S_{vi}	L_i	H	$F_{static\ i}$	$F_{inertial\ i}$	$F_{dyn\ i}$	$\Delta F_{seismic}$
1	0.10	1.78	0.20	1.60	1.88	1.14	0.16	0.26	0.42
2	0.30	1.58	0.20	1.60	1.88	1.01	0.16	0.33	0.49
3	0.50	1.38	0.20	1.60	1.88	0.88	0.16	0.40	0.56
4	0.70	1.18	0.20	1.60	1.88	0.76	0.16	0.47	0.63
5	0.90	0.98	0.20	1.60	1.88	0.63	0.16	0.54	0.70
6	1.10	0.78	0.20	1.60	1.88	0.50	0.16	0.61	0.77
7	1.30	0.58	0.20	1.60	1.88	0.37	0.16	0.69	0.84
8	1.50	0.38	0.20	1.60	1.88	0.24	0.16	0.76	0.91
9	1.70	0.18	0.28	1.60	1.88	0.16	0.22	1.16	1.38

Table C.3. Calculation of design tensile stresses due to seismic loads in geotextile reinforcements for Test 2-11 using FHWA method

Calculation of Tensile Load in Geotextiles for TEST 2 using FHWA Recommendations

$a_{max(table)}/g$	0.2717652
A_m	0.320
θ	17.76
K_A	0.238
K_{AE}	0.447
ΔK_{dyn}	0.21

H	1.88
L	1.14
K_{AH}	0.19
K_{AEH}	0.35
ΔK_{dynH}	0.17

Φ	(backfill)	38.00
γ	(backfill)	16.50
Mobilized interface friction angle	(backfill)	38.00
Φ	(reinforced soil)	38.00
γ	(reinforced soil)	16.50

W_w	4.32
W_i	32.26
W_r	36.58

W_i'	26.06
W_A	18.55

Block depth	0.10
Block unit weight	23.00

R_S	28.58
P_{IR}	9.73
P_{AEH}	7.87
FS_{sl}	1.62

P_I	5.94

Tensile stresses in geotextiles

									2001	2009
Layer Number	Elevation	Z_{vi}	S_{vi}	L_i	H	$K\,\sigma_{vi}$	L_a	Le	T_{md}	T_{md}
1	0.10	1.78	0.20	1.04	1.88	5.51	0.05	0.99	1.09	0.660
2	0.30	1.58	0.20	1.04	1.88	4.89	0.15	0.89	0.98	0.660
3	0.50	1.38	0.20	1.04	1.88	4.27	0.24	0.80	0.87	0.660
4	0.70	1.18	0.20	1.04	1.88	3.65	0.34	0.70	0.77	0.660
5	0.90	0.98	0.20	1.04	1.88	3.03	0.44	0.60	0.66	0.660
6	1.10	0.78	0.20	1.04	1.88	2.41	0.54	0.50	0.55	0.660
7	1.30	0.58	0.20	1.04	1.88	1.79	0.63	0.41	0.45	0.660
8	1.50	0.38	0.20	1.04	1.88	1.18	0.73	0.31	0.34	0.660
9	1.70	0.18	0.28	1.04	1.88	0.56	0.83	0.21	0.23	0.660
							Sum	5.41	5.94	5.94

Table C.4. Calculation of design tensile stresses due to seismic loads in geotextile reinforcements for Test 2-11 using NCMA method

Calculation of Tensile Load in Geotextiles for TEST 2 using NCMA Segmental Retaining Walls Seismic Design Manual

$A=a_{max(table)}/g$	0.2717652
k_h (int)	0.320
θ (int)	17.76
k_h (ext)	0.14
θ (ext)	7.74
K_A	0.238
K_{AE} (int)	0.447
$\Delta K_{dyn\ (int)}$	0.21
K_{AE} (ext)	0.312
$\Delta K_{dyn\ (ext)}$	0.07
W_w	4.32
W_i	32.26
W_r	36.58
R_S	28.58
P_{IR}	4.13
P_{AEH}	6.32
$FS_{sliding}$	2.74
$FS_{overturning}$	2.44

H	1.88
L	1.14
K_{AH}	0.19
$K_{AEH\ (int)}$	0.35
$\Delta K_{dynH\ (int)}$	0.17
$K_{AEH\ (ext)}$	0.25
$\Delta K_{dynH\ (ext)}$	0.06
W_i'	26.06

Φ	(backfill)	38.00
γ	(backfill)	16.50
Mobilized interface friction angle, δ	(backfill)	38.00
Φ	(reinforced soil)	38.00
γ	(reinforced soil)	16.50

Block depth	0.10
Block unit weight	23.00

Reinforcement loads

Layer Number	Elevation	Z_{vi}	S_{vi}	L_i	H	$F_{static\ i}$	$F_{inertial\ i}$	$F_{dyn\ i}$	$\Delta F_{seismic}$
1	0.10	1.78	0.20	1.04	1.88	1.10	0.15	0.24	0.38
2	0.30	1.58	0.20	1.04	1.88	0.98	0.15	0.30	0.45
3	0.50	1.38	0.20	1.04	1.88	0.85	0.15	0.37	0.52
4	0.70	1.18	0.20	1.04	1.88	0.73	0.15	0.43	0.58
5	0.90	0.98	0.20	1.04	1.88	0.61	0.15	0.50	0.65
6	1.10	0.78	0.20	1.04	1.88	0.48	0.15	0.56	0.71
7	1.30	0.58	0.20	1.04	1.88	0.36	0.15	0.63	0.78
8	1.50	0.38	0.20	1.04	1.88	0.24	0.15	0.69	0.84
9	1.70	0.18	0.28	1.04	1.88	0.16	0.21	1.06	1.27

Table C.5. Calculation of design tensile stresses due to seismic loads in geotextile reinforcements for Test 3-10 using FHWA method

Calculation of Tensile Load in Geotextiles for TEST 3 using FHWA Recommendations

$a_{max(table)}/g$	0.28038
A_m	0.328
θ	18.16
K_A	0.238
K_{AE}	0.454
ΔK_{dyn}	0.22

H	1.88
L	0.85
K_{AH}	0.19
K_{AEH}	0.36
ΔK_{dynH}	0.17

Φ	(backfill)	38.00
γ	(backfill)	17.00
Mobilized interface friction angle	(backfill)	38.00
Φ	(reinforced soil)	38.00
γ	(reinforced soil)	17.00

W_w	4.32
W_i	23.97
W_r	28.29

W_i'	26.85
W_A	18.98

Block depth	0.10
Block unit weight	23.00

R_S	22.11
P_{IR}	10.22 (NCMA)
P_{AEH}	8.19
FS_{sl}	1.20

P_I	6.22

Tensile stresses in geotextiles

									2001	2009
Layer Number	Elevation	Z_{vi}	S_{vi}	L_i	H	$K\,\sigma_{vi}$	L_a	Le	T_{md}	T_{md}
1	0.10	1.78	0.15	0.75	1.88	5.67	0.05	0.70	0.81	0.415
2	0.20	1.68	0.10	0.75	1.88	5.35	0.10	0.65	0.75	0.415
3	0.30	1.58	0.10	0.75	1.88	5.04	0.15	0.60	0.70	0.415
4	0.40	1.48	0.10	0.75	1.88	4.72	0.20	0.55	0.64	0.415
5	0.50	1.38	0.10	0.75	1.88	4.40	0.24	0.51	0.58	0.415
6	0.60	1.28	0.10	0.75	1.88	4.08	0.29	0.46	0.53	0.415
7	0.70	1.18	0.10	0.75	1.88	3.76	0.34	0.41	0.47	0.415
8	0.80	1.08	0.10	0.75	1.88	3.44	0.39	0.36	0.41	0.415
9	0.90	0.98	0.10	0.75	1.88	3.12	0.44	0.31	0.36	0.415
10	1.00	0.88	0.10	0.75	1.88	2.80	0.49	0.26	0.30	0.415
11	1.10	0.78	0.10	0.75	1.88	2.49	0.54	0.21	0.25	0.415
12	1.20	0.68	0.10	0.75	1.88	2.17	0.59	0.16	0.19	0.415
13	1.30	0.58	0.10	0.75	1.88	1.85	0.63	0.12	0.13	0.415
14	1.40	0.48	0.10	0.75	1.88	1.53	0.68	0.07	0.08	0.415
15	1.50	0.38	0.10	0.75	1.88	1.21	0.73	0.02	0.02	0.415
16	1.60	0.28	0.10	0.75	1.88	0.89	0.78	0.00	0.00	0.000
17	1.70	0.18	0.23	0.75	1.88	0.57	0.83	0.00	0.00	0.000
							Sum	5.40	6.22	6.22

Table C.6. Calculation of design tensile stresses due to seismic loads in geotextile reinforcements for Test 3-10 using NCMA method

Calculation of Tensile Load in Geotextiles for TEST 3 using NCMA Segmental Retaining Walls Seismic Design Manual

$A=a_{max(table)}/g$	0.28038
k_h (int)	0.328
θ (int)	18.16
k_h (ext)	0.14
θ (ext)	7.98
K_A	0.238
K_{AE} (int)	0.454
$\Delta K_{dyn\,(int)}$	0.22
K_{AE} (ext)	0.315
$\Delta K_{dyn\,(ext)}$	0.08

H	1.88
L	0.85
K_{AH}	0.19
$K_{AEH\,(int)}$	0.36
$\Delta K_{dynH\,(int)}$	0.17
$K_{AEH\,(ext)}$	0.25
$\Delta K_{dynH\,(ext)}$	0.06

Φ	(backfill)	38.00
γ	(backfill)	17.00
Mobilized interface friction angle, δ	(backfill)	38.00
Φ	(reinforced soil)	38.00
γ	(reinforced soil)	17.00

Block depth	0.10
Block unit weight	23.00

W_w	4.32
W_i	23.97
W_r	28.29

W_i'	26.85

R_S	22.11
P_{IR}	4.37
P_{AEH}	6.54
$FS_{sliding}$	2.03
$FS_{overturning}$	1.34

Reinforcement loads

Layer Number	Elevation	Z_{vi}	S_{vi}	L_i	H	$F_{static\ i}$	$F_{inertial\ i}$	$F_{dyn\ i}$	$\Delta F_{seismic}$
1	0.10	1.78	0.15	0.75	1.88	0.85	0.11	0.19	0.30
2	0.20	1.68	0.10	0.75	1.88	0.54	0.08	0.14	0.22
3	0.30	1.58	0.10	0.75	1.88	0.50	0.08	0.16	0.24
4	0.40	1.48	0.10	0.75	1.88	0.47	0.08	0.18	0.25
5	0.50	1.38	0.10	0.75	1.88	0.44	0.08	0.20	0.27
6	0.60	1.28	0.10	0.75	1.88	0.41	0.08	0.21	0.29
7	0.70	1.18	0.10	0.75	1.88	0.38	0.08	0.23	0.31
8	0.80	1.08	0.10	0.75	1.88	0.34	0.08	0.25	0.32
9	0.90	0.98	0.10	0.75	1.88	0.31	0.08	0.27	0.34
10	1.00	0.88	0.10	0.75	1.88	0.28	0.08	0.28	0.36
11	1.10	0.78	0.10	0.75	1.88	0.25	0.08	0.30	0.38
12	1.20	0.68	0.10	0.75	1.88	0.22	0.08	0.32	0.39
13	1.30	0.58	0.10	0.75	1.88	0.18	0.08	0.33	0.41
14	1.40	0.48	0.10	0.75	1.88	0.15	0.08	0.35	0.43
15	1.50	0.38	0.10	0.75	1.88	0.12	0.08	0.37	0.45
16	1.60	0.28	0.10	0.75	1.88	0.09	0.08	0.39	0.46
17	1.80	0.18	0.23	0.75	1.88	0.13	0.17	0.93	1.10

Table C.7. Calculation of design tensile stresses due to seismic loads in geotextile reinforcements for Test 4-15 using FHWA method

Calculation of Tensile Load in Geotextiles for TEST 4 using FHWA Recommendations

$a_{max(table)}/g$	0.39768
A_m	0.418
θ	22.71
K_A	0.249
K_{AE}	0.562
ΔK_{dyn}	0.31

H	1.88
L	0.85
K_{AH}	0.20
K_{AEH}	0.45
ΔK_{dynH}	0.25

Φ	(backfill)	37.00
γ	(backfill)	16.40
Mobilized interface friction angle	(backfill)	37.00
Φ	(reinforced soil)	37.00
γ	(reinforced soil)	16.40

W_w	4.32
W_i	23.12
W_r	27.45

W_i'	25.90
W_A	18.77

Block depth	0.10
Block unit weight	23.00

R_S	20.68
P_{IR}	12.65 (NCMA)
P_{AEH}	9.38
FS_{sl}	0.94

P_I	7.86

Tensile stresses in geotextiles

									2001	2009
Layer Number	Elevation	Z_{vi}	S_{vi}	L_i	H	$K\sigma_{vi}$	L_a	Le	T_{md}	T_{md}
1	0.10	1.78	0.20	0.75	1.88	5.80	0.05	0.70	1.96	0.982
2	0.30	1.58	0.20	0.75	1.88	5.14	0.15	0.60	1.68	0.982
3	0.50	1.38	0.20	0.75	1.88	4.49	0.25	0.50	1.40	0.982
4	0.70	1.18	0.20	0.75	1.88	3.84	0.35	0.40	1.12	0.982
5	0.90	0.98	0.20	0.75	1.88	3.19	0.45	0.30	0.84	0.982
6	1.10	0.78	0.20	0.75	1.88	2.54	0.55	0.20	0.56	0.982
7	1.30	0.58	0.20	0.75	1.88	1.89	0.65	0.10	0.28	0.982
8	1.50	0.38	0.20	0.75	1.88	1.24	0.75	0.00	0.01	0.982
9	1.70	0.18	0.28	0.75	1.88	0.59	0.85	0.00	0.00	0.000
							Sum	2.81	7.86	7.86

Table C.8. Calculation of design tensile stresses due to seismic loads in geotextile reinforcements for Test 4-15 using NCMA method

Calculation of Tensile Load in Geotextiles for TEST 4 using NCMA Segmental Retaining Walls Seismic Design Manual

$A=a_{max(table)}/g$	0.39768
k_h (int)	0.418
θ (int)	22.71
k_h (ext)	0.20
θ (ext)	11.25
K_A	0.249
K_{AE} (int)	0.562
$\Delta K_{dyn\ (int)}$	0.31
K_{AE} (ext)	0.367
$\Delta K_{dyn\ (ext)}$	0.12

H	1.88
L	0.85
K_{AH}	0.20
$K_{AEH\ (int)}$	0.45
$\Delta K_{dynH\ (int)}$	0.25
$K_{AEH\ (ext)}$	0.29
$\Delta K_{dynH\ (ext)}$	0.09

Φ	(backfill)	37.00
γ	(backfill)	16.40
Mobilized interface friction angle, δ	(backfill)	37.00
Φ	(reinforced soil)	37.00
γ	(reinforced soil)	16.40

Block depth	0.10
Block unit weight	23.00

W_w	4.32
W_i	23.12
W_r	27.45

W_i'	25.90

R_S	20.68
P_{IR}	6.01
P_{AEH}	7.12
$FS_{sliding}$	1.58
$FS_{overturning}$	1.04

Reinforcement loads

Layer Number	Elevation	Z_{vi}	S_{vi}	L_i	H	$F_{static\ i}$	$F_{inertial\ i}$	$F_{dyn\ i}$	$\Delta F_{seismic}$
1	0.10	1.78	0.20	0.75	1.88	1.16	0.19	0.36	0.55
2	0.30	1.58	0.20	0.75	1.88	1.03	0.19	0.46	0.65
3	0.50	1.38	0.20	0.75	1.88	0.90	0.19	0.55	0.75
4	0.70	1.18	0.20	0.75	1.88	0.77	0.19	0.65	0.85
5	0.90	0.98	0.20	0.75	1.88	0.64	0.19	0.75	0.94
6	1.10	0.78	0.20	0.75	1.88	0.51	0.19	0.85	1.04
7	1.30	0.58	0.20	0.75	1.88	0.38	0.19	0.95	1.14
8	1.50	0.38	0.20	0.75	1.88	0.25	0.19	1.05	1.24
9	1.70	0.18	0.28	0.75	1.88	0.16	0.27	1.60	1.87

Table C.9. Calculation of design tensile stresses due to seismic loads in geotextile reinforcements for Test 5-7 using FHWA method

Calculation of Tensile Load in Geotextiles for TEST 5 using FHWA Recommendations

$a_{max(table)}/g$	0.41597
A_m	0.430
θ	23.27
K_A	0.198
K_{AE}	0.483
ΔK_{dyn}	0.28

H	0.93
L	0.43
K_{AH}	0.15
K_{AEH}	0.36
ΔK_{dynH}	0.21

Φ	(backfill)	42.00
γ	(backfill)	19.00
Mobilized interface friction angle	(backfill)	42.00
Φ	(reinforced soil)	42.00
γ	(reinforced soil)	19.00

W_w	1.07
W_i	6.63
W_r	7.70

W_i'	7.33
W_A	4.73

Block depth	0.05
Block unit weight	23.00

R_S	6.93(NCMA)
P_{IR}	3.61
P_{AEH}	2.08
FS_{sl}	1.22

P_I	2.03

Tensile stresses in geotextiles

									2001	2009
Layer Number	Elevation	Z_{vi}	S_{vi}	L_i	H	$K\,\sigma_{vi}$	L_a	Le	T_{md}	T_{md}
1	0.05	0.88	0.10	0.38	0.93	2.46	0.02	0.35	0.46	0.254
2	0.15	0.78	0.10	0.38	0.93	2.18	0.07	0.31	0.40	0.254
3	0.25	0.68	0.10	0.38	0.93	1.90	0.11	0.26	0.34	0.254
4	0.35	0.58	0.10	0.38	0.93	1.62	0.16	0.22	0.28	0.254
5	0.45	0.48	0.10	0.38	0.93	1.34	0.20	0.17	0.23	0.254
6	0.55	0.38	0.10	0.38	0.93	1.06	0.24	0.13	0.17	0.254
7	0.65	0.28	0.10	0.38	0.93	0.78	0.29	0.09	0.11	0.254
8	0.75	0.18	0.10	0.38	0.93	0.50	0.33	0.04	0.05	0.254
9	0.85	0.08	0.13	0.38	0.93	0.22	0.38	0.00	0.00	0.000
							Sum	1.58	2.03	2.03

Table C.10. Calculation of design tensile stresses due to seismic loads in geotextile reinforcements for Test 5-7 using NCMA method

Calculation of Tensile Load in Geotextiles for TEST 5 using NCMA Segmental Retaining Walls Seismic Design Manual

$A=a_{max(table)}/g$	0.41597
k_h (int)	0.430
θ (int)	23.27
k_h (ext)	0.21
θ (ext)	11.75
K_A	0.198
K_{AE} (int)	0.483
$\Delta K_{dyn\,(int)}$	0.28
K_{AE} (ext)	0.309
$\Delta K_{dyn\,(ext)}$	0.11

H	0.93
L	0.43
K_{AH}	0.15
$K_{AEH\,(int)}$	0.36
$\Delta K_{dynH\,(int)}$	0.21
$K_{AEH\,(ext)}$	0.23
$\Delta K_{dynH\,(ext)}$	0.08

Φ	(backfill)	42.00
γ	(backfill)	19.00
Mobilized interface friction angle, δ	(backfill)	42.00
Φ	(reinforced soil)	42.00
γ	(reinforced soil)	19.00

Block depth	0.05
Block unit weight	23.00

W_w	1.07
W_i	6.63
W_r	7.70

W_i'	7.33

R_S	6.93
P_{IR}	1.75
P_{AEH}	1.55
$FS_{sliding}$	2.10
$FS_{overturning}$	1.16

Reinforcement loads

Layer Number	Elevation	Z_{vi}	S_{vi}	L_i	H	$F_{static\ i}$	$F_{inertial\ i}$	$F_{dyn\ i}$	$\Delta F_{seismic}$
1	0.05	0.88	0.10	0.38	0.93	0.25	0.05	0.09	0.14
2	0.15	0.78	0.10	0.38	0.93	0.22	0.05	0.11	0.16
3	0.25	0.68	0.10	0.38	0.93	0.19	0.05	0.14	0.18
4	0.35	0.58	0.10	0.38	0.93	0.16	0.05	0.16	0.21
5	0.45	0.48	0.10	0.38	0.93	0.13	0.05	0.18	0.23
6	0.55	0.38	0.10	0.38	0.93	0.11	0.05	0.21	0.26
7	0.65	0.28	0.10	0.38	0.93	0.08	0.05	0.23	0.28
8	0.75	0.18	0.10	0.38	0.93	0.05	0.05	0.26	0.31
9	0.85	0.08	0.13	0.38	0.93	0.03	0.06	0.36	0.43

Table C.11. Calculation of design tensile stresses due to seismic loads in geotextile reinforcements for Test 6-7 using FHWA method

Calculation of Tensile Load in Geotextiles for TEST 6 using FHWA Recommendations

$a_{max(table)}/g$	0.38756					
A_m	0.412	H	1.93	Φ	(backfill)	41.00
θ	22.38	L	0.85	γ	(backfill)	18.50
K_A	0.208	K_{AH}	0.16	Mobilized interface friction angle	(backfill)	41.00
K_{AE}	0.482	K_{AEH}	0.36	Φ	(reinforced soil)	41.00
ΔK_{dyn}	0.27	ΔK_{dynH}	0.21	γ	(reinforced soil)	18.50

W_w	2.22			Block depth	0.05
W_i	28.56	W_i'	32.67	Block unit weight	23.00
W_r	30.78	W_A	17.92		

R_S	26.76		
P_{IR}	14.37	P_I	7.38
P_{AEH}	8.97		
FS_{sl}	1.15		

Tensile stresses in geotextiles

									2001	2009
Layer Number	Elevation	Z_{vi}	S_{vi}	L_i	H	$K\ \sigma_{vi}$	L_a	Le	T_{md}	T_{md}
1	0.05	1.88	0.10	0.80	1.93	5.45	0.02	0.78	0.82	0.410
2	0.15	1.78	0.10	0.80	1.93	5.16	0.07	0.73	0.77	0.410
3	0.25	1.68	0.10	0.80	1.93	4.87	0.11	0.69	0.72	0.410
4	0.35	1.58	0.10	0.80	1.93	4.58	0.16	0.64	0.67	0.410
5	0.45	1.48	0.10	0.80	1.93	4.29	0.21	0.59	0.63	0.410
6	0.55	1.38	0.10	0.80	1.93	4.00	0.25	0.55	0.58	0.410
7	0.65	1.28	0.10	0.80	1.93	3.71	0.30	0.50	0.53	0.410
8	0.75	1.18	0.10	0.80	1.93	3.42	0.34	0.46	0.48	0.410
9	0.85	1.08	0.10	0.80	1.93	3.13	0.39	0.41	0.43	0.410
10	0.95	0.98	0.10	0.80	1.93	2.84	0.43	0.37	0.39	0.410
11	1.05	0.88	0.10	0.80	1.93	2.55	0.48	0.32	0.34	0.410
12	1.15	0.78	0.10	0.80	1.93	2.26	0.52	0.28	0.29	0.410
13	1.25	0.68	0.10	0.80	1.93	1.97	0.57	0.23	0.24	0.410
14	1.35	0.58	0.10	0.80	1.93	1.68	0.62	0.18	0.19	0.410
15	1.45	0.48	0.10	0.80	1.93	1.39	0.66	0.14	0.15	0.410
16	1.55	0.38	0.10	0.80	1.93	1.10	0.71	0.09	0.10	0.410
17	1.65	0.28	0.10	0.80	1.93	0.81	0.75	0.05	0.05	0.410
18	1.75	0.18	0.23	0.80	1.93	0.52	0.80	0.0025	0.00	0.410
							Sum	7.02	7.38	7.38

Table C.12. Calculation of design tensile stresses due to seismic loads in geotextile reinforcements for Test 6-7 using NCMA method

Calculation of Tensile Load in Geotextiles for TEST 6 using NCMA Segmental Retaining Walls Seismic Design Manual

$A=a_{max(table)}/g$	0.38756
k_h (int)	0.412
θ (int)	22.38
k_h (ext)	0.19
θ (ext)	10.97
K_A	0.208
K_{AE} (int)	0.482
$\Delta K_{dyn\ (int)}$	0.27
K_{AE} (ext)	0.312
$\Delta K_{dyn\ (ext)}$	0.10

H	1.93
L	0.85
K_{AH}	0.16
$K_{AEH\ (int)}$	0.36
$\Delta K_{dynH\ (int)}$	0.21
$K_{AEH\ (ext)}$	0.24
$\Delta K_{dynH\ (ext)}$	0.08

Φ	(backfill)	41.00
γ	(backfill)	18.50
Mobilized interface friction angle, δ	(backfill)	41.00
Φ	(reinforced soil)	41.00
γ	(reinforced soil)	18.50

Block depth	0.05
Block unit weight	23.00

W_w	2.22
W_i	28.56
W_r	30.78

W_i'	32.67

R_S	26.76
P_{IR}	6.76
P_{AEH}	6.76
$FS_{sliding}$	1.98
$FS_{overturning}$	1.12

Reinforcement loads

Layer Number	Elevation	Z_{vi}	S_{vi}	L_i	H	$F_{static\ i}$	$F_{inertial\ i}$	$F_{dyn\ i}$	$\Delta F_{seismic}$
1	0.05	1.88	0.10	0.80	1.93	0.55	0.05	0.16	0.21
2	0.15	1.78	0.10	0.80	1.93	0.52	0.05	0.18	0.23
3	0.25	1.68	0.10	0.80	1.93	0.49	0.05	0.21	0.25
4	0.35	1.58	0.10	0.80	1.93	0.46	0.05	0.23	0.28
5	0.45	1.48	0.10	0.80	1.93	0.43	0.05	0.25	0.30
6	0.55	1.38	0.10	0.80	1.93	0.40	0.05	0.27	0.32
7	0.65	1.28	0.10	0.80	1.93	0.37	0.05	0.30	0.34
8	0.75	1.18	0.10	0.80	1.93	0.34	0.05	0.32	0.37
9	0.85	1.08	0.10	0.80	1.93	0.31	0.05	0.34	0.39
10	0.95	0.98	0.10	0.80	1.93	0.28	0.05	0.37	0.41
11	1.05	0.88	0.10	0.80	1.93	0.26	0.05	0.39	0.44
12	1.15	0.78	0.10	0.80	1.93	0.23	0.05	0.41	0.46
13	1.25	0.68	0.10	0.80	1.93	0.20	0.05	0.44	0.48
14	1.35	0.58	0.10	0.80	1.93	0.17	0.05	0.46	0.51
15	1.45	0.48	0.10	0.80	1.93	0.14	0.05	0.48	0.53
16	1.55	0.38	0.10	0.80	1.93	0.11	0.05	0.50	0.55
17	1.65	0.28	0.10	0.80	1.93	0.08	0.05	0.53	0.57
18	1.75	0.18	0.23	0.80	1.93	0.12	0.11	1.27	1.37

Table C.13. Calculation of design tensile stresses due to seismic loads in geotextile reinforcements for Test 7-7 using FHWA method

Calculation of Tensile Load in Geotextiles for TEST 7 using FHWA Recommendations

$a_{max(table)}/g$	0.39787
A_m	0.419
θ	22.71
K_A	0.208
K_{AE}	0.489
ΔK_{dyn}	0.28

H	1.93
L	1.45
K_{AH}	0.16
K_{AEH}	0.37
ΔK_{dynH}	0.21

Φ	(backfill)	41.00
γ	(backfill)	18.50
Mobilized interface friction angle	(backfill)	41.00
Φ	(reinforced soil)	41.00
γ	(reinforced soil)	18.50

W_w	2.22
W_i	49.99
W_r	52.21

W_i'	32.67
W_A	17.92

Block depth	0.05
Block unit weight	23.00

R_S	45.38
P_{IR}	14.61
P_{AEH}	9.05
FS_{sl}	1.92

P_I	7.50

Tensile stresses in geotextiles

									2001	2009
Layer Number	Elevation	Z_{vi}	S_{vi}	L_i	H	$K\ \sigma_{vi}$	L_a	Le	T_{md}	T_{md}
1	0.05	1.88	0.10	1.40	1.93	5.45	0.02	1.38	0.58	0.417
2	0.15	1.78	0.10	1.40	1.93	5.16	0.07	1.33	0.56	0.417
3	0.25	1.68	0.10	1.40	1.93	4.87	0.11	1.29	0.54	0.417
4	0.35	1.58	0.10	1.40	1.93	4.58	0.16	1.24	0.52	0.417
5	0.45	1.48	0.10	1.40	1.93	4.29	0.21	1.19	0.50	0.417
6	0.55	1.38	0.10	1.40	1.93	4.00	0.25	1.15	0.48	0.417
7	0.65	1.28	0.10	1.40	1.93	3.71	0.30	1.10	0.46	0.417
8	0.75	1.18	0.10	1.40	1.93	3.42	0.34	1.06	0.45	0.417
9	0.85	1.08	0.10	1.40	1.93	3.13	0.39	1.01	0.43	0.417
10	0.95	0.98	0.10	1.40	1.93	2.84	0.43	0.97	0.41	0.417
11	1.05	0.88	0.10	1.40	1.93	2.55	0.48	0.92	0.39	0.417
12	1.15	0.78	0.10	1.40	1.93	2.26	0.52	0.88	0.37	0.417
13	1.25	0.68	0.10	1.40	1.93	1.97	0.57	0.83	0.35	0.417
14	1.35	0.58	0.10	1.40	1.93	1.68	0.62	0.78	0.33	0.417
15	1.45	0.48	0.10	1.40	1.93	1.39	0.66	0.74	0.31	0.417
16	1.55	0.38	0.10	1.40	1.93	1.10	0.71	0.69	0.29	0.417
17	1.65	0.28	0.10	1.40	1.93	0.81	0.75	0.65	0.27	0.417
18	1.75	0.18	0.23	1.40	1.93	0.52	0.80	0.6025	0.25	0.417
							Sum	17.82	7.50	7.50

Table C.14. Calculation of design tensile stresses due to seismic loads in geotextile reinforcements for Test 7-7 using NCMA method

Calculation of Tensile Load in Geotextiles for TEST 7 using NCMA Segmental Retaining Walls Seismic Design Manual

$A=a_{max(table)}/g$	0.39787
k_h (int)	0.419
θ (int)	22.71
k_h (ext)	0.20
θ (ext)	11.25
K_A	0.208
K_{AE} (int)	0.489
$\Delta K_{dyn\ (int)}$	0.28
K_{AE} (ext)	0.315
$\Delta K_{dyn\ (ext)}$	0.11

H	1.93
L	1.45
K_{AH}	0.16
$K_{AEH\ (int)}$	0.37
$\Delta K_{dynH\ (int)}$	0.21
$K_{AEH\ (ext)}$	0.24
$\Delta K_{dynH\ (ext)}$	0.08

Φ	(backfill)	41.00
γ	(backfill)	18.50
Mobilized interface friction angle, δ	(backfill)	41.00
Φ	(reinforced soil)	41.00
γ	(reinforced soil)	18.50

Block depth	0.05
Block unit weight	23.00

W_w	2.22
W_i	49.99
W_r	52.21

W_i'	32.67

R_S	45.38
P_{IR}	6.94
P_{AEH}	6.80
$FS_{sliding}$	3.30
$FS_{overturning}$	3.18

Reinforcement loads

Layer Number	Elevation	Z_{vi}	S_{vi}	L_i	H	$F_{static\ i}$	$F_{inertial\ i}$	$F_{dyn\ i}$	$\Delta F_{seismic}$
1	0.05	1.88	0.10	1.40	1.93	0.55	0.05	0.16	0.21
2	0.15	1.78	0.10	1.40	1.93	0.52	0.05	0.19	0.23
3	0.25	1.68	0.10	1.40	1.93	0.49	0.05	0.21	0.26
4	0.35	1.58	0.10	1.40	1.93	0.46	0.05	0.23	0.28
5	0.45	1.48	0.10	1.40	1.93	0.43	0.05	0.26	0.31
6	0.55	1.38	0.10	1.40	1.93	0.40	0.05	0.28	0.33
7	0.65	1.28	0.10	1.40	1.93	0.37	0.05	0.30	0.35
8	0.75	1.18	0.10	1.40	1.93	0.34	0.05	0.33	0.38
9	0.85	1.08	0.10	1.40	1.93	0.31	0.05	0.35	0.40
10	0.95	0.98	0.10	1.40	1.93	0.28	0.05	0.38	0.42
11	1.05	0.88	0.10	1.40	1.93	0.26	0.05	0.40	0.45
12	1.15	0.78	0.10	1.40	1.93	0.23	0.05	0.42	0.47
13	1.25	0.68	0.10	1.40	1.93	0.20	0.05	0.45	0.49
14	1.35	0.58	0.10	1.40	1.93	0.17	0.05	0.47	0.52
15	1.45	0.48	0.10	1.40	1.93	0.14	0.05	0.49	0.54
16	1.55	0.38	0.10	1.40	1.93	0.11	0.05	0.52	0.56
17	1.65	0.28	0.10	1.40	1.93	0.08	0.05	0.54	0.59
18	1.75	0.18	0.23	1.40	1.93	0.12	0.11	1.30	1.41

Table C.15. Calculation of design tensile stresses due to seismic loads in geotextile reinforcements for Test 8a-9 using FHWA method

Calculation of Tensile Load in Geotextiles for TEST 8 using FHWA Recommendations

$a_{max(table)}/g$	0.36535
A_m	0.396
θ	21.62
K_A	0.208
K_{AE}	0.468
ΔK_{dyn}	0.26

H	1.93
L	1.45
K_{AH}	0.16
K_{AEH}	0.35
ΔK_{dynH}	0.20

Φ	(backfill)	41.00
γ	(backfill)	18.50
Mobilized interface friction angle	(backfill)	41.00
Φ	(reinforced soil)	41.00
γ	(reinforced soil)	18.50

W_w	2.22
W_i	49.99
W_r	52.21

W_i'	32.67
W_A	17.92

Block depth	0.05
Block unit weight	23.00

R_S	45.38
P_{IR}	13.83
P_{AEH}	8.78
FS_{sl}	2.01

P_I	7.10

Tensile stresses in geotextiles

									2001	2009
Layer Number	Elevation	Z_{vi}	S_{vi}	L_i	H	$K\,\sigma_{vi}$	L_a	Le	T_{md}	T_{md}
1	0.05	1.88	0.10	1.40	1.93	5.45	0.02	1.38	0.55	0.395
2	0.15	1.78	0.10	1.40	1.93	5.16	0.07	1.33	0.53	0.395
3	0.25	1.68	0.10	1.40	1.93	4.87	0.11	1.29	0.51	0.395
4	0.35	1.58	0.10	1.40	1.93	4.58	0.16	1.24	0.49	0.395
5	0.45	1.48	0.10	1.40	1.93	4.29	0.21	1.19	0.48	0.395
6	0.55	1.38	0.10	1.40	1.93	4.00	0.25	1.15	0.46	0.395
7	0.65	1.28	0.10	1.40	1.93	3.71	0.30	1.10	0.44	0.395
8	0.75	1.18	0.10	1.40	1.93	3.42	0.34	1.06	0.42	0.395
9	0.85	1.08	0.10	1.40	1.93	3.13	0.39	1.01	0.40	0.395
10	0.95	0.98	0.10	1.40	1.93	2.84	0.43	0.97	0.39	0.395
11	1.05	0.88	0.10	1.40	1.93	2.55	0.48	0.92	0.37	0.395
12	1.15	0.78	0.10	1.40	1.93	2.26	0.52	0.88	0.35	0.395
13	1.25	0.68	0.10	1.40	1.93	1.97	0.57	0.83	0.33	0.395
14	1.35	0.58	0.10	1.40	1.93	1.68	0.62	0.78	0.31	0.395
15	1.45	0.48	0.10	1.40	1.93	1.39	0.66	0.74	0.29	0.395
16	1.55	0.38	0.10	1.40	1.93	1.10	0.71	0.69	0.28	0.395
17	1.65	0.28	0.10	1.40	1.93	0.81	0.75	0.65	0.26	0.395
18	1.75	0.18	0.23	1.40	1.93	0.52	0.80	0.6025	0.24	0.395
							Sum	17.82	7.10	7.10

Table C.16. Calculation of design tensile stresses due to seismic loads in geotextile reinforcements for Test 8a-9 using NCMA method

Calculation of Tensile Load in Geotextiles for TEST 8 using NCMA Segmental Retaining Walls Seismic Design Manual

$A=a_{max(table)}/g$	0.36535
k_h (int)	0.396
θ (int)	21.62
k_h (ext)	0.18
θ (ext)	10.35
K_A	0.208
K_{AE} (int)	0.468
$\Delta K_{dyn\ (int)}$	0.26
K_{AE} (ext)	0.305
$\Delta K_{dyn\ (ext)}$	0.10

H	1.93
L	1.45
K_{AH}	0.16
$K_{AEH\ (int)}$	0.35
$\Delta K_{dynH\ (int)}$	0.20
$K_{AEH\ (ext)}$	0.23
$\Delta K_{dynH\ (ext)}$	0.07

Φ	(backfill)	41.00
γ	(backfill)	18.50
Mobilized interface friction angle, δ	(backfill)	41.00
Φ	(reinforced soil)	41.00
γ	(reinforced soil)	18.50

Block depth	0.05
Block unit weight	23.00

W_w	2.22
W_i	49.99
W_r	52.21

W_i'	32.67

R_S	45.38
P_{IR}	6.37
P_{AEH}	6.67
$FS_{sliding}$	3.48
$FS_{overturning}$	3.38

Reinforcement loads

Layer Number	Elevation	Z_{vi}	S_{vi}	L_i	H	$F_{static\ i}$	$F_{inertial\ i}$	$F_{dyn\ i}$	$\Delta F_{seismic}$
1	0.05	1.88	0.10	1.40	1.93	0.55	0.05	0.15	0.20
2	0.15	1.78	0.10	1.40	1.93	0.52	0.05	0.17	0.22
3	0.25	1.68	0.10	1.40	1.93	0.49	0.05	0.19	0.24
4	0.35	1.58	0.10	1.40	1.93	0.46	0.05	0.22	0.26
5	0.45	1.48	0.10	1.40	1.93	0.43	0.05	0.24	0.28
6	0.55	1.38	0.10	1.40	1.93	0.40	0.05	0.26	0.31
7	0.65	1.28	0.10	1.40	1.93	0.37	0.05	0.28	0.33
8	0.75	1.18	0.10	1.40	1.93	0.34	0.05	0.30	0.35
9	0.85	1.08	0.10	1.40	1.93	0.31	0.05	0.33	0.37
10	0.95	0.98	0.10	1.40	1.93	0.28	0.05	0.35	0.39
11	1.05	0.88	0.10	1.40	1.93	0.26	0.05	0.37	0.41
12	1.15	0.78	0.10	1.40	1.93	0.23	0.05	0.39	0.44
13	1.25	0.68	0.10	1.40	1.93	0.20	0.05	0.41	0.46
14	1.35	0.58	0.10	1.40	1.93	0.17	0.05	0.43	0.48
15	1.45	0.48	0.10	1.40	1.93	0.14	0.05	0.46	0.50
16	1.55	0.38	0.10	1.40	1.93	0.11	0.05	0.48	0.52
17	1.65	0.28	0.10	1.40	1.93	0.08	0.05	0.50	0.54
18	1.75	0.18	0.23	1.40	1.93	0.12	0.10	1.20	1.30

REFERENCES

ANCO Engineers, 2010, *Typical Sample Training Material*, http://www. ancoengineers.com/wpimages/TYPICAL TRAINING MATERIAL.pdf.

Bathurst, R. J. and K. Hatami, 1998, "Seismic Response Analysis of a Geosynthetic Reinforced Soil Retaining Wall", *Geosynthetics International*, 5(1&2), pp. 127-166.

Balluff Data Sheet, *BTL6-A_10-M_-A1-S115 Micropulse AT Transducer in Round Profile Housing*, No. 823 110, pp. 3.

Bathurst, R. J., 1998, *Segmental Retaining Walls Seismic Design Manual*, National Concrete Masonry Association (NCMA), Herndon, Virginia, USA.

Bathurst, R. J., K. Hatami, and M. C. Alfaro, 2002, "Geosynthetic-Reinforced Soil Walls and Slopes – Seismic Aspects", in S. K. Shukla (ed.), *Geosynthetics and Their Applications*, pp. 327-392, Thomas Telford.

Bathurst, R. J. and M. C. Alfaro, 1996, "Review of Seismic Design, Analysis and Performance of Geosynthetic Reinforced Walls, Slopes and Embankments", *Third International Symposium on Earth Reinforcement*, 12-14 November 1996, Fukuoka, Kyushu, Japan.

Bathurst, R. J. and Z. Cai, 1995, "Pseudo-Static Seismic Analysis of Geosynthetic Reinforced Segmental Retaining Walls", *Geosynthetics International*, 2, No. 5, pp. 787-830.

Bathurst, R. J., Z. Cai, and M. J. Pelletier, 1996, "Seismic Design and Performance of Geosynthetic Reinforced Segmental Retaining Walls", *Proceedings of the 10th Annual Symposium of the Vancouver Geotechnical Society*, Vancouver, British Columbia, Canada.

Berg, R. R., B. R. Christopher, and N. C. Samtani, 2009, *Design of Mechanically Stabilized Earth Walls and Reinforced Soil Slopes – Volume I*, U.S. Department of Transportation, Federal Highway Administration, Record No. FHWA-NHI-10-024 FHWA GEC 011-Vol I, November.

Boğaziçi University Department of Earthquake Engineering, 2009, *Shaking Table Laboratory*, http://www.koeri.boun.edu.tr/depremmuh/shakingtable/shakingtable.htm

El-Emam, M. and R. J. Bathurst, 2004, "Experimental Design, Instrumentation and Interpretation of Reinforced Soil Wall Response Using a Shaking Table", *International Journal of Physical Modelling in Geotechnics*, 4(4), pp. 13-32.

El-Emam, M. and R. J. Bathurst, 2005, "Facing Contribution to Seismic Response of Reduced-Scale Reinforced Soil Walls", *Geosynthetics International*, 12(5), pp. 215-238.

El-Emam, M. and R. J. Bathurst, 2007, "Influence of Reinforcement Parameters on the Seismic Response of Reduced-Scale Reinforced Soil Retaining Walls", *Geotextiles and Geomembranes*, Volume 25, Issue 1, pp. 33-49, February.

El-Emam, M., R. J. Bathurst, and K. Hatami, 2004, "Numerical Modeling of Reinforced Soil Retaining Walls Subjected to Base Acceleration", *13th World Conference on Earthquake Engineering*, Vancouver BC, 15.

Elias, V., B. R. Christopher, and R. R. Berg, 2001, *Mechanically Stabilized Earth Walls and Reinforced Soil Slopes, Design and Construction Guidelines*, U.S. Department of Transportation, Federal Highway Administration, Publication No. FHWA-NHI-00-043, March.

Enünlü, A. K., 2007, *Investigation of Dynamic Behavior of Geosynthetic Reinforced Soil Retaining Structures under Earthquake Loads*, Ph.D. Thesis, Boğaziçi University.

Fujii, T., J. Izawa, J. Kuwano, M. Ishihara, and J. Nakane, 2006, "Prediction of Deformation of Retaining Walls of Geosynthetic-Reinforced Soil under Large Earthquakes", *8th International Conference on Geosynthetics,* 18-22 September 2006, Yokohama, Japan.

Güler, E. and A. K. Enünlü, 2009, "Investigation of Dynamic Behavior of Geosynthetic Reinforced Soil Retaining Structures under Earthquake Loads", *Bull Earthquake Eng.*, 7, pp. 737-777.

Helwany, S. M. B., M. Budhu and D. McCallen, 2001, "Seismic Analysis of Segmental Retaining Walls. I: Model Verification", *Journal of Geotechnical and Geoenvironmetal Engineering*, pp. 741-748, September.

Iai, S., 1989, *Similitude for Shaking Table Tests on Soil-Structure-Fluid Model in 1g Gravitational Field*, Report of the Port and Harbour Research Institute Vol. 27 No. 3 Sept. 1988.

Kadayıfçı, A., 2005, *Influence of Various Parameters on Seismic-Induced Permanent Displacement of Geosynthetic Reinforced Segmental Retaining Walls*, M.S. Thesis, Boğaziçi University.

Koseki, J., R. J. Bathurst, E. Güler, J. Kuwano, and M Maugeri, 2006, "Seismic Stability of Reinforced Soil Walls", *8th International Conference on Geosynthetics,* 18-22 September 2006, Yokohama, Japan.

Latha, G. M. and A. M. Krishna, 2008, "Seismic Response of Reinforced Soil Retaining Wall Models: Influence of Backfill Relative Density", *Geotextiles and Geomembranes*, Volume 26, pp. 335-349.

Lee, K. Z. Z., N. Y. Chang, and H. Y. Ko, 2010, "Numerical Simulation of Geosynthetic-Reinforced Soil Walls under Seismic Shaking", *Geotextiles and Geomembranes*, Volume 28, pp. 317-334.

Ling, H. I., H. Liu, V. Kaliakin, and D. Leshchinsky, 2004, “Analyzing Dynamic Behavior of Geosynthetic-Reinforced Soil Retaining Walls”, *Journal of Engineering Mechanics*, ASCE, 130(8), pp. 911-476.

Ling, H. I., H. Liu, and Y. Mohri, 2005a, “Parametric Studies on the Behavior of Reinforced Soil Retaining Walls under Earthquake Loading”, *Journal of Engineering Mechanics*, ASCE, 131(10), pp. 1056-1065.

Ling, H. I., Y. Mohri, D. Leshchinsky, C. Burke, K. Matsushima, and H. Liu, 2005b, “Large-Scale Shaking Table Tests on Modular-Block Reinforced Soil Retaining Walls”, *Journal of Geotechnical and Geoenvironmental Engineering*, ASCE, 131(4), pp. 465-476.

Ling, H. I., S. Yang, D. Leshchinsky, H. Liu, and C. Burke, 2010, “Finite-Element Simulations of Full-Scale Modular-Block Reinforced Soil Retaining Walls under Earthquake Loading”, *Journal of Engineering Mechanics*, ASCE, 136(5), pp. 653-661.

Pelletier, M. J., 1996, *Investigation of the Seismic Resistance of Reinforced Segmental Walls Using Small-Scale Shaking Table Testing*, MEng Thesis, Royal Military College of Canada.

Schmertmann, J. H., 1978, *Guidelines for Cone Penetration Test, Performance and Design*, U.S. Department of Transportation, Federal Highway Administration, Report No. FHWA-TS-78-209.

Seed, H. B. and R. V. Whitman, 1970, “Design of Earth Retaining Structures for Dynamic Loads”, *Proceedings of the ASCE Specialty Conference: Lateral Stresses in the Ground and Design of Earth Retaining Structures*, pp. 103-147, Ithaca, New York.

Segrestin, P. and M. J. Bastick, 1988, “Seismic Design of Reinforced Earth Retaining Walls – The Contribution of Finite Element Analysis”, *Theory and Practice of Earth Reinforcement: Proceedings of the International Geotechnical Symposium on Theory* *and Practice of Earth Reinforcement, IS-Kyushu '88*, Fukuoka, Japan, pp. 577-582, Balkema, Rotterdam.

Tamura, Y., 2006, "Lessons Learnt from the Construction of Geosynthetic-Reinforced Soil Retaining Walls with Full-Height Rigid Facing for the Last 10 Years", *8th International Conference on Geosynthetics*, 18-22 September 2006, Yokohama, Japan.

Watanabe, K., Y. Munaf, J. Koseki, M. Tateyama, and K. Kojima, 2003, "Behaviors of several types of model retaining walls subjected to irregular excitation", *Soils and Foundations*, 43(5), 13-27.

Wolfe, W. E., K. L. Lee, D. Rea, and A. M. Yourman, 1978, "The Effect of Vertical Motion on the Seismic Stability of Reinforced Earth Walls", *Proceedings of the ASCE Symposium on Earth Reinforcement*, Pittsburgh, Pennsylvania, USA, pp. 856-879.